BuMines OFR 96-83

A minerals research contract report
DECEMBER 1982

A STUDY OF EXPLOSION-PROOF ENCLOSURES

Contract H0377052
Southwest Research Institute

Bureau of Mines Open File Report 96-83

BUREAU OF MINES
UNITED STATES DEPARTMENT OF THE INTERIOR

The views and conclusions contained in this document are those of the authors and should not be interpreted as necessarily representing the official policies or recommendations of the Interior Department's Bureau of Mines or of the U. S. Government.

FOREWORD

This report was prepared by Southwest Research Institute, San Antonio, Texas, under USBM Contract Number H0377052. The contract was initiated under the Health and Safety Technology Program. It was administered under the technical direction of the Pittsburgh Research Center with Mr. Lawrence W. Scott acting as Technical Project Officer. Mr. Alan G. Bolton, Jr., was the contract administrator for the Bureau of Mines. This report is a summary of the work completed on this contract during the period September 1977 to October 1982. This report was submitted by the author on December 3, 1982.

The authors gratefully acknowledge the leadership and guidance given to the project by Messrs. Lawrence W. Scott and Roger L. King of the USBM. Special thanks are given to Mr. Kurt Thistlethwaite for conducting the enclosure tests and to Mr. Stephen E. Stewart, Mrs. Cathy Dean, Mr. Victor Hernandez, and Mrs. Rosemary Rivas for their valuable assistance in the preparation of this report.

TABLE OF CONTENTS

TABLE OF CONTENTS (Cont'd.)

TABLE OF CONTENTS (Cont'd.)

TABLE OF CONTENTS (Cont'd.)

LIST OF ILLUSTRATIONS

LIST OF ILLUSTRATIONS (Cont'd.)

LIST OF ILLUSTRATIONS (Cont'd.)

LIST OF ILLUSTRATIONS (Cont'd.)

LIST OF ILLUSTRATIONS (Cont'd.)

LIST OF ILLUSTRATIONS (Cont'd.)

LIST OF ILLUSTRATIONS (Cont'd.)

LIST OF ILLUSTRATIONS (Cont'd.)

LIST OF ILLUSTRATIONS (Cont'd.)

LIST OF ILLUSTRATIONS (Cont'd.)

LIST OF ILLUSTRATIONS (Cont'd.)

LIST OF TABLES

LIST OF TABLES (Cont'd.)

1.0 EXECUTIVE SUMMARY

Work documented in this report was performed by Southwest Research Institute (SwRI) for the U. S. Bureau of Mines (USBM) under Contract Number H0377052. The contract was initiated under the Health and Safety Technology Program and covered the time period from September 1977 through December 1982.

Initially the purpose of this contract research was to determine the level of safety in enclosures which had been certified as explosion proof (XP) under Schedule 2G [1]. Results and discoveries in the initial work led to an expansion of the contract to cover five major areas of research. These are:

- Selection of the computational method
- Margins of safety in XP enclosures
- Weld quality in XP enclosures
- Reliability of XP enclosures with windows and lenses
- Performance tests for XP enclosures

Several tasks were performed in each of these major areas. Key findings and conclusions are:

Selection of the Computational Method

- The ANSYS finite element computer program has all of the features required for the analysis of XP enclosures, and it was chosen for the analyses presented in this report.

- MARC has most of the features required for the analysis of XP enclosures, but lacks steady-state heat transfer in shell elements (at the time of the survey) and was judged not to be as user friendly as ANSYS.

- ADINA has many of the features required for the analyses performed, but lacks thin shell elements and pre- and post-processors.

Margins of Safety in XP Enclosures

- Dynamic effects, produced by explosions of methane and air, are insignificant in most enclosures. Dynamic effects may be important if unusually high pressures occur (pressure piling) or if the enclosure is unusually large.

- There are wide variations in the margins of safety for different enclosures. One enclosure had a factor of safety less than one.

- None of the enclosures tested ruptured at an internal pressure of 150 psig.

- Weld joints in one enclosure partially failed at pressures as low as 60 psig, and permanent deformations of 0.31 in./ft were

produced in the enclosure by a pressure of 150 psig. These are substantially larger than the allowable permanent deformation of 0.040 in./ft permitted by MSHA in the Explosion Test.

- At locations other than the cover seal, only one enclosure leaked during the hydrostatic test at pressures below 150 psig. A small leak occurred at 140 psig in the first hydrostatic test of one luminaire. The leak was at the sealing surface of a window to the enclosure body.

Weld Quality in XP Enclosures

- Small manufacturers do not have well-documented welding practice.
- Large manufacturers have welding procedures and most adhere, at least partly, to AWS welding codes.
- Joint design is similar for all of the manufacturers, but knowledge of joint efficiency was poor.

Reliability of Enclosures with Windows

- Enclosure resonances fall within the range of vibrations (5 Hz - 10,000 Hz) measured on typical mining machines.
- Amplification factors (ratio of acceleration amplitude measured on the enclosure to the input amplitude) were as high as 23 on some enclosures. These amplification factors were based on accelerations measured normal to window surfaces.
- High local stresses and moderately high bending stresses are induced in windows and lenses by the Schedule 2G Impact Test; however, impact energies in the mine far exceed those produced by the impact test, and so all windows should be protected by guards.
- Low stresses are produced in free windows and lenses by the Schedule 2G Thermal Shock Test. Much higher stresses are introduced if the entire enclosure is heated to 150°C, and the window is then quenched from one side.
- Heat and UV light degrade polycarbonate windows and adhesive materials that are used in some XP enclosures. Accelerated aging tests are needed and were developed for the qualification of such materials for use underground.
- A more suitable material than polycarbonate for XP enclosure windows and lenses may be polycarylate, a plastic with good heat and UV resistance.

Performance Tests and Acceptance Criteria

- A Ruggedness Test should be based on the possibility of impact by rock falls and mining equipment such as a shuttle car.

- The maximum potential energy which can be generated by rock fall is very high, and it is impractical to design for such an energy level.

- Protection from 60% of roof falls requires that exposed surfaces be designed for a kinetic energy of 3700 ft-lb/ft^2, based on data from past roof falls.

- Battery box covers should be designed to withstand the proposed Ruggedness Test unless future work shows that the exposure to roof falls of battery operated equipment is less than that of the mining machine.

The key findings given above and other results which are documented in the report led to the following recommendations:

- A design guide should be prepared for XP enclosures to unify the design effort of enclosure manufacturers.

- A structural performance test, such as the one described in Appendix E, should be used by MSHA in the certification of enclosures.

- MSHA should require that XP enclosures be fabricated according to an American Welding Society (AWS) Standard. AWS D14.4 is recommended.

- Materials, such as polycarbonates and adhesives, which are known to be degraded by heat and UV radiation should be approved for use in XP enclosures only after appropriate environmental testing. Recommended accelerated aging tests, which are designed to represent the mining environment, are given in Appendix K.

- Vibration tests should be performed on selected enclosures to determine how well they withstand, over their expected service life, vibration levels on typical mining machines.

- Before a Ruggedness Test is finalized, additional work is recommended to relate, if possible, damage to mining equipment produced by rock fall to the severity of the rock fall accident.

2.0 INTRODUCTION

2.1 Background and Overview

For the past several years the U. S. Bureau of Mines (USBM) has been preparing to update Schedule 2G [1]. In support of this effort the Bureau has funded contract research to provide information and data which are necessary for such a revision. The work reported herein, performed under USBM Contract No. H077052, was awarded as part of this overall research effort.

The purpose of the initial research performed under this contract was to determine the margins of safety in explosion-proof (XP) enclosures, which were designed and certified according to the current schedule. Results from this work provide baseline data on the current schedule from which a new schedule can be formulated. The aim of the Bureau is to provide equal or greater levels of safety in the revised schedule.

Margins of safety in XP enclosures were evaluated by a combination of analysis and testing. An analytical program was first selected based on a review of available analytical methods. Section 3.0 describes the survey which led to the selection of the finite-element computer program, ANSYS, as the primary analytical tool.

The analyses and hydrostatic tests performed on the enclosures are documented in Section 4.0. Both ANSYS and closed-form solutions were used to calculate maximum strains and stresses in the enclosures. These analyses treated elastic and plastic material behavior, weld joint strength, bolt deformations, and both static and dynamic internal pressure loads. Corresponding strains and displacements were measured during the hydrostatic tests for comparison with analytical predictions. Safety factors, computed as described in Section 5.0, were based on both the analyses and the experiments.

As a result of the work on safety factors, other areas were discovered which required aditional research. For example, the study of dynamic loads produced by internal explosions of methane and air led to a literature survey on pressure piling which is reported in Appendix D. Weld failures which occurred during hydrostatic tests revealed the need for an evaluation of weld quality in the fabrication of XP enclosures. A survey was conducted to evaluate the welding practices of six enclosure manufacturers. This survey is described in Section 6.0, and notes on the welding code recommended for the fabrication of XP enclosures are included as Appendix I.

The reliability of enclosures with windows was also evaluated as part of this study. These evaluations, reported in Section 7.0, addressed the effects of vibrations on windows or lenses in enclosures; the suitability of the Schedule 2G Impact Test and Thermal Shock Test for the qualification of enclosure windows; and the degrading effects of the mine environment on adhesives and polycarbonate materials that are used in explosion-proof luminaires.

Finally, the Mine Safety and Health Administration (MSHA) and the USBM plan to base future certification of enclosures upon a series of performance tests similar to the Explosion Test now conducted. Consequently, SwRI was asked to prepare performance tests for strength and ruggedness and to propose acceptance criteria for battery box covers. Results of these tasks are documented in Section 8.0. Recommendations based on the studies performed under this contract are given in Section 9.0.

2.2 Relationship to Other USBM Contract Research

Other investigators are performing or have performed contract research for the USBM which is related to the work reported herein. The reference list includes citations to the work which could be applied in this study. One contract in particular (USBM Contract H0387009 [2]) has ongoing work which relates directly to this research. This work is also being conducted by Southwest Research Institute, and part of it represents continuations of studies documented on this report.

Specifically, Contract H0387009 includes the following tasks which relate to this work.

Accelerated Aging of Polycarbonates and Adhesives - This task follows the test plan, documented in Appendix K, for the accelerated aging of enclosure window materials.

Quality Assurance for XP Enclosures - The need for this work was discovered through the survey of weld quality in XP enclosures and the aging problems associated with some window materials in XP luminaires.

Thermal Analysis of Windows in XP Enclosures - This work is a direct extension of the work reported in Section 7.4. Finite-element solutions cover more realistic window and enclosure geometries.

Preparation of a Design Guide for XP Enclosures - This work, initiated under Contract H0377052 (under which the work reported herein was performed), was transferred to Contract H0387009 so that results from the accelerated aging tests and the thermal analyses could be included in its development. Much of the information in the guide will be taken from the material presented in this report.

Preliminary results and conclusions from the above work are cited in appropriate sections of this document.

3.0 SELECTION OF COMPUTATIONAL METHOD

3.1 Computational Requirements

Guidelines for selection of a computational method were based primarily upon requirements for static and dynamic analyses of enclosures. Additionally, the availability of the program to the USBM and to the mining industry, ease of program use, and future requirements that may arise at the USBM (such as the need to predict temperature distributions throughout the enclosures) were considered.

The following analytical requirements were identified:

(1) Compute deflections, strains, and stresses in four different enclosures for static internal pressure.

(2) Compute deflections and strains beyond the elastic limit of the material.

(3) Compute the size of gaps between cover and flange which will occur in the enclosures when loaded.

(4) Compute the response of enclosures for dynamic pressures which vary with time.

To meet these requirements, the code selected must have certain features which can be broadly classified under the categories of Modeling Capabilities, Response Types, Loading, and Input/Output.

Modeling Capabilities. To accurately and efficiently describe the geometry of enclosures, the code selected must have a library of finite elements which includes general shells, three-dimensional beams, three-dimensional solids, and gap elements. For axisymmetric enclosures, axisymmetric shell and solid elements would greatly improve modeling efficiency. In addition, for elastic-plastic analyses, substructuring can reduce the solution cost because parts of the structure which remain elastic can be identified and partitioned from the remainder of the structure. Friction will occur between the cover and the flange and might be important for some types of enclosures. A friction element in the finite element library would permit the effect of friction to be investigated.

Response Types. For the analysis of enclosures, it is important to consider linear and nonlinear static, as well as linear and nonlinear transient, types of analyses. Nonlinearities are those produced by material plasticity and changes in geometry associated with gaps which may occur in the structure or large deflections in general. However, before these analyses are conducted, a model analysis should be performed to calculate the natural frequencies and mode shapes of the structure. This is necessary to allow the analyst to determine which, if any, modes of the structure will probably be excited.

In addition, to meet anticipated future needs of the government and mining industry for the design and qualification of Schedule 2G enclosures, the method should be able to calculate transient temperatures of the enclosures and perform transient thermal stress analyses for these temperatures.

Loading: The loadings can be classified on the basis of whether the analysis is static or dynamic. For both the static and dynamic cases, the program should have the capability of applying concentrated nodal loads or distributed pressures over the faces of the elements. The program should also be able to calculate the static deformations and stresses if the steady-state temperature distribution is specified.

The dynamic analysis should have the capability of applying time dependent concentrated and distributed spatially varying loadings. A thermal transient analysis should be able to be superimposed on the dynamic analysis if the temperature time history is known.

Input/Output: It is extremely important for the program to have the capability for nodal and element generation. This greatly simplifies the input since repeated nodal locations and elements are formulated from master sets. A computer graphic capability is also indispensable because it is very difficult, if not impossible, to "debug" the finite element input without being able to view the structure. The ability to view the deformed shapes and resultant stress contour plots is an invaluable aid in reviewing and interpreting the numerical results. These plots allow the user to quickly determine if gaps are developed in the structure and to identify the location and intensity of stress concentrations.

The restart capability is also an important feature in nonlinear problems. It allows the user to conduct an analysis for a certain time duration, to look at the results, and restart the program from the last calculated time step. The capability also allows for solutions which may have bifurcations.

3.2 Computer Code Survey and Evaluation

In our selection process, numerous finite element computer programs were scanned to see if their features matched our requirements. The choice was quickly narrowed to five general purpose programs which have most of the features required. These were:

ADINA
ANSYS
MARC
NASTRAN
NONSAP

NASTRAN was not selected because it lacked gap elements, and current government versions lack provisions for metal plasticity. Letters were written to the developers of the four other programs to obtain up-to-date information on program features and to establish the availability of the program for installation at government facilities.

The inquiry concerning NONSAP was directed to Professor Wilson, University of California, Berkeley, who developed the program in cooperation with Dr. Bathe, at MIT. Professor Wilson indicated that development work on NONSAP was stopped in 1973 and that the program has been superseded by ADINA, which is under development by Dr. Bathe at MIT. Therefore, at this point, NONSAP was dropped from further consideration.

Of the remaining programs, all are currently being maintained and can be implemented on a government computer or accessed on the CDC Cybernet system. Table 3.1, which summarizes program features that are important for the analysis of Schedule 2G enclosures, was compiled for these three remaining computer codes. Information was taken principally from replies by the program developers and from the User's Manuals for the programs. Based upon the information of Table 3.1 and upon our general knowledge of the programs, the following recommendations regarding their use for the analysis of Schedule 2G enclosures were made:

ADINA. This program was not recommended for the analysis of the Schedule 2G enclosures. ADINA seems to be more of a research tool and requires a great deal of sophistication on the part of the user. It also does not have thin shell elements. These would have to be formulated from the three-dimensional solid element, and the loss of accuracy is uncertain. It would be impractical to use more than one element through the thickness.

Processors for geometry and stress contour plotting are not available with the ADINA program and must be obtained elsewhere. This would be an expensive capability to develop.

MARC. Although MARC had most of the capabilities required for a complete analysis of Schedule 2G enclosures, it does not have shell elements for steady-state or transient heat transfer. For these analysis types, it was found that the three-dimensional solid must be used, which would significantly increase the analysis costs, both in engineering manpower and computation times.

Also, from a purely subjective point of view, MARC does not appear to be user-oriented. Program documentation indicates that the analyst must have a solid background in theoretical mechanics and finite element methods.

ANSYS. The general purpose finite element program ANSYS was chosen for use on this project. Table 3.1 shows that ANSYS has essentially all of the features necessary for the analysis. The only capability which ANSYS lacks is an elastic-plastic quadrilateral shell element. Dr. Gabriel De Salvo of Swanson Analysis Systems, Inc., indicated that there is no inherent problem in adding this element type to the ANSYS library; however, Dr. De Salvo expressed concern about the accuracy of the quadrilateral plastic element [3].

ANSYS has been in use at SwRI for over seven years. During this time we have been impressed by the program's capability to solve a wide range of problems. Program documentation is extensive and easy to read.

TABLE 3.1. PROGRAM CAPABILITIES

	ELASTIC		SMALL DEFORMATION ELASTIC-PLASTIC		LARGE DEFORMATION ELASTIC-PLASTIC		HEAT TRANSFER	
	Static	Dynamic	Static	Dynamic	Static	Dynamic	Steady-State	Transient
MODELING CAPABILITIES								
Plane Elements								
△ Shell	1,2*	1,2	1,2	1,2	1,2	1,2	1	1
▭ Shell	1,2	1,2	2	2	2	2		
Curved Elements								
△ Shell	2	2	2	2	2	2		
▭ Shell	2	2	2	2	2	2		
Solid								
(Indicate Num. No. of Nodes) 1,2	20	20	20	20	20	20	20	20
3	21	21	21	21	21	21	21	21
Other								
Gap	1,2,3	1,2,3	1,2,3	1,2,3	1,2,3	1,2,3	--	--
Friction	1,2	1,2	1,2	1,2	1,2	1,2	--	--
Substructuring	1	1	na	na	na	na	1	1
RESPONSE TYPES								
Harmonic	--	1,3	--	--	--	--	--	--
Linear Transient	--	1,2,3	--	--	--	--	--	1,2,3
Non-Linear Transient	--	--	--	1,2,3	--	1,2,3	--	1,2,3
Eigenvalues and Eigenvectors	--	1,2,3	--	--	--	--	--	--
LOADING								
Static								
Concentrated	1,2,3	--	1,2,3	--	1,2,3	--	1,2,3	--
Distributed	1,2,3	--	1,2,3	--	1,2,3	--	1,2,3	--
Thermal	1,2,3	--	1,2,3	--	1,2,3	--	--	--
Dynamic								
Concentrated	--	1,2,3	--	1,2,3	--	1,2,3	--	1,2,3
Distributed	--	1,2,3	--	1,2,3	--	1,2,3	--	1,2,3
Thermal Transient	--	1,2,3	--	1,2,3	--	1,2,3	--	--
Harmonic	--	1,3	--	1,3	--	1,3	--	--
Time Dependent	--	1,2,3	--	1,2,3	--	1,2,3	--	1,2,3
INPUT/OUTPUT								
Node And Element Generation	1,2,3	1,2,3	1,2,3	1,2,3	1,2,3	1,2,3	1,2,3	1,2,3
Geometry Plotting	1,2	1,2	1,2	1,2	1,2	1,2	1,2	1,2
Contour Plotting	1,2	1,2	1,2	1,2	1,2	1,2	1,2	1,2
Time Dependent Plotting	na	1,2	na	1,2	na	1,2	na	1,2
File Manipulation	1,2,3	1,2,3	1,2,3	1,2,3	1,2,3	1,2,3	1,2,3	1,2,3
Restart	1,2,3	1,2,3	1,2,3	1,2,3	1,2,3	1,2,3	1,2,3	1,2,3

*ADINA has no conventional shell finite elements. It has a three-dimensional solid element which can be used as a thick shell.

ANSYS = 1
MARC = 2
ADINA = 3

ANSYS has a User's Manual, an Examples Manual, Verification Manual, and a recently published Theoretical Manual. Institute analysts have also found the staff at Swanson Analysis Systems, Inc., to be very cooperative in answering any questions about the program.

3.3 General Procedure for Analysis with ANSYS

The ANSYS program provides an efficient solution to enclosure analysis problems. The computer solution is generally accomplished with the following steps:

1. Select the type of analysis to be performed (elastic, elastic-plastic, dynamic or thermal).

2. Model the problem in terms of the program approximations (grid geometry, element type specification, element property specification, etc.).

3. Prepare the input for the computer program.

4. Check the input data.

5. Run the data with the program to yield a solution.

6. Interpret the results from this solution.

7. Modify the structure and/or model until an acceptable solution is obtained.

The selection of the type of analysis to be performed will be clear from the type of information required about the enclosure. Vibrational response requires a dynamic nodal analysis, thermal shock analysis requires a transient thermal analysis, and so on.

For each type of analysis, different types of modeling elements must be selected. ANSYS has a large number of element types available, allowing flexibility in the modeling of the structure. The program has a very large capacity, so that the model may include great detail. The program also is efficient for small problems, so that a series of simple models may be run at little cost. A single model may be used for the heat transfer analysis, the stress analysis, and the dynamic analyses, with only a change in the element type. Once the model of the structure has been defined, utilization of ANSYS's multiple level element and nodal point generation subroutines can reduce the amount of data required to define the enclosure (for the program) and the time required to prepare the input data.

In all enclosure analyses the data was checked before submitting it for a solution. This was done in ANSYS by a geometry plot run, which produced plots of the geometry or sections of the geometry, as viewed from a specified orientation. Nodal points and elements were numbered in these geometry plots. The geometry plot was generally made as soon as the elements and nodal points were defined. This report contains several of these geometry plots as figures.

After the entire input data deck was completed, a check run was generally made. This run reads all input data, checks formats on the cards, produces additional geometry plots if desired, checks for the completeness of the materials data, checks for inconsistencies in the element definitions, and tabulates the computer resources required for the final solution. A successful check run usually assures a successful solution for the actual analysis run.

The computer solution from an ANSYS finite element analysis usually resulted in a large quantity of printout, in the form of tables of displacements and/or stresses. This is not, generally, a convenient format for interpretation so graphical displays of the output results were usually obtained. ANSYS output graphics included stress and temperature contours, distorted shapes, amplitude-frequency plots, response spectrum plots, and force, displacement, velocity or acceleration versus time plots.

4.0 ANALYSIS AND TESTING OF SCHEDULE 2G ENCLOSURES

4.1 Enclosure I Analysis and Testing

4.1.1 Two-Dimensional Elastic Analyses

Two-dimensional calculations were performed for the larger of the two box-like enclosures provided to SwRI by USBM. This enclosure, identified as Enclosure I, is shown in Figure 4.1. The purpose of the two-dimensional analysis was to check stresses which can be expected at known pressure levels and to study deflections in the flange to which the cover is bolted.

4.1.1.1 Finite Element Models

Four two-dimensional finite element models were generated. These four models were created to study the behavior of the flange-side shell and side shell-bottom weld connections and the bolted connection between the cover and the flange. The strength of Schedule 2G enclosures is very dependent upon the strength of the welded and bolted connections, and these models were used to evaluate modeling approaches for these joints and to approximate stresses and deflections in the enclosure. Each of the four models is described below, and they are shown in Figures 4.2-4.5.

Case I (Figure 4.2):

- Elastic flange with area below weld modeled using solid elements
- Flange rigidly connected to cover at two attachment points
- Side and bottom shells attached using shell elements

Case II (Figure 4.3):

- Elastic flange with area below modeled using shell elements
- Flange connected to cover with bolt and one attachment point
- Side and bottom shells attached using one solid element for weld

Case III (Figure 4.4):

- Elastic flange with area below weld modeled using shell elements
- Flange connected to cover with bolt and one attachment point
- Side and bottom shells attached using refined solid element model for weld and adjacent shells

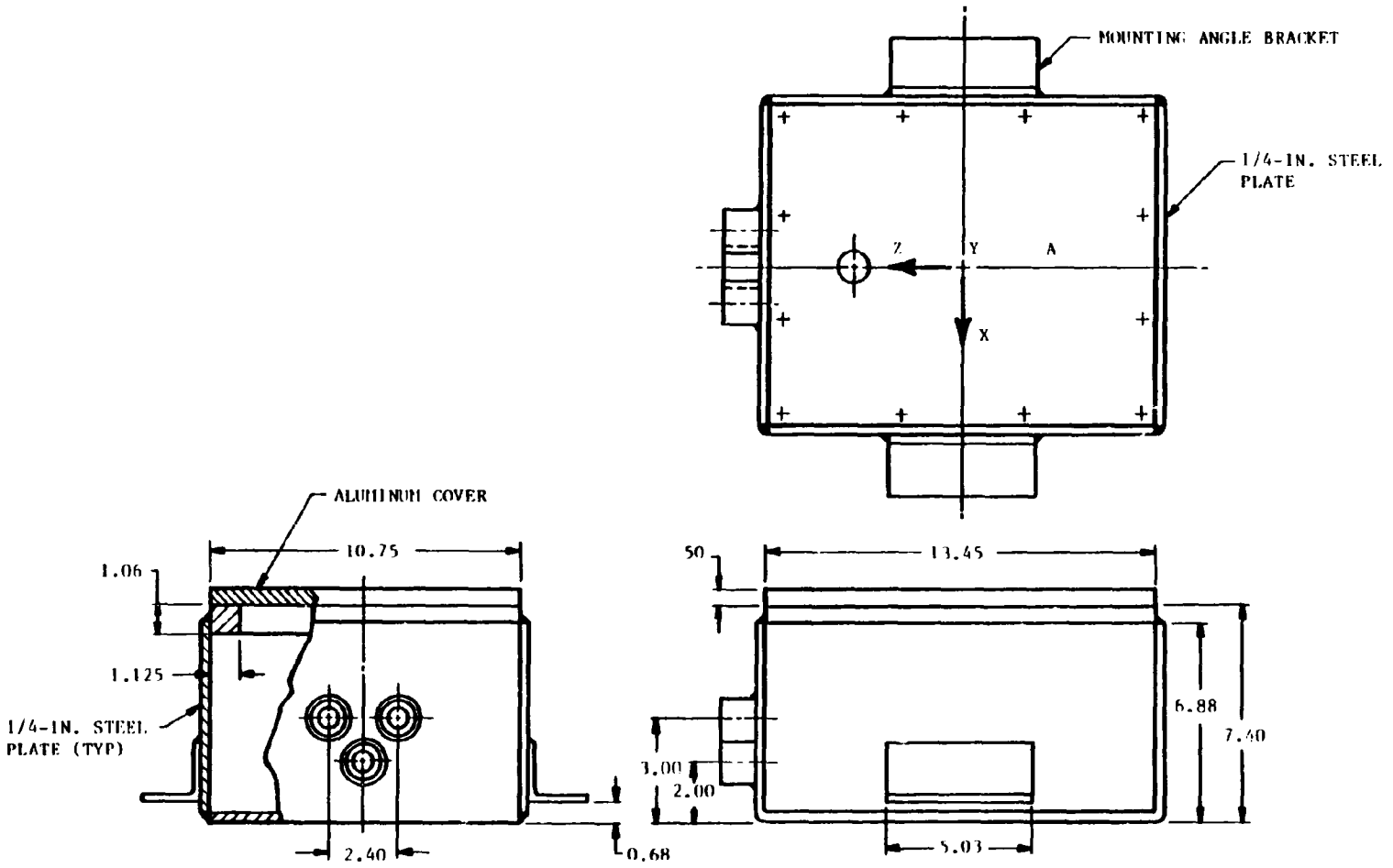

FIGURE 4.1. ENCLOSURE I (ALL DIMENSIONS IN INCHES)

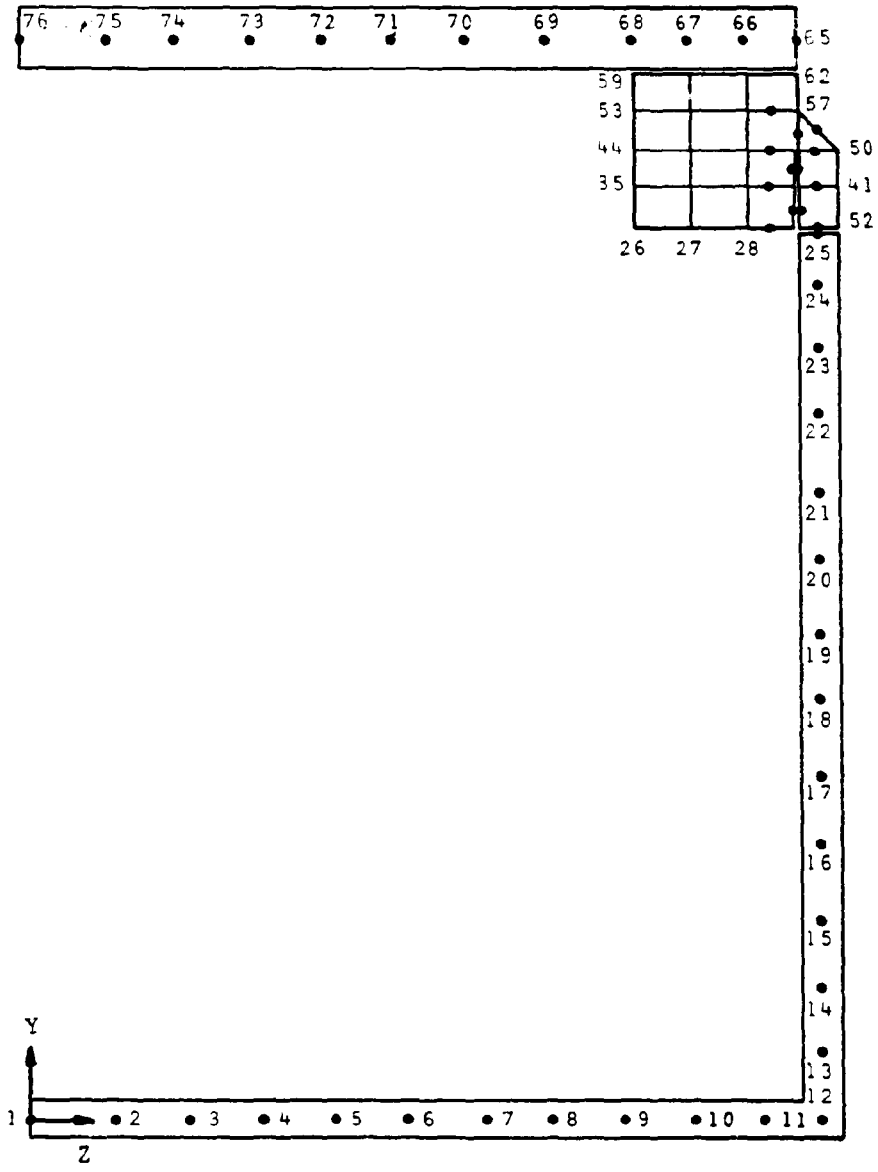

FIGURE 4.2. CASE I - FINITE ELEMENT MODEL

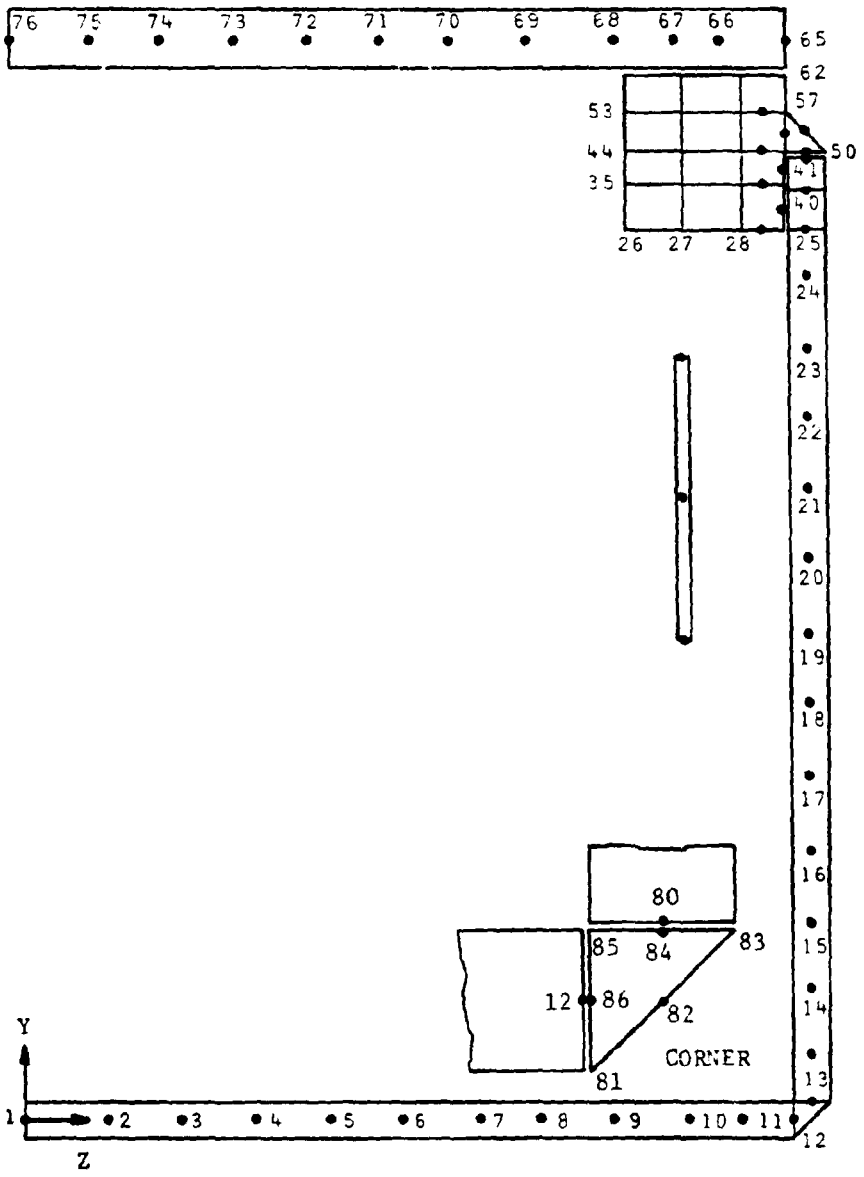

FIGURE 4.3. CASE II - FINITE ELEMENT MODEL

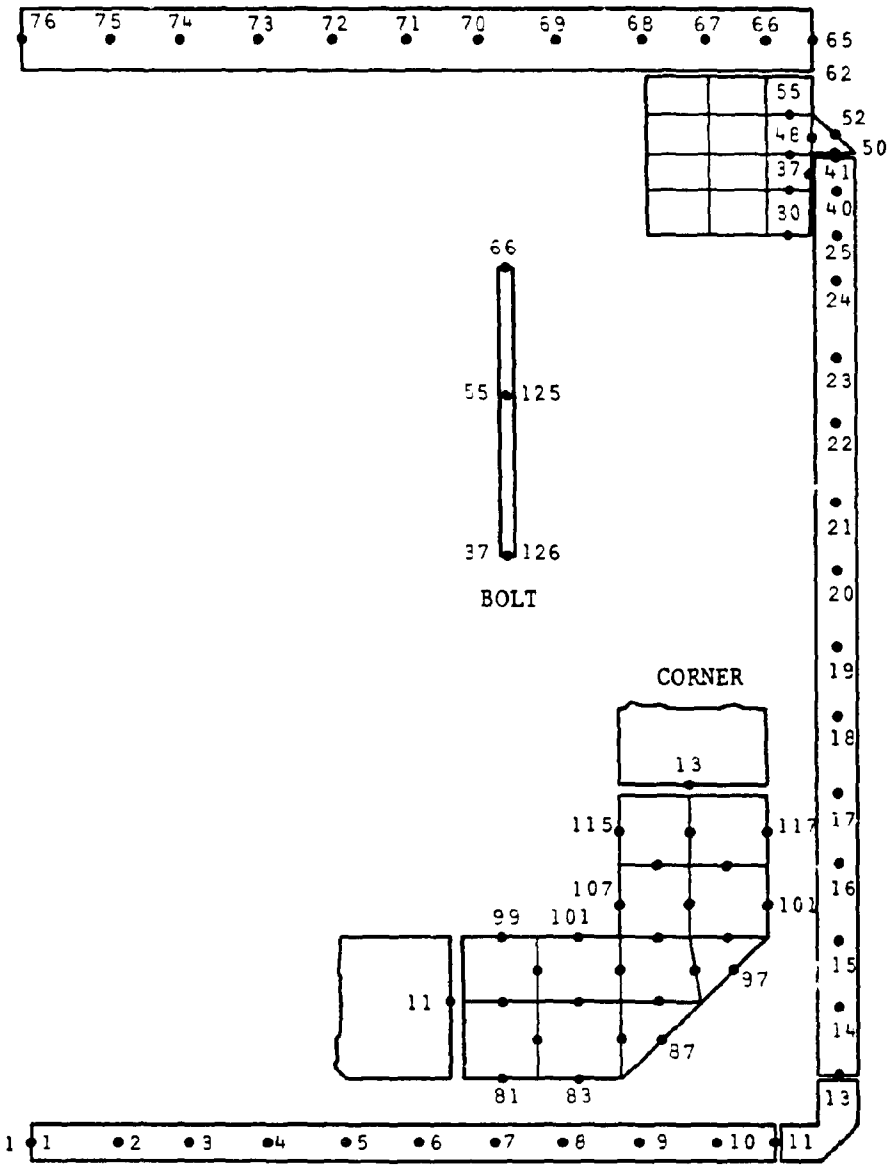

FIGURE 4.4. CASE III - FINITE ELEMENT MODEL

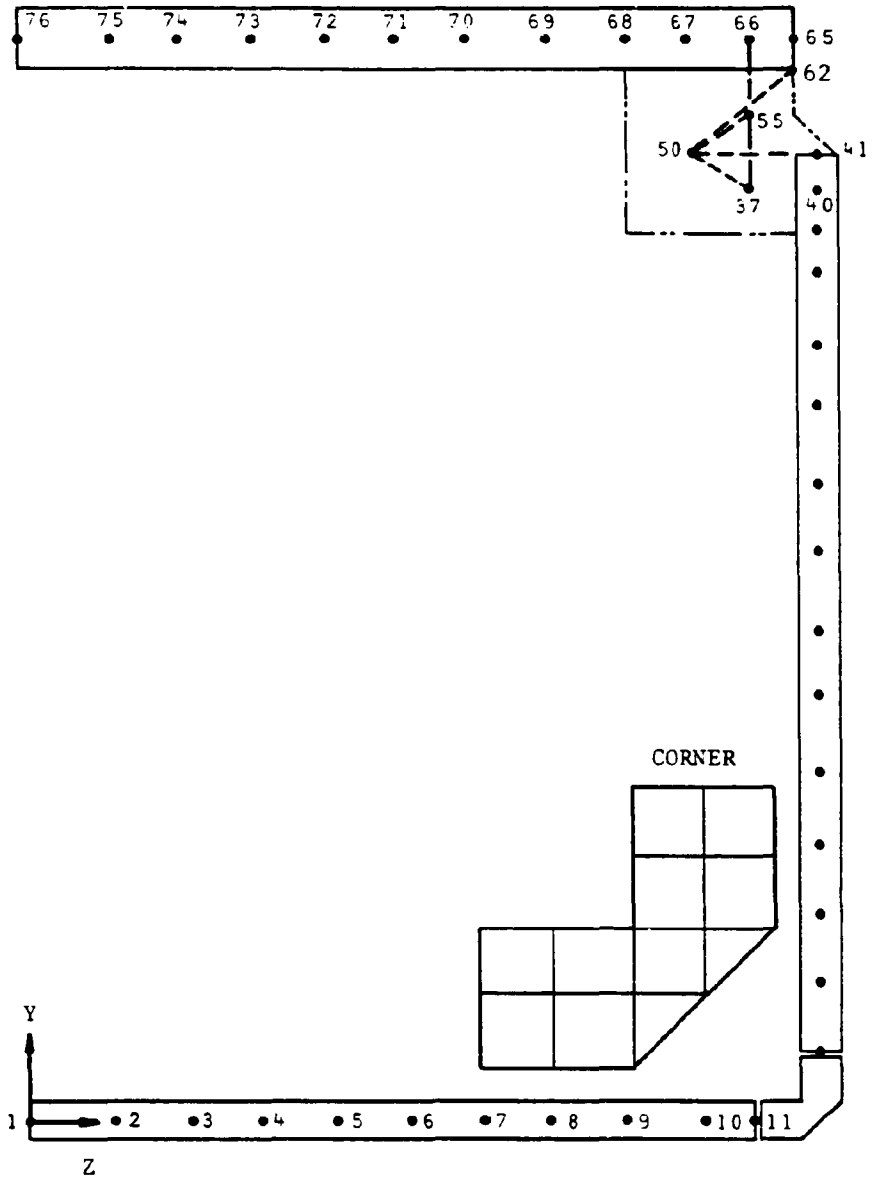

FIGURE 4.5. CASE IV - FINITE ELEMENT MODEL

Case IV (Figure 4.5):

- Rigid flange cross-section with flange connected to side shell using constraint equations
- Center of rigid flange connected to cover with bolt and constraint equations
- Side and bottom shells attached using refined solid element model for weld and adjacent shells

All the models were pressurized with a 100-psi internal pressure. The pressure was applied to the gap region between the flange and side shell and to the area between the flange and cover extending out to the bolt location. The pressurized areas and the geometric boundary conditions are shown in Figure 4.6. The geometric boundary conditions were taken as

$$U_x = U_y = \theta_z = 0 \text{ at node 1}$$

$$U_x = \theta_z = 0 \text{ at node 76}$$

U_i and θ_i are displacements and rotations in the i-th direction.

4.1.1.2 Results

The differences in the solutions for each case can best be evaluated by plotting the resulting inner and outer fiber stresses. Figures 4.7-4.9 show the direct plus bending and direct minus bending stresses for the cover, side shell, and bottom shell components. From these graphs, the following conclusions can be drawn concerning the stress distributions in the various components:

Cover:
(1) The stresses in the cover are low compared with those in the side and bottom shells.

(2) The maximum stresses for Case I are higher than the other cases (probably due to the increased flexibility at the flange-side shell joint).

(3) The replacement of the elastic flange with constraint equations has little effect on the stresses in the cover (Cases II and III compared with Case IV).

Side and Bottom Shells:
(1) The replacement of the elastic flange with constraint equations has little effect on the stresses in the side shell (Case IV compared with Cases II and III).

(2) There appears to be a stress concentration at the bottom and side shell intersections (Cases I and II compared with Cases III and IV).

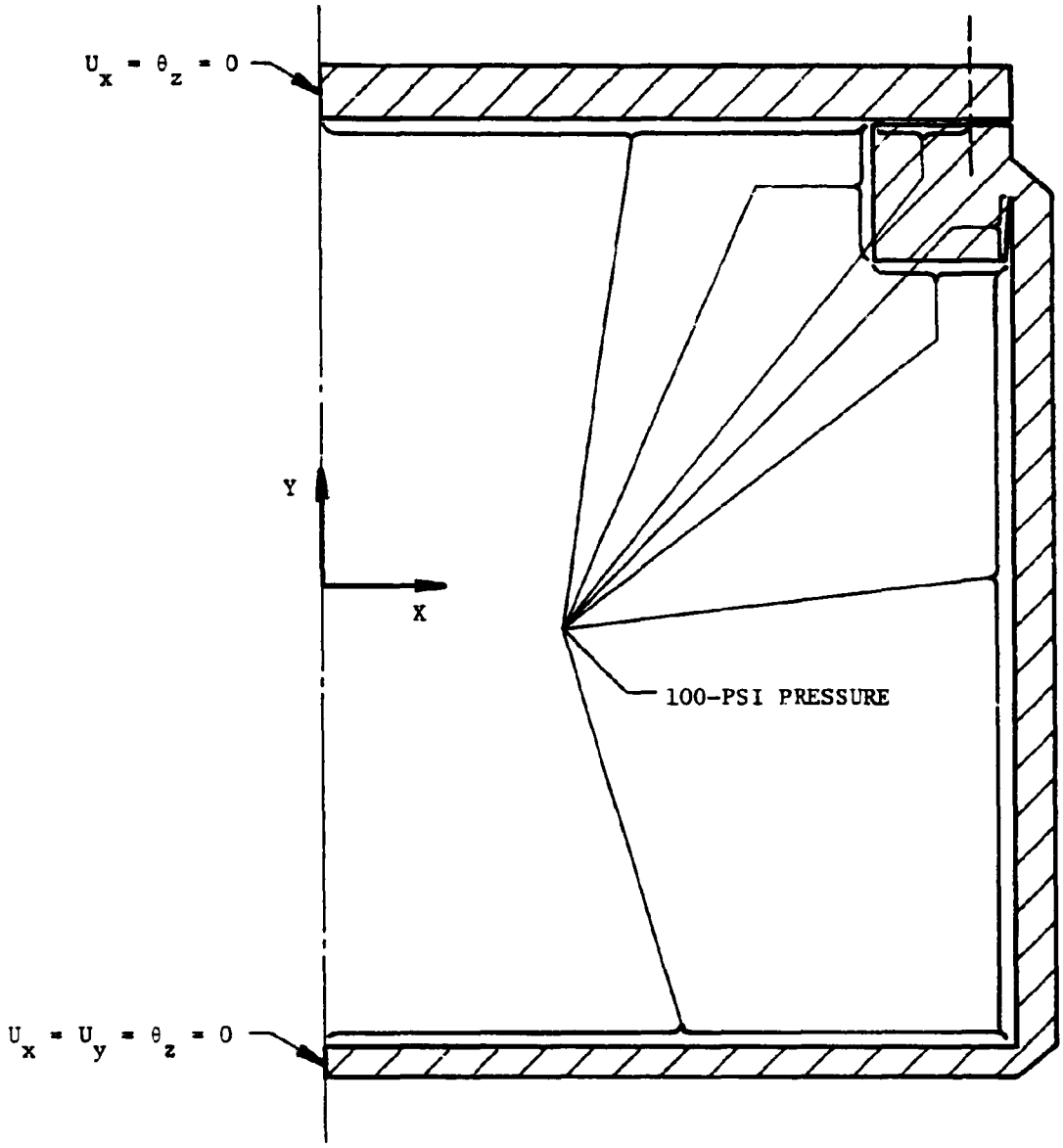

FIGURE 4.6. APPLIED PRESSURE AND GEOMETRIC BOUNDARY CONDITIONS

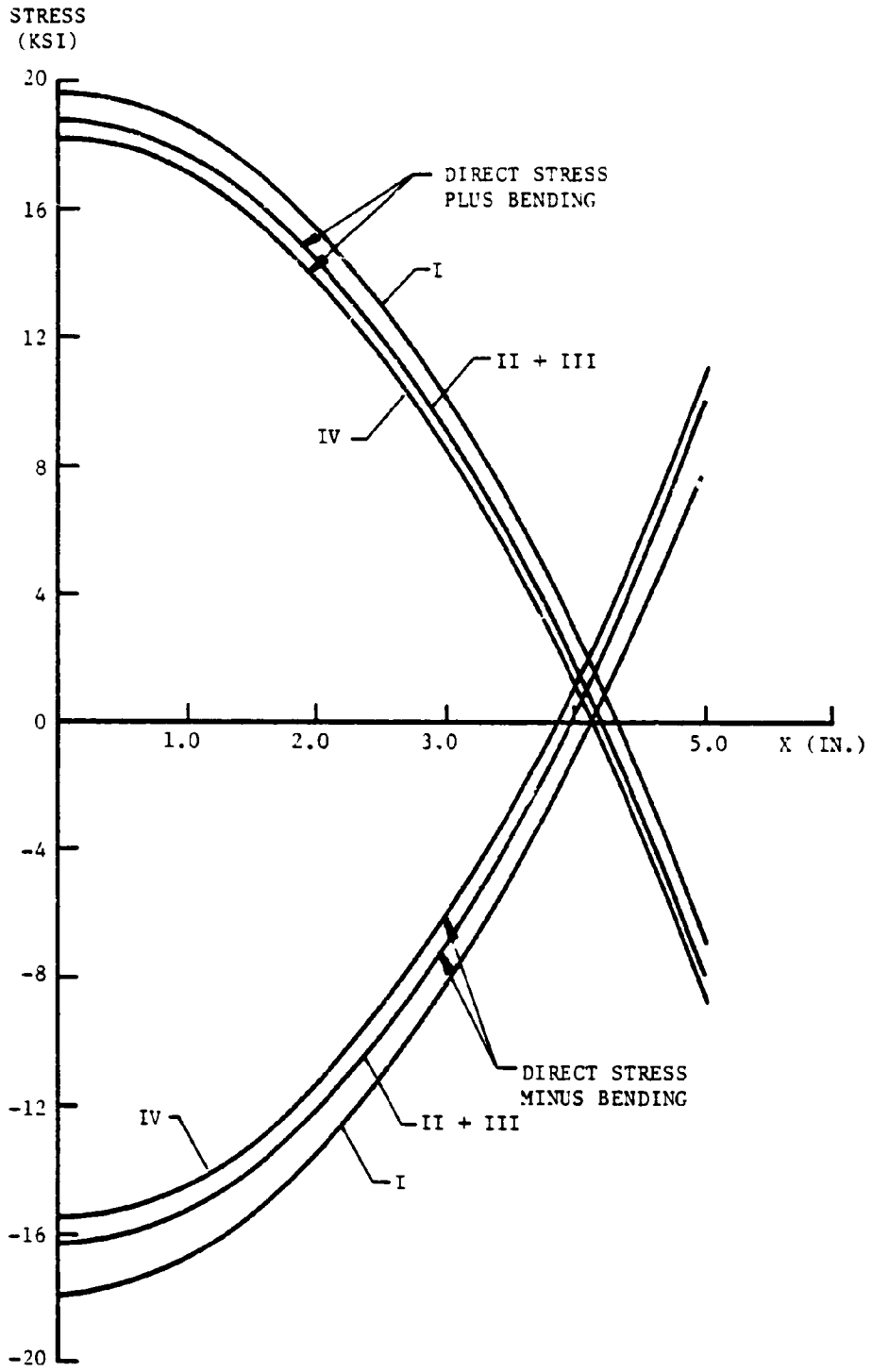

FIGURE 4.7. STRESSES IN THE COVER

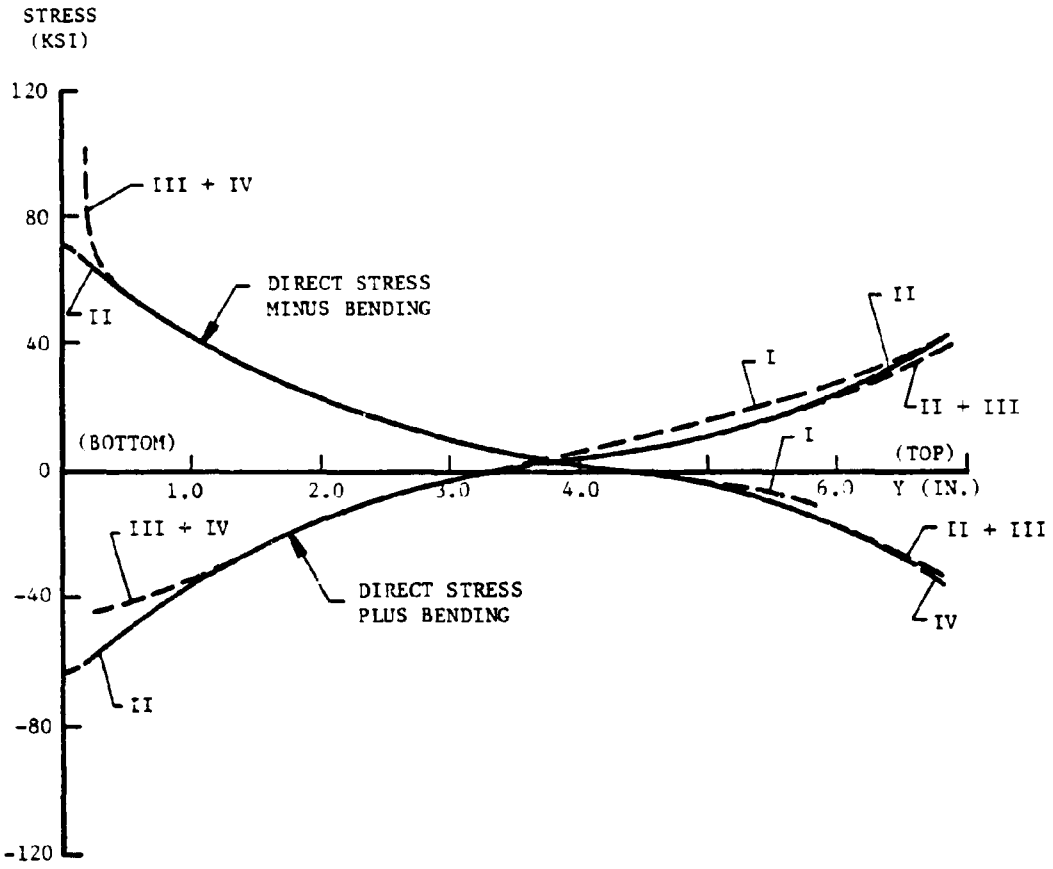

FIGURE 4.8. STRESSES IN SIDE SHELL

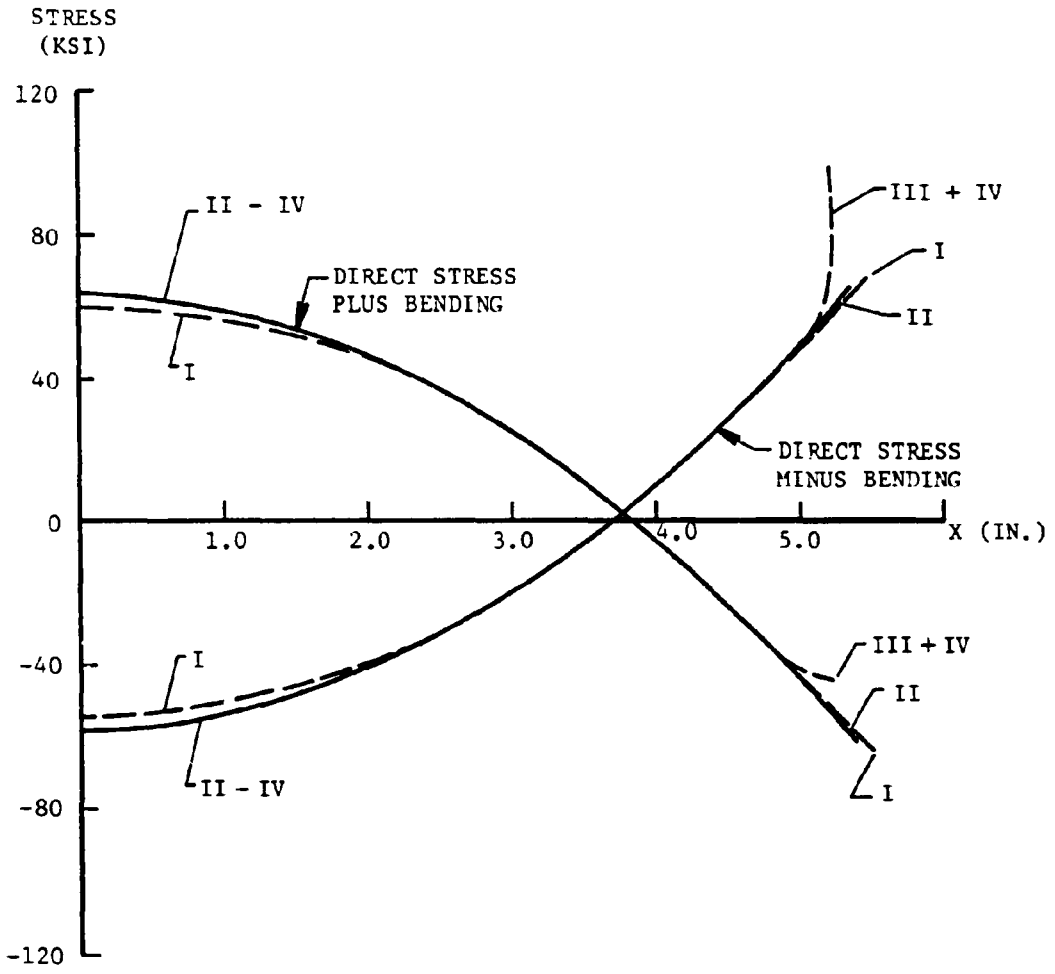

FIGURE 4.9. STRESSES IN BOTTOM SHELL

(3) There appears to be no change in the stress solution when the bottom and side shell weld is represented by a single solid element rather than intersecting shells.

In summary, the two-dimensional analyses showed that distortions in the cross-section of the elastic flange are not significant and that the side plates are accurately represented by shell elements. Stress concentrations are present at the welded joints, but much finer meshes than those used would be required to accurately resolve these stresses. Such fine meshs are not practical for these analyses, particularly for the three-dimensional analyses to follow. MSHA accepts plasticity in Schedule 2G enclosures, so high localized stresses which might exceed the yield stress are not particularly important. Thus, the three-dimensional analyses described in the next section are based upon the use of beam elements for the flanges (which ignore distortions in the cross-section of the flange) and shell elements to represent the sides, bottom, and cover of the enclosure.

4.1.2 Three-Dimensional Elastic Analysis

The two-dimensional models of Enclosure I, which were used in the analyses described in the preceding section, ignored the effects produced by plate bending in two directions. These effects are important for Enclosure I because its width and length are approximately equal (see Figure 4.1). The three-dimensional models described in this section were developed using beam elements to represent the flanges and shell elements to represent the plates. Results from the two-dimensional analyses showed that these elements gave a good representation of the enclosure behavior.

4.1.2.1 Verification of FEM Mesh Size

Before proceeding with the development of the three-dimensional models, it was necessary to estimate the accuracy of the solutions obtained from the chosen finite element mesh. The most expedient way of making this estimate was to compare the solution obtained from closed-form, analytical methods with the finite element results. To do this, the cover was represented as a rectangular flat plate supported along its edges and subjected to a uniform loading (see Figure 4.10). Timoshenko [4] gives analytical solutions for this case and presents solutions for plate aspect ratios equal to 1.2 and 1.3. The aspect ratio (plate length divided by plate width) for the cover is 1.256, so a sufficiently accurate approximation can be obtained by simply averaging the given solutions. The results given by Timoshenko [4] for a simply supported aluminum plate with

$$b/a = 1.25$$

$$E = 10 \times 10^6 \text{ psi}$$

$$\nu = 0.30$$

and a 100-psi uniform pressure are:

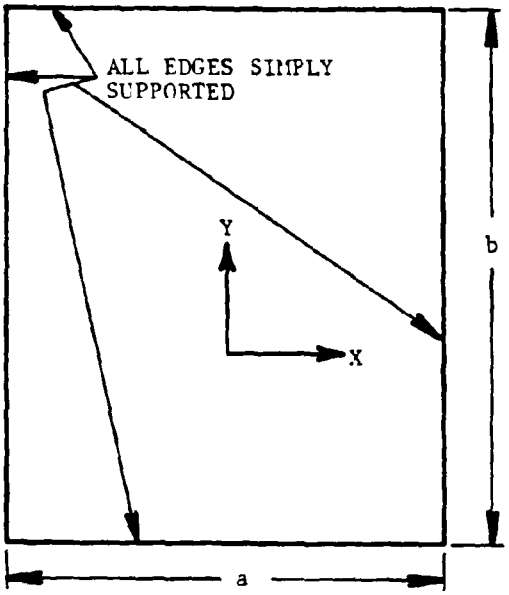

a = 10.75 IN.

b = 13.50 IN.

ASPECT RATIO

$\frac{b}{a}$ = 1.256

CASE I - SIMPLY SUPPORTED EDGES

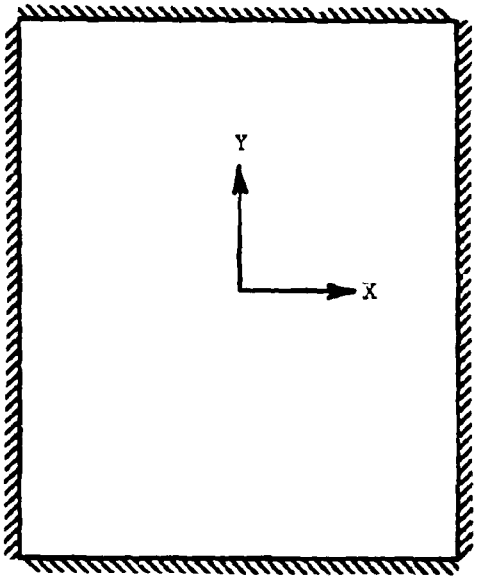

CASE II - EDGES COMPLETELY FIXED

FIGURE 4.10. GEOMETRY FOR COVER

Along y = 0			Along x = 0		
x/a	σ_x (psi)	σ_y (psi)	y/b	σ_x (psi)	σ_y (psi)
0.4	7,391	4,840	0	18,319	13,923
0.3	12,536	8,750	0.1	17,570	13,646
0.2	15,864	11,593	0.2	15,407	12,703
0.1	17,723	13,341	0.3	11,760	10,678
0.0	18,319	13,923	0.4	6,615	6,809

where σ_x and σ_y are bending stresses in the x and y directions, respectively. The maximum deflection at the center of the plate corresponding to this solution is

$$\delta_{max} \ (x = a/2, \ y = 0) = 0.07012 \text{ in.}$$

For the built-in edge case, the stress solution is available only at the following points:

Location	σ_x (psi)	σ_y (psi)
x = a/2 y = 0	18,388	15,516
x = 0 y = b/2	4,647	15,490
x = 0 y = 0	8,681	6,240

The corresponding deflection at the center of the plate is:

$$\delta_{max} \ (x = a/2, \ y = 0) = 0.02118 \text{ inch}$$

The finite element model of the cover is shown in Figure 4.11. Because the cover is symmetric about the x and y axes, only one-quarter of the structure was included in the model. The model shown has 78 elements and 52 nodes. Triangular elements were used because they can also treat plastic behavior (plastic behavior will be treated in a later section using the same mesh). The mesh in the vicinity of the boundary is reduced to account for the increased stress gradients in this region. Nodes along the boundary were constrained in translation and rotation, depending on whether the cover is simply supported or fixed. Nodes along the symmetry planes were given the symmetry boundary conditions, i.e.,

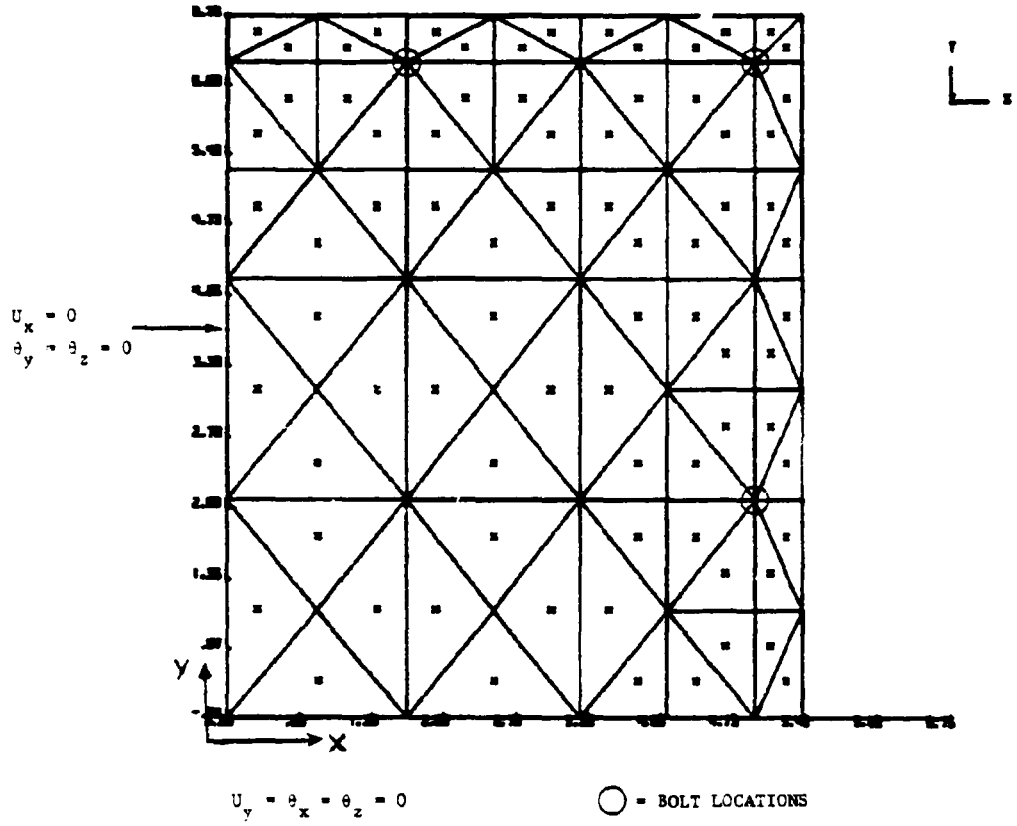

FIGURE 4.11. FINITE ELEMENT MESH OF 1/4 MODEL OF COVER

$$\delta_y = \theta_x = \theta_z = 0 \text{ along } y = 0$$

$$\delta_x = \theta_y = \theta_z = 0 \text{ along } x = 0$$

where δ_i and θ_i are displacements and rotations in the i-ith direction.

The classical analytical and computed finite element solutions for the maximum deflection at the center of the plate are:

	δ_{max} (in.)		
	Analytical	Finite Element	% Difference
Simply Supported	0.07012	0.07289	4.0
Fixed	0.02118	0.02251	6.3

Figure 4.12 plots the bending stresses given by the two solution methods for the simply supported case. As the figure shows, the correlation is good, and the solutions differ by less than 10% for the higher stresses. It should be remembered that the stresses for the finite element solution are not along the planes x = 0 and y = 0, but are computed at the element's centroid (located by the symbol "x" in Figure 4.11). There will be some difference in stresses from this condition alone.

The stresses in the cover with fixed edges are shown in Figure 4.13. Although the stresses obtained from the analytical solution are given only at the plate center and plate boundary, the graph indicates the two solutions closely agree.

These comparisons showed that both the displacements and stresses obtained by closed-form analytical solutions and by finite element methods agree within engineering accuracy. Therefore, it was concluded that the finite element mesh of Figure 4.11 adequately represented the cover.

4.1.2.2 Characteristics of Three-Dimensional FEM Model

The next step in the analysis was to construct a three-dimensional model using beam elements for the flanges and bolts, shell elements for the flat plates, and a grid spacing approximately equal to that verified for the cover. Because the enclosure is symmetric about vertical planes, passing through the center of the sides*, only one-quarter needed to be modeled. A schematic of one-quarter of the enclosure, which identifies the structural components, is given in Figure 4.14, and a corresponding view of the FEM model is given in Figure 4.15.

---

*This ignores the fact that there are penetrations in only one end of the enclosure. These penetrations are well reinforced and should not be weak points in the enclosure. Thus, a quarter of the enclosure without the reinforced penetrations is represented by the model.

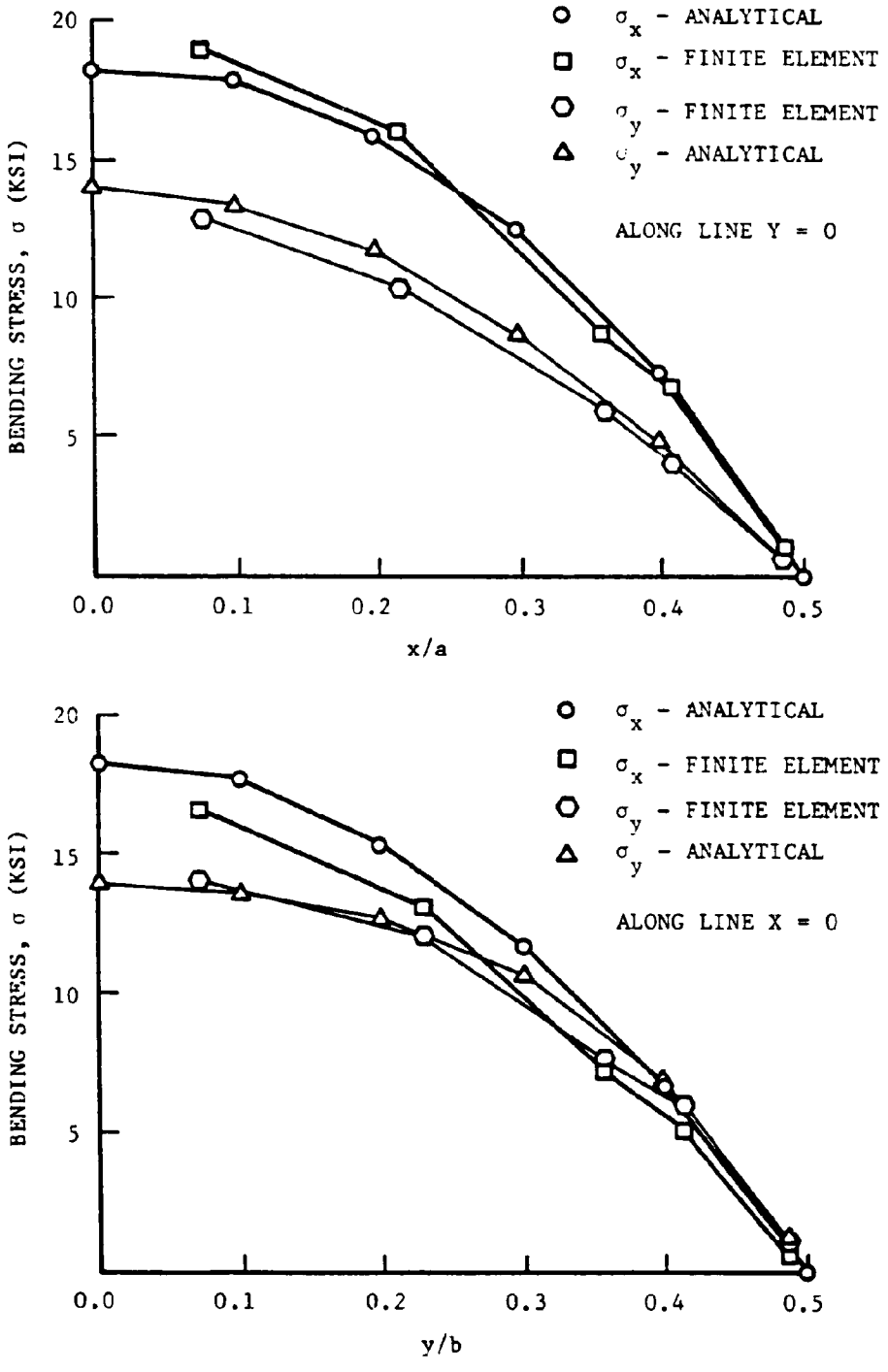

FIGURE 4.12. FINITE ELEMENT AND ANALYTICAL STRESS SOLUTIONS - SIMPLY SUPPORTED

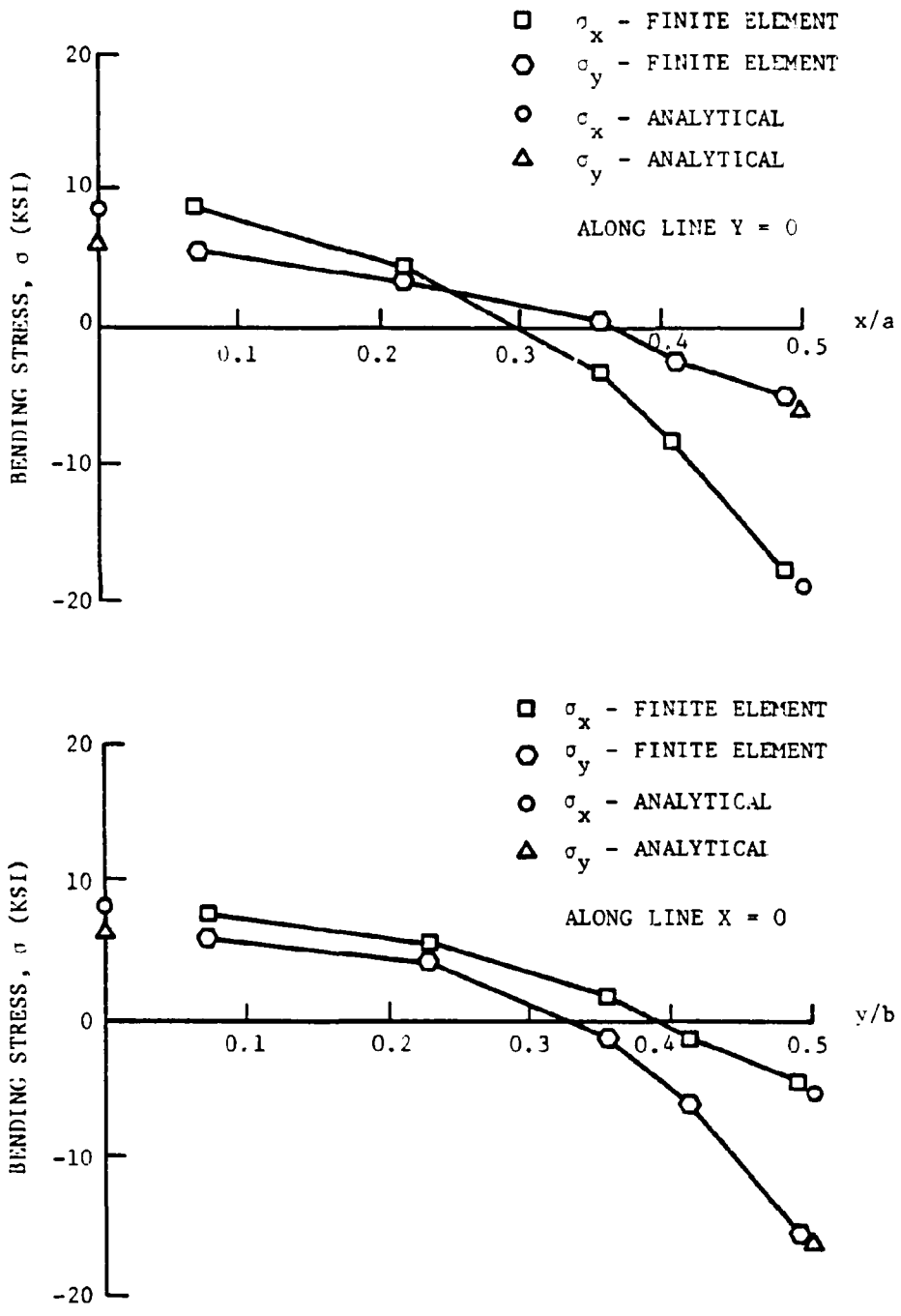

FIGURE 4.13. FINITE ELEMENT AND ANALYTICAL STRESS SOLUTIONS - FIXED EDGES

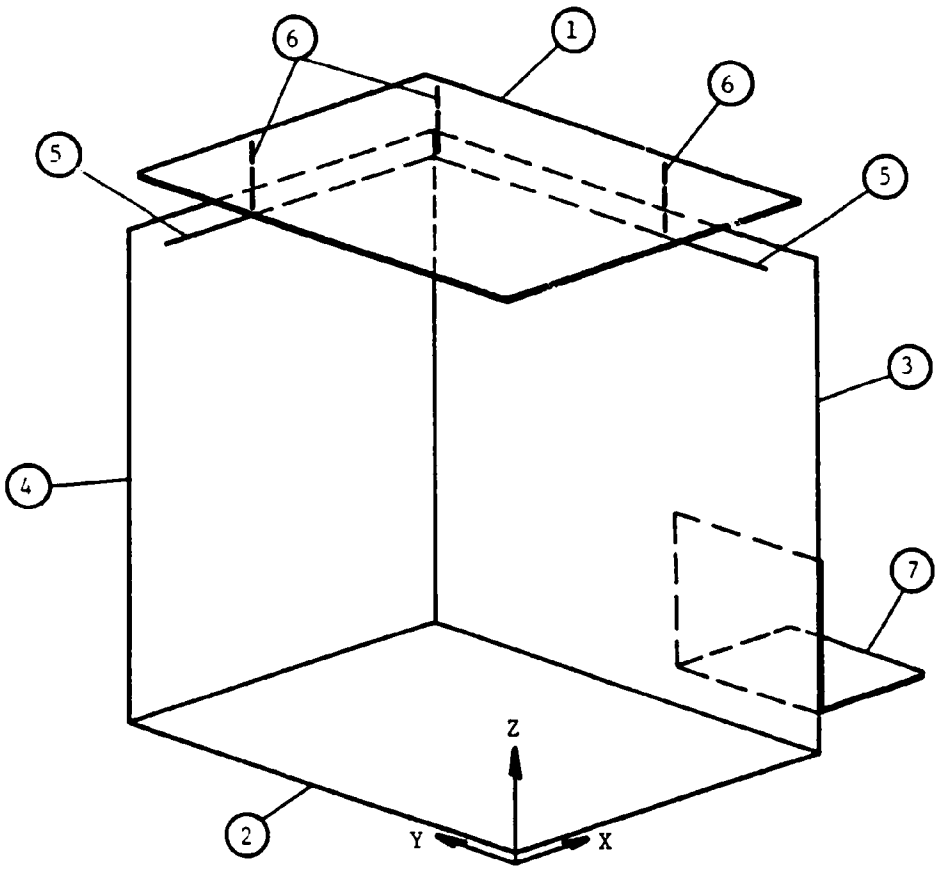

1 COVER
2 BOTTOM
3 SIDE
4 BACK (OR END)
5 FLANGE
6 BOLT
7 ANGLE IRON

FIGURE 4.14. QUARTER MODEL OF ENCLOSURE I LOOKING FROM INSIDE

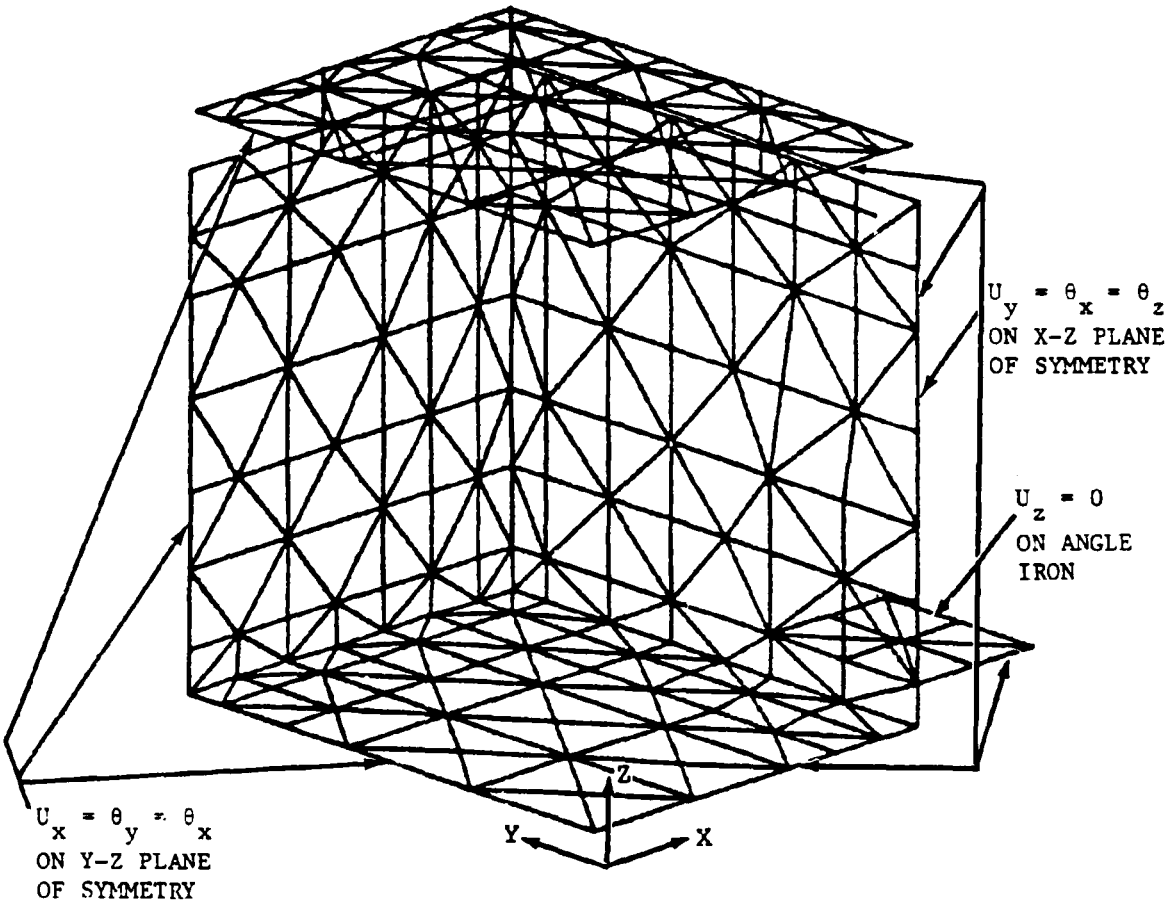

FIGURE 4.15. THREE-DIMENSIONAL FINITE ELEMENT GRID
OF ENCLOSURE I

The entire model has 254 nodes with six degrees of freedom (three translational and three rotational) per node. Each of the components shown in Figure 4.14 contains the following element types:

	Component	Element Types	Number
1.	Cover	Triangular Shell	78
2.	Bottom	Triangular Shell	78
3.	Side	Triangular Shell	94
4.	Back	Triangular Shell	86
5.	Flange	Three-Dimensional Beam	12
6.	Bolts	Three-Dimensional Beam	6
7.	Angle Iron	Triangular Shell	16
			370 Total

The various components were connected together with constraint equations to ensure that the boundary compatibilities will be correctly modeled. Figure 4.16 shows a sectional view formed by slicing the structure with an x-z plane at a bolt near the side shell. The points A through G denote nodal locations in the finite element model and are connected together as described below.

(a) Flange to Side Shell: Node A (center of flange) and Node B (top of side shell) are connected together as a rigid body. The constraint equations are

$$
\begin{aligned}
UX_B &= UX_A \\
UY_B &= UY_A + 0.6875\ ROTZ_A \\
UZ_B &= UZ_A - 0.6875\ ROTY_A \\
ROTX_B &= ROTX_A \\
ROTY_B &= ROTY_Z \\
ROTZ_B &= ROTZ_A
\end{aligned}
$$

(b) Flange to Edge of Cover: Node C (edge of cover) had the same vertical displacement (z direction) as Node H. The constraint equation relative to Node A is

$$UZ_C = UZ_A - 0.5625\ ROTY_A$$

(c) Flange to Bottom of Bolt: Node D (bottom of bolt) was connected to Node A only in the translational degrees of freedom. The constraint equations are

$$
\begin{aligned}
UX_D &= UX_A - 0.6875\ ROTY_A \\
UY_D &= UY_A + 0.1125\ ROTZ_A \\
&\quad + 0.06875\ ROTX_A \\
UZ_D &= UZ_A - 0.1125\ ROTY_A
\end{aligned}
$$

(d) Flange to Bolt Position at Bottom of Cover: Node G (bolt position at bottom of cover) connected to Node A only in translation for the x and y displacements. The constraint equations are

$$
\begin{aligned}
UX_G &= UX_A + 0.53125\ ROTY_A \\
UY_G &= UY_A + 0.1125\ ROTZ_A - 0.53125\ ROTX_A
\end{aligned}
$$

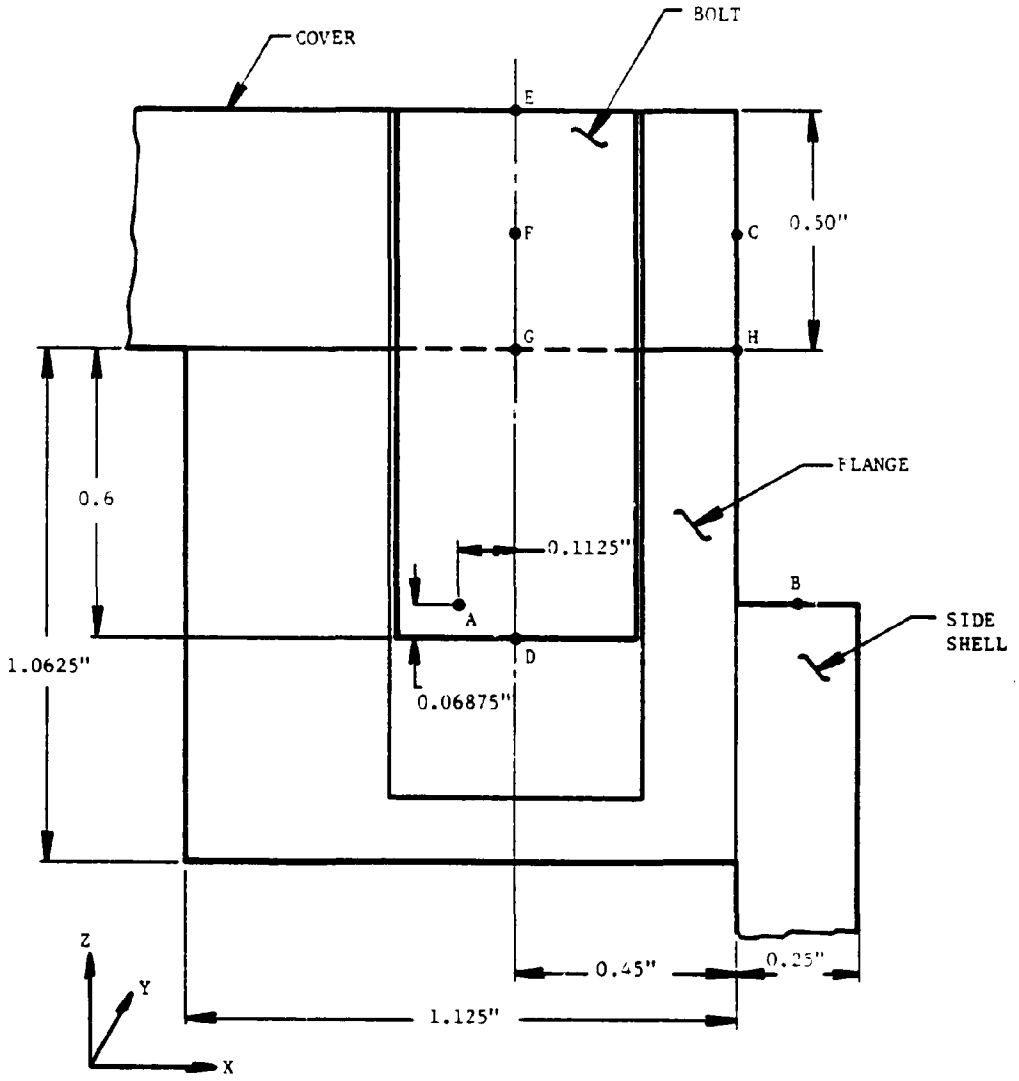

FIGURE 4.16. SCHEMATIC OF NODAL LOCATIONS USED IN CONNECTING COVER, FLANGE, AND SIDE SHELL

(e) Top of Bolt to Center of Cover: Node F (center of cover) and Node E (top of bolt) were connected as a rigid body except in the degree of freedom corresponding to torsion of the bolt. The constraint equations are

$$UX_E = UX_F + 0.25\ ROTY_F$$
$$UY_E = UY_F - 0.25\ ROTX_F$$
$$UZ_E = UZ_F$$
$$ROTX_E = ROTX_F$$
$$ROTY_E = ROTY_F$$

Nodes E to G and G to D were connected with beam elements which represent the bolts. At those positions where bolts were not present, the flange was connected to the side shell and cover as described in sections (a) and (b) above. Similar constraint equations were derived for the flange running in the x-direction.

After the finite element model had been assembled, the next step was to apply the prescribed boundary and loading conditions. For a symmetric structure loaded symmetrically, the nodes on the planes of symmetry were allowed no displacements normal to or rotations in the plane. Figure 4.15 shows the boundary conditions on the y-z and x-z symmetry planes. The node at the center of the support flange was constrained in the z-direction to prevent rigid-body movement of the enclosure in that direction. The structure was loaded by an 100-psi internal pressure over all interior surfaces.

4.1.2.3 Results of Elastic Analysis

Figure 4.17 shows an isometric view of the distorted and undistorted geometry of the enclosure. Outward deflections of the cover and bottom shell can be clearly seen. Contour plots of the principal stresses and perpendicular displacements in the cover are given in Appendix A. In all of the stress contour plots, the inside surface of the shell is that on the inside of the enclosure. Figures A.1-A.3 clearly show the effects of the bolts in the cover nearest the side and back edges and illustrate that the stress levels in the cover are well below 36 ksi, the yield stress of the 6061 aluminum alloy cover material.

Figures A.4-A.6 in Appendix A show contour plots of the principal stresses and normal displacements in the steel plating of the enclosure. They indicate that stress concentrations occur near the x-z and y-z planes of symmetry at the intersection of the side and back shells with the bottom shell.

It is instructive to identify those elements in which the von Mises combined stress exceeds the yield criterion. This criterion assumes that the structure will yield when the distortion energy equals the distortion energy in simple tension. A combined stress, called the von Mises stress, is defined as

$$\sigma_{vm} = \sqrt{1/2\ (\sigma_1 - \sigma_2)^2 + (\sigma_2 - \sigma_3)^2 + (\sigma_3 - \sigma_1)^2}$$

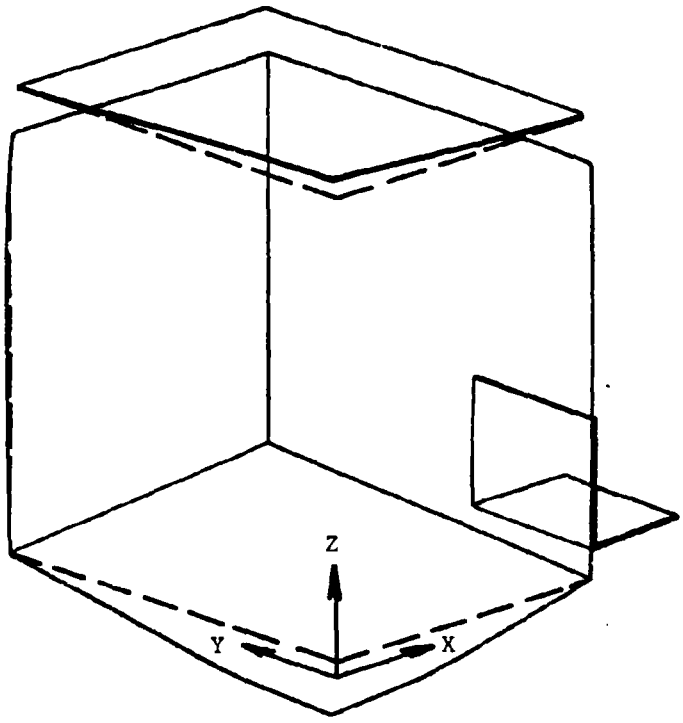

SOLID LINES - DEFORMED SHAPE

DASHED LINES - ORIGINAL SHAPE

FIGURE 4.17. DISTORTED GEOMETRY FOR 100-PSI INTERNAL PRESSURE LOADING

where σ_1, σ_2, σ_3 are principal stresses. The von Mises criterion expressed in terms of stresses states that yielding will occur when

$$\sigma_{vm} = \sigma_y$$

where σ_y is the yield stress in simple tension. For both the 6061 aluminum alloy used in the cover and the A36 structural steel used in the bottom, side, and back shells of Enclosure I, the yield value is 36 ksi.

For the elements indicated in Figures A.13-A.18, the combined stress at the centroid of the inside and/or outside surface is larger than 36 ksi. Remember that the values are for a 100-psi internal pressure and that the analysis is for an elastic structure loaded statically. Thus, this solution does not account for subsequent redistribution of stresses due to yielding or for the dynamics of the container. Nevertheless, the analysis does provide valuable information about the highly stressed areas and the applied pressures at which yielding will first occur. Figure A.14 shows that the structure will first yield on the interior of the side shell at its connection with the bottom. From a simple scaling of von Mises stresses, the applied pressure when the structure first begins to yield is

$$P = 100 \text{ psi} \times \frac{36 \text{ ksi}}{50 \text{ ksi}} = 72 \text{ psi}$$

At higher pressures the yielded zone will spread from the center along the side-bottom intersection as indicated in Figures A.12-A.15.

The second region to yield is at the intersection of the bottom and back shells in the vicinity of the y-axis. This area is far removed from the region which yielded first and will not be affected by the yielding which has already occurred. The pressure required to initially yield the region is

$$P = 100 \text{ psi} \times \frac{36 \text{ ksi}}{44 \text{ ksi}} = 82 \text{ psi}$$

Figures A.12-A.13 and A.16-A.17 show the yielded zone in this region.

Computed results also included stresses in the cover bolts for the 100-psi internal loading case. Figure 4.18 shows a schematic of the cover and bolts with the nonmenclature of the stress resultants. The axial (DIR), two bending (BZ and BY), and maximum (MAX and MIN) stresses are presented in Table 4.1. The results show that the bolts along the edges are more highly stressed than those in the corners. They also confirm the expected results that Bolt 1 along the side is subjected to more load than Bolt 3 along the back. The maximum bending stresses in these bolts are almost three times the axial or direct stress. This ratio may be too high because the bolt heads were constrained to rotate with the middle surface of the cover. This condition may not be realized in actual practice because the bolt holes are slightly larger than the bolt diameters and the bolt head may cock with respect to the cover. Thus, we expect that the calculated bolt bending stresses are higher than the stresses which would actually occur under these conditions.

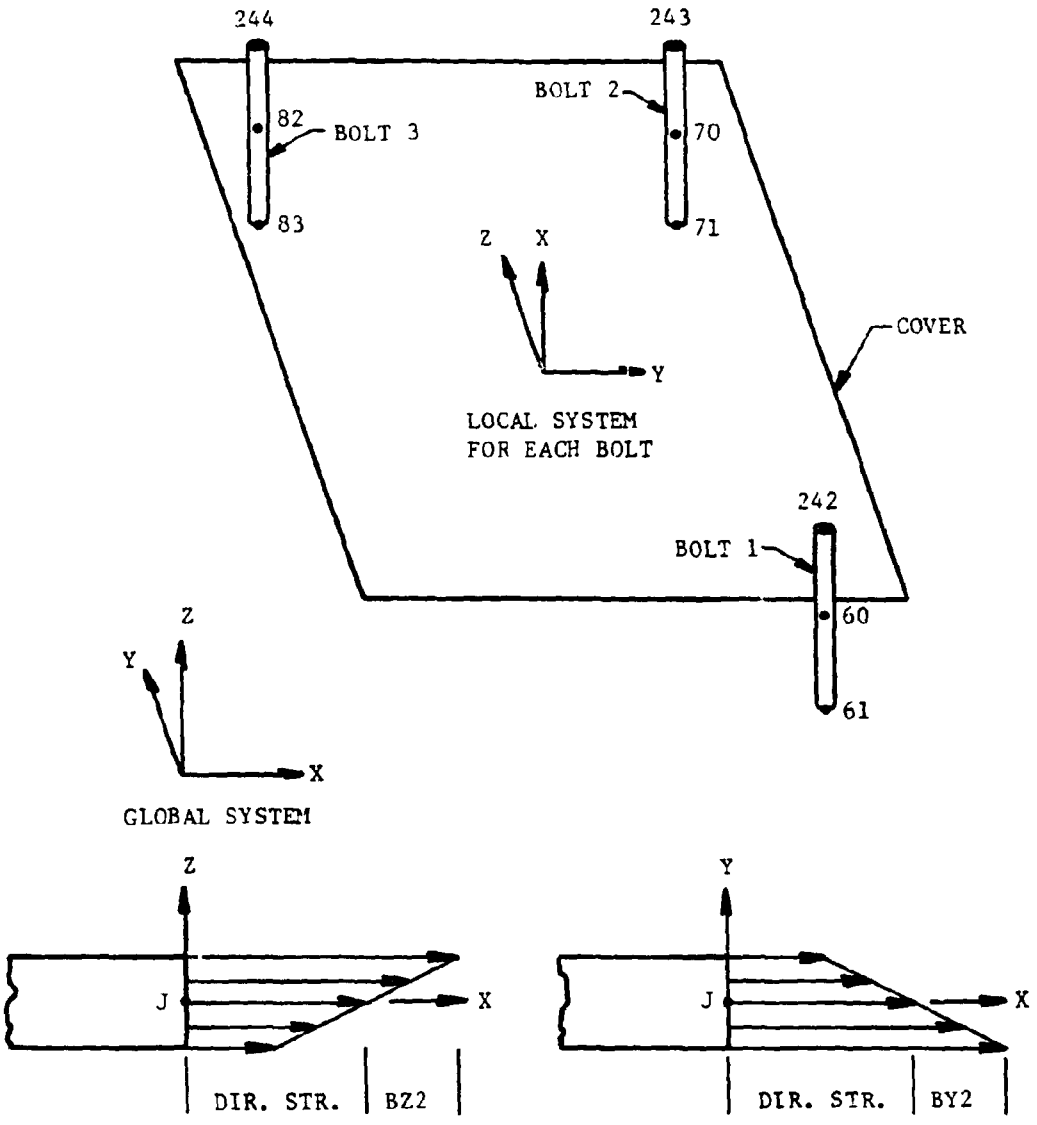

MAXIMUM = DIR. STR. + (BZ2) + (BY2)

MINIMUM = DIR. STR. + (BZ2) - (BY2)

FIGURE 4.18. SCHEMATIC OF COVER AND BOLTS

TABLE 4.1. SUMMARY OF BOLT STRESSES
UNDER 100-PSI INTERNAL PRESSURE

Bolt	Node Nos.	At Nodes	Dir.	BZ	BY	Max	Min
1	61-60	1	21157	0	0	21157	21157
		2	21157	5666	2199	26823	15491
	60-242	1	21157	5666	2199	26823	15491
		2	21157	60033	4438	81190	-38876
2	71-70	1	3929	0	0	3929	3929
		2	3929	1506	2325	6254	1604
	70-243	1	3929	1506	2325	7760	1604
		2	3929	8104	7207	12033	-4115
3	88-82	1	16573	0	0	16573	16573
		2	16573	1510	7307	23880	9266
	82-244	1	16573	1510	7307	23880	9266
		2	16573	4546	46693	63266	-30180

However, coupling these nodes would produce conservative stresses as far as design is concerned. The results do indicate that high-strength bolts should be used in order to prevent yielding.

Results from the calculations were also checked to see if gaps could develop between the cover and the flange. Recall from Figure 4.16 that the outer edge of the cover was coupled to the flange at locations corresponding to "H," which caused the cover and flange to move together at this location so that they could not separate. To see if gaps would form without the coupling, forces at the coupled nodes along the outer edge of the cover were checked. These forces were all negative, which indicated that the cover and flange were being pressed together rather than being forced apart. Thus, the prying action of the cover produced by the bolt is more than adequate to prevent the internal pressure from separating the cover and flange. These results show that the cover's outside edge will tend to seal against the flange, and no gaps will develop unless substantial elongation of the bolts occurs. Further, at 100 psi, bolt elongation is much less than the Maximum Experimental Safe Gap (MESG).

To study further the stresses produced in bolts and bolted covers for different cover thicknesses, bolt sizes, and bolt spacing, a series solution for a bolted cover on a rigid foundation was developed. This solution, given in Appendix B, was used to evaluate the effect of different cover thicknesses for Enclosure I and to calculate cover and bolt stresses for Enclosure II. All results are given in Appendix B, and they are also used in Section 5.0 for calculating safety factors.

4.1.3 Three-Dimensional Elastic-Plastic Analysis

The three-dimensional linearly elastic analysis of Enclosure I, described in the previous section, showed that stresses at several locations in the enclosure exceeded the material yield strength. Further, hydrostatic tests on the enclosure, reported in Section 4.1.5 and 4.1.6, showed (1) that permanent distortions develop in the enclosure at pressures below 150 psig and (2) that the weld joint separates at the intersection of the side and bottom shells, permitting plastic rotations of the joint. To describe this nonlinear behavior, material and geometric nonlinearity must be included in the model. This was done using the ANSYS computer code described previously, and an elastic-plastic analysis was performed. The finite element model was developed for this analysis by modifying the three-dimensional elastic model described in the previous section.

4.1.3.1 Characteristics of the Model

To utilize the three-dimensional model of Figure 4.15 for elastic-plastic behavior, the grid was first separated into two parts, as shown in Figure 4.19. One part models the behavior of that part of the enclosure which will remain elastic, and the other part models that in which plastic behavior is anticipated. The advantage of separating the model into two parts is computational efficiency. Computational costs for plastic behavior are high, so the plastic part is made as small as possible.

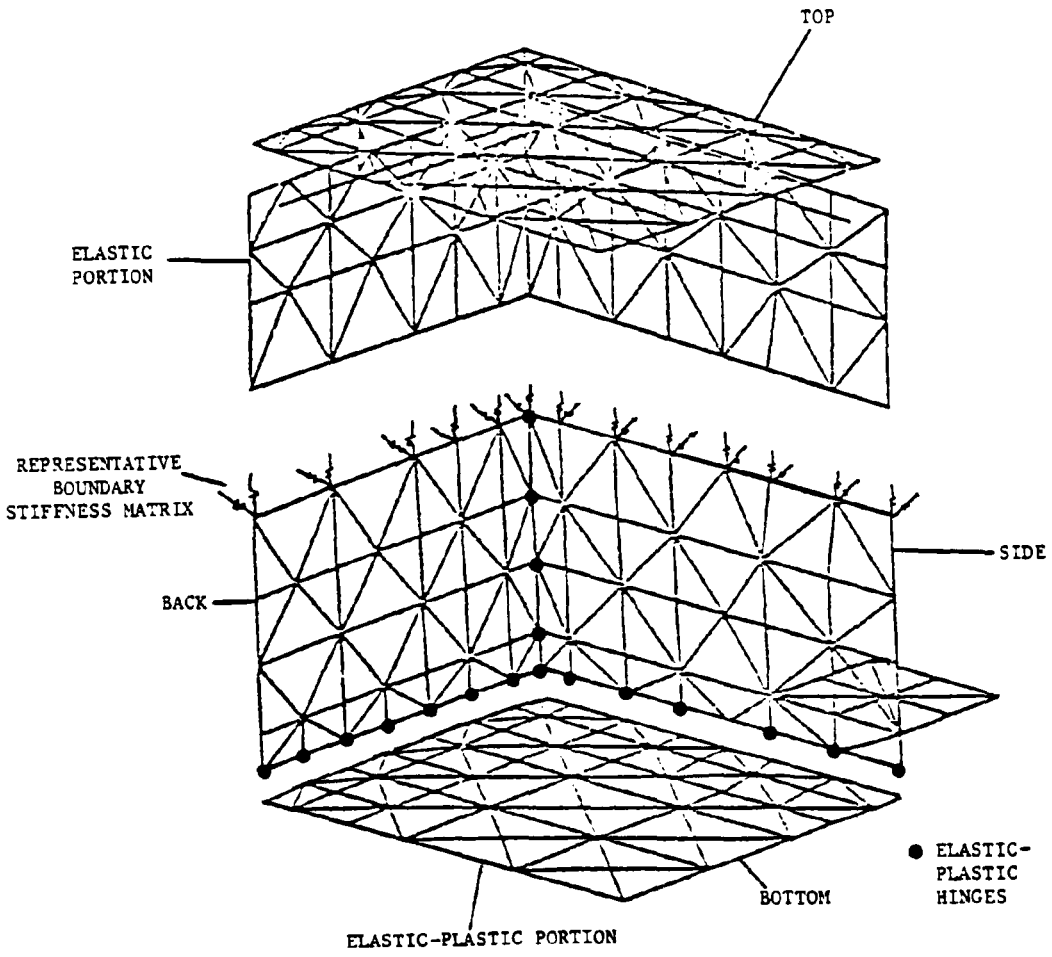

FIGURE 4.19. SUBSTRUCTURE MODEL FOR
ELASTIC-PLASTIC ANALYSIS

4.1.3.2 Finite Element Model

The boundary between the elastic and plastic portions of the model was chosen based on results from the experimental tests and previous analyses. The results indicated the structure above the boundary remained elastic during the loading and the plastic behavior in the elastic-plastic part of the material is well bounded by the elastic-plastic part. The hydrostatic tests on Enclosure I (see Section 4.1.5) showed that the welds joining the bottom to side and side to back sustained permanent deformations. That is, the initially perpendicular plate intersections did not remain normal to each other after loading. This phenomenon of weld yielding can be simulated in the analysis by an elastic/perfectly plastic hinge as shown in Figure 4.20. The hinge element requires knowledge of the stiffness, K, and the hinge moment at yielding, MMAX.

The elastic stiffness, K, was estimated by using results from the two-dimensional analysis of Enclosure I (see Section 4.1.1). This requires that the rotations at the weld-shell interfaces be known for a given applied moment on the weld. Figure 4.20 shows this schematically, and the joint elastic stiffness can be computed from the relationship

$$K = \frac{M}{\theta(I) - \theta(J)}$$

Figures 4.3 and 4.4 presented two levels of sophistication in the modeling of the weld at the intersection of the bottom and side shells. One would expect the values computed from Case III (Figure 4.4) to be more accurate because of the finer mesh in the bottom-side weld area. An analysis of the computer output indicates that

$$K \text{ (Case II, Figure 4.3)} = 1.244 \times 10^5 \frac{\text{in-lb}}{\text{rad}} \text{ in.}$$

$$K \text{ (Case III, Figure 4.4)} = 1.290 \times 10^5 \frac{\text{in-lb}}{\text{rad}} \text{ in.}$$

so both models give quite good agreement with each other. The actual elastic-plastic analysis used the values from Case III, however. Note that these K-values are on a "per inch" basis and must be multiplied by the appropriate factor accounting for the discrete spacing of hinges.

The hinge moment at complete yielding was assumed to equal that required to fully yield an equivalent beam in pure bending. Figure 4.20 shows the model and the hinge moment is

$$Mo = 2\sigma_o BH^2$$

where σ_o = material yield

$2B$ = width

$2H$ = thickness

For Enclosure I,

σ_o = 36,000 psi (A36-structural steel)

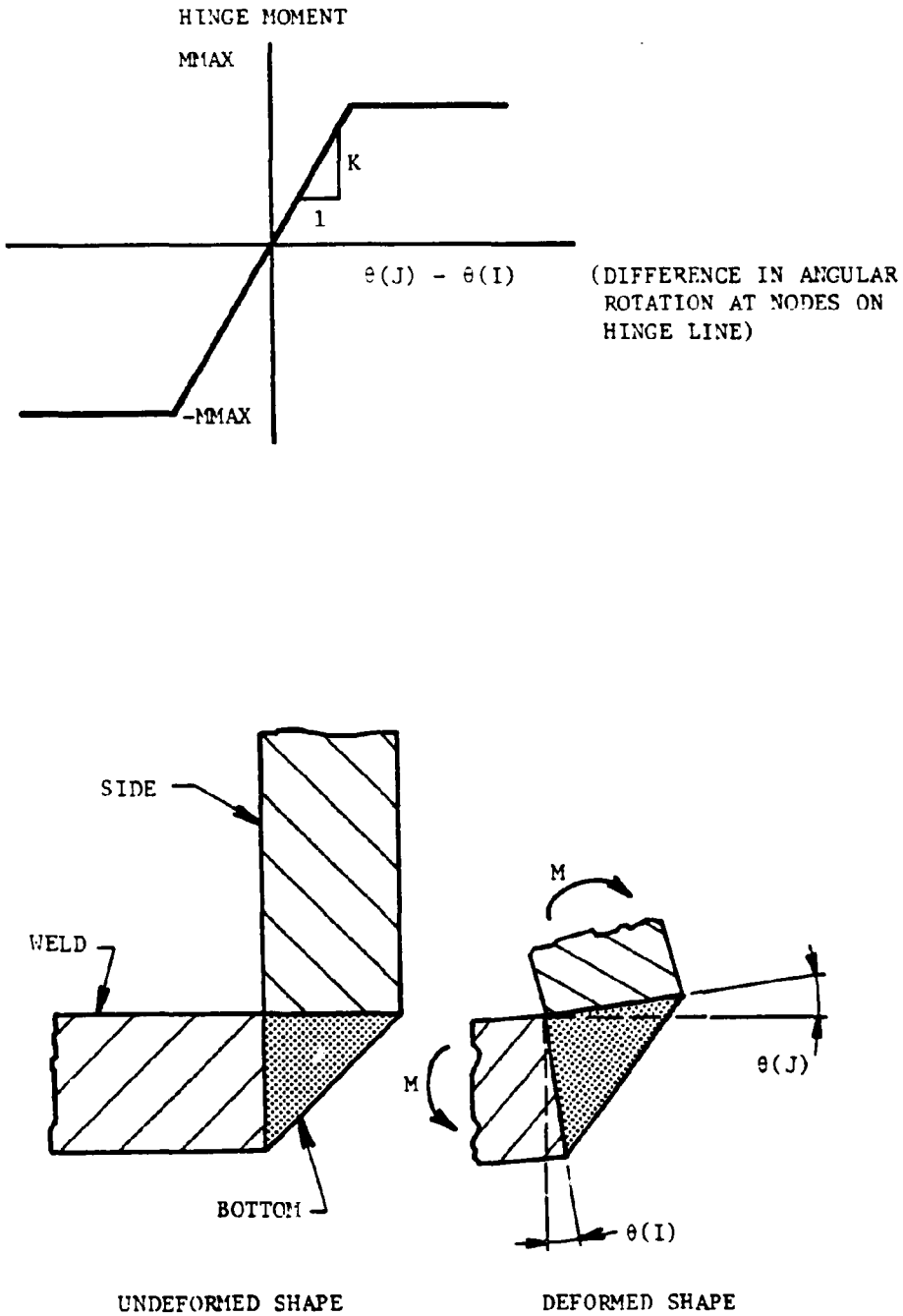

FIGURE 4.20. CHARACTERISTICS OF ELASTIC-PLASTIC HINGE AT WELD: MODELING OF WELD YIELDING AS ELASTIC-PLASTIC HINGE

$2H = 0.25\ (0.707) = 0.177$ in., minimum thickness through the weld

$2B$ = as determined by spacing of elastic-plastic spring elements

This gives

$$\frac{M_o}{2B} = (36{,}000)\left(\frac{0.177}{2}\right)^2 \quad \frac{\text{in-lb}}{\text{in}}$$

$$= 281 \quad \frac{\text{in-lb}}{\text{in}}$$

Values of the spring stiffness and yield moment must be given in units of in-lb/radian and in-lb, respectively. These can be obtained by multiplying the above values by the actual spacing between the elements.

For verification, the moment in the bottom plate, can be computed from the strains measured in the pressure tests. Figure 4.40 in Section 4.1.5 gives the strain 1/4 in. from the wall as

$$\varepsilon_{10} = \varepsilon_x = 0.00084$$

$$\varepsilon_{11} = \varepsilon_y = -0.00006$$

where ε_x is perpendicular to the side wall. This was the maximum value of ε_x which was recorded in the pressure test. As discussed in Section 4.1.5, the strain increased with load until the joint at the side wall yielded. Using this value of strain at yield, a good approximation for the peak moment can be obtained. Juvinal [5] gives an equation for the stress produced by biaxial strains as

$$\sigma_x = \frac{E}{(1-2\nu)}\left[\varepsilon_x + \nu\varepsilon_y\right]$$

$$\sigma_x = \frac{29 \times 10^6}{(1-0.09)}\left[(0.00084) + (0.3)(-0.00006)\right]$$

$$= 26{,}195 \text{ psi}$$

The relationship between moment and stress, neglecting the axial loading, is

$$\sigma = \frac{6M}{(2H)^2}$$

which gives

$$M = \frac{(2H)^2\sigma}{6} = \frac{(0.25)^2(26{,}195)}{6} = 273 \ \frac{\text{in-lb}}{}$$

This gives good agreement with the values estimated from simple beam theory, so

$$M_o = \text{Hinge Moment at Yielding} = 281 \times 2B \text{ in-lb}$$

where B is half of the spacing between hinge elements, was used in the FEM analysis. Nonlinear material properties of the elastic-plastic model are presented in Figure 4.21. The nodal constraints and couplings are the same as those in elastic analysis (Section 4.1.2.2, Figure 4.16).

The finite element program ANSYS was used to generate the model and compute strains and deflections beyond the elastic limit of the enclosure. The generated model was composed of the following elements:

Main Structure (Elastic-Plastic Model)

Components	Element Type	Description
Bottom, Side and Back	STIF48	Plastic Triangular Shell
Angle Iron	STIF48	Plastic Triangular Shell
Weld Joints	STIF58	Plastic Hinge
Upper Section (Including Cover)	STIF50	Substructure

Substructure (Elastic Model)

Components	Element Type	Description
Cover, Side & Back	STIF13	Elastic Flat Triangular Shell
Flange	STIF4	Three-Dimensional Elastic Beam
Bolts	STIF4	Three-Dimensional Elastic Beam
Weld Joints	STIF14	Spring Damper

To initiate the model, the enclosure was first pressurized to 70 psi. This is close to the pressure where yielding starts. During the next step, the pressure was increased to 100 psi and then in successive 25-psi increments until the internal pressure reaches 300 psi. The model was then depressurized using 50-psi increments back to 0 psi.

4.1.3.3 Results

Figure 4.22 shows the magnified deflection (dashed lines), along the center lines of bottom and side plates, superimposed over the undeflected structure (solid lines) during loading. The center of the bottom plate is subjected to the most deformation as expected. Figure 4.23 presents the displacement contour of the same section during unloading. The analytical prediction of the maximum residual displacement for 300-psi internal pressure is 0.35 inch.

In Figures 4.24 and 4.25, the displacements along center lines of bottom and back plates are plotted under loading and unloading, respectively.

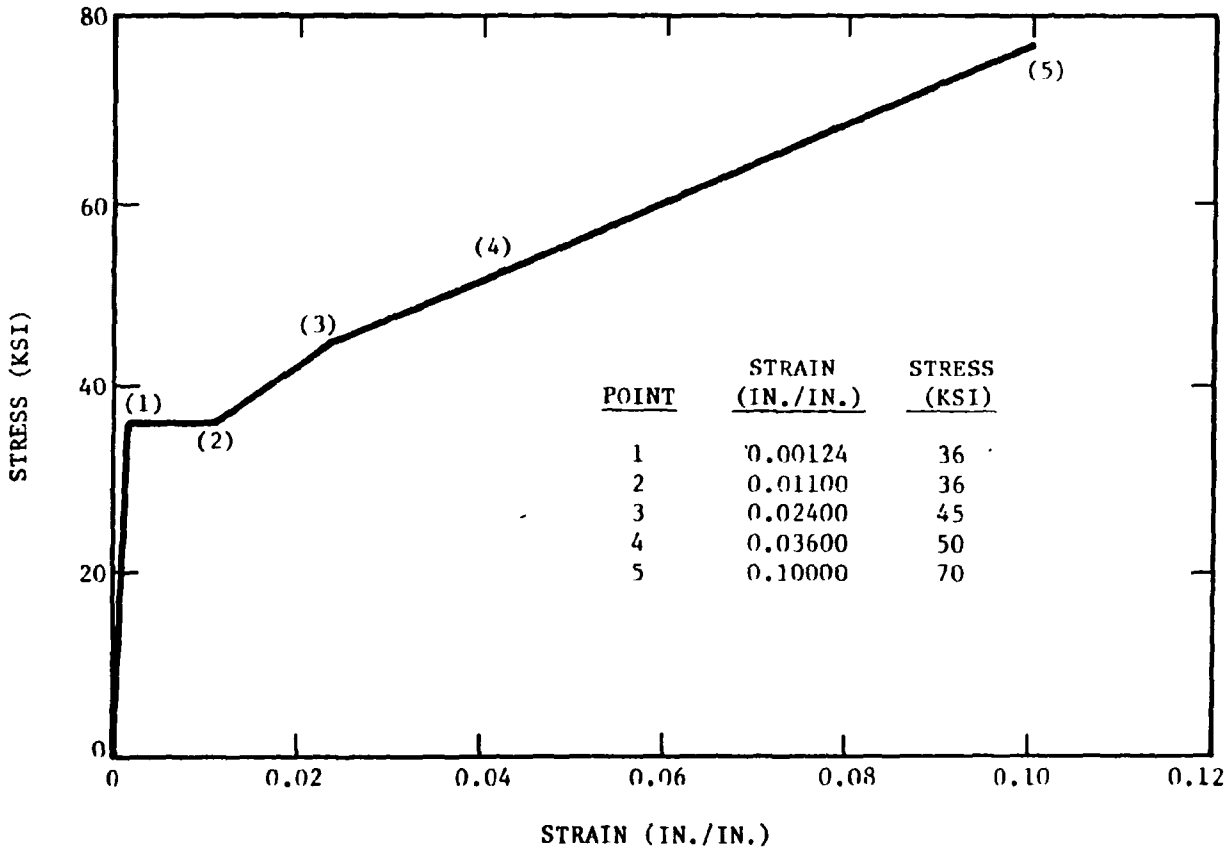

FIGURE 4.21. NONLINEAR MATERIAL PROPERTIES

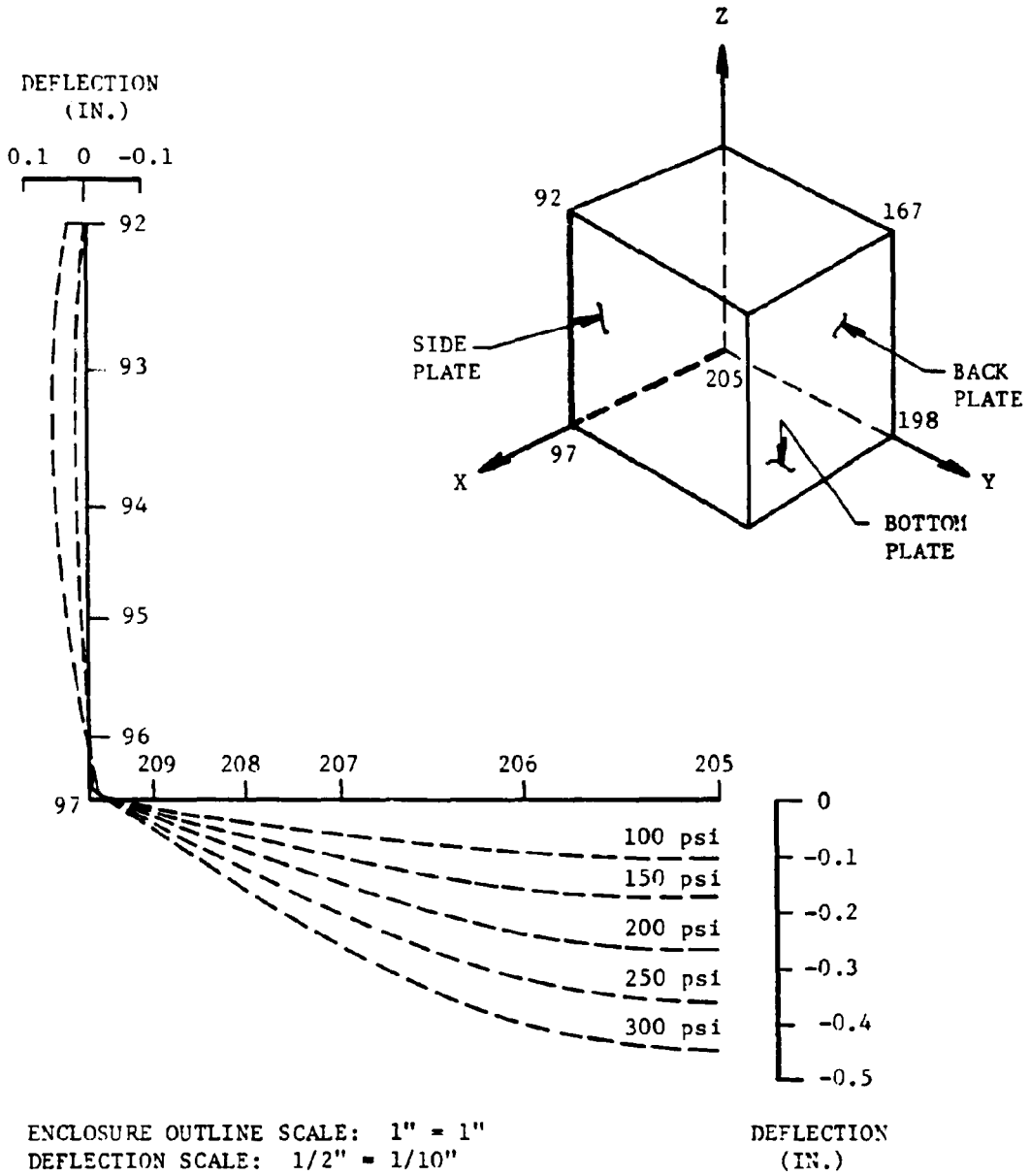

FIGURE 4.22. DEFLECTIONS AT CENTERLINES OF SIDE AND BOTTOM PLATES UNDER INCREASING LOAD (0-300 PSI)

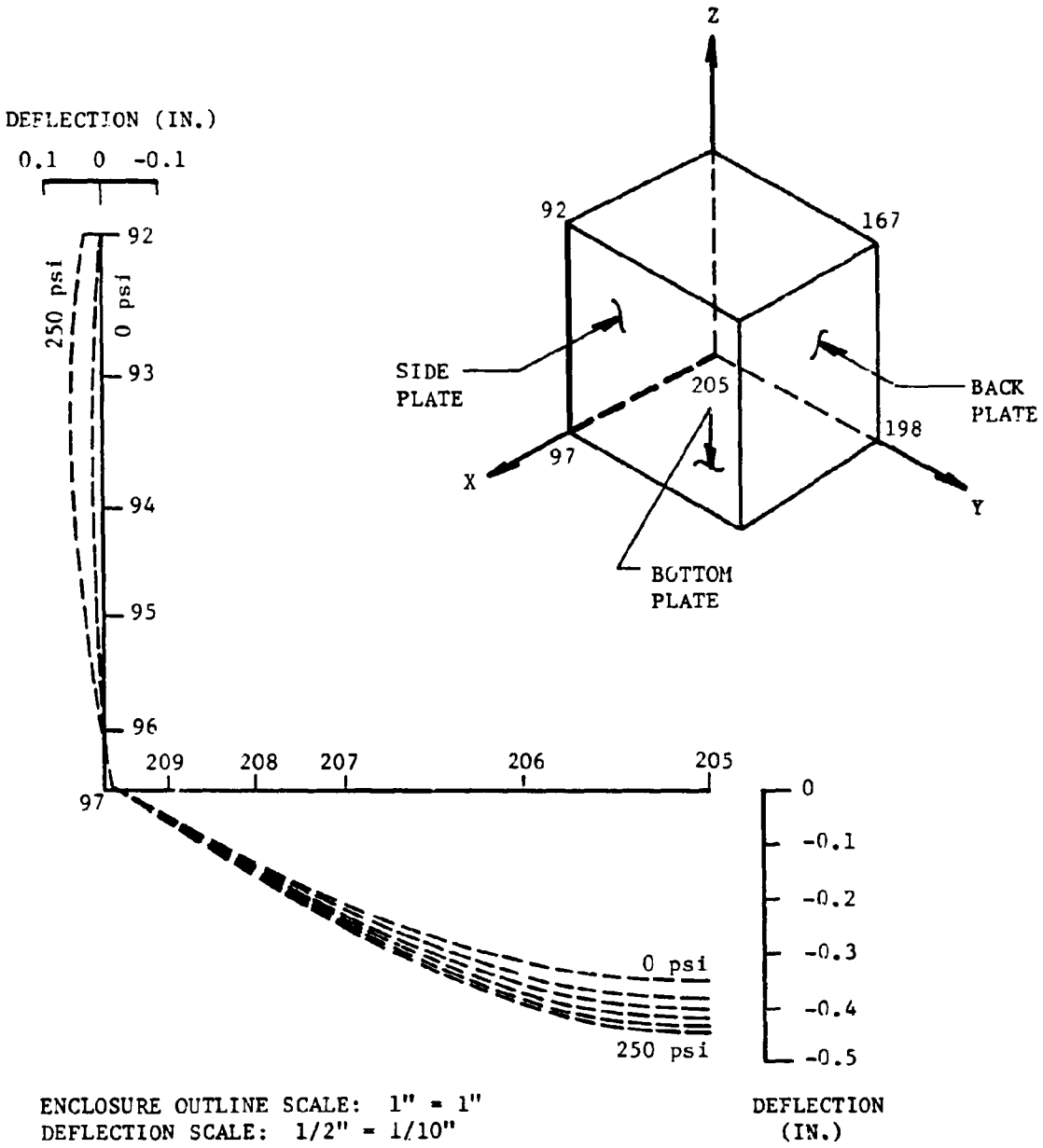

FIGURE 4.23. DEFLECTIONS AT CENTERLINES OF SIDE AND BOTTOM PLATES UNDER DECREASING LOAD (250-0 PSI)

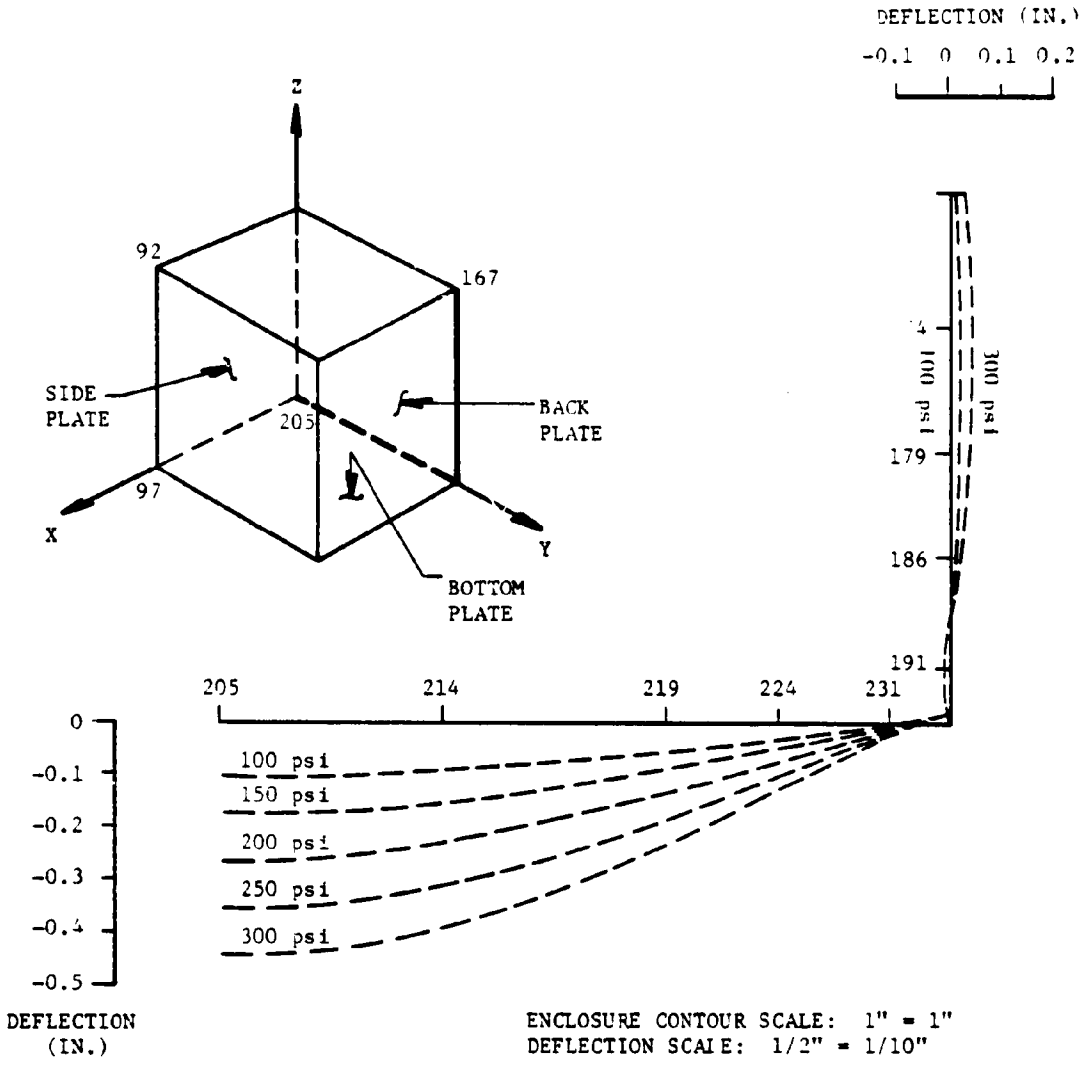

FIGURE 4.24. DEFLECTIONS AT CENTERLINES OF BACK AND BOTTOM PLATES UNDER INCREASING LOAD (0-300 PSI)

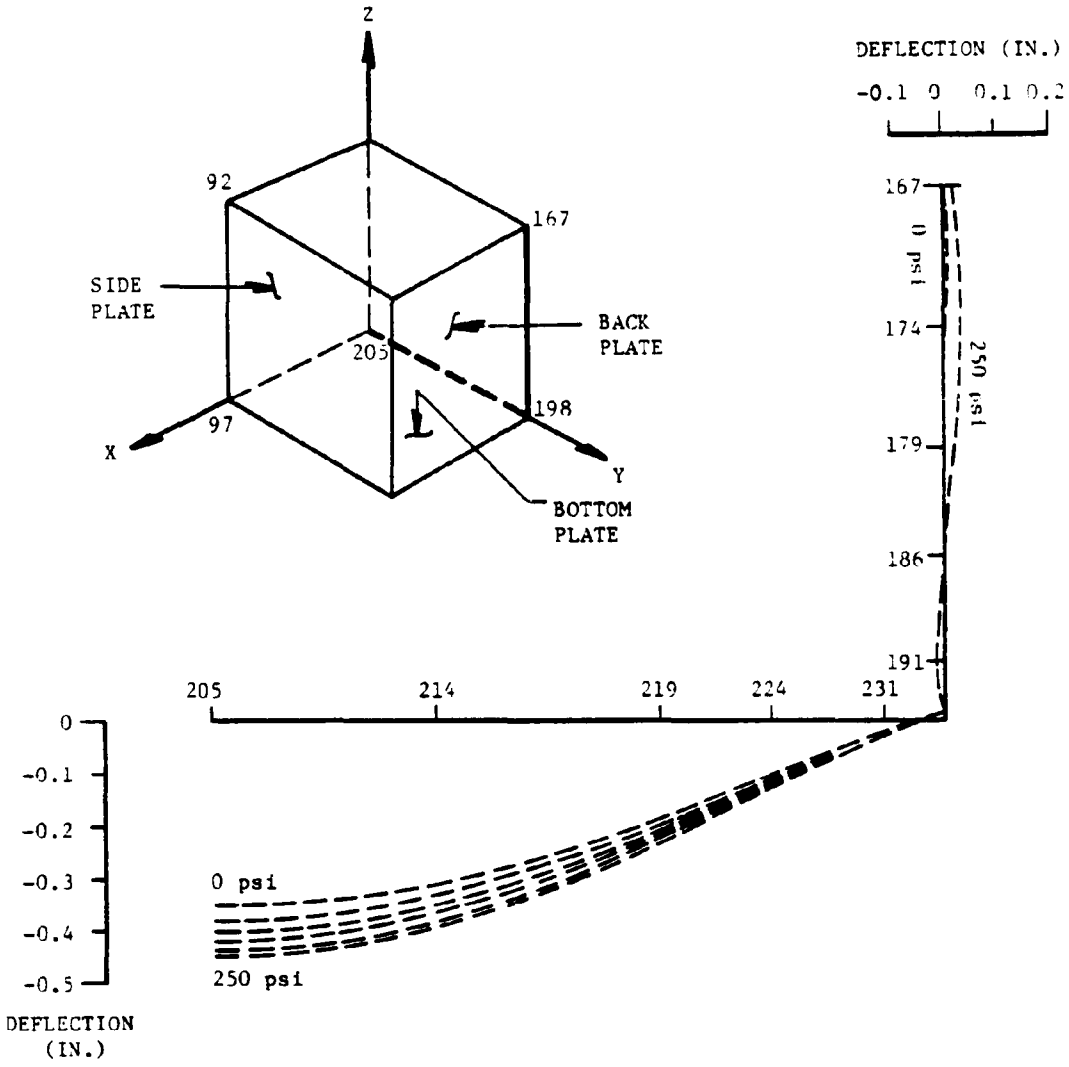

FIGURE 4.25. DEFLECTIONS AT CENTERLINES OF BACK AND BOTTOM PLATES UNDER DECREASING LOAD (250-0 PSI)

The principal conclusion derived from this study is that the elastic-plastic analysis provides more satisfactory solutions compared with those obtained from elastic finite element analysis. However, while the elastic-plastic prediction was in general agreement with the physical behavior of the enclosure, it failed to provide a good fit to the test results quantitatively. The comparison of these analytical and experimental results in Section 4.1.6 indicates that the properties of the weld joint (elastic-perfect plastic hinge) played a major role in this difference. Should more realistic bending stiffness of the hinge element be provided, the elastic-plastic analysis can prove to be an accurate method of computing the stress, strain, and deformation of the enclosure.

4.1.4 Dynamic Analysis of Enclosure I

In the mine, XP enclosures must contain the explosion of a methane-air mixture, should such a mixture form in the enclosure and be ignited. Overpressures produced in the enclosure by the explosion will occur rapidly and may cause greater stresses and deflection in the enclosure than would be produced by a static pressure of the same peak magnitude. This increase in the response of the loaded structure produced by a dynamic load is often accounted for by a dynamic load factor (DLF). The peak load (or pressure), when multiplied by the dynamic load factor, gives an equivalent static load which produces the same stresses and deflections as the dynamic load. The dynamic load factor is a function of the rise time and decay time of the loading, the shape of the load-time pulse, and the natural frequencies of the loaded structure. In this section the dynamic effects produced by a methane-air explosion inside Enclosure I are investigated.

4.1.4.1 Verification of FEM Mesh

To use the finite element model developed for the static analysis to determine the dynamic response, it is necessary to verify the model in some manner. This was done for the static case by subjecting the model of the cover to a uniform loading and comparing the deflections and stresses with the classical solutions (see Section 4.1.2). For the dynamic case, the model was verified by comparing the natural frequencies of the cover with those obtained from classical plate theory. The central question in the model analysis was the correct choice of dynamic degrees of freedom for the ANSYS computer program. Whereas classical theory gives an infinite set of natural frequencies, the finite element model produces a set equal to the number of dynamic degrees of freedom. The accuracy of the solution increases as this number increases, but so do the costs of obtaining a solution. Therefore, it behooves the user to select only those dynamic degrees of freedom consistent with the accuracy of the desired solution.

Figure 4.26 shows the locations of the 16 dynamic degrees-of-freedom chosen for the one-quarter model of the cover. Only dynamic degrees-of-freedom in the U_z direction, normal to the plate, were chosen because the lower modes are due to bending. Symmetric boundary conditions were given to those nodes on the planes (x-z and y-z) of symmetry so the solution will only contain symmetric modes and the corresponding

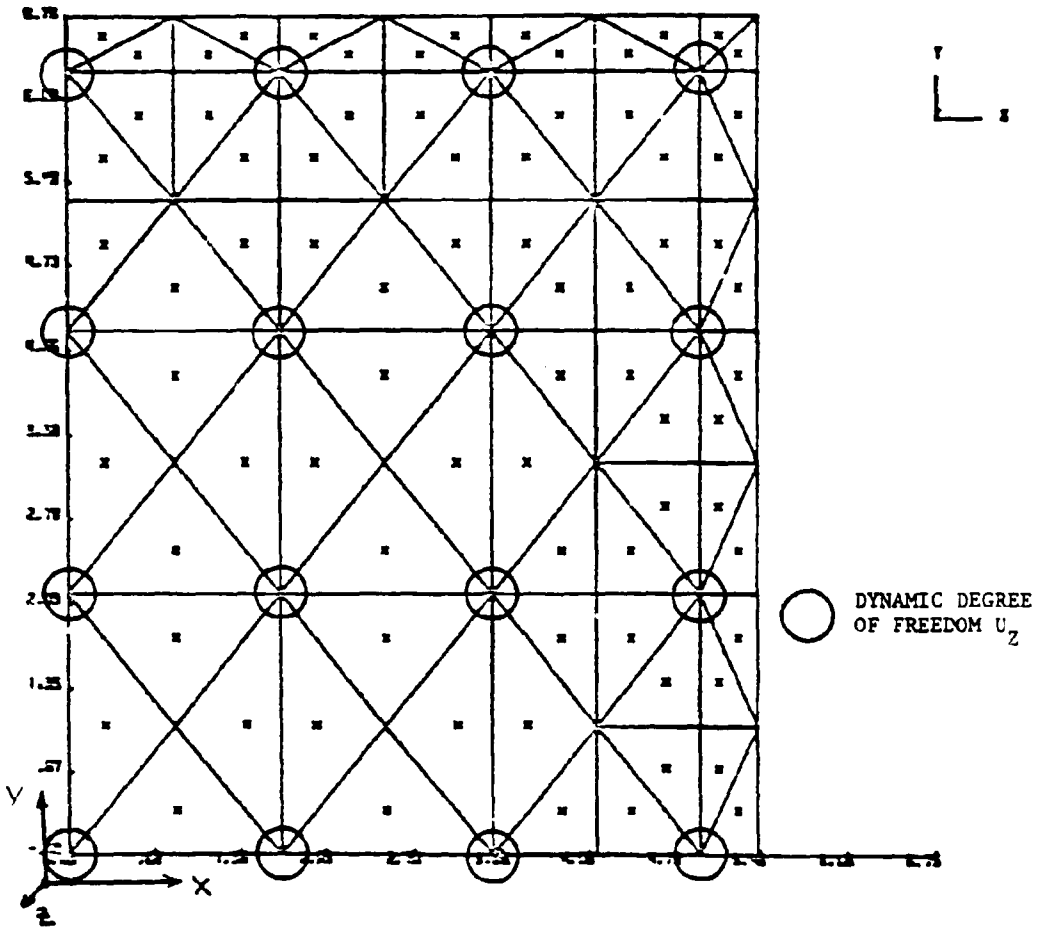

FIGURE 4.26. FINITE ELEMENT MESH OF 1/4 MODEL OF COVER
SHOWING DYNAMIC DEGREES OF FREEDOM

frequencies. Only these symmetric modes will be present in the solution if the plate is subjected to a uniform dynamic pressure loading as is the case for the enclosure.

Figures 4.27 and 4.28 show the first five mode shapes and natural frequencies for the simply supported and clamped cover. The natural frequencies can also be calculated analytically [6], and the results are presented in Table 4.2. Only the first three natural frequencies for the clamped case are given because of the limited analytical results. Nevertheless, the results betwen the finite element model and classical theory show excellent agreement, and it can be concluded that the model with the selected dynamic degrees of freedom will adequately represent the dynamic behavior of the cover. Therefore, this approach to selecting the dynamic degrees-of-freedom was applied to the three-dimensional model of Figure 4.15, which was used in the static pressure calculations, in order to calculate the natural frequencies of Enclosure I.

TABLE 4.2. NATURAL FREQUENCIES FOR CLAMPED AND SIMPLY SUPPORTED COVER MODELS

	Simply Supported Plate			Clamped Plate		
Mode	FE Model Hertz	Analytical Hertz	% Diff.	FE Model Hertz	Analytical Hertz	% Diff.
1	650	661	-1.7	1187	1213	-2.1
2	2674	2711	-1.4	3599	3638	-1.1
3	3796	3895	-2.5	5073	5255	-3.5
4	6002	5945	1.0	7561	----	----
5	6962	6812	2.2	8266	----	----

4.1.4.2 Estimation of Natural Frequencies

Sixteen dynamic degrees of freedom were selected normal to each of the four surfaces (top, bottom, side, and back) which gave a model with 64 degrees-of-freedom. In addition, all boundary conditions, which were imposed for the elastic analysis (see Figure 4.15, Section 4.1.2), were also imposed for the natural frequency determination.

Figure 4.29 shows the mode shapes and natural frequencies of Enclosure I for the first seven modes. The first mode represents essentially rigid body motion of the container vibrating in the Z-direction on the support flanges. Figure 4.30 schematically shows this behavior and indicates that this mode can be closely approximated by treating the container as rigid and the flanges as cantilever beams. The approximate frequency of 304 Hertz, computed with the simple model, is higher than the 224 Hertz computed by the ANSYS program because the flexibility of the container side wall at its connection with the angle iron, was ignored in the simple solution. This flexibility produced the side wall distortion evident in Figure 4.29 for the first mode shape.

The second mode (497 Hertz) involves primarily the bottom shell. For a plate with the properties of the bottom shell, the

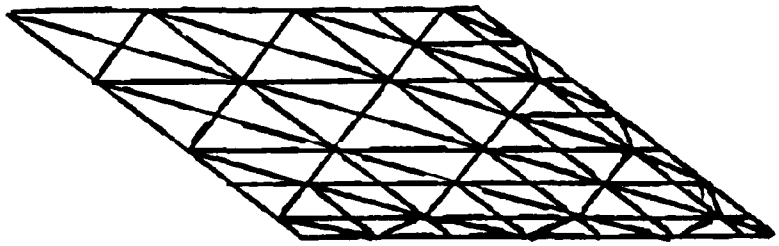

Undeflected Shape

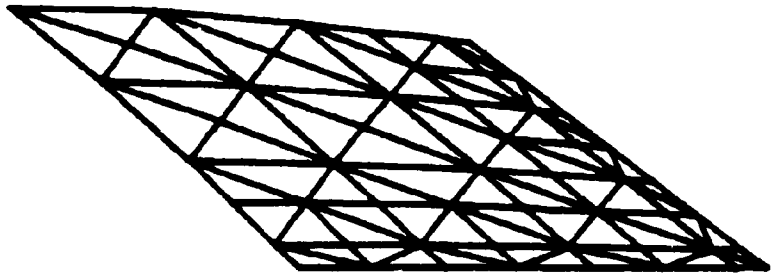

f_1 = 650 Hertz

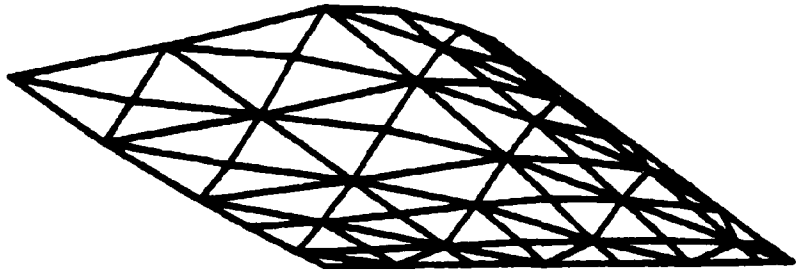

f_2 = 2674 Hertz

FIGURE 4.27. FIRST FIVE SYMMETRIC MODE SHAPES AND NATURAL FREQUENCIES FOR SIMPLY SUPPORTED PLATE

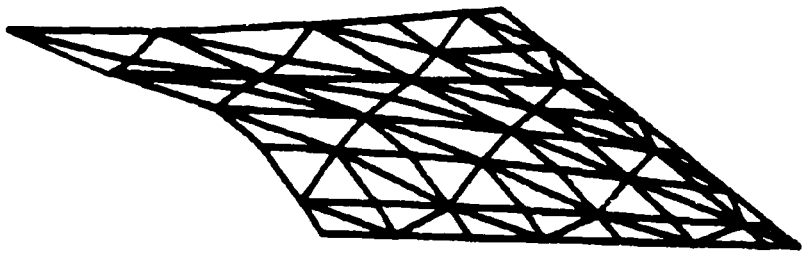

f_3 = 3796 Hertz

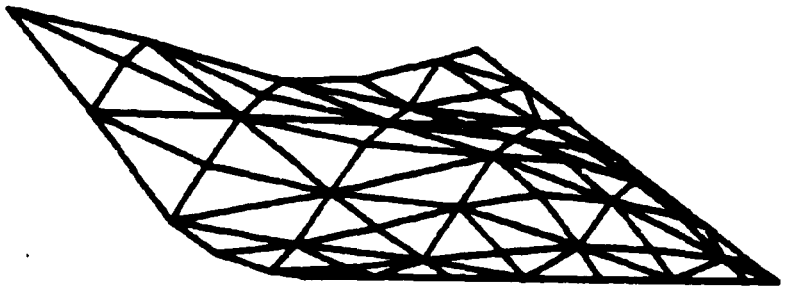

f_4 = 6002 Hertz

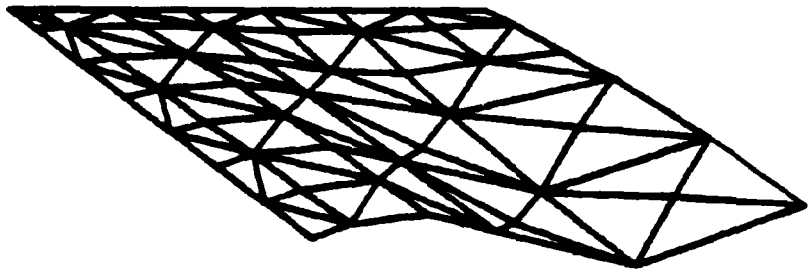

f_5 = 6962 Hertz

FIGURE 4.27. FIRST FIVE SYMMETRIC MODE SHAPES AND NATURAL FREQUENCIES FOR SIMPLY SUPPORTED PLATE (Concl'd)

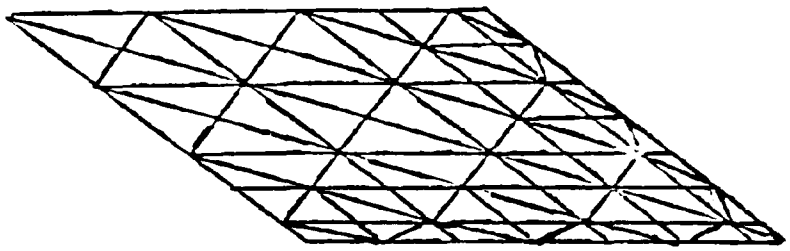

Undeflected Shape

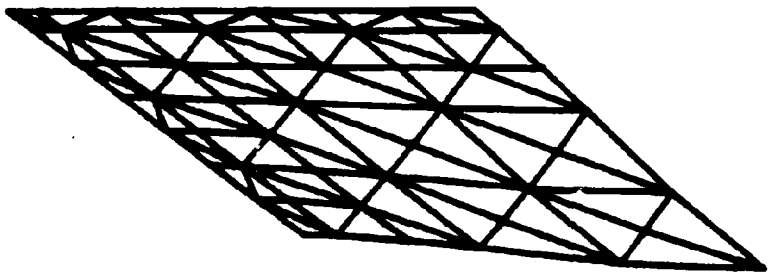

f_1 = 1187 Hertz

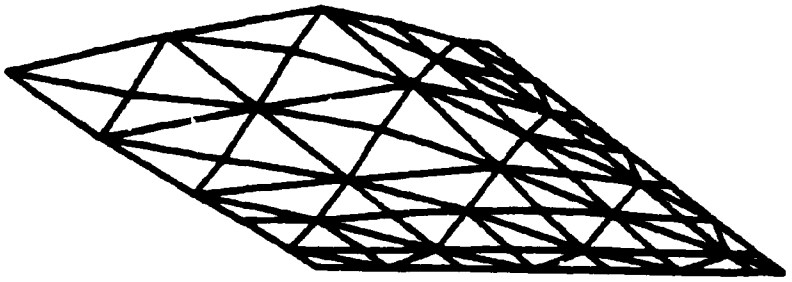

f_2 = 3599 Hertz

FIGURE 4.28. FIRST FIVE SYMMETRIC MODE SHAPES AND NATURAL FREQUENCIES FOR CLAMPED PLATE

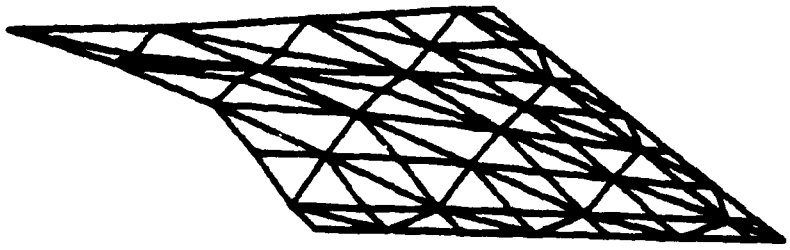

f_3 = 5073 Hertz

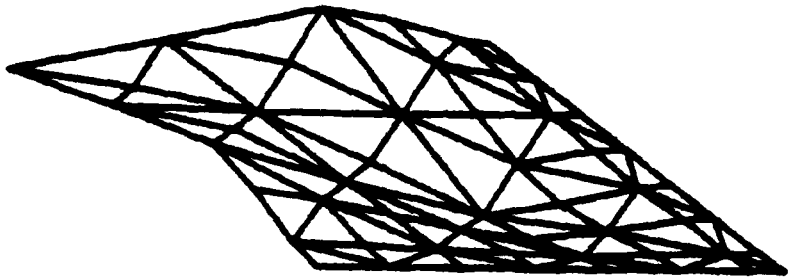

f_4 = 7561 Hertz

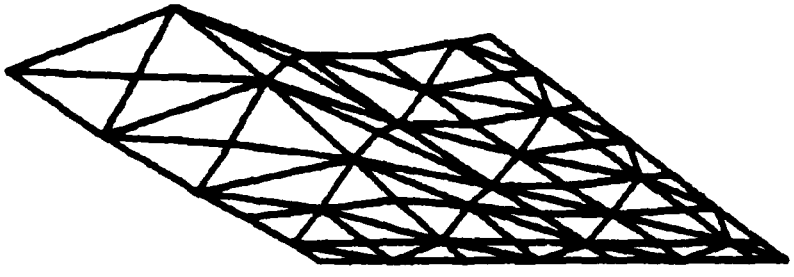

f_5 = 8266 Hertz

FIGURE 4.28. FIRST FIVE SYMMETRIC MODE SHAPES AND NATURAL FREQUENCIES FOR CLAMPED PLATE (Concl'd)

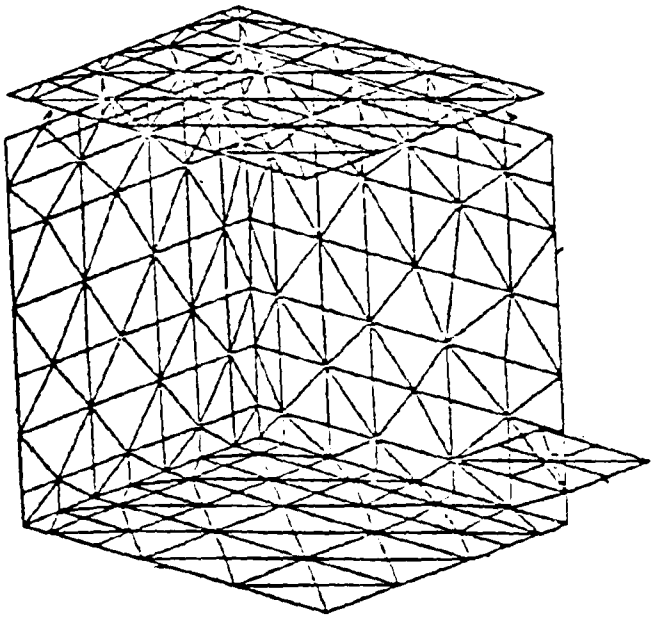

Undeflected Shape

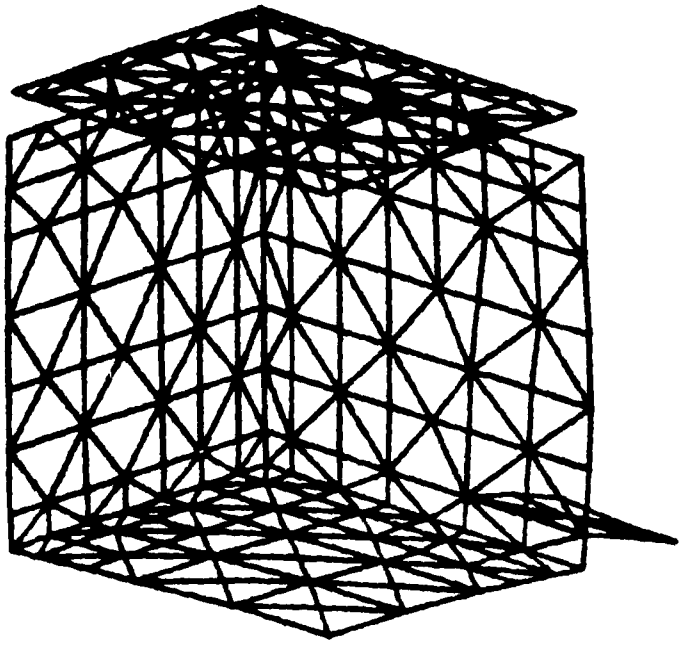

f_1 = 224 Hertz

FIGURE 4.29. FIRST SEVEN SYMMETRIC MODE SHAPES AND NATURAL FREQUENCIES FOR ENCLOSURE I

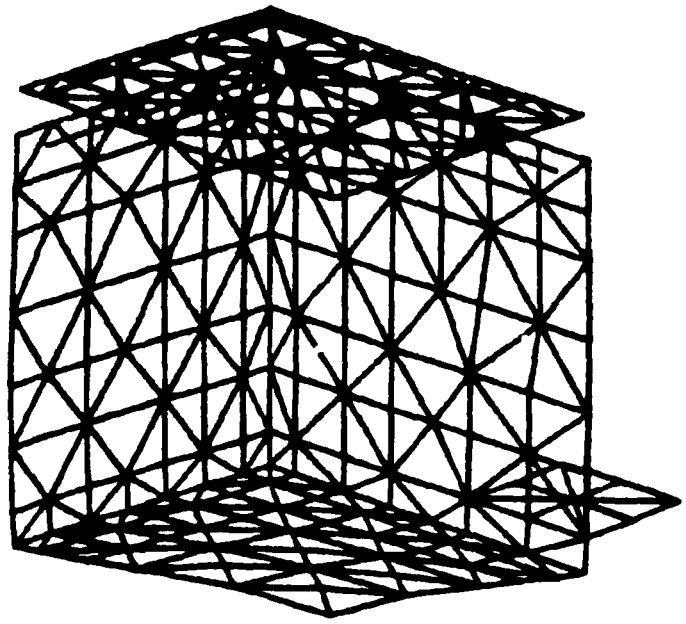

f_2 = 497 Hertz

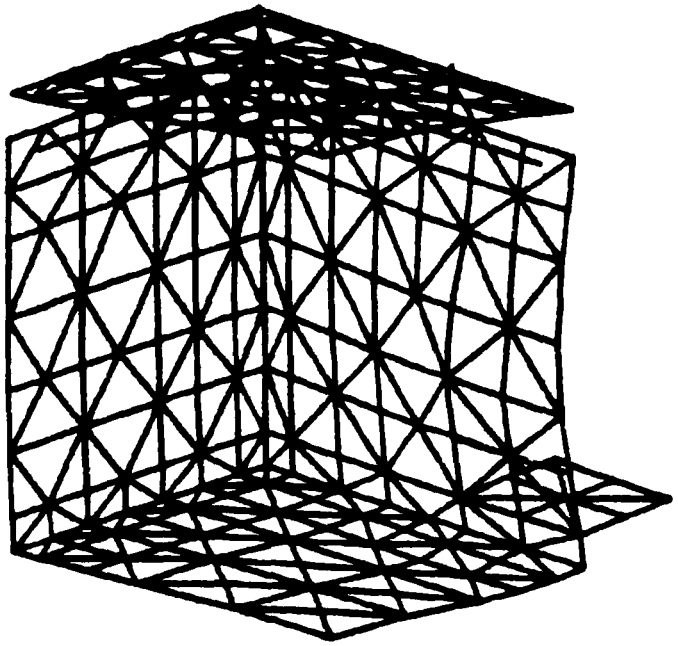

f_3 = 933 Hertz

FIGURE 4.29. FIRST SEVEN SYMMETRIC MODE SHAPES AND NATURAL FREQUENCIES FOR ENCLOSURE I (Cont'd)

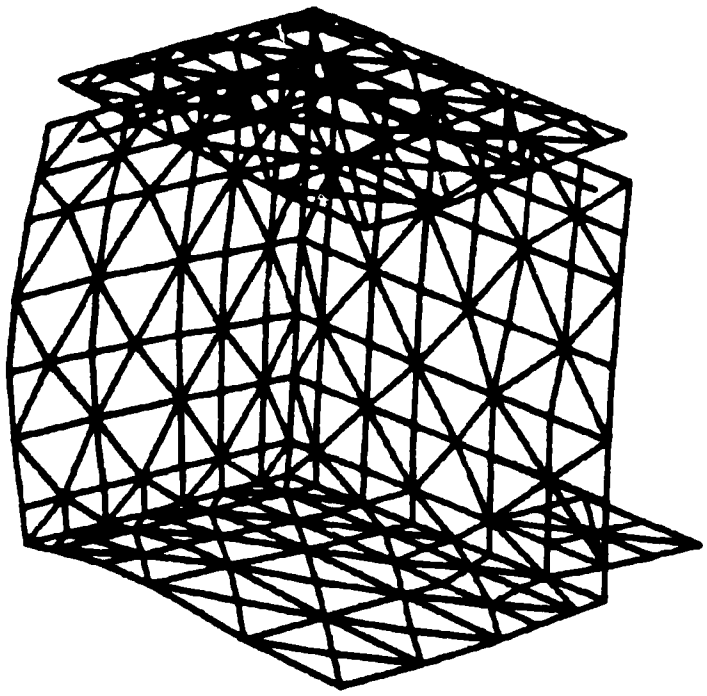

f_4 = 1014 Hertz

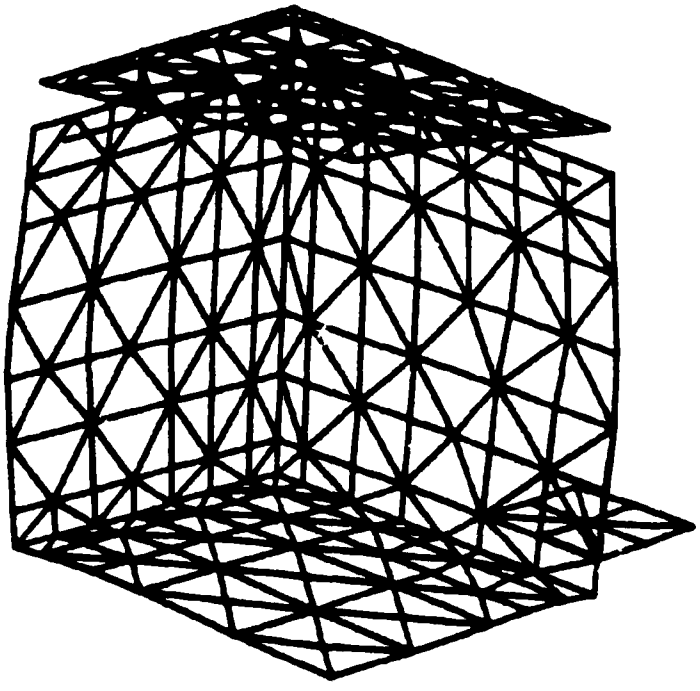

f_5 = 1135 Hertz

FIGURE 4.29. FIRST SEVEN SYMMETRIC MODE SHAPES AND NATURAL FREQUENCIES FOR ENCLOSURE I (Cont'd)

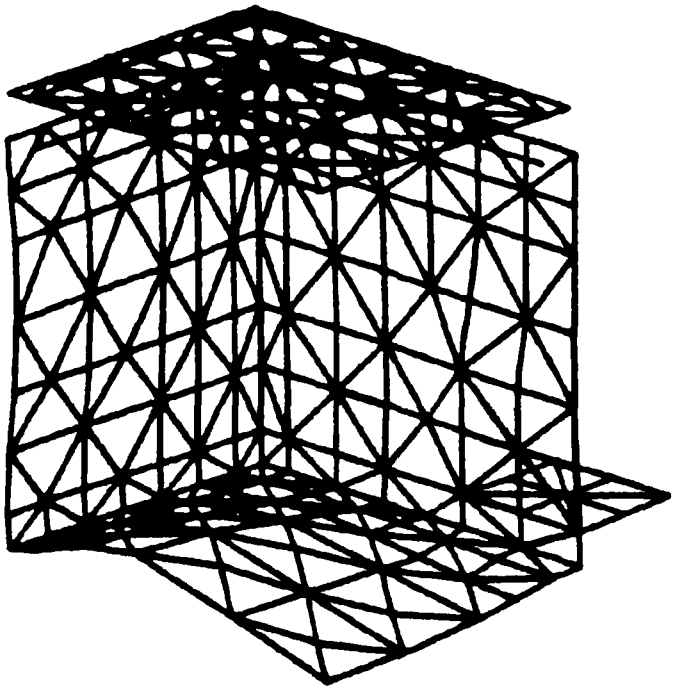

f_6 = 1564 Hertz

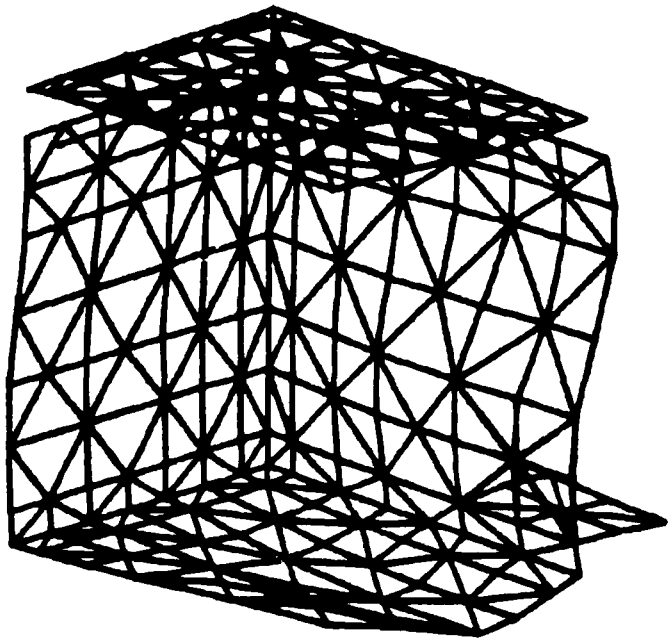

f_7 = 1960 Hertz

FIGURE 4.29. FIRST SEVEN SYMMETRIC MODE SHAPES AND NATURAL FREQUENCIES FOR ENCLOSURE I (Concl'd)

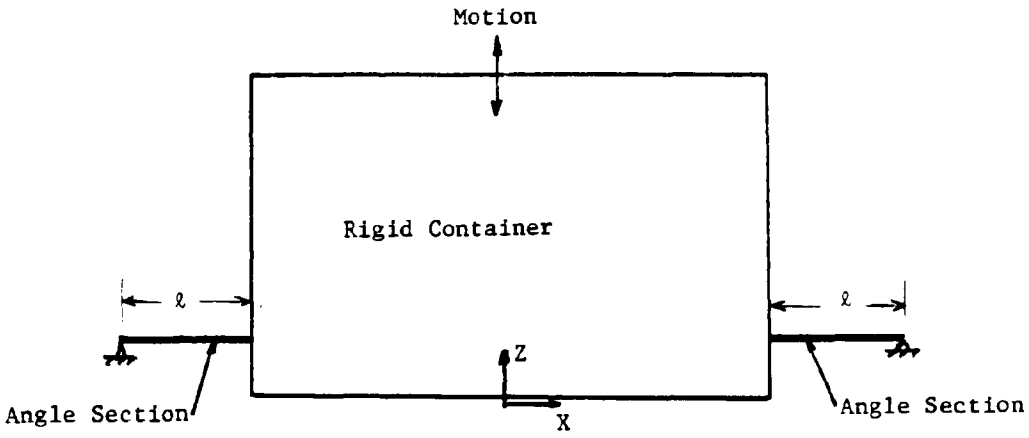

$$I_{\text{angle section}} = \frac{(2.515)\ (0.25)^3}{12}\ \text{in}^4 = 0.032747\ \text{in}^4$$

$$E = 29 \times 10^6\ \text{lb/m}^2 \qquad \ell = 1.00\ \text{in}$$

$$k = \frac{6EI}{\ell^3} = 5.698 \times 10^5\ \text{lb/in} \qquad m = 60.4\ \text{lbm}$$

$$f = \text{frequency} = \frac{1}{2\pi}\sqrt{\frac{K}{M}} = 304\ \text{Hertz}$$

FIGURE 4.30. FIRST VIBRATION MODE OF ENCLOSURE I

first natural frequencies for the simply supported and fixed cases are [6]:

f (simply supported) = 320 Hertz

f (fixed) = 594 Hertz

4.1.4.3 Character of the Dynamic Loading

Dynamic pressures are produced in an enclosure during the Explosion Test. These pressures are routinely measured by MSHA during testing and have also been measured by other investigators. For a spherical enclosure, a typical pressure-time history is given by Zabetakis [7] in Figure 4.31. To analyze the response of an enclosure for the explosion pressure; its magnitude, rise time, and duration must be known; however, because the enclosure is closed (usually tightly closed) during the Explosion Test and in service, the pressure does not decay rapidly; so, its duration can be treated as long relative to the response time of the enclosure. For this case only the peak pressure and rise time are needed.

The peak pressure which theoretically can occur in a closed volume from the ignition of a mixture of methane and air at the stoichiometric* ratio is 117 psig. This pressure is produced by complete combustion and assumes that no heat loss to the walls of the enclosure and, of course, no pressure piling occur. A more realistic upper limit for the pressure is the measured value shown in Figure 4.31. This pressure is for a 9.6% by volume methane-air mixture, which in practice gives the highest measured value of the explosion pressure. Also, this pressure was measured in a spherical chamber with central ignition, which is an idealized condition relative to most enclosure tests. Typical values of pressure measured by MSHA in the Explosion Test are 60-80 psig. Thus, a peak explosion pressure of 100 psig was taken as a reasonable value in this analysis.

The rise time of the explosion pressure, as well as its magnitude, is needed to calculate the response of the enclosure to the dynamic loads. Further, a short rise time generally produces a greater response in the enclosure than a long one. To determine the minimum rise time, it is convenient to use the maximum rise rate of the pressure. Again, the data in Figure 4.31 for spherical enclosures were used. Using the maximum rise rate determined for spherical enclosures will not guarantee that a minimum rise time for Enclosure I will be obtained, but using a minimum estimated rise time is conservative, and so the approach is appropriate for this analysis.

An approximate relationship between the time from ignition to peak pressure and the enclosure volume is given by Zabetakis [7] as

$$t = 75 \sqrt[3]{V}, \text{ ms} \qquad (4.1)$$

*Ratio at which there is, theoretically, just sufficient oxygen in the air for complete combustion of all of the methane. This ratio is 9.5% for methane and air.

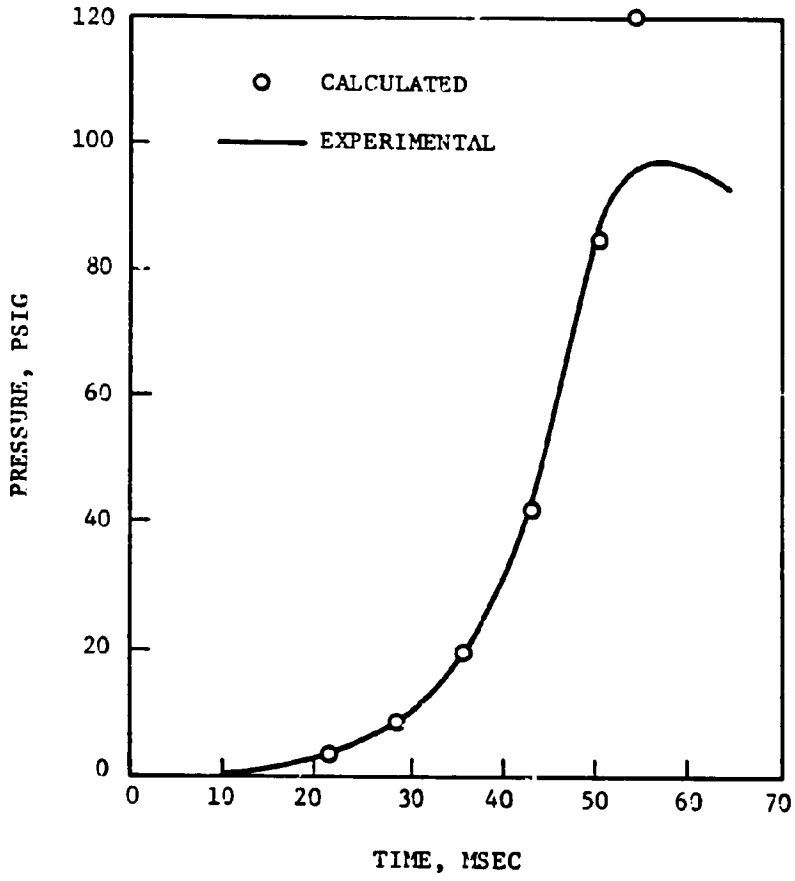

(a)

FIGURE 4.31. PRESSURE IN A 9-LITER SPHERICAL CHAMBER PRODUCED BY IGNITION OF A 9.6% (BY VOLUME) CH_4-AIR MIXTURE (REF. 7)

where V is in ft^3 and t is in milliseconds. This is not a minimum rise time, but Equation (4.1) can be used to scale a minimum rise time or maximum rise rate determined for one enclosure to enclosures with different volumes. A maximum rise rate for a 9-liter enclosure is estimated from Figure 4.31. Taking the tangent to the steepest part of the curve in Figure 4.31 gives a pressure rise rate of

$$P_{max} = \frac{97 \text{ psi}}{10.5 \text{ ms}} = 9.2 \text{ psi/ms} \qquad (4.2)$$

Combining equations (4.1) and (4.2) and taking a maximum pressure of 100 psig gives the following equation for the minimum rise time:

$$t_{r_{min}} = 21 \sqrt[3]{V}, \text{ msec} \qquad (4.3)$$

(V in ft^3)

Enclosure I has an internal volume of 0.60 ft^3, which gives a minimum rise time of 17.7 msec.

4.1.4.4 Calculation of the Dynamic Load Factor

Once the natural frequencies and rise time for the enclosure had been calculated, the dynamic load factor could be determined. The simplest approach for estimating the DLF is to base it on the fundamental frequency of the structure or component. With this approach, a single degree-of-freedom approximation can be used as described by Biggs [8]. For an elastic oscillator, the DLF for a loading which rises to a constant value (a suitable approximation for the pressure-time history in the enclosure) is given by Figure 4.32. It involves symmetric bending of the bottom and sides of the enclosure. Now, taking for t_r the value of 17.7 msec, as determined in the preceding section, the ratio of the rise time to frequency is

$$t_r/T = \frac{0.0177 \text{ sec}}{1/497 \text{ cyc/sec}} = 8.8$$

This value of t_r/T falls outside the range of Figure 4.32, but the maximum DLF is estimated to be about 5%. Note that longer rise times will only give lower values of the DLF.

The contribution of higher modes to the DLF is treated in Appendix C. The results show that for Enclosure I, neglecting all but the fundamental mode is entirely appropriate. Thus, for enclosures similar in size to Enclosure I, it can be concluded that dynamic effects produced by the ignition of methane and air without pressure piling produce insignificant dynamic effects. The effect of pressure piling would be to increase the magnitude of the pressures and reduce the rise time locally in the enclosure. It is still doubtful that, for pressures less than 200 psig, the dynamic effects will be significant. The results of a literature survey on pressure piling is included as Appendix D. It shows that the pressure magnitudes and impulses associated with pressure piling

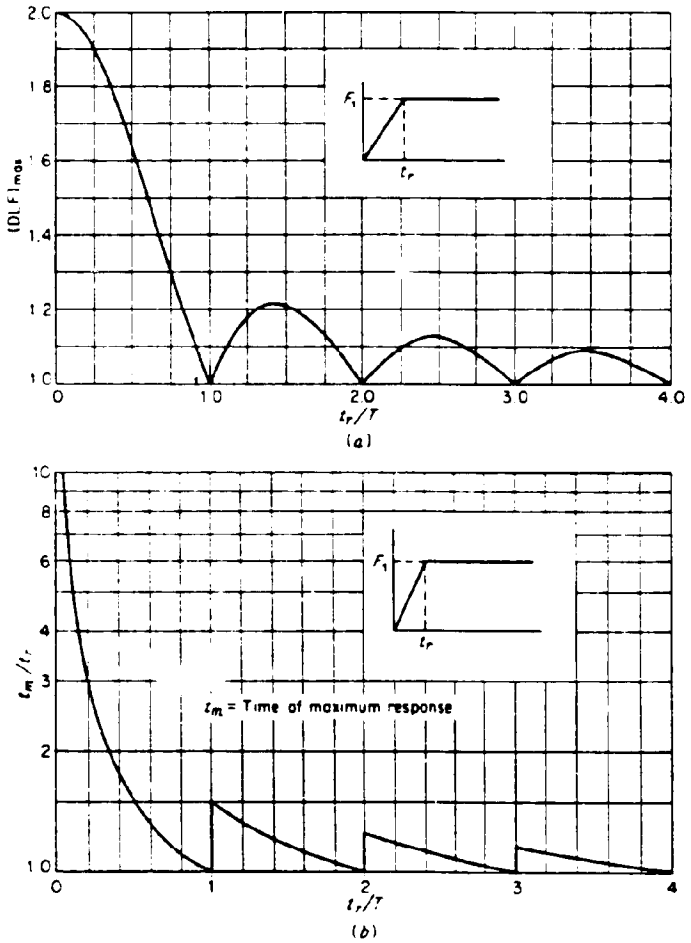

FIGURE 4.32. MAXIMUM RESPONSE OF ONE-DEGREE ELASTIC SYSTEMS (UNDAMPED) SUBJECTED TO CONSTANT FORCE WITH FINITE RISE TIME (FROM REF. 8)

cannot be predicted quantitatively based on the current state-of-the-art.

4.1.5 Testing of Enclosure I

Two very similar enclosures, which were identified as enclosures I and IA, were obtained and tested. The only obvious differences in the two enclosures were that Enclosure I had a threaded penetration through the cover and two mounting bars welded to the bottom on the inside of the enclosure, and Enclosure IA did not. Enclosure I was tested first as described in this section. Because of the substantial yielding which occurred in Enclosure I, Enclosure IA was obtained to more carefully measure the permanent distortions in the enclosure bottom plate. Testing of Enclosure IA is described in Section 4.1.6.

4.1.5.1 Methodology

Enclosure I was hydrostatically tested in accordance with the procedure given in Appendix E, "Structural Performance Test for Schedule 2G Enclosures." Figure 4.33 shows a schematic of the test apparatus. Hydraulic testing, as opposed to pneumatic testing, was chosen for safety reasons, and the amount of compressed air in the enclosure and in the reservoir was kept to a minimum.

Prior to testing the enclosure was instrumented with strain gages at five locations as shown in Figure 4.34. Three-element 45° single plane rosettes were used at each location, giving a total of 15 channels of strain data. The gage elements were identified as follows:

Rosette	Location	Element Orientation
1	Top of Cover	ε_1, ε_2, ε_3 — Looking from Top
2	Bottom (Inside)	ε_4, ε_5, ε_6 — Looking from Top
3	Bottom (Outside)	ε_7, ε_8, ε_9 — Looking from Top
4	Right Side (Inside)	ε_{10}, ε_{11}, ε_{12} — Looking from Outside
5	Back Side (Inside)	ε_{13}, ε_{14}, ε_{15} — Looking from Outside

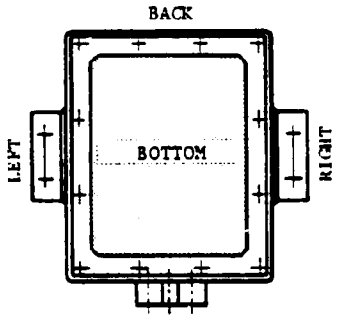

ENCLOSURE I WITHOUT COVER—LOOKING INSIDE

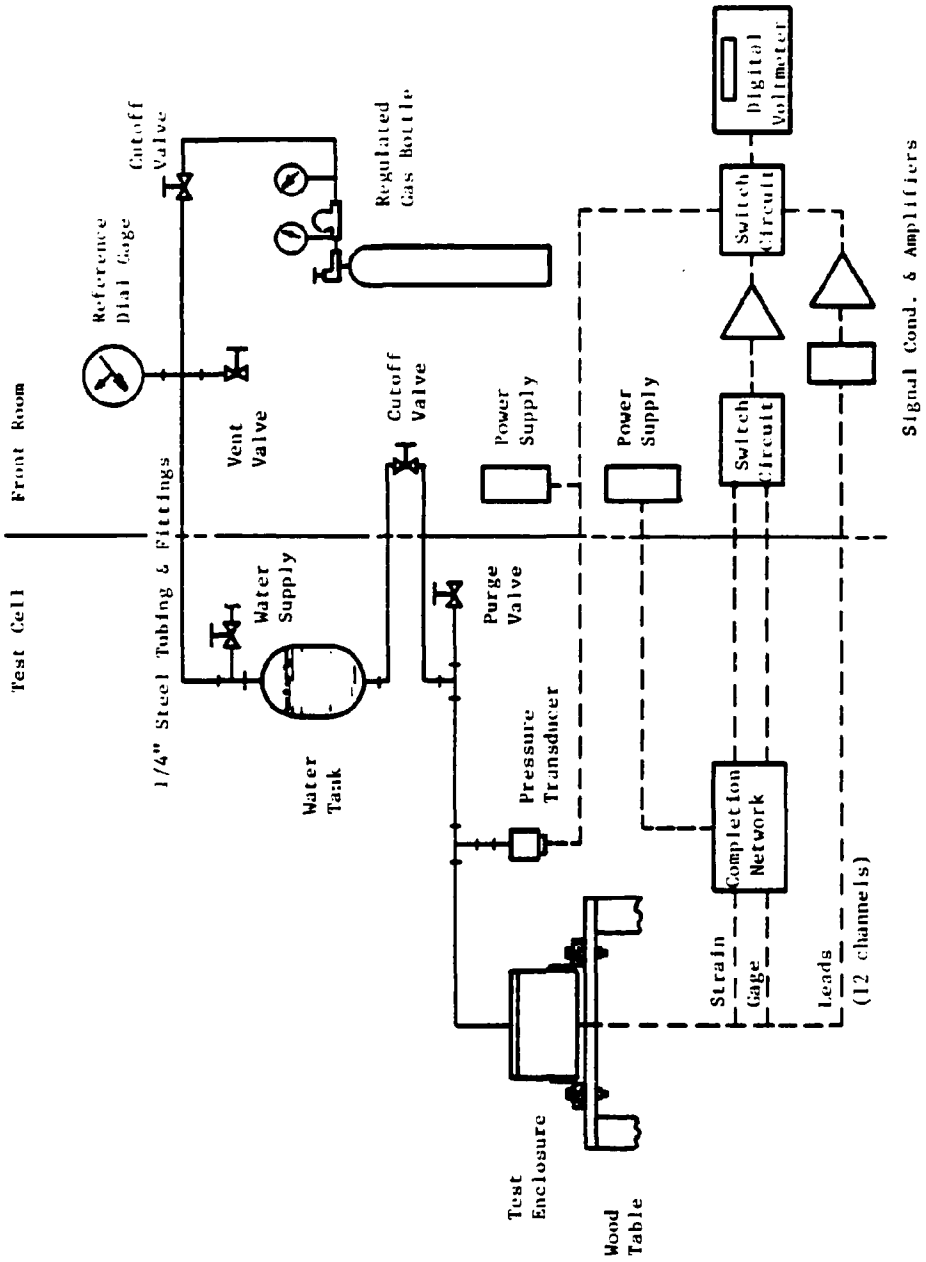

FIGURE 4.33. DIAGRAM OF EXPERIMENTAL SETUP

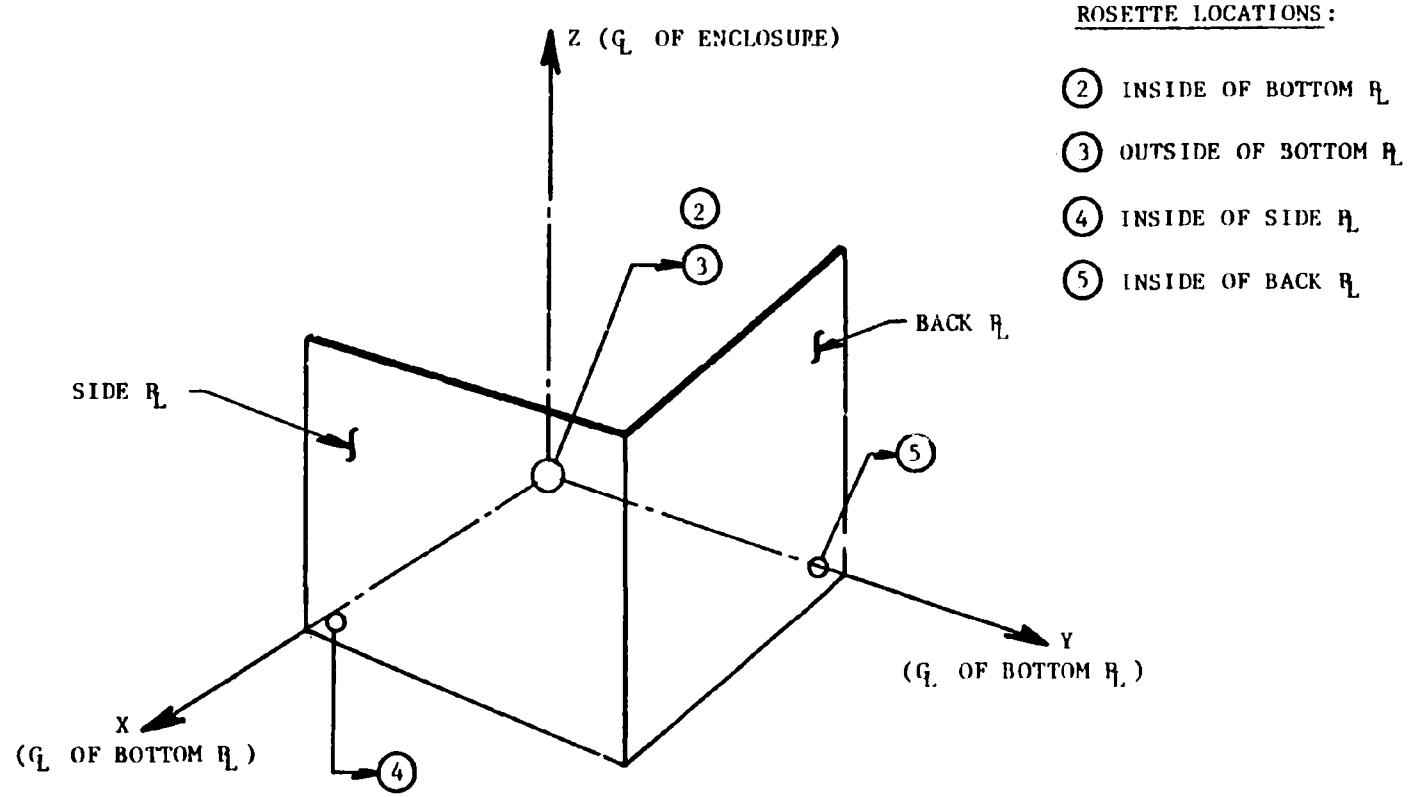

FIGURE 4.34. ROSETTE AND DISPLACEMENT GAGE LOCATIONS ON THE ONE-QUARTER MODEL OF ENCLOSURE I

Figure 4.35a is a photograph showing Rosettes No. 1 and No. 2 completely installed prior to waterproofing. Rosette No. 3 was located at the same point on the other side of Rosette No. 2. Figure 4.35b shows Rosette No. 2 again, as well as Rosettes No. 4 and No. 5.

Before the hydrostatic pressure tests, the lid was placed on the box and the 1/2-in. bolts "finger tightened" to determine the no-torque gap between the top and the box. Using flat feeler gages, gaps of 3 and 4 mils were present between the bolts on the short sides of the box. All bolts were then torqued one-half turn with a wrench, and no gaps could be found with a 2-mil feeler gage.

Three pressure tests plus a preliminary test were conducted on this enclosure. In the preliminary test, it was determined that vacuum grease effectively sealed the cover to the enclosure at pressures up to 100 psi. Therefore, it was decided to use vacuum grease on all the subsequent tests of Enclosure I. The preliminary test was also used to check out the strain gage circuits and the pressurization system.

Test No. 1 consisted of pressurizing the enclosure to 100 psig in 20-psi increments, recording 12 strain channels, and determining if any gaps could be measured with feeler gages. The 12 strain elements of Rosette Nos. 1-4 were recorded at each increment. A very small water leak was detected at 60 psig between the bolts on the back side of the enclosure. The leak increased slightly at 100 psig, but no measurable gap could be found with a 2-mil feeler gage.

Test No. 2 was similar to Test No. 1 except that one-quarter of the outside of the box was stress coated on the sides where strain gages were not used. The stress coat was used to obtain strain distributions and magnitudes on the end which contained the three circular penetrations. The outside surface was stress-coated, even though the larger tensile strains were expected on the inside surface. Coating was applied only to the outside because of the use of water to pressurize the enclosure and because depressurization would have been necessary to observe the status of an inside coating. No leaks occurred up to the maximum pressure used of 100 psig. In this test, Rosettes No. 1 and Nos. 3-5 were monitored. The stress coat showed no cracks up to the 100-psig pressure, indicating that tensile strains were below the 600 μin./in. threshold determined from tests of the calibration bars. (The bars were sprayed at the same time the enclosure was coated.) At 100 psig an air leak was found in the pressurization system so that Test No. 2 was terminated for repair. Testing was resumed after repair. This test was identified as Test No. 3 so that repeated strain gage readings could be identified.

Test No. 3, the final test on Enclosure I, was to have taken the box to failure or to the limit of the pressurization system. In this test the pressure was increased in 40-psi increments to 80 psig and 20-psi increments from then on. Measurements of gaps as well as observation of the stress coat were continued in this test. The first

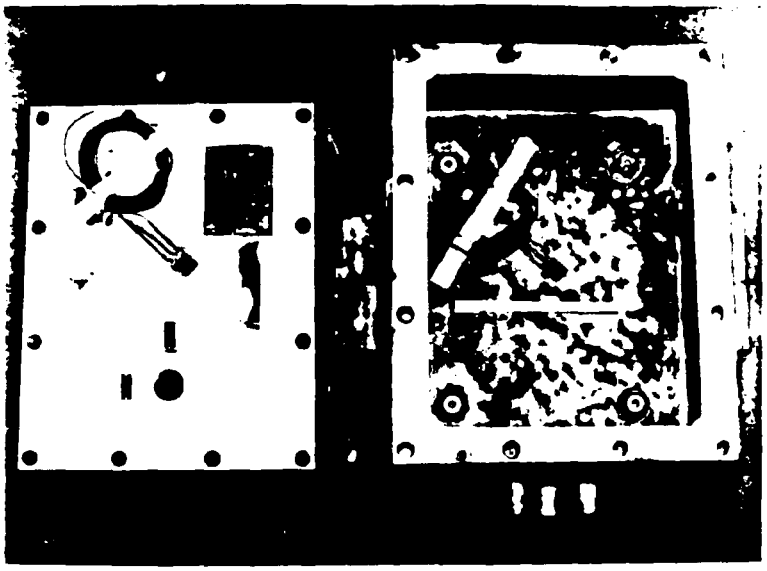

(a)

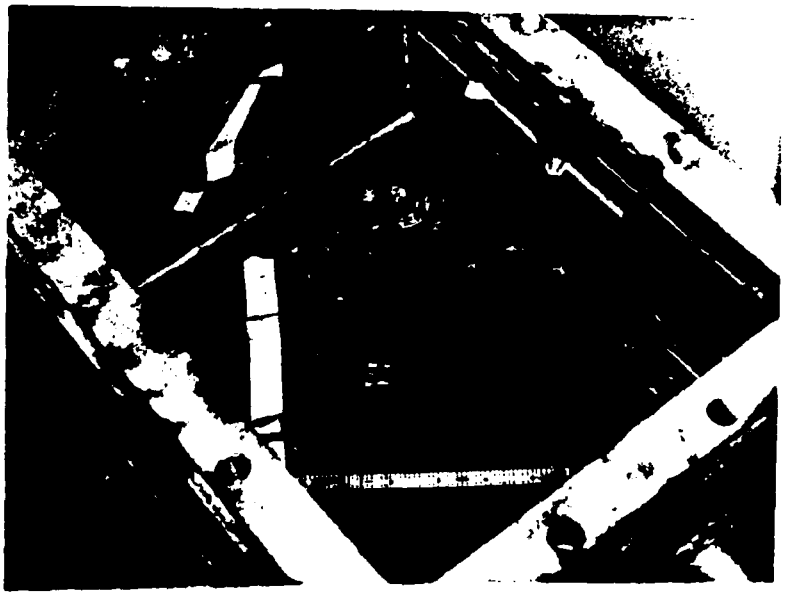

(b)

FIGURE 4.35. INSTRUMENTED 2G ENCLOSURE I

cracks in the stress coat were visible at a pressure of 120 psig, at a location approximately in the center of the side wall. There were no strain gages in this location, but calculated strains were +514 μin. at 120 psig (scaling linearly from results at 100 psig). This correlation is well within experimental scatter with stress coat unless environmental cconditions are better controlled than for the enclosure test. The important result from the stress-coating was that no cracking occurred around the penetrations at pressures up to 180 psig. No further stress coat observations were made until the test was completed.

Water leaking was first observed between pressures of 120 and 140 psig at the box-lid interface. Leaks increased to steady water sprays as the pressure increased. At a pressure of 180 psig, a 2-mil feeler gage could not be inserted between the cover and the flange, even at the point of the greatest leakage. At a pressure of 200 psi the torque on the bolts was increased from 60 to 80 ft-lb to try to reduce the leak rate and be able to continue pressurization to a higher pressure. Strains at this pressure indicated that the enclosure was well past yielding at several measurement points. At 220 psig, the last strain mesurements were made. Pressure was then increased quickly to the limit of the pressure system to see if the box would fail. However, at a pressure of approximately 290 psig, as indicated by the pressure transducer near the enclosure, the water in the tank was gone and high pressure air began leaking from the box at such a high flow rate that the air regulator could not keep up with it. The test was ended at this time. Inspection of the enclosure revealed significant bulging of the bottom as shown in Figure 4.36. Feeler gage checks revealed that all gaps at leak areas were smaller than 2 mils, which indicates that no permanent bolt set occurred. Removing the lid showed the vacuum grease had been blown out at points where the leaks had been observed during the test.

4.1.5.2 Results

The strain data recorded in the three tests are presented graphically in Figures 4.37-4.41. Data for each rosette are plotted on one graph and compared to the analytical predictions for pressures up to 150 psig. All tensile strains are positive, and compressive strains are negative. The data from the three experiments are repeatable for each strain element and compare relatively well with the analytical predictions in the elastic range. In every case, the strains measured with each rosette are magnitude consistent with the predictions, i.e., the element within each rosette which was supposed to measure the largest strains did, etc

4.1.5.3 Analytical-Experimental Comparisons with Elastic Analyses

Initial yielding of the box was predicted to occur at about 82 psig, at the intersection of the side wall and the shell. At the strain gage locations, yielding occurred at higher pressures. Maximum strains were recorded at the center of the enclosure bottom (Rosette No. 3) and on the back wall of the enclosure near the intersection of the wall and the bottom (Rosette No. 5). Agreement with analytical predictions is good out to about 100 psig where yielding occured.

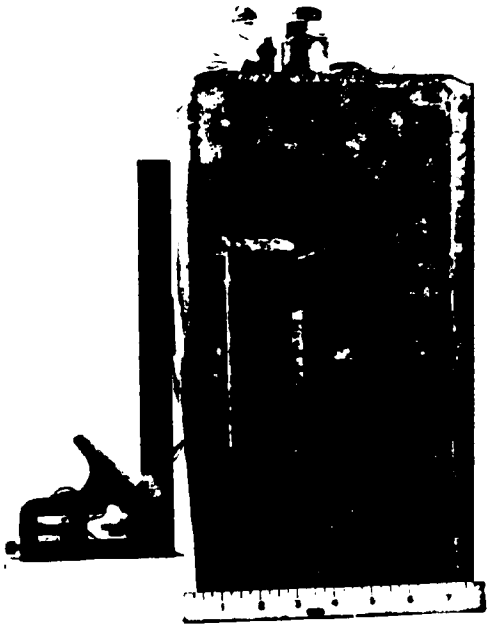

FIGURE 4.36. DEFORMATION OF ENCLOSURE I

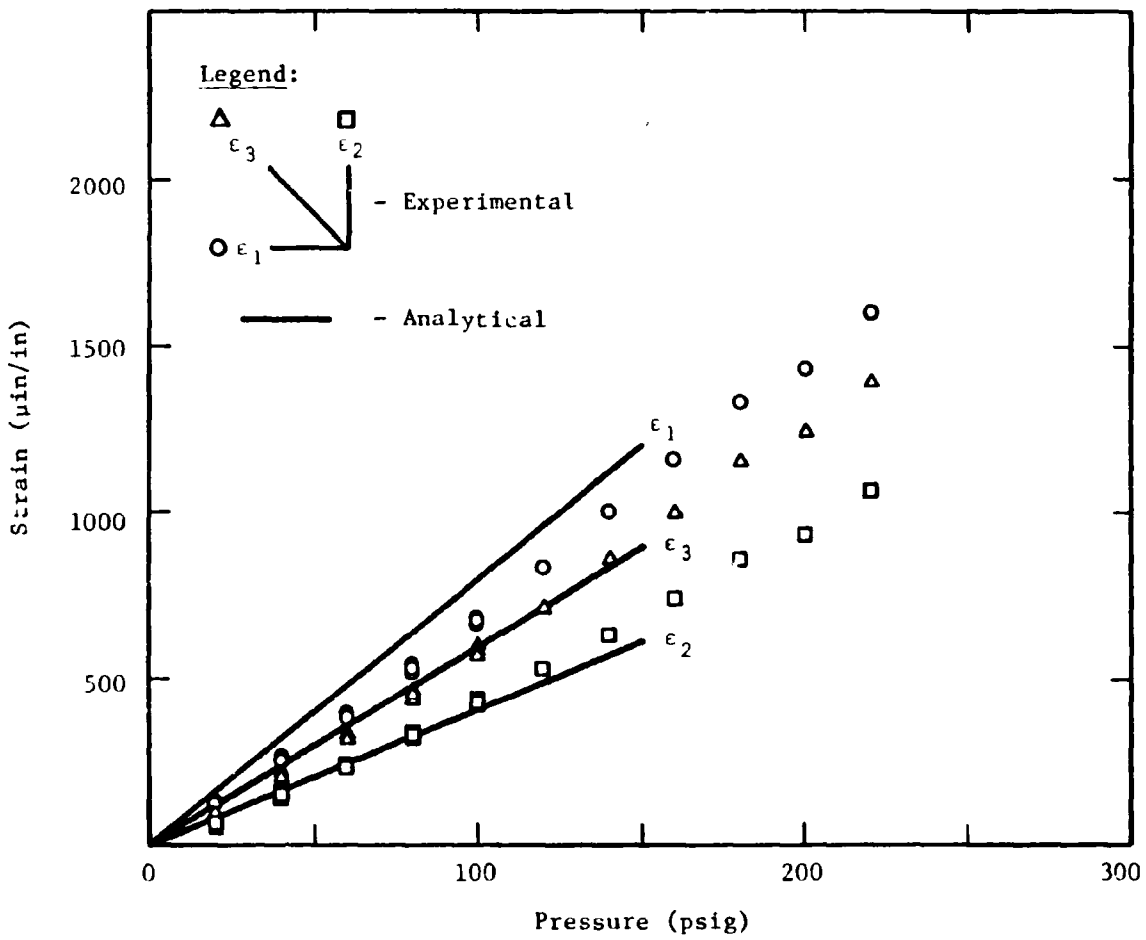

FIGURE 4.37. ROSETTE NO. 1 DATA COMPARISON

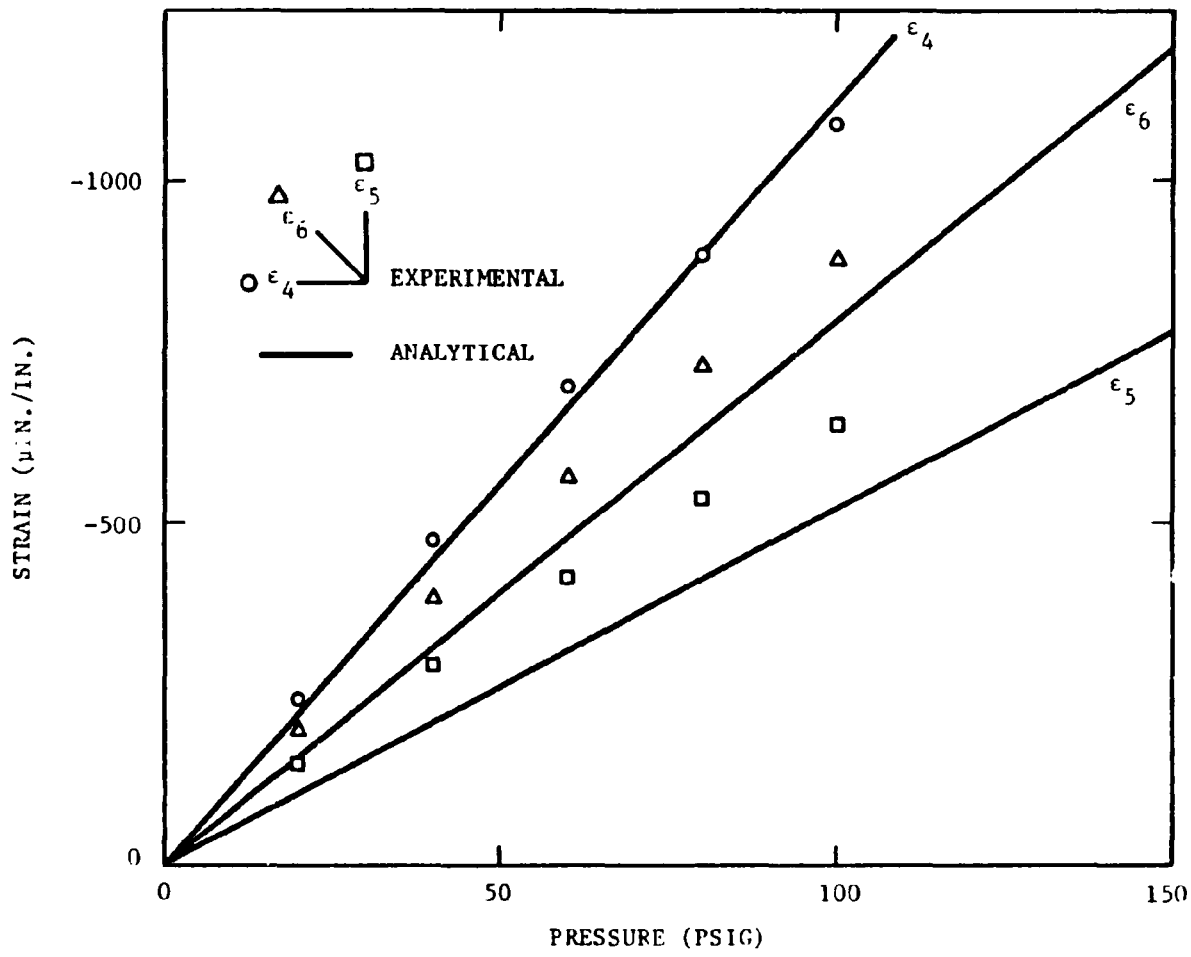

FIGURE 4.38. ROSETTE NO. 2 DATA COMPARISON

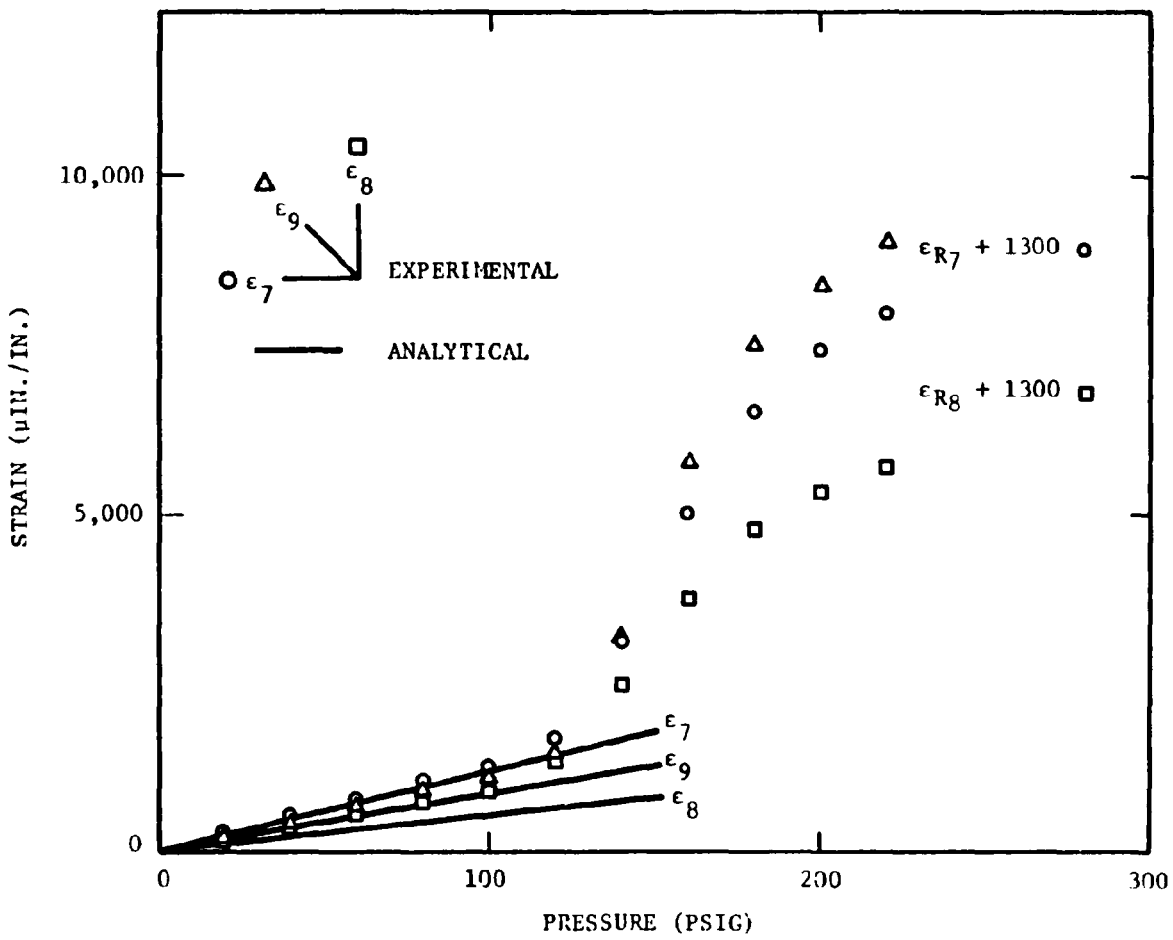

FIGURE 4.39. ROSETTE NO. 3 DATA COMPARISON

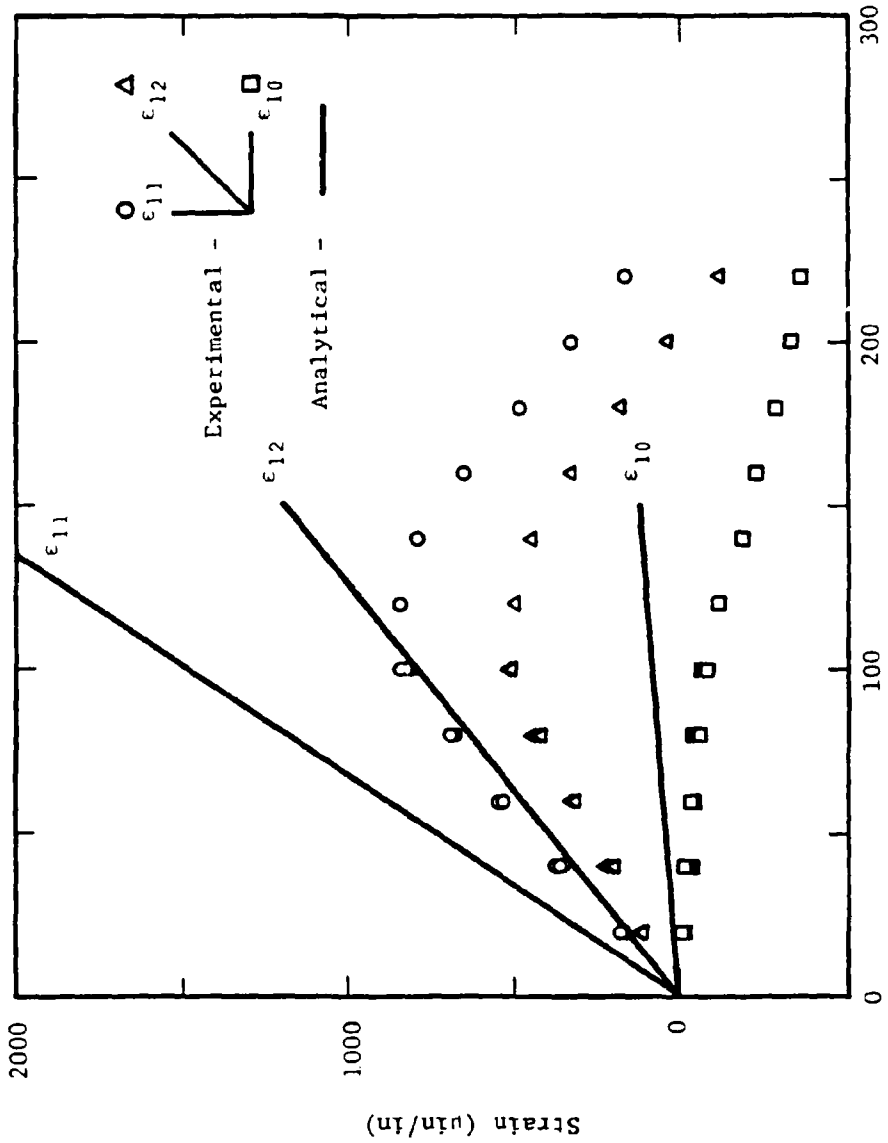

FIGURE 4.40. ROSETTE NO. 4 DATA COMPARISON

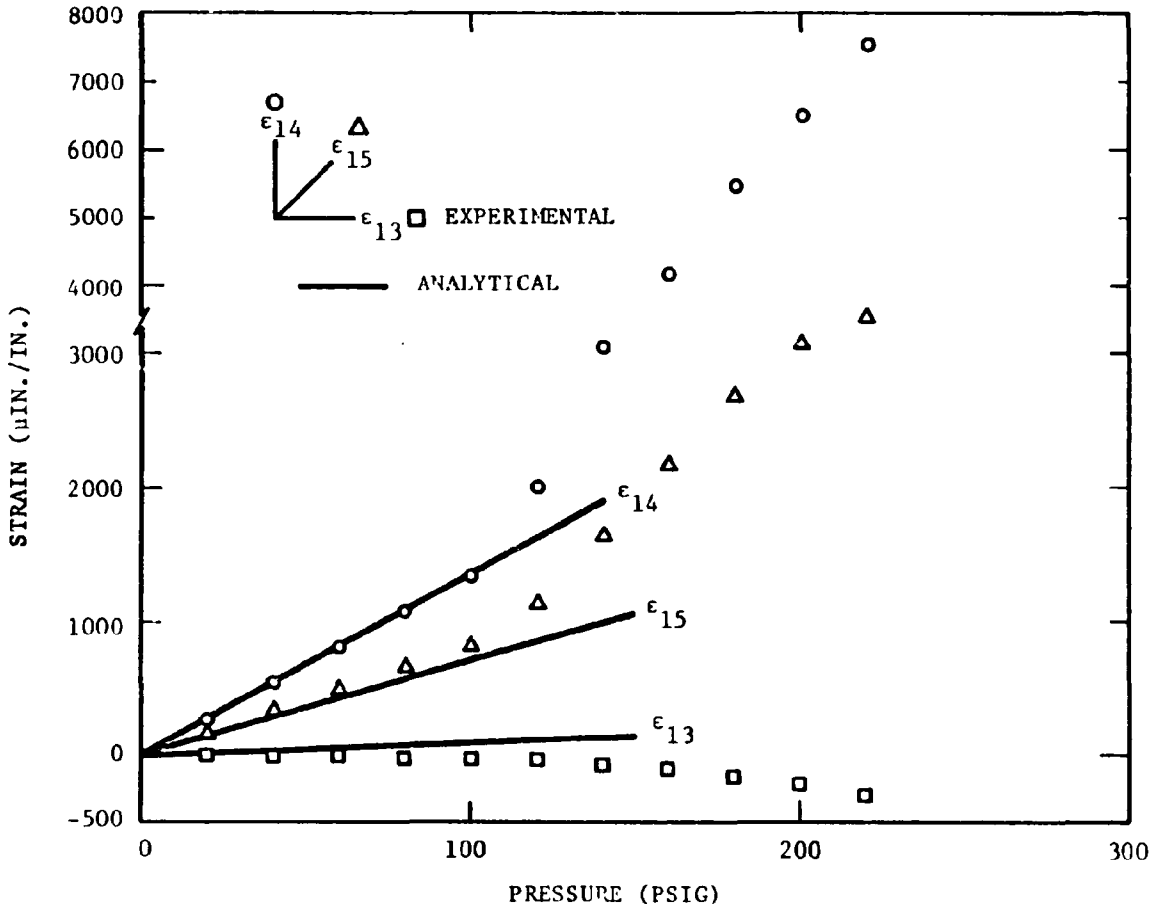

FIGURE 4.41. ROSETTE NO. 5 DATA COMPARISON

The most unusual behavior occurred at Rosette No. 4 (side shell near the bottom). Here the strain increased linearly over a very short range (out to 60-80 psig). With increasing pressure the strain on two elements gradually stopped increasing, reversed direction, and crossed the zero axis before the end of the test. This unusual phenomenon was caused by yielding in the weld joint between the bottom and the side shell at very low hydrostatic pressures. A simple diagram of a two-dimensional slice through the box (Figure 4.42) illustrates what happened. The moment at the gage location, M_a, is found from the free-body diagram.

$$M_a = M_W + \frac{pa^2}{2} - \frac{pba}{2} \quad \text{(in-lb/in)}$$

$$= M_W + \frac{pa}{2}(a - b)$$

Because b >> a, the moment produced by the second term in the expression for M_a is negative. If the system remains elastic, both M_W and the term pa/2 (a - b) increase linearly with pressure, and the net moment at the gage M_a, (and thus the stress) increases linearly.

At Rosette No. 4 the strain is initially positive and linear. It quickly becomes nonlinear and eventually reverses sign. This behavior is produced by early yielding of the weld joint. The moment in the weld increases linearly to about 60 psi, where yielding of the weld begins. The increasing negative moment produced by the pressure term then dominates and reverses the strain. This behavior is shown schematically in Figure 4.43. Strains at all other gages behave as expected. Strains in the top are essentially linear, indicating little or no local yielding, and strains increase rapidly after yielding in the bottom and back of the enclosure where strains were high. At Rosette No. 2 on the inside of the bottom of the enclosure, strains were measured only out to 100 psi on Test No. 1.

It is clear from the strain data and from the permanent deformation in the bottom of the enclosure that substantial plastic deformation occurred. Past examination of the weld at the junction of the bottom and side shells also revealed substantial tearing of the weld on the inside of the enclosure (the corner weld joint opened up on the inside). Because bottom deflections were not measured during the test, the onset of permanent deformation in the bottom could not be predicted. During testing of Enclosure IA, described in the next section, permanent bottom deflections were measured.

4.1.6 Testing of Enclosure IA

As noted previously, this was the second of two very similar enclosures to be tested. This enclosure was purchased for testing from Service Machine Co., Huntington Beach, West Virginia. The purpose of this test was to monitor more carefully the permanent deformations in the enclosure. Also, two bolts were instrumented in this test to verify the treatment of the bolts in the finite element model described in Section 4.1.2.

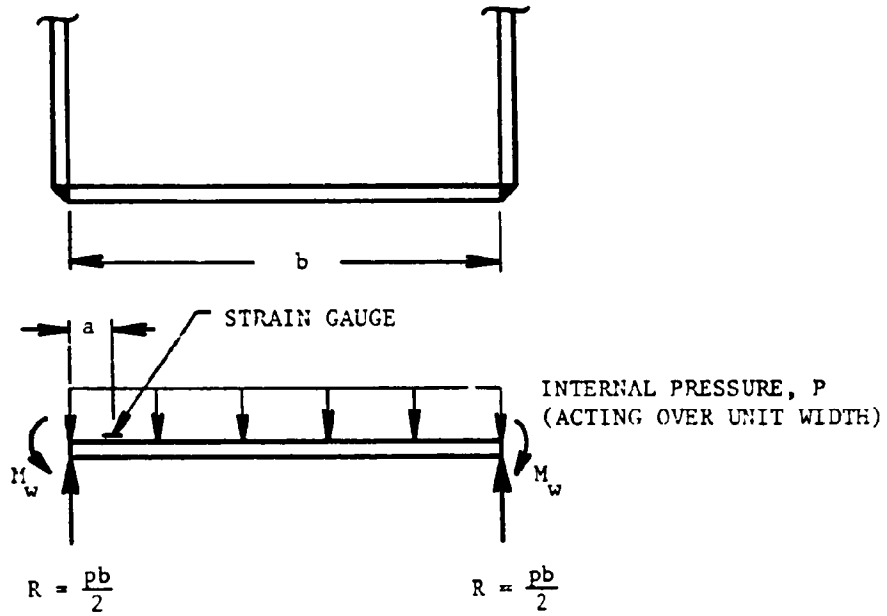

a. UNIT STRIP FROM BOTTOM OF ENCLOSURE

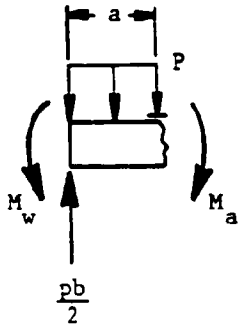

b. FREE-BODY OF LEFT END OF STRIP

FIGURE 4.42. SECTION THROUGH ENCLOSURE I

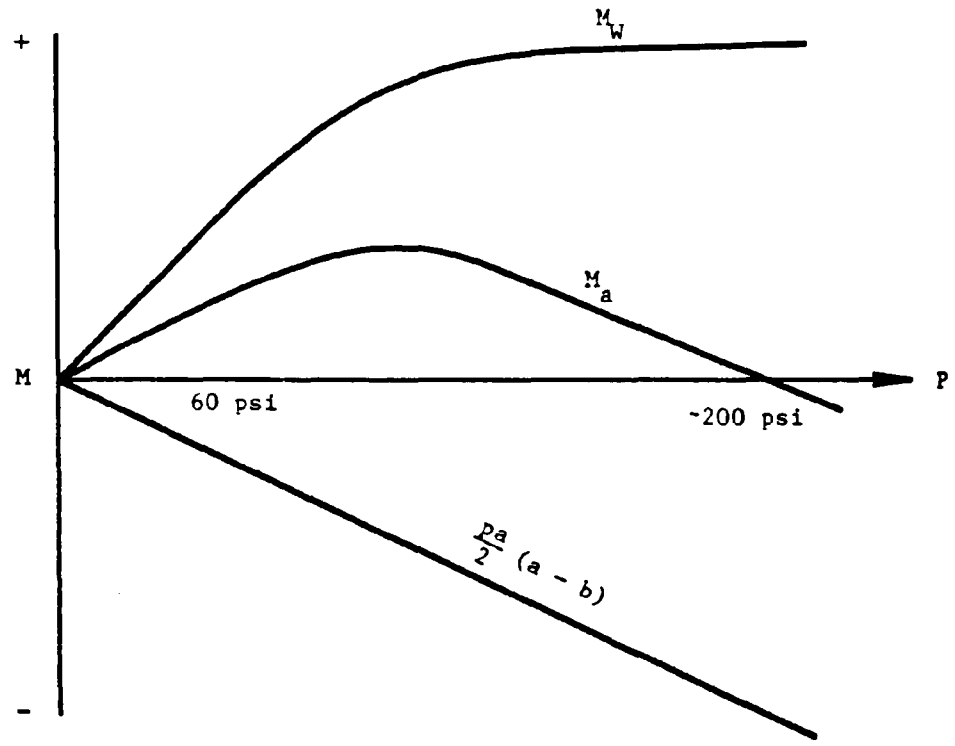

FIGURE 4.43. SCHEMATIC OF MOMENTS
AT ROSETTE NO. 4

4.1.6.1 Methodology

Enclosure IA was instrumented with four rosettes located at locations 2, 3, 4, and 5, as shown for Enclosure I in Figure 4.34. Rosette No. 1 (on the cover) was omitted in this test because of the low strains recorded previously. In addition, three dial displacement gages were used to measure the deformation across the width of the bottom of the enclosure. A fourth displacement sensor was used to monitor the flame gap between the aluminum cover and the rim of the enclosure. Finally, two instrumented bolts were installed to measure bending and axial loads at two bolt locations. Figure 4.44 shows the three internal rosettes and an external one completely installed prior to waterproofing. Figure 4.45 shows the enclosure mounted on a wooden table ready for testing. The two instrumented bolts can also be seen in this figure.

The same pressurization system used for hydrostatic testing of Enclosure I was also used to pressurize Enclosure IA. The enclosure was first filled completely with water. A reinforced neoprene rubber gasket, 1/32 in. thick, was used to seal the enclosure cover. The twelve 1/2-in. bolts, including the two internally gaged, were torqued to 60 ft-lb.

Test No. 5 of this project was begun by pressurizing the enclosure in 20-psi increments up to 80 psi. Pressure was then increased in 10-psi increments to a pressure of 120 psig. At 120 psig the pressure increments were increased to 20 psi for the remainder of the test. To obtain residual deformations on the bottom of the enclosure, the hydrostatic pressure was dropped to zero after each pressurization step. This procedure was repeated up to 180 psig, at which point the pressure was increased without returning to zero pressure between pressure steps. Water began to leak around some of the bolts at 140 psig. At a pressure of 200 psig, the torque on the bolts was increased to 80 ft-lb to decrease the water leaks and allow continuation of the test to higher pressures. The test was ended at a pressure of 300 psig because of large water leaks at the bolts.

4.1.6.2 Results

Inspection of the enclosure after the test revealed similar bulging of the bottom, shown in Figure 4.46, as had been experienced by Enclosure I. However, as depicted in Figure 4.47, the sides of Enclosure IA also experienced significant permanent deformations. These were not observed on Enclosure I.

Displacements measured during the test are given in Table 4.3. Slopes are also given for comparison with the criteria for permanent deformation of 0.04 in. per linear foot, as specified in Schedule 2G of the CFR [1]. The slope is calculated between each pair of gages, giving two slopes for each pressure increment. For this calculation the slope is assumed to be linear between the dial indicators, which have a spacing of 2-5/8 inches. Note that the slope is greatest near the edge of the enclosure and that the Schedule 2G criteria are exceeded between 100 and 110 psig. A high slope near the side wall also supports the observation made for Enclosure I that the weld joint between the side wall and the bottom plate is very weak in bending.

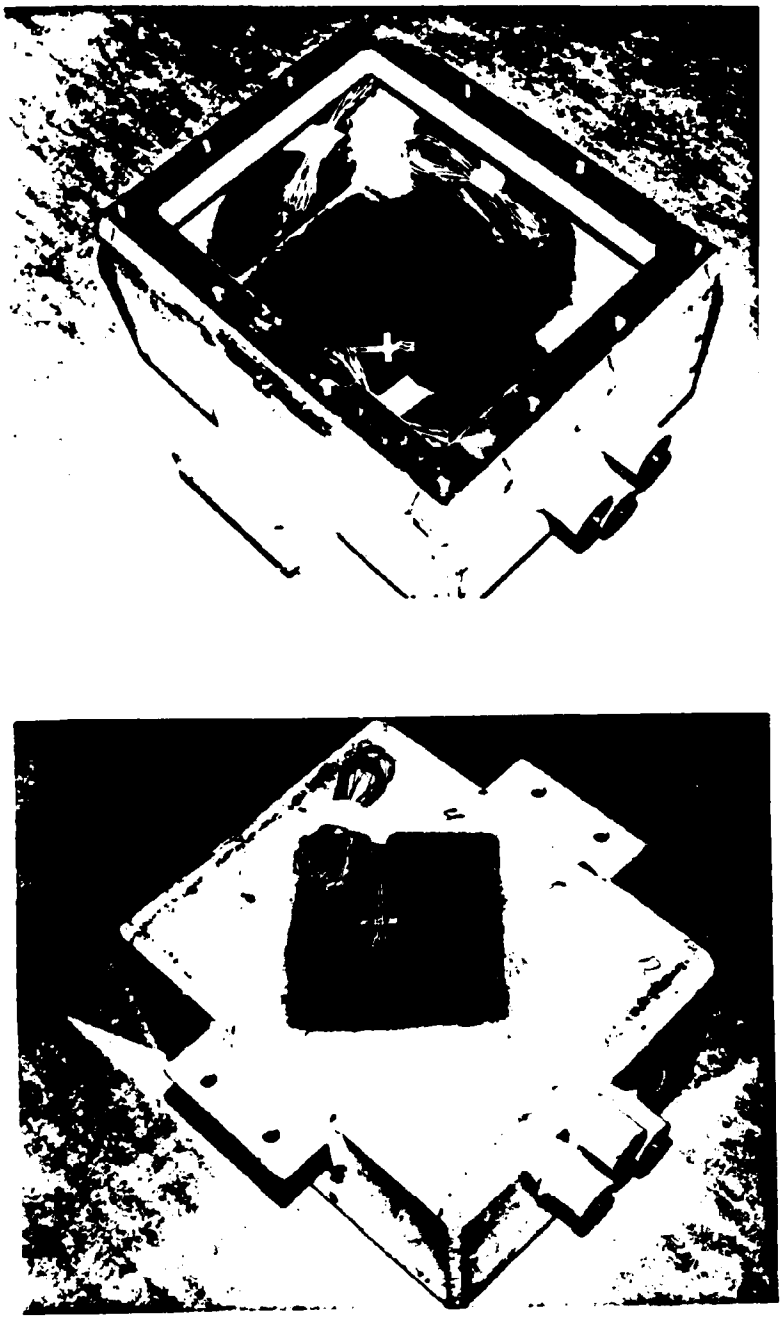

FIGURE 4.44. ENCLOSURE IA INSTRUMENTED WITH FOUR STRAIN GAGE ROSETTES

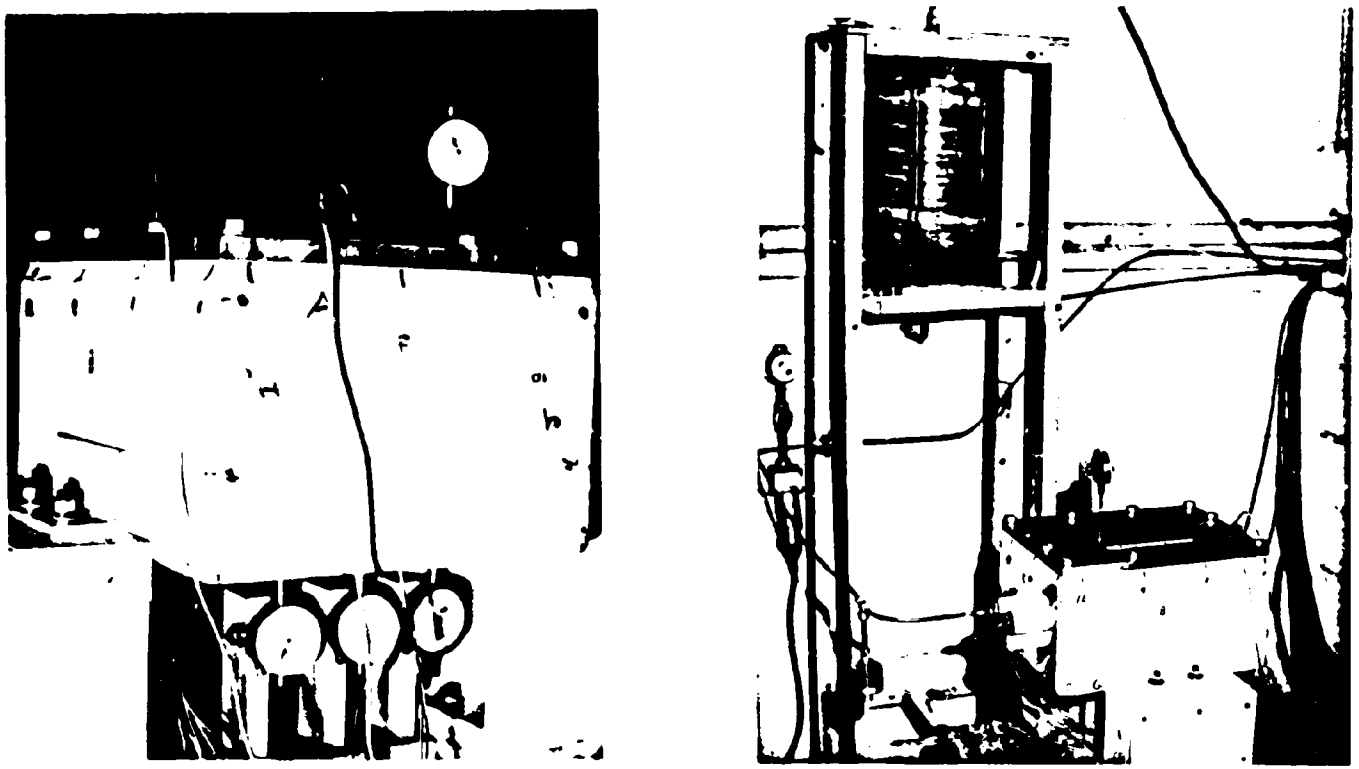

FIGURE 4.45. ENCLOSURE IA READY FOR TESTING

FIGURE 4.46. BOTTOM DEFORMATION
OF ENCLOSURE IA

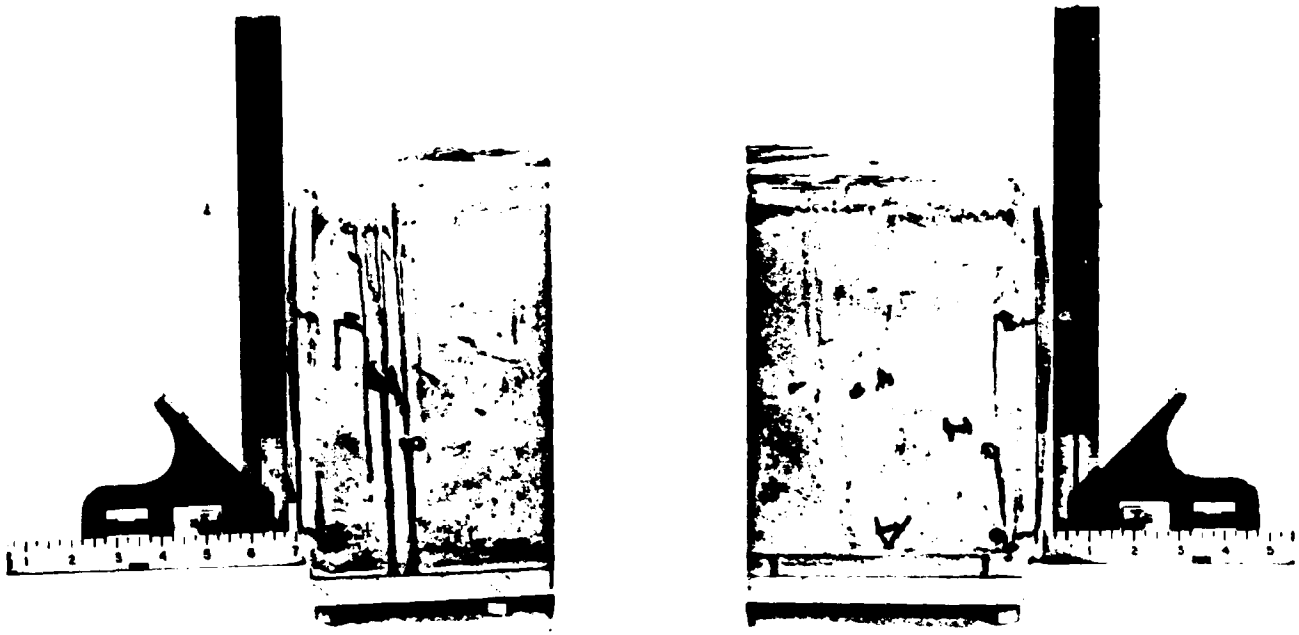

FIGURE 4.47. DEFORMATION OF SIDES ON ENCLOSURE IA

TABLE 4.3. DISPLACEMENT DATA AND CALCULATED SLOPES

Pressure (psig)	L_1	L_2	L_3	Residual Slope (in/ft)	
				Center	Edge
0	0	0	0	0	0
20	0	0	0	0	0
40	0	-0.5	+0.5	0.0023	-0.0046
60	0	-0.5	+0.5	0.0023	-0.0046
80	+4	+2.5	+1.5	0.0069	0.0046
90	+7.5	+5.0	2	0.0114	0.0137
100	11.5	8	2.5	0.0160	0.0251
110	22.5	15	3	0.0343	0.0549
120	32	21	3	0.0503	0.0823
130					
140	88	57	3	0.1417	0.2011
150					
160	167	109	3.5	0.2651	0.4823
170					
180	235	155	6	0.3657	0.6811

The strain data recorded on Test No. 5 are presented graphically in Figures 4.48-4.51. Strain data from each rosette are plotted on one graph. Comparing these data to those at corresponding locations on Enclosure I (Section 4.1.5), one can observe similar strain behavior at corresponding measurement points. The analytical predictions (straight lines) up to 150 psig are also included in each graph. As was the case in the Enclosure I testing, Rosette No. 4 (side shell near bottom) again produced the most unusual behavior. As for Enclosure I, this behavior is explained by failure of the weld joint between the side and bottom of the enclosure. This failure is not complete rupture, but cracking and loss of bending strength. Data from this and the other three rosettes show consistency in magnitude and sign (tensile or compressive) with earlier measurements on Enclosure I. In every case the element within each rosette which was supposed to produce the largest strain did, etc. Except for Rosette No. 4, the rosettes indicated maximum strains which exceeded the yield point of the material.

Two of the bolts used in Enclosure IA were internally gaged and calibrated to obtain the combined axial and bending loads during the testing using two strain gages recorded individually. To compute the axial or bending load by itself, data from both gages were required. Unfortunately, one gage became inoperative just prior to testing. Therefore, only the bolt located next to one of the corners along the long side of the enclosure yielded data from which the axial and bending loads could be computed. These data are presented in Figure 4.52.

4.1.6.3 Analytical-Experimental Comparisons

The analytical predictions for linear elastic behavior (see Section 4.1.2) are shown as straight lines on the strain plots in Figures 4.48-4.51. The analytical results are extended out to 150 psig even though nonlinear behavior occurs much earlier. Prior to the onset of nonlinear behavior, the analytical and experimental strains agree well for Rosettes Nos. 2, 3, and 5. As for Enclosure No. I, the strains at Rosette No. 4 are affected by yielding in the weld joint, which occurs very early in the test. This unusual behavior was discussed for Enclosure I in Section 4.1.5.3

Because of the yielding of Enclosures I and IA at relatively low pressures, an elastic-plastic analysis of these enclosures was performed as described in Section 4.1.3. For comparison with the experimental results, displacement and strains were determined at the gage locations used in the experiments. Experimental displacement measurements utilized three dial displacement gages (see Figure 4.45) to measure residual deformation along the width of the bottom of Enclosure IA. Figures 4.53 and 4.54 are the analytical results of displacements at gage locations 1 (center) and 2 (quarter distance from side plate). Figures 4.55 and 4.56 compare the experimental to the calculated residual displacements at these two locations. It is noted that the theoretical predictions are initially higher, but then lower, than the test results. The possible reasons for this difference are:

1. The weld joints were weaker in the actual enclosures than the F.E. model. Geometric changes

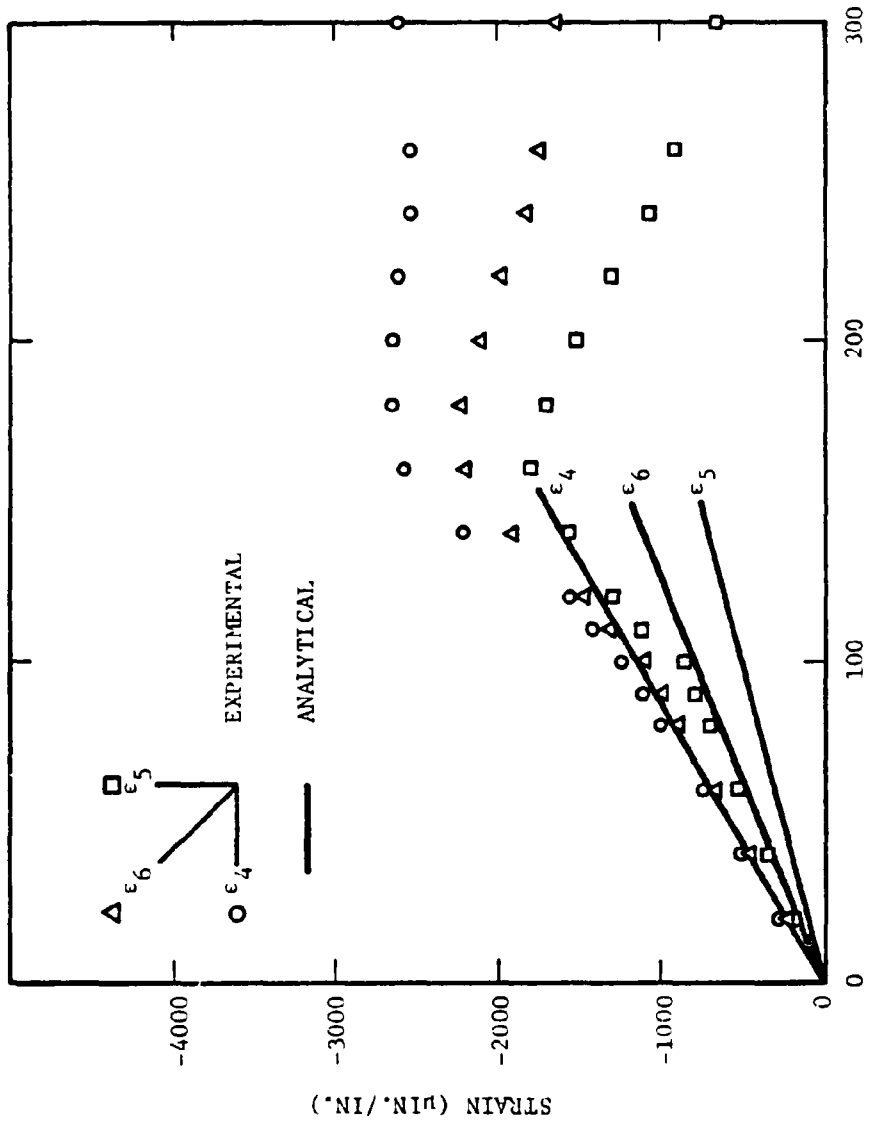

FIGURE 4.48. ROSETTE NO. 2, ENCLOSURE IA

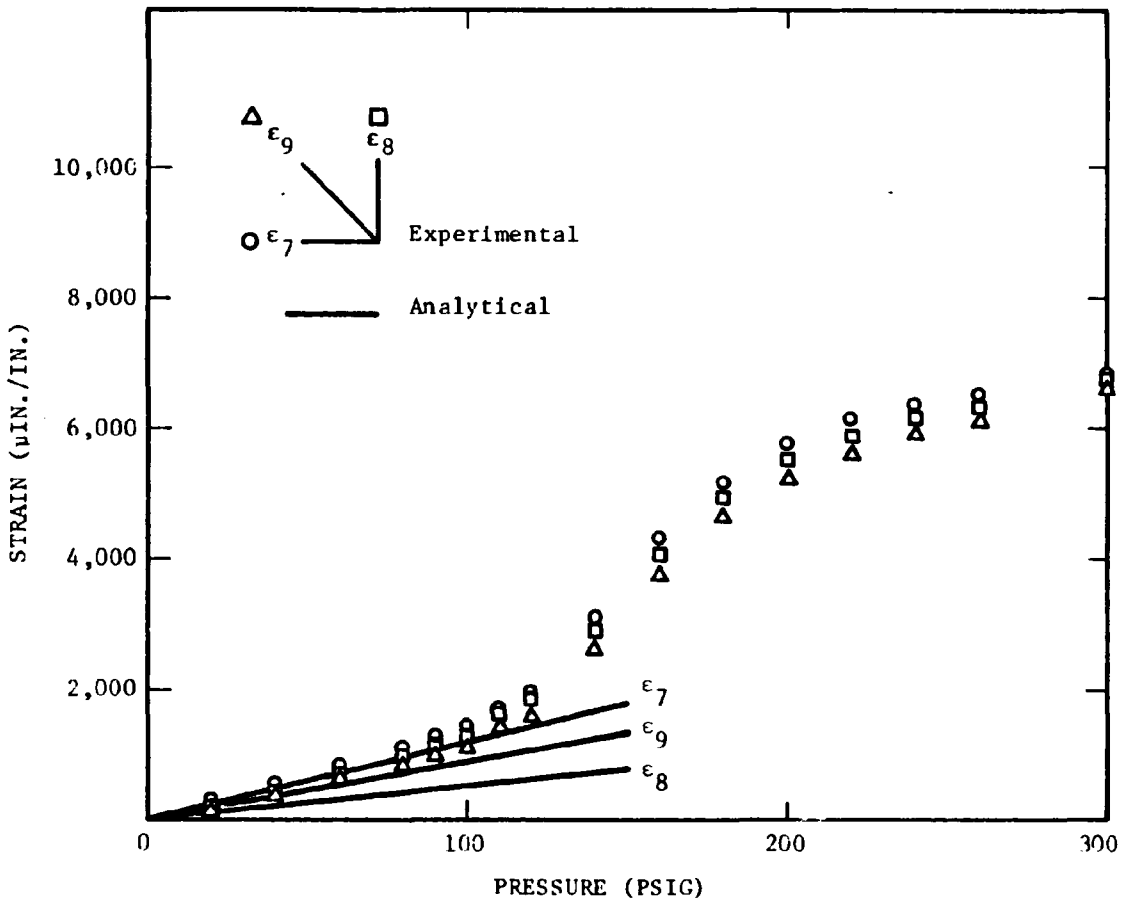

FIGURE 4.49. ROSETTE NO. 3, ENCLOSURE IA

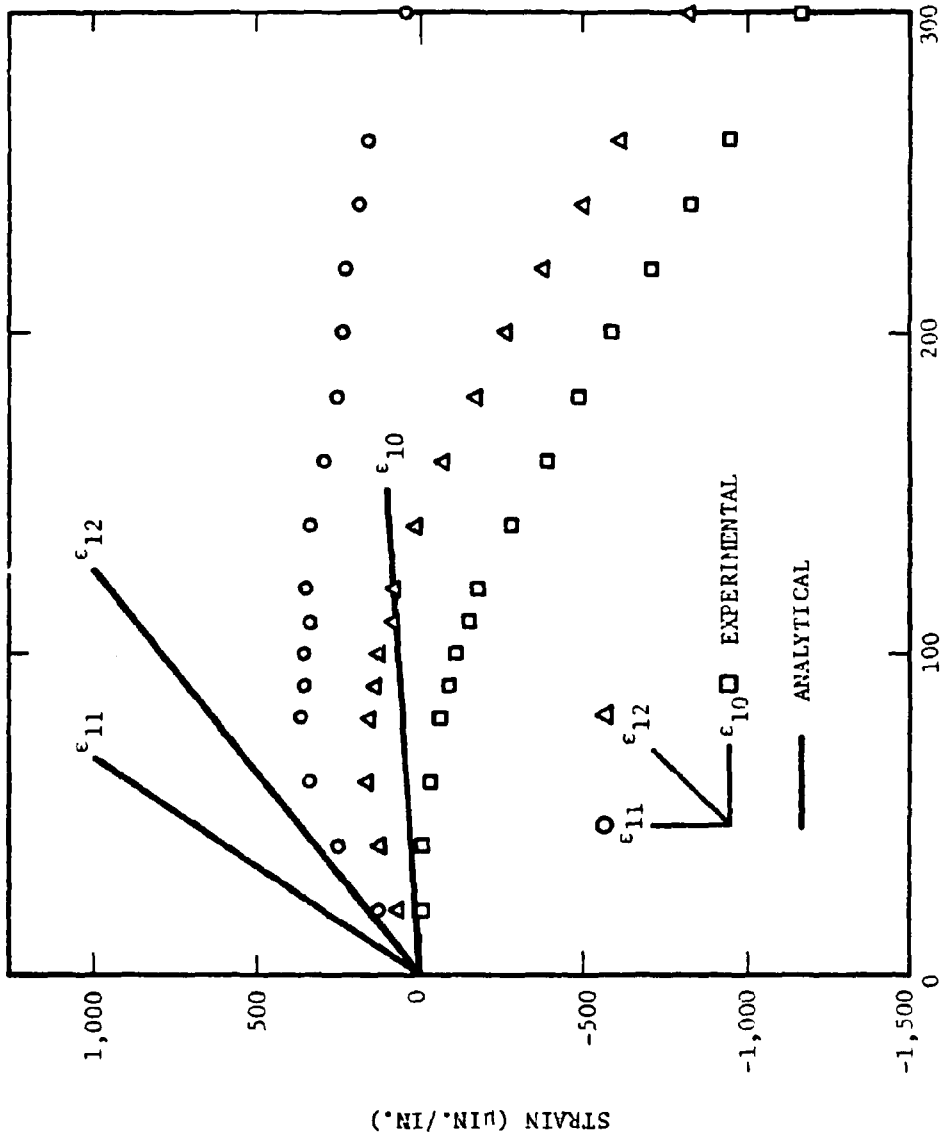

FIGURE 4.50. ROSETTE NO. 4, ENCLOSURE 1A

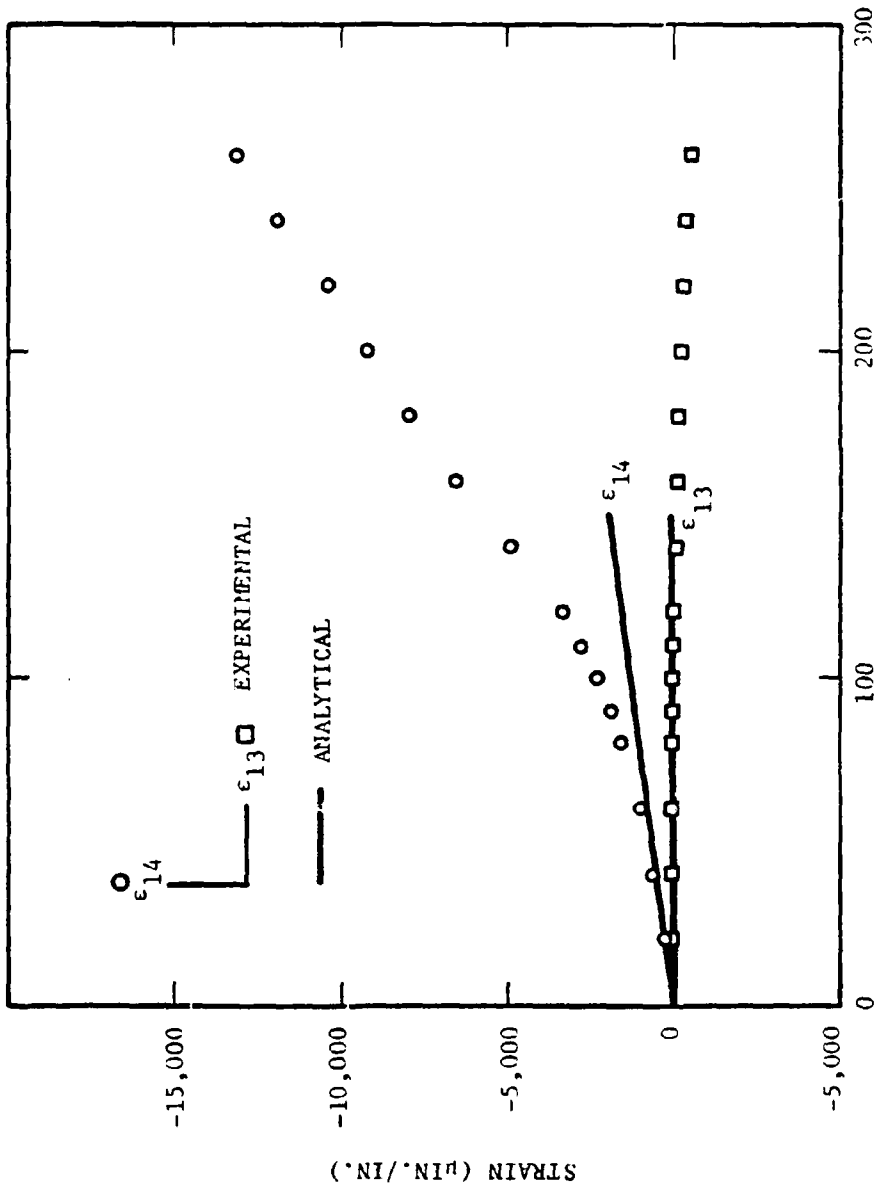

FIGURE 4.51. ROSETTE NO. 5, ENCLOSURE IA

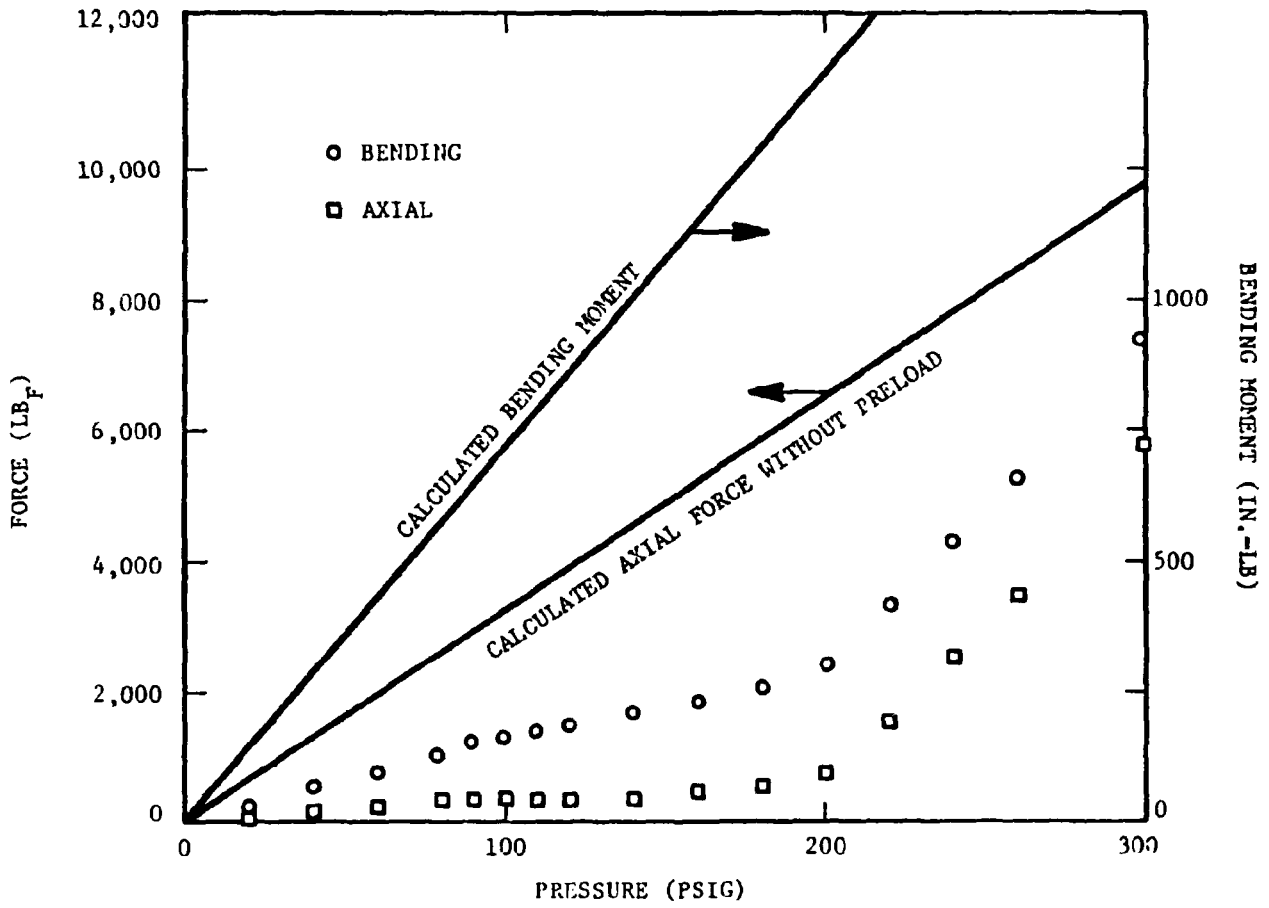

FIGURE 4.52. FORCES AND MOMENTS IN THE BOLTS

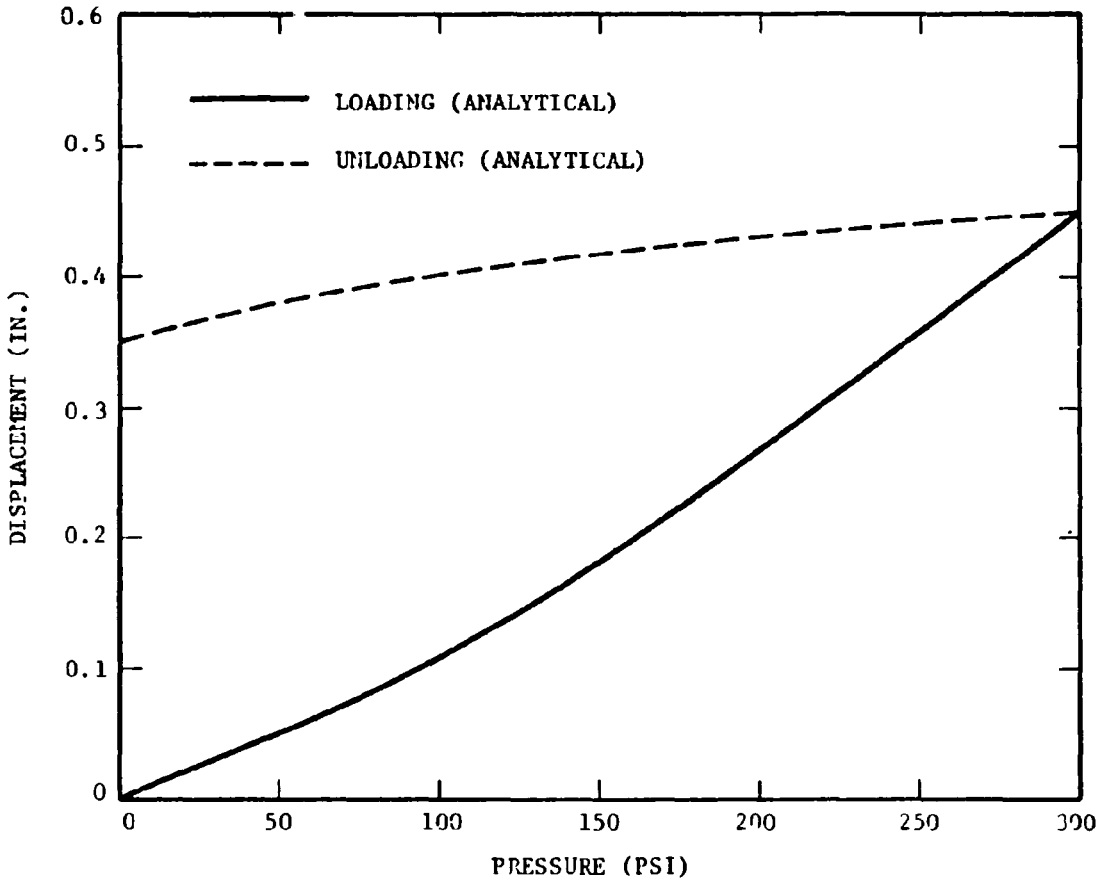

FIGURE 4.53. ANALYTICAL DISPLACEMENT AT GAGE LOCATION NO. 1

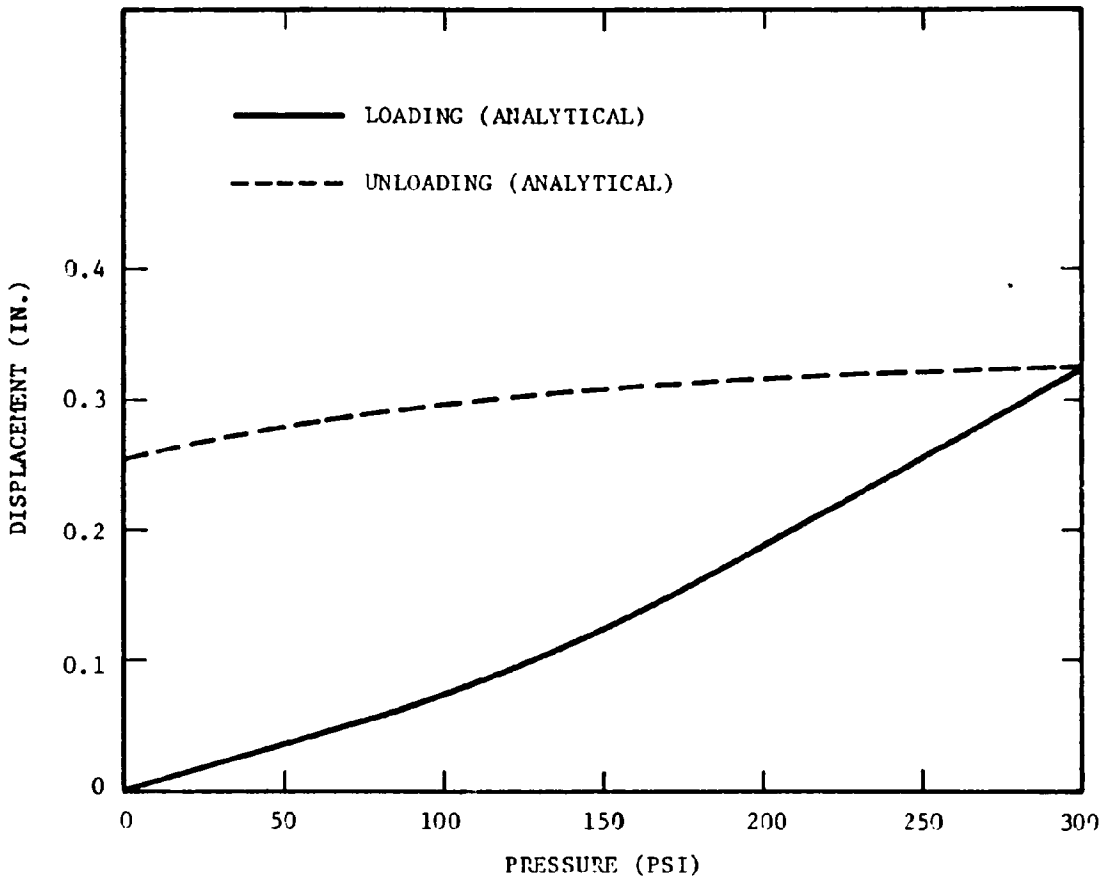

FIGURE 4.54. ANALYTICAL DISPLACEMENT AT GAGE LOCATION NO. 2

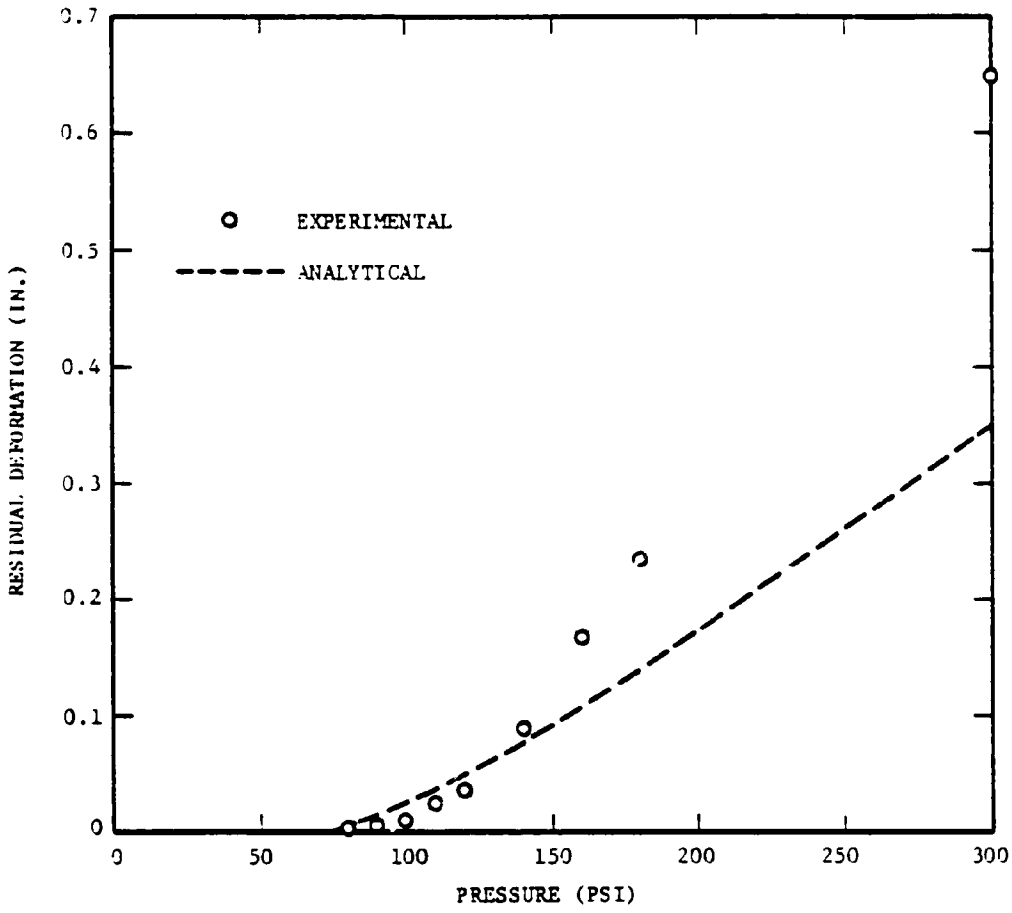

FIGURE 4.55. COMPARISON OF EXPERIMENTAL AND ANALYTICAL RESIDUAL DEFORMATION AT GAGE LOCATION NO. 1

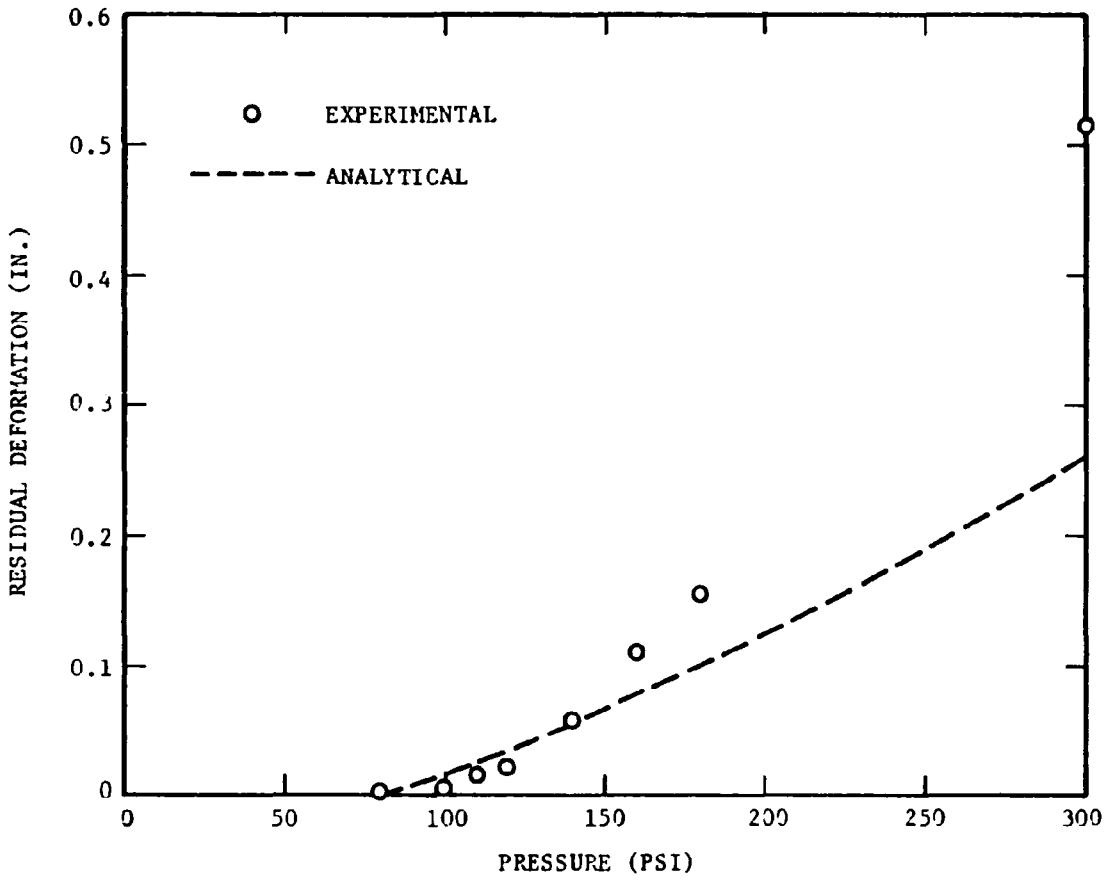

FIGURE 4.56. COMPARISON OF EXPERIMENTAL AND ANALYTICAL RESIDUAL DEFORMATION AT GAGE LOCATION NO. 2

and the cracking of the joint reduce the effective weld width and thickness, which in turn reduce the bending strength and yield higher deformation. This cracking was not modeled in the analysis.

2. The plastic stress-strain relationship used in the analysis may not have corresponded exactly with the true material behavior.

Enclosure IA was also instrumented with four strain gages at locations 2, 3, 4, and 5 (see Figure 4.34); however, the test did not provide strain information under unloading. Figures 4.57, 4.58, 4.59, and 4.60 compare the strain-pressure curves from the analysis to the experimental results repeated from Figures 4.48-4.51. The analytical strains conform in both sign and magnitude with the test results. The negative values in the figures indicate compressive strains. At locations 2, 3, and 5, the predicted strains are less than the experimental data for the same reasons as stated above. At Rosette No. 4, following material yielding, the analytical model predicted greater strain in the vertical direction (gage ε_{11}) than observed in the experimental results. In the experiment, this rosette was mounted inside the side plate, 3/16 in. beneath the angle iron and only 1/4 in. above the weld joint. This area is subjected to tensile strain produced by the moment in the joint. Therefore, the cracking of the weld joint reduces the bending stiffness in the weld and results in lower tensile strain at this region. In Figure 4.59, the model also exhibits unusual behavior under unloading. This is caused by yielding of the analytical hinge at the weld joint during unloading plus other changes in the model associated with the yielding. Overall, the comparisons between the analytical prediction and experimental results are good. Some refinement in the analytical description of the weld failure would have made the correlation even better.

4.2 Enclosure II Analysis and Testing

Enclosure II was provided by the USBM to SwRI for analysis and testing. Its manufacturers and previous usage were unknown. Basic dimensions of the enclosure are given in Figure 4.61. In comparison with Enclosure I (Figure 4.1), its design and fabrication are seen to be very different. It has an inside flange, a massive plate at the end with penetrations, and a steel cover. Plates are joined in Enclosure II by a partial penetration weld from both sides.

Enclosure II was analyzed and tested using the same procedures described for Enclosure I. Thus, the explanation for Enclosure II will be shortened. Also, because of the modeling experience gained for Enclosure I, the two-dimensional models were omitted in this analysis.

4.2.1 Elastic Analysis

4.2.1.1 Characteristics of the FEM Model

Enclosure II was symmetric about a vertical plane passing through its center and parallel to its longer sides, so only one-half of the complete container needed to be modeled. Further, the end

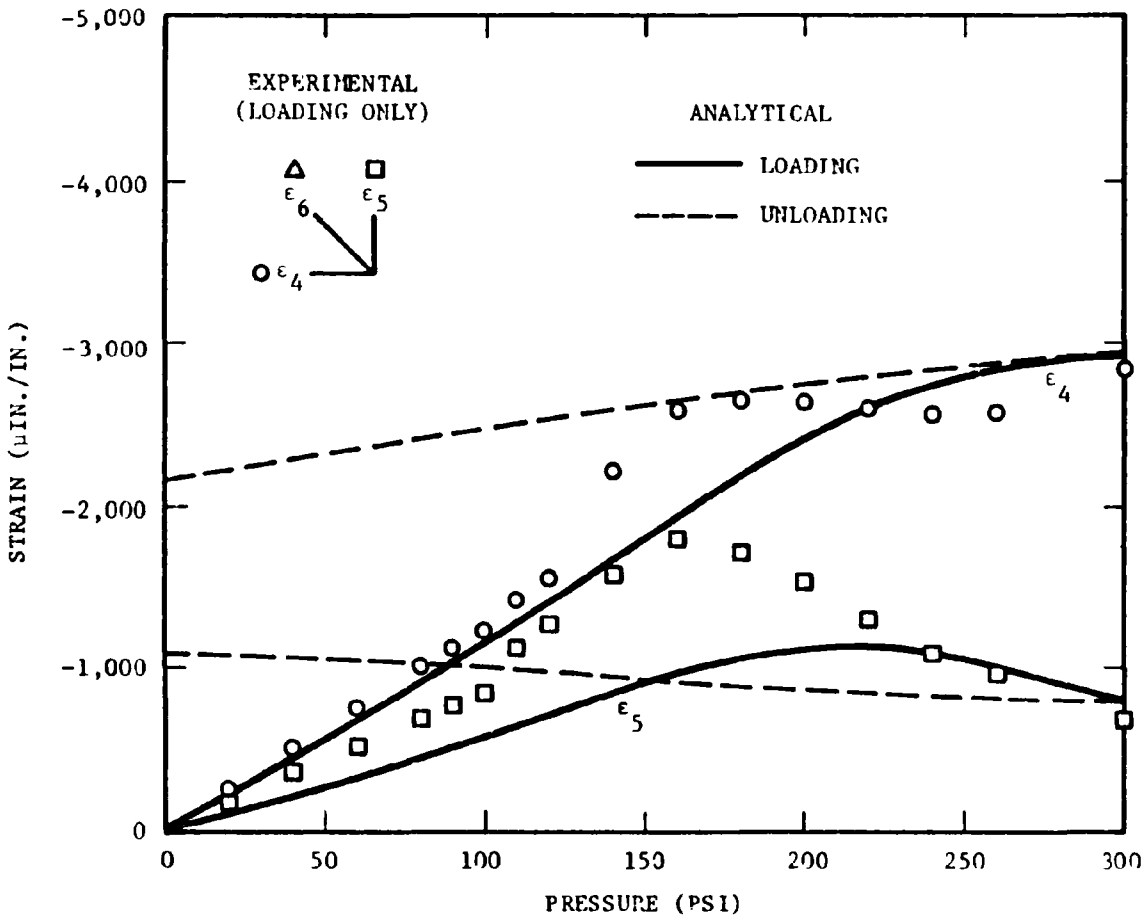

FIGURE 4.57. COMPARISON OF EXPERIMENTAL AND ANALYTICAL STRAINS AT ROSETTE NO. 2

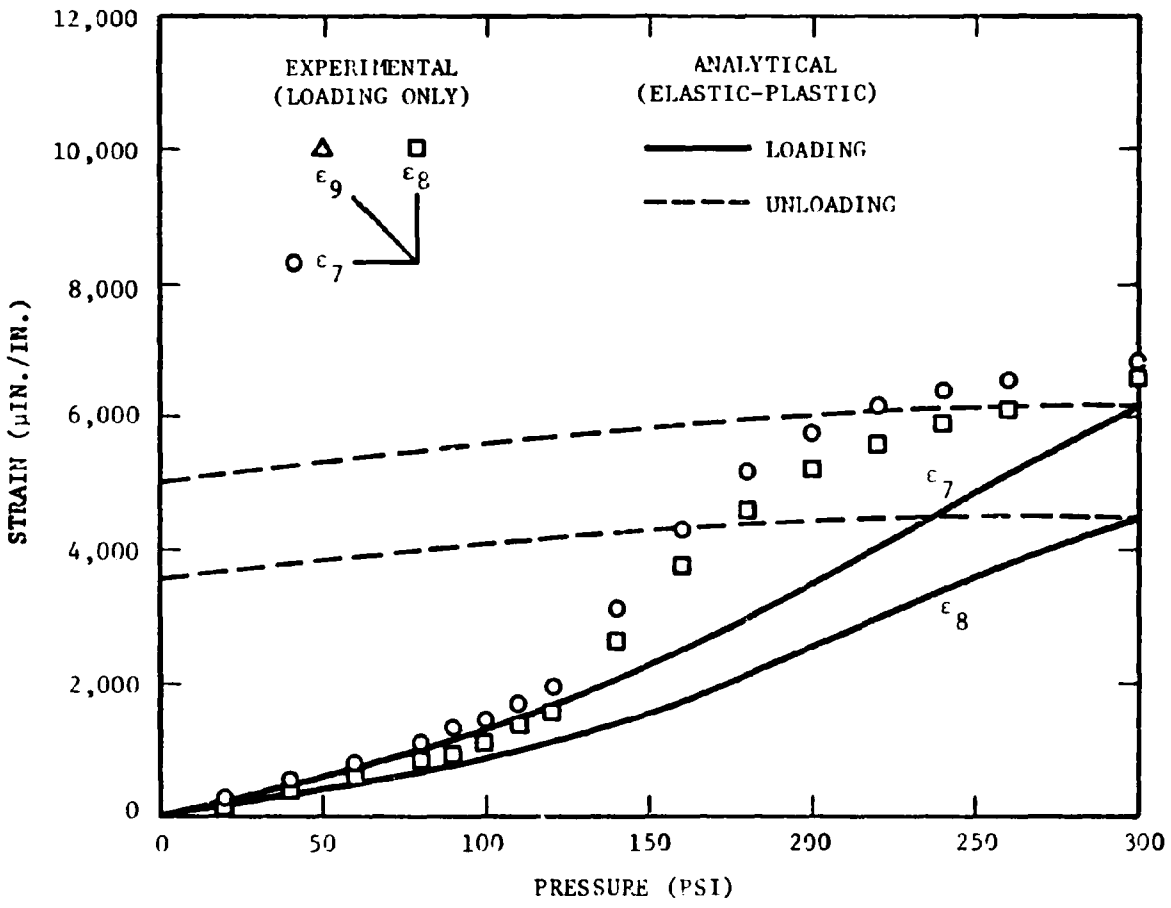

FIGURE 4.58. COMPARISON OF EXPERIMENTAL AND ANALYTICAL STRAINS AT ROSETTE NO. 3

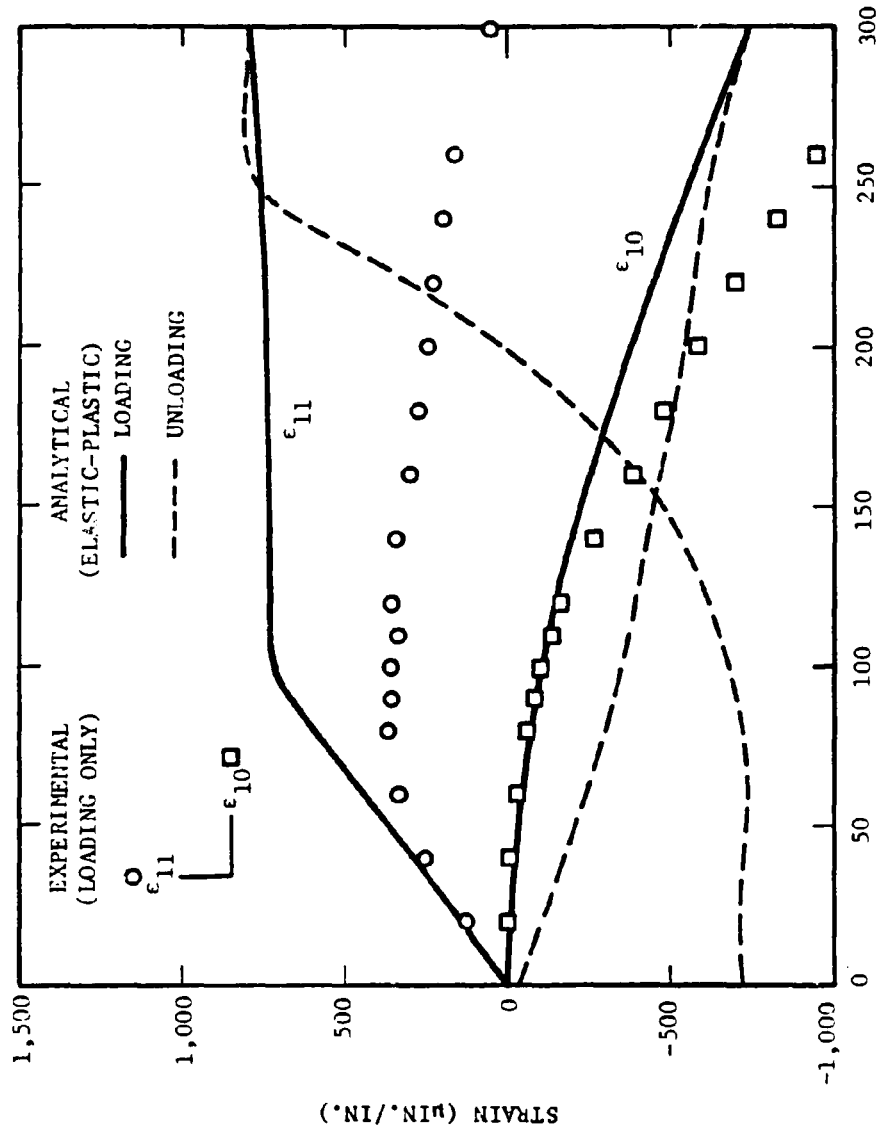

FIGURE 4.59. COMPARISON OF EXPERIMENTAL AND ANALYTICAL STRAINS AT ROSETTE NO. 4

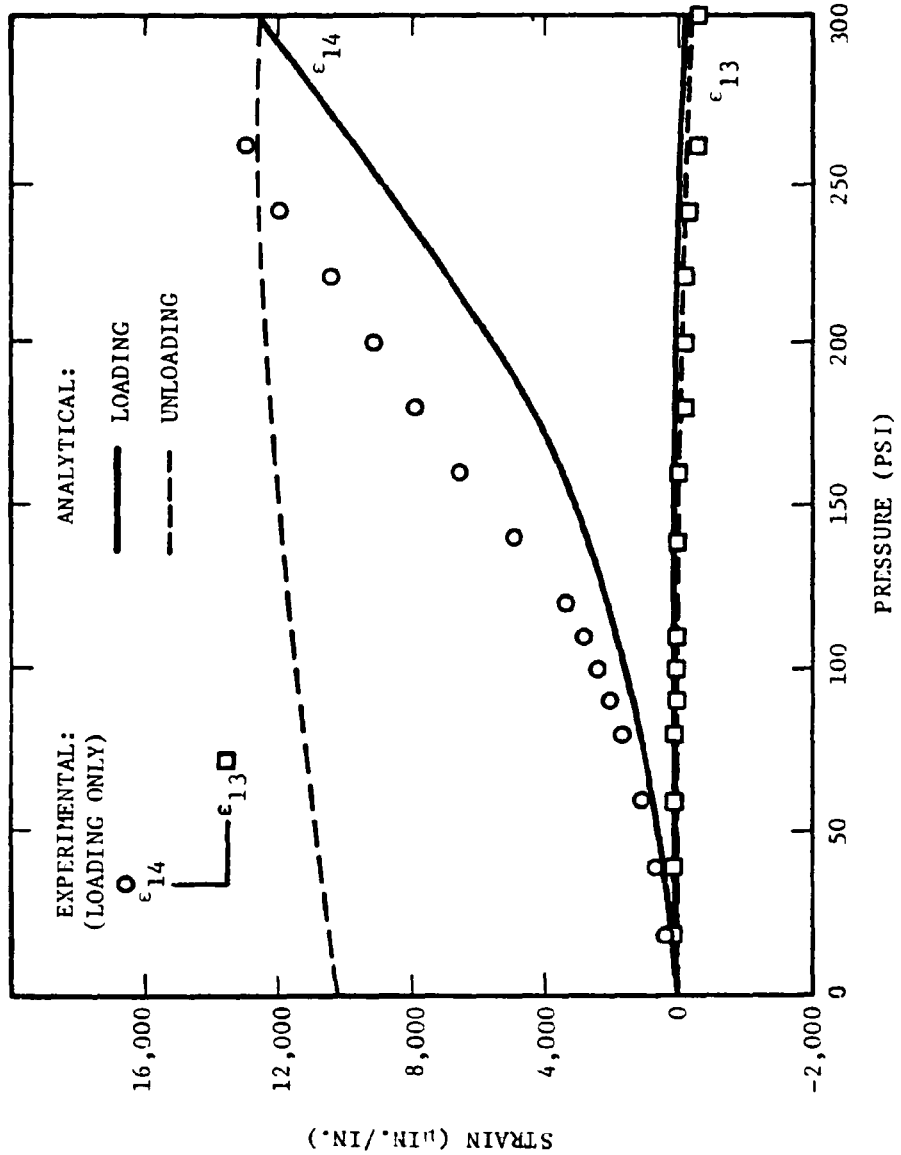

FIGURE 4.60. COMPARISON OF EXPERIMENTAL AND ANALYTICAL STRAINS AT ROSETTE NO. 5

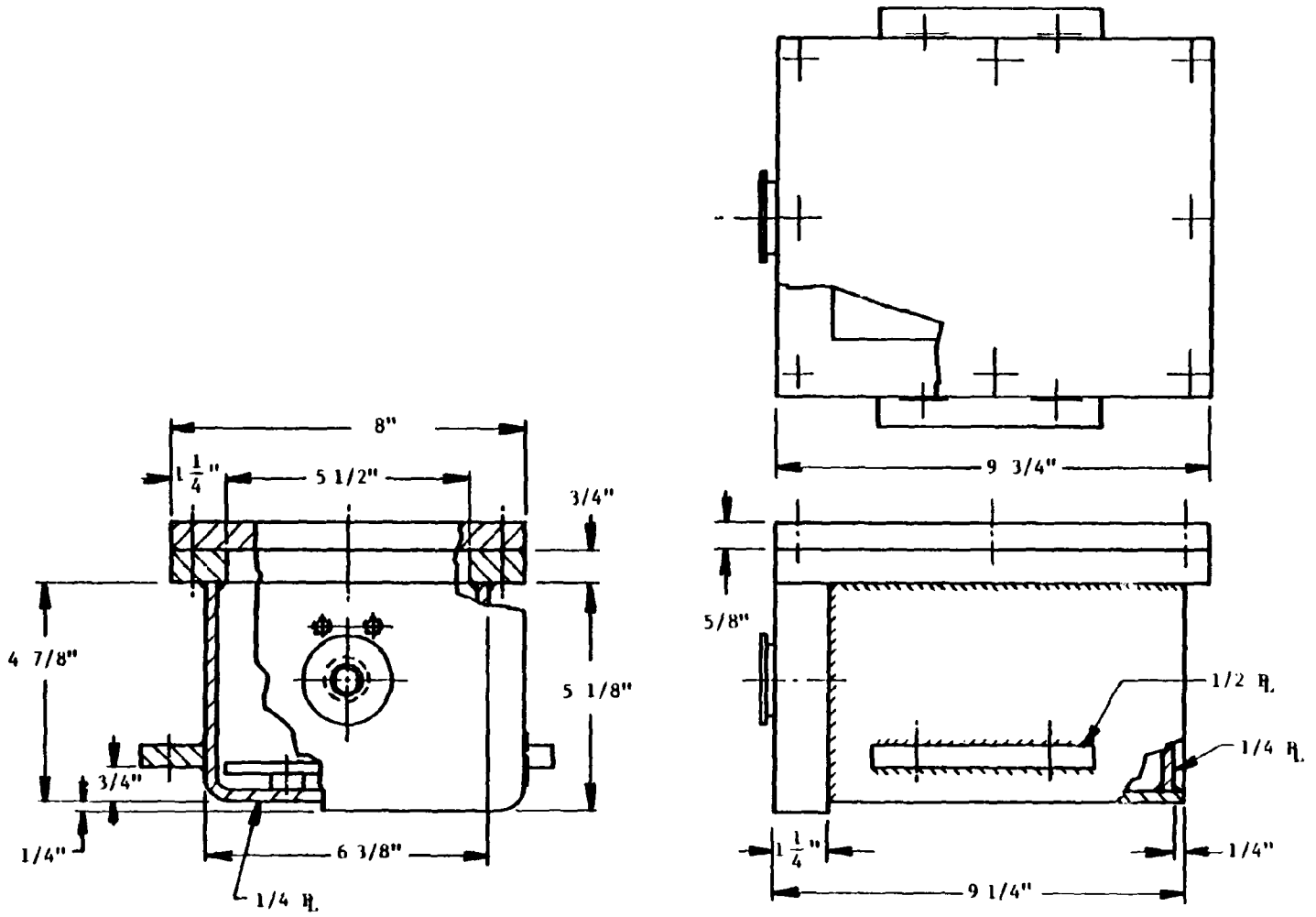

FIGURE 4.61. ENCLOSURE II

of the enclosure comprised of the 1-1/4-in.-thick plate was treated as rigid because its stiffness was very large compared to that of the 1/4-in. shell.

The model had approximately 334 nodes with six degrees of freedom (three rotational and three translational) per node. Each of the various components contained the following element types:

Component	Element Types	Number
Cover	Triangular Shell	134
Bottom	Triangular Shell	90
Side	Triangular Shell	126
Back	Triangular Shell	69
Flange	Three-Dimensional Beam	15
Bolts	Three-Dimensional Beam	0
Support Plate	Triangular Shell	15
		459 Total

An isometric view of the assembled model is shown in Figure 4.62. The cover, flange, and box shell were connected together with constraint equations as in the analysis of Enclosure I (for details see Section 4.1.2).

For the elastic analysis, the model was loaded with a 100-psi internal pressure. All nodes on the y-z plane of symmetry were given the symmetric boundary conditions.

$$U_x = \theta_y = \theta_z = 0$$

where U_i and θ_i are displacements and rotations in the i-th coordinate direction.

4.2.1.2 Results

Stress and displacement contour plots for the various components are shown in Figures F.1 through F.10 in Appendix F. If these plots are compared with those of Enclosure I, in Appendix A, one will see that they qualitatively agree very well. The only exception is for the covers in the neighborhood of bolts. This is to be expected since each cover has a different bolt configuration. The computer results indicate that the stress levels in Enclosure II are significantly below those of Enclosure I by factors ranging from three to five. In fact, for this 100-psi pressure loading, no von Mises stresses in the shell structure of Enclosure II exceeded the A36 steel yield stress of 36 ksi.

It is instructive to indicate which regions will yield when the internal pressure is increased. Figures F.11-F.13 in Appendix F show elements with a von Mises stress which exceeds 10 ksi for the 100-psi internal pressure (the 10-ksi level was an arbitrarily chosen value). Since the stresses in the shell vary linearly with pressure up to yield, the analysis predicts yield to occur first at the location of the highest induced stress. This location of maximum induced stress

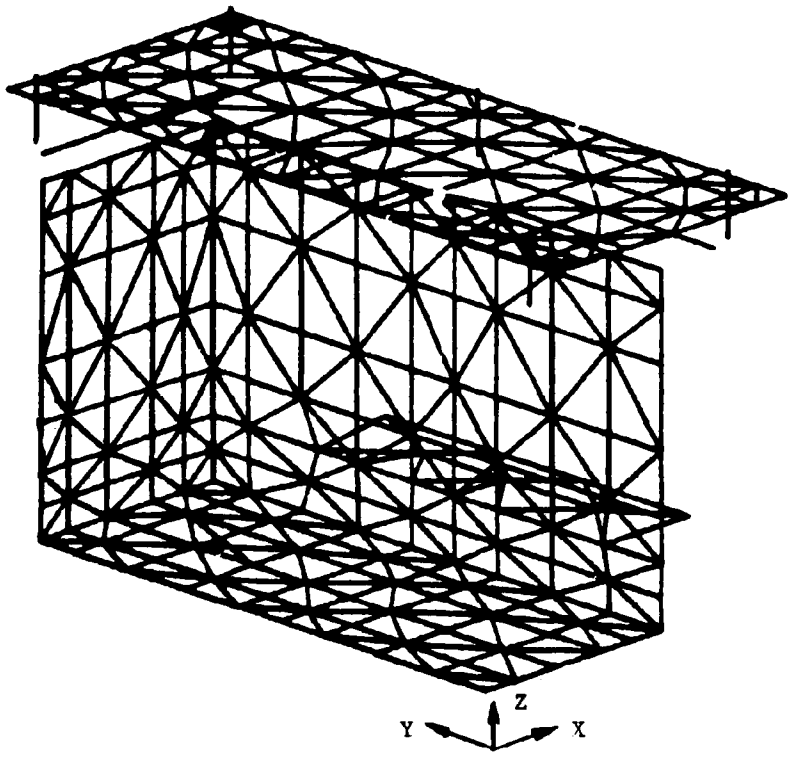

FIGURE 4.62. FINITE ELEMENT MESH
OF ENCLOSURE - LOOKING
FROM INSIDE

(at 100 psi) is in the bottom shell and is shown in Figure F.11 of Appendix F. The pressure required to induce a yield stress at this location is

$$P_{yield} = \frac{100 \text{ psi}}{15 \text{ ksi}} \times 36 \text{ ksi}$$

$$= 240 \text{ psi}$$

Note that the region of initial yielding in Enclosure II is adjacent to the initial yield location which was on the interior side shell for Enclosure I.

Bolt stresses were much lower for this enclosure than for Enclosure I. The most highly stressed bolt was in the center of the long side. For this bolt the direct (axial) stress was 18,496 psi and the bending stress was 19,876 psi. Thus the combined maximum stress was 38,372 psi. Recall that these stresses are for 100-psig internal pressure.

4.2.2 Testing

4.2.2.1 Methodology

The enclosure was instrumented with four, three-element 45°, single-plane rosettes. The rosettes were located on the enclosure as follows:

Rosette	Location	Element Orientation	
1	Right Side (Outside)	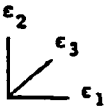	Looking from Outside
2	Bottom (Inside, Center and Close to Front Side)	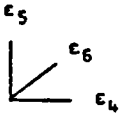	Looking from Top and Right Side
3	Bottom (Inside, Center and Close to Right Side)	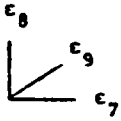	Looking from Top and Right Side
4	Back Side (Inside)	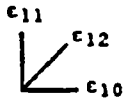	Looking from Inside

These gage locations are marked in Figure 4.63. Figure 4.64(a) shows Rosette No. 1 completely installed, and Figure 4.64(b) shows the interior installations for Rosettes Nos. 2-4.

The pressurization system used for Enclosure I was also used to test Enclosure II, except in these tests the pressure limit was increased from 285 psig to 500 psig. On this enclosure, the gap between the flange and the cover was monitored at two points, using dial indicators as shown in Figure 4.65. Because of the much higher pressures to which Enclosure II was tested, it was unsafe to manually check the cover-to-flange gaps with feeler gages, as was done on Enclosure I. Furthermore, 25 different pressure steps were made during the testing, and stopping at each step to enter the test cell and make the gap measurements would have been too time consuming. The two dial indicators were visible through a port in the test cell wall and were safely and easily monitored through a sight glass at every pressure increment.

After strain gaging, the enclosure was placed in the test cell and the cover attached without a gasket. The bolts were "finger tightened" to determine the no-torque gap between the lid and the box. Using flat feeler gages, gaps of 2 and 3 mils were detected, primarily along the short sides between bolt positions and around two of the corners. About one full turn with a torque wrench (15-20 ft-lb) was required to close all these gaps to less than 2 mils.

With the gasket in place, thickness measurements were made around the flange to determine the added gap produced by the gasket (by comparing to previous measurements made without the gasket). As would be expected, the added gap measurements ranged from 0.030 to 0.035 inch. To develop the necessary clamping force, the eight 3/8-in. bolts on the enclosure were torqued to 45 ft-lb, close to the maximum allowable torque for the No. 5 bolts used [9,10,11].

Prior to conducting the test, a preliminary test using pressure steps of 50 and 100 psig was made to check the complete measurement system and ensure pressure system integrity. Enclosure II was then pressurized to 500 psi in 20-psi increments. Water pressure was monitored using a strain gage pressure transducer and digital voltmeter, and voltage readings of the 12 strain elements were recorded at each pressure increment. In addition, the two dial gages were observed and recorded on several steps throughout the test pressure range.

At 200 psig, a small water leak was observed around a bolt. Pressurization continued up to 260 psi, at which point another water leak was detected at a second bolt and the first leak continued to grow. No yielding was apparent at any strain element. Because the pressure reached was just over half of the maximum pressure anticipated, it was decided to depressurize and take corrective action.

When removing the lid, it was noticed that some of the bolts were removed at a much lower torque than had been used to install them. Visual inspection showed that the lock washers were deforming beneath the bolts, allowing the lid to raise and reducing the pressure on the gasket. This problem was corected by installing double flat washers on

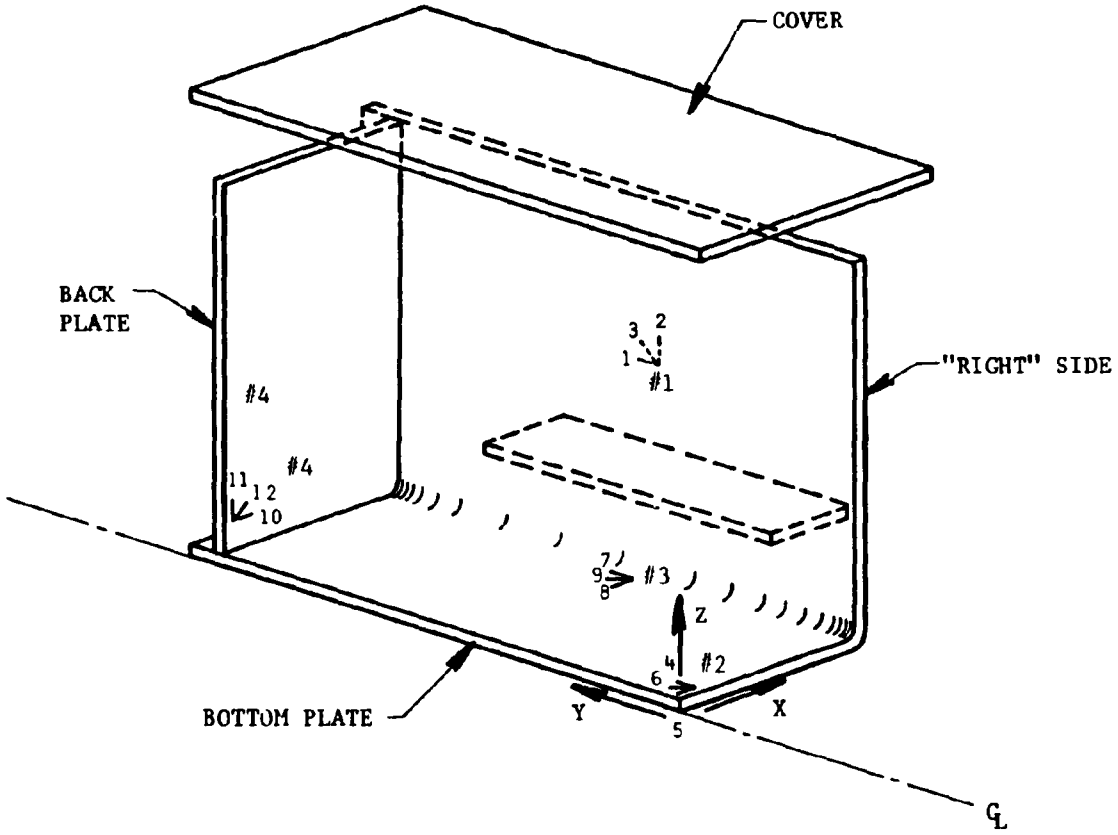

VIEW FROM INSIDE
(FRONT PLATE NOT SHOWN)

FIGURE 4.63. SCHEMATIC OF STRAIN GAGE LOCATIONS FOR ENCLOSURE II

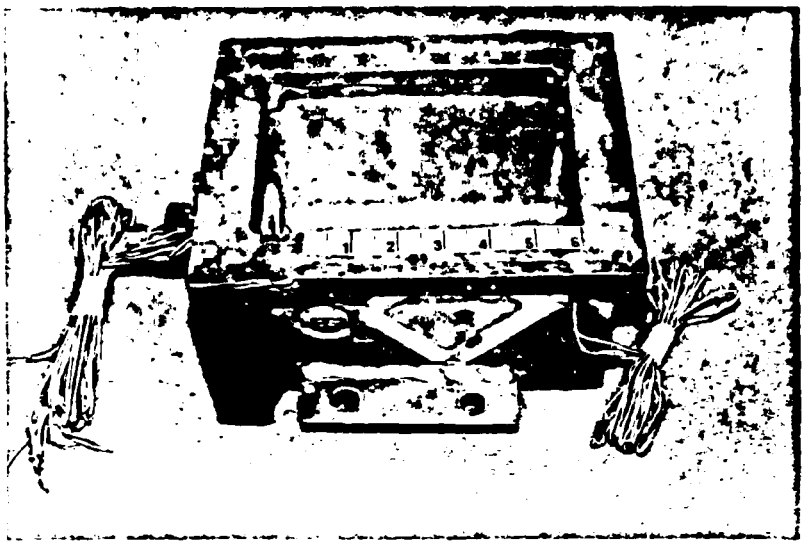

(a) View of Right Side (Front to Left)

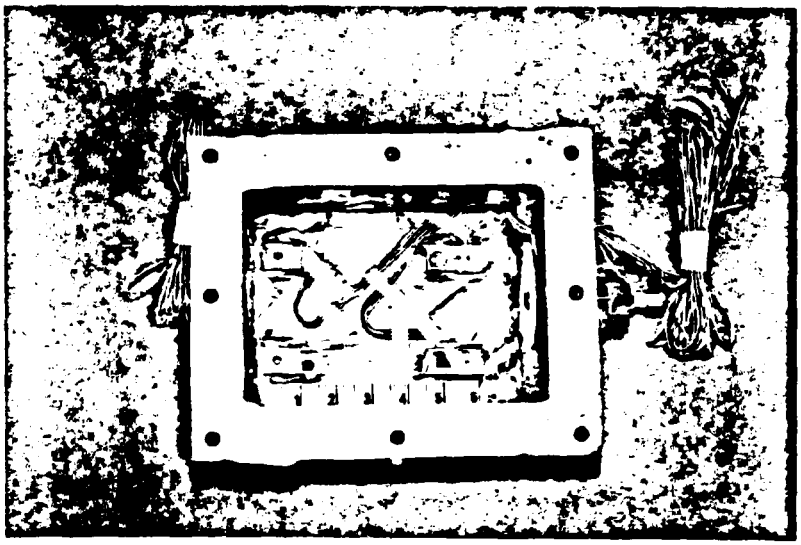

(b) View from Top (Front to Right)

FIGURE 4.64. INSTRUMENTED 2G ENCLOSURE II

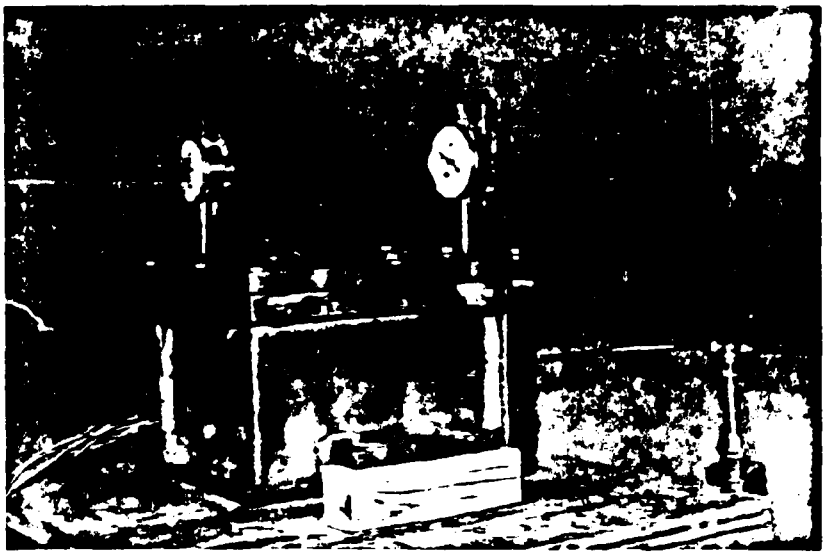

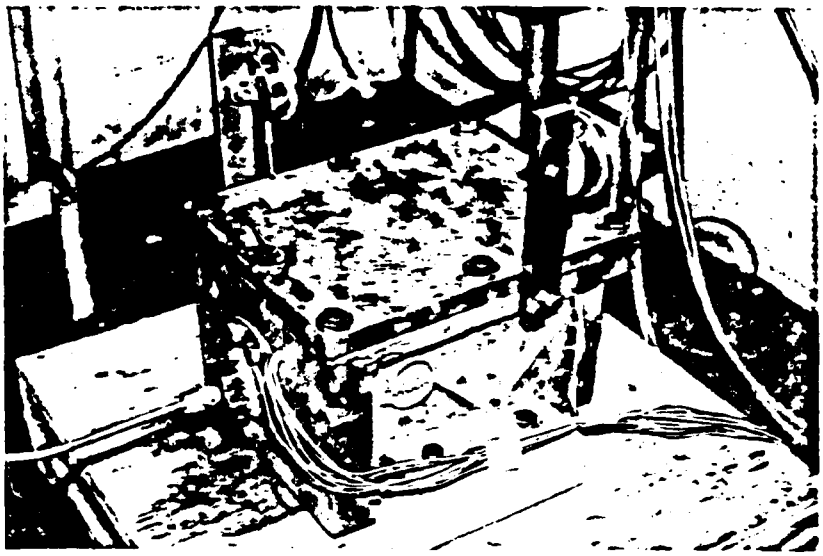

FIGURE 4.65. ENCLOSURE II WITH DIAL GAGES

all bolts. Another cause for the water leaks was the high in-plane elasticity of the neoprene rubber gasket. The gasket was being forced outward under the action of the internal pressure. To correct this problem, a reinforced neoprene rubber gasket of the same thickness was substituted for the unreinforced one used in the first attempt.

The new gasket was installed and the lid bolted on the enclosure with 50 ft-lb of torque. Pressure was increased in 80-psi increments up to 240 psi to check the earlier strain readings. Agreement with the first set of strain measurements was excellent, readings deviating only ± 1 μin./in. Pressurization then continued in 20-psi increments to 500 psig. Very slight water leaks around two bolts developed at 460 psig, but posed no problems, and the test continued to the maximum pressure.

The two dial indicators measuring the cover-flange gap were observed throughout the test, and at the 500-psig pressure they showed an increase between the cover and the enclosure of only 0.9 and 1.2 mils. The gasket was able to expand sufficiently within this gap enlargement to retain a tight seal. No water leaks were observed around the flange interface. Upon depressurization, the dial gage readings returned to zero.

4.2.2.2 Results

The strain data recorded on this test are presented in Figures 4.66-4.69. Strain measurements and analytical predictions for the three elements of each rosette are included on one graph. Tensile strains are given positive values. Yielding is not readily apparent at the gage locations. The strains at Rosette No. 2 show nonlinear behavior, but the magnitudes of the strains are below the yield strain of the steel plates. Higher strains occurred at other locations, such as at Rosette No. 3, but the strain behavior remained linear. Possible reasons for nonlinearity in Rosette No. 2 are discussed in the analytical-experimental comparisons which follow.

Displacement measurements on the bolts showed no permanent set, so no permanent increase in the flange-to-cover gap should occur at pressures up to 500 psig. Bending in the bolts was not measured for this enclosure.

4.2.2.3 Analytical-Experimental Comparisons

Analytical predictions can be compared with the measured strains for each gage element in Figures 4.66-4.69. Except for Rosette No. 2 the correlation is good. Small differences such as for elements 1 and 2 in Rosette No. 1 can be caused by slight misalignment between the gage axes and the axes in the F.E. model. Three factors may have caused the disagreement which occurred at gage location No. 2:

(1) Stiffening of the bottom of the enclosure at gage location No. 2 produced by the two standoff pieces welded to the bottom plate near the gage. These two pieces can be seen in Figure 4.64(b) near the right end (front) of the box.

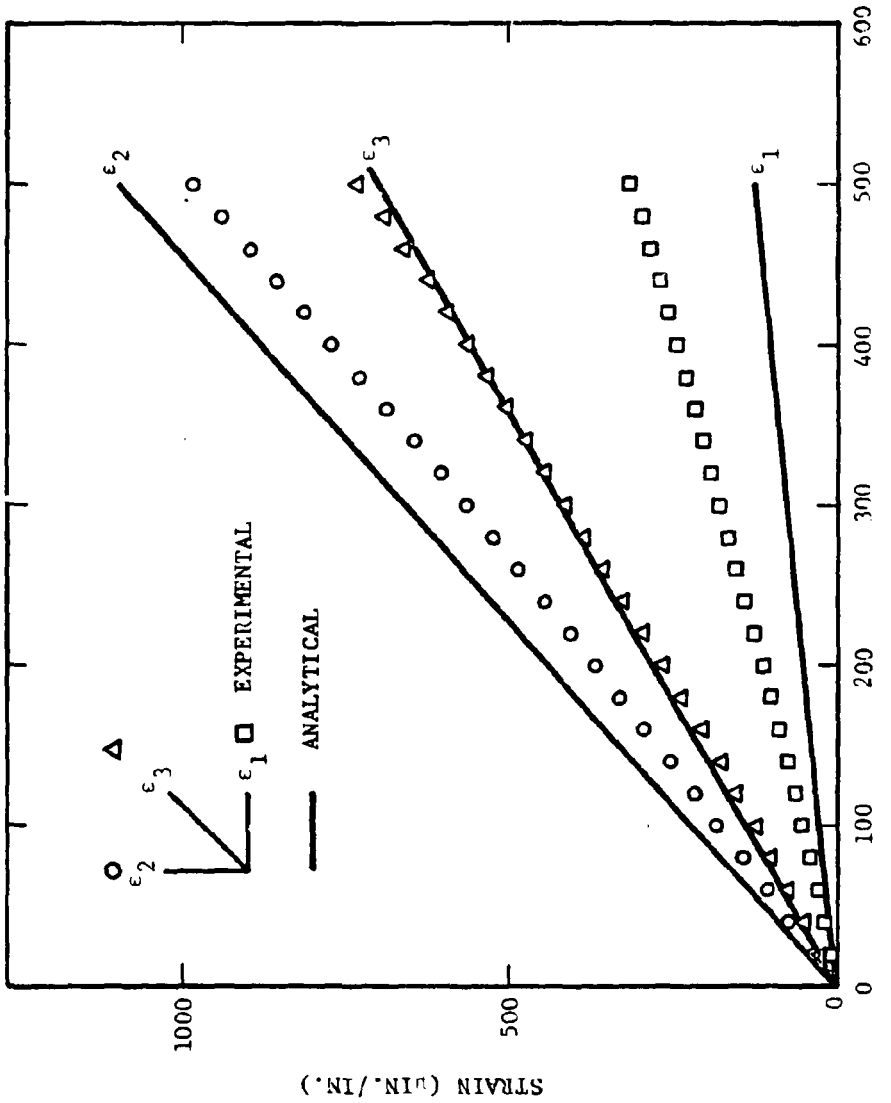

FIGURE 4.66. ROSETTE NO. 1 DATA COMPARISON

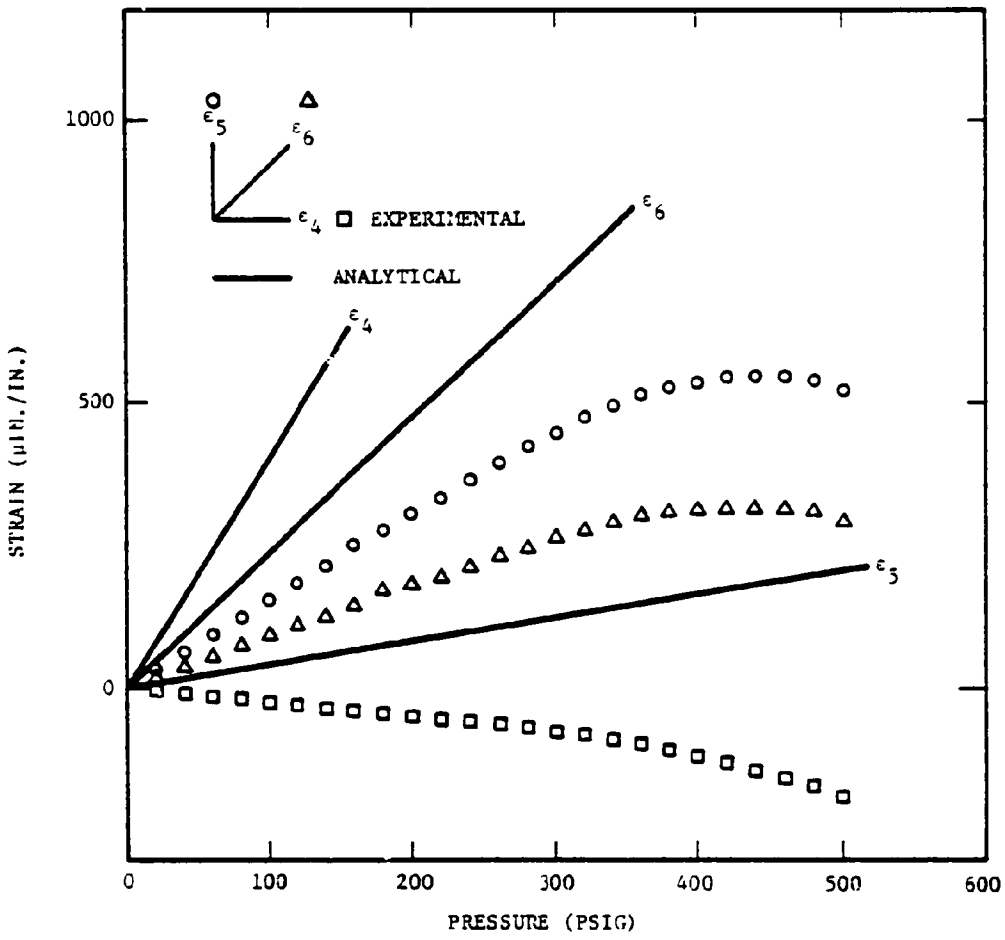

FIGURE 4.67. ROSETTE NO. 2 DATA COMPARISON

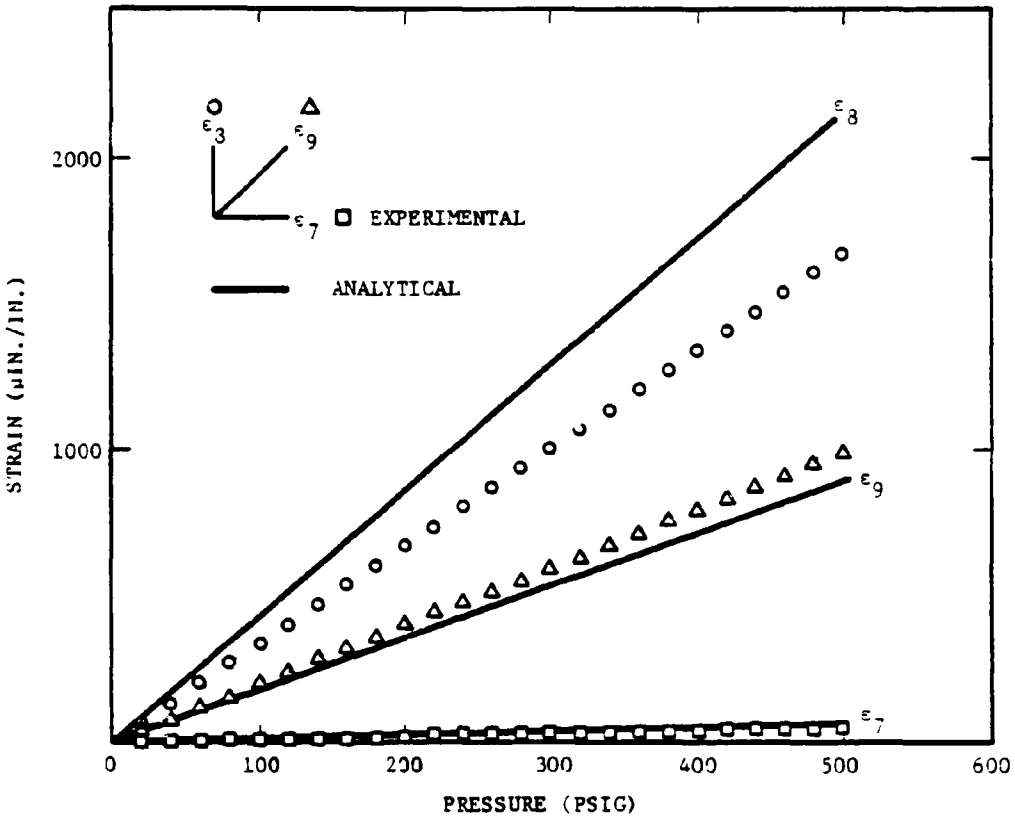

FIGURE 4.68. ROSETTE NO. 3 DATA COMPARISON

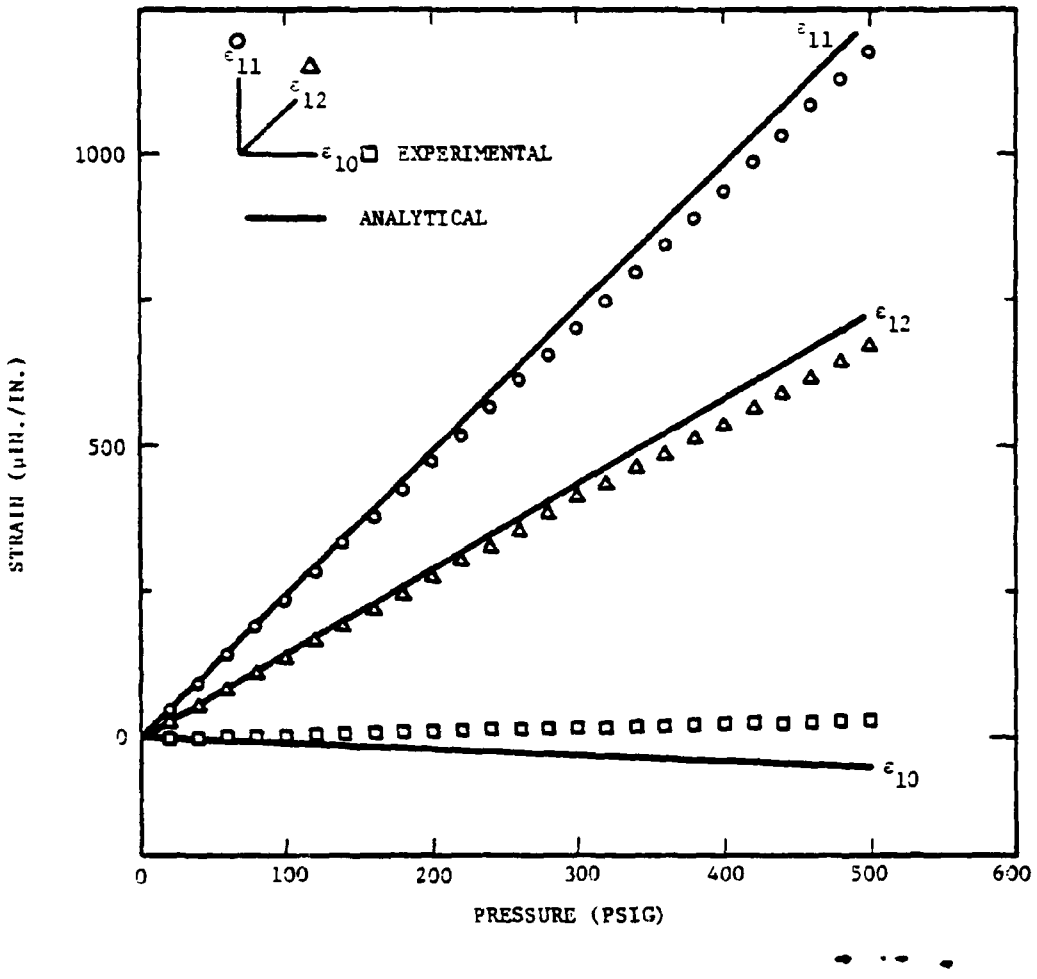

FIGURE 4.69. ROSETTE NO. 4 DATA COMPARISON

(2) Some yielding in the weld between the bottom plate and the front of the enclosure, which gave the bottom plate a boundary condition intermediate to fully clamped and simply supported. Fully clamped was assumed in the analysis.

(3) Some creep of the adhesive which held the gage in place.

At this time the principal cause of the analytical-experimental disagreement is believed to be the effect of the standoff pieces welded to the bottom of the enclosure. They act to reduce bending in the bottom plate at the gage location and can produce the basic disagreement in the slopes of the calculated and measured strains at low pressures. These stiffeners were omitted in the analysis because they will have little effect on peak strains and stresses in the enclosure, although they do affect strains locally at some locations. In addition to the general disagreement, some yielding of the weld or creep of the adhesive obviously occurred because of the concave nature of the strain-pressure plot (Figure 4.67). This behavior is characteristic of the strain observed in Enclosure No. 1 when the weld between the bottom plate and the side shell yielded. The true cause for the concave nature of the trace was not determined. Sectioning of the box through the weld in question might have revealed inadequate penetration or bonding, but visual examination showed no cracking or obvious yielding in the weld.

4.3 Enclosure III Analysis and Testing

Enclosure III was provided to SwRI by the USBM. As shown in Figure 4.70, the enclosure is a rectangular shaped luminaire, made of cast aluminum, with rectangular side windows and a circular end window. The windows are made from tempered soda lime glass with the side windows being 3/4 in. thick and the end window being 5/8 in. thick. An elastic analysis of this structure for a static internal pressure was conducted using the finite element method. Hydrostatic tests were then conducted and comparisons were made between the experimental and analytical results.

4.3.1 Elastic Analyses

4.3.1.1 Characteristics of the Finite Element Model

Enclosure III appeared, qualitatively speaking, to be rigid, with 0.75 in. thick glass side and top windows and a 1-1/4 in. thick aluminum end plate containing the penetrations for the electrical connections. Because of this rigidity, it was felt that the critical components of the container, i.e., windows and disk-shaped end section, could be analyzed by assuming that the remaining enclosure is rigid. This substructuring approach allowed for a more detailed study of the stress distributions in these parts than could have been economically obtained if the complete container were analyzed. Three such structures, along with their corresponding loading and boundary conditions, were analyzed. They were designated as:

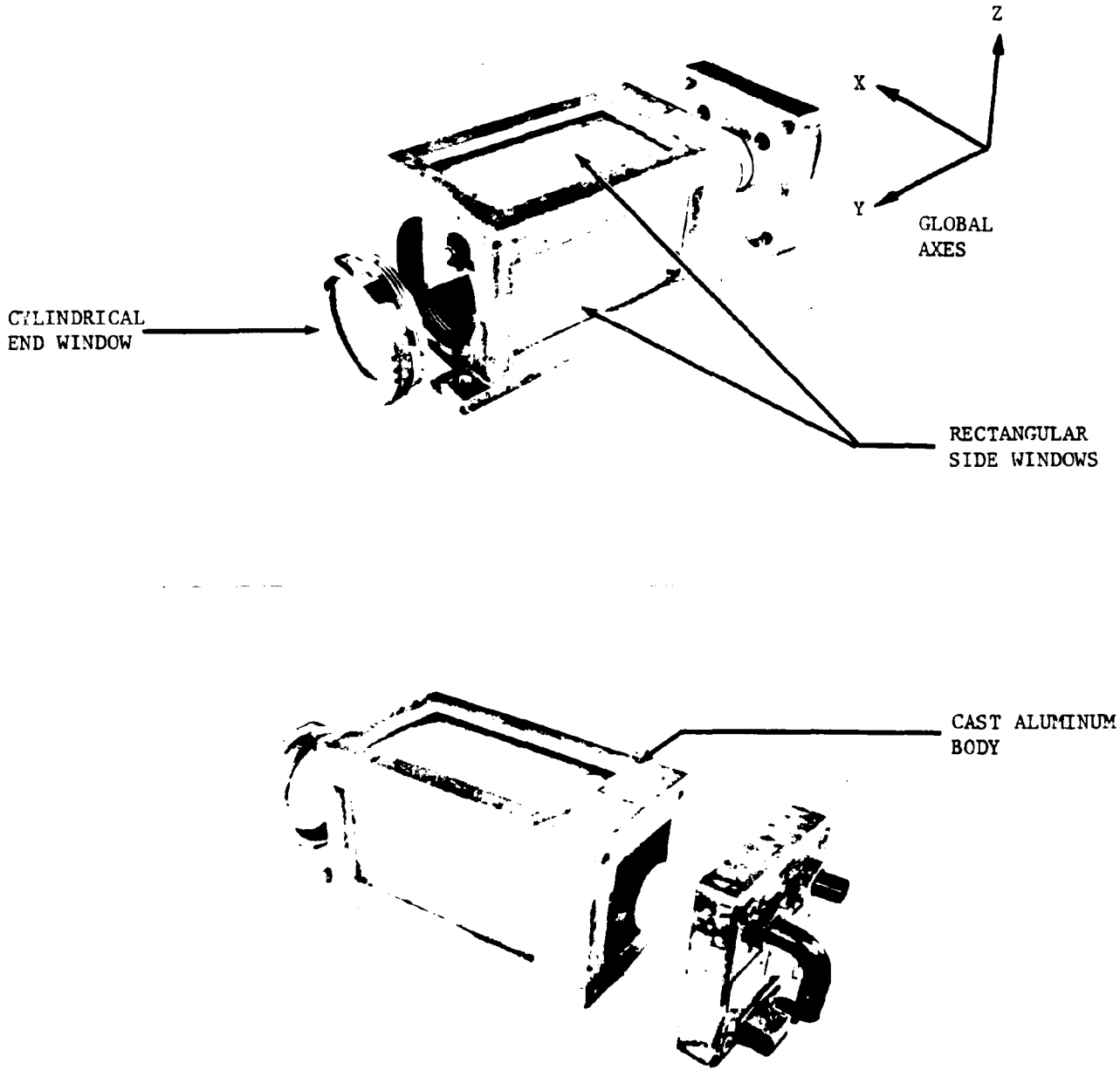

FIGURE 4.70. ENCLOSURE III -
LUMINAIRE WITH WINDOWS

Model I - Quarter-Symmetry Model of the Rectangular Windows Using Three-Dimensional Finite Elements

Model II - Axisymmetric Model of Cylindrical End Window

Model III - Two-Dimensional Plane Strain Model of the Luminaire's Cross-Section

The glass, aluminum, and epoxy cement in the models were assigned the following physical properties:

Glass - Young's Modulus $E = 10.0 \times 10^6$ psi
Poisson's ratio $\nu = 0.25$

Aluminum $E = 10.0 \times 10^6$ psi
$\nu = 0.30$
Epoxy Cement $E = 0.4 \times 10^6$ psi
$\nu = 0.35$

In these analyses all models were loaded with a 100-psi internal pressure. Since the solution assumes linear elastic behavior, deflections and stresses for other pressures were obtained by direct scaling.

Model I - Rectangular Window

The side and top glass windows are thick flat plates supported in a metal frame by an adhesive material. Figure 4.71 shows the geometry of the window only. Because the windows are symmetric about the local XZ and YZ planes, only one-quarter of the windows need to be modeled. A mesh for one-quarter of the window is given in Figure 4.72. It contains two solid elements through the thickness. Solid elements were chosen instead of plate elements because thin plate theory is not accurate for low breadth-to-thickness ratios, which these plates have. The model had a total of 18 elements, with each element having either 8 or 20 nodes, depending on the shape function used. The 20-node element is more accurate than the 8-node, but requires significantly more computer time to obtain a solution.

Now consider the support of the windows in the enclosure. The top window (+Z-direction in Figure 4.70), for example, is supported by the aluminum structure on its two long sides, and the aluminum is in turn bonded to the side windows. On the ends of the window the aluminum structure is more substantial and is not bonded to other components.

Three cases were analyzed. In the first case deformations in the structure were ignored and simple support for the window edges was assumed. In the second case bonding between the aluminum and the side windows was ignored, and support beams, pinned at the corners of the windows, were coupled to the window to represent the constraint by the aluminum. In the third case support springs were added to the aluminum beams to simulate the restraint provided by the bonding to the side windows. This latter case is more representative of the enclosure so long as there is good adhesion of the epoxy to the aluminum and the

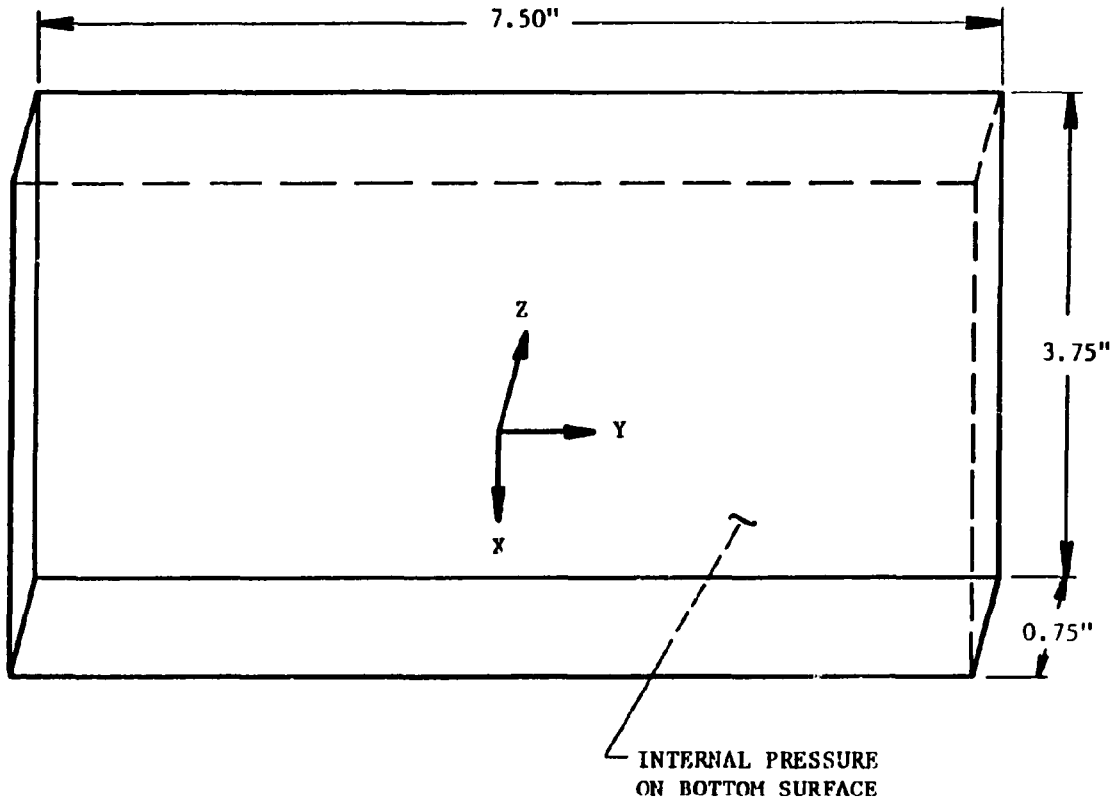

FIGURE 4.71. GEOMETRY OF RECTANGULAR WINDOWS IN ENCLOSURE III

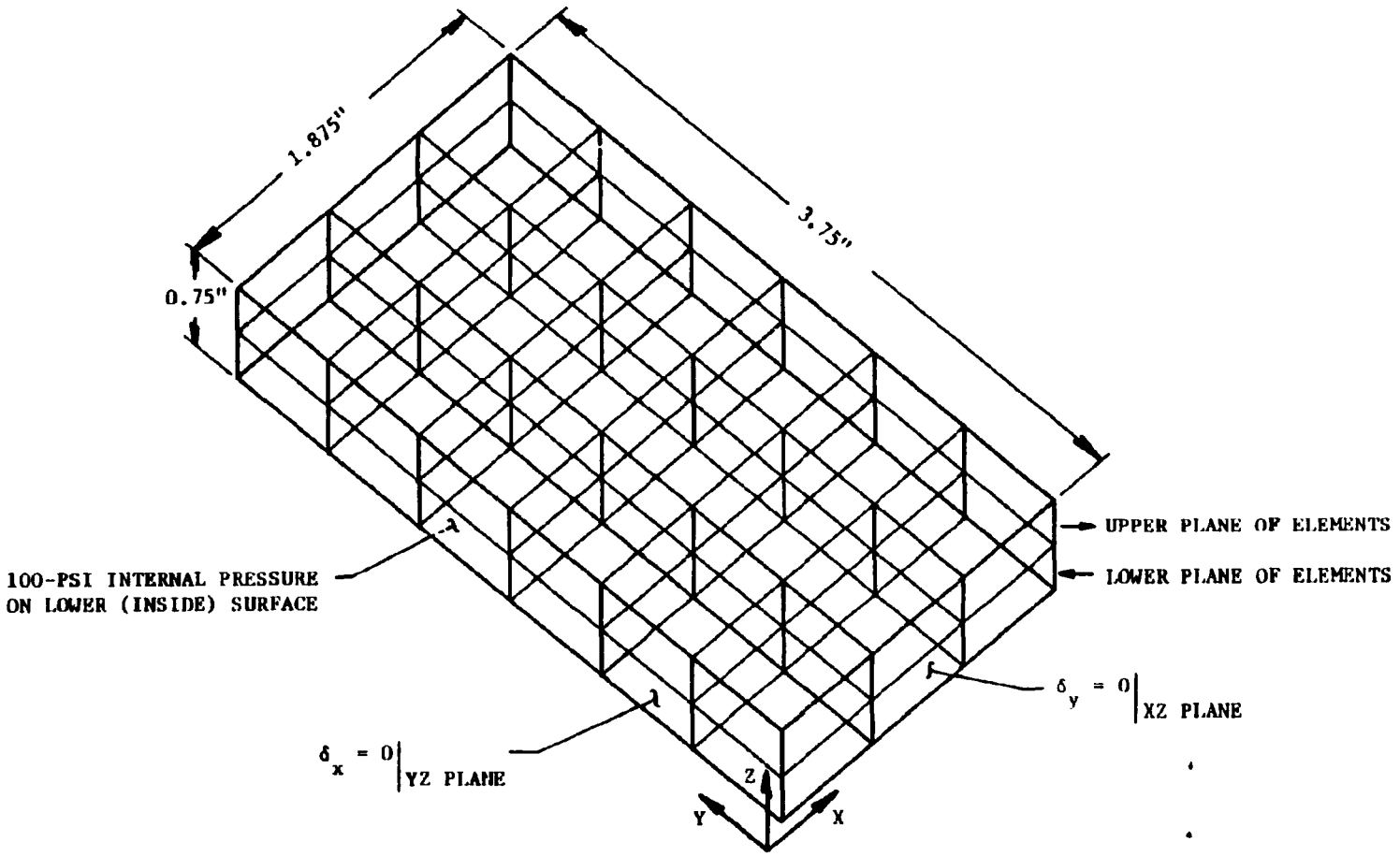

FIGURE 4.72. FINITE ELEMENT MESH OF ONE-QUARTER OF THE RECTANGULAR WINDOW--ENCLOSURE III

glass. The finite element mesh of the one-quarter of the window, with the beams and springs included in the model, is shown in Figure 4.73.

Model II - Cylindrical End Window

The end window consists of a cylindrical glass disk supported in an aluminum retaining ring by an adhesive material. The retaining ring is threaded and screws directly into the end of the enclosure. A cross-sectional view cut through any diameter of the disk is shown in Figure 4.74. Because the disk is a body of revolution, and therefore axisymmetric, the analysis was reduced from three to two dimensions. This reduction greatly reduced costs relative to a three-dimensional analysis and gave the same solution accuracy. Figure 4.75 shows the finite element mesh and the boundary and loading conditions. The window was pressurized uniformly on the inside and fully constrained along the outside threaded portion. The boundary condition preventing radial motion ($\delta_x = 0$) on the axis of rotation arises from the symmetry condition.

The model has nodes at each element intersection as well as nodes on selected element midsides. These midside nodes give improved accuracy in regions where high stress concentrations are expected. Locations of these nodes are indicated in Figure 4.75.

Model III - Luminaire Cross-Section

The purpose of the two-dimensional model of the luminaire cross-section was to treat more accurately the interaction between the rectangular glass windows, adhesive mterial, and aluminum support structure. This was accomplished by analyzing the container as if it were infinitely long. With this assumption, effects at the ends of the container were neglected, but the model should give reasonably accurate results for peak stresses and deflections near the mid-plane (a plane perpendicular to the Y-axis in Figure 4.70) of the luminaire.

Figure 4.76 gives a cross-sectional view of the enclosure with the glass, adhesive, and aluminum components; it shows that the structure is symmetric about a vertical centerline. The container was treated as though it were infinitely long, and a two-dimensional plane strain finite element model was formulated. Plane strain means that all strain components normal to the plane of Figure 4.76 are zero.

The half symmetry finite element model of the cross-section is shown in Figure 4.77. The elements in regions of expected high stress concentrations also contain midside nodes, although they are not shown. The nodes on the Y-axis were restrained in the X-direction, and for the loading condition, pressure was applied to the inside surface.

4.3.1.2 Analytical Results

Results of calculations performed using the previously described models are given in the following sections. Graphical results are for stresses computed at the element centroids. Surface stresses are usually higher than centroidal stresses, and these were given

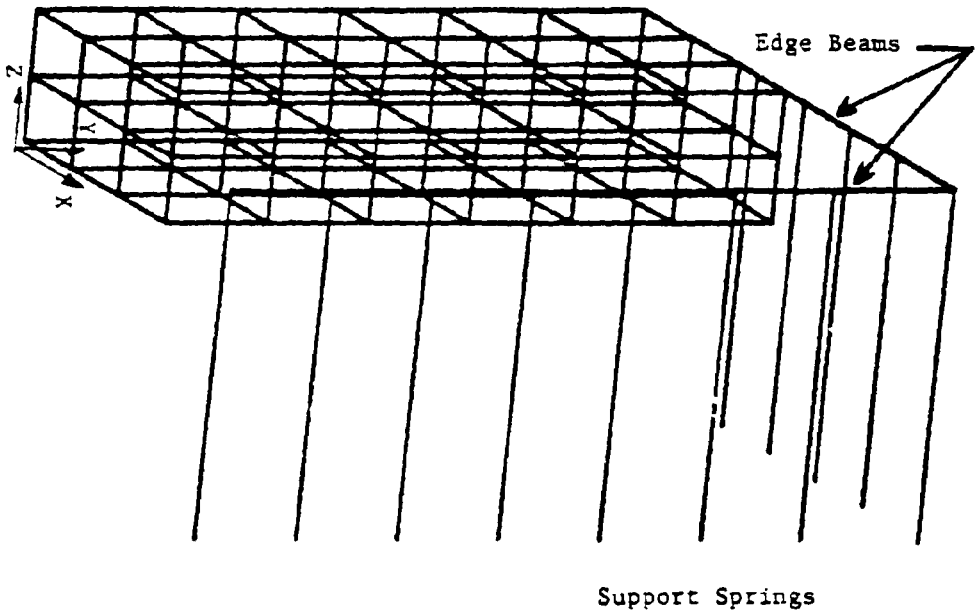

4.73. FINITE MESH OF ONE-QUARTER OF THE RECTANGULAR WINDOW WITH EDGE BEAMS AND SUPPORT SPRINGS

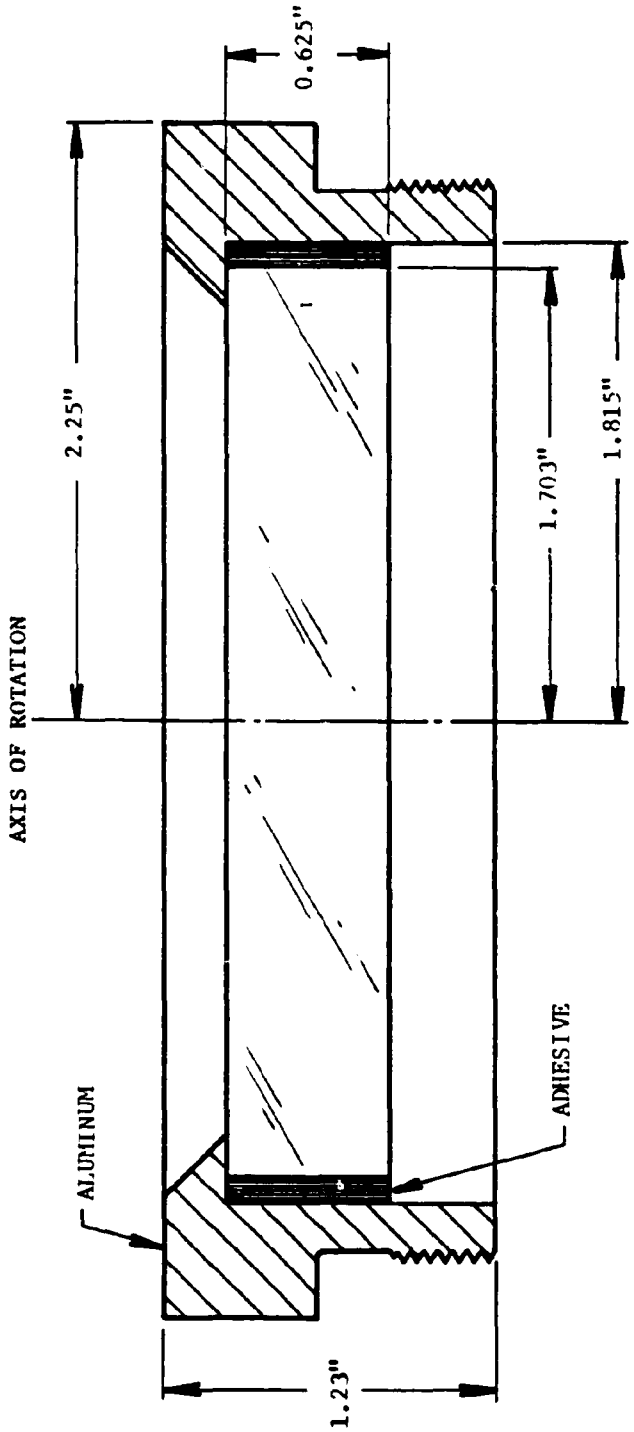

FIGURE 4.74. SCHEMATIC OF CYLINDRICAL END DISK

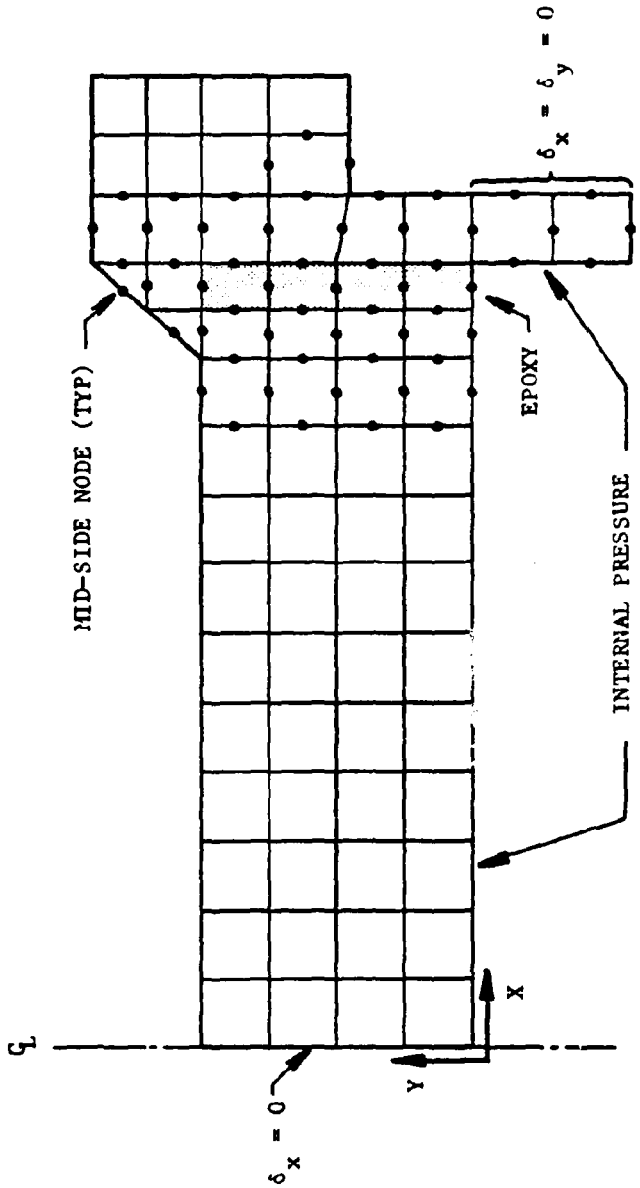

FIGURE 4.75. FINITE ELEMENT MODEL OF CYLINDRICAL END WINDOW

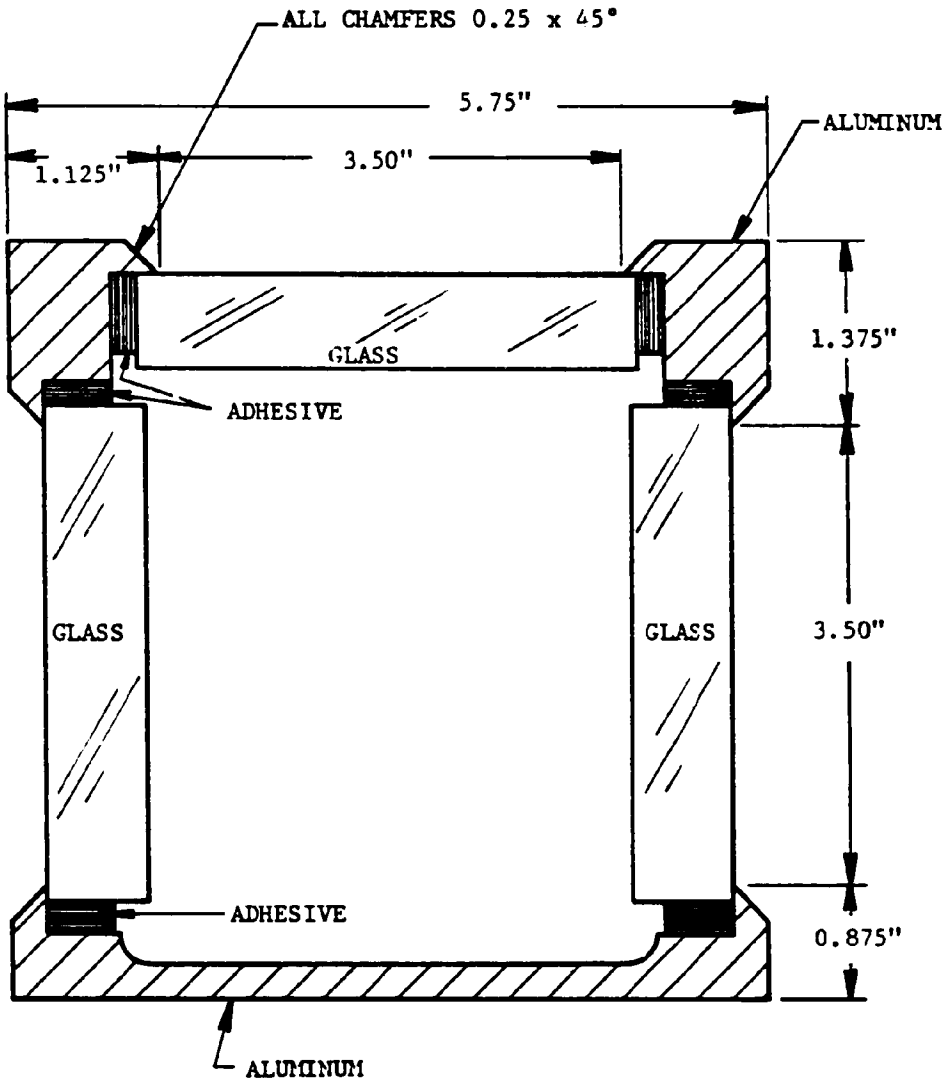

FIGURE 4.76. CROSS-SECTIONAL VIEW OF ENCLOSURE III

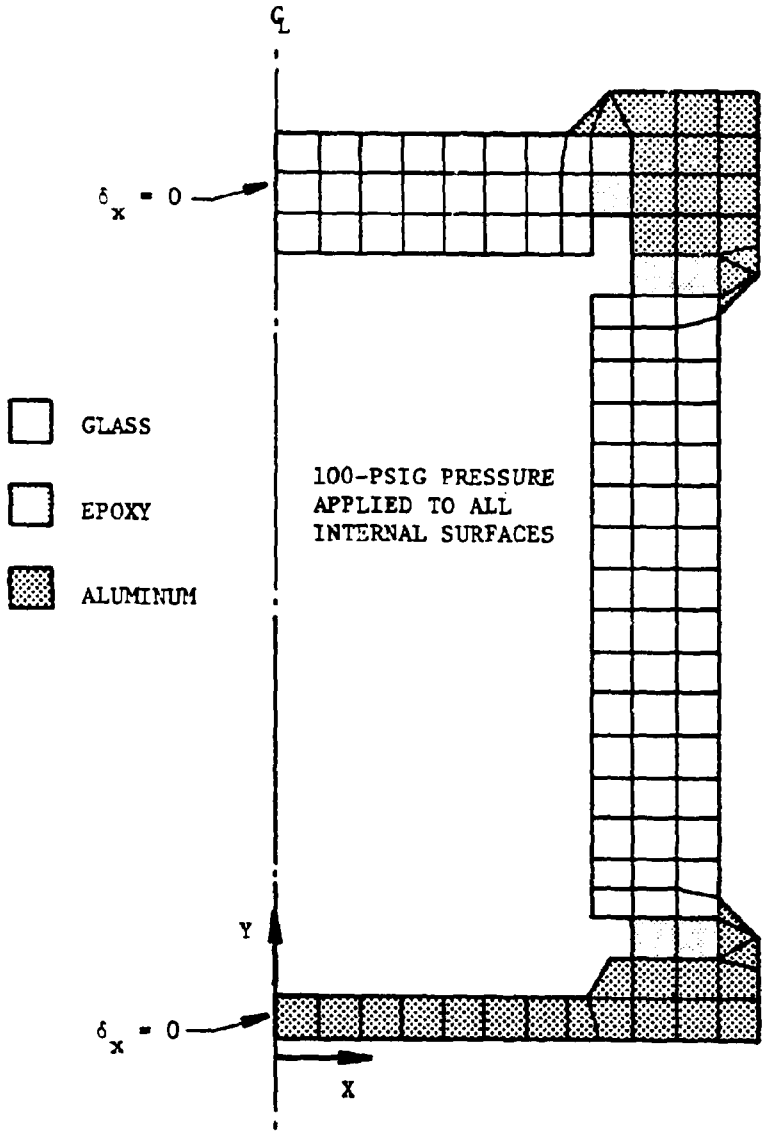

FIGURE 4.77. FINITE ELEMENT MESH
OF MODEL III

only in the printed output. Peak stresses for each model (usually surface stresses) are noted.

Results for Model I - Rectangular Window

Figures G.1-G.12 in Appendix G give stress contour plots for the maximum and minimum tensile stresses and for the maximum shear stresses at the centroids of the upper and lower planes of elements. Results are given only for the models with edge beams. These plots show that the peak centroidal stresses occur at the center of the window for both support conditions, i.e., with and without the contribution of the side windows. From the computer printout it was found that the surface stresses also peak at the center and are greater than the centroidal stresses. These peak surface stresses are shown on the finite model (shown without the support beams and springs) in Figure 4.78. Peak stresses are given for all three support conditions. Even though the simple support is an idealized representation of the support conditions, results for this case are not markedly different from the case with support springs.

Additional calculations were made for the windows in Enclosure III using handbook formulas [12] for glass windows with idealized support conditions. These results are given in Appendix H.

Results for Model II - Cylindrical End Window

A displaced geometry plot for the cylindrical end window is given in Figure 4.79. The displaced geometry is shown by solid lines, and the deflection at the center of the window corresponds to an internal pressure of 100 psig. Stress contour plots for this model are given in Figures G.13 through G.16. Recall that these stresses correspond to the element centroids. Maximum stresses in the glass occur at the center of the window, as expected, and peak stresses in the aluminum frame occur in the lip which retains the window. Note that the maximum von Mises stress occurs in the aluminum lip, but that all stresses are far below yield.

Tabulated results, which include surface stresses, were examined to find the peak stresses which occur in the model. As indicated by the contour plots, peak stresses in the glass should occur at the center of the window and, in the aluminum, near the lip. These maximums are shown in Figure 4.80. Peak stresses in the glass and aluminum are about the same and are well below the material yield strength. The peak stress in the epoxy is low and is only about 22% of the peak stress in the glass.

Results for Model III - Luminaire Cross-Section

The deformed geometry for Model III is presented in Figure 4.81. Boundary conditions fix the enclosure at the center of the bottom plate so that all displacements are positive. The maximum distortions occur in the bottom plate. Stress contour plots for the model are given in Figures G.17 through G.21. The contours indicate that maximum stresses occurred in the aluminum casting near the junction of the bottom

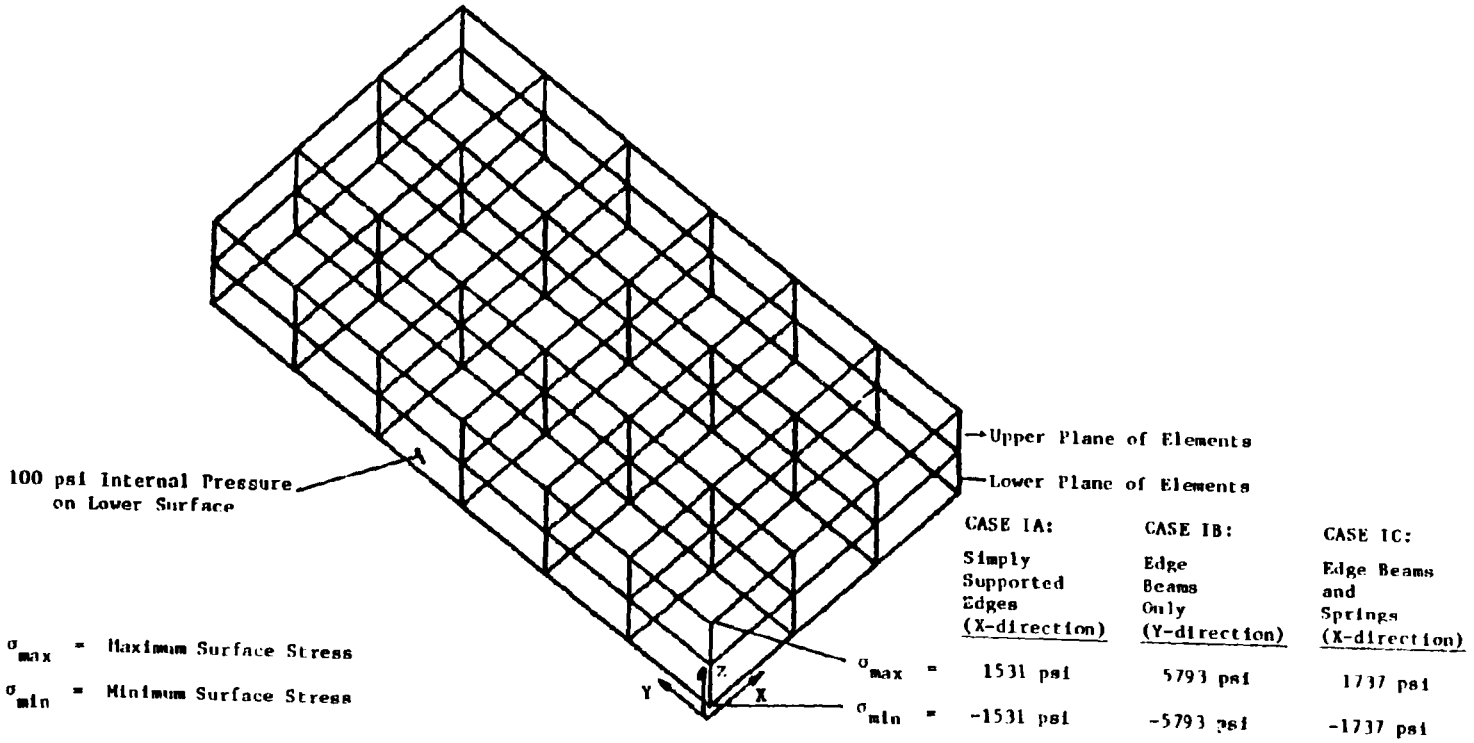

	CASE IA: Simply Supported Edges (X-direction)	CASE IB: Edge Beams Only (Y-direction)	CASE IC: Edge Beams and Springs (X-direction)
σ_{max} =	1531 psi	5793 psi	1737 psi
σ_{min} =	-1531 psi	-5793 psi	-1737 psi

FIGURE 4.78. LOCATIONS AND MAGNITUDES OF PEAK STRESS COMPONENTS FOR MODEL I - RECTANGULAR WINDOWS

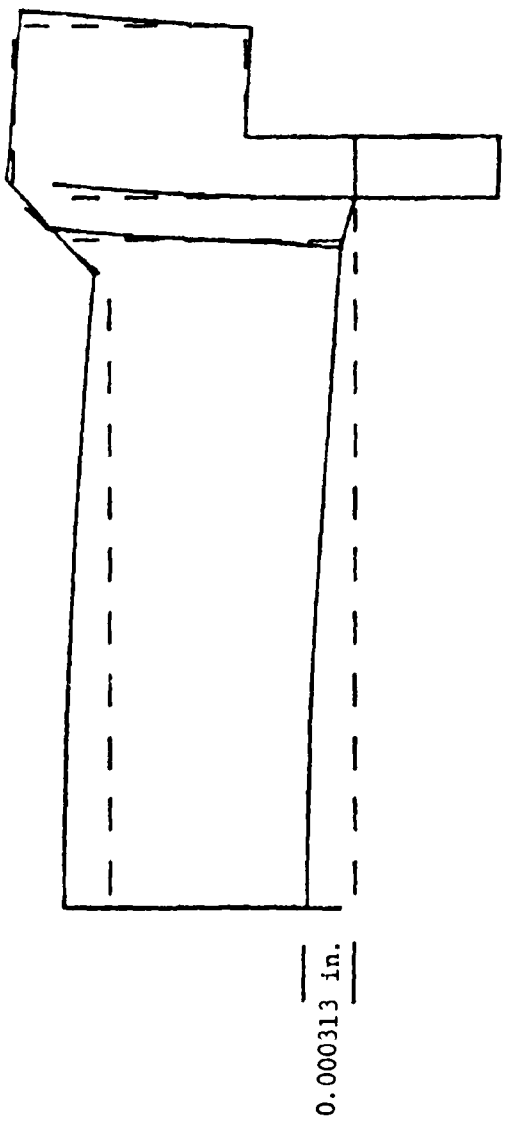

FIGURE 4.79. UNDISPLACED AND DISPLACED GEOMETRY
CYLINDRICAL END WINDOW (MODEL II)

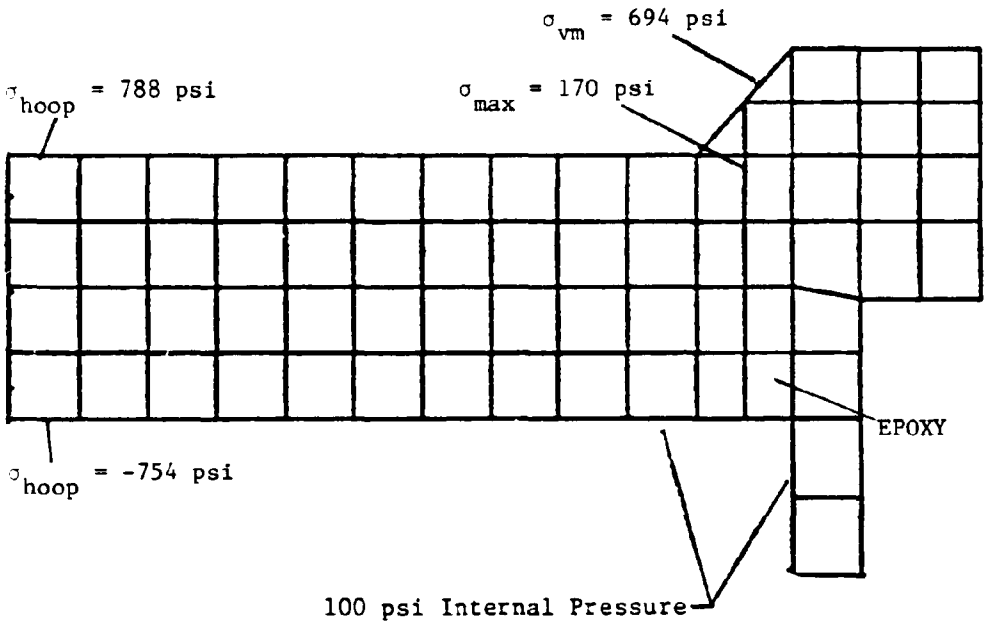

σ_{hoop} = Hoop Surface Stress

σ_{vm} = von Mises Surface Stress

σ_{max} = Maximum Surface Stress

FIGURE 4.80. LOCATIONS AND MAGNITUDES OF PEAK STRESS COMPONENTS IN CYLINDRICAL END DISKS

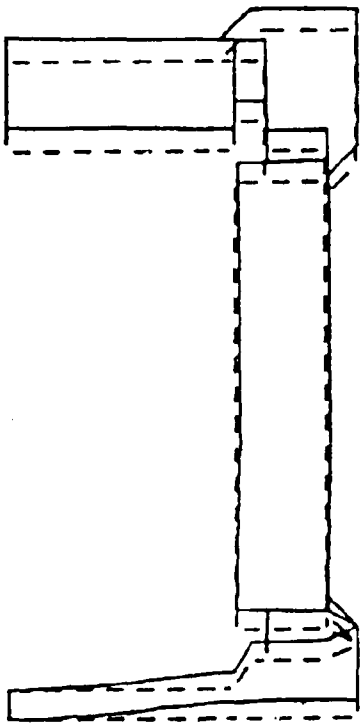

--- Undeformed Geometry

—— Deformed Geometry

FIGURE 4.81. UNDEFORMED AND DEFORMED GEOMETRY--MODEL III

plate and the side wall. This supports the observations from the displacement plots.

Tabulated output from the calculations were examined to identify the maximum stresses in the various parts of the model. These are shown in Figure 4.82. Note that the maximum stress does occur in the aluminum casting at the transition from the bottom plate to the side wall. The second highest stress occurs at the center of the bottom plate. Results for this model can be compared with those from Model I by examining stresses in the top window as given in Figures 4.78 and 4.82. These are tabulated below:

	Stresses (psi) Maximum	Minimum
Model I - 3-D Model of Top Window		
Case IB - Edge beams only	5793	-5793
Case IC - Edge beams plus support springs	1737	-1737
Model III - Cross-Section Model	2133	-1620

As expected, results for Model I with the support springs agree better with the cross-section model. The difference in peak stress between Case IC for Model I and Model III is produced by the restraint at the short side of the window, which is ignored in Model III. Recall that for Model III the window is assumed to be infinitely long in the Y-direction shown in Figure 4.70. The importance of good bonding between the epoxy, the aluminum, and the window is clear from the results of Cases IB and IC of Model I.

Comparisons between these results and those obtained from hydrostatic testing of Enclosure III are given in the next section.

4.3.2 Testing

Hydrostatic testing of Enclosure III and comparisons between experimental and analytical results are described in this section. Hydrostatic tests were performed to aid in the evaluation of the analytical predictions and to provide independent data with which to determine safety factors in the enclosure. Strain and displacement gages were used to monitor the enclosure behavior under the internal pressure loading.

4.3.2.1 Methodology

In order to measure strains induced by the hydrostatic pressure, five strain gage rosettes were installed at various locations on the enclosure. Four of these were 90°, two-element rosettes mounted on the glass windows, and the fifth was a three-element rosette mounted inside on the bottom of the aluminum casting near one of the long sides. Enclosure III, with gages installed, is shown in Figure 4.83. Each of the four two-element rosettes was centrally mounted on the glass panels, and the elements were parallel to the edges of the enclosure. One element was parallel to the short side of the window (transverse element), and

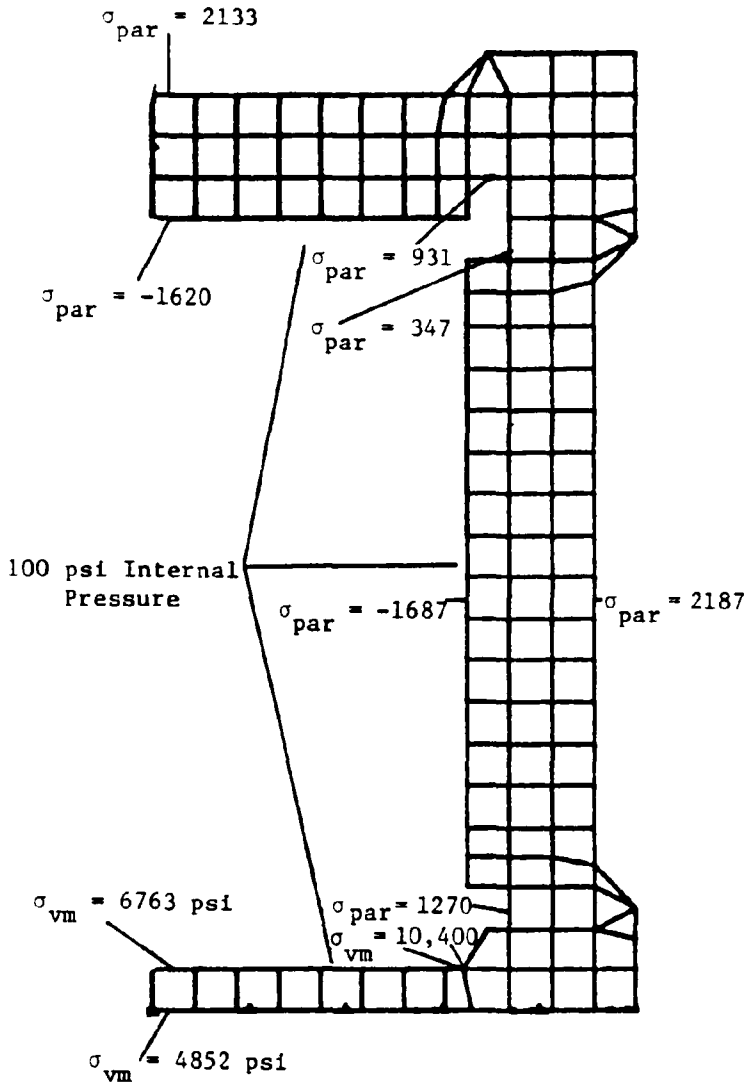

σ_{par} = Parallel Surface Stress

σ_{vm} = von Mises Surface Stress

FIGURE 4.82. LOCATIONS AND MAGNITUDES OF PEAK STRESS COMPONENTS IN PLANE STRAIN MODEL

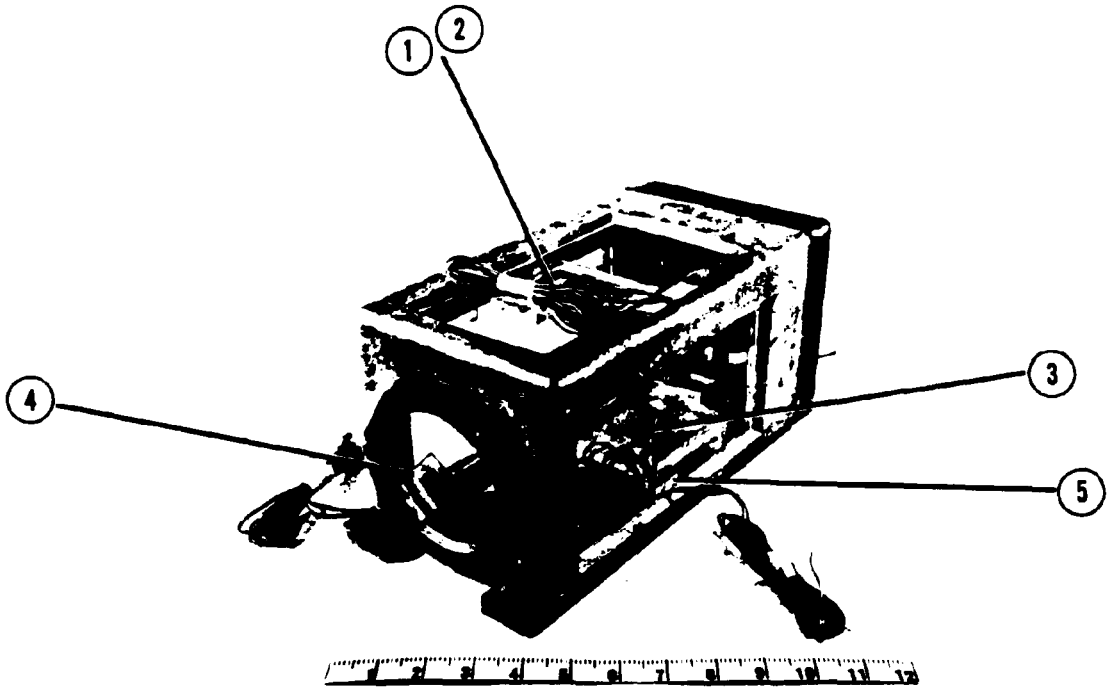

FIGURE 4.83. ENCLOSURE III WITH STRAIN GAGES INSTALLED

the other was parallel to the long side of the window (longitudinal element). Three of the two-element rosettes were externally mounted and one internally mounted opposite one of the external rosettes. The rosettes were numbered as follows: Rosette No. 1 was mounted on the outside of the top window; Rosette No. 2 was mounted on the inside of the top window; Rosette No. 3 was installed on the outside of one of the side windows; Rosette No. 4 was placed on the cylindrical end window, and Rosette No. 5 was mounted internally on the enclosure bottom surface.

In addition to the strain gages, two dial displacement gages were used to monitor the flange gap and to record center deformation in the bottom of the enclosure. The enclosure was mounted vertically with the cylindrical window at the bottom, to facilitate filling with water and pressurization. Figure 4.84 shows the enclosure ready for testing. Testing was performed by increasing the hydrostatic pressure in 20-psig increments. The enclosure was to have been pressurized up to the limit of the system, 500 psig, or until failure occurred. The test was terminated after taking data at a pressure of 230 psig. Higher pressures could not be achieved and maintained because of substantial water leaks through three cracks which developed in the aluminum casting. Small leaks also occurred through the 1/32-in.-thick neoprene gasket installed at the flange gap. However, these small leaks were inconsequential compared to the ones through the cracks in the aluminum housing. Figure 4.85 shows the cracks which occurred at three of the beveled corners on two of the openings for the glass panels.

4.3.2.2 Results

Valid strain data were obtained from all gages except for Rosette No. 5 on the aluminum bottom plate of the luminaire. All elements in this gage showed substantial drift during the test. The drift was attributed to loss of resistance to ground. Results for gages 1 through 4 are given in Figures 4.86 through 4.89. Analytical results are also shown in these figures, and experimental-analytical comparisons are made in the next section.

Recorded strains are linear over most of the loading range for gages 1, 2, and 3. Some non-linearity occurs at the beginning and end of the loading range in the transverse element of Rosette No. 3. This indicates some slight change in the boundary conditions with increasing load. Rosette No. 4 on the circular end window shows considerable non-linearity. Again, because the glass should be linear out to its breaking point, this non-linearity is caused either by changes in the window support or in the gage to window adhesion with increasing load.

The maximum tensile strain was recorded on element 1 of Rosette No. 1. This strain was 940 μin./in. and corresponds to a peak stress of approximtely 9,400 psi. The maximum compressive strain was recorded on Rosette No. 2, the opposing gage, and gives a compressive stress of approximately 10,100 psi. These stresses are quite high, but with tempered glass, which has high initial compressive surface stresses, it is possible to sustain these stresses without failure. The significance of these stresses will be further discussed in Section 5.0, which presents the safety factors computed for the enclosures. The displacement gages

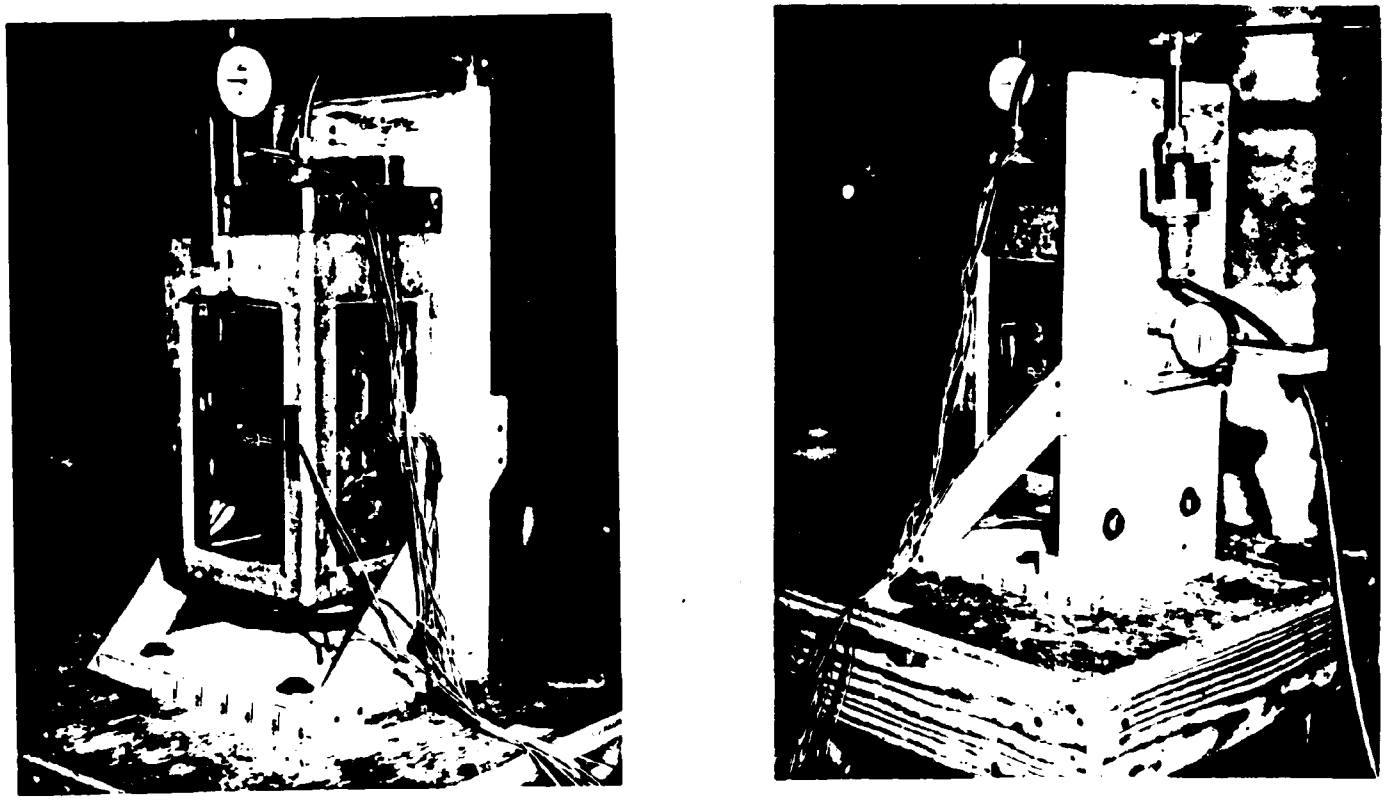

FIGURE 4.84. ENCLOSURE III READY FOR TESTING

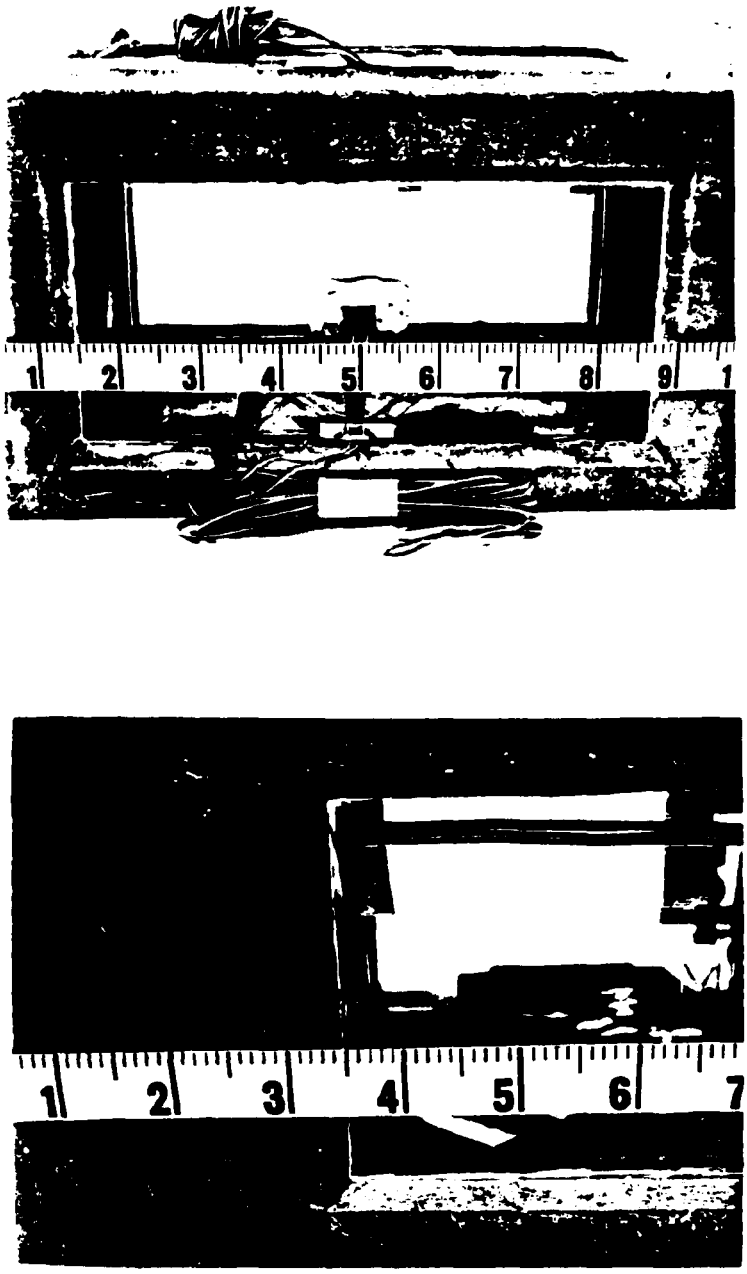

FIGURE 4.85. CRACKS IN THE ALUMINUM CASTING OF ENCLOSURE III WHICH OCCURRED DURING TESTING

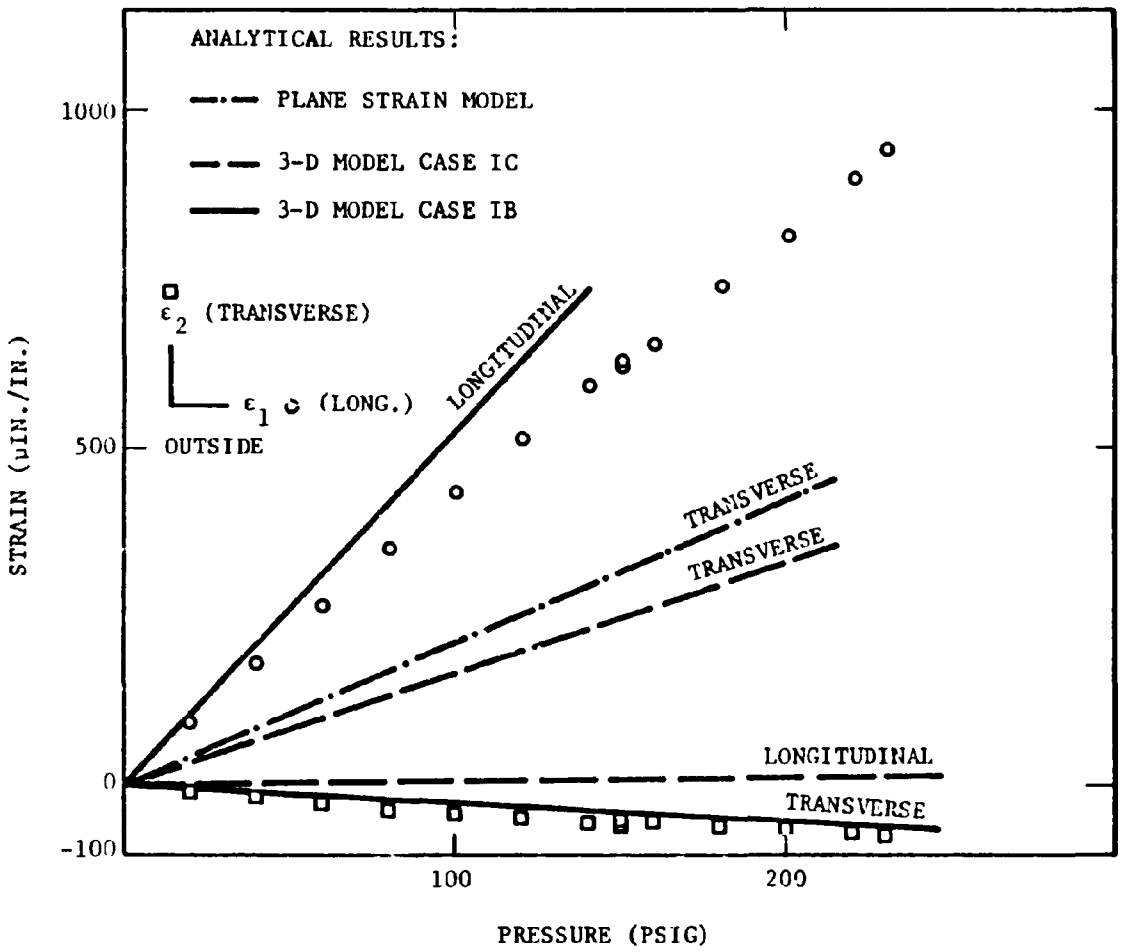

FIGURE 4.86. ROSETTE NO. 1, ENCLOSURE III

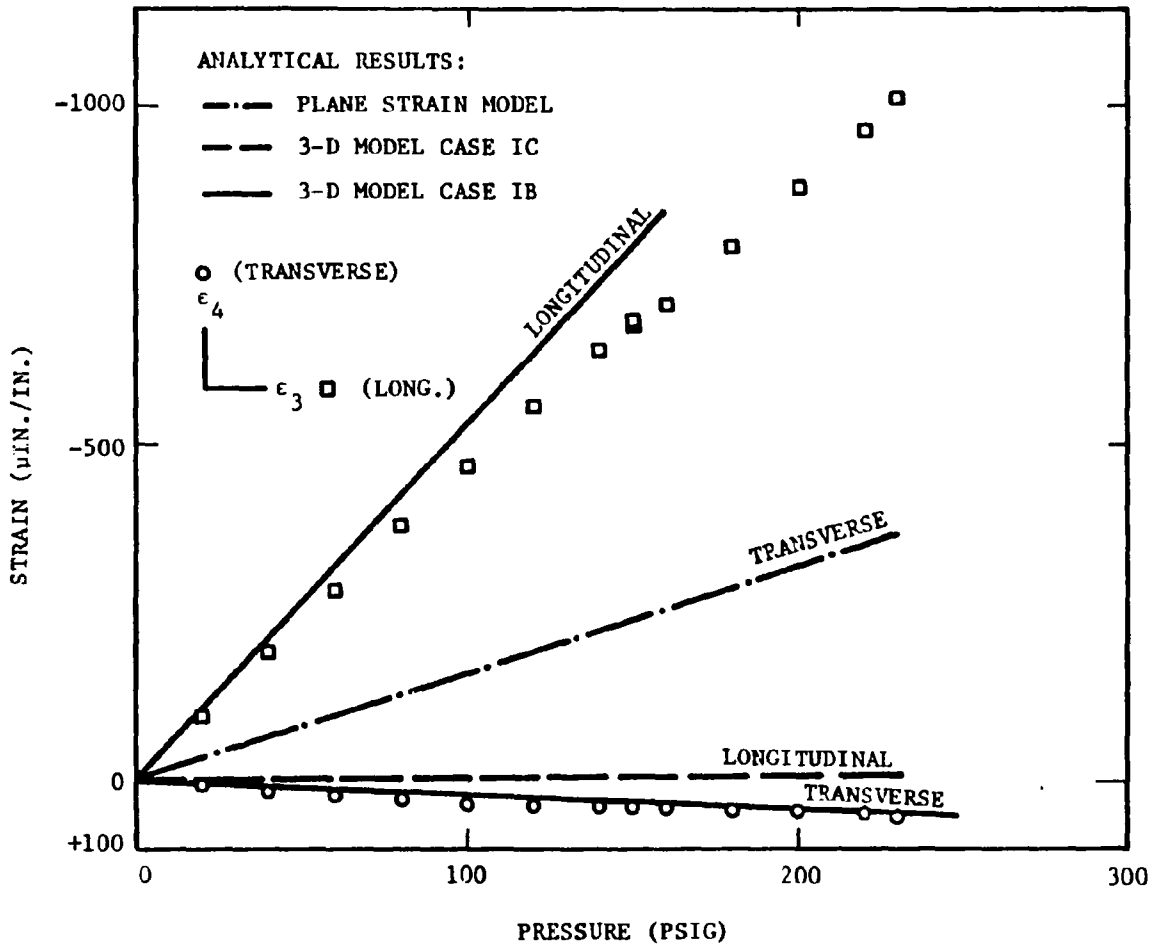

FIGURE 4.87. ROSETTE NO. 2, ENCLOSURE III

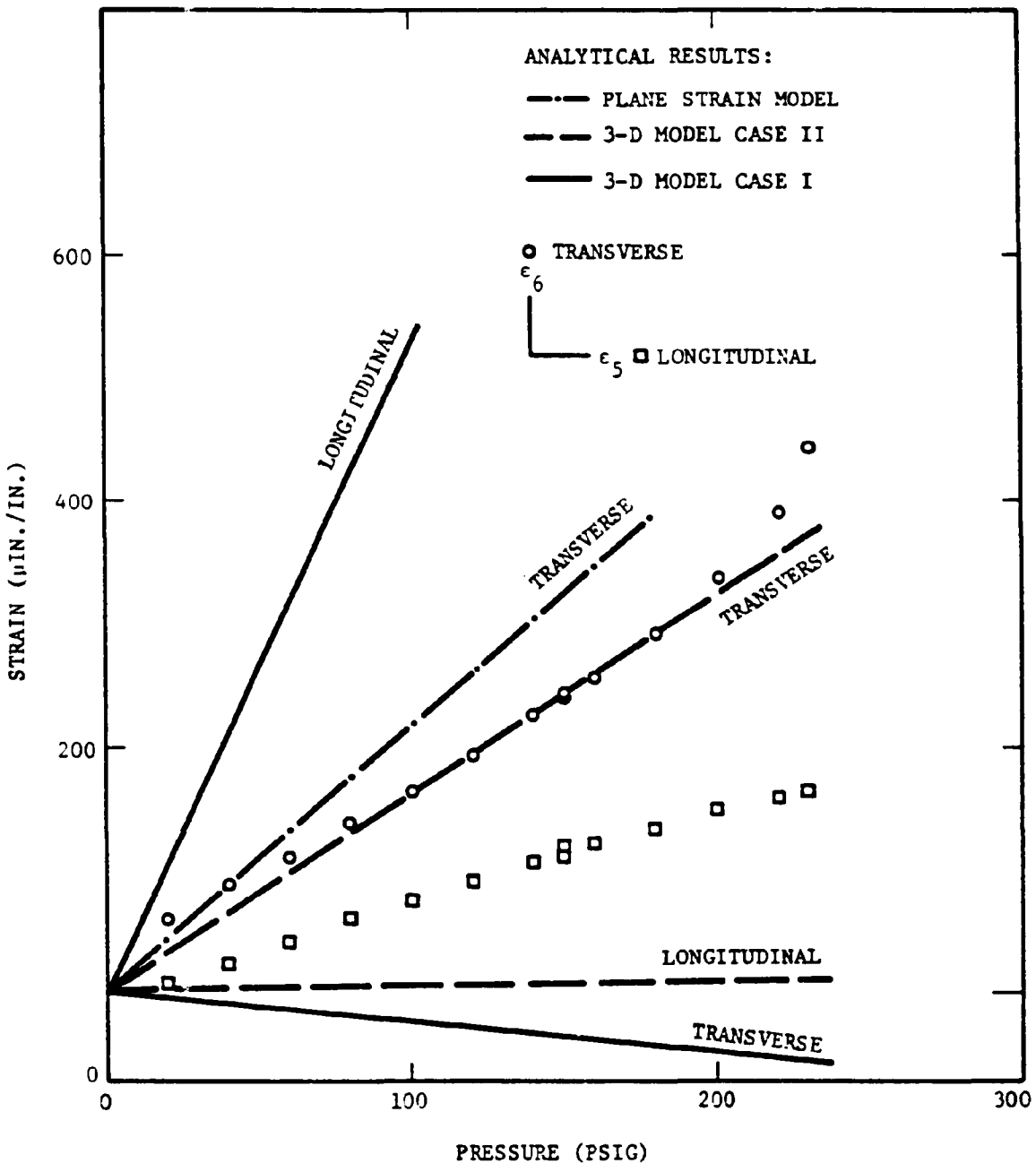

FIGURE 4.88. ROSETTE NO. 3, ENCLOSURE III

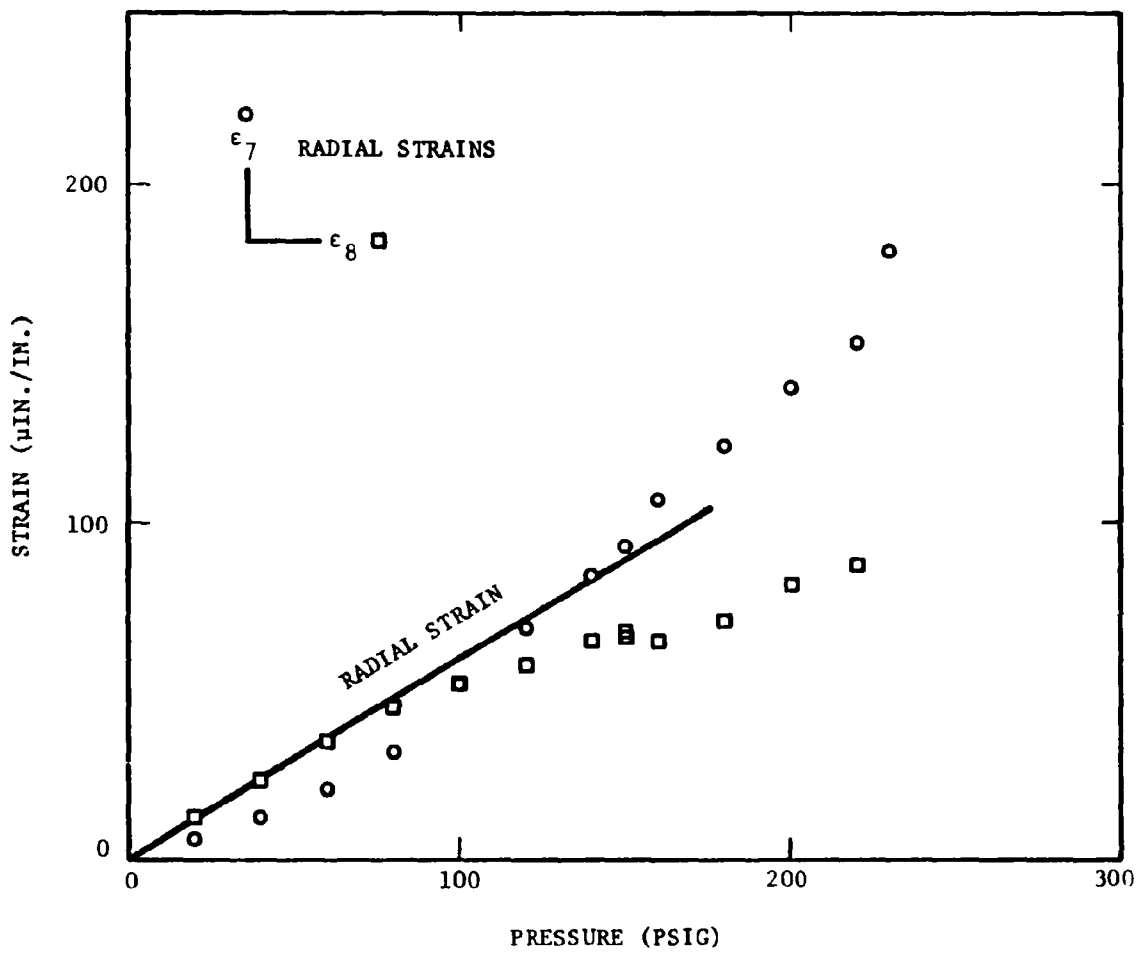

FIGURE 4.89. ROSETTE NO. 4, ENCLOSURE III

showed no permanent deformations in either the bolts or in the bottom of the enclosure.

4.3.2.3 Analytical-Experimental Comparisons

Some very important conclusions, about the structural behavior of the luminaire, were reached when the analytical and experimental results were compared. Solid lines in Figure 4.86 through 4.89 give the analytical predictions of strains in the windows of the luminaire. The analytical results are linear because they are based upon a linear elastic analysis.

Consider first Rosettes No. 1 and No. 2. These are opposing gages, one on each side of the top window (Figure 4.83). Three sets of analytical results are compared to the measured results. For the plane strain model (Model III) and for Case IC of the window three-dimensional model, the maximum strains are in the transverse direction and are in good agreement with each other. Both of these results are based on analytical models which assume a good bond between the glass and the aluminum for the rectangular windows. On the other hand, Case IB for the three-dimensional ignores the bond between the side windows and the aluminum structure (formed by the epoxy). For this case, then, the top window is supported only by the aluminum frame just as though the side windows were not present. Fortunately, in the analytical model, pressures can still be applied to the top window for such a configuration.

Notice in Figures 4.86 and 4.87 that the results for Case IB are in much better agreement with the measured strains, which were a maximum in the longitudinal direction. It shows that the aluminum frame alone does not provide significant restraint to the longitudinal edges (long sides) of the windows. Most of the load is transferred to the ends of the window where the aluminum frame is stiffer. Therefore, it is clear that there was not good bonding between the window and the aluminum frame for the side windows. This observation is further supported by the failures which occurred in the aluminum framework at the corners of the side windows. These cracks show that high bending stresses occurred in the frame at these locations. Had the frame been bonded to the side windows, these failures would not have occurred.

An obvious question is "Why didn't leakage occur between one of the side windows and the frame under pressure?" Leakage at this location was prevented by the silastic which was placed between the glass and the "retainer lip" as a seating compound. Even if this bond were broken, internal pressure would produce a tight seal.

Results for one of the side windows are compared in Figure 4.88. For the transverse strains, experimental results agree well with Case IC of the three-dimensional model. This may imply that the bond between the top window and the aluminum frame was good, or it may only be a consequence of the fact that adequate support along the longitudinal edge of the window is provided by the bottom of the enclosure. Note that measured longitudinal strains are higher than those predicted by Case IC. Most likely, this was caused by the side window having good longitudinal support along its bottom edge and more flexible support

(because of inadequate bonding) along the top edge. This particular support condition could not be simulated in the one-quarter symmetry model (Model I) or in the cross-section model (Model III) used in the analyses. Further, we attempted to remove the windows to examine the bond, but found that they could not be removed without breaking the glass or destroying the bond. Sections cut normal to the longitudinal axis of the enclosure would have revealed the bond, but equipment was not available to make such section cuts.

Comparisons for the circular end window are shown in Figure 4.89. Agreement between analysis and experiment is very good in the linear range.

4.4 Enclosure IV Analysis and Testing

Enclosure IV was purchased from Crouse-Hinds Company. Because all other enclosures provided to SwRI by the USBM had been rectangular in shape, a cylindrical enclosure was selected. This enclosure, shown in Figure 4.90, was constructed of cast gray iron, had a threaded top (which was sealed by an O-ring), and had ports for up to four electrical penetrations. The enclosure purchased had two ports which were drilled and fitted with removable plugs. In service, this enclosure serves as a junction box or ballast box in mine lighting systems.

4.4.1 Elastic Analyses

4.4.1.1 Characteristics of the Finite Element Model

Photographs of Enclosure IV (Figure 4.90) show that the cover is essentially axisymmetric about a vertical axis through the enclosure. This condition of symmetry allowed the use of a two-dimensional rather than a three-dimensional finite element model for the cover.

The two-dimensional model is shown in Figure 4.91. Each element in the model is an axisymmetric ring with midside nodes (the midside nodes are not shown). For the quadrilateral elements, this gives eight nodes per element, and these extra nodes allow the structure to be represented with a relatively coarse mesh. This model was loaded with a uniform pressure over three regions consisting of the inside surface, the external threads, and the lower half of the O-ring groove. Nodes on the axis of symmetry were not allowed to displace in the radial (X) direction, and nodes on the external threads were constrained from moving in the Y-direction. The loading and boundary conditions are shown in Figure 4.91.

The condition of axisymmetry could not be used on the body of the enclosure, and a three-dimensional model was made. However, the structure is almost symmetric about the two vertical planes passing through its center. This double-symmetry condition permitted the enclosure to be accurately described by a quarter-symmetry model, that is, only one quarter of the enclosure body was included in the finite element grid. This reduction in model size saved considerable effort in the model formulation and computer costs in the solution.

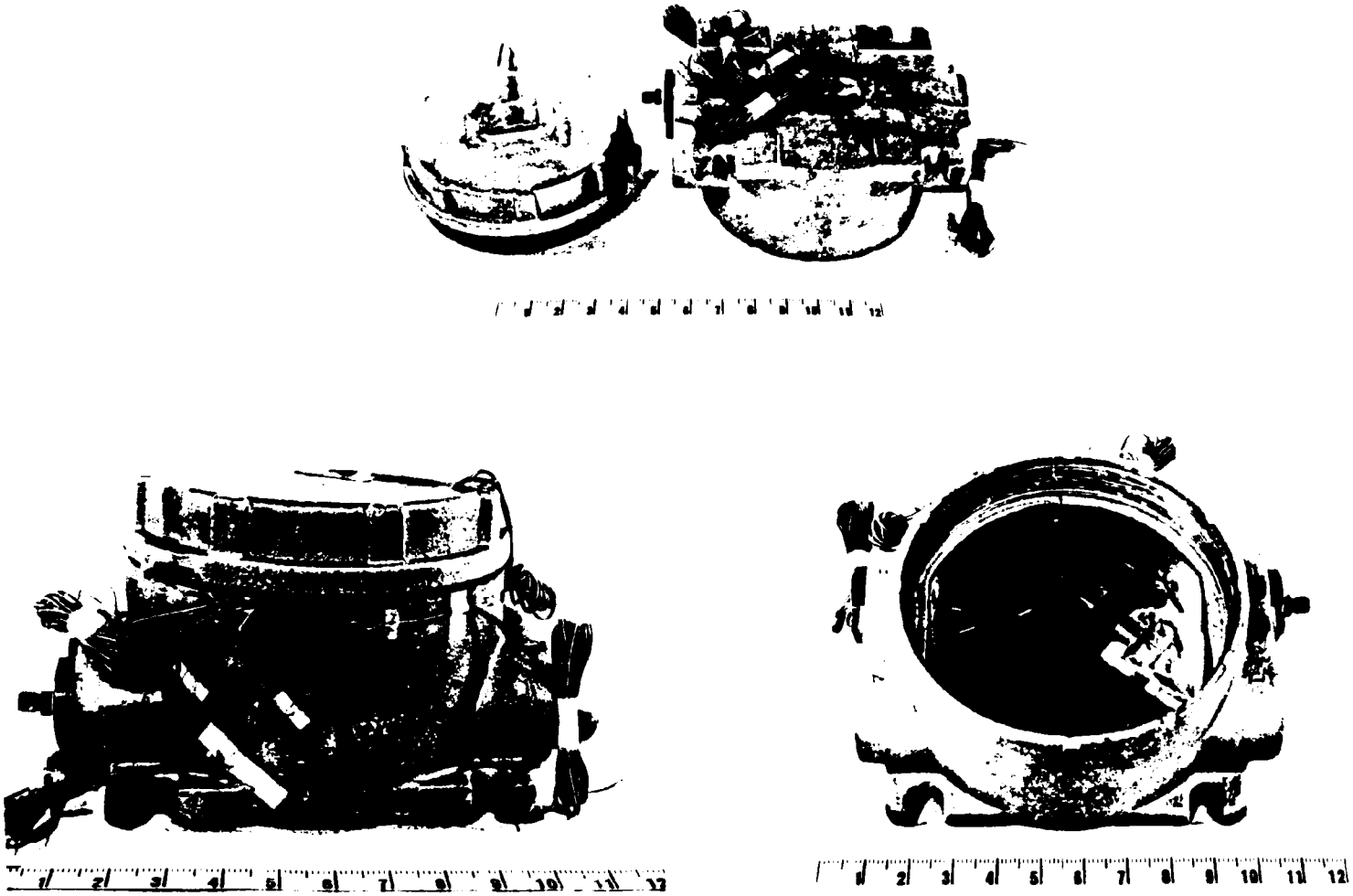

FIGURE 4.90. ENCLOSURE IV WITH STRAIN GAGES INSTALLED

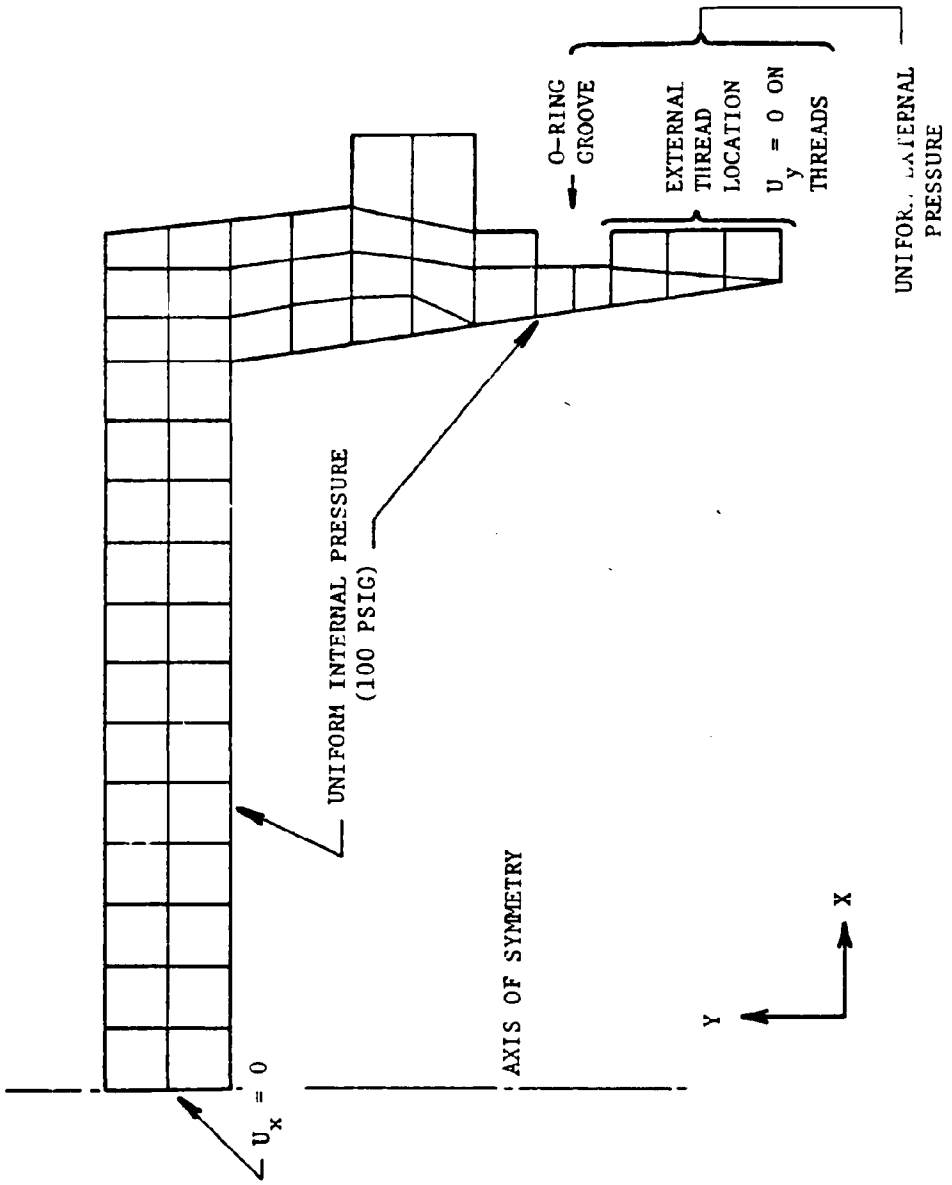

FIGURE 4.91. AXISYMMETRIC FINITE ELEMENT MODEL

Figure 4.92 defines the global coordinate system for the analysis and shows an isometric view of that portion of the enclosure bounded by the XZ and YZ planes. An abrupt change in thickness occurs in the cylindrical wall section at the bottom of the threads used for retaining the cover and is also shown on this figure. The abrupt change in thickness was included in the finite element model by defining two separate surfaces along this discontinuity line and connecting them together with constraint equations in the ANSYS program. The mathematical requirement for their connection was that plane sections remain plane.

Figure 4.92(b) shows the finite element grid for the enclosure body. It contained 48 three-dimensional isoparametric solid elements, which are designated as STIF 95 in ANSYS. Each element has 20 nodes, with nodes located along the edges of the cube-shaped solid to allow representation of curved boundaries. A 15-node version was used to model wedge-shaped solids.

The model was loaded by a uniform pressure applied over its internal surfaces, and symmetry boundary conditions were applied on those surfaces defining the quarter symmetry. These conditions require that all the U_y displacements at nodes on the XZ plane and all the U_x displacements at nodes on the YZ plane be zero. Figure 4.92(a) shows these loading and boundary conditions.

4.4.1.2 Results

Calculations of enclosure strains and stresses, using the finite element models described in the preceding section, were made for the assumptions that the material was homogenous and had a modulus of elasticity of 29×10^6 psi. This value was used because the true modulus of the material was unknown at the time the calculations were made and because, for a linearly elastic analysis, the results could be scaled for different elastic moduli just as they were scaled for different internal pressures.

Preliminary comparisons with experimental results, to be presented in Section 4.4.2, revealed very poor agreement between analysis and experiment and led to the conclusion that the modulus of the material was very different from the assumed value of 29×10^6 psi. Values of the elastic modulus reported in the literature for gray cast iron ranged from 8×10^6 to 25×10^6 psi, depending upon carbon content and general composition.

To establish actual values for the stiffness and strength of the gray cast iron in Enclosure IV, material tests were conducted on six specimens cut from the cover and three specimens cut from the bottom plate of the enclosure body. Results of these tests are given in Tables 4.4 and 4.5 for the cover and body of the enclosure, respectively. It was surprising to find such a wide variation in the elastic modulus for the two parts of the enclosure. The modulus for the body is three to four times higher than that for the cover. A visual inspection of the fractured tensile specimens revealed that the cover had a much larger grain structure than the body, which indicates a more brittle material. These differences were probably due to the casting

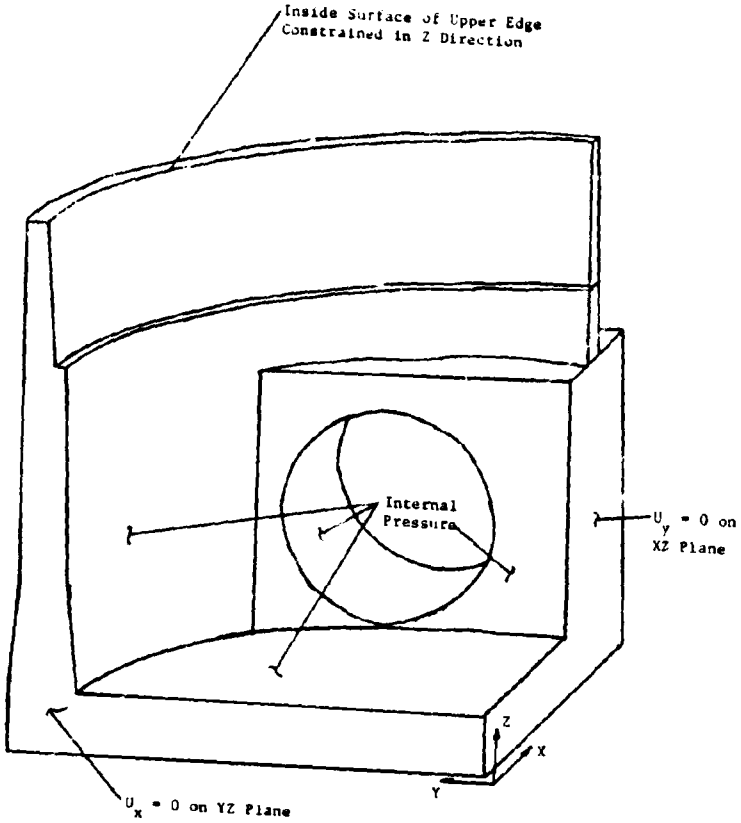

(a) LOADING AND BOUNDARY CONDITIONS

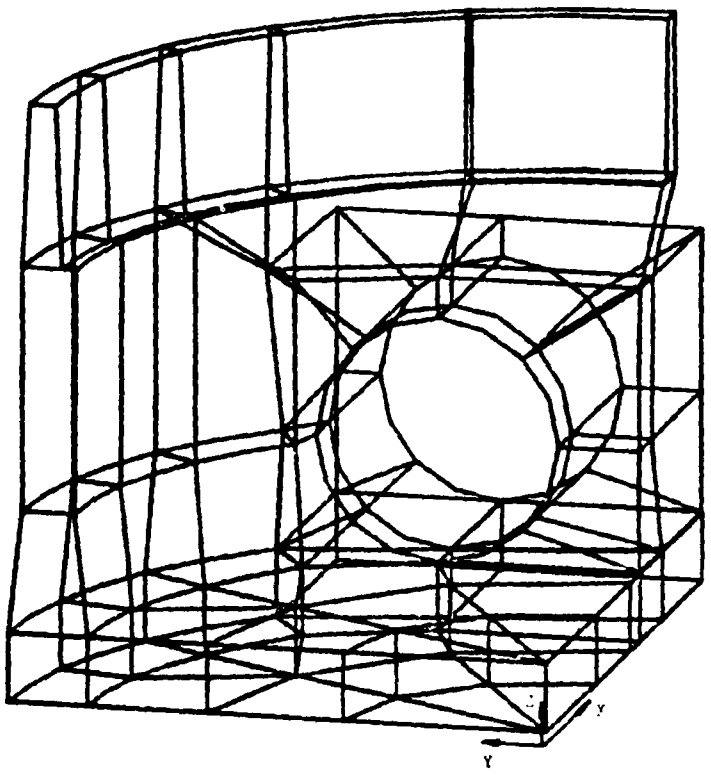

(b) FINITE ELEMENT GRID

FIGURE 4.92. ONE-QUARTER SYMMETRY MODEL OF ENCLOSURE IV

TABLE 4.4 MATERIAL TEST RESULTS FOR THE COVER OF ENCLOSURE IV

Specimen No.	Dia. (in.)	0.2% Off-Set Load (lb)	Max. Load (lb)	Yield Stress (ksi)	Ultimate Stress (ksi)	Elastic Modulus (psi)
1*	0.251	850	960	17.2	19.4	---
2	0.254	875	1070	17.3	21.1	7.4×10^6
3	0.250	820	1000	16.7	20.4	7.8×10^6
4	0.248	800	1020	16.3	20.8	7.4×10^6
5**	0.252	1036	1236	20.8	24.8	5.7×10^6
6**	0.250	1055	1225	21.5	24.9	5.7×10^6
AVERAGE PROPERTIES				18.3	21.9	6.8×10^6

*Specimen broke outside of the gage section.

**Orientation of specimens 5 & 6 was different from specimens 1 - 4.

TABLE 4.5 MATERIAL TEST RESULTS FOR THE BODY OF ENCLOSURE IV

Test No.	Elastic Modulus (Clip Gage) (ksi)	Elastic Modulus (Strain Gage) (ksi)	Yield Stress (ksi)	Ultimate Stress (ksi)
1	17.6×10^6	24.3×10^6	33.0	48.2
2	24.4×10^6	23.5×10^6	30.7	46.5
3	23.5×10^6	25.4×10^6	30.8	47.4
Average Properties	21.8	24.4	31.5	47.4

process. Calculated results, which follow, were scaled by the ratio of the average elastic modulii in Tables 4.4 and 4.5 to 29 x 10^6 psi.

Because of the unusual geometry of Enclosure IV, contour plots of stresses were not obtained. Instead, strains were determined at locations near the strain gage locations used in the hydrostatic test of the enclosure. Strain gage locations on the enclosure body are shown in Figure 4.93. These gage locations were not matched exactly by element centroids or surface nodes in the finite element calculations; thus, point-for-point comparisons between analysis and experiment were not possible. Locations on the finite element grid, where results were obtained for comparison with experiment, are shown in Figures 4.94 and 4.95. Comparisons with Figure 4.93 show that the locations of measured and computed stresses can be as much as 1 in. apart.

Surface strains determined from the finite element calculations at the locations shown in Figures 4.94 and 4.95 are given in Table 4.6. Note that the x and y directions of the strains correspond to local element axes and are not exactly parallel with the strain gage axes (Figure 4.93), nor do the locations exactly coincide. Values in the table have been scaled to give the results at 500 psig and for the correct values of the elastic modulus. The resulting scale factors were:

	Modulus Scaling		Pressure Scaling		Resulting Scale Factor
Cover:	$\frac{29 \times 10^6 \text{ psi}}{6.8 \times 10^6 \text{ psi}}$	x	$\frac{500 \text{ psi}}{100 \text{ psi}}$	=	21.3
Base:	$\frac{29 \times 10^6 \text{ psi}}{24.4 \times 10^6 \text{ psi}}$	x	$\frac{500 \text{ psi}}{100 \text{ psi}}$	=	5.94

Strain values given in Table 4.6 are quite low even for 500 psig, which is much higher than the design pressure of 150 psig. The highest strain level of 1297 μin./in. in the center of the cover is still well below the yield strain of the material which is estimated to be

uniaxial stress: $\varepsilon_y = \frac{18{,}300}{6.8} = 2690$ μin./in.

biaxial stress: $\varepsilon_y = \frac{1}{6.8}[18{,}300 - (0.3)(18{,}300)] = 1880$ μin./in.

Thus, if these strain values are confirmed by the experiments, the enclosure is much stronger than necessary to satisfy Schedule 2G requirements. Also, the safety factors for this enclosure will be high as shown in Section 5.4.

4.4.2 Testing

4.4.2.1 Methodology

For hydrostatic testing, strain gages were placed at six locations on this enclosure. These locations were shown previously

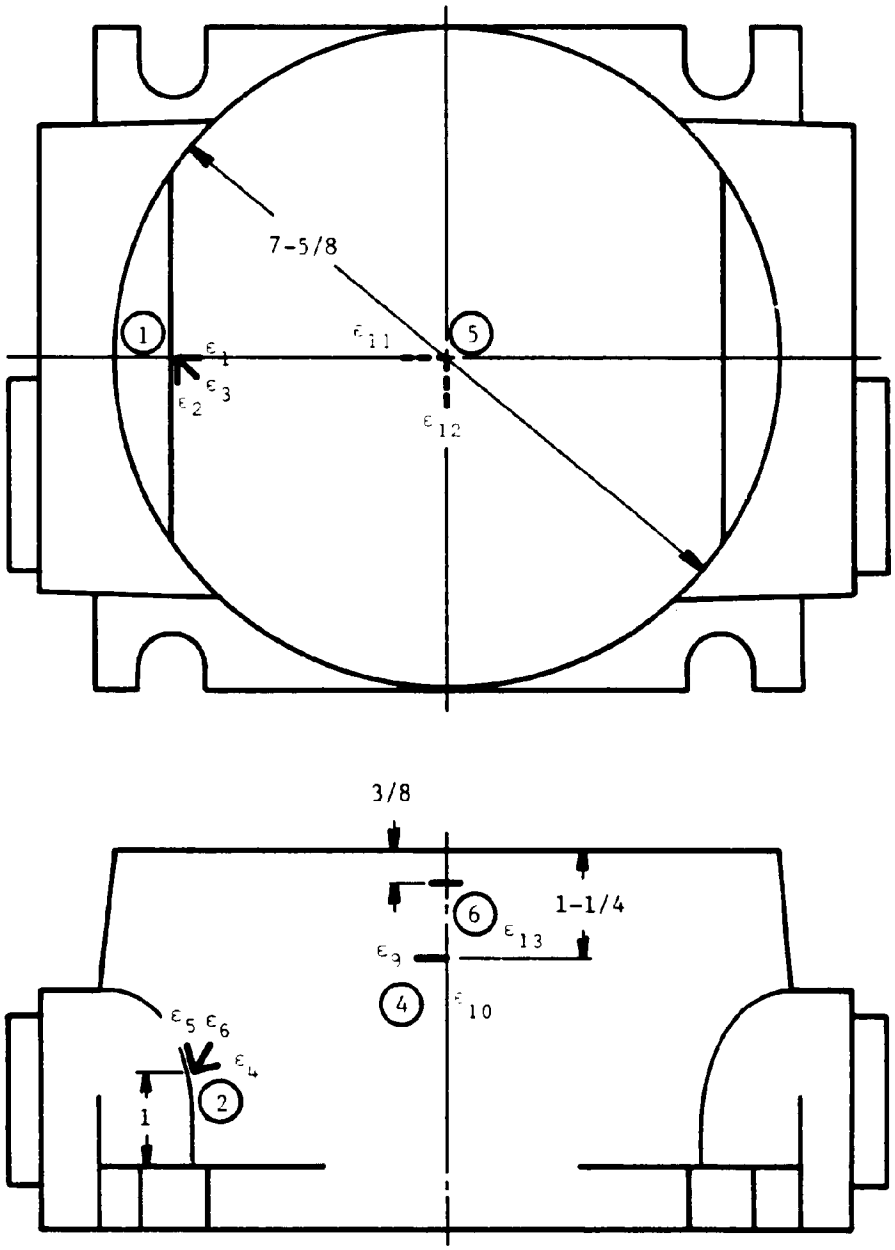

FIGURE 4.93. STRAIN GAGE ROSETTE LOCATIONS ON BASE OF ENCLOSURE IV

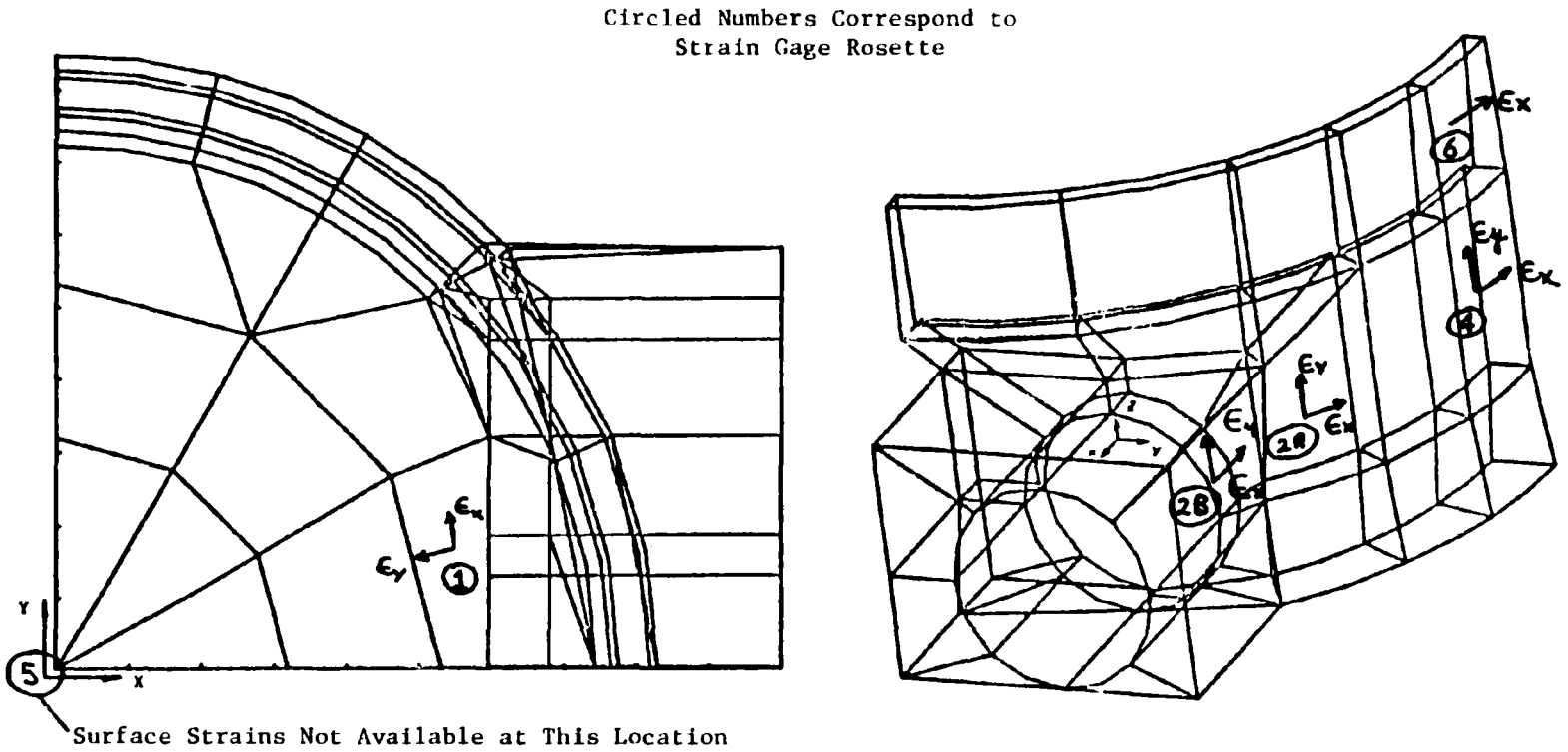

a. VIEW ALONG +Z AXIS

b. ISOMETRIC VIEW FROM OUTSIDE ENCLOSURE - WITHOUT BOTTOM

FIGURE 4.94. SOLID MODEL OF BASE SHOWING LOCATIONS WHERE SURFACE STRAINS ARE COMPUTED

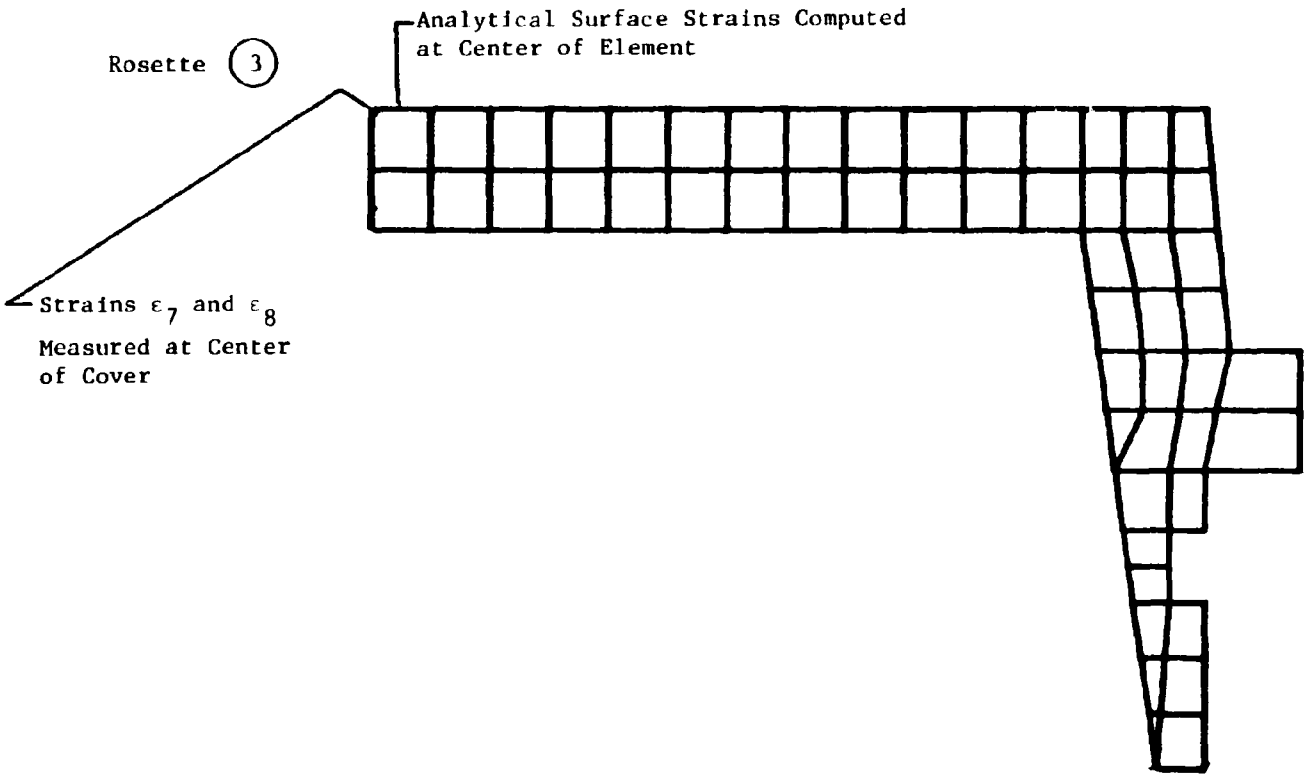

FIGURE 4.95. TWO-DIMENSIONAL MODEL OF COVER

TABLE 4.6 VALUES OF SURFACE STRAINS AT LOCATIONS SHOWN IN FIGURES 4.94 AND 4.95 - 500 psig INTERNAL PRESSURE

Strain Location	Strain μin./in. ϵ_x	ϵ_y
1 : Bottom of the base inside surface	-52	412
2 A: Outside surface of the base near the port	29	76
2 B: Outside surface of the base on the port	21	29
3 : Outside surface of cover near the center	1293 (radial)	1297 (hoop)
4 : Outside surface of the base near the top	77	62
5 : Bottom of the base - inside surface - center of enclosure	no available strain data	
6 : Outside surface of the base below the internal threads	217	----

in Figure 4.93. A three-element rosette was installed at location 1, which is inside the enclosure, near one end and centered on the longitudinal center line. Locations 2, 4, and 6, on the side of the enclosure, had three-element, two-element, and single-element strain sensors installed, respectively. Two-element rosettes were installed at locations 3 (on the top) and 5 (on the bottom) of the enclosure.

Pressure was applied in 20-psi increments from 0 to 220 psig and increased in 40-psig steps all the way to 500 psig. No water leaks developed over the entire pressure range. The O-ring seal between the screwed-on top and the body of this enclosure proved to be much more effective than the clamped-on gasket or metal-to-metal contact (with vacuum grease) that was used on the other enclosures tested.

4.4.2.2 Results

Experimental strain data for Enclosure IV are given by the symbols in Figures 4.96 through 4.101. Analytical results, for later comparison, are given by the solid lines. Locations and orientations of the gages are shown photographically in Figure 4.90 and schematically in Figure 4.93 of the previous section. All gages except for Rosette No. 2 exhibit fairly linear behavior. For Rosette No. 2, the element which is parallel to the line of intersection of the port and the cylindrical portion of the base is linear, and the two elements which are normal to this line of intersection show nonlinear behavior at very low strains. Because these strains are so low, these nonlinearities are attributed to the adhesive rather than to the substrate (metal) behavior. Note that the results are linear at the higher pressures.

Rosettes 3 and 5 on the top and bottom of the enclosure show good symmetrical behavior (strains on each gage element are nearly equal, as they should be). Comparing the results for Rosette No. 4 and Gage No. 6 on the side of the enclosure shows a slightly higher circumferential strain at Gage No. 6. Gage No. 6 is on the thinner section of the cylinder and should record a high circumferential strain. The axial (vertical) strain at Rosette No. 4 (ε_{10}) is small, as expected.

4.4.2.3 Experimental-Analytical Comparisons

The finite element analysis consistently underpredicted strain on the enclosure cover. Considering that the mesh on the base was rather coarse and that the locations of calculated and measured strain do not correspond, some disagreement was expected; however, the reasons for consistently lower predictions are unclear. The underpredictions on the base are most obvious at gage locations 4 and 6 where the calculated circumferential strains should have been reasonably accurate. Evaluating the predicted strains at locations nearer the gage locations could have yielded better comparisons, but the additional effort and costs associated with the interpolations were not warranted.

In direct opposition to the predictions for the base, the predictions for the cover were too high. This is shown in Figure 4.98 for Rosette No. 3. Note in Table 4.4 that cover properties were not

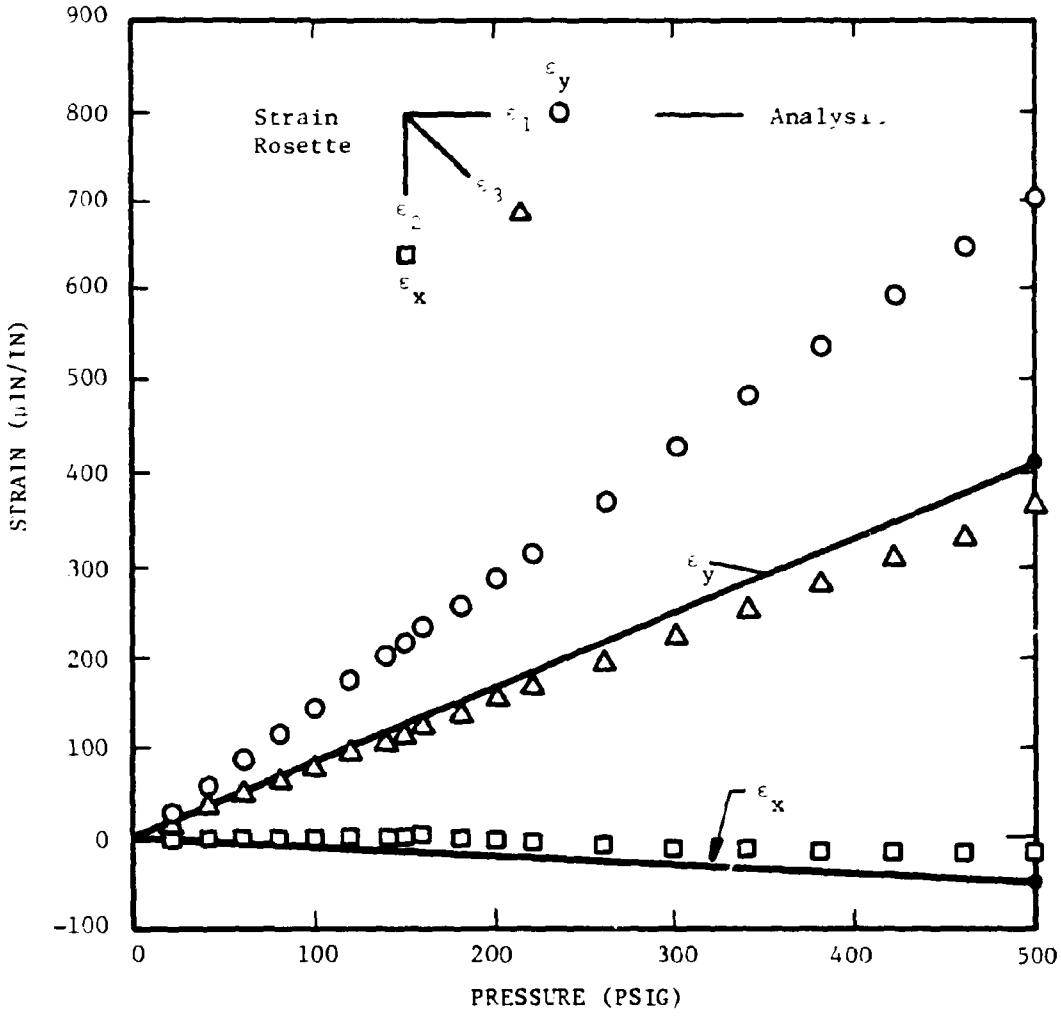

FIGURE 4.96. MEASURED AND ANALYTICAL STRAINS, ROSETTE NO. 1, ENCLOSURE IV

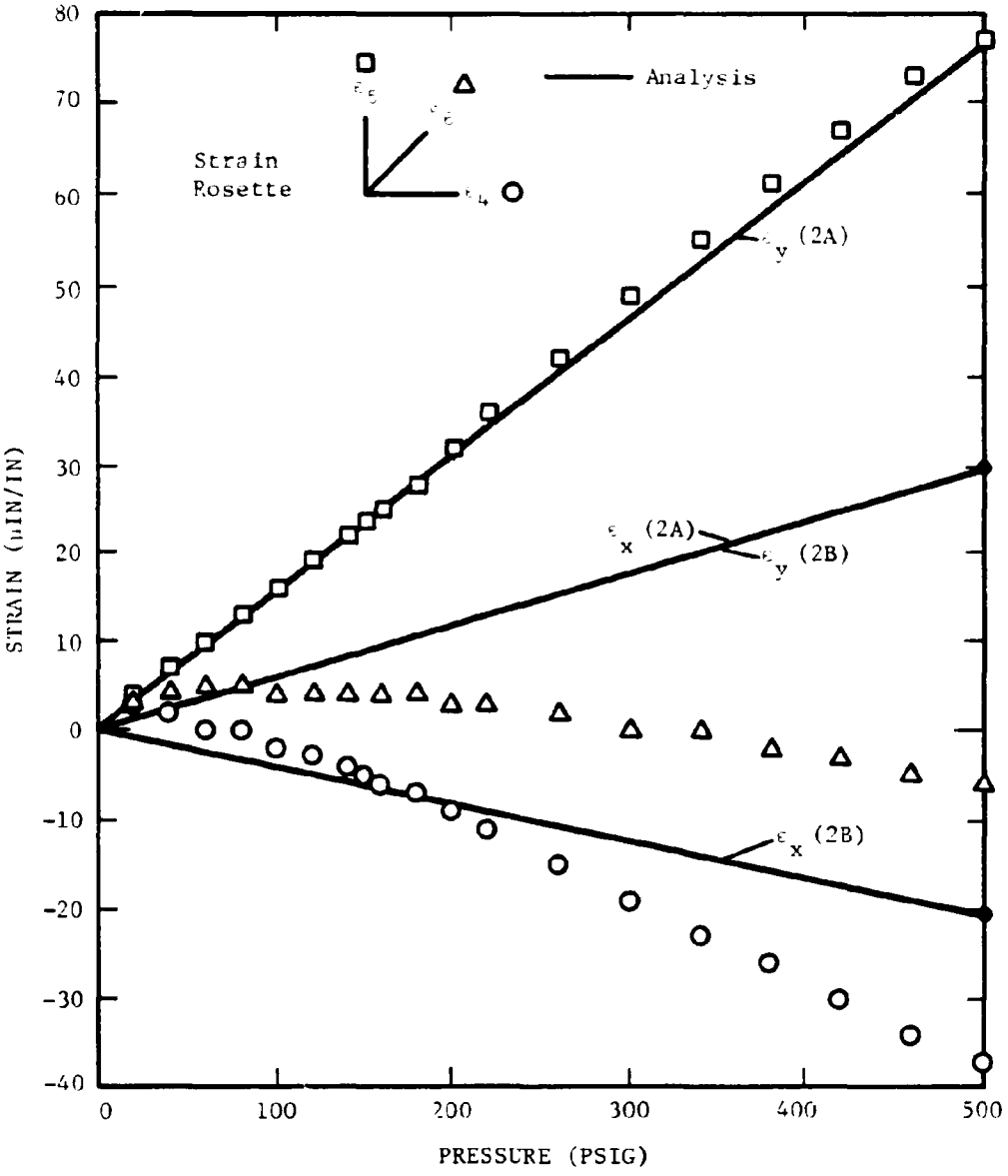

FIGURE 4.97. MEASURED AND ANALYTICAL STRAINS, ROSETTE NO. 2, ENCLOSURE IV

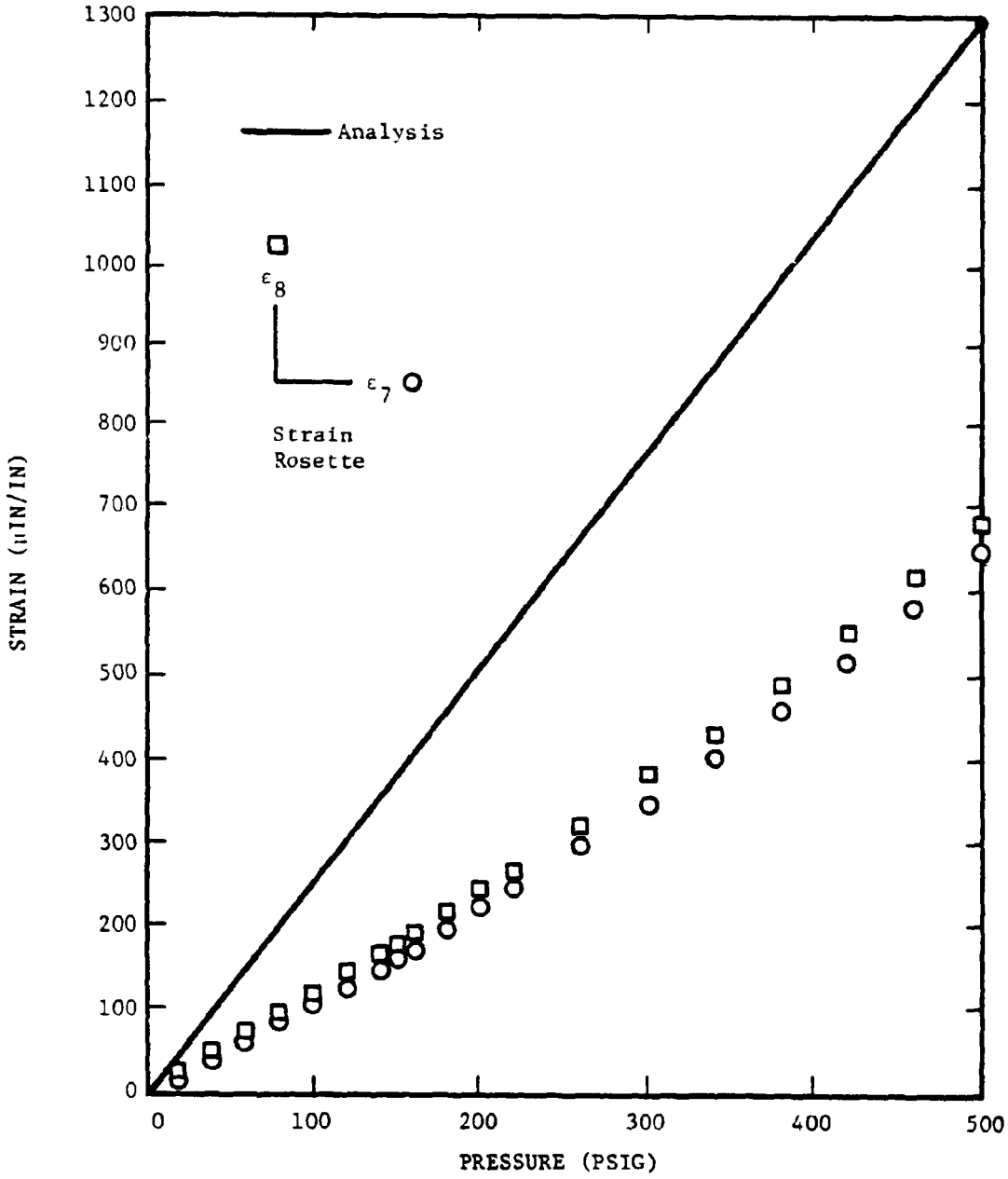

FIGURE 4.98. MEASURED AND ANALYTICAL STRAINS, ROSETTE NO. 3, ENCLOSURE IV

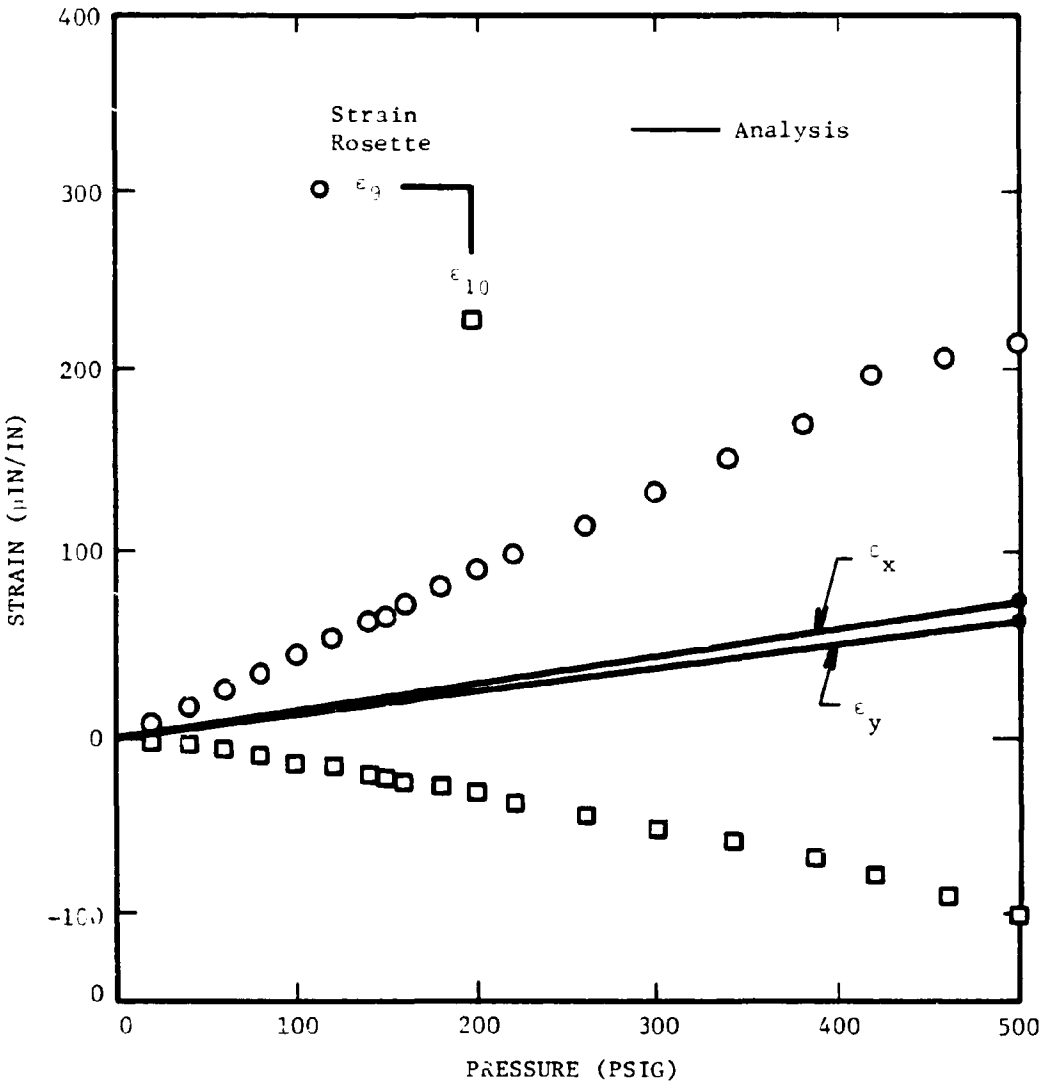

FIGURE 4.99. MEASURED AND ANALYTICAL STRAINS, ROSETTE NO. 4, ENCLOSURE IV

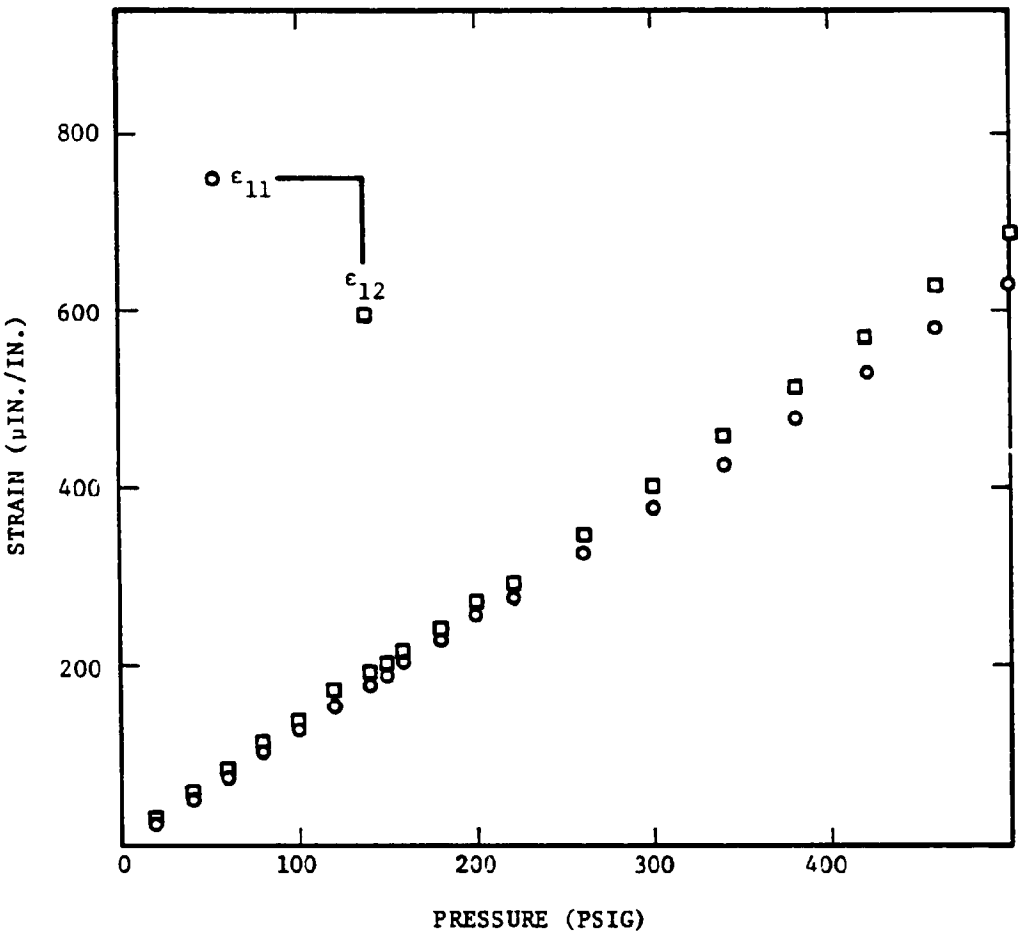

FIGURE 4.100. MEASURED STRAINS, ROSETTE NO. 5, ENCLOSURE IV

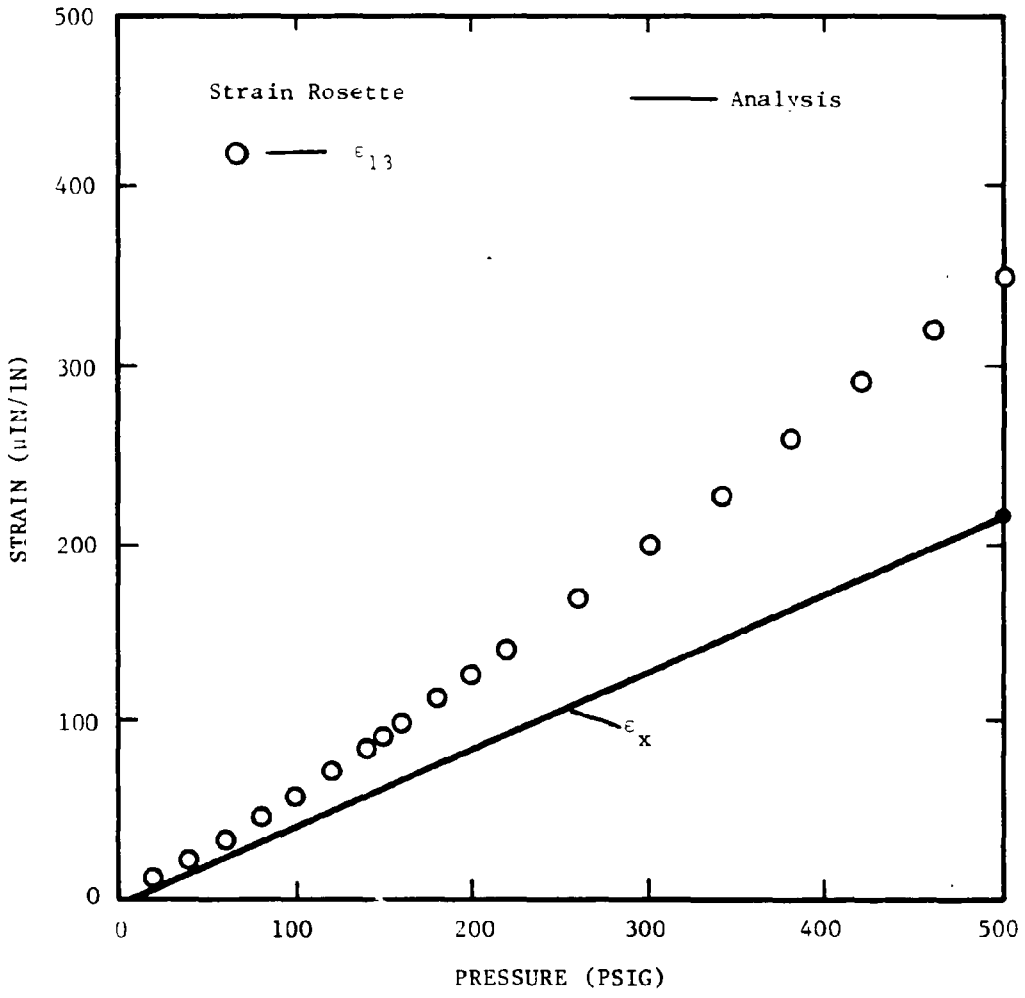

FIGURE 4.101. MEASURED AND ANALYTICAL STRAINS, GAGE NO. 6, ENCLOSURE IV

uniform. This asymmetry in the material properties was not treated in the model and could account for some of the disagreement.

Overall, the analytical predictions for this enclosure were the least accurate of the four enclosures analyzed and tested. It shows that finite element models cannot be used routinely in design without very accurate knowledge of the material properties and without using a safety factor of approximately 2 to cover modeling uncertainties for difficult geometric shapes.

5.0 SAFETY FACTORS IN SCHEDULE 2G ENCLOSURES

Based upon the analyses and testing reported in Section 4.0 and upon such other analyses as were required, safety factors were calculated for Enclosures I through IV. Calculation of the safety factors took into consideration the following factors:

(1) Peak stresses and strains in the enclosures
(2) Collapse loads for internal pressure
(3) Permanent deformations in the enclosures
(4) Bolt stresses

Dynamic effects were shown to be unimportant in Section 4.1.4 and so were not considered in these calculations. Also, the safe gap was found to decrease under load and remain unchanged following unloading, in the absence of bolt axial deformations. Thus, by addressing bolt stresses, changes to the safe gap are also addressed indirectly.

5.1 Enclosures I and II

Enclosures I and II were fabricated of ductile materials and can undergo limited plastic material behavior without fear of rupture. Just such behavior was observed in tests on Enclosure I as reported in Sections 4.1.5 and 4.1.6. Thus, for these enclosures safety factors were based on collapse loads (the formation of fully plastic mechanisms), permanent deformations, and bolt stresses.

5.1.1 Allowable Collapse Loads

Before the term safety factors can be defined, it is necessary to review the concept of collapse loads in elastic-plastic structures. Suppose that the structure shown in Figure 5.1 is subjected to a loading P_o applied over its surface in some manner. As P_o is gradually increased from zero, the stresses and strains will be elastic, until at a load, denoted by P_o^*, the stresses at some point in the body reach the yield stress of the material σ_o. If the load P_o is now removed, there will be some permanent deformation in the structure. Instead, if P_o is further increased from P_o^*, there will be a value of the load, denoted by P_o^{**}, for which the structure remains in equilibrium, but the displacements can increase indefinitely, geometry changes being ignored. This load P_o^{**} is defined as the collapse load or limit load. The collapse load is obviously dependent on the yield stress and stress strain behavior of the material.

Figure 5.2 shows a somewhat idealized representation of the stress strain characteristics of mild steel. The yield stress is approximately 36 ksi. After yielding, the stress remains almost constant over some strain interval and then increases slightly due to strain hardening. The condition that further deformations require an additional loading is called strain or work hardening. In conventional elastic-plastic analyses, strain hardening is ignored, and the material is assumed to be elastic, perfectly plastic. This is a valid engineering approximation since the amount of work hardening for metals is small. The approximation

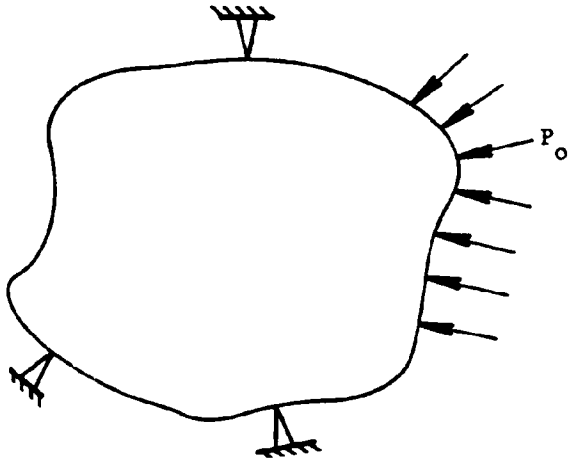

FIGURE 5.1. GENERAL STRUCTURE SUBJECTED TO ARBITRARY LOADING P_o

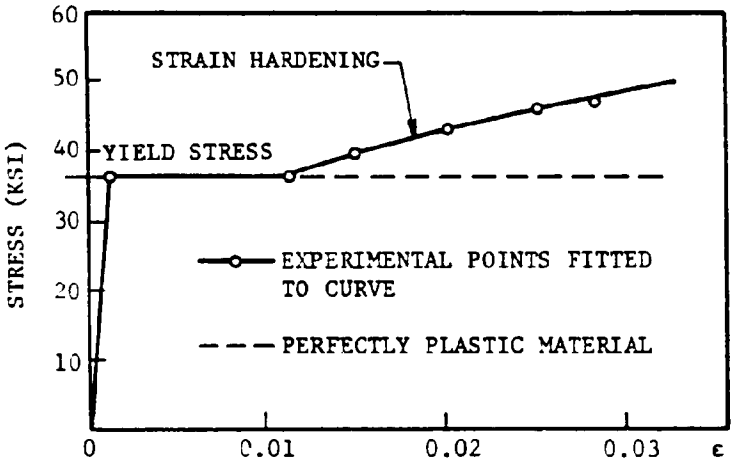

FIGURE 5.2. STRESS STRAIN CURVE FOR MILD STEEL

is also conservative because it produces collapse loads which are smaller than the actual ones.

To illustrate how collapse loads are determined, consider a simply supported beam carrying a uniformly distributed load P_o (force/length) shown in Figure 5.3(a). The corresponding shear and bending moment diagrams are given in Figures 5.3(b) and 5.3(c). Since the problem is statically determinant, the internal beam loads can be computed only from the equilibrium conditions. As the load P_o is increased from zero, the stress distributions at the beam's center section change from elastic to fully plastic as shown in Figure 5.4. When the collapse load P_o^{**} is reached, the maximum internal movement at the center section is developed (Figure 5.3(d)) and a hinge will form. The beam will collapse as shown in Figure 5.3(d). By integrating the stress distribution over the beam's cross section, the collapse moment for a rectangular beam can be computed to be

$$Mo^{**} = \frac{\sigma_o b h^2}{4} \tag{5.1}$$

where σ_o is the yield stress. In terms of the load, the moment at the center span is

$$M = \frac{P_o a^2}{2} \tag{5.2}$$

and the collapse load intensity is

$$P_o^{**} = \frac{\sigma_o b h^2}{2a^2} \tag{5.3}$$

For a uniformly loaded clamped beam, fully plastic moments must be developed at the center span end supports before the beam can collapse. This case is illustrated in Figure 5.5. It can be shown to collapse by plastic hinges forming as shown in Figure 5.5(d) at a collapse load of

$$P_o^{**} = \frac{\sigma_o b h^2}{a^2} \tag{5.4}$$

which is twice the collapse load for the simply supported beam.

In actual practice, the deformations for the fixed beam case would not increase without bound because changes in geometry would cause membrane forces to be developed along the beam's neutral axis. The collapse load was based on simple beam theory, which assumes the neutral axis is

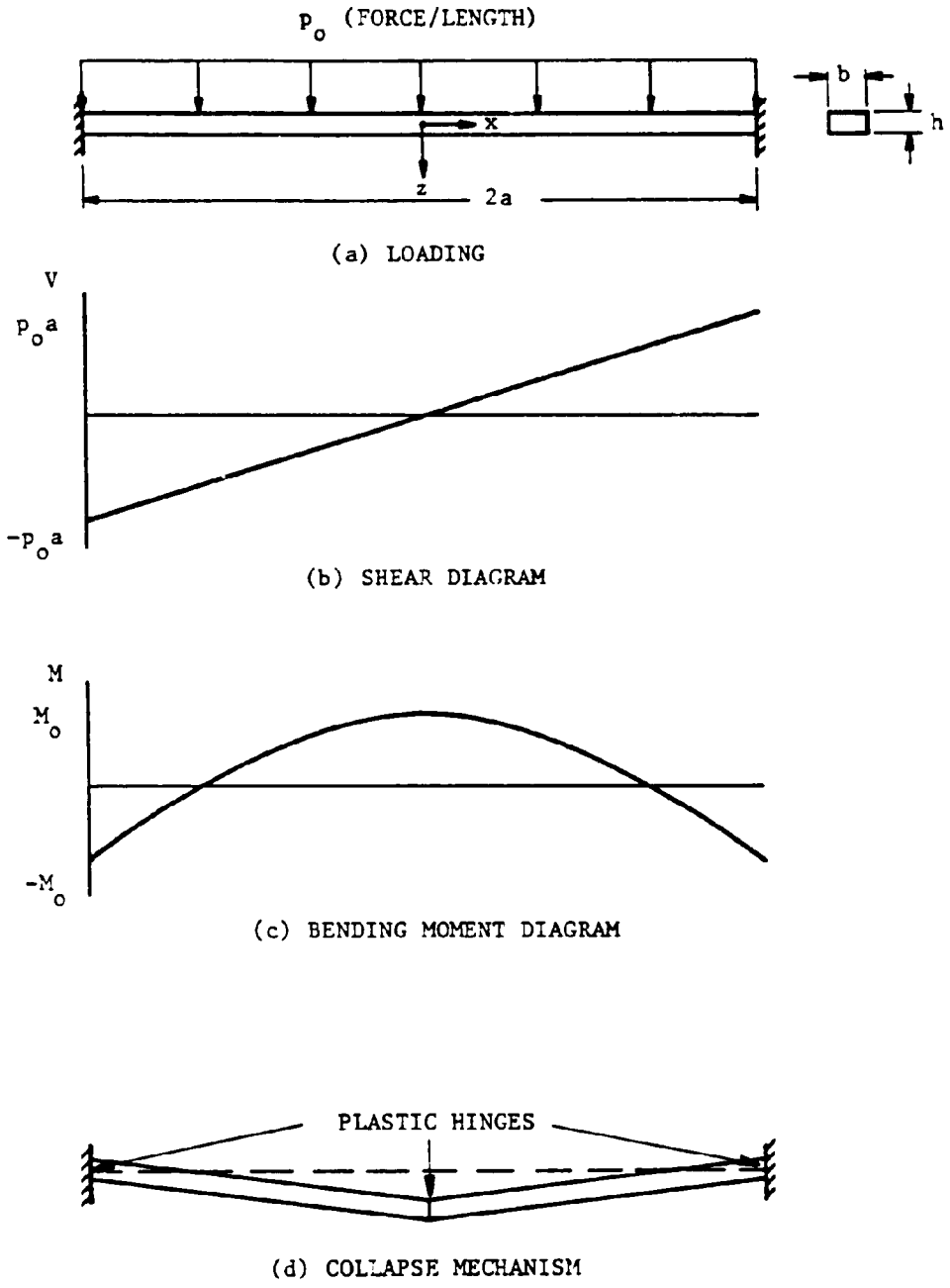

FIGURE 5.3. SIMPLY SUPPORTED BEAM UNDER UNIFORM LOADING

σ_o = YIELD STRESS

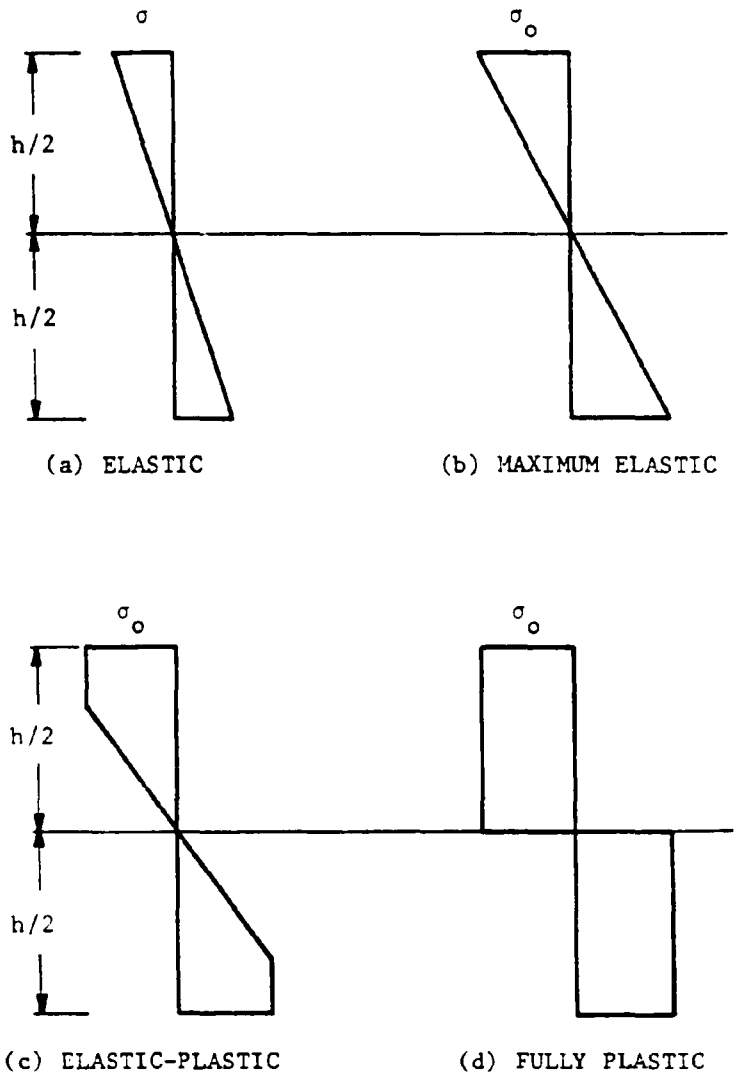

FIGURE 5.4. STRESS DISTRIBUTIONS
IN ELASTIC BEAMS

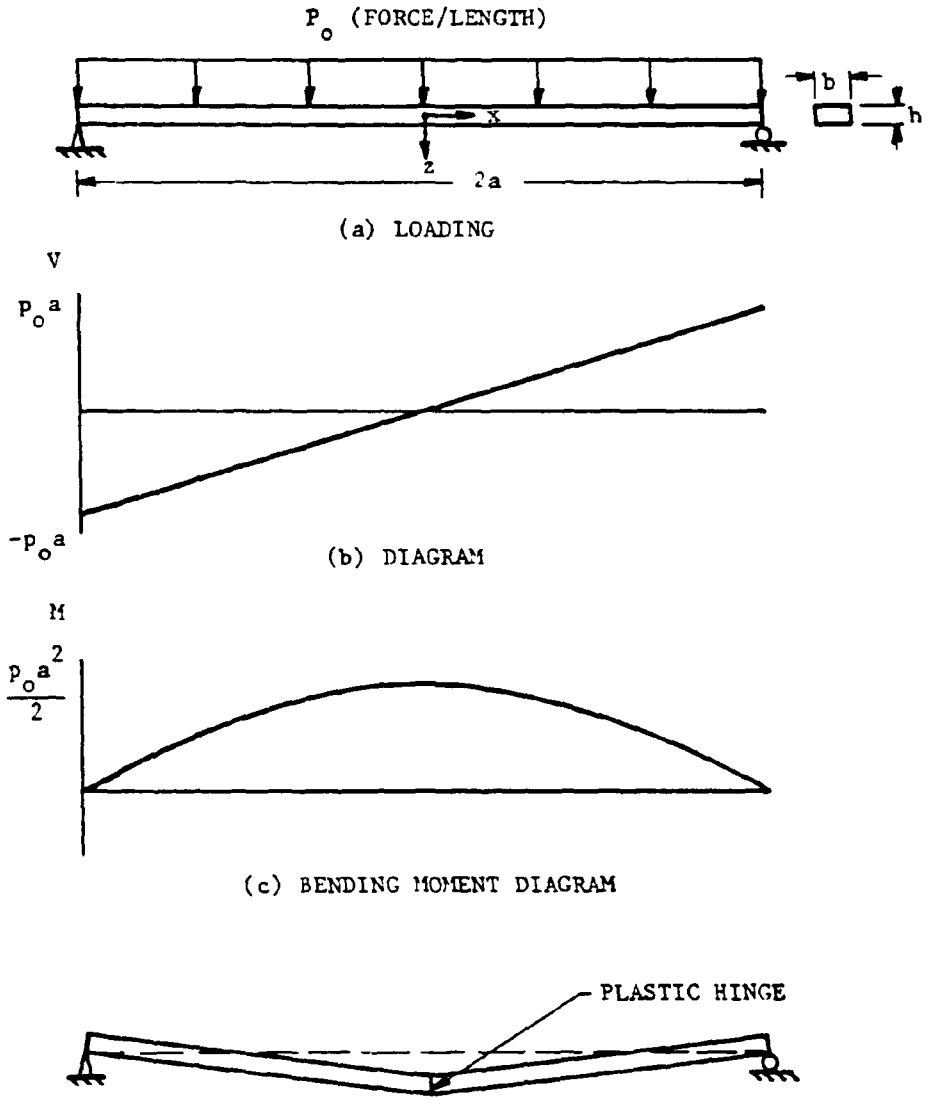

FIGURE 5.5. CLAMPED BEAM UNDER UNIFORM LOADING

inextensional and stress free. An analogous situation exists for plates forming the sides in the Schedule 2G enclosures. Therefore, the computed collapse load could be considered a lower bound for structures capable of developing membrane behavior.

Consider now the collapse load of rectangular plates subjected to clamped and simply supported boundary conditions. Much of the research in this area in recent years comes from the problem of ship slamming and the incurred damage. The similarities in the plate structures of a ship and Schedule 2G enclosures and the dynamic loads imposed on each enable both systems to be analyzed by the same techniques.

We treat first the fully clamped plate shown in Figure 5.6. The plate is subjected to a uniform pressure applied normal to its surface, and plastic hinges will form along the lines shown. Jones and Walters [13] give the collapse pressure as

$$P_c = \frac{3\sigma_o}{(a^2/h^2)\ (3 - 2\xi_o)} \quad \text{(fully clamped plate)} \qquad (5.5)$$

where

$$B = a/b \text{ (plate aspect ratio)}$$

$$\xi_o = B\left[\sqrt{3 + B^2} - B\right]$$

For a simply supported plate, the collapse load is one-half that of a fully clamped plate, i.e.,

$$P_c = \frac{3\sigma_o}{2(a^2/h^2)\ (3 - 2\xi_o)} \quad \text{(simply-supported plate)} \qquad (5.6)$$

The expressions presented by Equations (5.5) and (5.6) reduce to those of an infinitely long reactangular plate or beam when the aspect ratio is reduced to zero (B = 0). It must be remembered that the beam loading is given in terms of force/unit length. To obtain pressure, Equations (5.3) and (5.4) must be divided by the beam width b.

Once the collapse load of a structure has been determined, it is a simple procedure to define a safety factor. Hodge [14] and others in the field made the reasonable definition that the safety factor is the ratio of the applied load to the collapse or limit load. Therefore, the determination of the collapse load and of the safety factors can be considered as essentially equivalent. Using the relationships presented above, collapse loads were calculated for Enclosures I and II.

In box-like structures such as Enclosures I and II, the rectangular plates forming the top, bottom, and sides are neither fully clamped nor simply supported. The actual restraint lies somewhere between the two conditions. Equations (5.5) and (5.6) can, therefore, be used to bound the collapse load from below and above. Table 5.1 gives the geometrical parameters associated with Enclosures I and II and the results

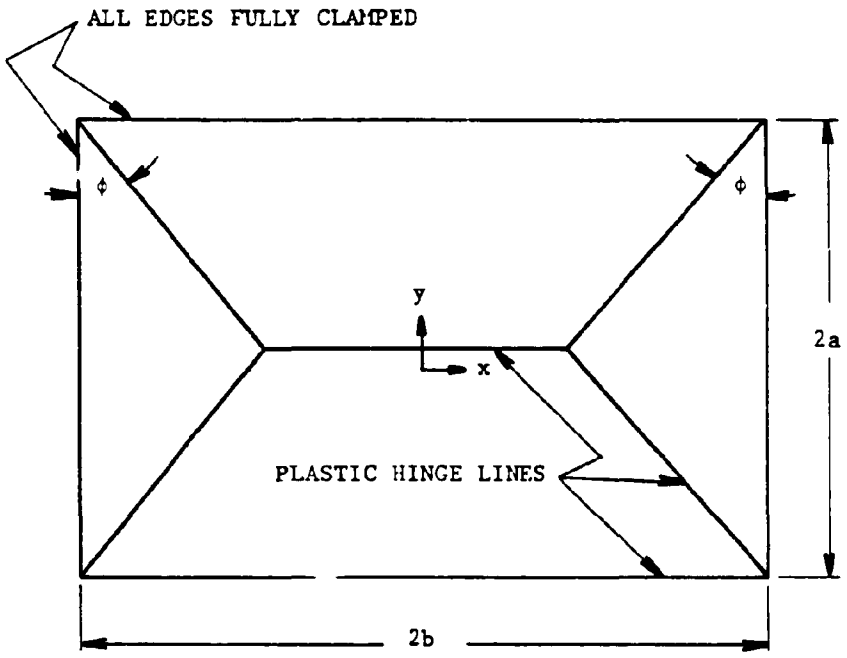

FIGURE 5.6. FULLY CLAMPED PLATE SUBJECTED TO UNIFORM PRESSURE

TABLE 5.1. UPPER AND LOWER BOUNDS FOR COLLAPSE PRESSURES FOR ENCLOSURES I AND II

ENCLOSURE I

Component	a = Height (in.)	b = Width (in.)	Thickness (in.)	Aspect Ratio (B)	ξ_o	Yield Stress (ksi)	Collapse Pressure (psi) Lower Bound	Upper Bound	Average
Top	6.75	5.375	0.50	1.26	1.11	36	380	760	570
Bottom	6.875	5.50	0.25	1.25	1.11	36	92	183	138
End	3.375	5.50	0.25	0.61	0.75	36	198	395	297
Side	3.375	6.875	0.25	0.49	0.64	36	172	345	259

ENCLOSURE II

Component	a = Height (in.)	b = Width (in.)	Thickness (in.)	Aspect Ratio (B)	ξ_o	Yield Stress (ksi)	Collapse Pressure (psi) Lower Bound	Upper Bound	Average
Top	4.875	4.00	0.625	1.22	1.10	36	1109	2219	1664
Bottom	3.9375	3.0625	0.25	1.29	1.12	36	286	573	430
End	2.375	3.0625	0.25	0.78	0.87	36	475	950	713
Side	2.375	3.9375	0.25	0.60	0.74	36	394	787	591

of the lower and upper bounds for the collapse pressure as computed from Equations (5.5) and (5.6). The last column represents an attempt to obtain a collapse pressure corresponding to the actual boundary condition of the plates. It is simply an average of the upper and lower bound collapse pressures.

The calculations agree well with the experimental test results. For Enclosure I the internal pressure was increased from zero to 290 psig, and large permanent plastic deformations were observed in the bottom. No permanent deformations could be seen in the remainder of the structure. These observations agree with the average collapse pressure calculations. They indicate a limit load for the bottom shell of 138 psig and that the end and top will not collapse at 290 psig. The averaged limit load for the side was calculated to be 259 psig, but it must be remembered that the sides of Enclosure I were reinforced by 1.00 in. x 1.00 in. x 0.25 in. angle sections.

For Enclosure II, the pressure was increased from zero to 500 psig, and no permanent deformations were observed. The averaged collapse pressures from Table 5.1 indicate that only the bottom shell would reach its limit load at 430 psig. The bottom is effectively clamped at its boundary with the 1-1/4-in.-thick end plate, and this end condition would raise the collapse pressure in the actual tests toward the upper bound pressure of 573 psig.

Schedule 2G enclosures must be designed to withstand a minimum internal pressure of 150 psig. Using this pressure along with the collapse loads in Table 5.1, the safety factors in Table 5.2 were computed for Enclosures I and II. This table gives both the lower and upper bounds as well as an averaged value. The overall safety factor for a given structure should be based upon the minimum safety factor of each of its components. If the averaged value is considered representative of the actual containers, the safety factors for the two enclosures, based on the collapse loads, are:

Safety Factor

Enclosure I = 0.9

Enclosure II = 2.9

These values indicate that the design of Enclosure I is not adequate and that Enclosure II is overdesigned for internal pressure. The result for Enclosure I was qualitatively confirmed by the hydrostatic test results reported in Sections 4.1.5 and 4.1.6 even though no catastrophic failures were observed. Calculations of safety factors based on residual permanent deformations, as covered in the next section, give more quantitative results.

5.1.2 Allowable Permanent Deformations

The work by Jones in References [15] and [16] addresses the problem of large, permanent deflections of rectangular plates subjected to static and dynamic pressure loads. The amount of damage or dishing of the plates is measured in terms of the maximum permanent deformation. Jones [16]

TABLE 5.2. SAFETY FACTORS FOR ENCLOSURES I AND II FOR A DESIGN PRESSURE OF 150 PSIG

	Enclosure I			Enclosure II		
Component	Lower Bound	Upper Bound	Average	Lower Bound	Upper Bound	Average
Top	2.5	5.1	3.8	7.4	14.8	11.1
Bottom	0.6	1.2	0.9	1.9	3.8	2.9
End	1.3	2.6	2.0	3.2	6.3	4.8
Side	1.1	2.3	1.7	2.6	5.2	3.9

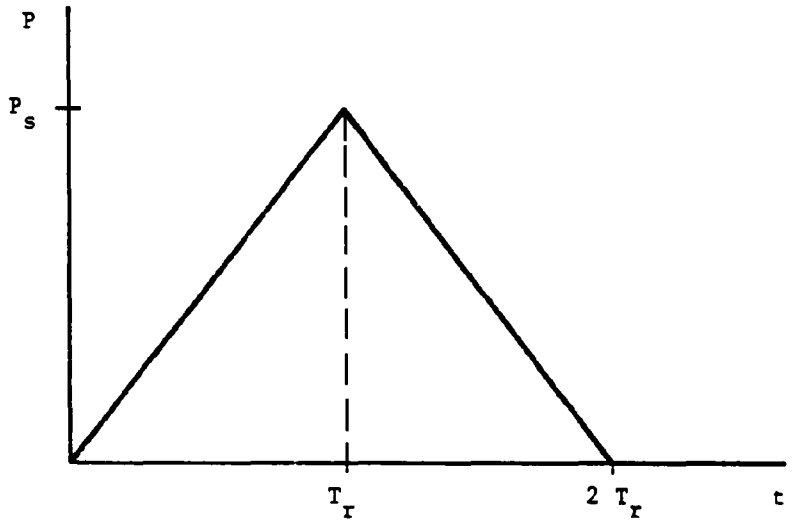

FIGURE 5.7. TRIANGULAR PRESSURE PULSE

states that if the plate is subjected to a triangular pressure pulse such as shown in Figure 5.7, dynamic effects must be considered when

$$\frac{2\,T_r}{T} > 1 \tag{5.7}$$

where

T_r = pressure rise time

T = longest natural period of plate

As was shown in Section 4.1.4, the ratio T_r/T for Enclosure I is bounded by

$$8.4 < \frac{T_r}{T} < 24.9 \tag{5.8}$$

and so Equation (5.7) is certainly satisfied. The rise time and natural period for Enclosure II will also satisfy Equation (5.7).

The relationships between damage and applied pressure are given in Reference [16] for clamped and simply supported plates by

$$\frac{P_s}{P_c} = 1 + \frac{W_o^2}{3h^2}\left[\frac{\xi_o + (3 - 2\xi_o)^2}{3 - \xi_o}\right] \quad \text{when} \quad \frac{W_o}{h} \leq 1 \quad \text{(clamped)}$$

$$= \frac{2W_o}{h}\left[1 + \frac{\xi_o\,(2 - \xi_o)}{3 - \xi_o}\left(\frac{h^2}{3W_o^2} - 1\right)\right] \quad \text{when} \quad \frac{W_o}{h} \geq 1 \tag{5.9}$$

and

$$\frac{P_s}{P_c} = 1 + \frac{4W_o^2}{3h^2}\left[\frac{\xi_o + (3 - \xi_o)^2}{3 - \xi_o}\right] \quad \text{when} \quad \frac{W_o}{h} \leq 1/2 \quad \text{(simply supported)}$$

$$= \frac{4W_o}{h}\left[1 + \frac{\xi_o\,(2 - \xi_o)}{3 - \xi_o}\left(\frac{h^2}{12W_o^2} - 1\right)\right] \quad \text{when} \quad \frac{W_o}{h} \geq 1/2 \tag{5.10}$$

where

W_o = maximum permanent lateral displacements (damage)
P_s = peak pressure
P_c = collapse pressure [see Equations (5.5)and (5.6)]
h = plate thickness
$\xi_o = B\,[\sqrt{3 + B^2} - B\,]$
B = plate aspect ratio (a/b)

These expressions are in fairly good agreement with experimental tests conducted by Hooke and Rawlings [17] on clamped, mild steel rectangular plates with aspect ratios in the range $1/3 \leq B \leq 1$. We can use Equations (5.9) and (5.10) to predict the permanent deformations in the bottoms of Enclosures I and II expected during the experimental tests. The maximum applied pressures during the tests were

$$\begin{aligned} P_s &= 290 \text{ psig for Enclosure I} \\ P_s &= 500 \text{ psig for Enclosure II} \end{aligned} \tag{5.11}$$

and the lower and upper bounds for the collapse pressures from Table 5.1 are

$$\begin{aligned} 92 < P_c < 183 \text{ psig for Enclosure I} \\ 286 < P_c < 573 \text{ psig for Enclosure II} \end{aligned} \tag{5.12}$$

If the above pressures along with the appropriate geometric quantities are used in Equations (5.9)and (5.10), the bounds for the maximum permanent deformation expected in the bottoms of Enclosures I and II are

$$\begin{aligned} 0.35 \leq W_o \leq 0.40 \text{ in. for Enclosure I} \\ 0 \leq W_o \leq 0.20 \text{ for Enclosure II} \end{aligned} \tag{5.13}$$

The lower displacement bound for Enclosure II is zero because the upper bound collapse pressure is greater than the applied pressure.

The measured maximum permanent deformation in Enclosure I was approximately 0.50 in., and no residual displacements were observed in Enclosure II. These observations agree fairly well with the displacements given in Equation (5.13). The only disconcerting point is that the upper displacement bound for Enclosure I is less than the measured value. We have no explanation for this difference.

Equations (5.9) and (5.10) can also be used very easily to compute the maximum applied pressure to give permanent deformations less than 0.04 in. per linear foot. Based on the smallest dimension of the bottom plates, the allowable deformations and W_o/h ratios for Enclosures I and II are

$$\begin{aligned} W_o &= 0.0183 \text{ in.} \\ W_o/h &= 0.073 \end{aligned} \qquad \text{Enclosure I} \tag{5.14}$$

and

$$\begin{aligned} W_o &= 0.0102 \text{ in.} \\ W_o/h &= 0.041 \end{aligned} \qquad \text{Enclosure II} \tag{5.15}$$

The pressures for the clamped, simply supported, and "averaged" conditions are

Enclosure	Simply Supported Lower Bound	Clamped Upper Bound	"Average"
1	94 psig	183 psig	138 psig
2	286 psig	573 psig	430 psig

and indicate that at 150 psig Enclosure I would have exceeded the 0.04 in. per linear foot requirement. Enclosure II would experience no permanent deformations at 150 psig. Again, these results are consistent with the hydrostatic tests reported in Section 4. Measurements of residual permanent displacements in Enclosure IA (Section 4.1.6) showed that the allowable permanent set of 0.040 in./ft was reached at 110 psig. Using the measured value for Enclosure IA and the calculated value above for Enclosure II, the safety factors based on permanent deformations are found to be:

TABLE 5.3 SAFETY FACTORS BASED ON AN ALLOWABLE PERMANENT DEFORMATION OF 0.040 In./Ft.

Enclosure	Pressure for 0.040 in./ft	Design Pressure (psig)	Safety Factor S.F.
1	110	150	0.73
2	430	150	2.87

These safety factors are slightly lower than those based on the collapse pressures as given in Section 5.1.1. Before the final safety factors could be established for the two enclosures, bolt stresses were also considered.

5.1.3 Bolt Stresses

Safety factors in the bolts for Enclosures I and II were computed from the finite element results given in Section 4, from the series solution given in Appendix B, and from the test results for Enclosure IA as given in Section 4.1.6. For these calculations, only the results for the bolt which had the maximum stress were used. Allowable strengths for bolts are usually given in terms of an axial load and do not include the effect of bolt bending. Because both axial loads and bending were present in the cover bolts, the safety factors were based upon an allowable stress. Using specifications for Armco fasteners, a Grade 5 bolt (the type used in the enclosures tested), with a diameter of 1/4 to 1 in., has the following material properties.

Yield strength: $\sigma_y = 92{,}000$ psi

Ultimate strength: $\sigma_u = 120{,}000$ psi

Safety factors in the bolts were based on the yield stress. This was consistent with the calculations of safety factors for the enclosure walls and covers, which were based on yield mechanisms and small permanent deformations.

The safety factor is simply the allowable stress divided by the calculated stress and therefore should be greater than one. Two safety factors were computed. One was based upon the direct or axial stress and the other upon the axial plus bending stress. This gives a clearer indication of how the bolt will behave under load. If the safety factor, based upon the direct plus bending stresses, is less than one, then yielding will occur. Yielding will redistribute the load and reduce the bending stress in the bolt. If the safety factor based on direct stress alone is greater than one, then the bolt may be adequate because bolt bending is limited in the enclosures by the stiffness of the covers.

Safety factors for the bolts in Enclosure I and II are given in Table 5.4. Stresses for Enclosure I were taken from Table 4.1 and Appendix B. Stresses for Enclosure II were taken from Section 4.2.1. All stresses were scaled to 150 psig internal pressure. For Enclosure I, safety factors are computed for three different cover thicknesses to demonstrate the effect on the bolt of using thinner covers.

The safety factors of Table 5.4 show that the bolts in Enclosure I are marginal and that those in Enclosure II are adequate. Both of these enclosures have been tested to pressures above 150 psig, and no bolt failures occurred. Also, the comparisons between analysis and experiment for bolt loads in Enclosure IA showed that the analytical predictions were higher than measured values. It was assumed in the analyses that the bolt had rotated with the cover. This is a conservative assumption and is probably the reason why calculated bolt forces exceeded measured ones.

5.1.4 Minimum Safety Factors for Enclosures I and II

Safety factors were computed for Enclosures I and II based on (1) collapse pressures for the enclosure bottom and side plates, (2) permanent deformations in the bottom and side plates, and (3) stresses in the cover bolts. These results are contained in Tables 5.2, 5.3, and 5.4, respectively. A survey of the results shows that the minimum safety factor for Enclosure I (S.F. = 0.73) is based upon permanent deformation of the bottom of the enclosure and that the minimum safety factor for Enclosure II (S.F. = 1.60) is based upon the bolt stress. It should also be noted that the S.F. = 1.60 is conservative for Enclosure II because this value is based upon bolt bending, and failure of the bolt is not likely to occur until the axial loads in the bolt exceed the bolt yield stress. Based upon axial bolt loads alone, the safety factor for the bolts would be 3.32.

Also note that the minimum safety factors computed for Enclosure I for the three types of failure were all about the same (S.F. = 0.9, 0.73 and 0.75); however, for Enclosure II the minimum safety factors were S.F. = 2.9, 2.87, and 1.60 based on collapse pressure, permanent deformation, and bolt stresses, respectively.

5.2 Enclosure III

The preceding sections addressed the question of safety factors in Enclosures I and II. These safety factors were based on the concept of

TABLE 5.4. SAFETY FACTORS FOR BOLTS
IN ENCLOSURES I AND II
(150-psig Internal Pressure)

	Direct Stress		Direct Plus Bending Stress	
	σ_A, psi	S.F.	σ_M, psi	S.F.
Enclosure I				
ANSYS Solution (1/2" cover)	31,736	2.90	121,785	0.75
Series Solution (1/2"cover)	41,888	2.20	107,151	0.86
Series Solution (3/8"cover)	44,297	2.08	117,348	0.78
Series Solution (1/4"cover)	44,679	2.06	136,283	0.68
Enclosure II				
ANSYS Solution	27,744	3.32	57,558	1.60
Series Solution	20,961	4.39	45,200	2.03

computing the so-called collapse load and deformations in an elastic-plastic structure. The ratio of the collapse or limit load to the applied load was defined as the safety factor. However, in components which are fabricated from glass, this procedure is no longer valid. Glass does not exhibit the property of plastic flow and has no yield point. Fracture always occurs in tension and before there is ever any permanent deformation in the glasss. Likewise, cast materials, also found in this enclosure, exhibit low ductility and no clearly defined yield point. Thus, the safety factors for Enclosure III will be based only on the peak stresses in its components, principally in the glass, and not on its elastic-plastic behavior.

It would appear from the preceding remarks that the safety factor for Enclosure III should have been based upon the fracture strength of glass in tension. But this approach was not totally satisfactory because additional factors, such as annealing, tempering, and service condition, have a significant effect on the fracture strength. For example, Reference 18 reports the following data for establishing a suitable design stress for an annealed piece of glass.

	psi
Average short-time breaking stress (from test)	8,000
Minimum probable breaking stress	4,800
Minimum long-time breaking stress	1,920
Design stress (Safety Factor = 2)	960

Reference 18 further indicates that experience has shown, for annealed glass, that suitable working stresses in tension may be between 500 psi and 1,500 psi, while for tempered glass they may be taken between 1,500 psi and 4,000 psi.

For additional information SwRI contacted an engineer in the New Products Division of PPG Industries. He reported that the soda lime glass, used in this enclosure, has a short-time modulus of rupture of approximately 6,000 psi. Short-time is defined as about one-tenth second or equal to the duration of a sonic boom. When the duration becomes long term, which is on the order of several hours, the strength drops to about 3,000 psi.

The strength of the structure supporting the glass was also considered. Not only is cast aluminum somewhat brittle, but experience has shown that the condition of the bearing surfaces which support the glass and their alignment can be extremely important in establishing the glass fracture loads. Any excessive deformations of the supporting structure under load can set up high bending stress in the glass and reduce the overall strength or the enclosure. For these reasons the yield strength of the cast aluminum was taken as the design criteria upon which the safety factors in the body of the enclosure were based. A third component in Enclosure III was the epoxy which bonded the glass to the aluminum. As noted in the finite element analysis of Section 4.3, this epoxy had a yield strength of approximately 10,000 psi.

Based on the information available for the three materials, as discussed in the paragraph just preceding, SwRI established the following

failure criteria for use in computing the safety factors of Enclosure III:

Glass: Failure will occur when the largest principal stress reaches the short-time modulus of rupture of 6,000 psi.

Aluminum: Failure will occur when the von Mises stress reaches the yield stress of 18,000 psi. This value is reported in Reference 13 for No. 319-F aluminum, which is believed to be the commercial No. 319 aluminum specified on the Control Products, Inc., engineering drawings.

Epoxy: Failure will occur when the principal stress reaches 10,000 psi. This is SwRI's best estimate for Dolph's two-part, carbon-filled epoxy.

Peak stresses in Enclosure III were computed with three different finite element models as described in Section 4.3. The three models were:

Model I - Side or Top Windows

IA - with idealized simple support
IB - with edge beams only
IC - edge beams bonded to side windows

Model II - Circular End Window and Frame

Model III - Two-Dimensional Cross-Sectional Model

Peak stresses for an internal pressure of 100 psig were summarized for these three models in Figures 4.78, 4.80 and 4.82. Stresses from these figures were scaled to an internal pressure of 150 psig and used to calculate the safety factors given in Table 5.5.

As discussed in Section 4.3.2.3, Model IB gives the most realistic description of the support conditions of the rectangular windows. This model also produces the lowest factor of safety in the glass (S.F. = 1.3). It should also be noted that tensile stresses as high as 9,400 psi were measured in the glass without failure. This stress is substantially higher than the 6,000 psi design criteria used to compute the safety factors. So, it is clear that some glass can withstand higher stresses than the design values recommended by the manufacturers; however, it is our opinion that in general the lower allowable of 6,000 psi should be used for tempered soda lime glass.

The minimum factor of safety for the enclosure is 1.2 and is based upon bending stress in the bottom of the enclosure. This stress did not occur at the location of the cracking which was observed during the hydrostatic test. Cracking occurred in the corners of the opening for the side windows as shown in Figure 4.85. These cracks first appeared about 200 psig and were sufficiently large to stop the test at 230 psig. The factor of safety associated with this cracking can be estimated from the test as

TABLE 5.5 PEAK STRESSES AND SAFETY FACTORS
FOR ENCLOSURE III: 150-PSI INTERNAL PRESSURE

Model	Glass	S.F.	Aluminum	S.F.	Epoxy	S.F.
I - Side or Top Windows						
A - Simple Support	2297	2.6	NA	NA	NA	NA
B - Top Window with Edge Beams	8690	0.70	13,838	1.3	NA	NA
C - Top Window with Edge Beams on Foundation Springs	2606	2.3	1,250	14.4	NA	NA
II - Cylindrical	1182	5.1	1,041	17.3	255	39.2
III - Plane Strain Model of Cross Section	3281	1.8	15,600	1.2	1905	5.2

NOTE: All stresses in psi

$$\text{Safety Factor (S.F.)} = \frac{\text{Peak Stress}}{\text{Failure Criteria Stress}}$$

$$S.F. = \frac{200 \text{ psig}}{150 \text{ psig}} = 1.33$$

Thus, S.F. = 1.2 as listed in Table 5.5 still controls the safety factor for Enclosure III.

5.3 Enclosure IV

Enclosure IV was constructed of gray cast iron and thus was treated as a brittle material in the calculation of safety factors. Tests on specimens from the enclosure showed widely varying properties between the cover and the enclosure body. The cover of the enclosure also exhibited brittle behavior, with the yield stress and ultimate stress differing by as little as 11% in some specimens (see Table 4.5). Although not indicated in Table 4.5, these specimens also exhibited low ductility and fracture surfaces revealed large grain structure characteristic of cast brittle materials.

Because of the brittle nature of the cast material in Enclosure IV, safety factors were based upon the material yield stress. The average yield stress for the cover was chosen for both components of the enclosure because variations which can occur in the casting might also result in a lower strength casting for the body of some enclosures. This value is

$$\sigma_y = 18{,}300 \text{ psi}$$

and is less than the minimum ultimate stress measured for any specimen.

Peak calculated strains in Enclosure IV are given in Table 4.7. The maximum strain was predicted to occur at the center of the cover. At 500 psig internal pressure this strain is

$$\varepsilon_{max} = 1297 \text{ } \mu\text{in./in.}$$

At the center of the cover a biaxial state of strain exists and the yield strain, for σ_y = 18,300 psi, would be

$$\varepsilon_y = \frac{1}{E}(\sigma_1 - \nu\sigma_2) \tag{5.16}$$

$$= \frac{1}{6.8}\,[18{,}300 - (0.3)(18{,}300)] = 1{,}830 \text{ } \mu\text{in./in.}$$

The average elastic modulus for the cover was used in the calculation and Poissons ratio, ν, was taken as 0.3.

Using the yield strain given by Equation (5.16) as the failure criterion and the maximum strains listed in Table 4.7, the safety factors given in Table 5.6 were computed. Safety factors in Enclosure IV are clearly the highest of all the enclosures analyzed. Also, the numbers are probably conservative because the calculated strains used in the calculations were generally higher than measured values (see Section 4.4.2.2).

TABLE 5.6 SAFETY FACTORS IN ENCLOSURE IV
FOR 150-PSIG INTERNAL PRESSURE

Component	Max. Strain @ 150 psig (μin/in)	Yield Strain (μin/in)	Safety Factor
Cover	389	1880	4.83
Body	124	1880*	15.16

*Biaxial state of stress taken as the lower limit.

TABLE 5.7 SUMMARY OF SAFETY FACTORS
FOR THE ENCLOSURES

Enclosure No.	Enclosure Description	Enclosure Volume (in^3)	Minimum Strength Component	Safety Factor
I	Steel Rectangular Box - Al Cover	926	Enclosure Bottom	0.73
II	Steel Rectangular Box & (Small) Cover	234	Cover Bolts	1.60
III	Rectangular Luminaire - Al Casting	~140	Bottom Plate - Al Casting	1.20
IV	Cylindrical Junction Box - Steel Casting	142	Cover - Steel Casting	4.83

5.4 Safety Factors Summarized

Safety factors for the four enclosures analyzed in this study were calculated in the preceding sections. For each enclosure, multiple factors of safety were calculated for different components and with different finite element models. Table 5.7 summarizes the minimum factor of safety for each enclosure. This is the safety factor which governs the failure mode of the enclosure; the others were calculated for evaluation and comparison only.

As Table 5.7 shows, there is a wide variation in the strength of Schedule 2G enclosures. Also, all of these enclosures have passed the MSHA explosion test. The design criterion of 150 psig used to compute the factors of safety in Table 5.7 is a more severe load than the internal explosion of methane and air (see Section 4.1.4.3). Thus, Enclosure I shows a safety factor of less than one even though it has been certified as explosion proof.

Note also that all of the enclosures have an internal volume which is greater than the maximum volume of 124 $in.^3$ in paragraph 18.31 of Schedule 2G. Based only on the requirements of paragraph 18.31, all of the enclosures would have the same minimum wall structures regardless of their size. This fact may contribute to the trend in Table 5.7 toward lower safety factors for larger enclosures. Because Enclosure III is a luminaire, it is in a somewhat different class from the other three enclosures.

It should be emphasized that these safety factors are based only on internal pressure loads. Although the safety factor of the luminaire (Enclosure III) is greater than that for Enclosure I, Enclosure I may be much more rugged in the mine environment. The luminaire is much more apt to be damaged by impact than are the other enclosures because of the brittle nature of the glass. Ruggedness of enclosures in the mine environment is discussed in Section 8.3.

6.0 ESTABLISH WELD QUALITY STANDARDS

Following the hydrostatic testing of Enclosures I and II (see Sections 4.1 and 4.2), the welds were examined visually and by radiography on selected joints. The visual examinations revealed that some joint designs were being used which have low efficiency for static and dynamic loads. Further, some of these low efficiency joints, which were used at the junction of side and bottom plates, failed during the hydrostatic testing. This was observed on Enclosure I. Failure in this case did not involve sudden rupture, or even leakage. The weld joint simply opened up along the fusion line and lost all moment continuity. Radiographs revealed that partial penetration weld joints were used and continuous porosity defects were entrapped in the weldment.

From these examinations, it was apparent that weld quality in some XP enclosures was inadequate and that more specific welding requirements were perhaps required. To establish more clearly the level of weld quality maintained in the fabrication of XP enclosures, SwRI was funded to conduct a modest survey of the industry.

6.1 Survey of Welding Practices

Southwest Research Institute, in cooperation with the Bureau of Mines, conducted a survey to determine the existing welding practices used by the mining equipment industry in the fabrication of XP enclosures. Six companies were visited which can be approximately classified as follows:

Two, Large: Number of Employees $\geq$ 150
One, Intermediate: 150 $\geq$ Number of Employees $\geq$ 50
Two, Small: 50 > Number of Employees

At each of the companies visited, discussions were held with the people most responsible for weld quality. At most large companies this was the welding engineer and head of Q.A.; at intermediate sized companies it was the chief design and Q.A. engineers; and at smaller companies it was the production manager. Most visits included tours of the fabrication shops and inspection areas.

A list of nine questions was prepared in advance and specifically covered on each visit. The questions were formulated jointly by representatives of SwRI, USBM, and MSHA. Along with the onsite observations, they formed the basis of the judgments regarding weld quality in the industry.

6.2 Survey Results

Table 6.1 summarizes the questions asked and responses to the survey. Company attitudes toward meeting American Welding Society (AWS) welding requirements are apparently divided. Activity in this direction is either being implemented or being considered by the larger manufacturers, while the smaller companies are depending more on the MSHA certification of their XP enclosures. The specific welding requirements acknowledged were the AWS D14.3-77, "Specification for Welding Earthmoving and Construction

TABLE 6.1. SURVEY SUMMARY

COMPANY	1	2	3	4	5	6
COMPANY SIZE	LARGE	LARGE	LARGE	MEDIUM	SMALL	SMALL
1. How do you meet Part 18.31(a)(2), Title 30, of the CFR?	Submit XP enclosures to MSHA.	Submit XP enclosures to MSHA.	Drawings note Part 18.32, Title 30, of CFR.	Use past practice. Depend on MSHA for testing.	Use past practice. Depend on MSHA for testing.	Use past practice Depend on MSHA for testing.
2. Do you meet any specific codes or standards for welding? Are you familiar with D14.4-77 or D-14.3-77?	Installing D14.3.	No, intend to meet D14.3.	No, looking at D14.3.	No, believe practice exceeds codes.	No.	No.
3. Describe your welding practice.	SMAW, GMAW, FCAW, and SAW.	SMAW, GMAW, and FCAW.	SMAW, GMAW, and FCAW.	SAW and GMAW with special fixtures.	SMAW and GMAW.	SAW and GMAW with special fixtures.
4. Can you supply copies of your						
(a) welding procedures,	Yes.	Partial.	No.	None, except drawings.	None available.	None.
(b) weld quality assurance procedures,	Yes.	None.	Reviewed. Not released.	Workmanship standards.	None.	None.
(c) welder qualification standard?	Will test AWS.	Plan AWS testing.	None.	None.	None.	None.
5. Do you distinguish between welding on explosion-proof containers and other equipment?	Yes, use best welders only.	No, same as mining machines.	No, same as mining machines.	Yes, use SAW and most experienced	Yes, use best welders.	Yes, use most experienced welders.
6. Is any of your welding subcontracted?	Yes, subcontractor is well-known.	Yes, receive and inspect.	Yes, most XPs are subcontracted.	Yes, some.	Yes, some.	No.
7. How is joint design determined?	Engineering and design agreement.	Drawing review by manufacturing and engineering.	Issued by engineering standards group.	Past experience of successful enclosures.	Use joints successful in the past.	Past experience of successful enclosures.
8. Do you keep records of the manufacturing process for enclosure?	Yes, identify and tests.	No, except router.	No records.	No, shop order for each job.	No records.	No records.
9. Do you test enclosures?	Yes, 100% air and 100% hydrostatic.	No tests except visual testing.	No tests except visual testing.	No tests except visual testing.	No tests except visual testing.	No tests.

Equipment." This "consensus" specification was formulated by large earthmoving and construction equipment manufacturers of self-propelled and on- and off-highway machinery. Such products as crawler tractors, motor graders, end loafers, off-highway trucks, power shovels, backhoes, truck and crawler cranes, draglines, and similar equipment are considered to be included in this description. Manufacturers of continuous mining machines were not participants, nor were they represented in drafting this document.

Replies on present welding practices, as shown in Table 6.1 for Question 3, were summarized by listing the welding processes used. Special fixtures are used and automatic welding is practiced by several manufacturers which use the submerged arc welding (SAW) process. Every manufacturer employs the semiautomatic flux core (FCAW) or gas metal arc welding (GMAW) processes to some extent on XP enclosures. Only one company had fully developed welding procedures which were ready to be issued at the time of the visit. Similarly, testing and qualification of welders had not been performed by any of the companies, although two were planning to test welders soon in accordance with AWS requirements.

Control of welding on XP enclosures which are subcontracted is based more on personal knowledge of the welders and on receiving visual inspection than on any code or test requirements. The trend seems to favor companies performing nearly all of their own welding. In general, very little weld joint design effort is given to XP enclosures, and the joint configurations are predominantly determined from past experience. However, some application of AWS prequalified joint designs was found. All of the larger companies employed welding engineers, and all were actively engaged in the joint designs. One company was found to test enclosures and keep traceable records; the others depend on the MSHA testing and certification process. Only the company which kept traceable records had an active and formalized quality assurance program. No intent to review or suggest quality assurance measures was considered in these surveys.

Based on these survey results, the following conclusions were reached:

(1) The survey has shown that the basic weld joint designs and quality measures that are applied to XP enclosures are largely dependent upon the original qualification testing performed by MSHA. Five out of six manufacturers do no testing. Half of the companies or less use AWS prequalified joint designs. None of the companies have qualified their own welding procedures, and two are beginning to qualify their welders to AWS standards. Therefore, it is recommended that a specific set of minimum welding and acceptance requirements be applied to the manufacture of XP enclosures.

(2) Half of the six companies are addressing the AWS D14.3-77, "Specification for Welding Earthmoving and Construction Equipment," without any specific weld joint design efficiency being applied. Since the survey has revealed that five out of six companies use partial penetration joints, and in many cases, this is further diminished by the use of single-sided welds only, the application of a minimum classification for weldment

designs should be specified. In addition, some original testing or calculation of the joint efficiencies should be applied to each enclosure design. Therefore, the AWS D14.4-77 Standard, "Classification and Application of Welded Joints for Machinery and Equipment," Classes I through V Joints, should be specified as the minimum requirement for enclosures.

(3) Visual testing and acceptance of enclosure weldments are the only measures of weld quality provided by five out of six companies. Therefore, it is considered necessary to use only qualified welding procedures, qualified welders, joint designs of known efficiency, and to inspect by the direct visual observation method of examination (as a minimum) for the fitup, root bead, and final weld surfaces of each enclosure joint. Acceptance standards for weldments should also be set in accordance with AWS D14.4 requirements.

6.3 Recommendations

Based upon the survey results, it is clear that a welding specification is needed by the industry to unify the welding procedures, to provide guidance in all areas of the welding process, and particularly tc provide much needed guidance in weld joint design efficiency. SwRI recommends AWS D14.4 as the most appropriate welding code for the fabrication of XP enclosures. It is self contained and provides sufficiently detailed information for users to perform the five functions necessary for good welding practice, i.e.,

(1) Welding procedure specification
(2) Welding procedure qualification
(3) Welder or welding operator qualification
(4) Joint design
(5) Acceptance criteria for weldments

To solicit comments from XP enclosure manufacturers on the use of AWS D14.4, a copy of the welding code and a set of explanatory notes were sent to representative companies for comment. The explanatory notes and accompanying cover letter are included as Appendix I.

Welding code AWS D14.4 is referred to heavily in the explanatory notes, and a copy must be on hand for ready reference if the notes are to be understood. The explanatory notes were mailed to representative companies under signature of the USBM. Only one reply was received. This reply, from one of the larger manufacturers, suggested their full support for the recommendation to adopt AWS D14.4 as a requirement for the manufacture of XP enclosures.

Welding requirements for XP enclosures are now specified in Part 18, Title 30 of the Code of Federal Regulations (Reference 1). The requirement now states:

18.31 Enclosures - joints and fastenings.

(a) Explosion-proof enclosures:

(1) Cast or welded enclosures shall be designed to withstand a minimum internal pressure of 150 pounds per square inch (gage). Castings shall be free from blow holes.

(2) Welded joints forming an enclosure shall have continuous gas-tight welds. All welds shall be made in accordance with American Welding Society Standards.

To establish a more specific welding requirement, Section 18.31(a)(2) should be revised to read:

(2) Welded joints forming an enclosure shall have continuous gas-tight welds. All welds shall be made in accordance with American Welding Society Standard D14.4 entitled "Classification and Application of Welded Joints for Machinery and Equipment," latest revision.

The purpose in recommending this standard is to provide for safe, uniform, minimum requirements for the manufacture of XP enclosures. It is surmised that no additional technical effort will be required by manufacturers to meet these requirements and to implement this standard. It is also believed that the majority of weld joint designs will not need to be revised in any way; however, welding procedures and welder qualification practices in accordance with the American Welding Society requirements will need to be established where they have not already been implemented.

7.0 RELIABILITY OF SCHEDULE 2G ENCLOSURES WITH WINDOWS

7.1 Background

If explosion-proof enclosures with windows are to operate reliably in an underground mining environment, each component of the enclosure must function properly. Metal components have proven their reliability through a long history of successful use. Relatively new materials, such as adhesives and polycarbonates, have not yet proven their reliability. The purpose of this task was to investigate those parameters which affect the reliability of enclosures with windows. It was not to develop Quality Assurance (Q.A.) procedures, but to develop information which will be directly applicable to the development of such procedures in the future.

To investigate the reliability of materials and components in the mine, one must understand the mine environment. A good survey of the environment underground is given by Francis and Lankford [19], from their study of acceptance testing criteria for adhesives and sealants for explosion-proof enclosures. In this task the environmental data in Reference [19] were supplemented with data from additional investigations. These new investigations were devoted primarily to defining the mechanical environment underground. The data were needed to formulate ruggedness criteria for enclosures (Section 8.3) and were also used for some of the evaluations performed in this task.

Based upon discussions with MSHA personnel and a review of the environmental data, it was concluded that evaluations were necessary to determine the effect of the inservice environment on enclosure materials and to determine how well Schedule 2G qualification tests represent inservice loads. The following tasks were selected:

- Evaluate the effect of vibrations on enclosures with windows
- Evaluate the Schedule 2G Impact Test
- Evaluate the Schedule 2G Thermal Shock Test
- Determine the effect of the inservice environment upon selected adhesives and polycarbonates which are used in enclosures

Results of these investigations are presented in the following sections.

7.2 Vibration Testing

7.2.1 Methodology

To study the effects of vibrations upon windows in explosion-proof enclosures, SwRI performed sinusoidal vibration sweep tests on three luminaires. The purpose of these tests was (1) to see if different types of window mountings produced differences in window response and (2) to see if excitation frequencies from mining equipment would excite resonances in the enclosures that might be detrimental to the window.

The luminaires tested were typical of those mounted on underground mining equipment. Each luminaire is identified below by type, manufacturer, and window description:

(a) Model & Type: 14812D Machine Light
Manufacturer: Control Products, Inc.
Window: Soda-lime plate glass, rectangular and round, seated with silicone and edge bonded with epoxy

(b) Model & Type: 500131-35 Fluorescent Lamp
Manufacturer: Joy Manufacturing Co.
Window: Polycarbonate tube, mechanically fastened, slip fit with O-ring seal

(c) Model & Type: MHL2 Headlight
Manufacturer: Crouse-Hinds Co.
Window: Tempered glass, round, mechanically fastened, no gasket or seating compound

These luminaires are shown in Figure 7.1. Note that the Control Products Luminaire is the same as Enclosure III, which was analyzed and hydrostatically tested as described in Section 4.3. Axes on the photographs identify the excitation (drive) and measurement axes for the vibration tests. For example, X-axis drive means that the excitation is being applied along the axis of the tube in the fluorescent lamp or perpendicular to the glass window in the MHL Headlight. Likewise, the measurement of vibration normal to the glass surface would be in the X-direction for the MHL Headlight, etc. This nomenclature is used in subsequent figures and refers to the axes and directions in Figure 7.1.

Before testing began, vibration data on different mining machines were reviewed to determine the expected frequency range of excitation on such equipment and to estimate vibration amplitudes. Vibration data reported by Patterson, et al. [20], provided the basis for the review. The data showed that significant vibration excitation can occur from ~50 Hz to ~10,000 Hz and that vibration levels can be as high as 19 g_{rms} (data taken with a 1/3-octave bandwidth filter). We did not attempt to excite the luminaires at these acceleration levels, but attempted only to identify the resonant frequencies within the above frequency range.

To cover the frequency range reported in the vibration data, sinusoidal sweep tests were performed from ~5 Hz to 10,000 Hz. An input acceleration level of 0.1 g (zero to peak) was used for all tests except the first. The first test was conducted with a 0.5 g (zero to peak) input. Measured responses exceeded 5 g's, so all subsequent excitation levels were lowered. The sweep from 5 Hz to 10,000 Hz was made in two parts, 5 Hz to 100 Hz and 100 Hz to 10,000 Hz. No resonances were observed in the 5 Hz to 100 Hz range for any of the enclosures, so those data are not presented; all data will cover the frequency range from 100 Hz to 10,000 Hz. A sweep rate of 30 Hz/sec was used in all tests for which data are presented. A few tests were also conducted with a sweep rate of 10 Hz/sec. Differences in the maximum responses were small, and no new frequencies were observed at the slower rate; thus, the majority of all tests were conducted at the higher sweep rate to reduce test time.

A total of 49 vibration tests were performed on the three enclosures exciting them along each of the three axes. Two acceleration

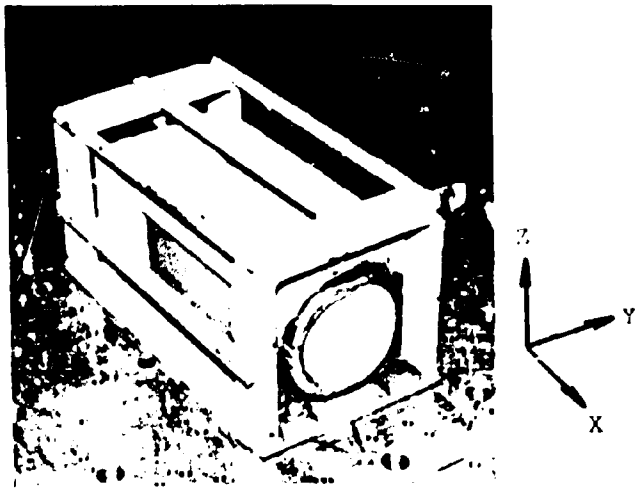

(a) Control Products, Inc., Luminaire

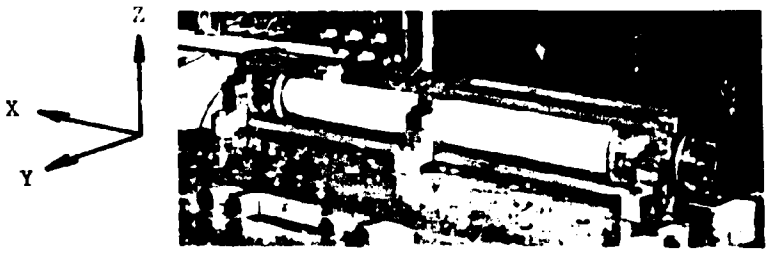

(b) Joy Manufacturing Co. Fluorescent Lamp

(c) Crouse-Hinds Co. MHL Headlight

FIGURE 7.1. REFERENCE AXES FOR VIBRATION TESTING

measurements were made per test. This large number of tests was conducted in an attempt to isolate the source of resonances when they were observed. Isolating the frequencies proved to be somewhat impractical because the accelerations from the resonances were transmitted throughout the enclosures. It was concluded that the important resonances for the windows were primarily those that produced the highest acceleration levels on the window in the direction normal to its plane. These vibrations would produce tension and/or compression in the seating compound (if any) between the window and the frame and place the adhesive (if any) that bonds the window to the enclosure in tension and/or shear. This is generally the direction of motion that would tend to unseat the window.

7.2.2 Results

Figures 7.2 through 7.4 show acceleration levels measured normal to the window surfaces for excitation in three mutually perpendicular axes. For the fluorescent luminaire, made from polycarbonate tube, these accelerations were arbitrarily measured in the vertical direction.

Figure 7.2 gives these results for the luminaire from Control Products. The top window was chosen as representative of the three rectangular windows in this enclosure, and Parts (a), (b), and (c) of Figure 7.2 give accelerations measured at the center of the top window for excitation in the X, Y, and Z axes, respectively (see Figure 7.1). Input acceleration for Part (a) was 0.5 g (zero to peak). All others are for inputs of 0.1 g (zero to peak). It is very clear from these graphs that the resonances that occur are not of the window, but of other components in the enclosure. They shift dramatically in frequency with changes in the direction of excitation. If the fundamental resonance of the window were being excited, it would be at the same frequency no matter the axis of excitation. Further, the fundamental frequency of the rectangular windows is ~7300 Hz for simple support conditions. The frequency at which the window will actually vibrate may be raised by some rotational restraint at the support or lowered by lateral support flexibility; however, it does not appear that the fundamental of the window is being excited because it does not occur for Z-axis drive, which is the drive axis most likely to excite the window.

The peaks in the response spectrum that occur at about 200, 500, 1700, 3700, and 6000 Hz show that significant amplification of the excitation acceleration can occur in the luminaires. As will be clear when the responses of the other luminaires are studied, the peak at ~200 Hz is common to all of them for Z-axis drive. Thus, this amplification is a consequence of the excitation system and will be ignored as a luminaire resonance. The second highest amplification is about

$$\frac{g_{output}}{g_{input}} = 23$$

which occurs at 3700 Hz. High and possibly detrimental accelerations of the window can occur in service if large excitation accelerations occur at this frequency. Smaller, but still significant, window vibration could be produced at any of the other, smaller peaks.

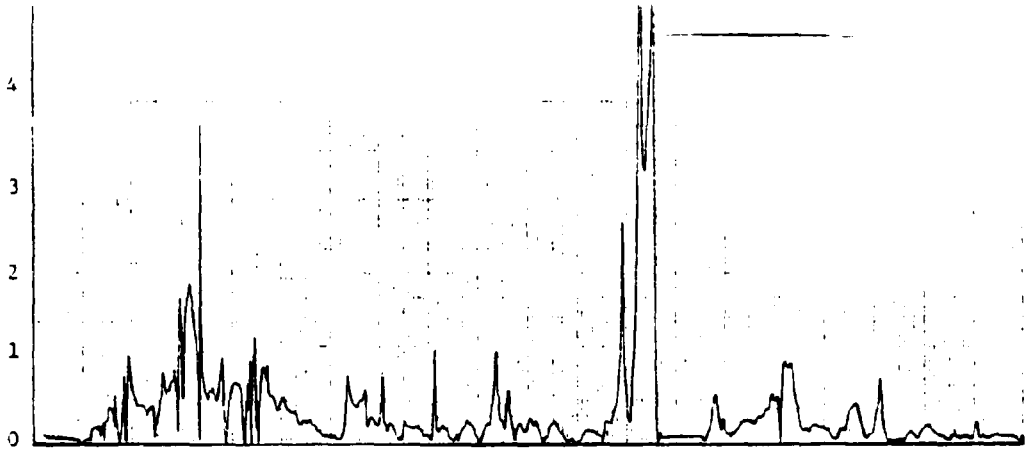

(a) X-Axis Drive, Top Window

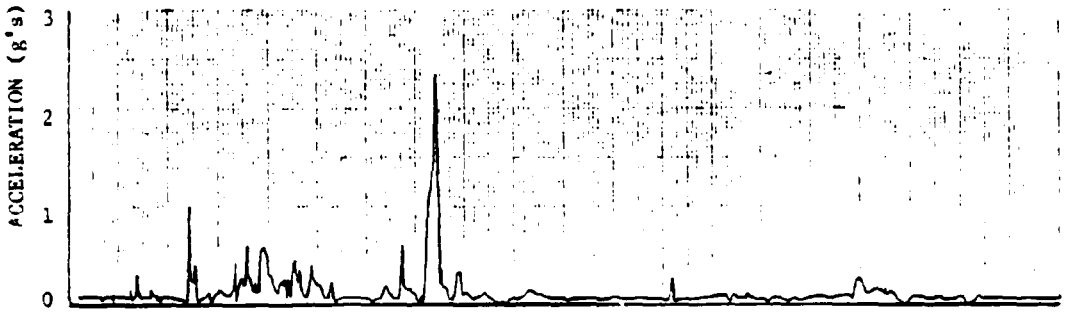

(b) Y-Axis Drive, Top Window

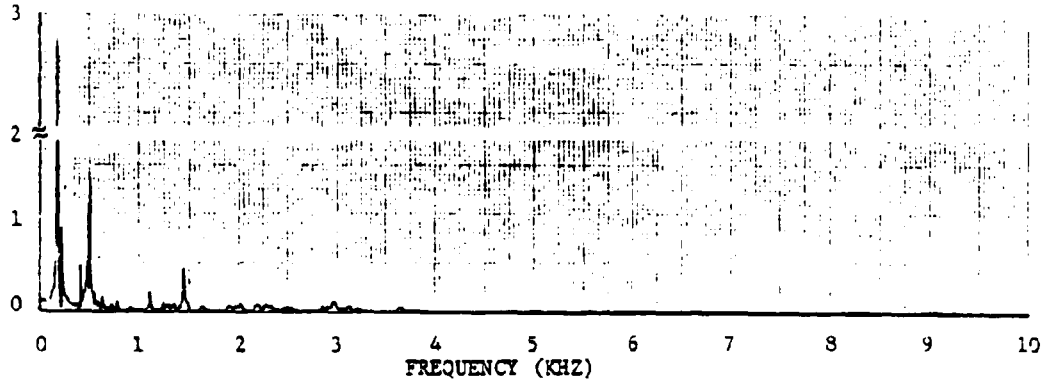

(c) Z-Axis Drive, Top Window

FIGURE 7.2. WINDOW ACCELERATIONS MEASURED NORMAL TO THE GLASS SURFACE - CONTROL PRODUCTS ENCLOSURE

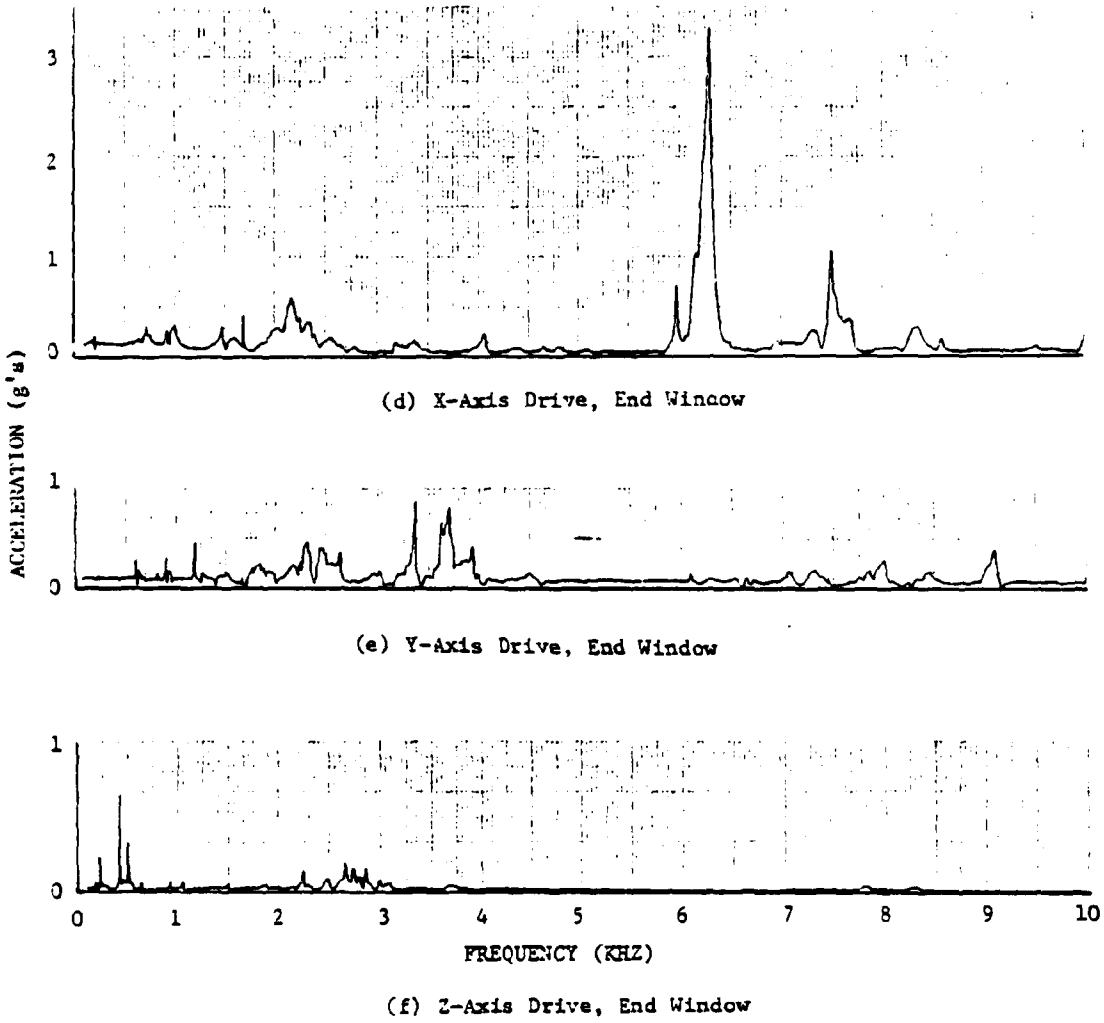

(d) X-Axis Drive, End Window

(e) Y-Axis Drive, End Window

(f) Z-Axis Drive, End Window

FIGURE 7.2. WINDOW ACCELERATIONS MEASURED NORMAL TO THE GLASS SURFACE - CONTROL PRODUCTS ENCLOSURE (Concl'd)

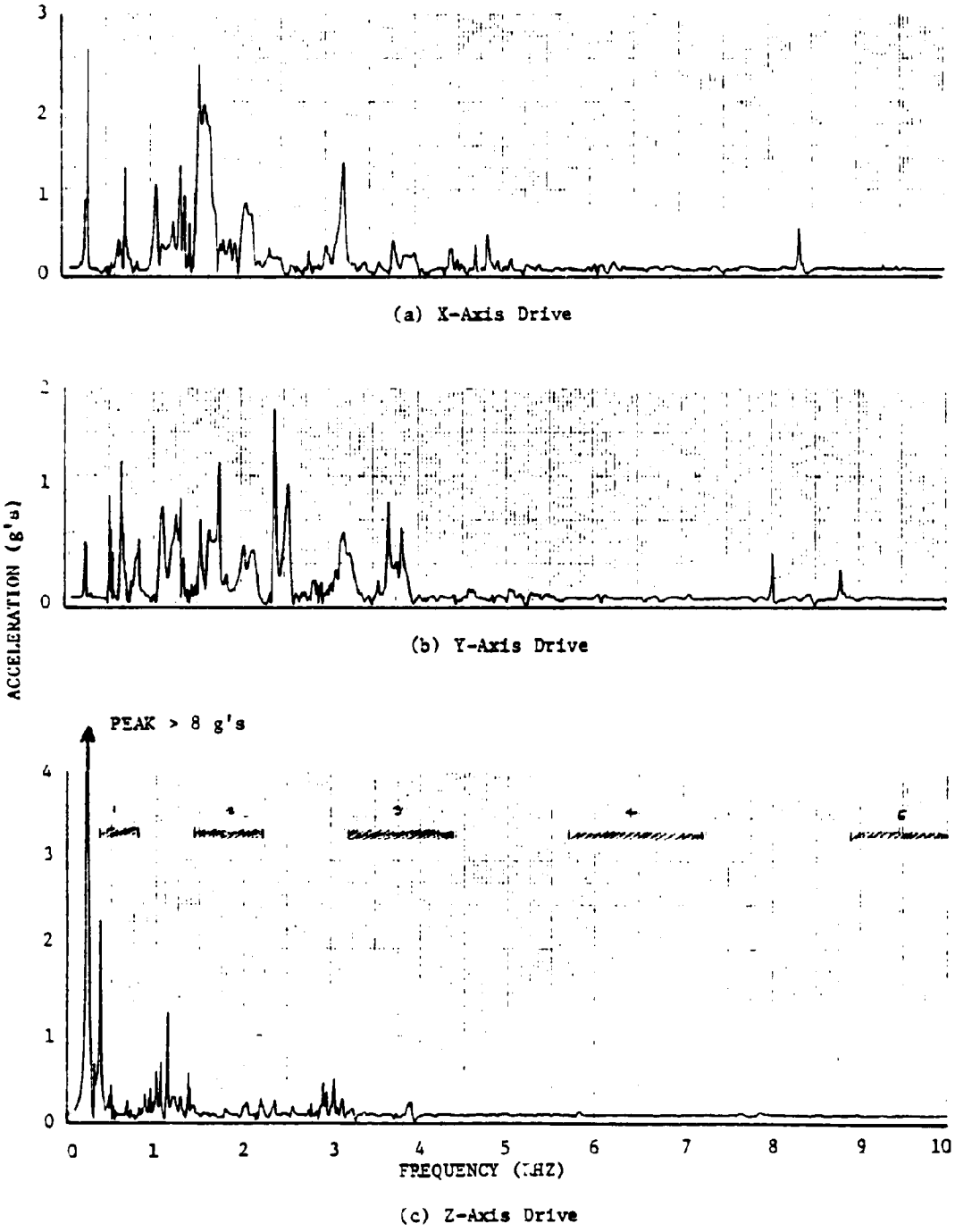

FIGURE 7.3. ACCELERATIONS MEASURED IN THE VERTICAL DIRECTION NEAR THE TUBE CENTER - FLUORESCENT LIGHT FIXTURE BY JOY MANUFACTURING CO.

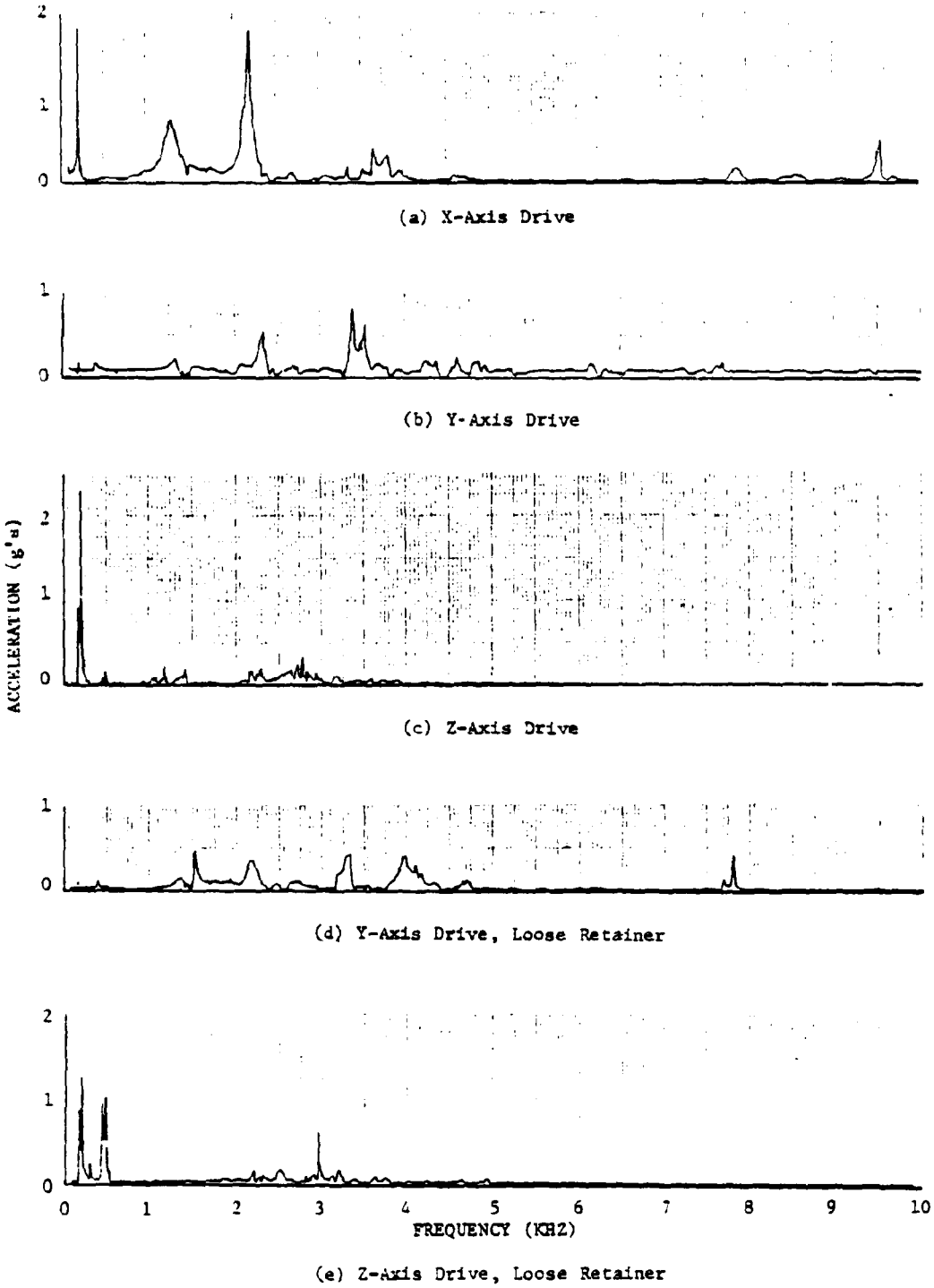

FIGURE 7.4. WINDOW ACCELERATIONS MEASURED NORMAL TO GLASS SURFACE (X-AXIS) - CROUSE-HINDS ENCLOSURE

Parts (d), (e), and (f) of Figure 7.2 show the effect of vibration on the round window in the end of the enclosure. Amplification factors are lower than for the top window. Note that the same spike appears in the top and end windows in the neighborhood of 6000 Hz for X-axis drive. All other resonance peaks for the end window are lower than for the top window. No others exceed 1.0 g (zero to peak), which produces an amplification factor of less than 10.

Results for the fluorescent lamp made by Joy Manufacturing Co. are given in Figure 7.3. The "window" in this lamp is a cylindrical tube, and vibration measurements were made in the Z-axis (normal to the cylindrical surface) near the tube center. Up to five resonant frequencies (longitudinal bending) of the tube occur in the range from 5 Hz to 10,000 Hz. These frequencies were calculated analytically and are shown as bands in Part (c) of the figure. The low end of each frequency band corresponds to the simple support solution for the tube, and the high end corresponds to clamped support solution. As the actual support conditions are between simple and damped restraint, the actual resonances will fall in the frequency band between these two bounds.

As for the Control Products luminaire, the spike at ~200 Hz is believed to be associated with the excitation equipment and is therefore ignored. Several other resonant spikes occur with amplification factors of about 22 to 26. Frequencies 4 and 5 calculated for the tube do not appear in the results; however, natural frequencies 1, 2, and 3 are probably among the spikes that occur within the respective bands. Resonances for this luminaire occur primarily below 4000 Hz.

Figure 7.4 gives results for the Crouse-Hinds MHL2 Headlight. The fundamental frequency of the window in this enclosure is between 5000 and 10,000 Hz, with the lower bound corresponding to simple support at the boundary. This frequency may be evident at 9500 Hz in Part (a). Note also that for y-axis drive with the window retainer loosened [Part (c)], a resonance peak occurs at about 7800 Hz. This could be the same resonant frequency, shifted by the change in boundary conditions.

Ignoring the resonance peak at ~200 Hz, as for the other luminaires, the maximum amplification is approximately 18 and occurs at 2200 Hz. Amplification is quite low at other resonant frequencies. The resonance at 3000 Hz in Part (e) is associated with the loose window retainer. It may be retainer or window rigid body motion. Although the window is mechanically retained without seating or sealing compound, the window in this enclosure experiences lower acceleration than windows in the other two luminaires. This effect is probably more a function of enclosure design than of window mounting It should be noted, however, that accidental loosening of the window retainer can introduce a new resonance and that if high input occurs at this frequency (~3000 Hz), damage to the window might easily occur.

7.2.3 Conclusions

These vibration tests have revealed that high amplification of input vibrations can occur in luminaires and can produce high accelerations that are normal to the plane of the windows. Thus, high

input vibrations at resonant frequencies have the potential to damage the windows or window mounts, but additional testing is required to quantify the effect of vibrations on enclosures. No clear picture emerges from these tests as to the best way to secure the window in place. The window that was secured only with a retainer ring functioned well when the retainer was tight. A potential problem with this arrangement is that the retainer can be loosened, but the probability of this occurring may be low. Dwell tests on these same enclosures might show that some mounting methods are more durable than others in a long-term vibration environment.

7.3 Evaluation of the Window Impact Test

7.3.1 Overview

The purpose of this evaluation was to determine the merit of the impact test for qualifying windows for use in the mine environment. To make the evaluation, the kinetic energy delivered to the lens by the impact test was compared to that which could be produced in the mine by various accidents. The criteria for a ruggedness test, presented in Section 8.3, are based on roof fall data and other postulated accidents, and so the kinetic energy produced by the impact test was compared to that recommended for the ruggedness test. In addition, the peak stresses in the lens produced by the impact test were compared to those which would be produced by the explosion test and a 150-psig hydrostatic test (see the Structural Performance Test, Section 8.2). Stresses in the lens produced by the impact test include both overall bending stresses and local contact stresses.

Schedule 2G Impact Test

The impact test, as defined in Paragraph 18.66 of Schedule 2G [1], is given below:

> *"(a) Impact tests. A 4-pound cylindrical weight with a 1-inch-diameter hemispehrical striking surface shall be dropped (free fall) to strike the window or lens in its mounting, or the equivalent thereof, at or near the center. Three or four samples shall withstand without breakage the impact according to the following table:*

Lens Diameter, (D), inches	Height of Fall, inches
$D < 4$	6
$4 \leq D < 5$	9
$5 \leq D < 6$	15
$6 \leq D$	24

In this study, a circular lens with two support conditions, simple and clamped, was analyzed to estimate the peak stresses produced by the impact test. The lens chosen for this study was half an inch thick, with an overall diameter of 6.375 inches. Since the lens was seated in a frame, the diameter from the center of the supports was between 5 and 6 inches. Therefore, the test cylinder had a free fall height of 15 inches as indicated above.

Lens Properties

The two most common glasses used as lenses for explosion-proof enclosures are borosilicates and soda-lime. The property and strength differences of these two glasses are within 10%. The properties of soda-lime glass (such as the float glass by PPG) were used in this study. They are:

E = Young's modulus = 10×10^6 psi
ν = Poisson's Ratio = 0.25
$\rho g = 9.1 \times 10^{-2}$ lb/in^3

The tensile strength of the soda-lime glass under static loading ranges from 4 to 10 ksi. If there is no pre-existing flaw, the tensile strength is approximately 4 to 5 times higher from empirical statistics. The compressive strength is considerably higher than the tensile strength.

7.3.2 Kinetic Energy in the Striking Cylinder

The kinetic energy produced by the 4-lb cylinder dropping 15 inches was calculated as:

$$\text{K.E.} = 1/2\ MV^2 = 1/2\ M\ (\sqrt{2gL})^2 = MgL = \overline{W}L = 5\ \text{(ft-lb)} \quad (7.1)$$

where M = mass of cylinder
g = gravitation acceleration
L = free fall distance
$\overline{W}$ = weight of cylinder.

The total kinetic energy level involved (5 ft-lb) in the impact test is almost nil compared with the kinetic energy of 3,700 ft-lb/ft^2 recommended for the ruggedness test (see Section 8.3). It is obvious that if the lens cannot withstand the load in the impact test, it is almost certain to fail under the ruggedness test. Further, the ruggedness test would almost certainly fail an unprotected lens even if it passed the impact test. However, the contact area under the impact test may be substantially smaller than that in the ruggedness test. The very localized radial tensile stress and vertical compressive stress can be detrimental and can initiate characteristic cone fractures. Contact stresses are addressed in Section 7.3.4

7.3.3 Bending Stresses Produced by the Impact

When a lens is subjected to vertical impact from a falling object, the kinetic energy released from the moving body can generate destructive pressure on the lens at the point of impact and cause the lens to vibrate laterally. To determine the peak tensile stress due to bending, an amplification factor (AMF) was introduced. It was defined as the maximum displacement caused by the peak pressure, divided by the displacement produced by the statically applied weight of the falling object.

The following simplifying assumptions were made in this study:

(1) The direction of cylinder impact is normal to the lens. The contact surface between the cylinder and the glass is very small with respect to the lens.
(2) Rebound of the cylinder is ignored.
(3) Deflection is small with respect to the plate thickness; i.e., there are no membrane effects.
(4) The lens takes its static deformation shape under the impact.

Under these assumptions, the maximum deflections and stresses were found from a consideration of energy in this system. When rebound of the cylinder is ignored, all of the kinetic energy of the cylinder is absorbed by the lens in terms of the strain energy, U. That is,

$$K.\ E. = U_{lens} \tag{7.2}$$

The kinetic energy is known from Section 7.3.2. By evaluating the strain energy of the lens in terms of its displacements, the displacements and stresses can be calculated.

7.3.3.1 Circular Lens with Simply Supported Boundary

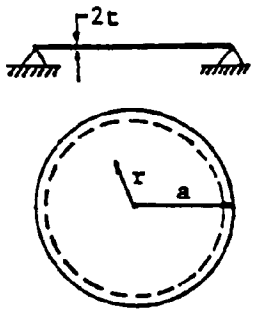

2t = 0.5 in

a = 3.1875 in

FIGURE 7.5. CIRCULAR PLATE WITH SIMPLY SUPPORTED EDGE

The deformation for this type of plate subjected to a concentrated load, P, at its center was derived by Timoshenko [4] and is given below:

$$W = \frac{P}{16\pi D}\left[\frac{3+\nu}{1+\nu}(a^2-r^2) + 2r^2 \log \frac{r}{a}\right] \tag{7.3}$$

where D is bending rigidity and is equal to 1.111×10^5 in-lb in this case.

Equation (7.3) can be written in terms of the maximum deflection at the center,

$$W_o = \frac{P}{16\pi D}\left[\frac{3+\nu}{1+\nu}\right] a^2 \tag{7.4}$$

which gives W in terms of W_o as

$$W = \left(\frac{1+\nu}{3+\nu}\right) \frac{W_o}{a^2} \left[\frac{3+\nu}{1+\nu} (a^2 - r^2) + 2r^2 \log \frac{r}{a}\right] \tag{7.5}$$

The total strain energy generated during the impact can be calculated as: (see Appendix J for details)

$$U = \frac{D}{2} \int_0^{2\pi} \int_0^a \left[\left(\frac{\partial^2 W}{\partial r^2} + \frac{1}{r} \frac{\partial W}{\partial r}\right)^2 - 2(1-\nu) \frac{1}{r} \frac{\partial W}{\partial r} \frac{\partial^2 W}{\partial r^2} \right] r dr d\theta$$

$$= 1.056 \times 10^5 \times W_o^2 \quad \text{(in-lb)} \tag{7.6}$$

Now, the displacement at the center of the plate under the peak load due to the impact, $(W_o)_i$, can be calculated by using Equation (7.2).

$$(W_o)_i = 2.384 \times 10^{-2} \text{ (in)}$$

The displacement at the center of the plate due to the statically applied weight of the cylinder is given by Equation (7.4) as

$$(W_o)_s = \frac{P}{16\pi D} \left(\frac{3+\nu}{1+\nu}\right) a^2 = 1.89 \times 10^{-5} \text{ in}$$

and now

$$\text{AMF} = \frac{(W_o)_i}{(W_o)_s} = \frac{2.384 \times 10^{-2}}{1.890 \times 10^{-5}} = 1261^* \tag{7.7}$$

For the lens shown in Figure 7.5, the maximum tensile stress occurs at the center of the surface opposite to the impact. This tensile stress is composed of the stress due to bending and the local stress due to bearing. Woinowsky-Krieger [4] provided an appropriate formula which accounts for both effects.

$$\sigma_t = \frac{P}{(2t)^2} \left[(1 + \nu) \left(0.485 \log \frac{a}{2t} + 0.52\right) + 0.48\right] \tag{7.8}$$

*Roark [21] provided a simplified equation for this factor. His equation states

$$\frac{\sigma_i}{\sigma_s} = \frac{W_i}{W_s} = 1 + \sqrt{1 + 2(h/w_s)} \quad \text{where h is the drop height.}$$

The AMP is calculated as

$$\text{AMP} = 1 + \sqrt{1 + \frac{(2)(15)}{1.89 \times 10^{-5}}}$$

The stress produced by the 4-lb load applied statically becomes:

$$(\sigma_t)_s = 25.88 \quad \text{psi}$$

The maximum tensile stress under impact was therefore calculated using Equation (7.7) as

$$(\sigma_t)_i = AMF \times (\sigma_t)_s = 1261 \times 25.88 = 32{,}634 \quad \text{psi}$$

7.3.3.2 Circular Lens with Clamped Edge

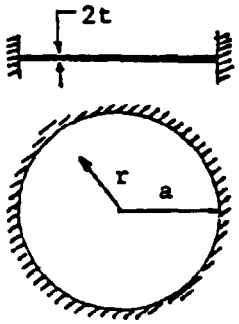

FIGURE 7.6 CIRCULAR LENS PLATE WITH CLAMPED EDGE

The deflection for a clamped circular plate loaded at the center can be expressed as

$$W = \frac{Pr^2}{8\pi D} \log \frac{r}{a} + \frac{P}{16\pi D}(a^2 - r^2) \tag{7.9}$$

or in terms of the displacement at center, W_o as

$$W = 2\frac{W_o}{a^2} r^2 \log \frac{r}{a} + \frac{W_o}{a^2}(a^2 - r^2) \tag{7.10}$$

Based on this expression for the displacement and the results in Appendix J the strain energy was calculated as

$$U = 2.749 \times 10^5 W_o^2 \quad \text{lb-in.} \tag{7.11}$$

Now using Equation (7.2) and a kinetic energy of 5 ft-lb, the center displacement produced by the impact was found from Equation (7.11) to be

$$(W_o)_i = 1.477 \times 10^{-2} \quad \text{in}$$

The center displacement of the lens under the weight of the cylinder is

$$(W_o)_s = \frac{P}{16\pi D} a^2 = 7.277 \times 10^{-6} \quad \text{in}$$

which gives an amplification factor of

$$\text{A.M.F.} = \frac{(W_o)_i}{(W_o)_s} = 2030 \qquad (7.12)$$

The maximum tensile stress occurs at the center of the surface opposite to the impact. It can be expressed as:

$$\sigma_t = \frac{P}{(2t)^2}(1 + \nu)\ (0.485 \log \frac{a}{2t} + 0.52) \qquad (7.13)$$

The static load of cylinder weight produces a tensile stress of

$$(\sigma_t)_s = 18.2 \text{ (psi)}$$

Multiplying the static stress by a dynamic load factor [Equation (7.12)], the impact stress becomes:

$$(\sigma_t)_i = \text{AMF} \times (\sigma_t)_s = 2030 \times 18.2 = 36{,}946 \text{ psi} \qquad (7.14)$$

7.3.3.3 Comparison with Other Tests

Table 7.1 summarizes the radial tensile stresses generated in the circular lens by the Impact Test, the Schedule 2G Explosion Test, and the Structural Performance Test (Section 8.2). In the Structural Performance Test, a 150-psig pressure is applied uniformly to the lens. Stresses were calculated using standard handbook formulas such as given in Appendix H. For these calculations, ideal edge support conditions (simply supported and clamped) were assumed.

In the Explosion Test the peak pressure without pressure piling can be as high as 117 psig (as discussed in Section 4.1.4), although it is normally much lower. Further, for this calculation, a minimum rise time of 17 msec was assumed to give a worst case loading. Using this minimum rise time the dynamic load factor (DLF) was calculated for the lens. This DLF, when multiplied by the static stress as given by the formulas in Appendix H, gave the stress listed in Table 7.1.

It is clear from these comparisons that the Impact Test produces far higher bending stresses than either the Explosion or the Structural Performance Tests. Further, the Explosion Test normally produces lower pressures than the 117 psig assumed for this study and thus causes substantially lower stresses than the Structural Performance Test. It should also be noted that the comparisons in Table 7.1 are based only on peak stress. Glass is known to be rate sensitive and glass manufacturers permit higher allowable stresses for short duration loads than for long duration loads (refer to Section 5.0). The allowable stress can vary by factors of 2-3. Even with a variation this large, it appears that the Impact Test is still more severe than the Structural Performance Test.

TABLE 7.1. COMPARISON OF BENDING STRESSES FOR THE IMPACT, EXPLOSION, AND STRUCTURAL PERFORMANCE TESTS

	UNIT	IMPACT TEST	EXPLOSION TEST	STRUCTURAL PERFORMANCE TEST
Load (or pressure)	#(psi)	4	(117)	(150)
Applied Area		Concentrated	Uniform	Uniform
Load Characteristics		Dynamic	Dynamic	Static
Rise Time	msec	-	17	-
Simply Supported				
AMF (DLF)		1206	(1.05)	-
Static Stress	psi	25.88	5,795	7,430
Dynamic Stress	psi	31,211	6,085	-
Fixed Edge				
AMF (DLF)		2030	(1.05)	-
Static Stress	psi	18.20	3,566	4,572
Dynamic Stress	psi	36,946	3,744	-

7.3.4 Local Contact Stresses

7.3.4.1 Calculation of the Maximum Stress

When the 4-lb cylinder with 1-in.-diameter hemispheric tip (refer to Section 7.3.1) drops 15 in. on the center of the circular lens (Figure 7.7), a very localized stress field is generated. This stress field is known as the Hertzian contact stress field, since Hertz was the first to calculate the pressure distribution and deformations arising during the contact of two linear-elastic solids. Timoshenko and Goodier [22] introduced a closed form solution of two spheres under impact by relating the contact force to the momentum of the impacting objects. Evans [23] extended the solution to the impact of a projectile and a planar surface; however, in Evans' study, the planar surface was assumed semi-infinite as compared to the size of the projectile. For the lens analyzed in the preceding section (Figure 7.7), the mass of the lens is only 0.376 x 10^{-2} lb-sec^2/in. as opposed to a mass of 1.035 x 10^{-2} lb-sec^2/in. for the impacting cylinder. Therefore, the force generated during the impact test was estimated by including the finite mass of the lens as given below:

$$P_{MAX} = 1.14 \times \left[\left(\frac{16}{9\pi^2} \right) \frac{V^6 R_1}{(K_1 + K_2)^2} \left(\frac{1}{\frac{1}{m_1} + \frac{1}{m_2}} \right)^3 \right]^{1/5} \qquad (7.15)$$

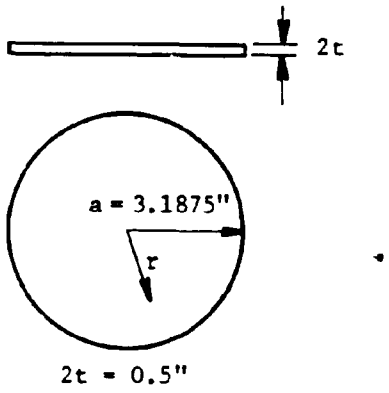

FIGURE 7.7. CIRCULAR LENS DIMENSIONS

where P_{max} = maximum impact force
V = impact velocity
R_1 = radius of the dropping cylinder

$K_1 = \frac{1 - \nu_1^2}{\pi E_1}$ for the dropping cylinder

$K_2 = \frac{1 - \nu_2^2}{\pi E_2}$ for the lens

ν = Poisson's ratio
E = Young's modulus
m_1 and m_2 are the masses of the cylinder and lens, respectively.

It is noted that Equation (7.15) is exactly the same as Evans' when m_2 approaches infinity. Using this relationship, the peak load delivered to the lens by the dropping cylinder was found to be

$$P_{max} = 5899 \text{ lb}$$

The contact duration can be estimated by using Timoshenko and Goodier's general equation as:

$$T = 3.214 \left[\left(\frac{9\pi^2}{16} \right) \frac{(K_1 + K_2)^2}{VR_1} \left(\frac{m_1 m_2}{m_1 + m_2} \right)^2 \right]^{1/5}$$

$$= 0.000212 \text{ sec} \qquad (7.16)$$
$$= 0.212 \text{ msec}$$

For comparison, the fundamental vibration period for the lens of Figure 7.7 can be found in Appendix J. These periods of

$T = 0.032$ msec for simply supported edges
$T = 0.0158$ msec for fixed edges

are well below the contact duration. Thus, the lens vibration was neglected in the analysis, and Hertzian quasi-static contact theory was used to calculate the peak stresses.

Under the impact load, the apex of the dropping cylinder and the glass plate are pressed together. There is local deformation near the point of contact. Assuming that both materials undergo elastic deformations, a circular contact surface is developed (see Figure 7.8). The radius of this contact surface was calculated as (References 24 and 25):

$$c = \left(\frac{4QPR_1}{3E_1} \right)^{1/3} \qquad (7.17)$$

where

$$Q = \frac{9}{16} \left[(1 - \nu_1^2) + (1 - \nu_2^2) \frac{E_1}{E_2} \right] \qquad (7.18)$$

For our conditions we find $c = 0.0652$ in.

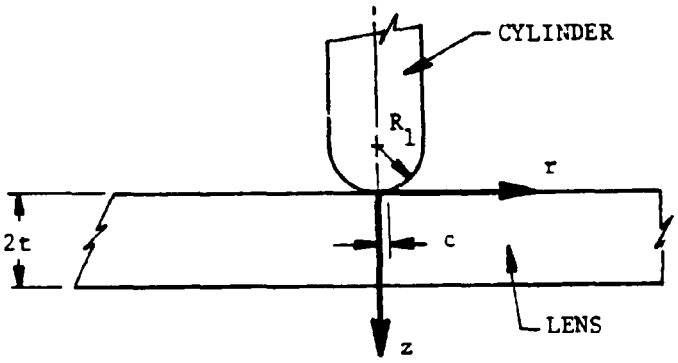

FIGURE 7.8. CONTACT GEOMETRY

The stress distributions around the contact area for general quadratic deformation surfaces were derived by Wilshaw [26]. Maximum compressive stresses are generated at the center of the contact surface. The principal stresses at this point are:

$$\sigma_z = (\sigma_z)_{MAX} = \frac{3}{2} \frac{P_{MAX}}{\pi c^2} = 662,559 \quad \text{psi} \quad \text{(compression)} \qquad (7.19)$$

$$\sigma_r = \sigma_\theta = -\frac{1+2\nu}{2} \sigma_z = -496,916 \quad \text{psi} \quad \text{(compression)} \qquad (7.20)$$

These compressive stresses are very high. However, they have almost the same order of magnitude. Thus, the area immediately below the center of contact appears to be a zone of nearly hydrostatic pressure. Glass usually has high compressive strength and is unlikely to fail under hydrostatic pressure. Figure 7.9 shows the stress distribution through the thickness at r = 0. Note that the local stresses diminish to zero at about half the thickness from the contact point.

The radial stress underneath the contact surface is compressive with its maximum at the center. However, it changes its sign close to the edge of the contact surface. It is this radial tensile stress that is most likely to initiate failure in the brittle glass material, because, at the location of this maximum radial tensile stress, σ_z is equal to zero; therefore, pure shear governs. This maximum tensile stress at the periphery of contact surface can be expressed as:

at $z = 0$, $r = c$

$$\sigma_r = -\sigma_\theta = \tau = \frac{1-2\nu}{3} \left(\frac{3}{2} \frac{P_{MAX}}{\pi c^2} \right) = 110, 427 \quad \text{psi} \qquad (7.21)$$

Figure 7.10 illustrates the surface tensile stress distribution. The tensile stress drops sharply away from the edge of

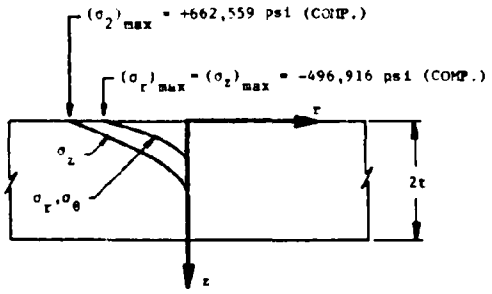

$$\sigma_z = q_{max} \frac{c^2}{c^2 + r^2}$$

where $q_{max} = \frac{3}{2} \frac{P_{max}}{\pi c^2}$

$$\sigma_r = q_{max} \left\{ (1+\nu) \left[\frac{z}{c} \arctan\left(\frac{c}{z}\right) - 1 \right] + \frac{c^2}{2(c^2+z^2)} \right\}$$

$$\tau_{max} = \frac{1}{2} (\sigma_2 - \sigma_r)$$

FIGURE 7.9. VERTICAL, RADIAL, AND TANGENTIAL STRESS DISTRIBUTIONS THROUGH THE THICKNESS AT r = 0

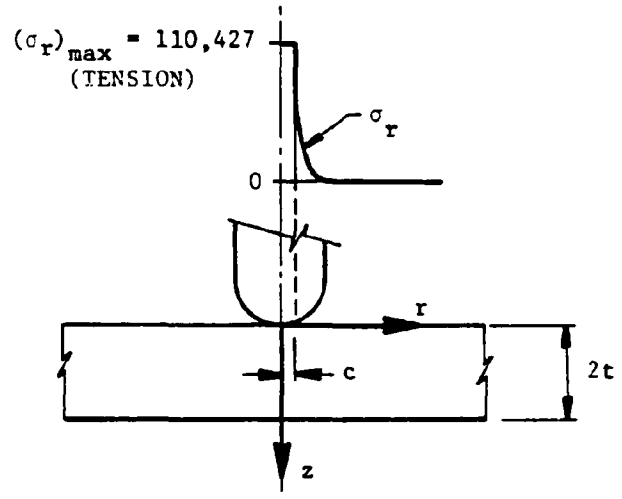

FIGURE 7.10. RADIAL TENSILE STRESS DISTRIBUTION ON THE SURFACE OF LENS

the contact surface. At the location approximately equal to the radius of the dropping cylinder, the local tensile stress is almost zero.

From Equation (7.21) it appears that an enormous amount of tensile stress exists at the edge of the contact surface. However, from previous experience, the lens appears to be intact during the impact test, according to visual observation. Since there are no labroatory results to support our analysis at the current time, the experiments carried out by Kirchner and Gruver [27] are used to illustrate the relationship of impact force and damage. In their test, an annealed soda-lime glass sheet (3/16 in. or 1/4 in. thick) was used, and the specimen was supported from the rear by a large steel block. A 3/4-in.-diameter portion of the center area was abraded by 3-mm-diameter glass spheres; the remainder was protected by a paper mask. Figures 7.11(a), 7.11(b), and 7.11(c) show the localized impact damage by glass spheres at velocities of 72 ft/sec, 187 ft/sec, and 377 ft/sec, respectively.

Impact forces and the maximum radial tensile stresses from Equation (7.21) are summarized in Table 7.2 for the Kirchner and Gruver [27] data and for the Impact Test. A complete circular crack was formed in the surface of the particular specimen when the maximum tensile stress is approximately equal to 84,000 psi. However, the crack was detected by optical and scanning electron microscopy. Such cracks may not be apparent visually. We cannot conclude from this that soda-lime glass has tensile (rupture) strength on the order of 84,000 psi. The possible impacts by more than one projectile can make the stress more pronounced in Kirchner and Gruver's test. The rigidity of the support also has an effect on the impact process.

Above, it was stressed that the tensile strength of the glass under impact can be four to five times higher than its normal tensile strength. That puts the tensile strength in the range of 20-40 ksi under impact load. This strength is substantially lower than the localized tensile stress calculated for the impact test. Thus, it appears that the impact test on the circular lens was severe and could have caused the lens to fail in flexure or could have produced local cracking at the point of impact. The circular lens analyzed is from an explosion-proof enclosure, so it must have passed the impact test without significant visible cracking; however, our calculations indicate that it was near failure.

7.3.4.2 Comparison of Contact and Bending Stresses

Table 7.3 compares the maximum contact stress to the flexure stresses produced by an internal explosion and by a 150-psig internal pressure. These comparisons show that the impact test is much more severe for the case studied than either the Schedule 2G Explosion Test or the proposed Structural Performance Test (150 psig). However, it is less severe than the proposed ruggedness test because of the higher impact energy for the ruggedness test. Thus, it is very unlikely that a glass lens could pass a ruggedness test, and it is apparent that the lens should be protected from the exposure to a rock fall or side impact (see Section 8.3).

(a) Velocity = 72 ft/sec

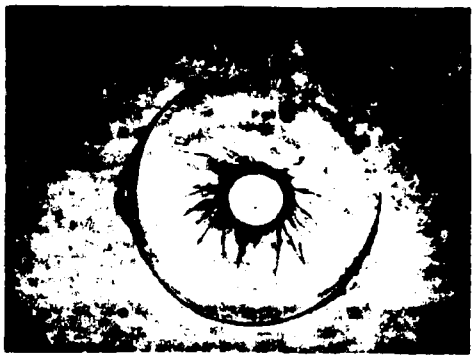

(b) Velocity = 187 ft/sec

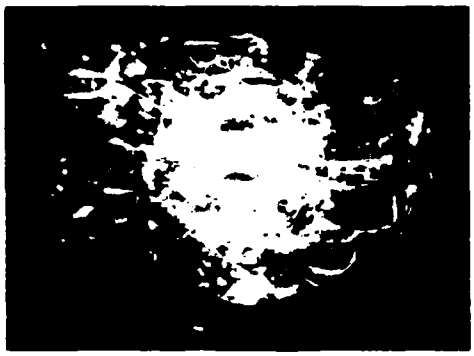

(c) V = 377 ft/sec

FIGURE 7.11. LOCALIZED IMPACT DAMAGE ON SODA-LIME GLASS BY GLASS SPHERES (1.5-mm RADIUS) AT VARIOUS SPEEDS

TABLE 7.2. IMPACT FORCES AND THE CORRESPONDING MAXIMUM TENSILE STRESSES

	Projectile Mass	Velocity	Maximum Impact Force	Maximum Tensile Stress	Description
	$\frac{\text{lb-sec}^2}{\text{in.}}$	(ft/sec)	(lb)	(psi)	
Kirchner and Gruver's Tests	1.142×10^{-7}	72.18	81.604	84.047	Circular Crack
	1.142×10^{-7}	187.01	255.774	122,311	Conical Crack
	1.142×10^{-7}	377.30	593.810	163,508	Crushing
Impact Test Study	1.035×10^{-2}	8.97	5899.000	110,427	Unknown

TABLE 7.3. MAXIMUM TENSILE STRESS PRODUCED BY IMPACT, RUGGEDNESS, AND PERFORMANCE TESTS

	Impact Test	Explosion Test	Structural Performance Test
Loading Characteristics	Dynamic	Dynamic	Static
Applied Area	0.13-in.-Diameter Circle	Uniform	Uniform
Load (or Pressure)	5,589 lb (Maximum Load)	(117 psi)	(150 psi)
Maximum Tensile Stress (psi) (S.S. Case)	110,427* 31,211**	6,085**	7,430**

NOTES: * Local Contact Stress
** Flexure Stress

7.3.4.3 Conclusions

When the 4-lb weight drops 15 in. onto the lens, the bending stresses calculated from the impact energy, on the basis of static bending formulae, reach 31-37 ksi. This value exceeds the 4-10 ksi static tensile strength of the glass. However, from previous experience, the glass did not break or exhibit cracks which can be detected with unaided eye. As was mentioned earlier, empirical statistics do indicate that the strength under impact can be 4 to 5 times higher than its normal strength. This is probably due to the fact that the glass allows some viscoelastic behavior under short duration impact. However, if there are pre-existing flaws in the glass, the cracks can degrade the strength (References 23 and 28) and the glass can fail in this particular case.

The bending stress can be the dominating factor for failure under static load or low-velocity impact. Under high-velocity impact, very high local stresses around the contact area can be more critical. The compressive wavefront will travel from the contact surface through the thickness with the maximum compressive stress occurring at the center of contact surface. Refracted tensile waves will be generated at the edge of the free surface. This tensile stress is of particular interest, since it can initiate the Hertzian (cone shape) crack and possible spalling. The localized effect involves a complicated mechanism. It depends upon the vibration period of the lens, the rise and decay time of the peak load, the stress wave traveling speed, the surface condition and the properties of the projectile, etc. Such spalling, while potentially important, was not addressed in this study.

Our conclusions from this evaluation of the impact test for lenses are:

(1) The impact test subjects the lenses to flexure stresses which are higher than those produced by the Schedule 2G Explosion Test or by 150-psig internal pressure.

(2) It assures that the lenses are suitable for "moderate" impacts, but more severe impacts can occur in the mine from which the lenses should be shielded.

(3) The proposed ruggedness test is more severe than the impact test, but lenses may not need to pass the ruggedness test if their orientations and/or locations do not expose them to the types of impact upon which the ruggedness test is based.

7.4 Evaluation of Thermal Shock Test

7.4.1 Closed-Form Solution for an Infinite Plate

In the Code of Federal Regulations, the thermal shock test for windows and lenses in explosion-proof enclosures is given as:

> *"§18.66(b) Thermal Shock Tests. Four samples of the window or lens will be heated in an oven for 15 minutes to a temperature of 150°C (302°F) and immediately upon withdrawal of the samples from the oven they will be immersed in water having a temperature between 15°C (59°F) and 20°C (68°F). Three of the four samples shall show no defect or breakage from this thermal shock test."*

In order to determine the severity of the thermal shock test, the maximum stresses it produces in the windows and lenses had to be calculated. These stresses are transient and are a function of temperature gradients. Therefore, analytical solutions of the stresses produced by thermal shock could be obtained only if the temperature distribution throughout the thickness at any time were known.

7.4.1.1 Transient Thermal Solution

The exact solution for transient temperature in a quenched plate has been developed in most heat transfer textbooks [29,30]. However, a few simplifying assumptions were necessary in order to obtain a closed form solution. These assumptions are:

(1) The lens is semi-infinite.

(2) The lens is suddenly placed in an environment with a constant temperature T.

(3) The temperature varies through the thickness of the lens only.

Figure 7.12 shows a plate with thickness t. Its mid-surface lies in the Y-Z plane with X denoting the distance from this plane. The thermal field in this plate can be expressed by using the heat conduction equation:

$$\frac{1}{a}\frac{\partial}{\partial \tau}\theta(\tau,x) = \frac{\partial^2}{\partial x^2}\theta(\tau,x) \qquad (7.22)$$

where

$\theta(\tau, X) = T(\tau, X) - T$

τ = time (min.)

$a = K/\rho C$ = thermal diffusivity (ft^2/min.)

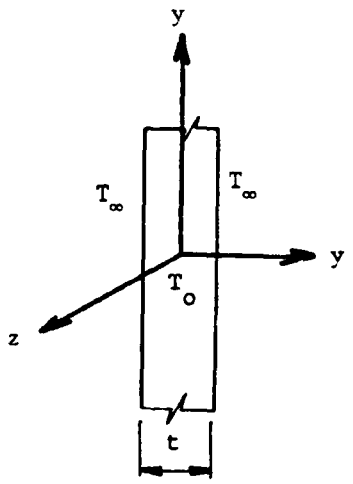

FIGURE 7.12. SECTION THROUGH THE LENS

It is noted that Equation (7.22) is a second-order partial differential equation and that the heat sink and source are excluded. A product solution was adopted to solve the equation.

The thermal parameter $\theta(\tau, X)$ can be written as:

$$\theta(\tau,x) = X(x)\,Q(\tau) \tag{7.23}$$

so that the general solution of the heat conduction equation now becomes

$$\theta(\tau,x) = C_1 e^{-a\lambda^2\tau}\,(C_2 \cos\lambda x + C_3 \sin\lambda x) \tag{7.24a}$$

or

$$\theta(\tau,x) = e^{-a\lambda^2\tau}\,(A \cos\lambda x + B \sin\lambda x) \tag{7.24b}$$

The parameters λ, C_1, C_2, C_3, A, and B are all constants. In order to determine coefficients, λ, A, and B, the following boundary conditions were used:

(1) Symmetry conditions:

$$\frac{\partial}{\partial x} T(\tau,x) = 0 \quad \text{or} \quad \frac{\partial}{\partial x}\theta(\tau,x) = 0 \quad @\ x = 0$$

(2) Convection Boundary Condition:

$$-\frac{\partial}{\partial x} T(\tau,x) = \frac{h}{k}\,[\,T(\tau,x) - T_\infty\,] \quad \text{at} \quad x = \pm\frac{t}{2}$$

or

$$-\frac{\partial}{\partial x}\theta(\tau,x) = \frac{h}{k}\theta(\tau,x) \quad \text{at} \quad x = \pm\frac{t}{2}$$

(3) Surface Boundary Condition:

$$\vartheta(o, x) = T_o - T_\infty$$

Based upon Boundary Condition (1), Coefficient B is equal to zero. From Boundary Condition (2), the following relationship exists:

$$\text{Cot}(\lambda L) = \frac{\lambda L}{B_i} \tag{7.25a}$$

where

$L = t/2$ and $Bi = hL/k$

Equation (7.25) has an infinite number of values that will satisfy λ. In other words, it can be written as

$$\text{Cot}(\lambda_n L) = \frac{\lambda_n L}{B_i} \tag{7.25b}$$

The characteristic values λ_n can be determined from the table prepared by Kantorovich and Krylov [31]. Coefficients A_n are calculated by using Boundary Condition (3). The resultant temperature distribution function is given below:

$$\frac{T(\tau,x) - T_\infty}{T_o - T_\infty} = 2\sum_{n=1}^{\infty}\left(\frac{\sin\lambda_n L}{\lambda_n L + \sin\lambda_n L\cos\lambda_n L}\right) e^{-a\lambda_n^2\tau}\cos\lambda_n x \tag{7.26a}$$

or

$$T(\tau,x) = T_\infty + 2(T_o - T_\infty)\sum_{n=1}^{\infty}\left(\frac{\sin\lambda_n L}{\lambda_n L + \sin\lambda_n L\cos\lambda_n L}\right) e^{-a\lambda_n^2\tau}\cos\lambda_n x \tag{7.26b}$$

7.4.1.2 Transient Stress Solution

Boley (1960) [32] derived the analytical solutions of the transient thermal stresses for plates of simple geometries with various boundary conditions. His theory was based upon the following assumptions:

(1) Small deflection
(2) No in-plane loading
(3) Plane sections remain plane.

(4) Temperature distribution varies through the thickness only.
(5) Temperature distribution at each time step is known.

A semi-infinite circular plate was analyzed in this study. The stress distribution by Boley [32] can be summarized below:

Case 1 - Circular Plate with Free Edges

$$\sigma_{xx} = \sigma_{yy} = \frac{1}{1-\nu}\left\{-\alpha E T + \frac{N_T}{t} + \frac{12 M_T}{t^3} y\right\} \tag{7.27}$$

where

ν = Poisson's ratio
α = thermal expansion
E = modulus of elasticity
T = temperature
t = plate thickness
y = distance from the mid-surface plane

$$N_T = \int_{-t/2}^{t/2} T\, dy$$

$$M_T = \int_{-t/2}^{t/2} Ty\, dy$$

Integration of M_T yields zero, and the equation becomes:

$$\sigma_{xx} = \sigma_{yy} = \frac{1}{1-\nu}\left\{-\alpha E T + \frac{N_T}{t}\right\} = \frac{1}{1-\nu}\left\{-2\alpha E (T_0 - T_\infty) \sum_{n=1}^{\infty}\right.$$

$$\times \left(\frac{\sin \lambda_n L}{\lambda_n L + \sin \lambda_n L \cos \lambda_n L}\right) e^{-a\lambda_n^2 \tau} \cos \lambda_n y + \frac{4\alpha E}{\lambda_n t} (T_0 - T_\infty) \sum_{n=1}^{\infty}$$

$$\left. \times \left[\frac{\sin \lambda_n L}{\lambda_n L + \sin \lambda_n L \cos \lambda_n L} e^{-a\lambda_n^2 \tau} \sin \lambda_n L\right]\right\} \tag{7.28}$$

The thermal stress equations listed above involve an infinite series of trigonometric functions, and the arguments of these functions are the roots of certain transcendental equations. The process of obtaining numerical solutions was programmed on a digital computer.

7.4.1.3 Numerical Evaluation

The arguments of the trigonometric function in Equation (7.26b) are the roots of the transcendental equations; that is

$$(\lambda_n L) \tan (\lambda_n L) = B_i = \frac{hL}{k} \qquad (7.29)$$

where

h = heat transfer coefficient (BTU/sec-in^2-°F)
k = thermal conductivity (BTU/sec-in-°F)

A table prepared by Carslow and Jaeger [33] gives the first six characteristic values of λ_n. A computer program for the solution of Equation (7.26b) was first written using just the first six values of λ_n. The solution showed small temperature perturbations at the beginning of the quenching process when temperature gradients are high. By examination of Equation (7.26b) it was found that when time is greater than 1 sec ($\tau > 1$ sec), six terms are sufficient for the infinite series to converge. However, when the magnitude of τ is approaching zero, the six terms no longer guarantee the convergence of the trigonometric series, and this resulted in the temperature perturbations. Thus, another program was developed to solve Equation (7.29), and the first twenty (20) characteristic values were used to estimate the temperature distribution.

To compute the temperature distributions, time zero was taken as the time at which the lens was first submerged in the cold water bath, and the initial temperature across the lens was assumed to be constant at 302°F. Figure 7.13 shows that the temperature at the surface plunges sharply due to the contact with cold water, whereas the rate of temperature drop is relatively slow at the mid-plane. At the end of 10 seconds, the temperature at mid-plane is still around 301°F. Also note in Figure 7.14 that, about two minutes after the lens is dipped into the water, the surface of the lens reaches its equilibrium temperature. However, it takes seven minutes for the entire lens to reach a uniform temperature of 59°F.

These transient temperatures were then used as input to calculate the in-plane stresses, as given by Equation (7.27). For a free, unsupported circular lens, the x-direction stress (σ_x) is equal to the y-direction stress (σ_y). Figures 7.15 and 7.16 illustrate the stresses at different locations versus time. As shown in Figure 7.15, the maximum tension stress occurs at the surface. This tension stress peaks at approximately 1.5 seconds after the quenching process starts, with a magnitude of 3700 psi. Maximum compression occurs at the mid-plane with a considerable time lag. Its maximum occurs at -30 seconds, with a magnitude of 500 psi.

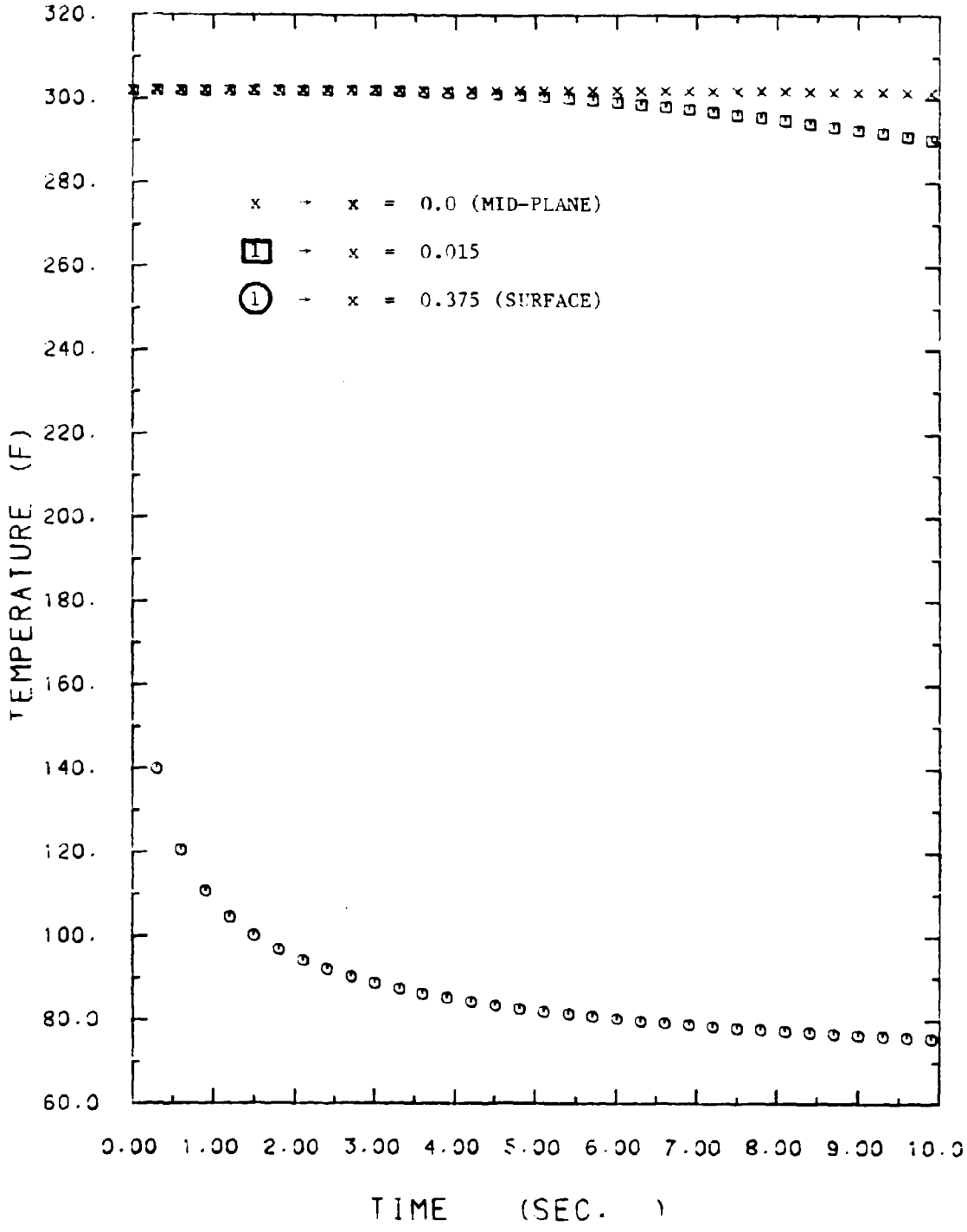

FIGURE 7.13. TEMPERATURE HISTORIES IN THE LENS

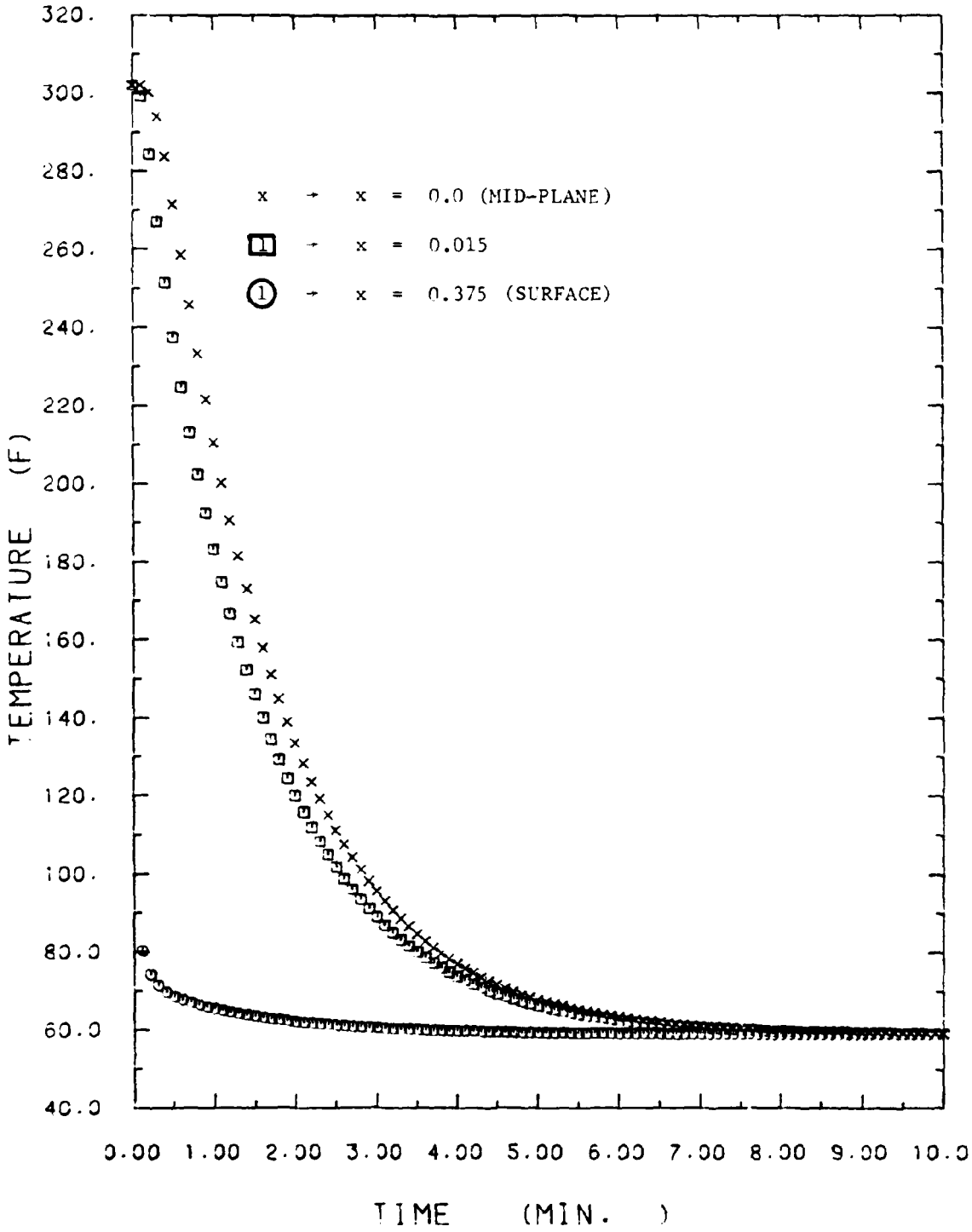

FIGURE 7.14. TEMPERATURE HISTORIES IN THE LENS

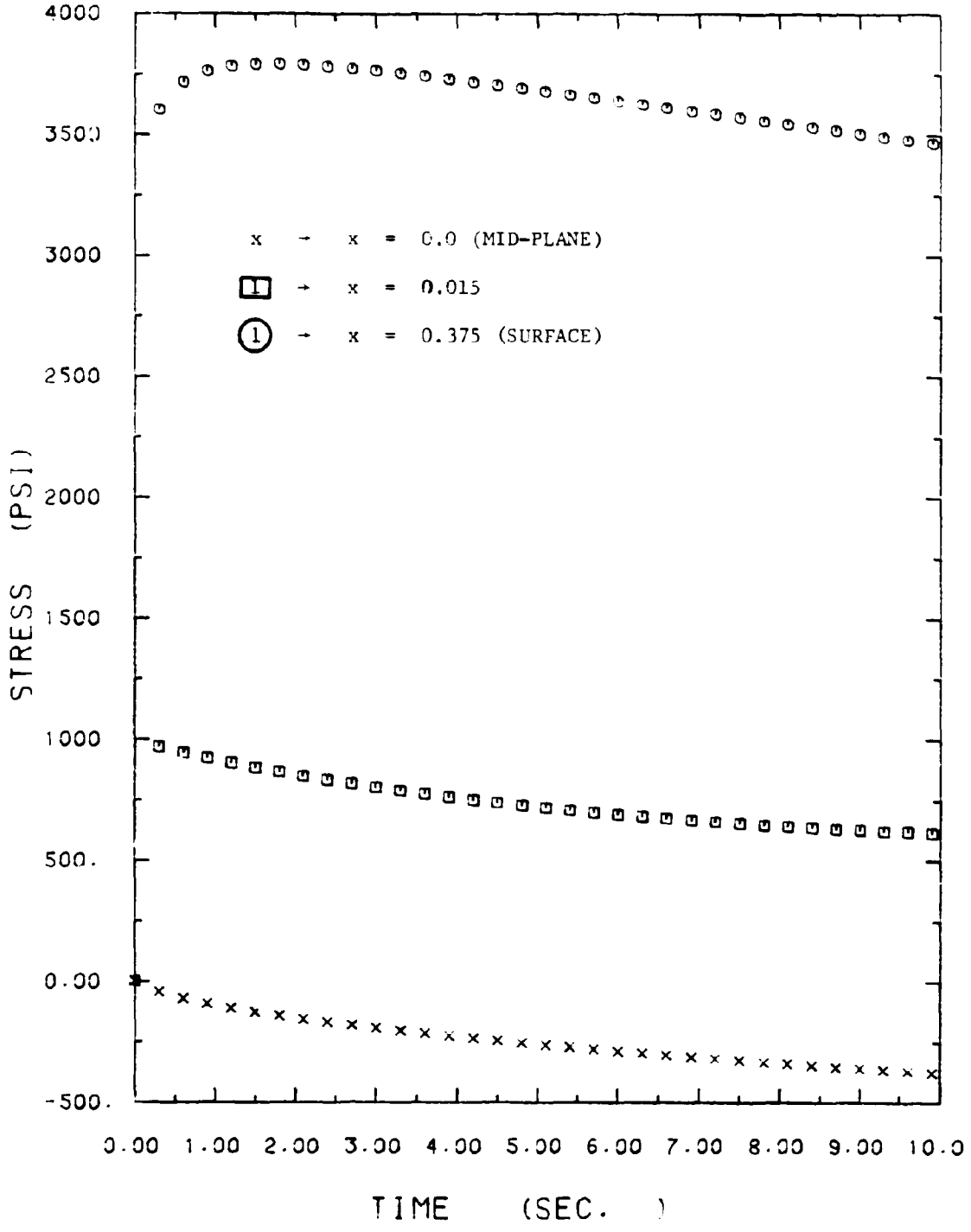

FIGURE 7.15. STRESS HISTORIES IN THE FREE, UNSUPPORTED LENS

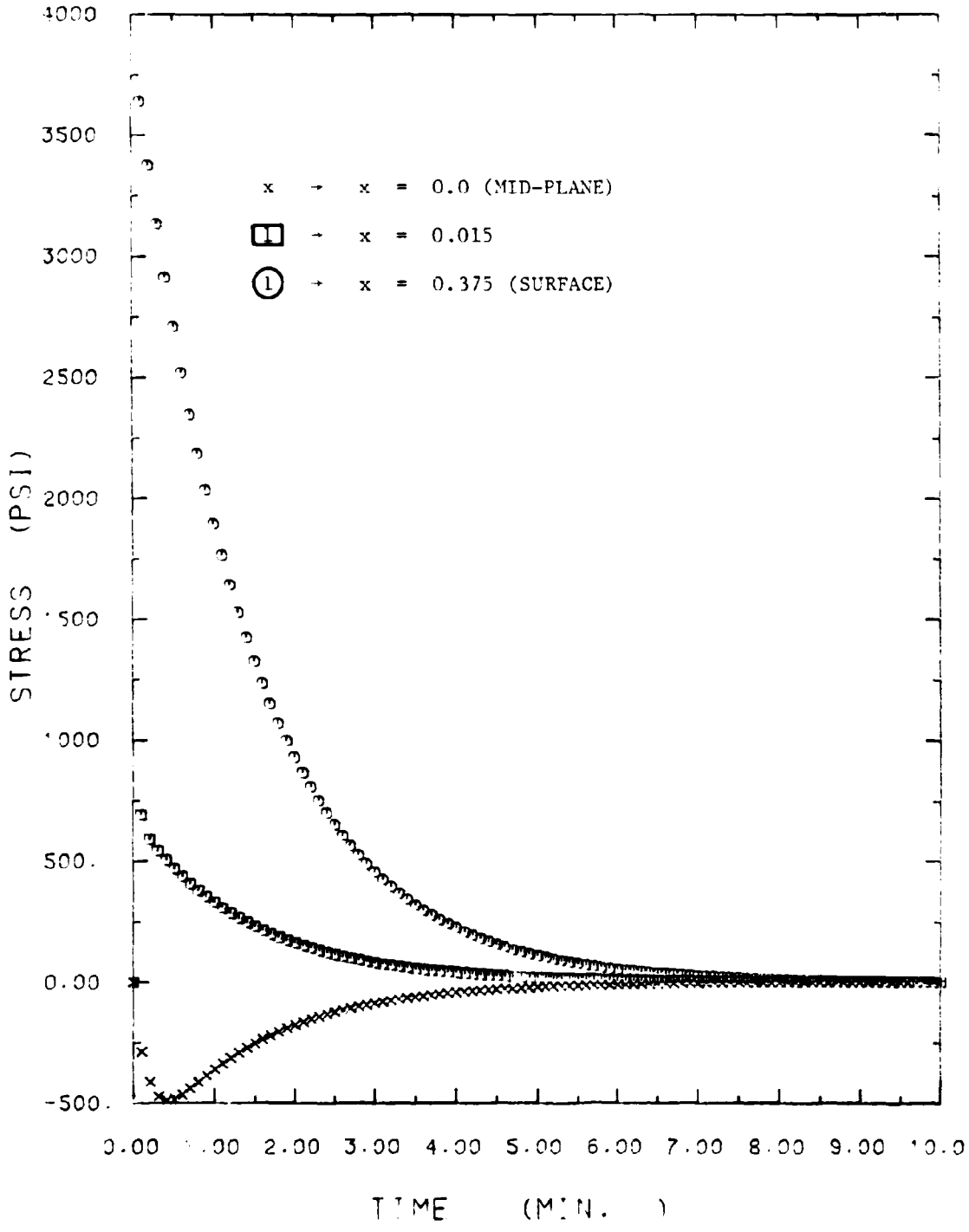

FIGURE 7.16. STRESS HISTORIES IN THE FREE, UNSUPPORTED LENS

If we compare the magnitude of the stresses produced by the Thermal Shock Test with those produced by the Impact Test, the Explosion Test, and the Structural Performance Test (see Sections 7.3.3 and 7.3.4), we find that the Thermal Shock Test produces lower stresses than the others. It should be noted that the thermally induced stresses were calculated for an infinite plate and thus are approximations to the true stresses.

To compute thermal stresses in a lens which is part of an enclosure requires that a finite element analysis be performed. Such an analysis for the thermally induced stresses was not part of the scope of work of this project. Finite element thermal analyses of enclosures were funded as part of USBM Contract H0387009 [2]. These results have not been completed, but preliminary, unpublished results show that stresses are strongly influenced by the method of support and, for some cases, the thermally induced stresses can be much higher than the 3700 psi calculated for the infinite lens. The results of the finite element analyses will be published in the future as part of the final report on USBM Contract H0387009 [2].

7.5 Evaluation of Polycarbonates and Adhesives

7.5.1 Introduction

Explosion-proof luminaires require transparent windows capable of withstanding (1) dynamic pressures generated by methane gas explosions inside the enclosures, (2) high temperatures generated by electric lamps located inside the enclosures, and (3) ultraviolet radiation generated by fluorescent and discharge type light sources. In addition, the windows must tolerate immersion in water and contacts with hydrocarbons without the initiation of cracking.

Glasses, and borosilicates in particular, have been found to be excellent for construction of windows in explosion-proof enclosures, as the physical properties of glass meet all of the operational requirements. In addition, glass retains its original physical properties for time periods in excess of 20 years even though being subjected continuously to high temperature, moisture, ultraviolet radiation, and hydrocarbons.

Thus, for all practical purposes an explosion-proof enclosure equipped with glass windows needs to be checked for structural competence only once prior to being placed in service. Subsequently, the windows need to be only periodically inspected for cracks and fractures. Since the lamps fail at relatively short time intervals (i.e., 1-2 years), the inspection of the window can be performed during replacement of the lamp. If cracks cannot be detected by visual inspection, it can be safely assumed that the window is structurally competent to remain in service until next inspection.

Since glass can safely operate in ambient temperatures in the $\leq 500°F$ range without significant decrease of physical properties, an accidental replacement of the burned out lamp with a lamp rated for larger

power consumption may raise the temperature above the 300°F design temperature, without compromising the pressure rating of the window.

A different case presents itself when the windows are fabricated from plastic. Not only are the physical properties of plastics totally dependent upon temperature, but also on composition of the ambient atmosphere (i.e., water vapor, hydrocarbons). In addition, exposure to heat and UV radiation ages plastics, so that their structural performance may become unacceptable in a very short period of time. Since the rate of aging is a function of temperature, exposure to UV radiation, and composition of the ambient atmosphere, the useful life span for a window fabricated from a particular plastic may vary by a factor of 10, depending on the actual operational environment. Thus, with plastic windows the accidental replacement of a burned out lamp with a lamp of higher power rating may be catastrophic, as the increase in ambient temperature will not only decrease the pressure rating of the window, but also its rated life span. These same comments are applicable to the adhesives which are used to bond or seal windows in enclosures; however, the adhesives are usually more protected from the environment (except for heat) than the polycarbonates and may be less highly stressed.

It is clear from the foregoing discussion that the effect of environmental factors on polycarbonates and adhesives is very important from the standpoint of reliability in Schedule 2G enclosures with windows. The purpose of this task was to establish an accelerated aging test program by which one could determine the short- and long-term effecs of the mine environment on polycarbonates and adhesives. The purpose of the tests will be to qualify window and lens materials for use in the mine environment and to provide data so that an allowable service life can be established.

Although not specifically addressed in this study, the inspection of plastic windows will be more tedious than for glass windows. Administratively, the inspections will probably require that (1) the type of plastic be noted on the window, (2) the design temperature of the window be noted on the window, (3) the date that the window was placed in service be noted and recorded in the equipment file, and (4) the date that the window should be removed from the enclosure and replaced with a new one be noted and recorded in the equipment file. Technically, the inspections may require that (1) the surface temperature of the window be measured for conformance to design values and (2) the surface of the window be inspected for cracks, crazing, and permanent deformations. When one considers that in a given mine location there may be hundreds of lamp enclosures with windows fabricated not only from different plastics, but also designed to operate at different temperatures, the inspection program would have to rely on storage of pertinent data in computers which would provide the inspectors for each inspection with printouts defining the inspection schedule. Obviously, the data file would need to be updated after every inspection and there would be many details to be worked out in such an inspection system.

The foregoing discussion on the difficulties associated with inspection of plastic windows in service is not intended to discourage the use of plastics for construction of windows in explosion-proof

enclosures, but to alert the USBM to the possible increase in administrative costs that could result from wide-scale utilization of plastic windows in luminaires. Alternately, the inspection program could be assigned to mine operators, with MSHA retaining only the supervisory function. A potential benefit of such an arrangement might be that by placing not only the acquisition and maintenance cost, but also the inspection cost, on the shoulders of mine operators, they would be in a better position to judge the cost effectiveness of glass versus plastic windows.

7.5.2 Candidate Plastic Materials

There are several transparent plastics for potential applications as windows in explosion-proof lamp enclosures. These plastics are listed in Table 7.4 in the order of increasing deflection temperatures.

The highest resistance to ultraviolet radiation and heat aging is exhibited by acrylic; however, its maximum service temperature in structural applications is limited to 150°F. In applications where the design temperature does not exceed 150°F, the service life of acrylic plastic windows subjected to ultraviolet radiation exceeds ten years.

The highest service temperature in a humid environment, excellent impact resistance, and good heat aging resistance are exhibited by polyphenylsulfone. Its service temperature in structural applications is 350°F. This plastic, however, deteriorates rather rapidly under ultraviolet radiation. In applications where the ultraviolet radiation is absent (i.e., incandescent lamps). the polyphenylsulfone windows will provide a long service life at 302°F, the maximum allowable design temperature for explosion-proof enclosures.

The best resistance to hydrocarbons is offered by transparent nylon; however, its relatively low service temperature of 200°F and impact resistance of only 1.1 ft-lb/in. do not make it very desirable for applications as windows in explosion-proof enclosures.

The highest impact resistance is found in polycarbonate materials; however, the service temperature is limited to 275°F, and polycarbonates have only fair resistance to UV and poor resistance to hydrocarbons. In fact, their resistance to hydrocarbons is less than for the other plastics. Also, it is toughness that degrades first under the influence of UV radiation, sustained heat, and moisture so that after several years the toughness of polycarbonate may decrease to the level of acrylic.

The best combination of physical properties demanded by windows appears to be offered by polyarylates. The high service temperature, good resistance to UV radiation, more than average toughness, and the retention of a very large percentage of room temperature strength at 300°F service temperature make polyarylate plastics an excellent candidate for windows in explosion-proof enclosures.

In summary, other plastics besides polycarbonates were identified as potentially suitable for windows in explosion-proof

TABLE 7.4. TRANSPARENT PLASTICS FOR PRESSURE RESISTANT WINDOWS

Plastic	ASTM-D-648 at 264 psi	Resistance to UV	ASTM-D-256 Izod Notch	ASTM-D-638 Tensile Strength	ASTM-D-638 Tensile Modulus	ASTM-D-638 Elongation at Break	ASTM-D-785 Hardness	Resistance to Hydro-carbons
Acrylic (Plexiglass® G)	+ 200°F	Excellent	0.4 ft.lbs/in	10,000 psi	400,000 psi	4-5 %	M-94	Fair
Nylon (AMIDEL®)	+ 250°F	Fair	1.1 ft.lbs/in	10,500 psi	280,000 psi	9 %	M-89	Good
Polycarbonate (LEXAN®)	+ 276°F	Fair	16 ft.lbs/in	9,500 psi	340,000 psi	110 %	M-70	Poor
Polyarylate (ARDEL®)	+ 340°F	Good	4.2 ft.lbs/in	9,500 psi	290,000 psi	50 %	?	Poor
Polysulfone (UDEL®)	+ 340°F	Poor	1.2 ft.lbs/in	10,200 psi	360,000 psi	50-100 %	M-69	Poor
Polephenylsulfone (RADEL®)	+400°F	Poor	12 ft.lbs/in	10,400 psi	310,000 psi	60 %	M-83	Poor

enclosures. Polyarylates appear to have the best combination of properties, primarily because of their relatively high service temperature and good UV resistance. Polycarbonates would be the second choice because of their high impact resistance, fair UV resistance, and moderately high service temperature. A test program is needed to establish empirically the combined effect of service temperature, UV, and moisture on the service life of transparent plastics serving as windows in explosion-proof enclosures (principally luminaires).

At the present time, only two types of plastics should be considered for the testing program; polycarbonates and polyarylates. Polycarbonates should be tested first because polycarbonate windows are already in service and the establishment of their service life is of utmost importance to the safety of miners. Polyarylates should also be tested because they appear to be a potential replacement for polycarbonates in current applications as explosion-proof windows. Since there are at the present time no polyarylate windows in service as explosion-proof windows, the testing of polyarylates does not have to be initiated immediately. The testing of polyarylate plastic would follow the same test procedures as polycarbonate plastic.

7.5.3 Accelerated Aging Tests

A procedure was developed for accelerated testing of plastics and adhesives which are used in explosion-proof enclosures. The test procedure, included as Appendix K, was developed to closely represent inservice conditions. It includes combined exposure to UV, heat, stress, humidity, and acid mine water spray.

Under this contract (H037052) the test equipment was fabricated and assembled. Testing was performed as part of USBM Contract H0387009 (Reference 2). The test procedure was subsequently changed from that included in Appendix K, as test conditions indicated. Two major changes and the reasons for them are

1. The lens thickness was reduced from 1/2 in. to 3/16 inch. This was done to produce higher stresses in the lens during pressurization.

2. Periodic cycling of the pressure in the fixture was stopped. At intervals of time, specimens were removed from the chambers and tested to failure. Both pressure tests and test coupons were used to measure material degradation. This procedure was initiated because early test results indicated that lenses were unlikely to fail within one year at pressures of 150 psig.

The complete test procedure will be included in the final report on Contract H0387009 [2]. Also included will be test results and recommended procedures for future testing.

8.0 PERFORMANCE TESTS FOR SCHEDULE 2G ENCLOSURES

8.1 Introduction

In the future MSHA plans to implement additional performance tests for the evaluation of explosion-proof enclosures. These tests will complement existing tests and will be designed to measure the performance of enclosures in critical areas such as strength and ruggedness. When enclosures are evaluated in this way, rather than by specifying certain dimensions as in part 18.31(b) of the CFR, then enclosure designers will have more freedom in their design approach.

Two performance tests were developed in this study. They are:

- a Structural Performance Test
- a Ruggedness Test

In addition, criteria are recommended for the qualification of battery box covers.

Only one of these test procedures has been verified by actual testing. Several enclosures were successfully tested following the procedures of the Structural Performance Test, and refinements to the test procedure were made as appropriate. The Ruggedness Test has not been verified. Further, additional work on this test is recommended before its adoption by MSHA. These recommendations are given in Section 8.3.

8.2 Structural Performance Test

8.2.1 Test Development

Schedule 2G [1] requires that explosion proof enclosures be designed for 150 psig and that they contain an internal explosion of methane and air. As shown in Section 4.1.4, dynamic effects produced by the explosion of methane and air are slight and the dynamic pressures produced are usually 80 psig or less. Thus, it is logical to base a test for strength upon a static pressure test at 150 psig with provisions for increasing the test pressure if unusually high pressures are observed in the MSHA explosion test.

The test procedure was developed based upon our general experience in hydrostatic testing and more specifically upon the hydrostatic testing of enclosures cited in Section 4.0. In addition, conversations were held with MSHA personnel [34] and the following general guidelines for the test were mutually agreed upon:

(1) The normal test pressure will be 150 psig, but provisions should be made for pressures up to 300 psig. Test pressures above 150 psig may be required if pressure piling is observed in the explosion tests.

(2) A pneumatic test should not be used because of the potential hazards of such a test. For pneumatic testing

MSHA would have to design a special testing chamber for personnel protection.

(3) Water or another dense liquid should be the test fluid. Water is the obvious choice because it is inexpensive and readily available.

(4) Failure criteria should be based on an allowable permanent deformation of 0.04 in./linear foot (as now specified for the explosion test) and on a maximum allowable cover-to-flange gap of 0.004 inch.

(5) The use of a feeler gage is the preferred method for checking the gap.

(6) Gasket material can be used so long as it does not interfere with the measurement of the gap. This means that the gasket material can be no closer than 1/8 in. to the outer edge of the flange if a feeler gage is to be used. It may be necessary simply to record the change in the gap which occurs as the result of a test. A gap greater than 0.004 in. may exist before the test because of the gasket. After the test, if this gap has increased less than a predetermined amount, then the test can be considered as successful. If this approach is used, it will be necessary to check the gap before testing and before a gasket is installed. Based on the pretest gap, a permissible change in the gap produced by the test can be established.

(7) The only direct recording instrumentation required is for internal pressure. Instrumentation such as strain gages is too expensive for the type of repetitive testing anticipated.

(8) Standard bolt torques will be used as specified by the manufacturer for bolt type and grade.

The Structural Performance Test which was developed according to the above guidelines is included as Appendix E.

One major problem which arose in the development and implementation of the test was: "How is the enclosure sealed so that test pressure can be maintained?" As noted in Section 4.0, leakage frequently occurred during the hydrostatic tests. Thus, a study of sealing methods was undertaken to find fast and reliable ways of sealing enclosures of arbitrary shape and size. This work, reported in the next section, became an integral part of the Structural Performance Test.

The Structural Performance Test of Appendix E evolved throughout this program. It was applied in its final form to the evaluation of the Pressure Test-Mine Environment, as documented in Section 8.2.3.

8.2.2 Evaluation of Sealants

Hydrostatic testing of enclosures requires an effective seal between the enclosure and its cover. Other penetrations must be sealed also, but the large seal area between the cover and the body of the enclosure presents the biggest problem to the test engineer. Covers can be large and irregular in shape, and so a sealant was sought which could be applied easily and quickly to enclosures of different geometry. Further, a sealant was sought which would seal the enclosure at pressures up to 300 psig. (A pressure of 300 psig is twice the static-design pressure and would only be reached if significant pressure piling, during the explosion test, dictated the need for higher static pressures in the Structural Performance Test.)

To determine the most suitable sealants for use in the Structural Performance Test, eight different sealants were evaluated as listed in Table 8.1. Sealants were evaluated which could be easily applied to large and/or oddly shaped enclosures. These sealants are applied as double-sided tapes, as brushed-on adhesives, or as caulking from a tube. Reinforced neoprene gaskets, which were found to work well in earlier hydrostatic tests on small, regular shaped enclosures (see Section 4.0), were not evaluated further.

All sealant tests were conducted using Enclosure I (Figure 4.1). The sealing surfaces for this enclosure lie in one plane, so it is clear that other sealing configurations can occur; however, two flat surfaces which press together, without sliding, can usually be found for sealing so that the results obtained should still apply. For screw-type joints the parts must be assembled before the sealant starts to cure or the relative sliding of the mating surfaces will destroy the seal.

Results of the sealant evaluations are summarized in Table 8.2. Twelve tests were conducted, including multiple tests with some sealants to study the effect of bead size, curing time, and sealant pattern. Figure 8.1 shows the sealant patterns evaluated. None of the sealants tested were satisfactory at pressures up to 300 psig, but sealant B (Table 8.1) performed well in all of its tests and held pressures up to 280 psig. In most tests the maximum pressures could have been increased even higher. There were no sudden ruptures of the seals which resulted in sudden pressure drops. The leaks were slow and progressive, and as long as makeup water could be supplied fast enough, the pressure could be increased. Tests were terminated when several drips or a small stream appeared.

It should be noted that the ease of application of some of the sealants influenced the uniformity of the bead and, perhaps, the performance of the sealant, also. Sealants B and E were supplied in caulking tubes and applied with a caulking gun (relatively easy to apply). All other "bead type" sealants were supplied in a squeeze tube (more difficult to apply). In spite of these differences, sealant B appears to be the superior sealant. Higher pressures can possibly be achieved by improved application techniques and bead patterns with some of the sealants.

TABLE 8.1. SEALANTS EVALUATED

Sealant Identification	Sealant Description	Evaluation Test Number
A	Form-a-Gasket® Aviation Permatex P/N 765-1210	#1
B	G.E. Silicone Construction 1200 Sealant Meets Spec. TT-S-00230C/00115438 (COM-NBS)	#2, #7, #12
C	3M, Scotch Mounting Tape, P.N. 4016 Double Adhesive Coated Foam Filled Tape	#3
D	Permatex Silicone Form-A-Gasket, RTV Blue Gasket Maker, P/N GBR, Item No. 80022, 3 oz Tube	#4
E	G. E. Silmate Silicone Rubber, RTV 1473	#5, #6
F	Permatex Handy Gasket Fast Cure Sealant, Part No. 80478, 2-Component Kit of Activator and Sealant	#8, #9
G	3/16-inch O.D., 1/8-inch I.D., Tygon Tubing	#10
H	Dayplas Hi-D Adhesive Backed Tape #1389.0, 503-5, (Manufactured by TFI Industries, 148 Parkway, Kalamazoo, Michigan 49006)	#11

*Reference to specific brands, equipment, or trade names in this table is made to facilitate understanding and does not imply endorsement by the Bureau of Mines.

TABLE 8.2. SUMMARY OF SEALING TESTS

Test No.	Sealant Identification	Application of the Sealant	Maximum Pressure (Psig)	Maximum Bolt Torque (Ft-Lb)	Comments
1	A	Sealant applied as a uniform coating to both mating surfaces	50	50	This sealant does not set - it remains tacky
2	B	1/4-in. straight bead inside the bolt hole (Figure 8.1)	200	40	Lid placed on "skimmed" sealant for curing - bolts finger tight
3	C	Tape laid inside of bolts (Figure 8.1)	200	60	At 40 ft-lb torque drips first appeared at 30 psig - at 60 ft-lb torque drips appeared at 160 psig
4	D	1/8-in. bead inside and around the bolt holes (Figure 8.1)	100	50	Sealant allowed to cure as in Test No. 2 - drips first appeared at 90 psig with 50 ft-lb torque
5	E	1/8-in. bead inside the bolt holes (Figure 8.1)	60	50	Lid placed on wet sealant and bolts torqued to 40 ft-lb before curing
6	E	1/8-in. bead inside the bolt holes (Figure 8.1)	120	60	Sealant cured without lid in place - drips first appeared at 100 psig
7	B	3/32-in. bead along centerline of bolt holes (Figure 8.1)	260	70	Sealant cured without lid in place - drips appeared at 240 psig
8	F	1/16-in. bead inside bolt holes (Figure 8.1)	140	60	Cured with lid in place - bolts finger tight - drips appeared at 120 psig
9	F	Same as for Test #8	100	60	Sealant cured with lid in place and bolts torqued to 40 ft-lb - drips appeared at 80 psig
10	G	Laid tubing inside bolt holes - overlapped ends 3 inches (Figure 8.1)	200	60	Used rubber cement to hold tubing during assembly - drips appeared at 180 psig
11	H	Laid tape inside the bolt holes (Figure 8.1)	40	60	
12	B	1/8-in. bead in zigzag pattern (Figure 8.1)	280	70	Lid placed on "skimmed" sealant for curing - bolts finger tight - drips appeared at 220 psig

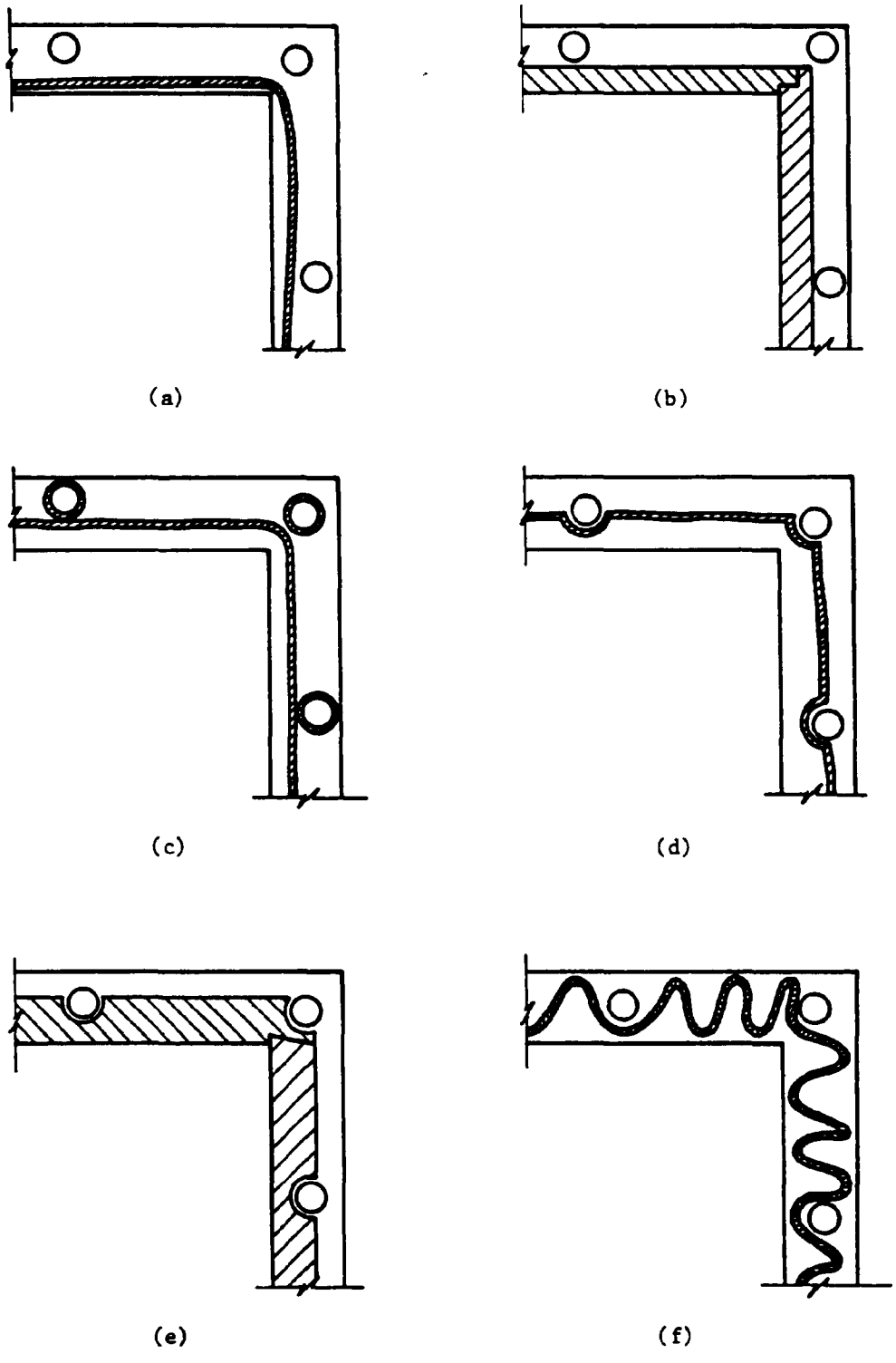

FIGURE 8.1. APPLICATION OF THE SEALANTS

From these tests, along with our earlier experience with reinforced neoprene gaskets, we recommend two methods of sealing the enclosures. These are:

- Sealant B (G.E. Construction Sealant, 1200 Series) - recommended for enclosures of all shapes and sizes
- Reinforced neoprene gaskets - recommended for small, regular shaped enclosures.

Application of these two sealants is described in the Structural Performance Test procedure of Appendix E.

8.2.3 Environmental Test/Structural Performance Test

As part of this study, evaluations were performed of the test series recommended for luminaires by Francis and Lankford [19]. The tests proposed are combined environmental exposure and static pressure tests. The purpose of these tests is to give a qualitative evaluation of adhesives and/or polycarbonates in luminaires after exposure to heat and light from the internal light source and to high humidity from acid mine water. As described in Reference 19, the two tests are:

Static Pressure Test

It is recommended that all luminaire design prototypes be subjected to a static pressure test, which is a modification of Paragraph 18.67, Title 30, CFR. In particular, the light source in each enclosure will be turned on and run continuously for a period of fourteen (14) days prior to the static test. The aim here is to assess the ability of the sealant/adhesive to withstand long-term thermal exposure. Immediately following this, a static pressure test will be carried out as per Paragraph 18.67, Title 30, CFR, using a gage pressure of 150 pounds per square inch.

Static Pressure Test, Mine Environment

It is recommended that all luminaire design prototypes be subjected to a pressure test similar to that described above, but carried out under humidity controlled environmental conditions. In this case, the luminaire light source will again be turned on and run continuously for a period of fourteen (14) days prior to the static pressure test. However, the luminaire during this time will be contained within an environmental chamber maintained at 20°C, with a 90% relative humdity environment. The moisture in the environment will be the acidic simulated mine water drainage solution developed by the U.S. Environmental Protection Agency. Following this exposure, the luminaire again is subjected to a static gage pressure of 150 pounds per square inch.

These two tests were performed on two luminaires, one fluorescent tube fixture manufactured by Joy Mining and Machinery Co. and one mercury vapor lamp manufactured by Control Products Co. These two fixtures were also subjected to the vibration sweep tests and are shown in parts (a) and (b) of Figure 7.1. The hydrostatic testing performed in these evaluations followed the test procedures of the Structural Performance Test.

8.2.3.1 Test Procedure

The test sequence for the enclosures was as follows:

1. Examined the two luminaires visually in as-received condition for deformations or damage.

2. Turned "on" the luminaires in the laboratory under normal RT conditions and left them "on" continuously for 14 days.

3. Subjected the luminaires to the Structural Performance Test.

4. Reexamined the luminaires for evidence of deformations or damage.

5. Turned "on" and left "on" the luminaires continuously for 14 days, in an environment which was maintained at a temperature of 20°C and a relative humidity of 90%.

6. Again subjected the luminaires to the Structural Performance Test.

7. Reexamined the luminaires for evidence of deformation or damage.

One exception was taken to the test procedure for the mine environment. Moisture in the environmental test did not simulate acid mine water. We do not believe that this deviation from the test procedure was significant for the enclosures tested. This conclusion is based upon accelerated aging tests being conducted under Contract H0387009 [2]. In these tests, which have been in progress for about twelve months, there has been no significant deterioration of polycarbonate lenses or RTV adhesives from a combination of high heat, UV radiation, and mine acid water spray. From these results, it does not appear that rapid aging is being produced by the mine acid water.

8.2.3.2 Test Evaluations

Our evaluations of the two tests recommended for luminaires was based upon the tests themselves, upon the results produced, and upon the results of accelerated aging tests on polycarbonates and adhesives which are being conducted under Contract H0387009 [2].

Observations on the Tests

The tests are easy to perform if the proper equipment is available. Facilities must be available for hydrostatically testing the luminaires, and an environmental chamber is required to control the temperature and humidity in the environmental exposure portion of the test. These facilities are available at SwRI, and so the tests progressed smoothly. We experienced no particular difficulty in preparing the

luminaires for hydrostatic testing or in returning the luminaires to service-ready condition following the tests. It is necessary to supply proper voltage and current to the luminaire, and the power requirements are usually different from 120 volts A.C. The proper power supply should be furnished by the manufacturer when the luminaire is submitted for approval.

One problem with the test equipment which must be addressed is the effect of acid mine water on the environmental chamber. The mine acid water will degrade all but the most stain resistant steels. Because the environmental chamber used in these tests serves many projects and has a mixture of metals in the humidity supply system, we took exception to the use of acid mine water in our tests. If MSHA implements these tests on a routine basis, a chamber must be used which is constructed totally of a high quality stainless steel or its equivalent.

Test Results

Results of tests on the two luminaires are given in Table 8.3. No discernible damage occurred to the luminaire from Joy Manufacturing. Any degradation which may have occurred from the 28 days of continuous operation (except for one stop to test the unit) was not apparent visually and did not affect the hydrostatic test results.

In the first hydrostatic test on the luminaire from Control Products, small leaks occurred at the junction of the lens and the enclosure and in the casting itself. The locations of these leaks are shown in Figure 8.2. Note that Location A is on the opposite side of the enclosure from that viewed in the photograph. The leak in the casting must be the result of porosity because no cracks were evident. The drip at the edge of the window increased to a stream at about 160 psig. Following the first hydrostatic test, small slivers of glass (see Figure 8.3) were found inside the enclosure. An examination of the lenses in the enclosure revealed that the slivers came from the free edge of the glass plates (see Figure 8.4). In the thermal analyses being performed under Contract H0387009 [2], this area of the lens was found to have high thermally induced stresses.

Results from the second hydrostatic test of the Control Products luminaire were similar to those for the first test. The drip from the casting occurred at a lower pressure than in the first test, but remained at the same level (an occasional drip); the leak at the edge of the window occurred at the same pressure as in the first test, but was slightly greater at 150 psig than at 160 psig in the first test. So, some deterioration of the Control Products luminaire may have occurred from the 28-day "burn" and the hydrostatic testing, but the evidence of the deterioration is slight in these tests.

Results of Accelerated Aging Tests

Preliminary results from accelerated aging tests being conducted on Contract H3877009 [2] indicate that rapid deterioration from UV, heat, and acid mine water does not occur in the polycarbonate and RTV tested (Lexan and GE 108, respectively). Fairly rapid deterioration in epoxy does occur, but it may not be revealed by the 28 days of continuous

TABLE 8.3. SUMMARY OF LUMINAIRE TESTS

Tests Performed	Luminaire from Control Products	Luminaire from Joy Manufacturing
2 Wk. Burn* at RT Max. Exterior Lens Temp. Results	~160°F No visual damage	141.5°F No visual damage
1st Hydrostatic Test Max. Pressure Results	160 psig Drip at edge of lens at 140 psig (Loc. A in Fig. 1). Drip from Al. casting at 160 psig (Loc. B in Fig. 1). Small slivers of glass from edge of the lens found in enclosure after testing (Figs. 2 & 3).	150 psig No damage or distortion
2 Wk. Burn* at 20°C & 90% RH Max. Exterior Lens Temp. Results	132°F No visual damage	114.5°F No visual damage
2nd Hydrostatic Test Max. Pressure Results	150 psig Drip from Al casting at 100 psig (Loc. B in Fig. 1). Small stream of water at edge of lens at 140 psig (Loc. A in Fig. 1). Stream increases to spray at 150 psig.	150 psig No damage or distortion

*Indicates that the lamp is on.

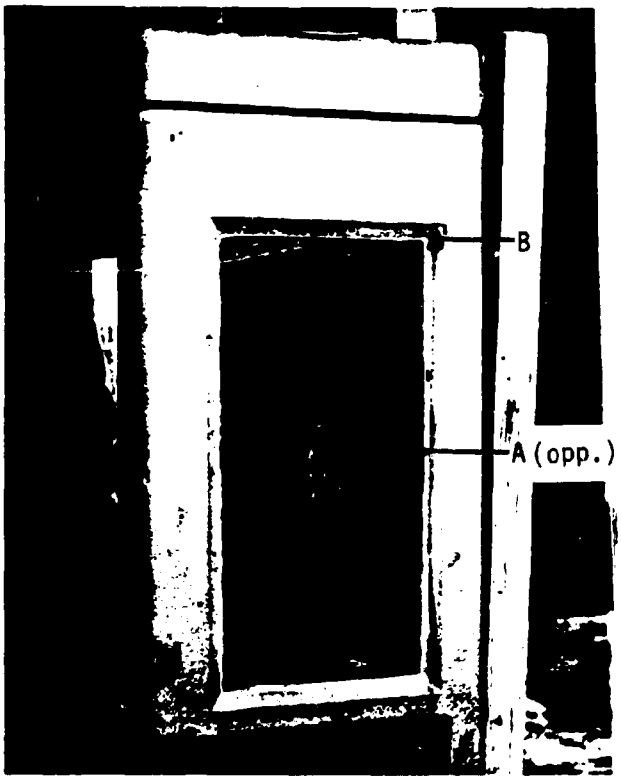

FIGURE 8.2. LUMINAIRE FROM CONTROL PRODUCTS

FIGURE 8.3. GLASS SLIVERS INSIDE
CONTROL PRODUCTS LUMINAIRE

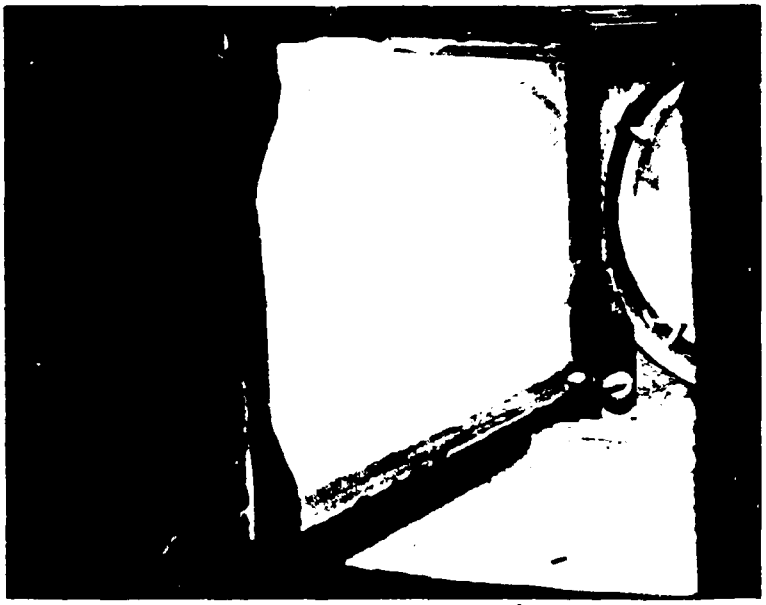

FIGURE 8.4. EDGES OF THE LENS WHERE GLASS BREAKAGE OCCURRED

operation at normal temperatures. Thus, continuous operation of the luminaires tested probably did not significantly affect their strength. This does not invalidate the tests as a means of screening enclosures for particularly unsuitable materials, nor does it guarantee that materials which pass the tests will survive for a long time in the mine environment. More extensive tests, such as the accelerated aging tests proposed in Appendix K, plus other tests that may be appropriate, are required for a thorough evaluation.

Conclusions and Recommendations from the Test Evaluations

Conclusions

- Special equipment is required to conduct the tests. The equipment required includes a hydraulic test apparatus and an environmental chamber. The environmental chamber must be resistant to acid mine water.

- The tests are straightforward and easy to perform with the proper test equipment.

- As a result of the tests, there was no evidence of deterioration in one luminaire and only slight evidence of deterioration in the other luminaire.

- Only the most unsuitable of materials will be significantly degraded by these tests.

- The test can be simplified by hydrostatic testing at the beginning and end of the 28-day illumination and exposure period. This approach may eliminate some luminaires from the 28 days of exposure testing.

Recommendations

- More extensive tests such as those recommended in Appendix K are required to determine the suitability of materials for long-term use in enclosures. We recommend that materials be pretested and selected from an approved products list which is based on valid test results.

- The tests evaluated should be performed for preliminary screening until such a list is available, and these tests should be performed before other MSHA testing (before the explosion test, impact test, thermal test, etc.).

8.3 Ruggedness Test

The environment in which Schedule 2G enclosures must operate underground can be very severe; so severe, in fact, that the loads produced by an internal explosion of methane and air may not govern the design of some components (covers, sides, surfaces) of the enclosure. That is, other loads may be greater. Also, as enclosures evolve, the venting of enclosures through explosion-proof vents may become permissible. If this occurs, then the internal pressure loads may be quite low and other design criteria, such as ruggedness, will control. The purpose of this work was to evaluate the environment in the mine and to identify suitable criteria which an enclosure should meet to ensure that it will function properly in the mine. Further, a testing procedure for e· 'osures, to evaluate their ruggedness, is recommended.

8.3.1 Environment in the Mine

To estimate the forces which can occur in typical mining operations (forces which can be applied to exposed surfaces of explosion-proof enclosures), we examined operating mines for evidence of damage and calculated forces which might be produced by different mine accidents. Specifically, the following forces were evaluated:

- Forces required to produce observed damage on a mining machine
- Contact forces when a mining machine strikes a rib (as in turning a corner)
- Impact forces when a shuttle car rams a mining machine
- Impact forces produced by rock falls

Rib burst can also produce substantial lateral forces which might damage an enclosure; however, we were unable to quantify the magnitude of these forces. Lateral forces produced by rib contact and vehicle impact can be large as well, and we believe that an enclosure designed to withstand these forces will be adequate.

8.3.1.1 Observed Damage

Estimates of forces were based on damage to mining machines observed in the Westland No. 2 mine. Observed damage included permanent deformations in a mine lighting guard mounted on the top of the miner and permanent deformations in a flat plate located on the side of the miner. Estimates of the damage-producing forces and kinetic energy are:

(1) Light guard: 1/2-in.-diameter bar 10 in. long with 1/2-in. permanent lateral deformation.

Uniform static force to deform the bar:
$F \sim 600$ lb

Kinetic energy (uniformly applied) to deform the bar: KE $\simeq$ 25 ft-lb

(2) Flat plate: 2 ft x 3 ft x 1/2 in. steel plate with a permanent deformation of 3/4 inch.

Uniform static force to deform the plate: F $\simeq$ 60,000 lb

Kinetic energy (uniformly applied) to deform the plate: KE $\simeq$ 3700 ft-lb

The estimates of the kinetic energy required to deform the plate and the bar are based on bending behavior only (no in-plane stretching). If the deformations in the plate are somewhat larger, about twice the plate thickness, then stretching may occur, and this greatly increases the energy that the plate can absorb. For example, if the plate deforms 1 in. and is sufficiently restrained at its boundary, the kinetic energy required for this deformation is

$$KE \simeq 14{,}300 \text{ ft-lb}$$

Likewise, if in-plane stretching is treated for a statically applied load, the force required to produce the 3/4-in. permanent deformation can be estimated from Equation 5.9 as

$$F = 217{,}000 \text{ lb}$$

Thus, the static force and kinetic energy required to produce the observed plate deformations are actually bounded by

$$3{,}700 \text{ ft-lb} \leq KE \leq 14{,}300 \text{ ft-lb} \qquad (8.1)$$

and

$$60{,}000 \text{ lb} \leq F \leq 217{,}000 \text{ lb} \qquad (8.2)$$

For the damage observed, the plate was not well restrained, and the forces and energy will be near the low end of the ranges shown.

8.3.1.2 Contact With a Rib

This force will most likely occur as a mining machine contacts a rib when turning a corner. An accurate determination of the peak forces produced during such an incident would require a dynamic analysis that includes the driving power of the miner to the track, track-to-floor friction, miner-to-rib friction, and rib lateral strength. We could not locate the results of such an analysis, and to undertake it ourselves was beyond the scope and resources of this project. We believe that a reasonable estimate of the upper bound of this contact force is the frictional force between the mining machine and the mine floor. Above this frictional force the miner slips sideways, relieving this contact pressure. If the frictional coefficient is taken as 0.70 [35], a 100,000-lb miner could produce a contact force of

$$F = 0.70\ (100{,}000\ \text{lb}) = 70{,}000\ \text{lb} \qquad (8.3)$$

This force can act in a direction almost parallel to or normal to the side of the miner. For cover enclosures, the force will be treated as normal to the miner side. This force should give a reasonable upper bound for slowly applied (quasi-static) forces which occur when a mining machine contacts the rib.

8.3.1.3 Miner-Shuttle Car Impact

When two bodies collide, the impact force depends upon their flexibility at the point of impact; however, even if this flexibility is unknown, the energy that must be absorbed during the impact can be determined. For simplicity, consider a shuttle car impacting a mining machine from the side. A typical shuttle car will weigh 60,000 lb and operate at speeds from 0 to 7 mph, with normal operating speeds being less than 5 mph. If we arbitrarily take 1 mph as a lower limit, the kinetic energy of the impact will be bounded by

$$2000\ \text{ft-lb}\ (1\ \text{mph}) \leq KE \leq 98{,}200\ \text{ft-lb}\ (7\ \text{mph}) \qquad (8.4)$$

If the mining machine slips sideways during the impact with the shuttle car, then the peak forces may be attenuated somewhat. This will occur only if the impact force exceeds the 70,000-lb force required to slide the mining machine, as estimated in the preceding section. Most likely, impacts will occur at the lower speeds, say 2 mph. At this velocity the impact energy is

$$KE \simeq 8000\ \text{ft-lb}$$

This value is a reasonable level for side impact. It is considerably above the lower limit of the energy required to produce the observed damage.

8.3.1.4 Rock Falls

The impact energy in rock falls was estimated both from roof fall data and from the work of Terzaghi. Terzaghi [36] gave rock loads for six different rock conditions as a function of the width and height of the mine opening. The general form of his equations is

$$H_p = C\ (B + H_T) \qquad (8.5)$$

where B and H_T are the breadth and height, respectively, of the mine opening and C is a coefficient that depends upon the rock conditions. C varies from 0.25 for moderately blocky and seamy rock to 1.10 for completely crushed, but chemically intact rock. Morley [37] suggests the following values to estimate a reasonable upper limit rock load for U.S. mines:

$$B = 20\ \text{ft}$$
$$H = 8\ \text{ft}$$
$$C = 0.50$$

These values give a rock load of 14 ft, which is a static load (for 160 lb/ft^3 rock) of

$$F = 2240 \text{ lb/ft}^2 = 15.6 \text{ psi} \quad (8.6)$$

This value is very close to the 15-psi requirement for canopies as required by U.S. Congress Federal Coal Mine Health and Safety Act of 1969 [38]. Enclosure covers, which are designed for 150-psi internal pressure, would obviously withstand this static load; however, in a roof fall, the rock column can drop up to 6 ft before striking the cover. This produces a kinetic energy at impact of

$$KE = 13,440 \text{ ft-lb/ft}^2 \quad (8.7)$$

As will be shown later, this kinetic energy, which must be dissipated by the cover, is much more detrimental to the cover than is the static load.

In addition to the work of Terzaghi, we analyzed data from underground roof falls reported in Reference 39. The data were analyzed and replotted to obtain kinetic energy which can be produced on the top of a mining machine by the rock impact. The original data reported in Reference 39 came from MESA (now MSHA) accident reports. These reports were primarily for years 1972 through 1975 (a few earlier reports were included), and the accident data were supplemented by additional inquiries to obtain more specific information.

Reference 39 gave the kinetic energy produced by a roof fall at the top of the protective canopy for a miner. This height was taken as 6 ft above the mine floor, but no higher than 1 ft below the mine roof. For XP enclosures, which are located on the top of the miner, the height above the mine floor was taken as 3 ft. These heights affect the kinetic energy in the roof fall because they determine the rock fall distance. An additional drop of 3 ft can significantly increase the energy in the falling rock.

Figure 8.5 gives the kinetic energy per unit of area at the top of the miner versus the cumulative percentage of roof falls. The data are bounded by upper and lower curves, and values are read from the lower bound which gives the highest kinetic energy at any percentage level. For example, based on these data, 60% of all roof falls should produce kinetic energy levels equal to or less than 3,700 ft-lb/ft^2. Thus, to protect against 60% of all roof fall accidents, XP enclosures* should be designed for a kinetic energy level from roof falls of

$$KE_{60} = 3,700 \text{ ft-lb/ft}^2 \quad (8.8)$$

To protect against 90% of all roof fall accidents, the enclosure should be designed for

$$KE_{90} = 16,000 \text{ ft-lb/ft}^2$$

The kinetic energy can be very large from roof falls. The largest reported accident gives a kinetic energy per square foot of

$$KE_{100} = 77,520 \text{ ft-lb/ft}^2$$

*This applies to the surface exposed to the roof of the mine.

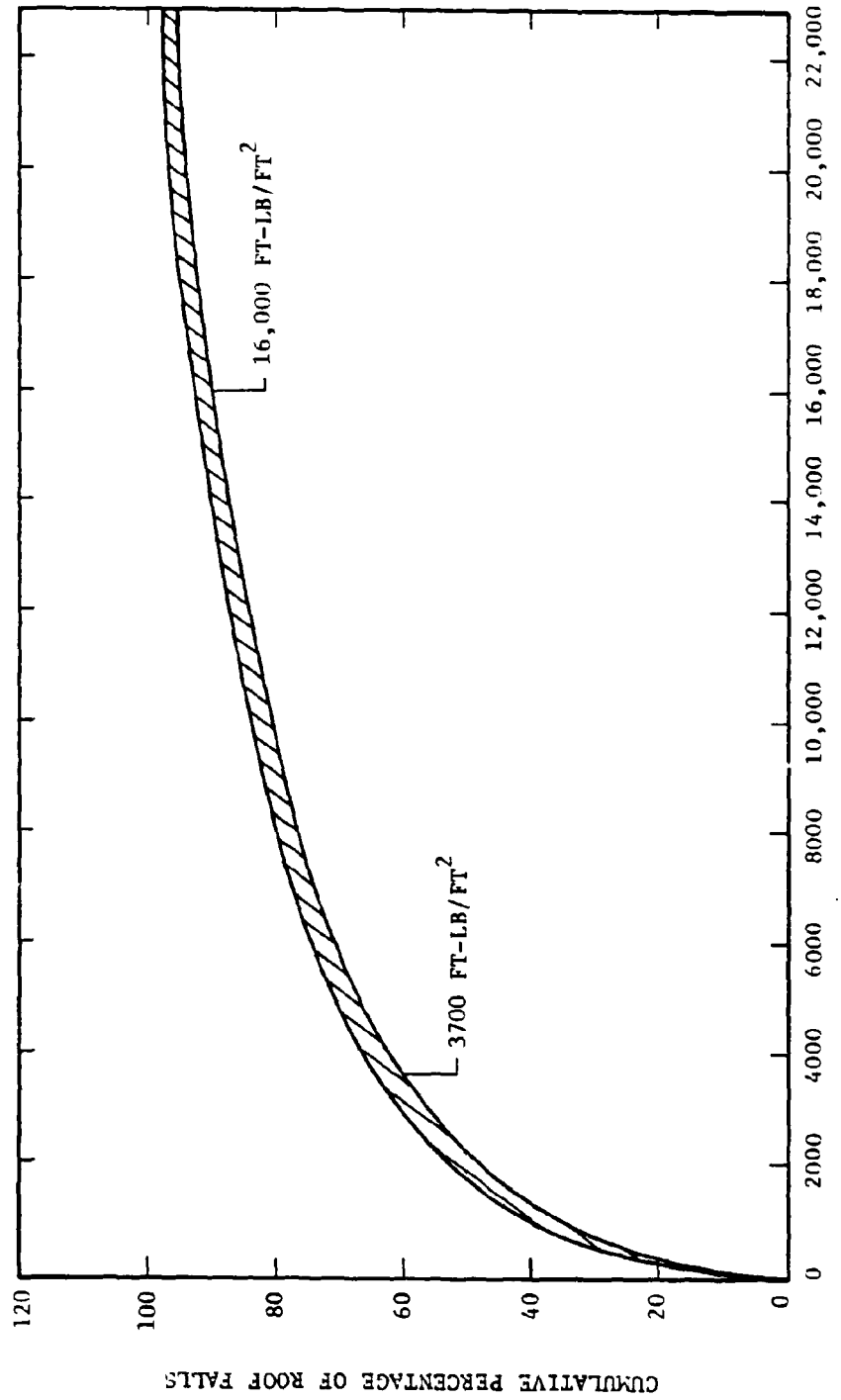

FIGURE 8.5. KINETIC ENERGY AT THE MINER TOP PRODUCED BY ROOF FALLS

It is interesting to note that the kinetic energy calculated from Terzaghi's work (Equation 8.7) corresponds to a protection level of about 86%, i.e.

$$KE_{86} \approx 13{,}440 \text{ ft-lb/ft}^2$$

These energy levels are very high and will govern the design of the exposed surface of an enclosure. To demonstrate this, consider a 2-ft by 3-ft enclosure cover designed from mild steel with a yield strength, σ_y, of 36,000 psi. Using Equation (5.6), the plate thickness to withstand a pressure of 150 psig was found to be

$$h^2 = \frac{2 Pa^2 (3 - 2\xi_o)}{3 \sigma_y} = \frac{(150 \text{ psig}) (12)^2 [3 - 2 (0.7928)]}{6 (36{,}000)}$$

$$h = 0.75 \text{ in.} \qquad (8.9)$$

To compute the required cover thickness for KE_{60} = 3,700 x 2 x 3 x 12 = 266,400 in-lb, energy relationships developed in Reference 40 were used. Equating the strain energy in the plate to the kinetic energy applied to the plate we obtained

$$U = 4 \sigma_y h^2 \left(\frac{w_o}{2Y}\right) \left[\frac{Y^2}{X} + X\right] + \frac{8}{\sqrt{3}} \sigma_y h^2 \left(\frac{w_o}{2Y}\right) Y = KE_{60}^* \qquad (8.10)$$

If the ratio of the plate center deflection, w_o, to the plate width, 2Y, is taken as 0.04 (maximum center deflection of 0.96 in. in the 2-ft x 3-ft plate), then the thickness required for KE_{60} is:

$$h^2 = \frac{266{,}400}{4 (36{,}000)(0.04) \left[\frac{(12)^2}{18} + 18 + \frac{2(12)}{\sqrt{3}}\right]} = 1.164 \qquad (8.11)$$

$$h = 1.08 \text{ in.}$$

These values are for illustration only and should be treated as approximate. Even though this cover plate is much thicker than would be required for 150-psig internal pressure, the thickness is not excessive for a 2-ft x 3-ft plate. Cover thickness could be reduced by internal supports.

For the calculation in Equation (8.11), a center deflection was assumed which is approximately equal to the plate thickness. Also, expressed as in./ft, the value is 0.96 in./ft across the narrow dimension of the plate. This is much higher than the deformation which would occur in the plate designed by Equation (8.9) for an applied pressure of 150 psig. If a smaller deflection had been used in Equation (8.11), the required plate thickness would have been much larger.

Thus, the kinetic energy level, KE_{60}, given by Equation (8.8) represents a very severe load on enclosures, and it is clearly impractical to protect against higher kinetic energy levels. It is also clear from the above calculations that KE_{60} represents a much more severe load than the 15-psi requirement now specified for canopies on mining equipment (Reference 38). Further, it seems inconsistent to design Schedule 2G enclosures for a load which is significantly higher than that specified for the canopy which directly protects the operator from a roof fall. Thus, additional work is recommended to better quantify the severity of rock falls and their effect on mining equipment. This work should address data on equipment damaged from rock falls and relate the damage to the kinetic energy in the fall as reported in Reference 39. In this way, a less severe criterion for roof falls can perhaps be established.

8.3.1.5 Summary of Environmental Effects

From the previously discussed investigations, the forces and energies which can occur in the mine are summarized as follows:

Based on Observed Damage

From above. $F \sim 600$ lb
$KE \sim 300$ in-lb

From the side: $60{,}000 \text{ lb} \leq F \leq 217{,}000 \text{ lb}$
$3{,}670 \text{ ft-lb} \leq \overline{KE} \leq 14{,}300 \text{ ft-lb}$
(observed damage is near the low end of this range)

Based on Accident Scenarios

From above: $F = 15.6$ psi
$KE \leq 77{,}520 \text{ ft-lb/ft}^2$
$KE_{60} = 3{,}700 \text{ ft-lb/ft}^2$

From the side: $F = 70{,}000$ lb (rib contact)
$2000 \text{ ft-lb (1 mph)} \leq KE \leq 98{,}200 \text{ ft-lb (7 mph)}$
(shuttle car impact)
(most likely impact velocities will be at low speed)

It is clear that the maximum energies and forces which can occur in the mine are much greater than the values based on the observed damage. Of course, the observed damage was very limited and did not include any equipment which had been impacted by significant rock fall.

8.3.1.6 Recommended Ruggedness Criteria

Based upon these studies, our recommendations for ruggedness criteria are:

- Test enclosure surfaces exposed to the roof to a kinetic energy level which will protect against 60% of the roof falls reported in Reference 39.

- Test enclosure surfaces exposed to side impacts to an energy level which corresponds to a 60,000-lb shuttle car impacting at 2 mph.

- Design protected surfaces to a kinetic energy level which is 10% of that required for side impact.

These recommendations correspond to the following energy levels:

Top Exposure: Test to KE = 3,700 ft-lb/ft^2

Side Exposure: Test to KE = 8,000 ft-lb

Protected Areas (such as under the operator's canopy):
Test to KE = 800 ft-lb

As noted in Section 8.1, we believe that additional work is necessary to better quantify damage from actual accidents, particularly from rock falls. This type of study will relate the damage potential which exists to the protection level that is actually needed to assure some prescribed level of safety.

8.3.1.7 Test Procedure

A ruggedness test to verify that these criteria are satisfied can be based on static or dynamic tests. A dynamic test (most likely a drop test) is preferred because it more accurately characterizes the postulated accidents which might damage the components. Also, while the energy level is a function of exposed area (for top exposure), it is independent of the area geometry. For top exposure, the drop weight should simulate broken rock. For side and "under canopy" exposure, a solid impacting mass is recommended. Although the kinetic energies can be high, drop weights need not exceed 1000 lb.

To develop a static test, an equivalent external pressure must be defined. This pressure will be a function of both area and geometry and adds uncertainty to the test. While this presure can be readily defined for regular geometries,it will be more difficult to define for complex shapes. Another difficulty is that the pressure must be applied externally to the enclosure and only over specified areas. Thus, a dynamic drop test is recommended which produces the kinetic energies specified.

8.4 Criteria for Battery Box Covers

The purpose of this task was to examine the criteria for battery box covers now included in Schedule 2G and to recommend suitable alternatives. With regard to cover strength, Schedule 2G now states:

"18.44 Battery boxes and batteries (exceeding 12 volts).

(a) A battery box (tray), including the cover, shall be made of steel the thickness of which is to be based on the total weight of the battery and tray, as follows:

Weight	*Thickness*
2,000 lb maximum	*3/16"*
2,001-4,500 lb	*1/4"*
Over 4,500 lb	*5/16"*

Materials other than steel that provide equivalent strength will be considered.

(b) Battery-box covers shall be lined with a flame-resistant insulating material, preferably bonded to the inside of the cover, unless equivalent protection is provided.

(c) Battery-box covers shall be provided with a means for securing them in closed position."

These requirements do not take into consideration the geometry of the tray, strength requirements, or tray design. They do not give the battery manufacturer any flexibility in the design and certainly stifle the development of new and better designs for battery boxes. Thus, the USBM and MSHA are seeking more suitable criteria upon which to base the certification of battery box covers. Further, MSHA plans to test the battery box covers for compliance with the criteria.

To better understand the current battery box requirements and their effects upon battery manufacturers, discussions were held with representatives of two battery manufacturers [41]. There was a general consensus among the representatives contacted that a performance standard for battery box covers is needed. This consensus was based upon a belief that MSHA accepts some batteries with inferior covers because they do not have good acceptance criteria or a performance test. They feel that the effort they spend to develop good designs places them at a financial disadvantage relative to companies that are less design conscious. Good performance criteria, properly enforced, would put all companies on an even footing. Additional comments include:

- There is a great need for improvement in the design of the battery tray cover. The major difficulty with current tray covers is that they warp easily and, once warped, are difficult to remove.
- Several features of the batteries should be considered by MSHA when choosing or setting a new criterion. These are:
  a. Ease of cover removal
  b. Prevention of shorting by the cover or by something that might be inserted into the battery if the cover should warp
  c. Battery contamination from coal dust or other particulate matter in the mine
  d. Battery performance
  e. Proper cooling and ventilation during recharging

f. Size limitations because batteries constructed to a new performance criterion might not be interchangeable with batteries in existing vehicles

g. Battery life

- Extending the height of tray partitions to provide support for the cover is feasible, but it will complicate the battery layout and fabrication because slots must be provided in these partitions for leads and drainage.

- The recommended performance criteria for battery box covers were that (1) no shorting occur and (2) warpage be sufficiently small that no item (such as the blade on a screwdriver) can be inserted into the battery without cover removal.

- Battery manufacturers do not know the magnitudes of the load that the tops of their batteries (not the covers) can withstand before shorting or other serious damage occurs. They suggested that such data could be generated by a series of relatively simple tests that utilize several existing cells potted in place as in normal battery assembly.

- The design of battery covers to resist roof falls is logical for battery covers that are exposed to the mine roof. There was no consensus as to whether or not the probability of roof fall was greater or less for a battery-operated vehicle than, for example, mining machinery operating nearer to the mine face.

There may be some justification for reducing the severity of the kinetic energy for the design of battery box covers below that for the design of enclosures. Justification for reducing the severity would have to be based on the location of battery operated vehicles and mining machines relative to the face. The mining machine is frequently exposed to unsupported roof falls near the cutting face, whereas battery operated vehicles are more likely to operate in areas with bolted roof support; however, we have no data to support a contention that the battery boxes are exposed to fewer roof falls than mining machines. Thus, for now we recommend that the KE_{60} criterion be applied to both battery box covers and to enclosures.

Calculations were made for battery covers under the assumption that partitions within the boxes can be extended above the tops of the cells to support the covers and that the covers are not clamped or bolted at the sides of the cases. Under these assumptions, the weakest part of the cover (for a uniform distribution of rock striking the cover) is an outside corner.* If membrane action is ignored, the cover deflections (or thickness for a specified deflection) can be computed from Equation (8.10). Applying Equation (8.10) to a steel battery box cover in which

*Refers to a corner of the cover defined by two intersecting partitions and two intersecting sides of the box.

the permanent cover deflections are set at

$$\frac{w_o}{L_y} = 0.10 ,$$

the cover thicknesses in Table 8.4 are obtained.

TABLE 8.4 THICKNESS OF A STEEL BATTERY BOX COVER
(σ_y = 36,000 psi)

Partition Spacing 2Y x 2X	Allowable Permanent Deflection (W_o)	Cover Thickness, h	
		KE_{60}	KE_{50}
6 in. x 8 in.	0.6 in.	0.35 in.	0.28 in.
10 in. x 10 in.	1.0 in.	0.40 in.	0.32 in.
12 in. x 18 in.	1.2 in.	0.53 in.	0.42 in.
24 in. x 36 in.	2.4 in.	0.74 in.	0.59 in.

Cover thicknesses for two different kinetic energy levels are given for comparison. It is clear that to keep battery covers light, the partitions must be closely spaced, higher strength steels must be used, or the kinetic energy level must be reduced. Alternately, new battery cover designs, which include support to the cover from the battery cells themselves, may evolve. Note also that large permanent deformations have been used in these calculations. We believe that large deformations should be permitted for battery box covers under roof fall conditions so long as provisions are made to avoid shorting battery components.

It is evident from the results in Table 8.4 that applying a kinetic energy level equal to KE_{60} to battery box covers may result in thicker covers than are now being used in the mine. Thus, before such a criterion is adopted by MSHA, SwRI recommends that two additional studies be made. One is a survey of mine roof fall accident data to determine, if possible, the probability of roof fall damage to battery box covers. This should be done in conjunction with a determination of the probability of damage to Schedule 2G enclosures located on mining machines. The other investigation which we recommend is a test to establish the crushing strength of battery cells in mine batteries. Again, this study may best be performed in conjunction with a study of alternate battery box cover designs.

What is proposed is basically a strength criterion for battery box covers. Other factors, such as venting, electrical insulation, and locking provisions are already covered adequately in Schedule 2G. The performance requirements for the battery would be that (1) no cells or electrical components be broken by the test, (2) the battery function properly, and (3) a straight rod, approximately 3/16 in. in diameter, cannot be inserted into the battery a sufficient distance to damage or short internal components.

9.0 KEY FINDINGS, CONCLUSIONS, AND RECOMMENDATIONS

9.1 Key Findings

The work described in preceding sections of this report covered five major areas of research. These are:

- Selection of a computational method
- Margins of safety in XP enclosures
- Weld quality in XP enclosures
- Reliability of XP enclosures with windows and lenses
- Performance tests for XP enclosures

Several tasks were performed in each of these areas. The key findings were:

Selection of the Computational Method

- The ANSYS finite element computer program has all of the features required for the analysis of XP enclosures, and it was chosen for the finite-element analyses documented in this report.

- MARC had most of the desired features for the analysis of enclosures, but lacked steady-state heat transfer capability in thin shell elements and, in our judgement, was less "user friendly" than ANSYS.

- ADINA had many of the desired analysis capabilities, but lacked thin shell elements and (at the time of evaluation) lacked pre- and post-processors.

Margins of Safety in XP Enclosures

- Dynamic effects, produced by explosions of methane and air, were found to be very small for the enclosures analyzed in this study.

- There are wide variations in the margins of safety for different enclosures. One enclosure had a factor of safety less than one.

- None of the enclosures tested ruptured at internal pressures of 150 psig.

- Weld joints in one enclosure partially failed at pressures as low as 60 psig, and permanent deformations of 0.31 in./ft were produced in the enclosure by a pressure of 150 psig.

- At locations other than the cover seal, only one enclosure leaked (during the hydrostatic test) at pressures below 150 psig. A small leak ocurred around the window at 140 psig in the first hydrostatic test of one luminaire.

- Safety factors tend to decrease with increasing enclosure volume.

- Physical properties can vary widely for some cast materials. These property variations affect the behavior of the structure under load. Further, these variations are difficult to model analytically (by finite-element methods, for example) because destructive tests are required to establish the properties, and the properties are known only in certain areas.

- The behavior of welded joints under load is difficult to predict and therefore to accurately describe in an analytical model. This is particularly true for low-efficiency joints. High-efficiency joints are more predictable.

Weld Quality in XP Enclosures

- Small manufacturers do not have well-documented welding practices.

- Large manufacturers have welding procedures, and most adhere, at least partly, to AWS welding codes.

- Joint design is similar for all of the manufacturers, but knowledge of joint efficiency was poor.

Reliability of Enclosures with Windows

- Enclosure resonances fall within the range of vibrations (5 Hz - 10,000 Hz) measured on typical mining machines.

- Amplification factors (ratio of acceleration amplitude measured on the enclosure to the input amplitude) were as high as 23 on some enclosures. These amplification factors were based on accelerations measured normal to window surfaces.

- High local stresses and moderately high bending stresses are induced in windows and lenses by the Schedule 2G Impact Test. These stresses exceed those produced by the Schedule 2G Explosion Test, the Structural Performance Test (Appendix E), and the Schedule 2G Thermal Shock Test.

- Low stresses are produced in free windows and lenses by the Schedule 2G Thermal Shock Test. Much higher stresses are introduced if the entire enclosure is heated to 150°C, and the window is then quenched from one side.

- Heat and UV light degrade polycarbonate windows and adhesive materials that are used in some XP enclosures.

- Polyarylate may be a more suitable material than polycarbonate for XP enclosure windows and lenses. It is a plastic with good heat and UV resistance and adequate toughness.

Performance Tests and Acceptance Criteria

- To assure that all enclosures are designed for 150-psig internal pressure, MSHA must implement a Structural Performance Test (described in Appendix E).

- Forces and impact energies which characterize the mine environment are dominated by those which can be produced by rock falls, by impacts between mining machinery, and by the impact of a mining machine with the rib.

- The maximum potential energy which can be generated by rock fall is very high, and it is impractical to design for such an energy level.

- Protection from 60% of roof falls requires that exposed surfaces be designed for a kinetic energy of 3700 ft-lb/ft^2, based on data from past roof falls.

- Battery box covers should be designed to withstand the proposed Ruggedness Test unless future work shows that the exposure to roof falls of battery operated equipment is less than that of the mining machine.

9.2 Conclusions

Based upon the key findings noted in the preceding section and other results reported herein, the following conclusions were reached:

- Nonhomogeneous material properties and weld joint stiffness and strength are not always well known. Because of these uncertainties in the input data, MSHA should not rely exclusively upon analytical methods for enclosure certification. MSHA could use a combination of analysis and testing for certification if they chose to do so.

- Dynamic effects, produced by explosions of methane and air, are insignificant in most enclosures. Dynamic effects may be important if unusually high pressures occur (pressure piling) or if the enclosure is unusually large.

- Some enclosures have been designed to withstand the MSHA Explosion Test and not 150-psig internal pressure. Enclosures should be hydrostatically tested by MSHA to assure that they will contain pressures equal to or greater than 150 psig.

- Most small enclosures (internal volume $\leq$ 124 in^3) have adequate margins of safety; larger enclosures may not have adequate safety margins.

- For a typical bolted cover, the flange gap will close outside the bolt line under load. Axial yielding of the bolt may cause the "unloaded gap" to increase from test to test; however, only a drastic bolt overload would cause the gap (as measured with a feeler gage) to increase under load.

- Joint efficiency is not well understood by many enclosure manufacturers.

- A uniform welding standard is needed for the manufacturer of XP enclosures.

- Enclosure resonant frequencies can be excited by mining machines, and the response amplitudes may be high enough to cause damage under prolonged excitation.

- High local stresses and moderately high bending stresses are produced in windows and lenses by the Schedule 2G Impact Test; however, impact energies which can be produced in the mine by mining accidents far exceed those produced by the impact test.

- Accelerated aging tests are needed to qualify plastics and adhesives for service underground. These materials should be qualified prior to their uses and restricted in service as dictated by the test results.

- A Ruggedness Test should be based on the possibility of impact by rock falls and mining equipment such as a shuttle car.

- Battery box covers should be designed to withstand the proposed Ruggedness Test unless future work shows that the exposure to roof falls of battery operated equipment is less than that of the mining machine.

9.3 Recommendations

Key findings and conclusions given in the preceding two sections, and other results which are documented throughout the report, led to numerous recommendations which are cited below. It is recommended that

- A design guide be prepared for XP enclosures to unify the design effort of enclosure manufacturers.

- A structural performance test, such as the one described in Appendix E, be used by MSHA in the certification of enclosures.

- MSHA utilize analytical methods as an aid to enclosure certification. A screening program for enclosures, to be used prior to testing, is one way that this recommendation can be implemented.

- MSHA require that XP enclosures be fabricated according to an American Welding Society (AWS) Standard. AWS D14.4 is recommended.

- Materials, such as polycarbonates and adhesives, which are known to be degraded by heat and UV radiation, be approved for use in XP enclosures only after appropriate environmental testing. Recommended accelerated aging tests, which are designed to represent the mine environment, are given in Appendix K.

- Vibration tests be performed on selected enclosures to determine how well they withstand, over their expected service life, vibration levels on typical mining machines.

- Before a Ruggedness Test is finalized, additional work is done to relate, if possible, damage to mining equipment produced by rock fall to the severity of the rock fall accident.

- Battery box covers be required to satisfy the requirements established for the Ruggedness Test, unless data from mine accidents shows that battery powered vehicles operate in a more benign environment than do mining machines. It is also recommended that new designs be evaluated for battery box covers which rely upon battery cell strength for support.

- Windows and lenses, particularly those made of glass, be protected from roof falls and side impacts.

10.0 REFERENCES

1. Code of Federal Regulations, Title 30, Mineral Resources, Part 18, Electric Motor Driven Mine Equipment and Accessories (revised as of July 1, 1977, also known as Schedule 2G).

2. U. S. Bureau of Mines Contract Number H0387009, "QA Standards for Bonding Materials Used in Explosion-Proof Enclosures," awarded to Southwest Research Institute under the technical direction of the Pittsburgh Mining and Safety Research Center, September 1978 (active as of December 1982).

3. Letter from Dr. G. J. DeSalvo to Dr. O. H. Burnside, dated November 1, 1977, and telephone conversations between Dr. DeSalvo and Dr. Burnside in November 1977.

4. Timoshenko, S., and Woinowsky-Kreiger, S., Theory of Plates and Shells, Second Edition, McGraw-Hill Book Company, New York, 1959.

5. Juvinal, R. C., Stress, Strain, and Strength, McGraw-Hill, 1967.

6. Leissa, A. W., Vibration of Plates, National Aeronautics and Space Administration Publication NASA SP-160, 1969.

7. Zabetakis, M. G., "Flammability Characteristics of Combustible Gases and Vapors," Bulletin 627, Bureau of Mines, 1965.

8. Biggs, J. M., Introduction to Structural Dynamics, McGraw-Hill Book Co., 1964.

9. Dann, R. T., "How Much Preload for Fasteners?," Machine Design, August 21, 1975, pp. 66-69.

10. Cobb, B. J., "Preloading of Bolts," Product Engineering, August 19, 1963, pp. 62-66.

11. Skidmore, R., "A Practical Approach to Accurate Determination of Thightening Torque for Bolts," Machine Design, January 9, 1958, pp. 133-136.

12. Shand, E. B., Glass Engineering Handbook, second edition, McGraw-Hill Book Company, Inc., New York, 1958.

13. Jones, N., and Walters, R. M., "Large Deflections of Rectangular Plates," Journal of Ship Research, Vol. 15, No. 2, June 1971.

14. Hodge, P. G., Plastic Analysis of Structures, McGraw-Hill Book Co., Inc., New York, 1959.

15. Jones, N., "A Literature Review of the Dynamic Plastic Response of Structures," The Shock and Vibration Digest, Vol. 7, No. 8, August 1975.

16. Jones, N., "Slamming Damage," Journal of Ship Research, Vol. 17, No. 2, June 1973.

17. Hooke, R., and Rawlings, B., "An Experimental Investigation of the Behavior of Clamped, Rectangular, Mild Steel Plates Subjected to Uniform Transverse Pressure," Proceedings, The Institute of Civil Engineers, Vol. 42, January 1969.

18. Alcoa Aluminum Handbook, Aluminum Company of America, Pittsburgh, Pennsylvania, 1957.

19. Frances, P. H. and Lankford, J., "Recommended Acceptance Testing Criteria for Adhesives and Sealants for Explosion-Proof Enclosures," Interium Technical Report prepared for the Bureau of Mines under USBM Contract No. H0387009, January 1980.

20. Patterson, W. N., Rubin, M. H., and Galaitsis, A. G., "Vibration Data for Continuous Miners," Report No. 3366, Contract No. HO-115113, U. S. Bureau of Mines, Pittsburgh, Pennsylvania, 1976.

21. Roark, R. J. and Young, W. G., Formulas for Stress and Strain, 1975, 5th Edition, McGraw-Hill Book Co.

22. Timoshenko, S. P., and Goodier, J. N., Theory of Elasticity, McGraw-Hill Book Company, Third Edition, 420-422, 1970.

23. Evans, A. G., "Strength Degradation by Projectile Impact," J. Amer. Ceram, Soc., 56 [8], Aug. 1973.

24. Huber, M. T., "Contribution to Theory of Contact of Elastic Solids," Ann. Physics, 14, 153-163 (1904).

25. Engel, P. A., Impact Wear of Materials, Elsevier Scientific Publishing Company, 1976.

26. Wilshaw, T. R., "The Hertzian Fracture Test," J. of Physics. Part D, Applied Physics, Vol. 4, 1971.

27. Kirchner, H. P., and Gruver, R. M., "Localized Impact Damage in Glass," Mat. Sci. & Enc., 28, 153-160 (1977).

28. Wiederhorn, S. M., and Lawn, B. R., "Strength Degradation of Glass Resulting from Impact with Spheres," J. of American Ceramic Soc., Sept., Oct. 1977.

29. Holman, J. P., Heat Transfer, McGraw-Hill Book Co., Inc., New York, 1972.

30. Arpaci, V. S., Conduction Heat Transfer, Addison-Wesley Publishing Co., 1966.

31. Kantorovich, L. V., and Krylov, V. I., Approximate Methods of Higher Analysis, New York - Groningen, Holland - Interscience-Noordhoof, 1958.

32. Boley, B. A., and Weiner, J. H., Theory of Thermal Stresses, John Wiley and Sons, Inc., 1960.

33. Carslaw, H. S., and Jaeger, J. C., Conduction of Heat in Solids, Oxford at the Clarendon Press, 1959.

34. Telephone Conversation between P. A. Cox, SwRI and Mr. Joe Uraco, MSHA, February 25, 1980. Letter from P. A. Cox, SwRI to Mr. Joe Uraco, MSHA, February 27, 1980.

35. Letter from Mr. R. J. Gunderman, Jeffery Mining, Machinery Division, Dresser Industries, Inc., to Mr. P. A. Cox, SwRI, January 18, 1980.

36. Terzaghi, Karl, Rock Defects and Loads on Tunnel Supports, republished in Rock Tunnelling with Steel Supports, by R. V. Proctor and T. L. White, Commerical Sheaving, Inc., Youngstown, Ohio, 1977.

37. Morley, L. A., "Battery and Battery-Charging Safety," Draft Final Report on USBM Grant Number G0155003, March 1980, (approximate date).

38. U. S. Congress Federal Coal Mine Health and Safety Act of 1969, Public Law 91-173, December 30, 1969, 83 Stat. 742.

39. "Design Criteria and Guidelines for Falling Object Protective Structures (FOPS)" Woodward Associates, Inc., Redlands, Calif., U.S. Dept. of Commerce Publication PB-259 254, 20 Feb. 1976.

40. Baker, W. E., Cox. P. A., Westine, P. S., Kulesz, J. J., and Strehlow, R. A., Explosion Hazards and Evaluation, Fundamental Studies in Engineering, Elsevier Scientific Publishing Co., Amsterdam, 1983.

41. Site visits and/or telephone conversations were held with the following individuals:

Mr. Marton Stanton
Mr. Frank Terrantino
Exride Power System Div.
Horshanna, PA

Mr. Franz Wagner
Mr. Jay Schaetzle
Mr. Tyrone Harris
C&D Batteries
Plymouth-Reading, PA

ANALYTICAL RESULTS FOR ENCLOSURE I

This appendix contains

- o stress contour plots
- o displacement plots
- o identification of elements with von Mises stress $\geq$ 36 ksi

for the cover, bottom, side, and back shell of Enclosure I. Refer to Figures 4.1 and 4.14 in Section 4.1.3 to identify the location and orientation of the components in the enclosure and the coordinate axes.

x = 11,327 psi
o = -2,494 psi
Contour Interval = 1,500 psi

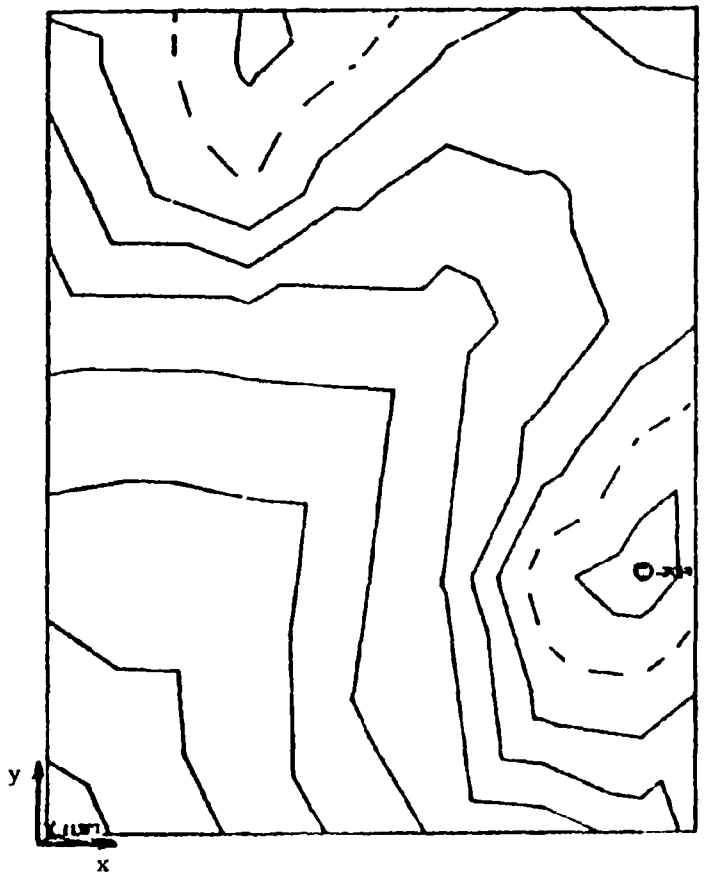

Maximum Stress

x = 8,323 psi
o = -7,723 psi
Contour Interval = 2,000 psi

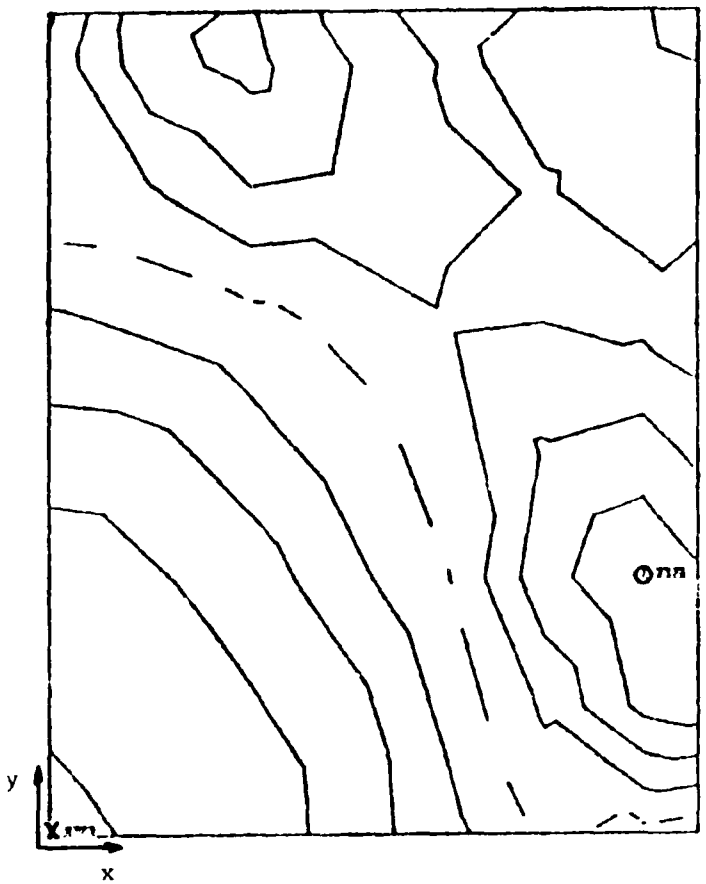

Minimum Stress

FIGURE A.1. PRINCIPAL STRESSES (OUTSIDE SURFACE) IN COVER

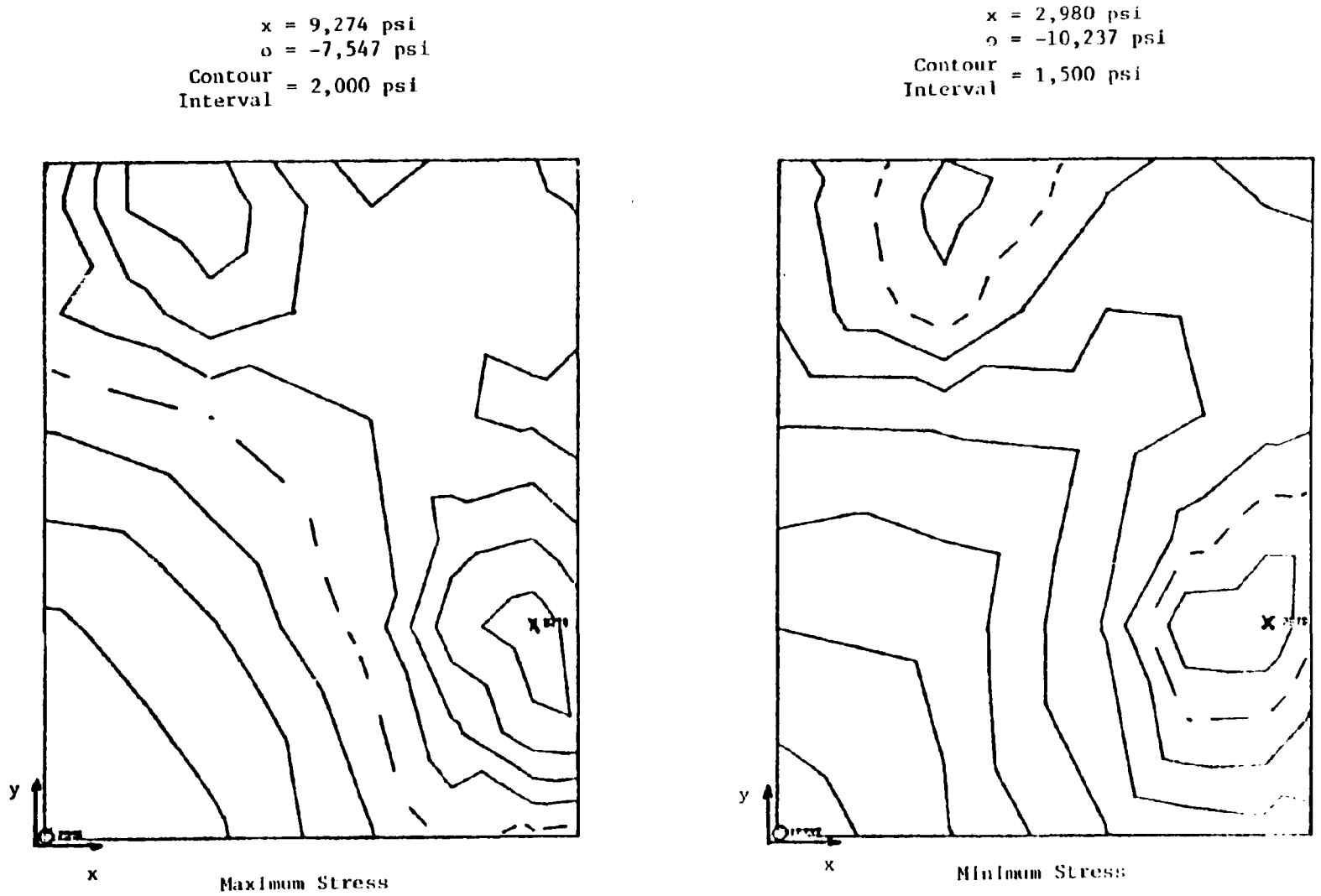

FIGURE A.2. PRINCIPAL STRESSES (INSIDE SURFACE) IN COVER

$x = 0.287 \times 10^{-1}$ in.

$o = -0.127 \times 10^{-3}$ in.

Contour Interval = 0.004 in.

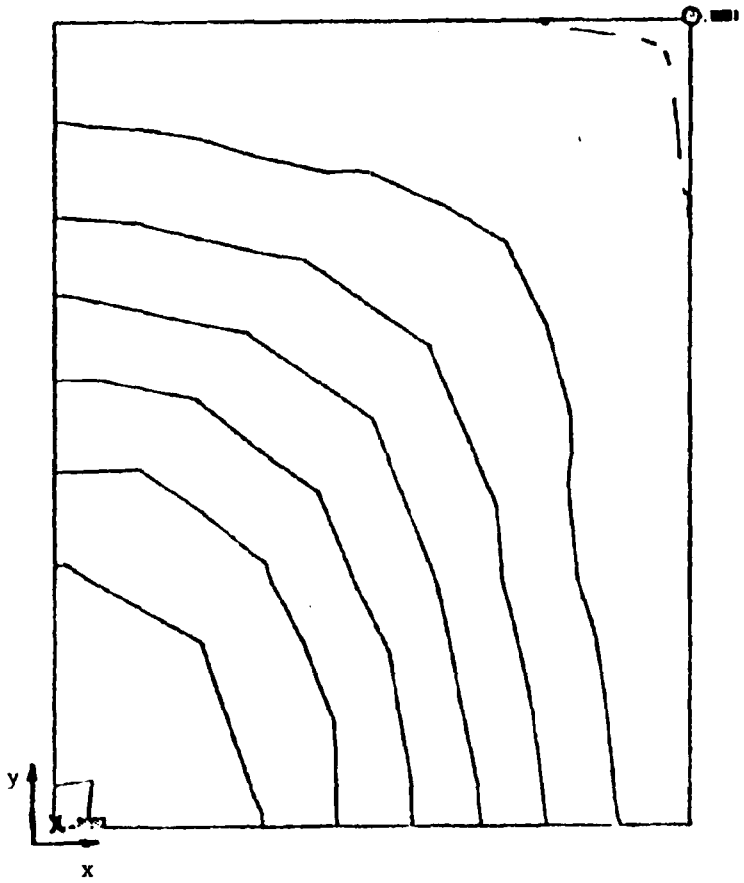

FIGURE A.3. PERPENDICULAR DISPLACEMENT IN COVER

x = 63,015 psi
o = -29,847 psi
Contour Interval = 10,000 psi

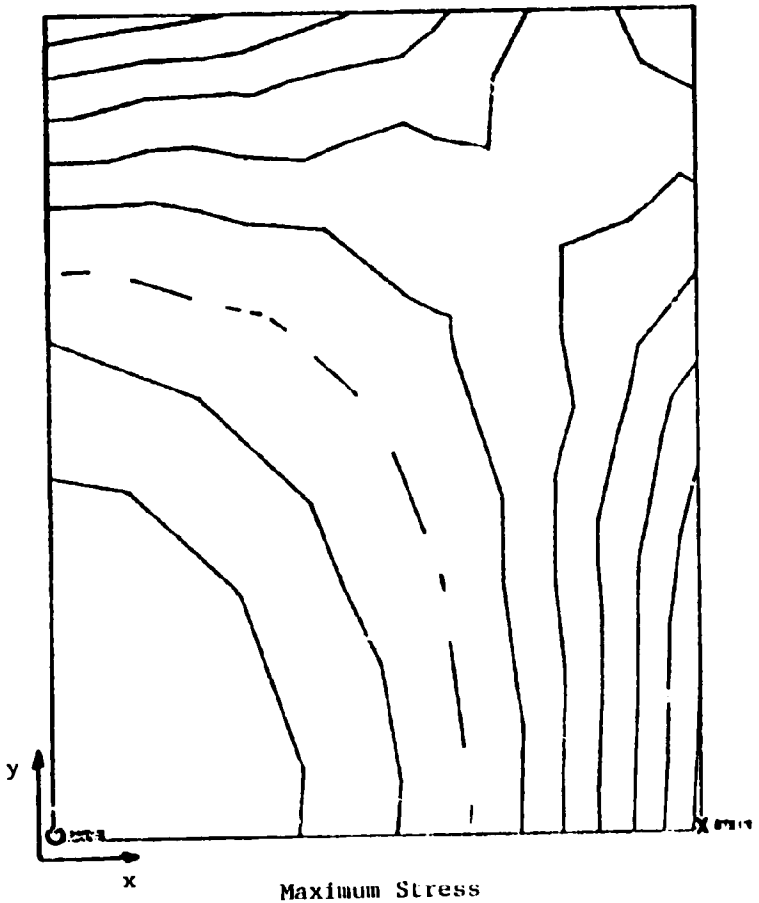

Maximum Stress

x = 19,443 psi
o = -43,591 psi
Contour Interval = 8,000 psi

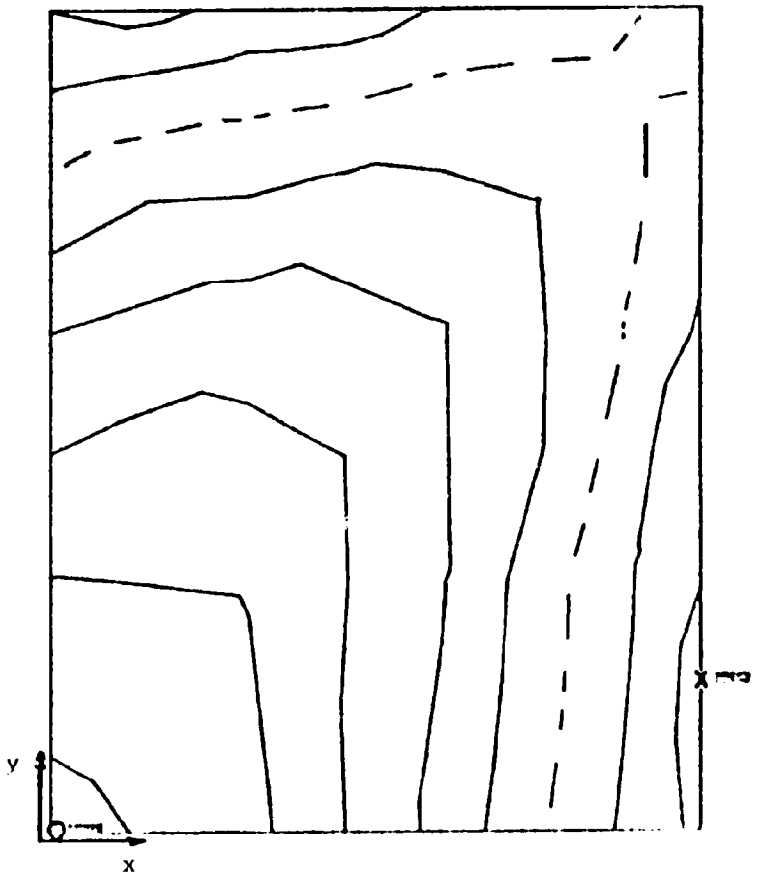

Minimum Stress

FIGURE A.4. PRINCIPAL STRESSES (INSIDE SURFACE) IN BOTTOM SHELL

x = 46,351 psi
o = -17,661
Contour Interval = 8,000 psi

x = 31,856 psi
o = -64,167 psi
Contour Interval = 15,000 psi

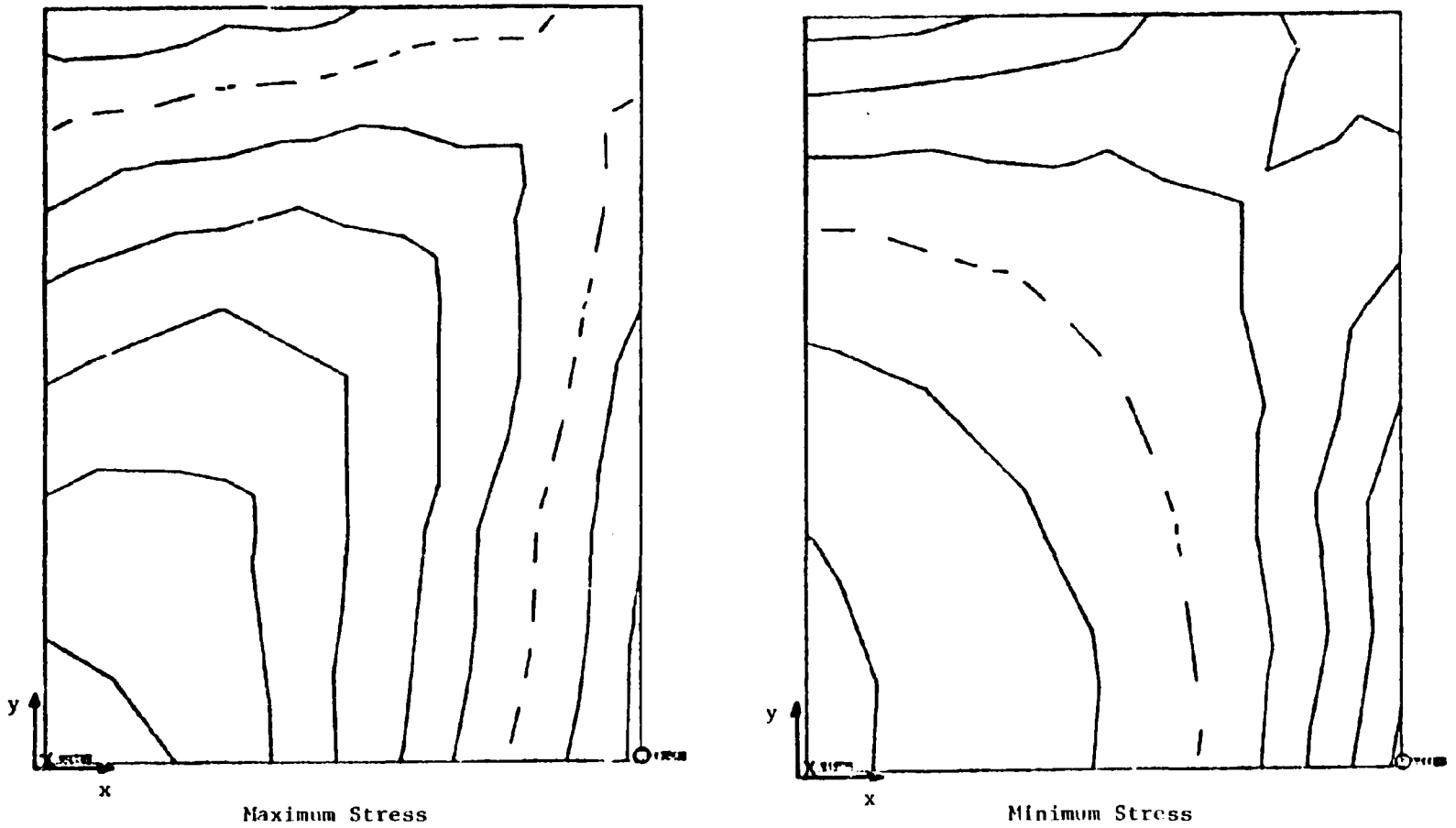

Maximum Stress

Minimum Stress

FIGURE A.5. PRINCIPAL STRESSES (OUTSIDE SURFACE) IN BOTTOM SHELL

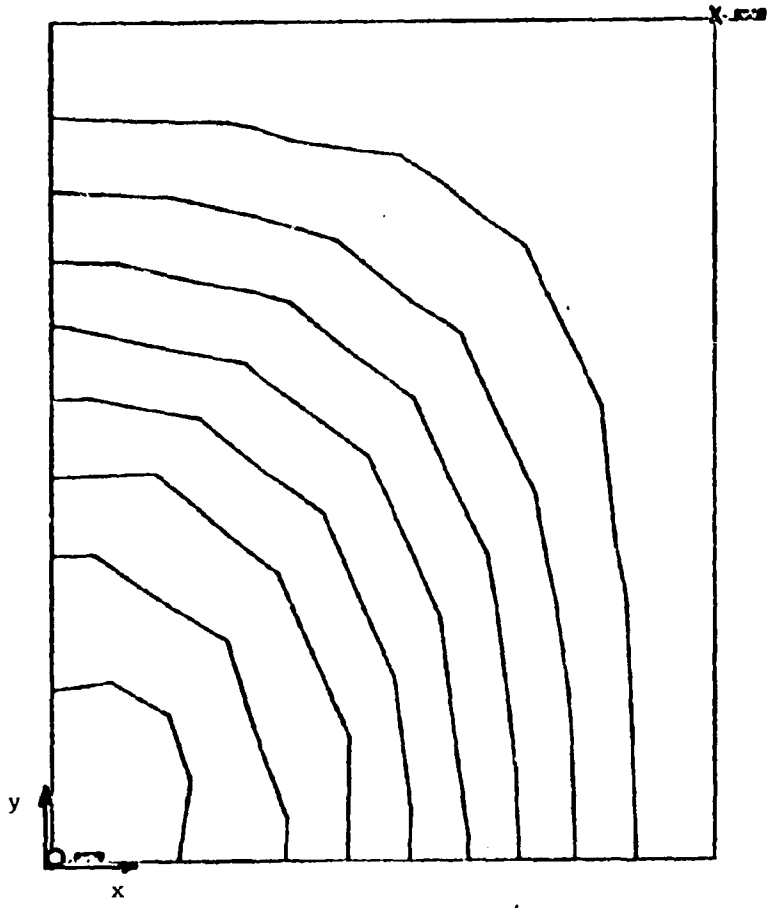

x = -0.459×10^{-4} in.

o = -0.879×10^{-1} in.

Contour Interval = 0.01 in.

FIGURE A.6. PERPENDICULAR DISPLACEMENTS IN BOTTOM SHELL

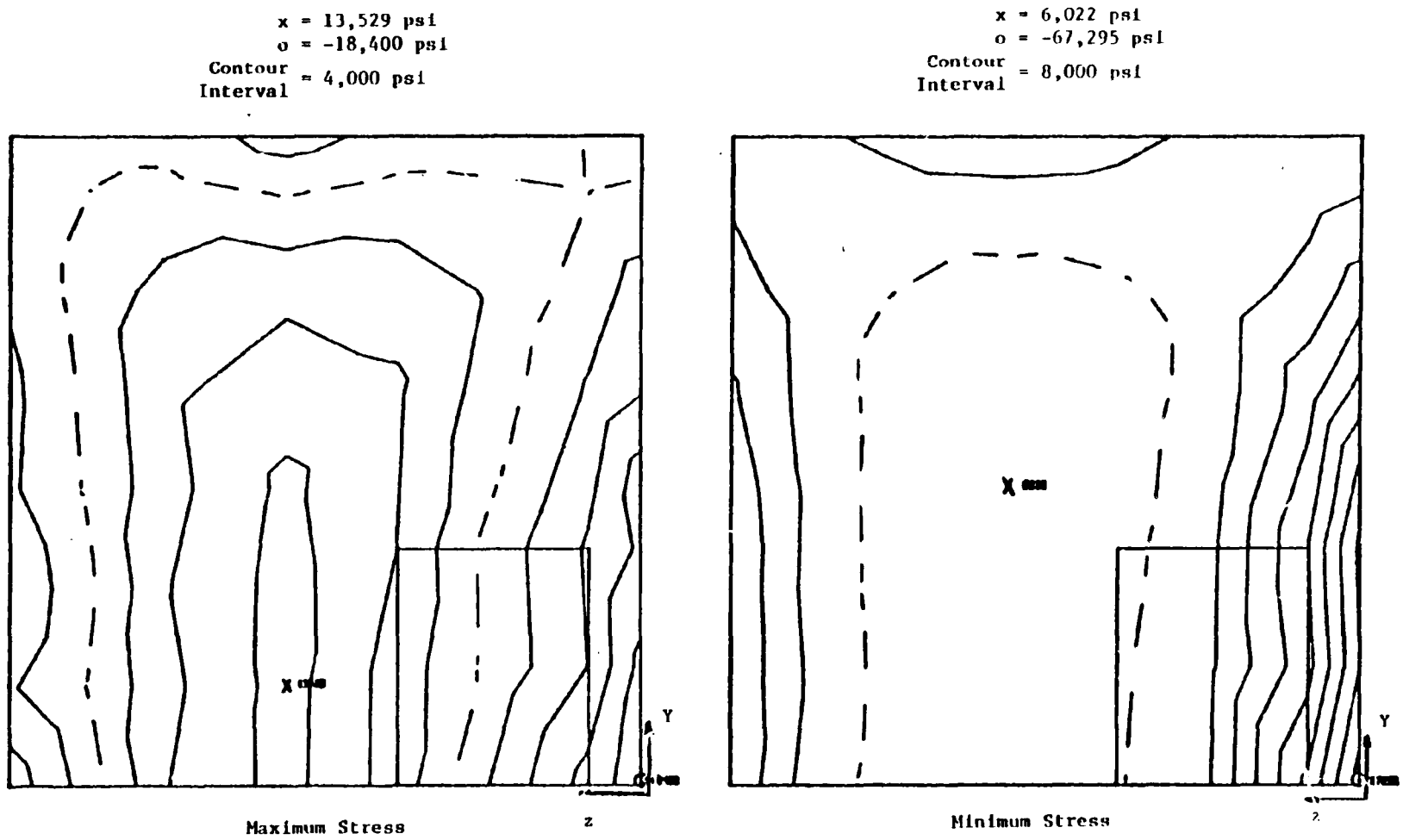

FIGURE A.7. PRINCIPAL STRESSES (OUTSIDE SURFACE) IN SIDE SHELL

x = 0.662×10^{-2} in.

o = -0.277×10^{-2} in.

Contour Interval = 0.001 in.

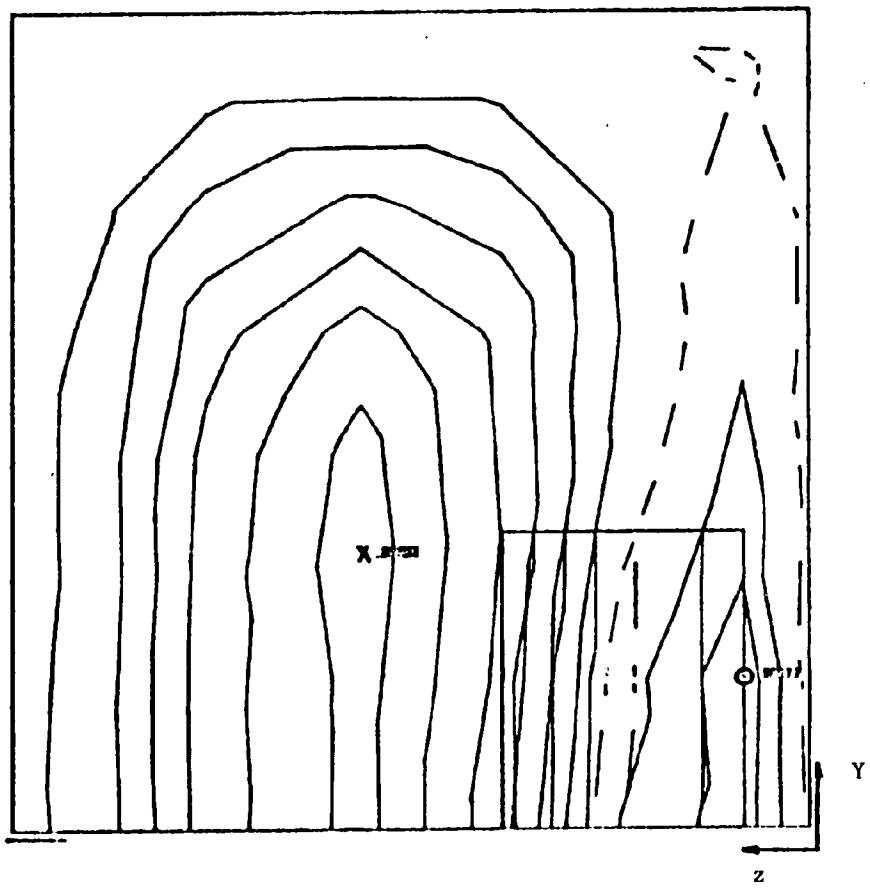

FIGURE A.8. PERPENDICULAR DISPLACEMENTS IN SIDE SHELL

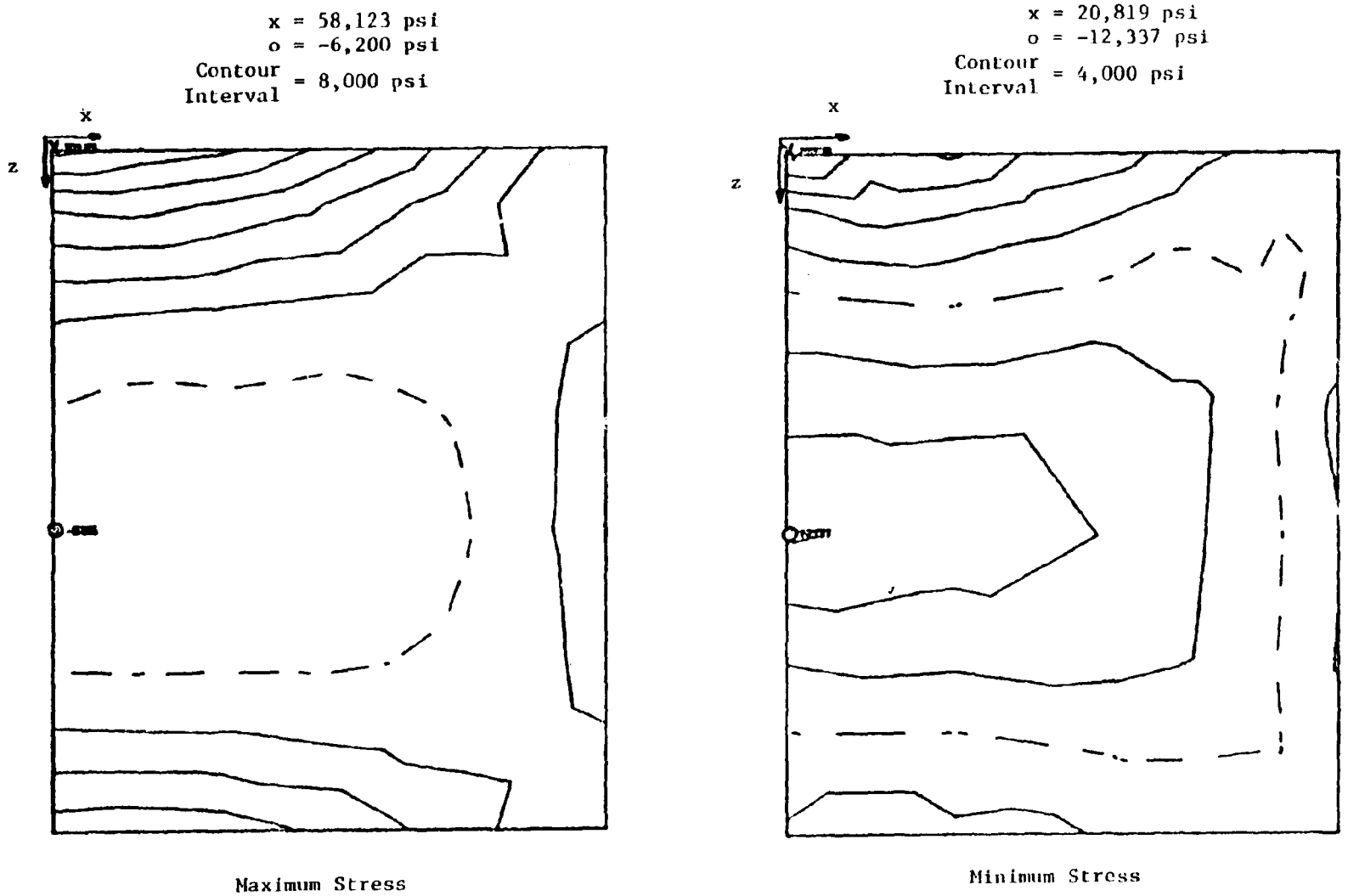

FIGURE A.9. PRINCIPAL STRESSES (INSIDE SURFACE) IN BACK SHELL

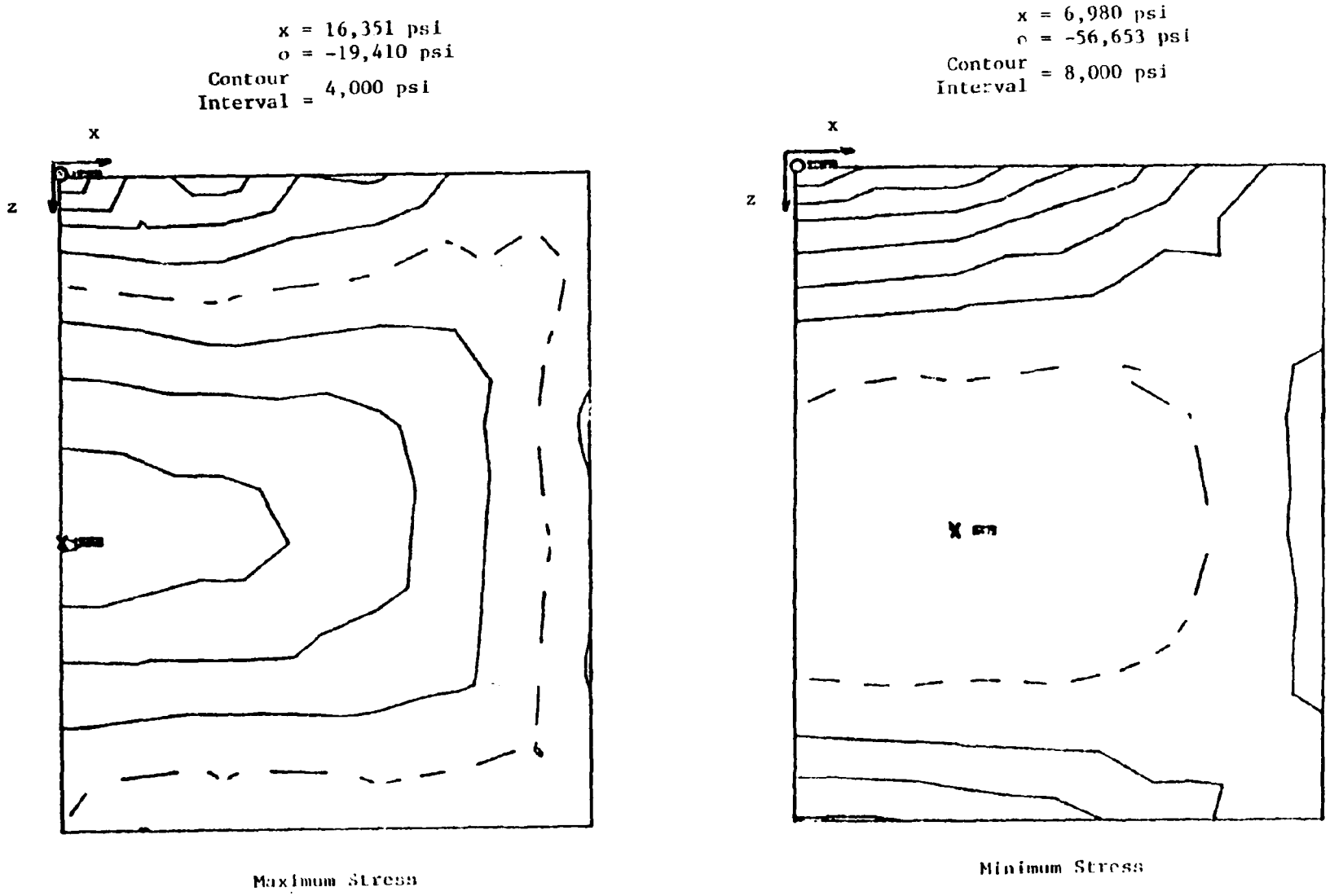

FIGURE A.10. PRINCIPAL STRESSES (OUTSIDE SURFACE) IN BACK SHELL

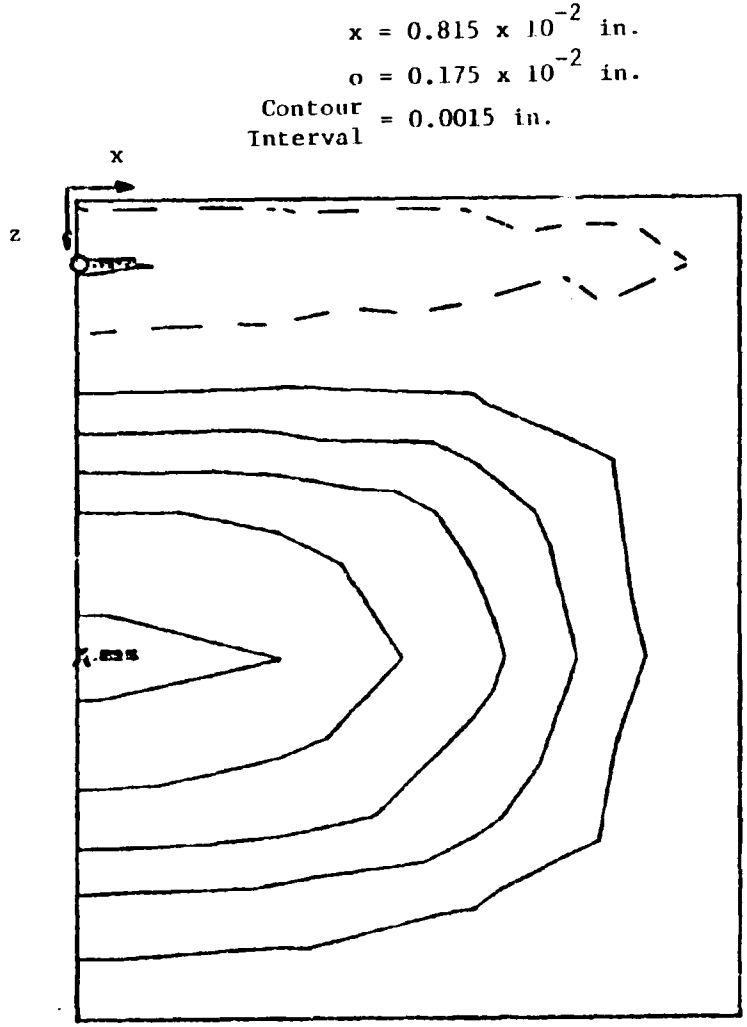

FIGURE A.11. PERPENDICULAR DISPLACEMENTS IN BACK SHELL

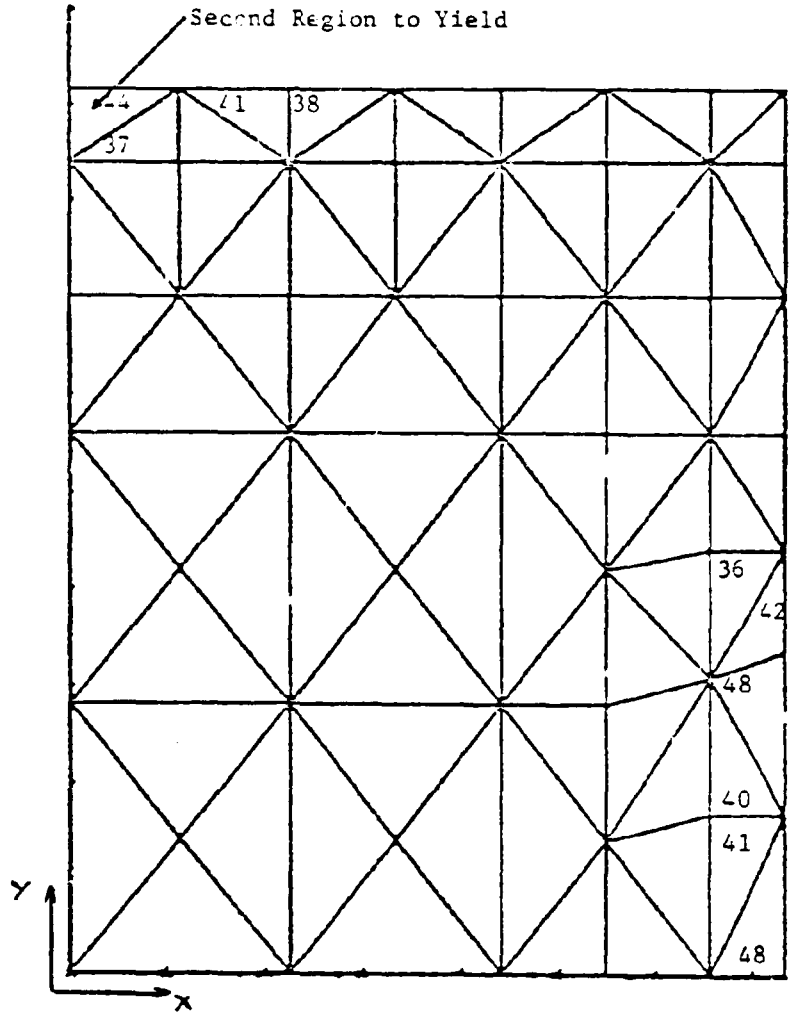

FIGURE A.12. ELEMENTS IN BOTTOM SHELL WITH VON MISES STRESSES EXCEEDING 36 KSI - INSIDE SURFACE

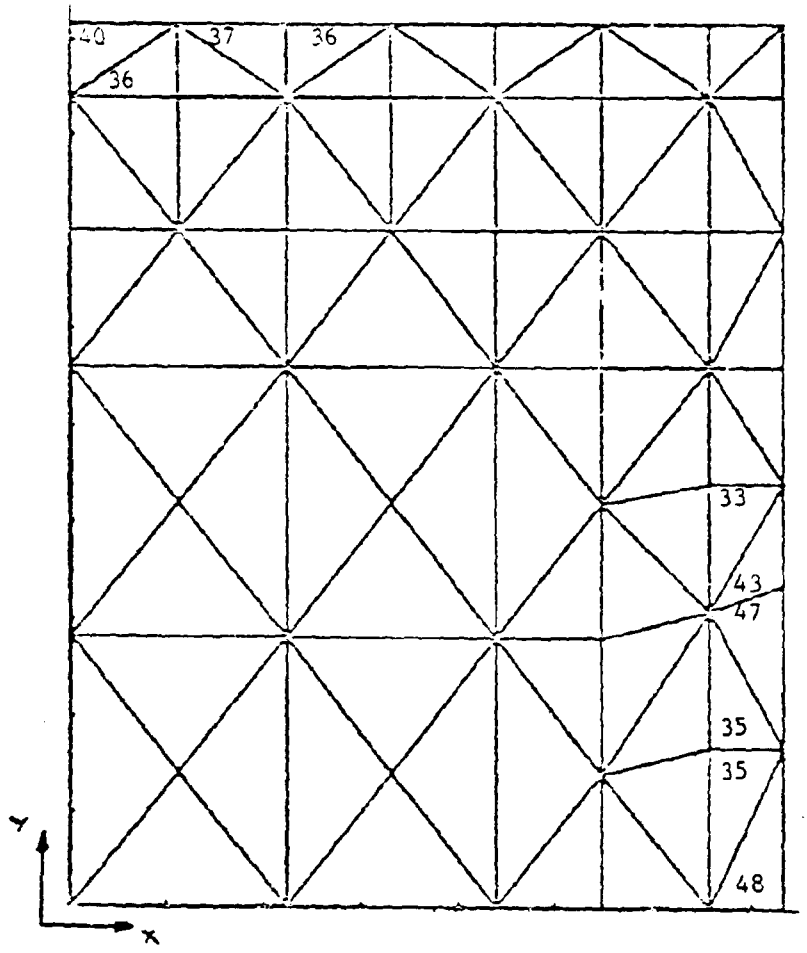

FIGURE A.13. ELEMENTS IN BOTTOM SHELL WITH VON MISES STRESSES EXCEEDING 36 KSI - OUTSIDE SURFACE

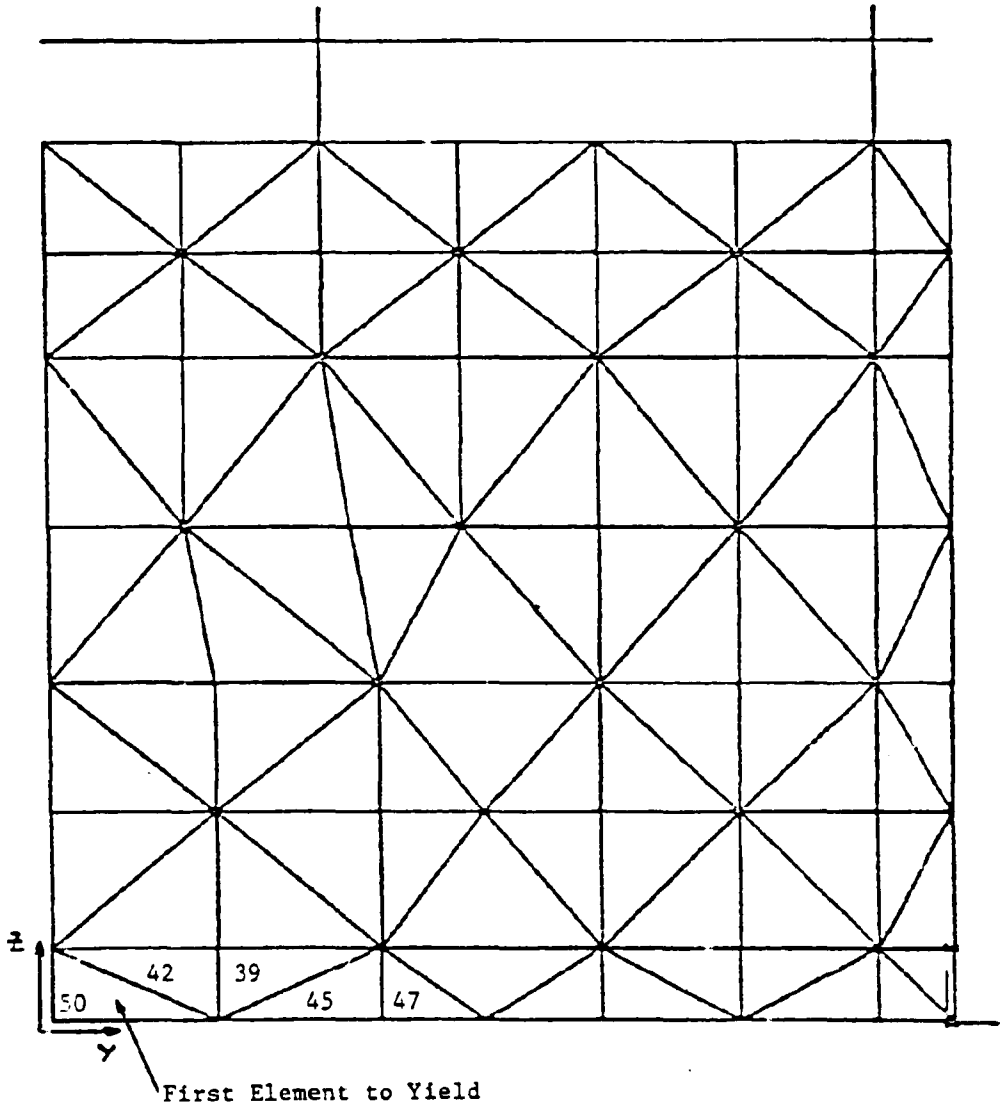

FIGURE A.14. ELEMENTS IN SIDE SHELL WITH VON MISES STRESSES EXCEEDING 36 KSI - INSIDE SURFACE

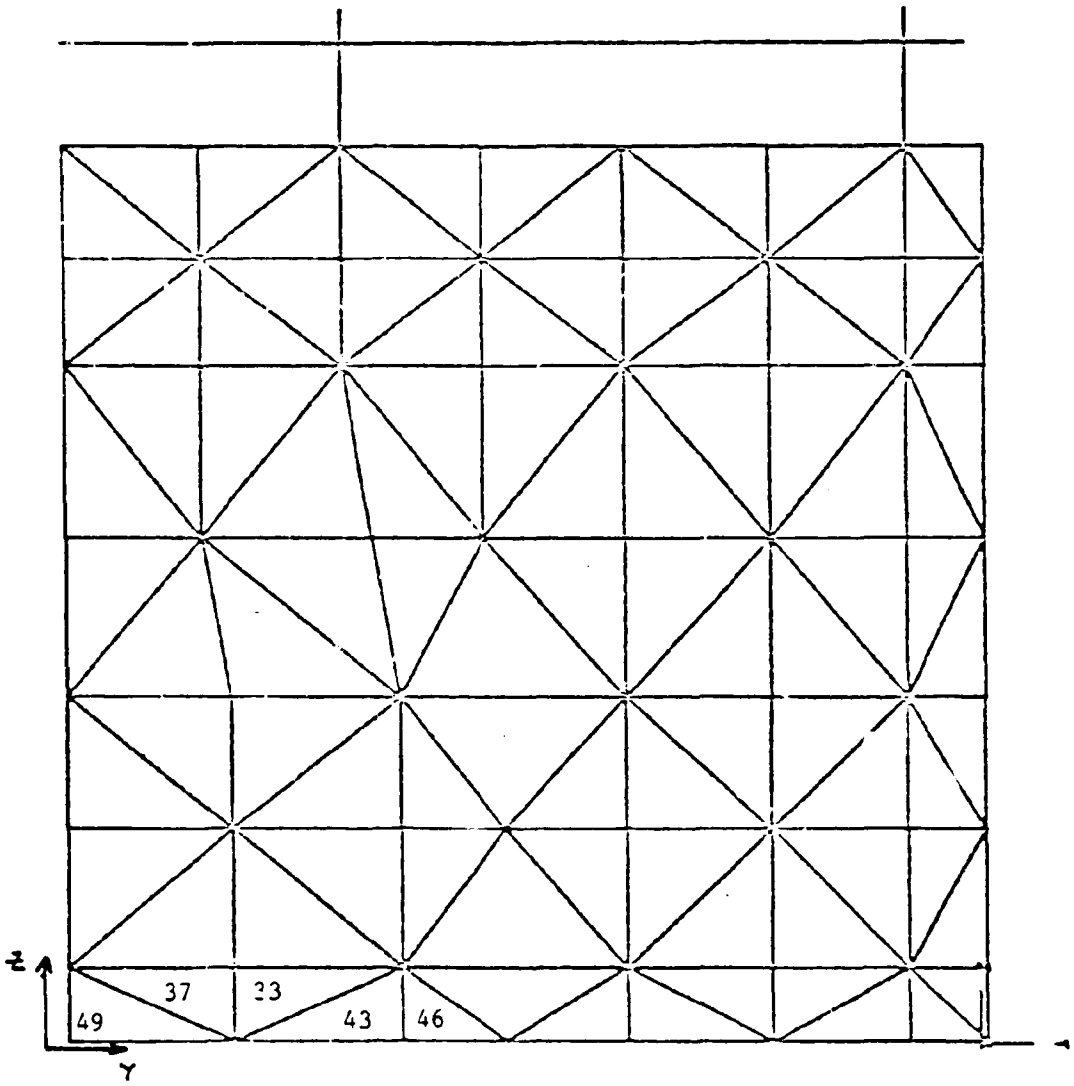

FIGURE A.15. ELEMENTS IN SIDE SHELL WITH VON MISES STRESSES EXCEEDING 36 KSI - OUTSIDE SURFACE

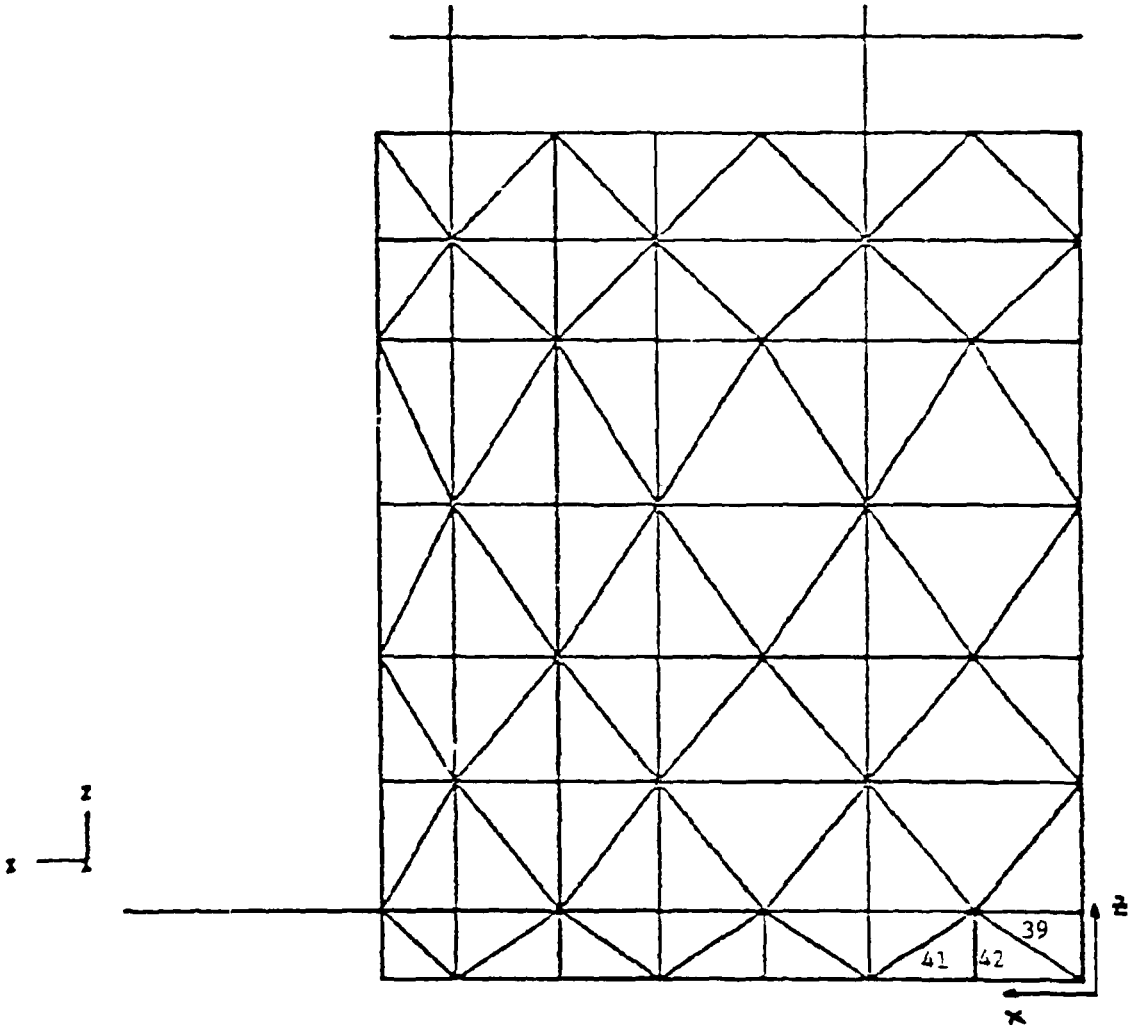

FIGURE A.16. ELEMENTS IN BACK SHELL WITH VON MISES STRESSES EXCEEDING 36 KSI - INSIDE SURFACE

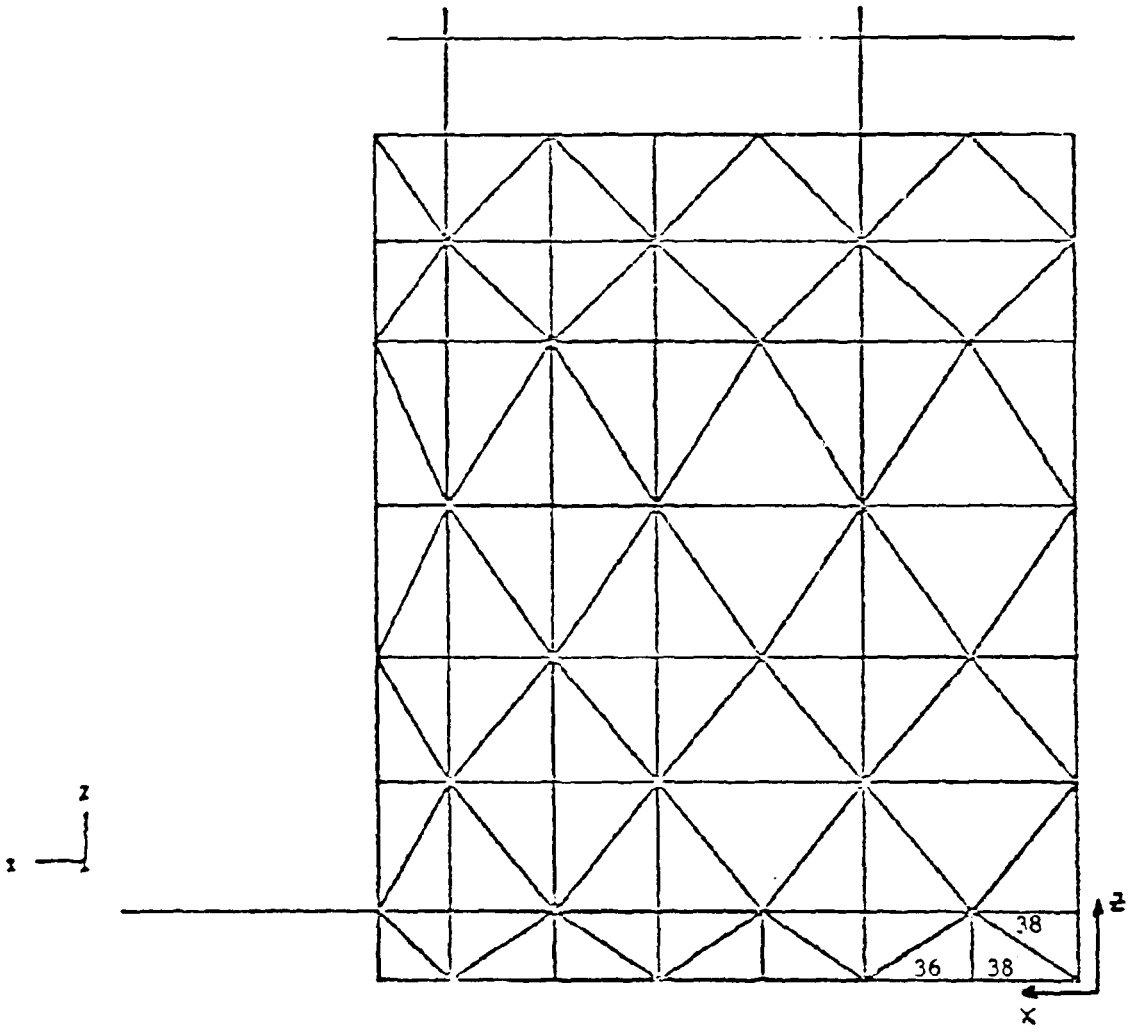

FIGURE A.17. ELEMENTS IN BACK SHELL WITH VON MISES STRESSES EXCEEDING 36 KSI - OUTSIDE SURFACE

APPENDIX B--SERIES SOLUTION FOR BOLT STRESSES

SERIES SOLUTION FOR BOLT STRESSES

This Appendix presents a means of computing bolt and cover stresses for simply supported rectangular covers with arbitrary bolt locations. An example problem is included based on Enclosure I, and the results are compared with the finite element computations for that enclosure. The effect of varying cover thickness is also demonstrated.

Solution Procedure

The analysis which follows is based upon several assumptions. The first concerns the boundary conditions at the edge of the cover. The cover is assumed to be simply supported, which means that all deflections and moments normal to the cover's edges are zero. Figure B.1 shows a schematic of a typical cover. The inside of the support flange is indicated by dashed lines, and the bolt locations correspond to those of Enclosure I. The boundary condition for moments on the free edge is well justified for this geometry. The boundary conditions for deflections assume that only the plate's edges contact the flange and that no gaps exist between the plate and flange. This last condition may not be satisfied for very thin covers with widely spaced bolts.

The second assumption requires that the bolt's elongation and slopes be equal to the cover's deflection and slopes at the individual bolt location. The bolt is also assumed to be completely fixed at its base and has no lateral deflection at the point it intersects the midplane of the cover. Figure B.2 illustrates the bolt's deformation pattern.

The assumption for the bolt deflections will be closely satisfied. However, the requirement that the bolt's and cover's slopes be equal depends on the thickness of the cover and the clearances between the bolt and its drilled hole in the cover. The analysis also does not consider the effects of the drilled bolt holes. The bolts are assumed to be attached to a solid cover at their discrete locations.

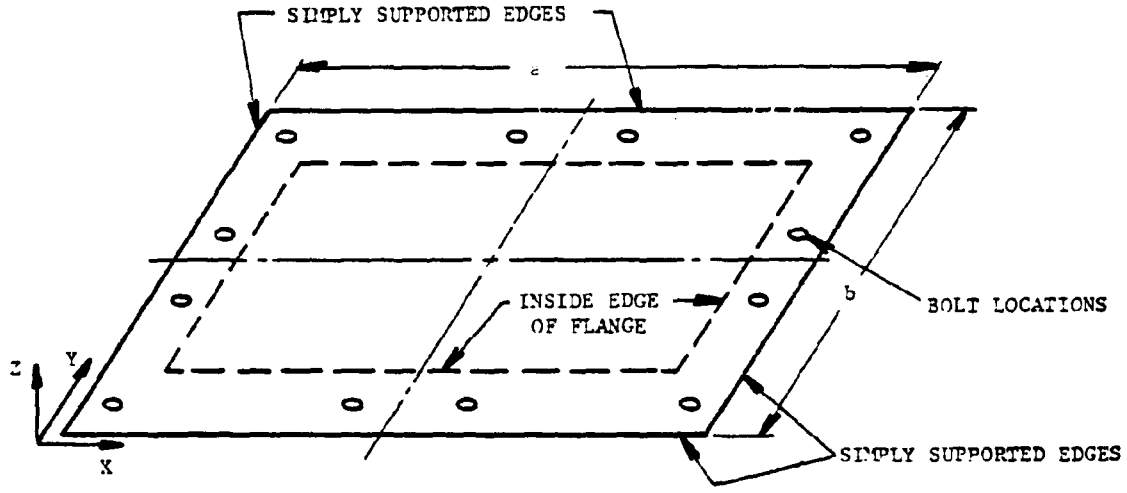

FIGURE B.1. GEOMETRY OF COVER WITH BOLT LOCATIONS

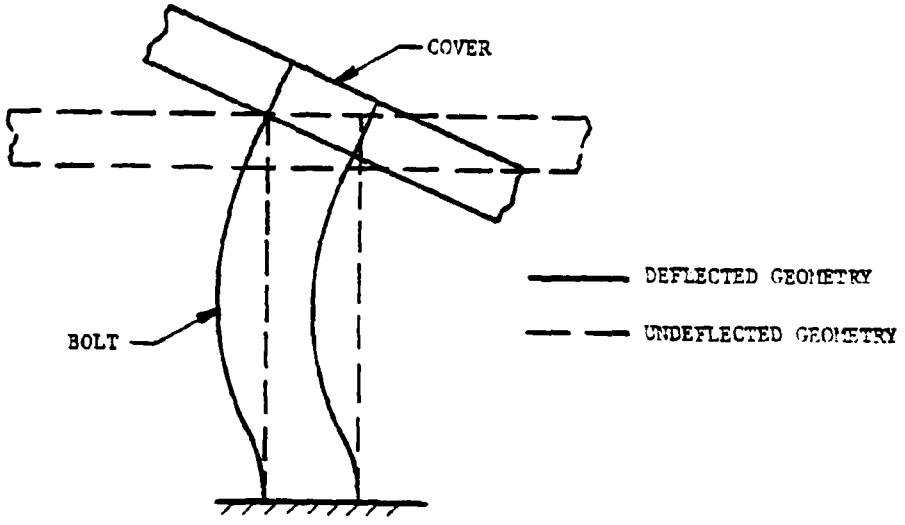

FIGURE B.2. DEFORMATION PATTERN OF BOLT AND COVER

The analysis requires that all stresses in the bolts and cover remain elastic. At the present time, this assumption is necessary to make the mathematical analysis tractable. This is conservative in that the computed safety factors will be smaller than the actual due to yielding in the bolts and plate. It may be possible to relax this restriction as the analytical techniques are further developed; however, for enclosures tested to date, the bolts and covers have remained elastic.

Since the determination of the safety factors in the bolts is based upon the foregoing assumptions, the analysis and solution techniques should be verified experimentally. This could be done by measuring strains in the bolts and deflections in the cover, as the enclosure is internally pressurized.

The simply supported plate shown in Figure B.1 represents the cover of Enclosure I and is loaded with a uniform internal pressure p_o. The deflection of the plate will be represented by a double sine series of the form

$$\omega(x,y) = \sum_{m=1}^{\infty} \sum_{n=1}^{\infty} a_{mn} \sin \alpha m X \sin \beta n y \qquad (B.1)$$

where

$$a_{mn} = \text{Fourier series coefficient} \qquad (B.2)$$

$$\alpha m = \frac{m\pi}{a}$$

$$\beta n = \frac{n\pi}{b}$$

For numerical computations the series will be truncated at a finite limit. The function $\omega(x,y)$ satisfies the boundary conditions that the deflection and moment vanish on the simply supported edges, i.e.,

$$\begin{aligned} \omega(o,y) &= 0 \\ \omega(a,y) &= 0 \\ \omega(x,o) &= 0 \\ \omega(x,b) &= 0 \end{aligned} \qquad (B.3)$$

and

$$
\begin{aligned}
M_x(o,y) &= -D\left[\frac{\partial^2\omega(o,y)}{\partial x^2} + \nu\,\frac{\partial^2\omega(o,y)}{\partial y^2}\right] = 0 \\
M_x(a,y) &= -D\left[\frac{\partial^2\omega(a,y)}{\partial x^2} + \nu\,\frac{\partial^2\omega(a,y)}{\partial y^2}\right] = 0 \\
M_y(x,o) &= -D\left[\frac{\partial^2\omega(x,o)}{\partial y^2} + \nu\,\frac{\partial^2\omega(x,o)}{\partial x^2}\right] = 0 \\
M_y(x,b) &= -D\left[\frac{\partial^2\omega(x,b)}{\partial y^2} + \nu\,\frac{\partial^2\omega(x,b)}{\partial y^2}\right] = 0
\end{aligned}
\tag{B.4}
$$

where D is the flexural rigidity of the plate

$$D = \frac{Eh^3}{12(1 - \nu^2)} \tag{B.5}$$

and

E = modulus of elasticity

ν = Poisson's ratio

h = plate thickness

M_x and M_y = the bending moments per unit length in the x and y directions

The Fourier coefficients a_{mn} will be determined by evaluating the total potential energy of the system and using the principle of stationary potential energy. If we let

U_b = strain energy in bending for the plate

U_f = strain energy for the bolts (fasteners)

Ω = potential energy of the internal pressure p_o

then the total potential energy of the system is

$$\pi = U_b + U_f + \Omega \tag{B.6}$$

The principle of stationary potential energy says that, for equilibrium

$$\delta\pi = \delta(U_b + U_f + \Omega) = 0 \tag{B.7}$$

where $\delta(\pi)$ is the first variation [B.1].

The strain energy of bending in the cover can be shown to be [B.2]

$$U_b = \frac{D}{2} \iint_{\text{area}} \left[(W_{xx} + W_{yy})^2 - 2(1 - \nu) \, (W_{xx} W_{yy} - W_{xy}^2) \right] dxdy \qquad (B.8)$$

The subscripts indicate partial differentiation with respect to the indicated variables. In terms of the assumed deflection shape for $\omega(x,y)$, Equation (B.8) can be evaluated to be

$$U_b = \frac{abD}{8} \sum_{m=1}^{\infty} \sum_{n=1}^{\infty} \left[(\alpha m^2 + \beta n^2)^2 \, a_{mn}^2 \right] \qquad (B.9)$$

or

$$U_b = \frac{abD\pi^4}{8} \sum_{m=1}^{\infty} \sum_{n=1}^{\infty} \left[\left(\frac{m^2}{a^2} + \frac{n^2}{b^2} \right)^2 a_{mn}^2 \right]$$

The potential energy of the constant applied pressure p_o is

$$\begin{aligned} \Omega &= \int_A \int -p_o \, \omega(x,y) \, dxdy \\ &= -p_o \int_A \int \left[\sum_{m=1}^{\infty} \sum_{n=1}^{\infty} a_{mn} \sin \alpha m X \sin \beta n y \right] dxdy \\ &= -p_o \sum_{m=1}^{\infty} \sum_{n=1}^{\infty} \frac{a_{mn}}{\alpha m \beta n} \cos \alpha m X \Big|_o^a \cos \beta n y \Big|_o^b \qquad (B.10) \\ &= -4p_o \sum_{m=1}^{\infty} \sum_{n=1}^{\infty} \frac{a_{mn}}{\alpha m \beta n} \\ &= \frac{-4p_o ab}{\pi^2} \sum_{m=1}^{\infty} \sum_{n=1}^{\infty} \frac{a_{mn}}{mn} \end{aligned}$$

where $a_{mn} = 0$ (for m or n odd)

To compute the strain energy in a typical bolt, we will assume that the bolt is fixed at its base and subjected to the axial force P; lateral shearing forces, V_{XT} and V_{YT}; and bending moments, M_{XT} and M_{YT}, shown in Figure B.3. The moments and shear forces at any section Z are

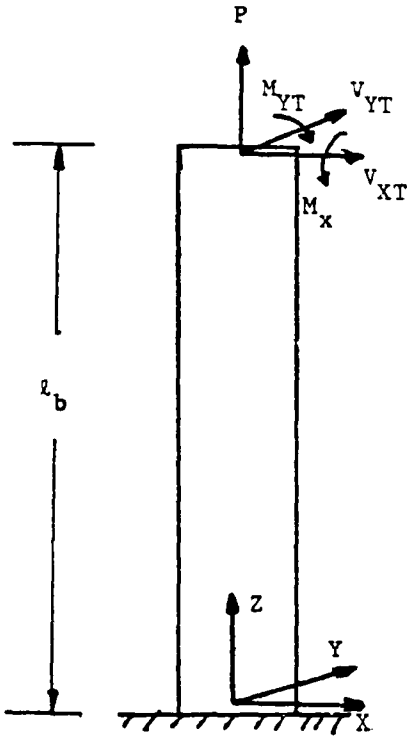

FIGURE B.3. GEOMETRY AND LOADING
FOR TYPICAL BOLT

$$
\begin{aligned}
M_x(z) &= M_{xT} - (\ell - z)\, V_{yT} \\
M_y(z) &= M_{yT} - (\ell - z)\, V_{xT} \\
V_x(z) &= V_{xT} \\
V_y(z) &= V_{yT}
\end{aligned}
\tag{B.11}
$$

where the subscript T denotes the top of the bolt. The strain energy can be expressed as the sum due to bending, shear, and axial elongation, i.e.,

$$
\begin{aligned}
U_f = {} & \frac{1}{2E_b I_b} \int_0^{\ell_b} [M_x^2(z) + M_y^2(z)]\,dz \\
& + \frac{Ks}{2A_b G_b} \int_0^{\ell_b} [V_x^2(z) + V_y^2(z)]\,dz \\
& + \frac{P^2 \ell_b}{2A_b E_b}
\end{aligned}
\tag{B.12}
$$

where

E_b = modulus of elasticity for bolt

G_b = shear modulus $\left(G = \frac{E}{2\,(1 + \nu)}\right)$

A_b = bolt cross-sectional area

I_b = area moment of inertia about any diameter

K_s = shear shape factor ($K_s = \frac{4}{3}$ for a circular cross-section)

ℓ_b = length of bolt

If the moments and shears in (B.11) are substituted into (B.12), evaluation of the integrals yields

$$U_f = \frac{\ell_b}{2E_b I_b}\left[M_{xT}^2 - M_{xT}\,V_{yT}\,\ell_b + \frac{\ell_b^2}{3}\,V_{yT}^2 + M_{yT}^2 + M_{yT}\,V_{xT}\,\ell_b + \frac{\ell_b^2}{3}\,V_{xT}^2\right] + \frac{K_s \ell_b}{2A_b G_b}\left[V_{xT}^2 + V_{yT}^2 + \frac{P^2 \ell_b}{2A_b E_b}\right] \tag{B.13}$$

The deflections and angular rotations may now be determined by using Castigliano's theorem, which states [B.3].

> When forces operate on an elastic system, the displacements corresponding to any force may be found by obtaining the partial derivative of the total strain energy with respect to that force, i.e.,

$$\delta_i = \frac{\partial \pi}{\partial F_i} \tag{B.14}$$

δ_i is the deflection at the point of application of F_i in the direction of F_i. From Equation (B.13), the generalized deflections at the top of the bolt can be expressed as

$$\delta_{xT} = \frac{\ell_b}{2E_b I_b}\left[M_{yT}\,\ell_b + \frac{2\ell_b^2}{3}\,V_{xT}\right] + \frac{K_s\,\ell_b\,V_{xT}}{A_b G_b} \tag{B.15}$$

$$\delta_{mT} = \frac{\ell_b}{2E_b I_b}\left[-M_{xT}\,\ell_b + \frac{2}{3}\,\ell_b^2\,V_{yT}\right] + \frac{K_s\,\ell_b\,V_{mT}}{A_b G_b} \tag{B.16}$$

$$\delta_{zT} = \frac{P\ell_b}{A_b E_b} \tag{B.17}$$

$$\frac{\partial \delta_{xT}}{\partial_x} = \theta_x = x - \text{slope at top} = \frac{\partial v}{\partial M_{yT}} = \frac{\ell_b}{2E_b I_b}\left[2M_{yT} + V_{xT}\,\ell_b\right] \tag{B.18}$$

$$\frac{\partial \delta_{yT}}{\partial_y} = \theta_y = y - \text{slope at top} = -\frac{\partial v}{\partial M_{xT}} = \frac{\ell_b}{2E_b I_b}\left[2M_{xT} - V_{yT}\,\ell_b\right] \tag{B.19}$$

If we assume that the lateral displacements at the top of the bolt are zero, then

$$\delta_{xT} = \delta_{yT} = 0 \tag{B.20}$$

and from Equations (B.15) and (B.16)

$$M_{yT} = -\left[\frac{2E_b I_b K_s}{A_b G_b \ell_b} + \frac{2}{3}\ell_b\right] V_{xT} = -\left[\frac{6E_b I_b K_s + 2A_b G_b \ell_b^2}{3A_b G_b \ell_b}\right] V_{xT} \tag{B.21}$$

$$M_{xT} = \left[\frac{2E_b I_b K_s}{A_b G_b \ell_b} + \frac{2}{3}\ell_b\right] V_{uT} = \left[\frac{6E_b I_b K_s + 2A_b G_b \ell_b^2}{3A_b G_b \ell_b}\right] V_{yT} \tag{B.22}$$

By substituting Equations (B.21) and (B.22) into (B.18) and (B.19), the slopes can be expressed only in terms of the moments at the top of the bolts

$$\theta_x = \frac{\ell_b}{2E_b I_b}\left[2 - \frac{3A_b G_b \ell_b^2}{6E_b I_b K_s + 2A_b G_b \ell_b^2}\right] M_{yT}$$

$$= \frac{\ell_b}{2E_b I_b}\left[\frac{12E_b I_b K_s + A_b G_b \ell_b^2}{6E_b I_b K_s + 2A_b G_b \ell_b^2}\right] M_{yT} \qquad \text{(B.23)}$$

$$= -\frac{\ell_b^2}{2E_b I_b}\left[\frac{12E_b I_b K_s + A_b G_b \ell_b^2}{3A_b G_b \ell_b^2}\right] V_{xT}$$

$$\theta_y = -\frac{\ell_b}{2E_b I_b}\left[2 - \frac{3A_b G_b \ell_b^2}{6E_b I_b K_s + 2A_b G_b \ell_b^2}\right] M_{xT}$$

$$= -\frac{\ell_b}{2E_b I_b}\left[\frac{12E_b I_b K_s + A_b G_b \ell_b^2}{6E_b I_b K_s + 2A_b G_b \ell_b^2}\right] M_{xT} \qquad \text{(B.24)}$$

$$= -\frac{\ell_b^2}{2E_b I_b}\left[\frac{12E_b I_b K_s + A_b G_b \ell_b^2}{3A_b G_b \ell_b^2}\right] V_{yT}$$

If the constants C_1, C_2, and C_3 are defined as:

$$C_1 = 12E_b I_t K_s + A_b G_b \ell_b^2$$

$$C_2 = 6E_b I_b K_s + 2A_b G_b \ell_b^2 \qquad \text{(B.25)}$$

$$C_3 = 3A_b G_b \ell_b^2$$

Equations (B.23) and (B.24) can be rewritten as:

$$\theta_x = \frac{\ell_b}{2E_b I_b}\frac{C_1}{C_2} M_{yT} \qquad \text{(B.26)}$$

$$= -\frac{\ell_b^2}{2E_b I_b}\frac{C_1}{C_3} V_{xT}$$

$$\theta_y = -\frac{\ell_b}{2E_bI_b}\frac{C_1}{C_2}M_{xT}$$

$$= -\frac{\ell_b^2}{2E_bI_b}\frac{C_1}{C_3}V_{yT} \qquad (B.27)$$

The above equations can be substituted into Equation (B.13) so that the total strain energy in the bolt can be expressed in terms of the rotations and axial displacement at the top

$$U_f = \frac{2E_bI_b}{\ell_b^2 C_1^2}\left[C_2^2 - C_2C_3 + \frac{1}{3}C_3^2\right]\left[\theta_x^2 + \theta y^2\right]$$

$$+ \frac{K_s\ell_b}{2A_bG_b}\left[\frac{2E_bI_bC_3}{\ell_b^2C_1}\right]^2\left[\theta_x^2 + \theta_y^2\right] \qquad (B.28)$$

$$+ \frac{A_bE_b\delta_{zT}^2}{2\ell_b}$$

Equation (B.28) can be simplified to

$$U_f = \frac{2E_bI_b}{\ell_b}\left[\frac{(12E_bI_bK_s + A_bG_b\ell_b^2)}{(12E_bI_bK_s + A_bG_b\ell_b^2)^2}\right]$$

$$x\ [3E_bI_bK_s + A_bG_b\ell_b^2]\ [\theta_x^2 + \theta_y^2] \qquad (B.29)$$

$$+ \frac{A_bE_b\delta_{zT}^2}{2\ell_b}$$

$$= \frac{E_bI_b}{2\ell_b}\left[\frac{12E_bI_bK_s + 4A_bG_b\ell_b^2}{12E_bI_bK_s + A_bG_b\ell_b^2}\right]$$

$$x\ [\theta_x^2 + \theta_y^2] + \frac{A_bE_b\delta_{zT}^2}{2\ell_b} \qquad (B.30)$$

Equation (B.30) yields the expected results that the strain energy in a bolt can be represented by a quadratic form in the displacement and rotation at the top of the bolt.

The total potential energy can now be written as

$$\pi = U_b + U_f + \Omega$$

$$= \frac{abD\pi^4}{8} \sum_{m=1}^{\infty} \sum_{n=1}^{\infty} \left[\left(\frac{m^2}{a^2} + \frac{n^2}{b^2} \right)^2 a_{mn}^2 \right]$$

$$+ K_1 \sum_{i=1}^{N} \left[\left(\sum_{m=1}^{\infty} \sum_{n=1}^{\infty} \frac{m\pi}{a} a_{mn} \cos \alpha m X_i \sin \beta_r Y_i \right)^2 \right.$$

$$\left. + \left(\sum_{m=1}^{\infty} \sum_{n=1}^{\infty} \frac{n\pi}{b} a_{mn} \sin \alpha m X_i \cos \beta_r Y_i \right) \right]^2 \qquad \text{(B.31)}$$

$$+ K_2 \sum_{i=1}^{N} \left(\sum_{m=1}^{\infty} \sum_{n=1}^{\infty} a_{mn} \sin \alpha m X_i \sin \beta_r Y_i \right)^2$$

$$- \frac{4p_o ab}{\pi^2} \sum_{m=1}^{\infty} \sum_{n=1}^{\infty} \frac{a_{mn}}{mn} \varepsilon_{mn}$$

where X_i, Y_i = location of i-th bolt

N = number of bolts

$$K_1 = \frac{E_b I_b}{2\ell_b} \left(\frac{12E_b I_b K_s + 4A_b G_b \ell_b^2}{12E_b I_b K_s + A_b G_b \ell_b^2} \right)$$

$$K_2 = \frac{A_b E_b}{2\ell_b}$$

$$\varepsilon_{mn} = \begin{cases} 1 \text{ if m } \underline{\text{and}} \text{ n odd} \\ 0 \text{ otherwise} \end{cases}$$

All bolts are assumed to have the same geometry and mechanical properties.

The principle of stationary potential energy, i.e.,

$$\delta\pi = \delta(U_b + U_f + \Omega) \tag{B.32}$$

can be expressed by taking the partial derivative of Equation (B.31) with respect to the generalized coordinate a_{pq}.

This yields

$$\begin{aligned}
&\frac{abD\pi^4}{4}\left[\left(\frac{p^2}{a^2}+\frac{q^2}{b^2}\right)^2 a_{pq}\right] \\
&+ 2K_1 \sum_{i=1}^{N}\left[\left(\sum_{m=1}^{\infty}\sum_{n=1}^{\infty}\frac{m\pi}{a}a_{mn}\cos\alpha m X_i \sin\beta n Y_i\right)\right. \\
&\left.\times\left(\frac{p\pi}{a}\cos\alpha p X_i \sin\beta q Y_i\right)+\left(\sum_{m=1}^{\infty}\sum_{n=1}^{\infty}\frac{n\pi}{b}a_{mn}\right.\right. \\
&\left.\left.\sin\alpha m X_i \cos\beta n Y_i\right)\left(\frac{q\pi}{b}\sin\alpha p X_i \cos\beta q Y_i\right)\right] \\
&+ 2K_2 \sum_{i=1}^{N}\left[\sum_{m=1}^{\infty}\sum_{n=1}^{\infty}a_{mn}\sin\alpha m X_i \sin\beta n Y_i\right] \\
&\times[\sin\alpha p X_i \sin\beta q Y_i] - \frac{4p_o ab\varepsilon_{pq}}{\pi^2 pq} = 0
\end{aligned} \tag{B.33}$$

Expression (B.33) represents an infinitely squared set of linear algebraic equations for the coefficients a_{pq}. To obtain a solution, the integer subscripts m and n must be truncated at a finite value. If m and n range from 1 to N, then expression (B.33) reduced to a set of N^2 equations. After the coefficients a_{pq} have been calculated, the deflections and stresses in the bolts and cover can be evaluated. This will be addressed in the discussion which follows.

The deflection and slope of the plate can be expressed as

$$\omega(x,y) = \sum_{m=1}^{N} \sum_{n=1}^{N} a_{mn} \sin \frac{m\pi x}{a} \sin \frac{n\pi y}{b} \tag{B.34}$$

$$\theta_x = \frac{\partial w}{\partial x} \sum_{m=1}^{N} \sum_{n=1}^{N} \frac{m\pi}{a} a_{mn} \cos \frac{m\pi x}{a} \sin \frac{n\pi y}{b} \tag{B.35}$$

$$\theta_y = \frac{\partial w}{\partial y} = \sum_{m=1}^{N} \sum_{n=1}^{N} \frac{n\pi}{b} a_{mn} \sin \frac{m\pi x}{a} \cos \frac{n\pi y}{b} \tag{B.36}$$

By evalutating the plate deflection at the bolt locations, the axial loads in the bolts can be directly computed from

$$\sigma_{axial} = \frac{E_b w(x,y)}{\ell_b} \tag{B.37}$$

The bending moments and shear forces at the top of the bolts can be found from Equations (B.23) and (B.24).

$$\begin{aligned}
M_{yT} &= \frac{2E_b I_b}{\ell_b} \left[\frac{6E_b I_b K_s + 2A_b G_b \ell_b^2}{12E_b I_b K_s + A_b G_b \ell_b^2} \right] \theta_x \\
M_{xT} &= -\frac{2E_b I_b}{\ell_b} \left[\frac{6E_b I_b K_s + 2A_b G_b \ell_b^2}{12E_b I_b K_s + A_b G_b \ell_b^2} \right] \theta_y \\
V_{xT} &= -\frac{2E_b I_b}{\ell_b^2} \left[\frac{3A_b G_b \ell_b^2}{12E_b I_b K_s + A_b G_b \ell_b^2} \right] \theta_x \\
V_{yT} &= -\frac{2E_b I_b}{\ell_b^2} \left[\frac{3A_b G_b \ell_b^2}{12E_b I_b K_s + A_b G_b \ell_b^2} \right] \theta_y
\end{aligned} \tag{B.38}$$

Equation (B.11) gives the relationship for the moment and shear at any location along the bolt's length. It indicates that the bending moment varies linearly, and the shear is constant with length. Therefore, the maximum moment occurs either at the top or bottom of the bolt. At the bottom the bending moments are

$$M_{xB} = M_{xT} - \ell_b V_{yT}$$
$$M_{yB} = M_{yT} - \ell_b V_{xT} \tag{B.39}$$

The bending and shearing stresses in the bolts can be found from the standard strength of materials relationships

$$\sigma = \frac{MC}{I} \tag{B.40}$$

$$\tau = \frac{VQ}{Ib} \tag{B.41}$$

where

- σ = bending stress
- τ = shearing stress
- M = bending moment
- V = transverse shear force
- c = distance from neutral axis to location bending stresses are to be computed
- I = area moment of inertia about neutral axis
- Q = static moment (about neutral axis) of cross-sectional area between free edge and plane through point being investigated
- b = minimum width or thickness at point in question

To determine the maximum stresses in a circular cross-section, Equations (B.40) and (B.41) reduce to

$$\sigma_{max} = \frac{32M}{\pi D_b^3} \tag{B.42}$$

$$\tau_{max} = \frac{16v}{3\pi D_b^2} \tag{B.43}$$

where D_b = the diameter of the bolt.

All information necessary to evaluate the bolt stresses is now available.

We will now turn to the stresses in the cover. The bending and twisting moments on a differential element of the plate, as defined by Reference B.4, are shown in Figure 8.4a, and the shearing forces are illustrated in Figure B.4b. The relationships between these quantities and the deflections in the plate are [B.4]

$$M_x = -D[W_{xx} + \nu W_{yy}]$$

$$M_y = -D[W_{yy} + \nu W_{xx}]$$

$$M_{xy} = -M_{yx} = D(1 - \nu)\, W_{xy} \qquad \text{(B.44)}$$

$$Q_x = \frac{\partial M_{yx}}{\partial y} + \frac{\partial M_x}{\partial x} = -D \frac{\partial}{\partial x} [W_{xx} + W_{yy}]$$

$$Q_y = \frac{\partial M_y}{\partial y} - \frac{\partial M_{xy}}{\partial x} = -D \frac{\partial}{\partial y} [W_{xx} + W_{yy}]$$

where w(x,y) can be evaluated from the series given by Equation (B.1). The maximum bending and shearing stresses in the plate at location (x,y) can be found from the relationships

$$(\sigma_x)_{max} = \frac{6M_x}{h^2}$$

$$(\sigma_y)_{max} = \frac{6M_y}{h^2} \qquad \text{(B.45)}$$

$$(T_{xy})_{max} = \frac{6M_{xy}}{h^2}$$

where h is the thickness of the plate.

By assuming the transverse shearing stresses T_{xz} and T_{yz} are distributed parabolically across the thickness of the plate, then

$$(T_{xz})_{max} = \frac{3}{2} \frac{Q_x}{h}$$

$$(T_{yz})_{max} = \frac{3}{2} \frac{Q_y}{h} \qquad \text{(B.46)}$$

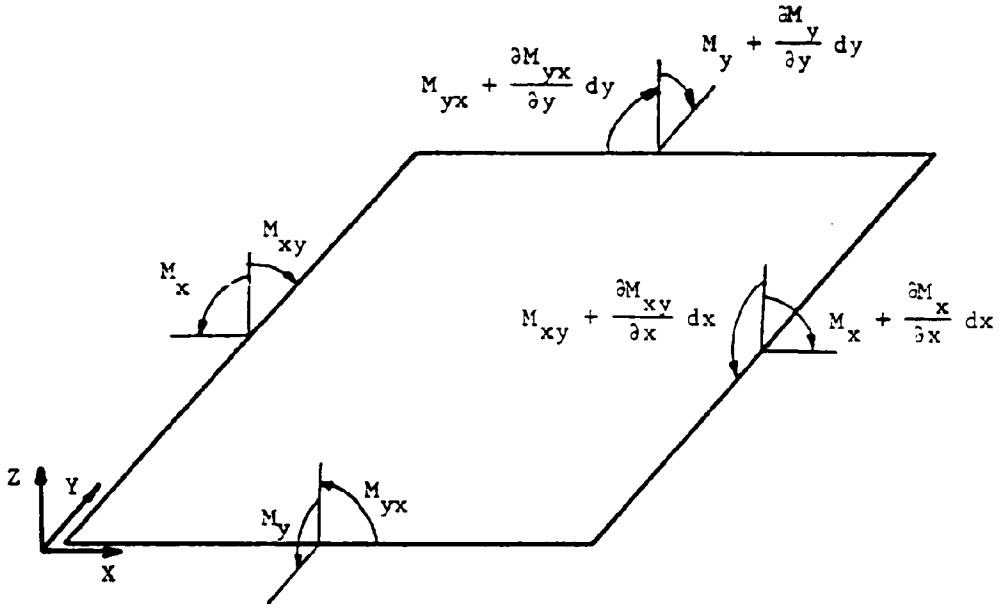

(a) Bending and Twisting Moments

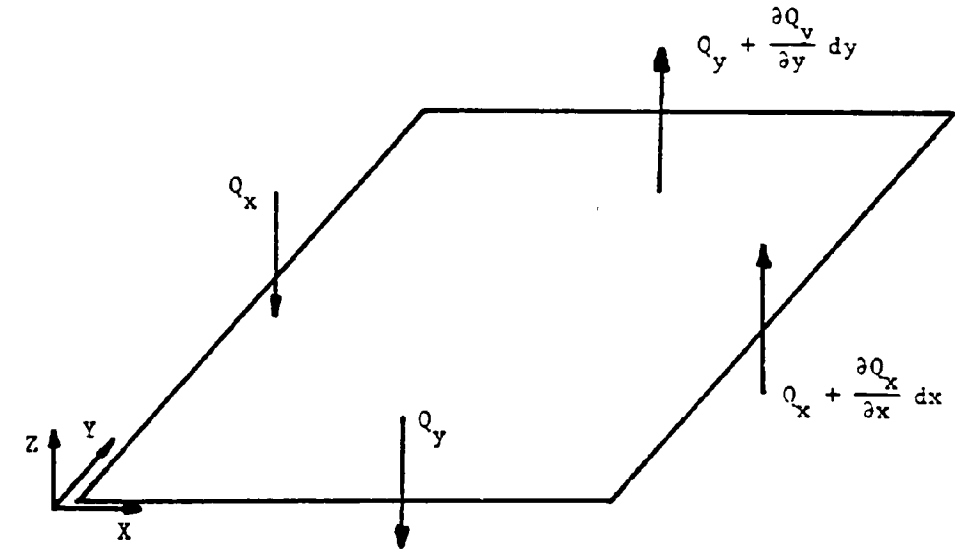

(b) Shearing Forces

FIGURE B.4. SIGN CONVENTION FOR PLATE LOADS

The theory developed up to this point will allow computation of the deflections and stresses in the cover and bolts. Because the determination of the coefficients a_{mn} requires the solution of a large set of simultaneous linear algebraic equations, it was expedient to program the theory for a computer. As a numerical example, the geometry and material properties for the cover and bolts of Enclosure I were used.

Example Calculations

The first set of results is for a simply supported flat plate subjected to uniform pressure. This example is presented only for verification of the numerical methods. In Section 4.1.2.1, finite element and analytical solutions from Reference B.4 were presented for a simply supported aluminum plate with the geometry of the cover for Enclosure I. Timoshenko's results taken at the center of the plate are compared with a nine-term series solution in Table B.1.

TABLE B.1. COMPARISON BETWEEN SERIES SOLUTION FOR A STAINLESS STEEL PLATE AND THE SOLUTION OF REFERENCE

	Deflection (in.)	σ_x Stress (psi)	σ_y Stress (psi)
Timoshenko's Analytical Solution [B.4]	0.07012	18,319	13,923
Series Solution	0.07139	18,138	13,560

The solutions in the table only differ by a few percent, and it can be concluded that the computer program for the series solution is yielding correct results.

The next task was to add the effects of the bolts. Bolt locations and physical properties were the same as in the finite element solution for Enclosure I (see Section 4.1.2 and Figure 4.11). The effective bolt length in the series solution was assumed to be 0.85 in., the distance

from the bottom of the bolt to the middle surface of the plate in the finite element model. A comparison of the two solution techniques is given in Table B.2. Results for the finite element solution are taken from Table 4.1 in Section 4.1.2.3.

TABLE B.2. COMPARISON BETWEEN SERIES AND FINITE ELEMENT SOLUTIONS

Bolt	Solution Procedure	Deflection (in.)	Axial Stress (psi)	Bending Stress Top of Bolt (psi) σ_x	Bending Stress Top of Bolt (psi) σ_y
1 (long side)	Finite Element	0.001332*	21,157	4,438	60,033
	Series	0.000818	27,925	5,046	43,509
2 (corner)	Finite Element	0.000252*	3,929	7,207	8,104
	Series	0.000041	1,406	2,181	2,220
3 (short side)	Finite Element	0.000828*	16,573	46,693	4,546
	Series	0.000642	21,906	33,680	4,972

*The deflections include rigid body motion as well as elongation of the bolts because of where constraint was applied in the F.E. model.

For bolts 1 and 2, the series solution gives higher values for axial stresses and lower values of bending stresses than the finite element solution. Nevertheless, the total axial plus bending stresses for the two methods are in reasonable agreement. For the corner bolt (bolt 2), the solutions do not agree well at all. The difference may be attributed to the constraint equations imposed on the bolt at the corner in the finite element analysis.

The series solution was also used to investigate the effects of varying such parameters as plate thickness, bolt dimensions, and bolt spacing on the stresses. Solutions for 0.375-in. and 0.25-in. cover thicknesses are summarized in Table B.3. These results show that both the plate and

TABLE B.3. PLATE AND BOLT STRESSES AS A FUNCTION OF PLATE THICKNESS FOR ENCLOSURE I

Plate Thickness	Deflection and Bending Stresses at Center of Plate			Bolt Axial and Bending Stresses								
				Bolt 1			Bolt 2			Bolt 3		
	δ(in.)	σ_x	σ_y	Axial	σ_x	σ_y	Axial	σ_x	σ_y	Axial	σ_x	σ_y
0.50	0.0186	11,012	8,656	27,925	5,046	43,509	1406	2131	2220	21,906	33,680	4,972
0.375	0.0369	18,970	14,884	29,531	8,650	48,834	- 830	1055	950	23,075	36,904	8,578
0.25	0.1100	42,254	33,081	29,786	16,903	61,069	-6557	9364	9092	23,769	43,881	17,077

bolt bending stresses increase rapidly with decreased plate thickness. This is a consequence of assuming that the bolt head rotates with the plate. A nonlinear solution would be required to account for separation of the bolt head and cover. It is also interesting to plot the plate's edge load distribution. Figure B.5 shows the distribution along two adjacent edges of the plate. In all cases the reaction is positive, which means there is no tendency for a gap to open up between the plate and support. Figure B.5 also indicates that with a 0.50-in. plate, the edge loads are more evenly distributed than for the other thicknesses. The results, therefore, confirm the choice of a 0.50-in. cover over the two other thicknesses investigated.

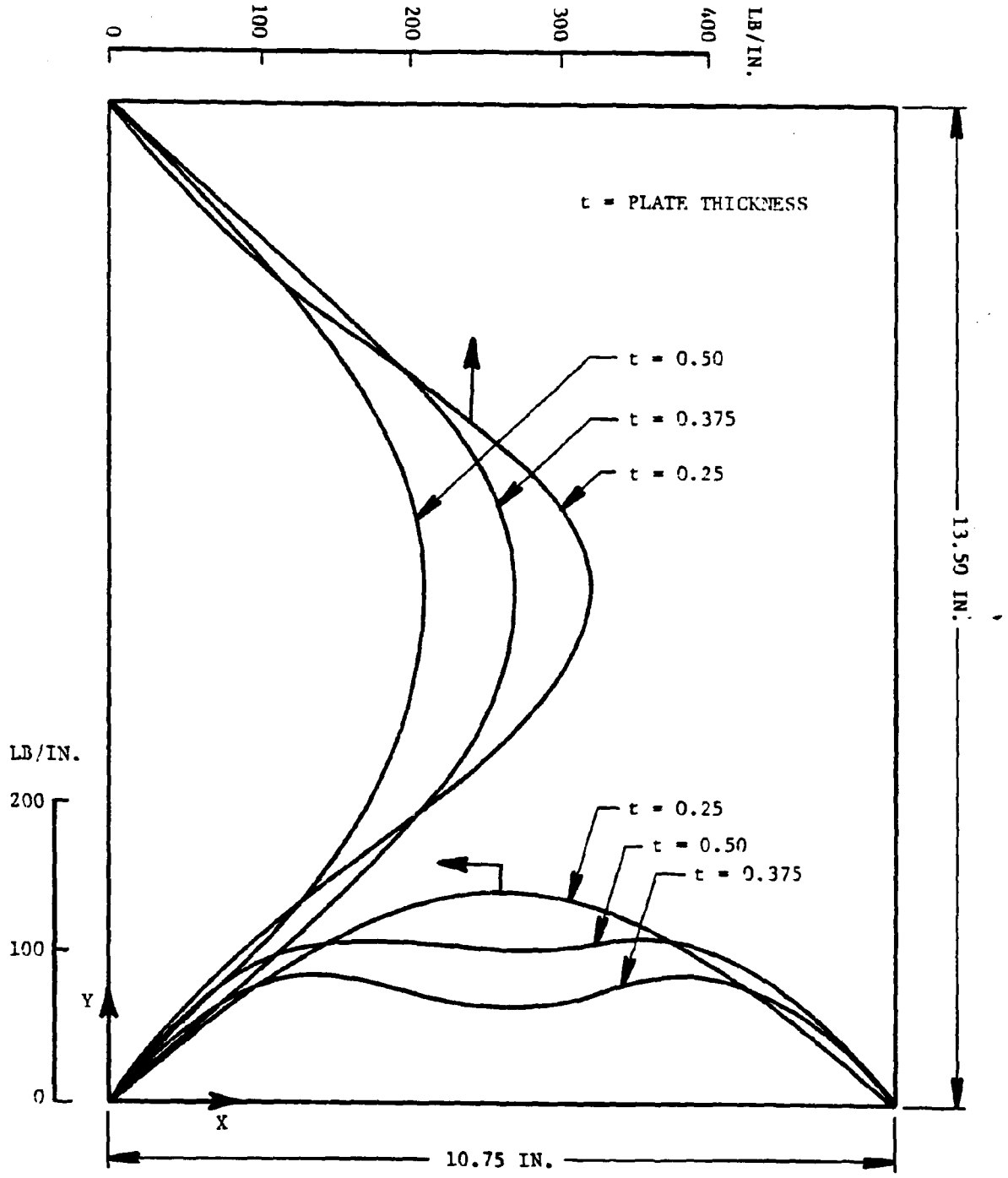

FIGURE B.5. PLATE EDGE REACTION DISTRIBUTION

REFERENCES

B.1. Fung, Y. C., Foundations of Solid Mechanics, Prentice-Hall, Inc. Englewood Cliffs, New Jersey, 1965.

B.2. Langhaar, H. L., Energy Methods in Applied Mechanics, John Wiley and Sons, Inc., New York, 1962.

B.3. Shigley, J. E., Mechanical Engineering Design, McGraw-Hill Book Company, New York, 1977.

B.4. Timoshenko, S., and Woinowsky-Krieger, S., Theory of Plates and Shells, McGraw-Hill Book Company, New York, 1959.

EFFECTS OF HIGHER VIBRATION MODES ON THE DYNAMIC RESPONSE OF ENCLOSURE I

In the computation of the dynamic load factor for Enclosure I, it was assumed that the contribution by the modes higher than the fundamental was negligible. This section presents the procedures for calculating the effects of the higher modes. The results are based upon the classical theory of a rectangular plate subjected to a ramp-type uniform pressure.

We will assume that the rectangular plate shown in Figure C.1(a) subjected to a uniform pressure q(t). The pressure increases with time according to the loading indicated by Figure C.1(b).

The partial differential equation of motion is:

$$D\left[\frac{\partial^4\omega(x,y,t)}{\partial x^4} + 2\frac{\partial^4\omega(x,y,t)}{\partial x^2\partial y^2} + \frac{\partial^4\omega(x,y,t)}{\partial y^4}\right] + \rho h\frac{\partial^2\omega(x,y,t)}{\partial t^2} = q(x,y,t) \qquad (C.1)$$

where D = flexural rigidity of plate $\frac{Eh^3}{12(1-\nu^2)}$

ρ = mass/unit volume

h = thickness of plate

q(x,y,t) = q(t) for a uniformly loaded plate

w(x,y,t) = deflection at point (x,y) at time t.

Since the plate is assumed to be simply supported along the edges, the boundary conditions are:

1. $\omega(o,y,t) = 0$
2. $\omega(a,y,t) = 0$
3. $\omega(x,o,t) = 0$
4. $\omega(x,b,t) = 0$

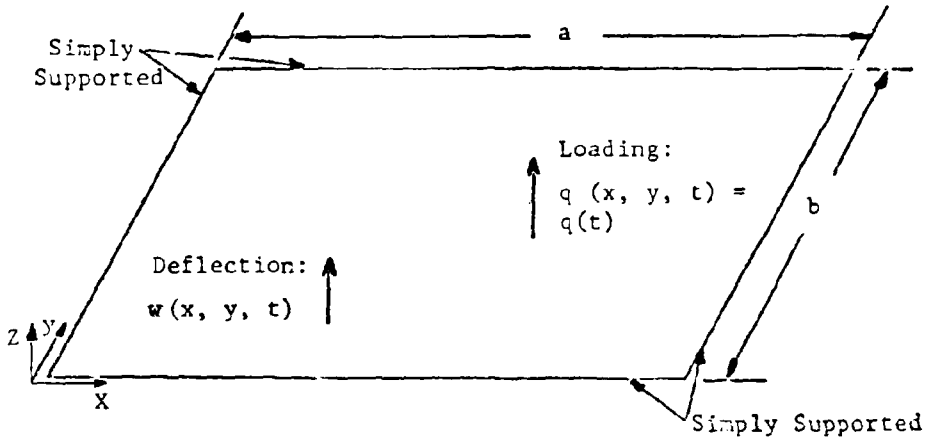

(a) Plate Geometry

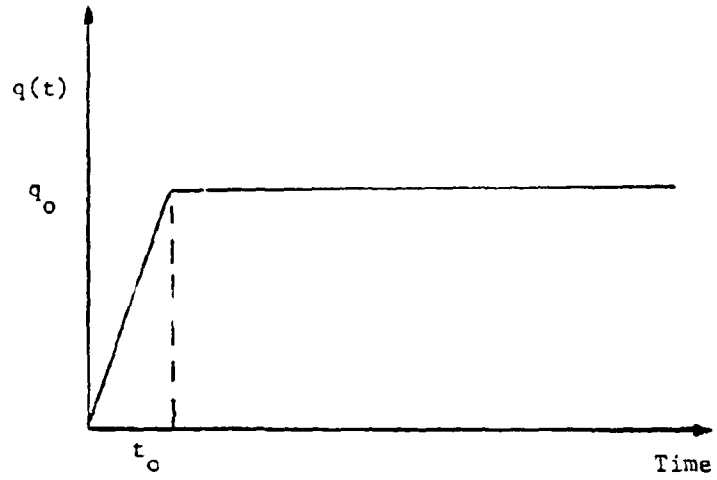

(b) Pressure Time History

FIGURE C.1. RAMP LOADING ON SIMPLY SUPPORTED PLATE

$$
\begin{aligned}
5.\quad & Mx(o,y,t) = -D\left[\frac{\partial^2\omega(o,y,t)}{\partial x^2} + \nu\frac{\partial^2\omega(o,y,t)}{\partial y^2}\right] \\
6.\quad & Mx(a,y,t) = -D\left[\frac{\partial^2\omega(a,y,t)}{\partial x^2} + \nu\frac{\partial^2\omega(a,y,t)}{\partial y^2}\right] \\
7.\quad & My(x,o,t) = -D\left[\frac{\partial^2\omega(x,o,t)}{\partial y^2} + \nu\frac{\partial^2\omega(x,o,t)}{\partial x^2}\right] \\
8.\quad & My(x,b,t) = -D\left[\frac{\partial^2\omega(x,b,t)}{\partial y^2} + \nu\frac{\partial^2\omega(x,b,t)}{\partial x^2}\right]
\end{aligned}
\qquad (C.2)
$$

For initial conditions, we will assume that the plate is underflected and at rest at the time t = 0. These give:

$$\omega(x,y,o) = 0$$

and (C.3)

$$\frac{\partial\omega(x,y,o)}{\partial t} = 0$$

The response of the plate will be solved using the Laplace transform approach. Details of the method can be found in references such as References C.1 and C.2. Taking the Laplace transform of Equation (C.1) with respect to time gives:

$$
\begin{aligned}
& D\left[\frac{\partial^4\bar{\omega}(x,y,s)}{\partial x^4} + 2\frac{\partial^4\bar{\omega}(x,y,s)}{\partial x^2\partial y^2} + \frac{\partial^4\bar{\omega}(x,y,s)}{\partial y^4}\right] \\
& + ph\left[S^2\bar{\omega}(x,y,s) - S\omega(x,y,o) - \frac{\partial\omega(x,y,o)}{\partial t}\right] = \bar{q}(s)
\end{aligned}
\qquad (C.4)
$$

where $\bar{\omega}(x,y,s)$ is the Laplace transform of $\omega(x,y,t)$ and $\bar{q}(s)$ is the transform of q(t).

The ramp loading shown in Figure C.1(b) can be written as

$$q(t) = q_o\frac{t}{t_o}\left[1 - S_{t_o}(t)\right] + q_oS_{t_o}(t) \qquad (C.5)$$

where the $S_{t_o}(t)$ is the unit step function defined by:

$$
\begin{aligned}
S_{t_o}(t) &= 0 \quad 0 < t < t_o \\
&= 1 \quad t \geq t_o
\end{aligned}
\qquad (C.6)
$$

The pressure q(t) correctly reduces to:

$$q(t) = \frac{q_o t}{t_o} \qquad 0 < t < t_o \tag{C.7}$$

$$= q_o \qquad t \geq t_o$$

The Laplace transform of q(t) then becomes:

$$\bar{q}(s) = \frac{q_o}{t_o}\left[\frac{1}{s^2} - \frac{t_o e^{-t_o s}}{s} - \frac{e^{-t_o s}}{s^2}\right] + \frac{q_o e^{-t_o s}}{s} \tag{C.8}$$

$$= \frac{q_o}{t_o s^2} - \frac{q_o e^{-t_o s}}{t_o s^2}$$

and with the initial conditions, Equation (C.4) reduces to

$$D\left[\frac{\partial^4 \bar{\omega}(x,y,s)}{\partial x^4} + 2\frac{\partial^4 \bar{\omega}(x,y,s)}{\partial x^2 \partial y^2} + \frac{\partial^4 \bar{\omega}(x,y,s)}{\partial y^4}\right] + \rho h\left[s^2 \bar{\omega}(x,y,s)\right] = \frac{q_o}{t_o s^2}\left[1 - e^{-t_o s}\right] \tag{C.9}$$

We will take the function $\bar{\omega}(x,y,s)$ to be:

$$\bar{\omega}(x,y,s) = \sum_{n=1}^{\infty} \sum_{m=1}^{\infty} \phi_{nm}(s) W_{nm}(x,y) \tag{C.10}$$

where $W_{nm}(x,y)$ are the free vibration mode shapes. These are given by:

$$W_{nm}(x,y) = \frac{2}{\sqrt{ab}} \sin \alpha_n X \sin \beta_m y \tag{C.11}$$

where

$$\alpha_n = \frac{n\pi}{a}, \quad \beta_m = \frac{m\pi}{b}$$

Note that $W_{nm}(x,y)$ are orthogonal and normalized to one, i.e.,

$$\int_0^b \int_0^a W_{nm}(x,y)\, W_{pq}(x,y)\, dxdy = 0 \qquad (n \neq p) \quad (m \neq q)$$

$$= 1 \qquad (n = p) \quad (m = q) \tag{C.12}$$

and of course, satisfy the boundary conditions given in Equation (C.2).

Substituting the expression for $\bar{w}(x,y,s)$ from Equation (C.10) into Equation (C.9) gives

$$\sum_{n=1}^{\infty}\sum_{m=1}^{\infty}\left\{ D\left[\alpha_n^4\,\phi_{nm}(s)\,W_{nm}(x,y) + 2\alpha_n^2\,\beta_m^2\,\phi_{nm}(s)\,W_{nm}(x,y) + \beta_m^4\,\phi_{nm}(s)\,W_{nm}(x,y)\right] + \rho h S^2\,\phi_{nm}(s)\,W_{nm}(x,y)\right\} = \frac{q_o}{t_o S^2}\left[1 - e^{-t_o s}\right] \tag{C.13}$$

If Equation (C.13) is multiplied by $W_{pq}(x,y)$ and both sides integrated over the area of the plate, the resulting expression becomes:

$$\begin{aligned}
&\left[D(\alpha_p^4 + 2\alpha_p^2\beta_q^2 + \beta_q^4) + \rho h S^2\right]\phi_{pq}(s) \\
&= \frac{2\,q_o}{\sqrt{ab}\,t_o S^2}\left[1 - e^{-t_o s}\right]\int_0^b\int_0^a \sin\alpha_p x \sin\beta_q y\,dx\,dy \\
&= \frac{2\,q_o}{\sqrt{ab}\,t_o S^2}\left[1 - e^{-t_o s}\right]\frac{1}{\alpha_p\beta_q}\cos\alpha_p x\,\Big|_0^a \cos\beta_q y\,\Big|_0^b \\
&= \frac{2q_o}{\sqrt{ab}\,t_o S^2\,\alpha_p\beta_q}\left[1 - e^{-t_o s}\right](\cos p\pi - 1)(\cos q\pi - 1) \\
&= \begin{cases} \dfrac{8q_o}{\sqrt{ab}\,\alpha_p\beta_q\,t_o S^2}\left[1 - e^{-t_o s}\right] & p \text{ and } q \text{ odd} \\ 0 & p \text{ or } q \text{ even} \end{cases}
\end{aligned} \tag{C.14}$$

The expression for $\phi_{pq}(s)$ now becomes:

$$\phi_{pq}(s) = \frac{\dfrac{8q_o}{\alpha_p\beta_q\sqrt{ab}\,t_o ph}\left[1 - e^{-t_o s}\right]}{S^2\left[S^2 + \dfrac{D}{ph}(\alpha_p^2 + \beta_q^2)^2\right]}, \quad (p, q \text{ odd}) \tag{C.15}$$

The inverse Laplace transform of $\phi_{pq}(t)$ is:

$$\phi_{pq}(t) = \frac{8q_o}{\alpha_p\beta_q\sqrt{ab}\,t_o\rho h}\left[\frac{1}{k^3}(kt - \sin kt)\right. \qquad (C.16)$$
$$\left. - \left(\frac{1}{k^3}(k(t - t_o)) - \sin k(t - t_o)\right) S_{t_o}(t)\right]$$

where

$$k^2 = \frac{D}{\rho h}(\alpha_p{}^2 + \beta_q{}^2)^2 \ , \ (p, q \text{ odd})$$

It is instructive to note that k is simply the natural frequency of free vibration for given integers p and q, i.e., $k = \omega_{pq}$. The complete solution is:

$$\omega(x,y,t) = \frac{16\ q_o}{ab\rho h t_o}\sum_{\substack{p=1\\(p,\ q\ \text{odd})}}^{\infty}\sum_{q=1}^{\infty}\frac{1}{\alpha_p\beta_q}\left[\frac{1}{k^3}(kt - \sin kt)\right. \qquad (C.17)$$
$$\left. -\left(\frac{1}{k^3}(k(t - t_o)) - \sin k(t - t_o)\right) S_{t_o}(t_o)\right] \sin \alpha_p X \sin \beta_q y$$

Since the general solution contains only odd integers p and q, the response will be symmetric about the midplanes of the plates. In the time interval $0 < t < t_o$, the solution reduces to:

$$\omega(x,y,t) = \frac{16\ q_o}{ab\rho h}\sum_{\substack{p=1\\(p,\ q\ \text{odd})}}^{\infty}\sum_{q=1}^{\infty}\frac{1}{k^2\alpha_p\beta_q}\left[\frac{1}{t_o}\left(t - \frac{\sin kt}{k}\right)\right] \qquad (C.18)$$
$$\sin \alpha_p X \sin \beta_q y$$

In the time interval $t > t_o$, the solution becomes:

$$\omega(x,y,t) = \frac{16\ q_o}{ab\rho h}\sum_{\substack{p=1\\(p,\ q\ \text{odd})}}^{\infty}\sum_{q=1}^{\infty}\frac{1}{k^2\alpha\ \beta}\left[1 + \frac{1}{kt_o}(\sin k(t - t_o) - \sin kt)\right] \qquad (C.19)$$
$$\sin \alpha_p X \sin \beta_q y$$

The expressions in the brackets of Equations (C.18) and (C.19) are analogous to the dynamic load factor given by Biggs [C.3], i.e.,

$$\begin{aligned} \text{DLF} &= \frac{1}{t_o}\left(t - \frac{\sin \omega t}{\omega}\right) \qquad 0 < t < t_o \\ &= 1 + \frac{1}{\omega t_o}\left(\sin \omega(t - t_o) - \sin \omega t\right) \qquad t \geq t_o \end{aligned} \tag{C.20}$$

The double summations in Equations (C.18) and (C.19) give the contributions of the higher modes, whereas Equation (C.20) involves a single degree-of-freedom system.

It is now instructive to examine some special cases of Equation (C.19). For a large pressure rise time t_o, the solution reduces to that of a plate loaded statically. That is, as t_o approaches infinity

$$\omega(x,y,t) = \frac{16\, q_o}{\pi^6 D} \sum_{\substack{p=1 \\ (p,q \text{ odd})}}^{\infty} \sum_{q=1}^{\infty} \frac{\sin \frac{p\pi}{a} X \sin \frac{q\pi y}{b}}{q\left(\frac{p^2}{a^2} + \frac{q^2}{b^2}\right)^2} \tag{C.21}$$

This expression agrees exactly with the static given by Timoshenko in Reference C.4.

To obtain the solution for a step loading, we let $t_o \to 0$ in Equation (C.19), and using L'Hospital's rule,

$$\omega(x,y,t) = \frac{16\, q_o}{abph} \sum_{\substack{p=1 \\ (p,q \text{ odd})}}^{\infty} \sum_{q=1}^{\infty} \frac{\sin \alpha_p X \sin \beta_q y}{\alpha_p \beta_q k^2} (1 - \cos kt) \tag{C.22}$$

Equation (C.22) agrees in form with that from Biggs for a single degree-of-freedom system.

We will now return to Equations (C.18) and (C.19) and define a dynamic load factor in the pq mode by the expressions:

$$DLF(p,q,t) = \frac{1}{t_o}\left(t - \frac{\sin W_{pq} t}{W_{pq}}\right) \qquad 0 < t < t_o$$

$$= 1 + \frac{1}{W_{pqt}} \left(\sin W_{pq}(t - t_o) - \sin W_{pq} t\right) \qquad t \geq t_o \tag{C.23}$$

The factor can be read directly from Figure C.2 if the frequency ω_{pq} and the rise time t_o are known. Equations (C.18) and (C.19) now can be written as:

$$\omega(x,y,t) = \frac{16\, q_o}{abph} \sum_{\substack{p=1 \\ (p,q \text{ odd})}}^{\infty} \sum_{q=1}^{\infty} \frac{DLF(p,q,t) \sin \alpha_p X \sin \beta_q y}{W^2_{pq}\, \alpha_p\, \beta_q} \tag{C.24}$$

The bending stresses in the plate are:

$$\partial x = \frac{\partial M_x}{h^2} \quad , \quad \partial y = \frac{\partial M_y}{h^2} \tag{C.25}$$

where the bending moments are given by:

$$M_x = -D\left[\frac{\partial^2 \omega}{\partial x^2} + \nu \frac{\partial^2 \omega}{\partial y^2}\right], \quad M = -D\left[\frac{\partial^2 \omega}{\partial y^2} + \nu \frac{\partial^2 \omega}{\partial x^2}\right] \tag{C.26}$$

In terms of the solution for the simply supported plate, the bending stresses become:

$$\partial x = -\frac{96 q_o D}{ab\rho h^3} \sum_{\substack{p=1 \\ (p,q \text{ odd})}}^{\infty} \sum_{q=1}^{\infty} \frac{DLF(p,q,t)}{W^2_{pq}} \left(\frac{\alpha_p}{\beta_q} + \nu \frac{\beta_q}{\alpha_p}\right) \sin \alpha_p X \sin \beta_q y \tag{C.27}$$

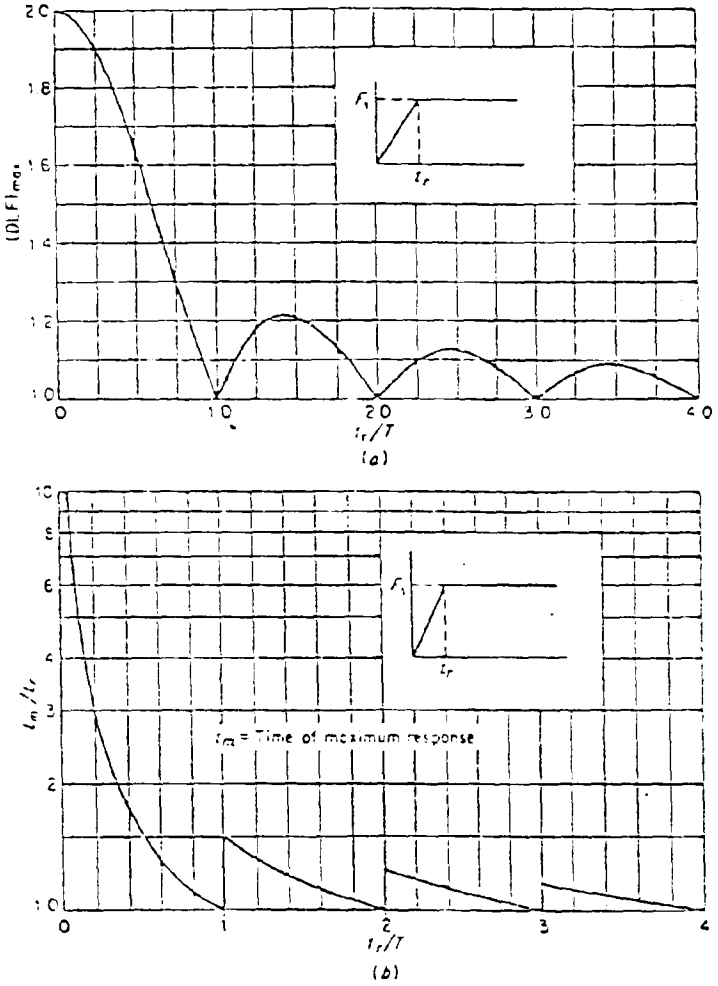

FIGURE C.2. MAXIMUM RESPONSE OF ONE-DEGREE ELASTIC SYSTEMS (UNDAMPED) SUBJECTED TO CONSTANT FORCE WITH FINITE RISE TIME (FROM REF. C.2)

$$\partial y = -\frac{96 q_o D}{ab\rho h^3} \sum_{\substack{p=1 \\ (p,q\ \text{odd})}}^{\infty} \sum_{q=1}^{\infty} \frac{DLF(p,q,t)}{W_{pq}^2} \left(\frac{\beta_q}{\alpha_p} + \nu \frac{\alpha_p}{\beta_q} \right) \sin \alpha_p X \sin \beta_q y \quad \text{(C.28)}$$

For a plate with the properties of the bottom of Enclosure I, the frequency ω_{pq} and corresponding period T_{pq} for p,q = 1, 3 are [C.5]:

ω_{pq} (rad/sec)/T (msec)			
↓p,q→	1	2	3
1	2014	4371	8300
	3.12	1.44	0.76
2	5697	8056	11984
	1.10	0.78	0.52
3	8352	14194	18126
	0.75	0.44	0.35

Using the shortest rise time of t_r = 17.7 msec determined in Section 4.1.4.3 the ratios of time t_r to natural periods, T_{pq}, are found to be

T_{pq}/t_r			
↓p,q→	1	2	3
1	5.7	12.3	23.3
2	16.1	22.7	34.0
3	23.6	40.2	50.6

When these ratios are used with Figure C.2, they show that the dynamic load factors higher than the first mode (p = 1, q = 1) are negligible, and even in the first mode the contribution is only about 5 percent. These results do not imply that, in computing deflections and stresses from

Equations (C.24), (C.27), and (C.28), only one term in the double summation should be taken, but only the DLF (p, q, t) can be neglected. The number of terms depends on how fast the series converges, which can be seen from the evaluation of a particular case.

These results using a simply supported plate to represent the bottom will be more conservative than the actual case since its response to dynamic loads will be greater. It appears, therefore, that a reasonable approach to evaluate the effects of dynamic response on enclosures with geometries similar to Enclosure I would be to treat each rectangular side as a simply supported flat plate. Each plate's natural periods could be calculated and compared with the duration of loading. Dynamic load factors could then be evaluated using the method outlined by Biggs [C.2]. Because of its simplicity, this approach certainly offers many advantages to the designer for the initial sizing of the containers and to the Bureau of Mines in checking the adequacy of proposed enclosure designs to dynamic response.

REFERENCES

C.1. Churchill, R. V., Operational Mathematics, McGraw-Hill Book Company, New York, 1958.

C.2. Nowacki, W., Dynamics of Elastic Systems, John Wiley and Sons, Inc., New York, 1963.

C.3. Biggs, J. M., Introduction to Structural Dynamics, McGraw-Hill Book Company, New York, 1964.

C.4. Timoshenko, S., and Woinowsky-Krieger, S., Theory of Plates and Shells, McGraw-Hill Book Company, New York, 1959.

PRESSURE PILING: A LITERATURE SURVEY

Introduction

As part of the current efforts by USBM and SwRI to determine the pressure safety factors in the Schedule 2G enclosure by computational and experimental analysis, this literature survey was undertaken to assess, at least qualitatively, the current understanding of pressure piling. For the Schedule 2G enclosure work, dynamic pressures in the enclosures are prescribed by USBM for input to computational procedures. The influence of pressure piling on dynamic response may be significant, and the possibility of pressure piling is recognized by USBM and MSHA personnel. It has, as yet, not been possible to know the causes of pressure piling to the degree that geometry, ignition source and location, and combustible gas mixture influences can be used to predict if pressure piling will occur, and, if it occurs, what pressures will be obtained. It is, instead, the purpose of this review to document the observations of pressure piling and to present, at least from the qualitative point of view, what factors influence the phenomenon or anomaly referred to as pressure piling or pressure heaping. Regarding the present Schedule 2G enclosure work being conducted by SwRI for the USBM, pressure piling is thought of as the increase in pressure in a compartmented enclosure above the pressures that would occur in the same volume without compartmentation. This pressure increase is a relative measure and may be considered abnormal compared to pressure obtained in a constant volume combustion process with a precombustion gas pressure at or very near standard atmospheric pressure.

Compartmentation alone does not lead to pressure piling, and, apparently, only under ideal conditions are high peak pressures observed. Also, because of the ever present problem of the presence of methane in gassy mines, methane combustion is of foremost interest to the USBM; however, other flammable gases may exist under some conditions (e.g., flammable decomposition products during electrical arcing through potting compounds) and could represent a hazard, as may pressure piling during the combustion of methane in air.

A Graphic Example of Pressure Piling

Grice and Wheeler report in Ref. D.1 results of a comprehensive study to demonstrate the magnitude of unusually high pressure and the rate of pressure rise that can occur as a result of pressure piling. They cite the importance of precompression of gas in the second of two connected compartments following ignition of the gas in the larger of two compartment volumes. Previously, precompression had been used to explain the high explosion pressure. They agreed with the conclusion of a much earlier work by Beyling in Germany that precompression of gas prior to burning in the second volume did affect the magnitude of pressure attained (120 psi or greater for stoichiometric methane and air initially at one atmosphere pressure reported by Beyling). But, they also emphasized the importance of the turbulence of the gas mixture in the second compartment or chamber produced by the inrush of gases before a relatively large burned or burning flame jet protruded into

the second, smaller chamber. Precompression is reported to be the main cause of the high pressure attained, but rising at a rapid rate and reaching an extraordinary peak in pressure is attributed to the turbulence and sizeable (large relative to flame volume and area of the flame surface) turbulent flame jet. In fact, higher pressure may have been attained than that concluded as probable by Grice and Wheeler owing to the types of pressure transducers used by Grice and Wheeler.

A large part of the report in Ref. D.1 was devoted to the instrumentation for measuring pressure and to ascertaining what pressure was probably attained from pressure-time records. Pressure transducers in current use for blast and explosion work do not have the mechanical leverages that Grice and Wheeler had to use in pressure transducers of the time.

Beyling had tested a cylinder 42.5 cm long and 33.5 cm in diameter (approximately 4.2 liters) divided at one-third the length by a partition with a 3-cm-diameter hole. Later he used a large vessel attached to a 3.6-liter vessel by a short, 2-cm-diameter tube. Beyling reported 240-psi peak pressure for 9.6% methane in air for the connected chambers; however, Grice and Wheeler estimated that 120-psi peak pressure was more probable due to the response exhibited by the type of pressure transducer used. Grice and Wheeler conducted several types of experiments, starting each one with 1 atmosphere initial pressure. A summary of their tests is given below.

1. Bronze spheres of 1, 2, and 8 liters, any two of which were connected by a short steel tube 7.6 cm long and 3.2 cm diameter or 2.5 cm diameter, were tested using 9.5% methane in air with an ignition source from an induction coil through a 1-cm spark gap. No unusual pressure was reported.

2. An 8-liter sphere divided in half by a brass plate with a 2.5-cm-diameter hole in the center was used to contain a 9.5% methane explosion. No unusual pressure was reported.

3. Flame movement studies were conducted using glass spheres of 500 and 250 cc containing 25% carbon monoxide with air to get a visible flame (methane and air flames are difficult to photograph). Spheres were connected by a 2-cm-long and 1.8-cm-diameter tube. Observations were:

   a. Flame appeared in larger volume and spread (more rapidly toward opening).

   b. Flame jet into smaller volume before all unburned gas in larger volume was consumed.

   c. Flame in smaller volumes died out; larger volume flame still burning.

   d. Oscillatory burning back and forth between large and small volumes until flames died out altogether.

4. A cubical iron box 96 liters in volume was connected to an 8-liter bronze sphere by a 7.5-cm-long and 2.5-cm-diameter steel

tube. The box was destroyed by an internal explosion of unrecordable intensity when 9.5% methane in air was ignited.

5. A 100-liter cylinder with domed ends and having a length equal to the cylinder diameter was connected to a 6-liter sphere by a 7.6-cm-long and 2.5-cm-diameter steel tube. With ignition in the far end of the larger volume of 9.5% methane in air, the pressure rose to 30 psi in the smaller volume and then jumped to a typical peak of approximately 200 psi (peak pressure varied between 145 and 235 psi). The peak was followed by a dip to a pressure below 100 psi and a return to about 115 psi. This was followed by a gradual cooling phase. Slightly leaner mixtures (8 to 8.5% methane in air) gave essentially the same results except the pressure returned to about 100 psi and then the cooling phase occurred in typical fashion.

Because 9.5% methane in air leads to an explosion pressure/initial pressure ratio of approximately 7.0*, a 250-psia pressure should result from a combined explosion of gas at an initial pressure of 35.7 psia, or greater than twice standard atmospheric pressure. In fact, Grice and Wheeler's experiments with the last configuration discussed above did show a gradual rise of initial (precombustion) gas pressure to between 20 and 30 psi.

Recognition of Pressure Piling as a Design Consideration

The Safety in Mines Research Annual Reports for the years 1953-1959 give accounts of pressure piling experiments conducted under the direction of the Electrical Research Association (E.R.A.) and the Department of Scientific and Industrial Research of Great Britain (D.S.I.R.). Emphasized in the experiments were a variety of electrical motor enclosures and other compartmented enclosures (conditioner boxes of diesel engines, core-cooled electric motors, and specially designed test enclosures), especially containing pentane and air. Peak pressures attained were greater than 500 psi. Such pressures were transient, localized, and of short duration. In one series of some 500 tests on a large core-cooled electric motor, pressure piling was common until the number of motor cooling ducts were reduced by one-half, thus reducing the forced cooling circulation in the motor casing.

In other tests in a special apparatus designed to investigate pressure piling, a one-cubic-foot cylinder was connected by a 1-in.-long, 1/8-in.-diameter duct to a 1/4-cubic-foot cylinder. Peak pressure attained was 820 psi. Additional data pertaining to the above mentioned studies may be found in Refs. D.2 through D.16.

An earlier work by Gleim (Ref. D.17) than reported in Ref. D.4 gives some eight factors that could result in "pressure heaping." The factors as described by Gleim in Ref. D.17 are:

1. Volume of explosive gas-mixture ignited

2. Gas composition of the mixture

---

*A ratio of 8 to 8.5 is probably more acceptable today and may be used for design purposes.

3. Coal dust present in the enclosure

4. Turbulent motion of the mixture

5. Gaps that seal or permit pressure release (e.g., enclosed equipment placement)

6. Opening sizes between compartments

7. Ignition point location

8. Heat transfer to enclosed equipment or surfaces.

In fact, Gleim cited four examples where one or more of the above factors could be attributed to having caused pressure piling, and, by modification of the factors, investigators were able to eliminate or greatly reduce the peak pressure observed. Unfortunately, Gleim's report did not describe experimental instrumentation, and thus, by today's standards in test reporting, the pressure observations may be considered qualitative at best.

Gleim and Marcy (Ref. D.4) report findings from studies with connected spheres that the rapid rise in pressure is due to turbulence of the gas and to the relative size of the flame ignition source to the compartment in which ignition occurs. Both turbulence and ignition source strength caused increase in pressure so long as ignition occurred in the larger of the interconnected chambers. Further, they report that the pressure attained in the smaller compartment was directly proportional to the initial pressure in the compartments; however, the rate of pressure rise was retarded by increasing the initial pressure for methane and air. In other reported tests described by Gleim and Marcy, a 1-ft-diameter tube, divided by 11 partitions with 4-in. holes over a distance of 106 ft, was filled with a methane and air mixture. Upon ignition of the mixture at one end, a flame speed of 2000 ft/sec was observed. The effect of each compartment divided by partitioning plates on the combustion process was to cause an increasing turbulence in each chamber as the flame projected into the unburned gas mixture. When a condensed explosive was used to initiate the combustion in the tube, a flame speed in excess of 6000 ft/sec was observed. Such flame velocities are in the regime of a detonation; however, a constant velocity was not attained, as is usually the case for detonation in a tube without obstructions.

To quantify the pressure piling effect, Gleim and Marcy conducted experiments within a 1-ft- by 1-ft- by 4-ft-long container. The container was partitioned in various ratios of volume using a plate.

The plate was provided with centrally located openings having a 10-in. diameter, an 8-in. diameter, a 4-in. diameter, a 4-in. square, and a 2-in. diameter for the various tested configurations. Pressure gages used for pressure measurements had a natural frequency above 2000 Hz and were of strain gage type construction. Gages had a 2-ms response to a step input and were operated with a 10-kHz carrier frequency. A 9.5% mixture of natural gas (91% methane, 8% ethane, and 1% nitrogen) in air was used as the test gas with ignition from a spark plug spark of unstated energy and duration.

As a reference condition, central ignition of an unpartitioned test configuration resulted in 80 psi. For a 7:1 volume ratio using the 10-in.-diameter orifice, the largest pressure developed was in the larger volume where ignition was near the center of the larger volume. Peak pressure developed was about 90 psi.

For 1:1 and 3:1 volume ratios, the 8-in.-diameter orifice tests resulted in high explosion peak pressures of approximately 125 psi, oscillations were recorded, and except for 3:1 volume ratio tests, the high peak pressure was not obtained in the smaller of the connected volumes. For a volume ratio of 7:1, peak pressures were approximately 80 psi and invariant with ignition location.

Using a 4-in.-diameter orifice plate configuration, a peak pressure of 195 psi was obtained for a volume ratio of 1:1. Ignition occurred at the midpoint of the first volume wall, and peak pressure occurred at the far end wall of the second volume. However, peak pressures of approximately 155 psi were obtained in the second volume for 1:1 volume ratio with ignition at various locations along the second volume wall. At volume ratios of 3:1, peak pressures of approximately 135 psi were obtained when ignition was along the wall of the first, larger volume. The peak pressures for 1:1, 3:1, and 7:1 volume ratios using a partition with a 4-in.-diameter orifice plate hole were, overall, higher than 80 psi, and pressure-rise time was often less than 15 ms to reach 80-90% of the peak pressure.

For a compartment volume ratio of 1:1 separated by an orifice plate having a 2-in.-diameter hole, a peak pressure of 315 psi was obtained. Ignition was at the side wall, but away from the hole connecting the two volumes. The mirror image test with ignition in the second volume resulted in a peak pressure in the second volume of 234 psi. The series of tests with the 2-in. holes indicate that highest pressures are obtained when ignition occurs away from the connecting passageway. With higher peak pressures, oscillations in pressure-time traces were considerable, and high pressures were transitory and fluctuated rapidly. Gleim and Marcy describe the high pressure results obtained in the 2-in. hole tests as being entirely different from that assumed to be as a result of pressure-piling.

In conclusion, Gleim and Marcy reveal that more-complicated commercial enclosures with their contents should be used to evaluate whether or not pressure piling may occur. This, they state, would at least provide the confidence to predict if pressure piling would occur that their study could not provide. Altogether, some of the features of connected chambers explosion pressures were consistent with other observations; however, there did not appear to be a systematic behavior, especially as tested volume ratios of 1:1 and 3:1 resulted in high peak pressures. What was clear was that a small opening or passage was more likely to give higher pressures than large openings, and high pressure could be expected in the chamber opposite that chamber where ignition occurred. They also suggest that tests be conducted using fast response pressure gages having diaphragms flush to the walls. Their suggestion indicates that they believed that resonance frequency of gages may have been excited in some testing or that frequency response may be inadequate in some tests that they conducted. Otherwise, their experiments did not provide a quantitative understanding of what they observed,

and they were unable to conclude what may cause pressure piling. As an observation, however, the pressure oscillations they observed may be present in the gas during burning. This phenomenon has been observed by others (Refs. D.18 and D.19, for example) where venting studies were conducted, and it is expected that acoustically driven oscillations and oscillation effects on the burning process may have important consequences and implications to enclosure structural integrity whether or not controlled venting is provided and whether or not enclosure compartmentation is found.

Mechanisms That Influence Enclosure Pressure History

To understand thoroughly the phenomenon that is referred to as pressure piling, the mechanisms that lead to flame propagation with acceleration from one chamber of an enclosure volume through an opening into another chamber must be known. In a recent experimental studies report by Solberg, Skramstad, and Pappas at Det norske Veritas (Ref. D.20), the mechanisms are described that lead to peaks in pressure-time histories. Because several mechanisms are at work simultaneously and are apparently coupled, no single mechanism may be attributed to the observed pressure histories for confined burning in adjacent volumes connected by an open passage. The probable causes for observed pressure peaks, pressure oscillations, and flame accelerations will be described below and some will be briefly discussed. If more conclusive and additional data are obtained or if an analytical model is proposed, the main principles and events leading to pressure piling may include the mechanisms. If some or all of the possible factors are not allowed for, then quations may be raised as to whether pressure piling is predictable or whether it may occur in experiments. In the case of an analytical model, the effects necessary to predict pressure piling should be included in the model for the model to represent a physically realistic analysis.

Parameters found to be important to the causes of pressure and burning magnitudes and rates, in addition to the geometry descriptors, are:

1. size of the enclosure
2. gas type and concentration
3. initiation location and strength
4. precompression of unburned gas in excess of normal precompression
5. flow induced acceleration
6. flame instabilities
    a. cellular flame instabilities
    b. oscillatory instabilities
    c. Taylor instabilities
    d. turbulent eddies

With regard to the above, the following observations may be made:

1. Subscale gas explosion experimental testing has been shown to give different results than full-scale model experiments.

2. For hydrocarbon gases except methane, cellular instability (described later) occurs in rich fuel-air mixtures.

3. A volume of explosive gas centrally ignited may result in more severe and rapid pressure rises than an end ignited gas mixture.

4. Precompression of explosive gas leads to higher peak combustion pressure. Gas in a second chamber, precompressed before flame arrival through a connecting passage and consequential ignition of the connected volumes gas, produces greater than normally expected pressure peaks.

5. As gas flow accelerates to pass through a connecting passage, the energy release rate is increased. This increase thereby increases the flow rate, and a positive feedback loop is evident.

6. Several flame instabilities of different natures are important to the rate of energy release.

    a. Flame surface is increased due to preferential diffusion of reactants caused by concentration gradients. The gradients result from flame front perturbation, and no perturbation is too small to create this effect and consequential increase in the pressure rise rate.

    b. Rayleigh's criteria provide for positive correlation between acoustic mode resonance and pressure oscillations. The frequency is not of a Helmholtz type and is connected with the flame passing through an opening.

    c. Differences between hot burned gas and unburned gas result in Taylor instabilities and flame front convolutions. A weak wave is produced through the passage, and acceleration of the energy release rate occurs, especially for a centrally ignited main chamber.

    d. At the boundary between burned and unburned gas, as between accelerated venting gas through the passage and secondary chamber gas, shear gradients produce turbulence and consequential accelerating energy release rate. Obstacles in the flow are not necessary for this turbulence to be produced.

It is anticipated that additional evidence of these mechanisms will be quantified to understand better the potential for pressure piling. However, the understanding of the mechanisms described above is not complete, particularly with regard to flame instabilities and especially the turbulence aspects (Ref. D.21). Precompression is more easily assessed, and since the ratio of combustion pressure to precompression is nearly constant for a gas mixture, all other parameters (e.g., temperature) being the same, the effect of precompression may be incorporated into an evaluation model with less difficulty

than would be required to evaluate flame instabilities. Whatever experiments or models one may propose to conduct or develop, a nonsteady analysis and corresponding structural analysis would be required to assess the importance of pressure piling unless data were available to prescribe a statically equivalent pressure for design evaluation.

Further References to Pressure Piling

Several references have been made to pressure piling in USBM reports and elsewhere. Often, however, a shortcoming is that references do not go on to describe what "pressure piling" means, nor are specific instances or examples given of the occurrence of pressure piling. These references do, however, indicate that in the event pressure piling occurs, the pressures that develop are large and may have serious consequences.

For example, in Mitchell's report on explosion-proof bulkheads (Ref. D.22), he states, *In the Bureau's Experimental Mine, for example, propagating explosions have developed from 1 to 127 psig, and in a few trials pressure piling caused higher, unrecordable pressures, and considerable damage.*

In his paper on rapidly applied pressures in enclosures, Smith, Ref. D.23, gives recognition to pressure piling:

> *It is known (Grice, 1929 and Titman & Haig, 1950) that, when ignition of an explosive mixture takes place in one of two interconnected compartments, and in certain other circumstances, 'pressure-piling' may occur in the other compartment if the ratio of their volumes is within certain limits. The enclosures used for the tests to be described were of simple internal design that did not lead to pressure-piling with its associated high pressures.*

Also, Marinovic (Ref. D.24) warns of pressure-piling dangers, but refers to the phenomenon as the "detonation effect" in his discussions on maximum safe gap of enclosures.

> *In the last ten or more years it has been found out in various countries that in case of flammable mixtures the maximum safety gap can be reduced due to other phenomena. This can be caused by the so called 'obstacle' effect, which with external obstacles in the vicinity of the gap can cause ignition of external atmosphere, or also by detonation effect, which can occur in casings with divided compartments or in casings of oblong form.*

Scott, Kennedy, and Zabetakis, Ref. D.25, describe briefly the work of Grice and Wheeler, Ref. D.1, with confined methane and air, and attribute the high explosion pressure to geometry as well as ignition location. Scott, Kennedy, and Zabetakis also point out that higher explosion pressure may be obtained with a slightly richer mixture than with the ideal, stoichiometric mixture (i.e., 10.2% as opposed to the ideal 9.5% methane). Also, 11% gives the same pressure as 9.5%, and an even richer mixture of approximately 11.9% will yield the same explosion pressure as an 8% methane, which was

found by Grice and Wheeler to give about the same peak pressure during a pressure piling incident as 9.5% methane in air.

Engel and Merritts, Ref. D.26, refer to pressure piling, but in fact do not experience it in their demonstrations. Stefanko and Morley, Ref. D.27 in discussions of USBM Schedule 2G comparison and IEC recommendations on mechanical strength, state the following:

> *Mechanical Strength. The comparison here has been already investigated thoroughly with the exception of pressure piling. Pressure piling refers to the development of abnormal pressure as a result of a gas-air mixture's accelerated burning rate (100)*. It is frequently caused by restricted configurations within enclosures. The IEC recognizes this problem can occur whenever an enclosure is subdivided and requires designs leading to pressure piling be precluded as far as it is practical. If not, the mechanical strength must be increased. The design specifications and testing requirements of Schedule 2G appear to eliminate the problem. However, if changing to performance, a requirement similar to IEC's is absolutely necessary."*

* *USBM, Schedule 2G, 1968.*

Another reference to pressure piling occurs in Ref. D.28; however, at the time of this writing, we were unable to acquire that research paper.

REFERENCES

D.1. Grice, C. S. W., and Wheeler, R. V., "Firedamp Explosions Within Closed Vessels: Pressure Piling," SMRB Paper 49 and ERA G/T 38, Leatherhead, Surrey, England, 1929.

D.2. Pearson, A. R., "Pressure Piling in Motor Enclosures and Its Effect on the Maximum Experimental Safe Clearance Between Shaft and Gland in Atmospheres Containing Coal Gas," E.R.A. G/T 136, Leatherhead, Surrey, England, 1941.

D.3. Horseley, J. A. B., "Flameproof Enclosures of Electrical Apparatus: Gaseous Explosions in Communicating Compartments: Influence of Turbulence on Pressure Piling," E.R.A. G/T 265, Leatherhead, Surrey, England, 1952.

D.4. Gleim, P. J., and Marcy, J. F., "A Study to Determine Factors Causing Pressure Piling in Testing Explosion-Proof Enclosures," 7th Conference of Directors, SMRE Paper 6, 1952. See also USBM RI 4904, 1952.

D.5. Staples, H., "The Pressure During Explosion of a Pentane-Air Mixture Inside a Core-Cooled Motor, Part 2," SMRE Research Report 27, 1951.

D.6. Staples, H., "The Pressure Generated During Explosion Inside a Core-Cooled Motor, Mixtures of Methane in Air and Hydrogen/Methane 85/15 in Air," SMRE Research Report 38, 1952.

D.7. Titman, H., and Haig, J., "The Pressure Generated During Explosion of a Pentane-Air Mixture Inside a Core-Cooled Motor, Part I," SMRE Research Report No. 11, 1950.

D.8. Smith, P. B., and Simpson, N., "Interim Report No. 3 on the Progress of Flameproof Motor Research: Tests with a Hydrogen/Methane/Air Mixture," E.R.A. D/C/T 102, 1957.

D.9. Smith, P. B., and Simpson, N., "Interim Report No. 4 on the Progress of Flameproof Motor Research: Tests with One-Half of Cooling Ducts Open," E.R.A. D/C/T 103, 1958.

D.10. Smith, P. B., and Simpson, N., "Interim Report No. 5 on the Progress of Flameproof Motor Research: Tests at Reduced Speeds with a Large Fan," E.R.A. D/C/T 105, 1959.

D.11. Maskow, H. M., "Explosion Processes in Subdivided Chambers in Electrical Equipment (The Behavior of Mixed Gases)," 11th Conference of Directors, SMRE Paper 17, 1963.

D.12. Woodhead, D. W., "Summarized Conclusions from Experiments with an 800 H.P. Core-Cooled Motor at SMRE During 1954-1958 (Stage II)," E.R.A. D/C/T 104, 1959.

D.13. Combe, A., Meyer, C., and Theiry, M., "Study of the Propagation of Flames in a Reaction Vessel Formed by Two Compartments Linked by a Duct," SMRE Translation 4734, 1958.

D.14. Brown, T. J. A., "Interim Report on the Progress of Flameproof Motor Research at SMRE Buxton, From November 1953 to February 1955," E.R.A. G/H/T 11, 1955.

D.15. Brown, T. J. A., "Interim Report No. 2 on the Progress of Flameproof Motor Research at SMRE Buxton, From October 1955 to February 1956," 1956.

D.16. Brown, T. J. A., "Pressure Piling in Compartmented Enclosures. Effects of Bore and Length of Connecting Tube in Explosions of Pentane/Air Mixtures," E.R.A. D/T 109, 1959.

D.17. E. J. Gleim, "Abnormal Pressures in Explosion-Proof Compartments of Electrical Mining Machines," USBM RI 2974, December 1929.

D.18. Zalosh, R. G., "Gas Explosion Tests in Roomlike Vented Enclosures," 13th Loss Prevention Symposium, AIChE, 1979.

D.19. Yao, C., "Explosion Venting of Low-Strength Equipment and Structures," Loss Prevention, Vol. 8, AiCHE, 1974.

D.20. Solberg, D. M., Skramstad, E., and Pappas, J., "Experimental Investigations on Partly Confined Gas Explosions," Veritas Report No. 79-0483, 1979.

D.21. Makepeace, R., "The Effect of Turbulence on the Combustion of Gases," Fire and Materials, Vol. 2, No. 3, 1978.

D.22. Mitchell, D. W., "Explosion-Proof Bulkheads, Present Practices," USBM RI 7581, 1971.

D.23. Smith, P. B., "The Behavior of Certain Enclosures Under Rapidly Applied Internal Pressures," SMRE Research Rept. 91.

D.24. Marinovic, N., "Effect of Short Circuits Inside Explosion Proof Enclosures on Propagation of Ignition," Electrotechnical Institute, Zagreb, Yugoslavia, 16th International Conference on Coal Mine Safety Research, I5, Washington, D. C., Sept. 1975.

D.25. Scott, G. S., Kennedy, R. E., and Zabetakis, M. G., "Gas Explosions and Their Prevention," USBM IC 7601, 1951.

D.26. Engel, H. H., and Merritts, M. W., "Lecture and Demonstration on Flame Propagation and Permissable and Explosion-Proof Electrical Equipment," USBM IC 7980, 1960.

D.27. Stefanko, R., and Morley, L. A., "Mine Electrical Systems Evaluation Explosion-Proofing of Mine Containers," USBM OFR 76(2)-75, USBM Grant No. GO-133077, 1974.

D.28. "Pressure Piling," Final Report on Research Work Plan No. 3501 03/02 2-28/9, Mining Safety Institute Leipzig - Versuchsstrecke Freiberg from HSE Translation 7113, Aug. 1977. (Bibliography reference no. 14 of "Thermosetting Resins for Small Flameproof Enclosures," by R. Sack and G. Grey, M.S.I. Leipzig Rept. EL 025/70, 3 Nov. 1972.)

STRUCTURAL PERFORMANCE TEST FOR SCHEDULE 2G ENCLOSURES

I. PURPOSE

The purpose of this structural performance test is to verify that explosion-proof enclosures are designed for a minimum static pressure of 150 psig.

II. DESCRIPTION OF TEST APPARATUS

In order to routinely test 2G enclosures for structural performance as specified in Part 18, Title 30 of the Code of Federal Regulations, the apparatus shown in Figure E.1 is required. This setup consists primarily of a water reservoir, a regulated nitrogen source, interconnecting hardware, and pressure sensing instrumentation. The use of water as the test fluid is recommended for reasons of safety. However, even with this safer fluid, the apparatus should be installed in two seprate test cells. The enclosure under test should be in a separate test cell from the individuals conducting the test.

The water tank should be at least 50 gallons in volume and be rated for 300-psig water service. If considerably larger volume enclosures are to be tested, a larger reservoir may be required, but note that the enclosure is initially filled from the water supply and not from the water tank. The tank only supplies makeup water in the event of leaks, etc.

A regulated high-pressure bottle of nitrogen (2000 psig) or the equivalent is used to provide the input pressure to the water tank. A reference dial gage with a range of 0-300 psig is installed near the nitrogen bottle. This dial gage is used as a rough reference of the pressure being applied and as a backup safety indicator of whether the system is under pressure or not.

The primary pressure indicator is the output voltage of an electro-mechanical pressure transducer installed near the test enclosure and used to sense the hydrostatic pressure being applied. This transducer, such as a Type 4-424-0010 made by Bell & Howell or an equivalent unit, should have a pressure range of 0 to 500 psig with full range output voltage of 5.0 volts. This type of transducer requires an unregulated power source of 12 to 30 volts DC and a simple digital voltmeter to display the output. The output voltage sensitivity is approximately 10 millivolts per psi of pressure. Thus, pressure can be read directly in psi's by simply dividing the number of millivolts indicated by 10. The accuracy of this transducer is $\pm$0.25% of full range output, which is equivalent to $\pm$1.25 psi.

III. MOUNTING OF TEST ENCLOSURE

The geometry, size, and complexity of the test enclosure will dictate how it is connected to the pressurization apparatus. The general procedure is to use an existing feedthrough, if available, and adapt it for connection to the pressure tubing. In the absence of an existing opening that can

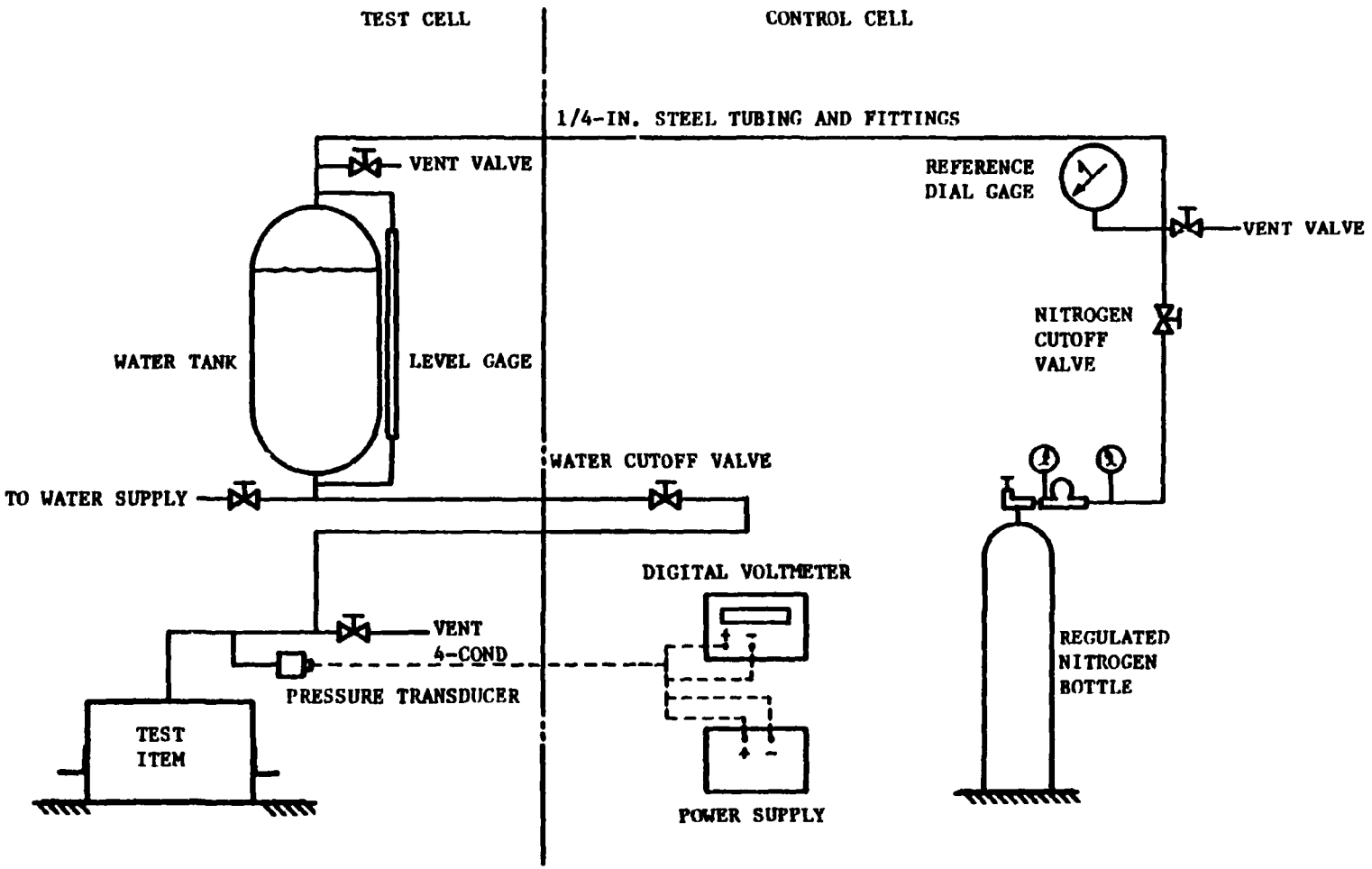

FIGURE E.1. HYDROSTATIC TEST APPARATUS

be used, a hole and pipe thread will have to be machined on the cover for pressurizing the enclosure.

Once a pressure connection is available, the next step is to provide a tight seal between the cover and the enclosure if one has not been provided by the manufacturer. Two sealing methods have been found to be satisfactory for hydrostatic testing. The most suitable method for the enclosure being tested can be used.

Method 1 (Suitable for small, regular shaped enclosures) - In this method a continuous gasket is cut from 1/16-in. thick reinforced neoprene. This gasket should extend outside the bolt circle, but no closer than 3/16 in. from the outer edge of the flange or cover. Clean the mating surfaces with acetone or an equivalent solvent before placing the gasket and closing the enclosure. No sealants are necessary. Bolts are torqued to their rated loads as given in Table E.1.

Method 2 (Suitable for enclosures of all sizes) - This method uses G.E. Silicon Construction Sealant, 1200 series, as a sealant. Clean the surfaces to be sealed with acetone or an equivalent solvent and apply the sealant in a uniform bead 1/16 - 1/8 in. in diameter. A zigzag pattern as shown in Figure E.2 has been found to work satisfactorily. Some sealant will be extruded from the outer edge of the enclosure by this method, but there will also be spaces for a feeler gage. Use heat lamps to raise sealant temperature above 110°F for a faster cure. The lid can be applied after the sealant "skims" or after it has cured completely. High humdity and high heat reduce the curing time. A faster cure should occur without the cover in place. Torque bolts to their rated torques as given in Table E.1.

Prior to connecting the enclosure to the pressurization system and bolting the cover, all surfaces should be checked for flatness so that a pretest baseline can be established. Deformations, if any, due to the hydrostatic test can then be determined. A steel straight edge should be used against every flat surface and any undulations measured and recorded. Measurements should include those across the width and length of each side, and, if necessary, across the two diagonals.

With all of the pretest measurements recorded, the enclosure is placed on the test stand with the sealing surface level and at the highest point on the enclosure. Connection is then made to the pressurization system and the enclosure is completely filled with water. Eliminate or minimize air pockets when filling the enclosure. The sealant or gasket is then applied and allowed to cure if necessary. Curing time can be accelerated with heat lamps.

The enclosure is now ready to be closed for pressurization. Top the enclosure with water if necessary (water can overflow), open the vent valve, install cover and torque bolts to rated load as given in Table E.1. Using feeler gages, the gap, if any, between the enclosure and its cover is measured and recorded on all sides of the enclosure with at least one measurement between each pair of bolts. If exuded sealant precludes

TABLE E.1. TORQUE WRENCH CHART BOLTS

GRADE MARKING		0-1-2	5	6	7	8	SUPER
BOLT DIAM.	THREAD PITCH	FOOT POUNDS					
1/4"	20	5.5	9.7	11.0	11.5	13.0	
	28	6.0	11.0	12.0	13.0	15.0	
5/16"	18	10.0	18.0	20.0	21.0	24.0	
	24	11.4	20.0	23.0	24.0	27.5	
3/8"	16	21.7	39.0	43.0	45.0	52.0	
	24	24.5	44.0	49.0	51.0	59.0	
7/16"	14	32.4	58.0	65.0	67.0	78.0	
	20	38.4	69.0	77.0	80.0	92.0	
1/2"	13	43.5	87.0	97.0	102.0	116.0	
	20	54.6	102.0	115.0	121.0	135.0	
9/16"	12	57.5	111.0	123.0	129.0	147.0	
	18	68.0	131.0	145.0	153.0	175.0	
5/8"	11	86.0	173.0	192.0	201.0	230.0	
	18	102.0	200.0	224.0	235.0	269.0	
3/4"	10	152.0	293.0	324.0	336.0	389.0	
	16	167.0	325.0	364.0	402.0	461.0	
7/8"	9	222.0	500.0	555.0	583.0	666.0	
	14	251.0	585.0	652.0	685.0	784.0	
1"	8	307.0	660.0	769.0	807.0	923.0	
	14	370.0	830.0	925.0	967.0	1111.0	

Courtesy Premier Industrial Corp.
Cleveland, Ohio

1. Specifications contained in this chart are correct to the best of our knowledge but we assume no liability as to accuracy. Consult the exact specifications as given by original equipment manufacturer.
2. Consult your service manual before adjusting or repairing any automatic transmission.
3. Any torque wrench is a delicate measuring instrument and should be treated with care. Should the pointer become bent by accident reset to zero when tool lies in rest position and accurate readings will result. Make certain pointer floats.
4. Craftsman repair and service tools available for all normal servicing requirements.

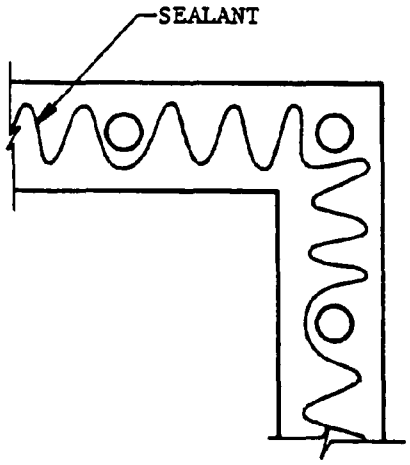

FIGURE E.2. RECOMMENDED SEALANT PATTERN

insertion of the feeler gages, it can be easily removed with a fine-bladed knife.

IV. PERFORMANCE TEST

After the enclosure has been connected to the water tank, the hydrostatic test is conducted as follows:

(1) Turn on voltmeter and power supply set at 15 VDC.

(2) Make sure water supply valve is closed.

(3) Close vent valve above water tank.

(4) Read and record pressure transducer output. This is 0-psig voltage output.

(5) Open water cutoff valve.

(6) Output of transducer may increase slightly as a result of the height of water in the water tank.

(7) Close vent valve by dial gage.

(8) Open nitrogen cutoff valve.

(9) Open regulator and gradually apply pressure to the system in 30 psi increments. The output of the pressure transducer will be approximately as follows:

Pressure	Change in Voltage
30	0.300
60	0.600
90	0.900
120	1.200
150	1.500

Actual voltages can be obtained from the calibration information supplied by the manufacturer.

(10) After each pressure step, close nitrogen cutoff valve and inspect the enclosure for water leaks. Very small leaks can be tolerated, particularly at the higher pressures.

(11) In case of a flowing leak, shut off nitrogen cutoff valve, close the water cutoff valve, and close the regulator. Open vent valve by reference dial gage. Reseal the enclosure before starting test again.

(12) After the test pressure reaches 150 psig, close the nitrogen cutoff valve.

(13) Shut off the regulator and open vent valve by reference dial gage.

(14) Close water cutoff valve.

(15) Measure and record the gap between the enclosure and its cover at the same locations surveyed after sealing.

(16) Remove enclosure.

(17) Remeasure and record flatness of each side to determine if any permanent deformations resulted from the hydrostatic pressure test.

V. ACCEPTANCE CRITERIA

The enclosure will have passed the structural performance if no deformations larger than 0.04 in./ft are measured on any side and if the gap has not increased more than 0.002 in. relative to pretest measurements.

APPENDIX F--GRAPHS OF ANALYTICAL RESULTS FOR ENCLOSURE II

ANALYTICAL RESULTS FOR ENCLOSURE II

This appendix contains

- o Stress Contour Plots
- o Displacement Contour Plots
- o Identification of Elements with Von Mises Stress $\geq$ 10 ksi

for the cover, bottom, side and back shells of Enclosure II. Refer to Figures 4.61 and 4.62 in Section 4.2.1 to identify the location and orientation of the components in the enclosure and the coordinate axes.

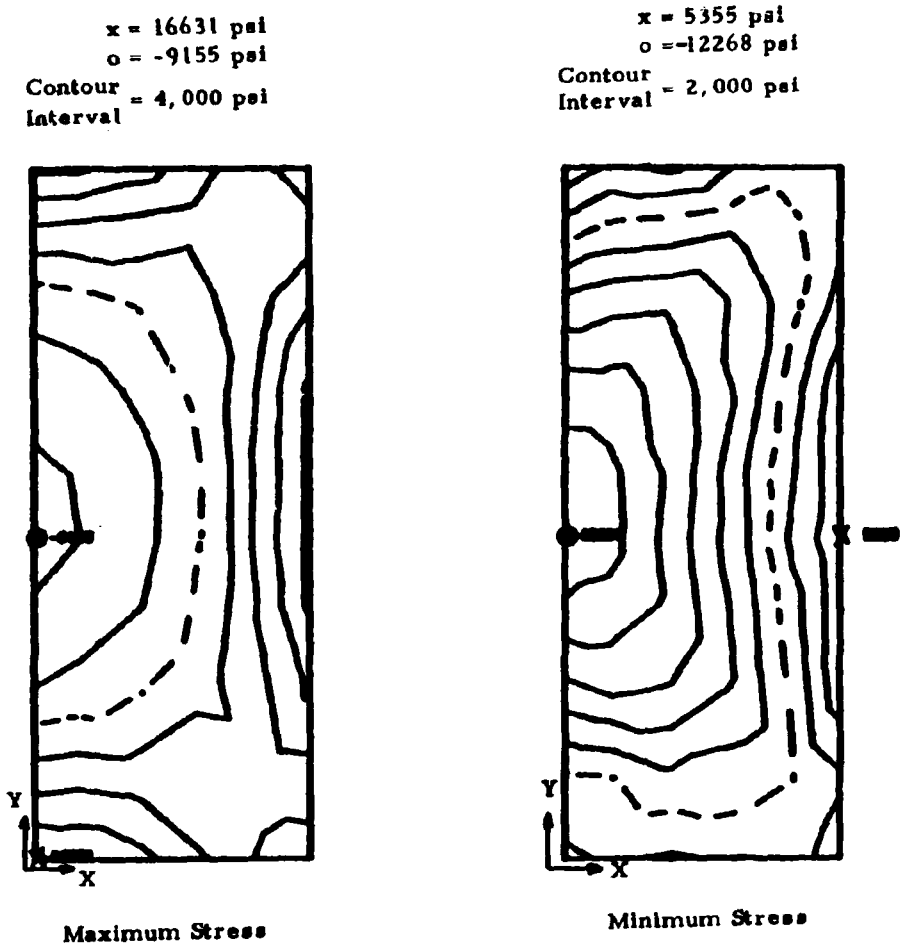

FIGURE F.1. PRINCIPAL STRESSES (INSIDE SURFACE) IN BOTTOM SHELL

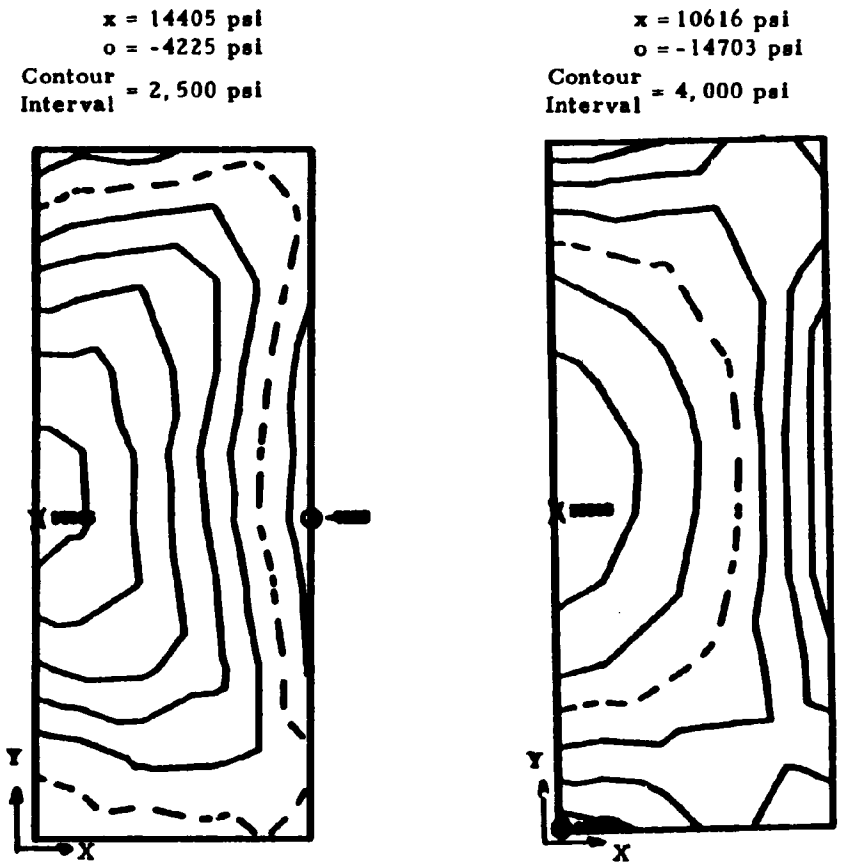

FIGURE F.2. PRINCIPAL STRESS (OUTSIDE SURFACE) IN BOTTOM SHELL

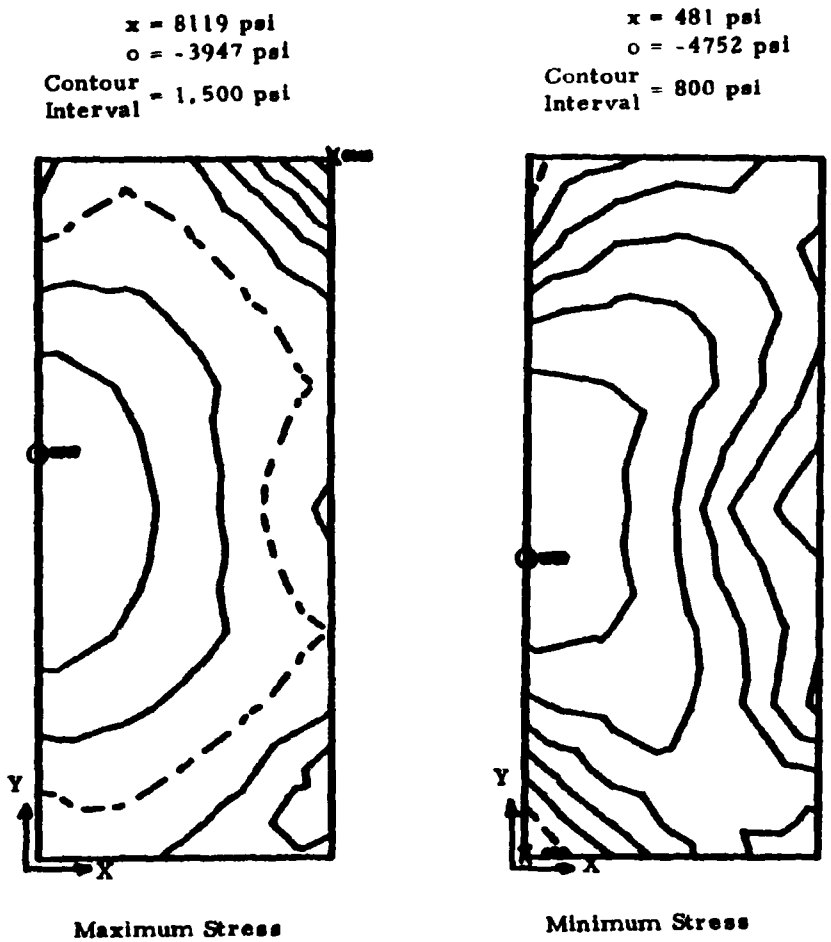

FIGURE F.3. PRINCIPAL STRESSES (INSIDE SURFACE) IN COVER

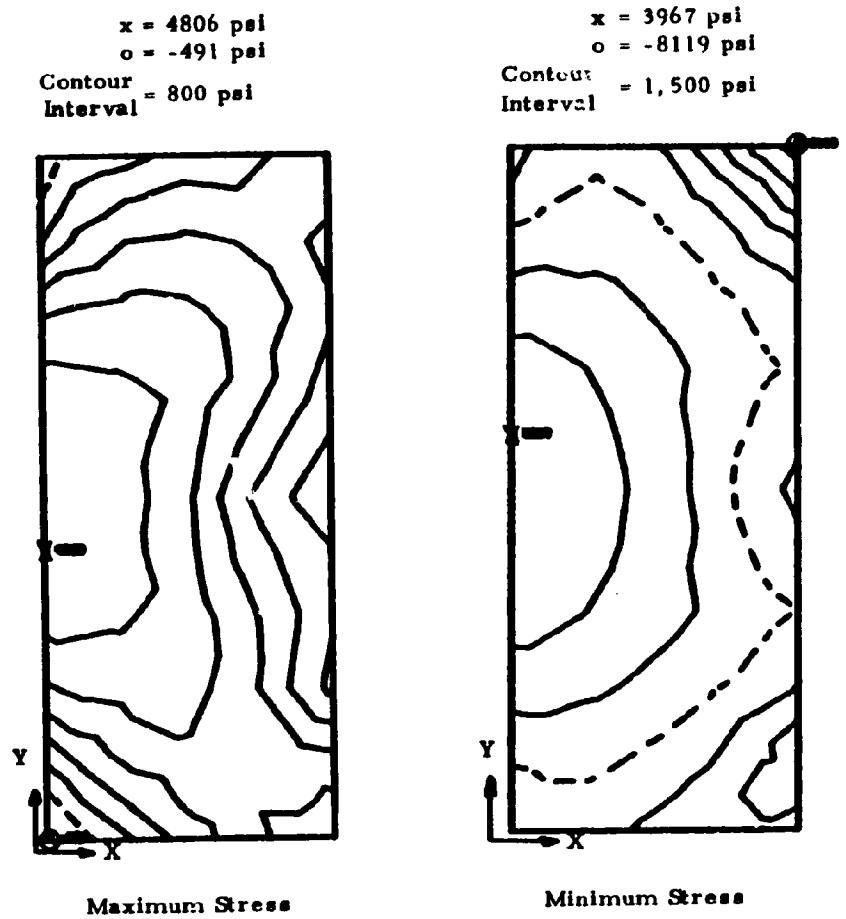

FIGURE F.4. PRINCIPAL STRESSES (OUTSIDE SURFACE) IN COVER

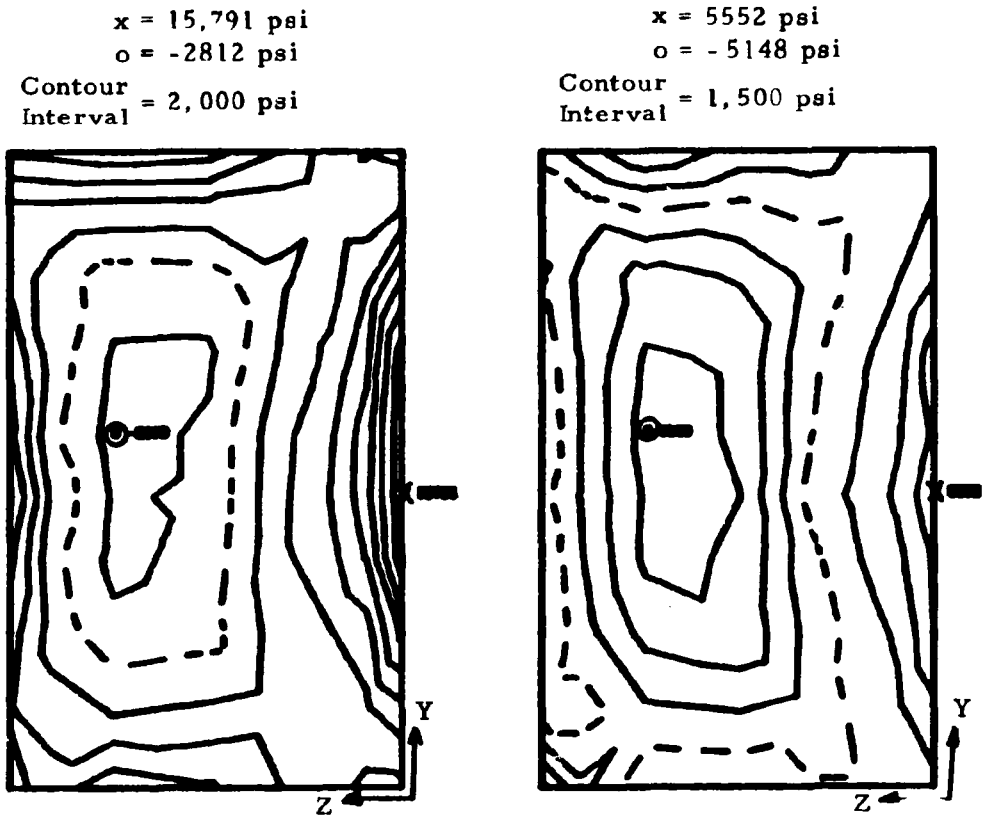

FIGURE F.5. PRINCIPAL STRESSES (INSIDE SURFACE) IN SIDE SHELL

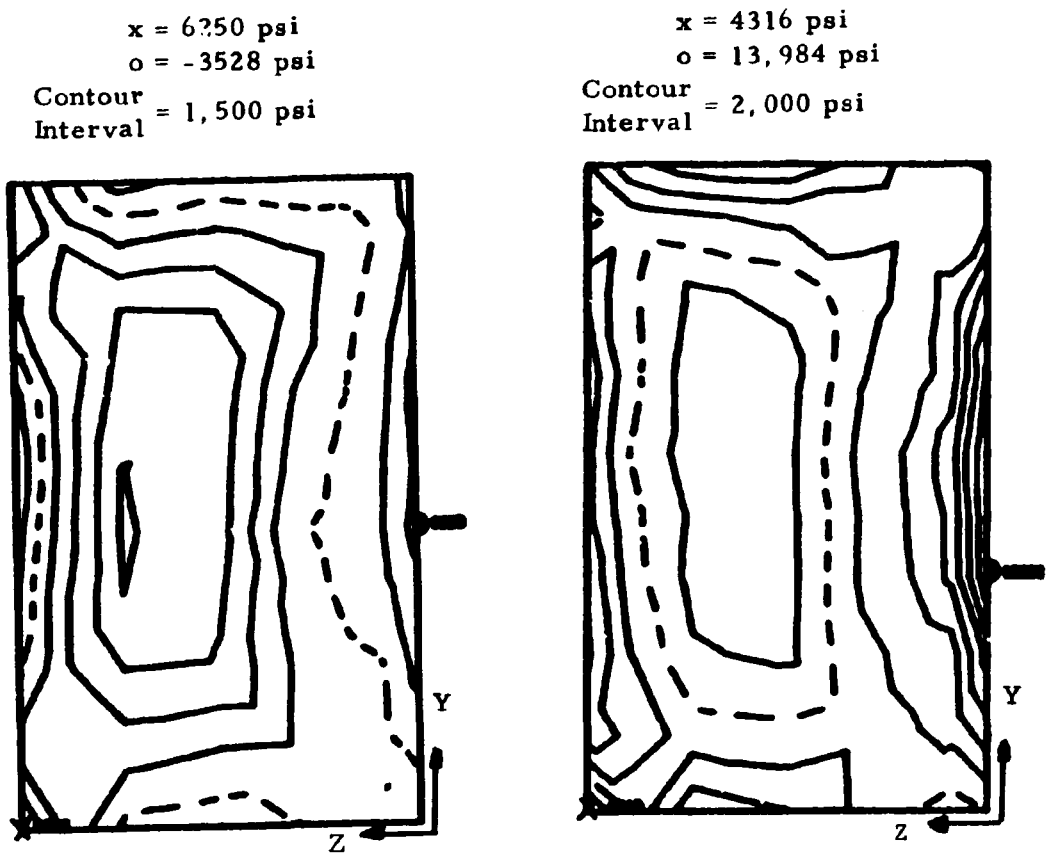

FIGURE F.6. PRINCIPAL STRESSES (OUTSIDE SURFACE) IN SIDE SHELL

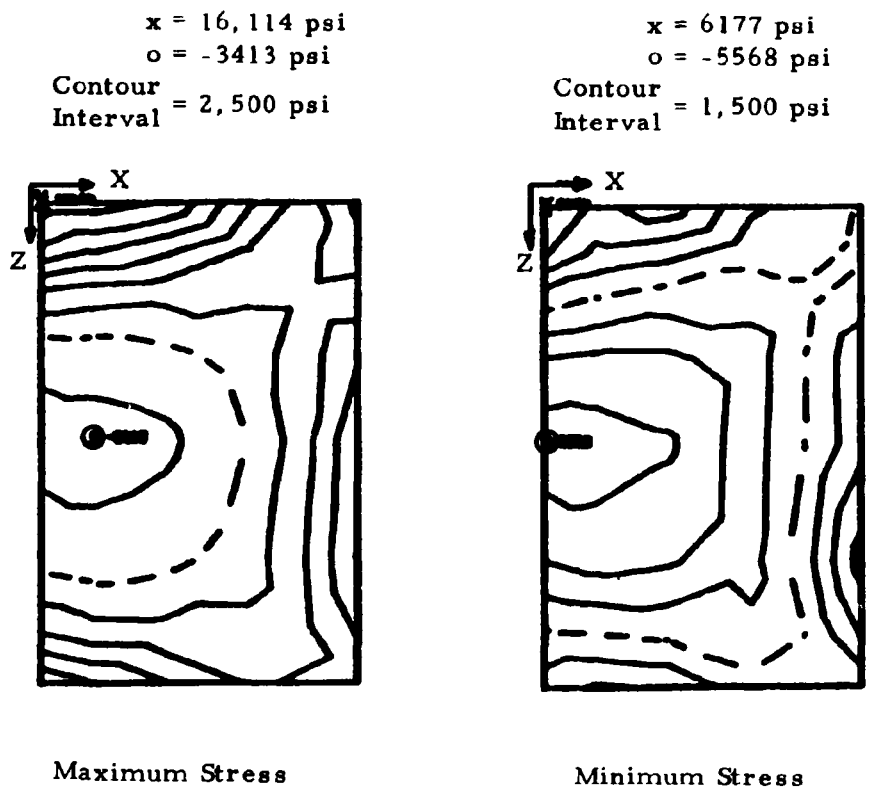

FIGURE F.7. PRINCIPAL STRESSES (INSIDE SURFACE) IN BACK SHELL

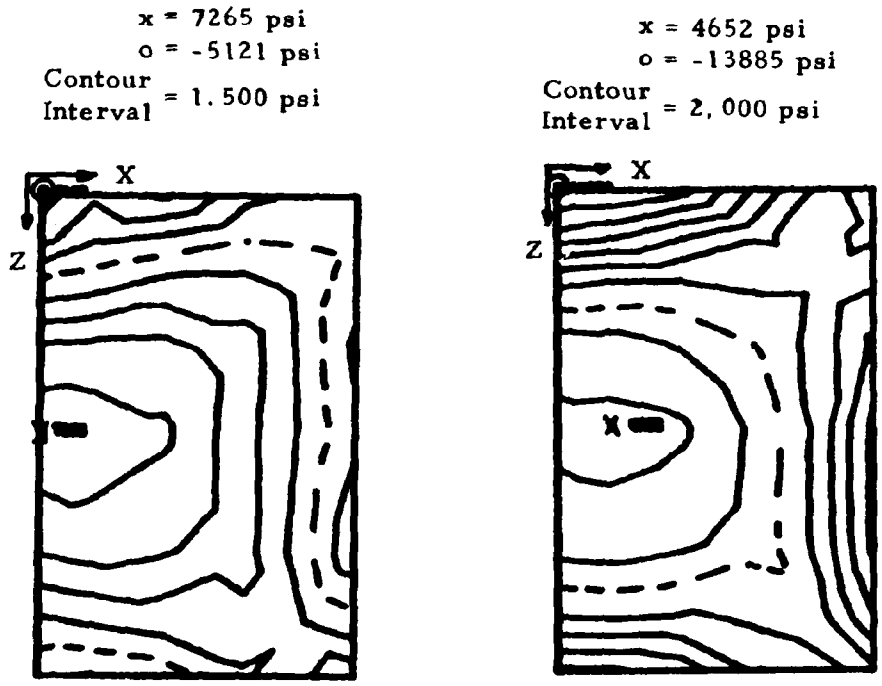

FIGURE F.8. PRINCIPAL STRESSES (OUTSIDE SURFACE) IN BACK SHELL

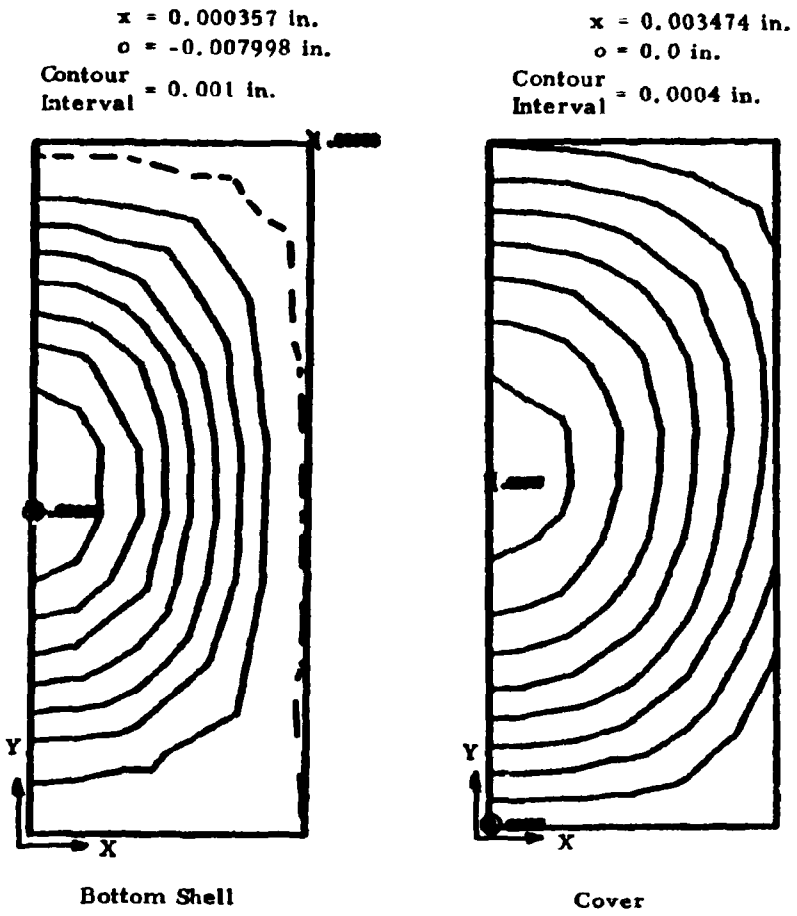

FIGURE F.9. PERPENDICULAR DISPLACEMENTS

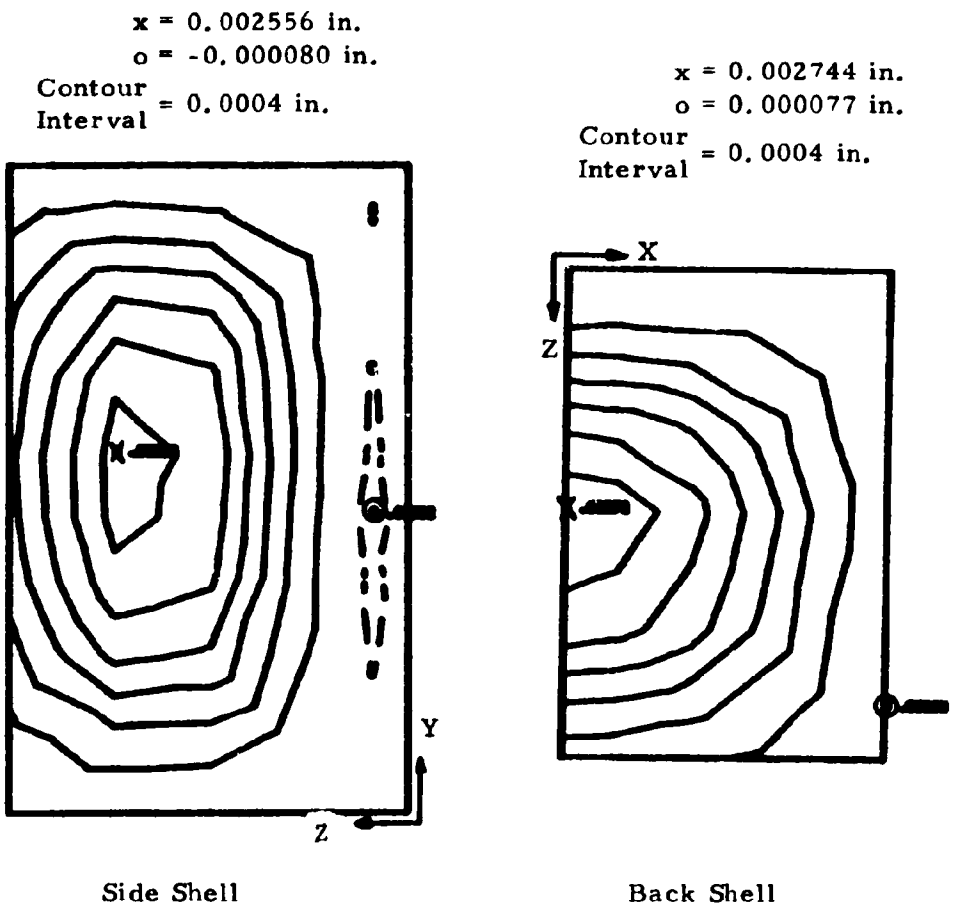

Side Shell

Back Shell

FIGURE F.10. PERPENDICULAR DISPLACEMENTS

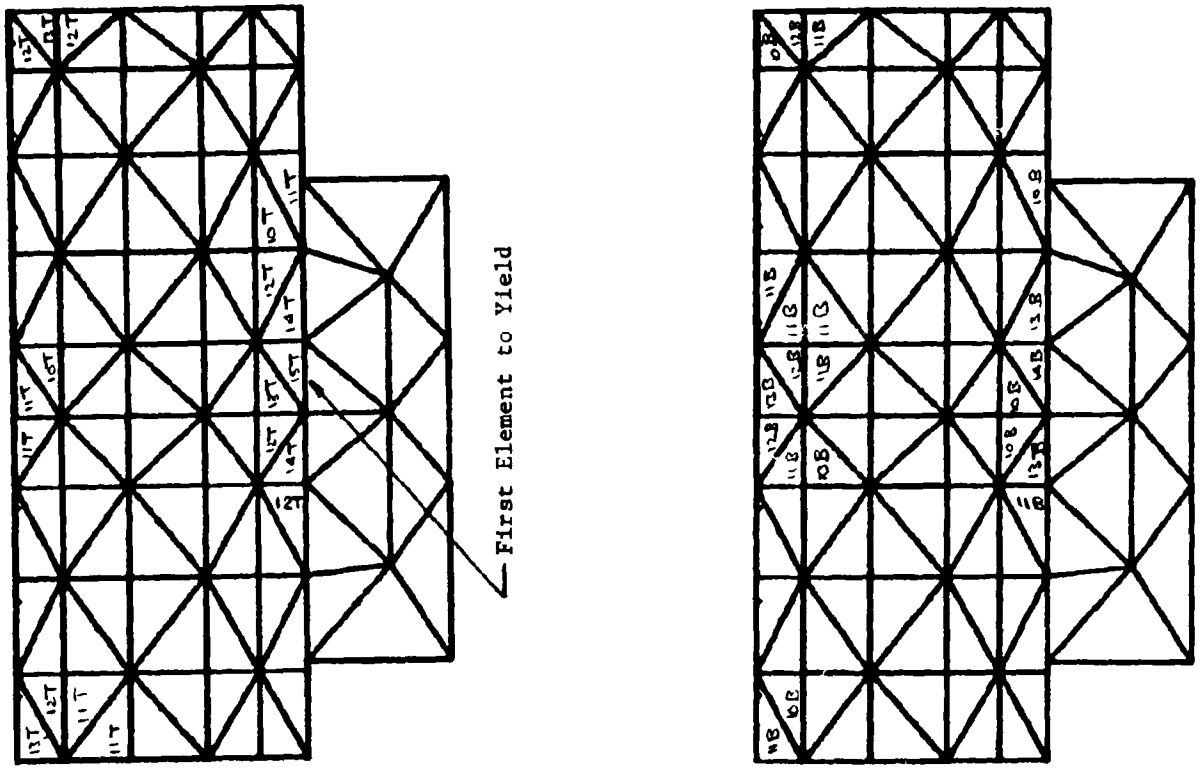

FIGURE F.11. ELEMENTS IN BOTTOM SHELL WITH VON MISES STRESSES EXCEEDING 10 KSI

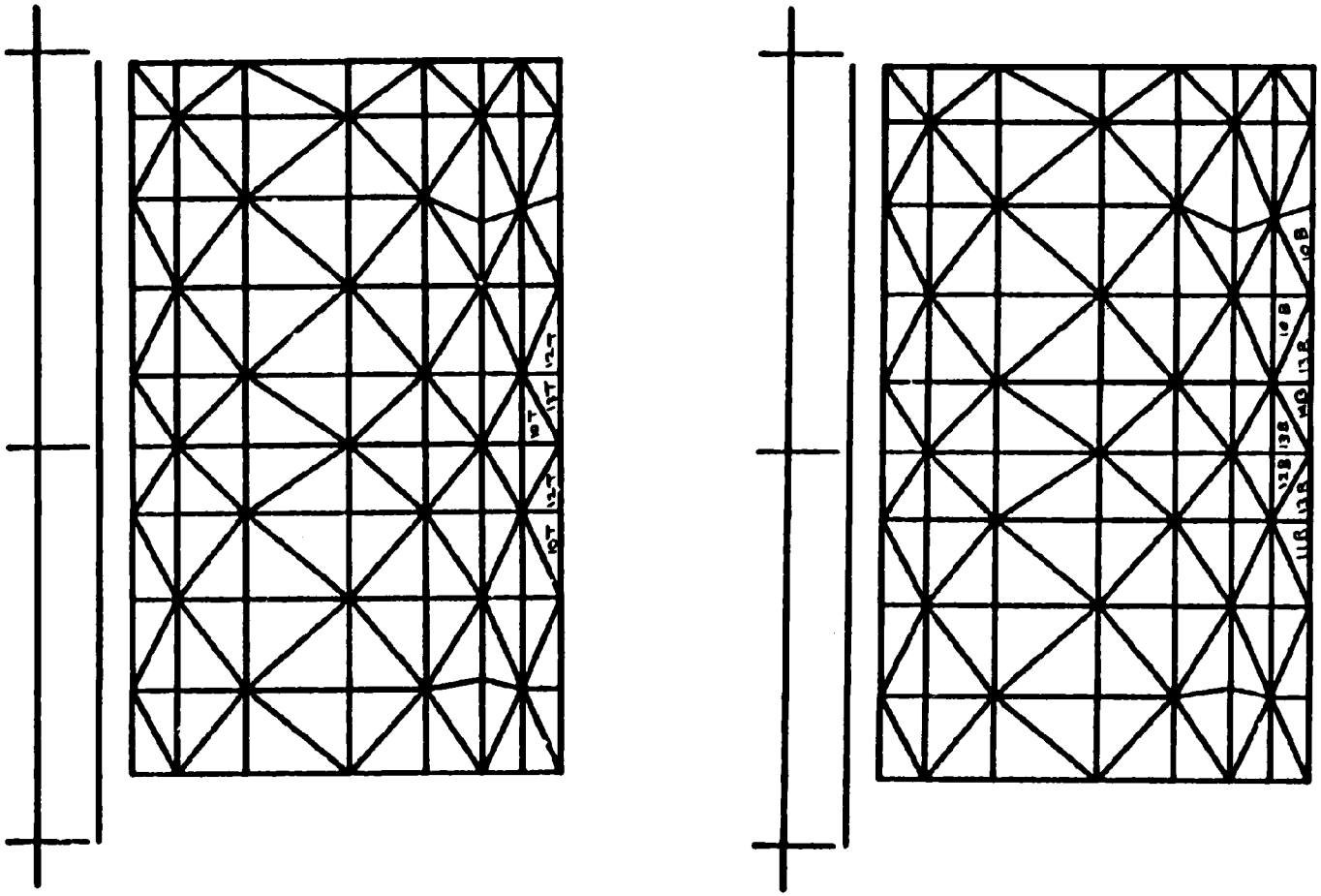

Outside Surface

Inside Surface

FIGURE F.12. ELEMENTS IN SIDE SHELL WITH VON MISES STRESSES EXCEEDING 10 KSI

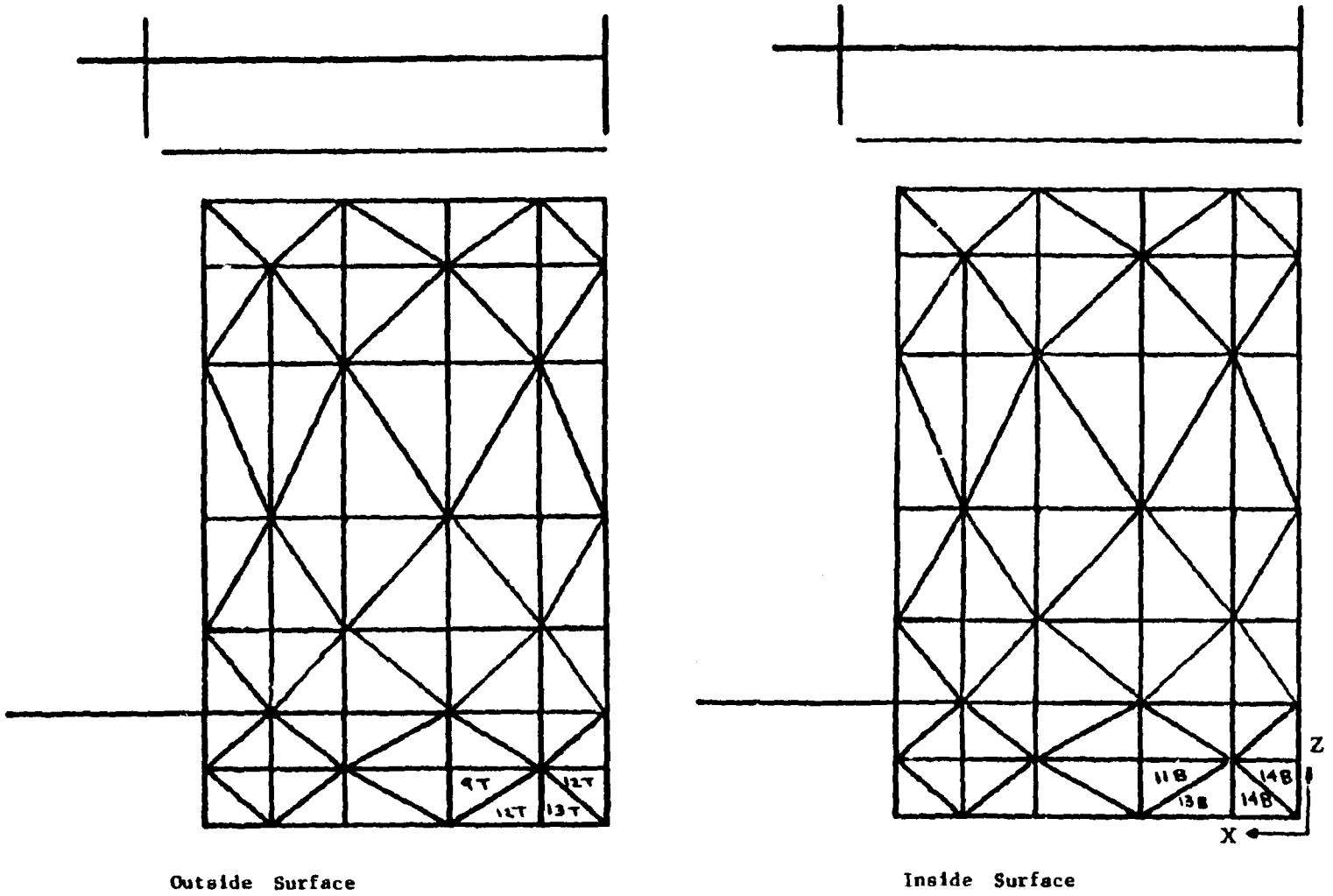

FIGURE F.13. ELEMENTS IN BACK SHELL WITH VON MISES STRESSES EXCEEDING 10 KSI

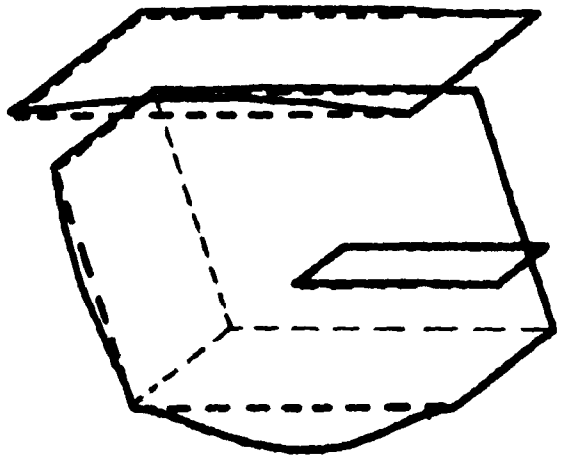

Solid Lines - Deformed Shape

Dashed Lines - Original Shape

FIGURE F.14. DISTORTED GEOMETRY FOR 100-PSI INTERNAL PRESSURE LOADING

APPENDIX G--STRESS CONTOUR PLOTS FOR ENCLOSURE III

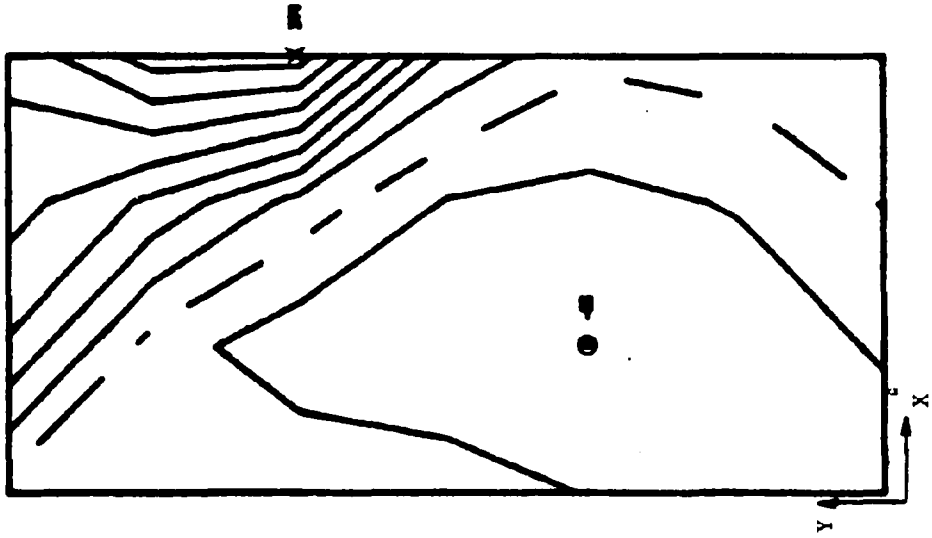

FIGURE G.1. MAXIMUM STRESS AT CENTROID OF LOWER PLANE OF ELEMENTS - RECTANGULAR WINDOW - EDGE BEAMS ONLY

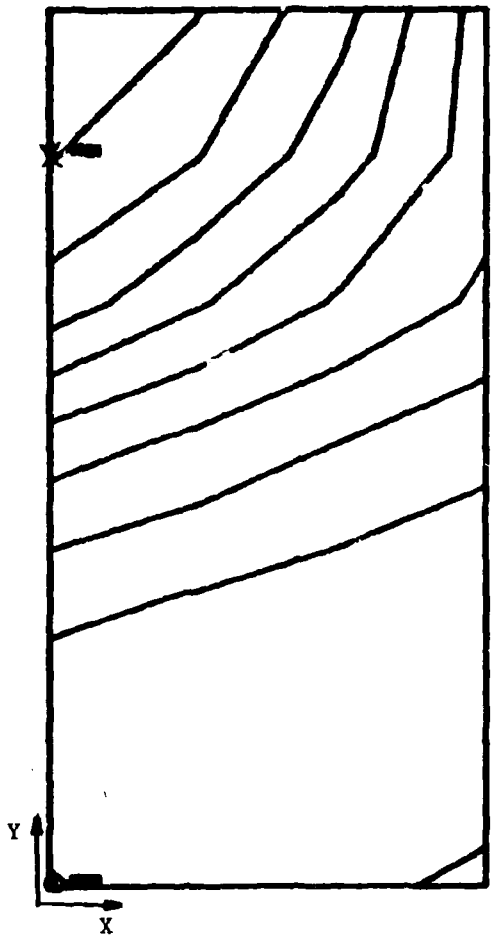

x max: -1185 psi
o min: -2805 psi

FIGURE G.2. MINIMUM STRESS AT CENTROID OF LOWER PLANE OF ELEMENTS - RECTANGULAR WINDOW - EDGE BEAMS ONLY

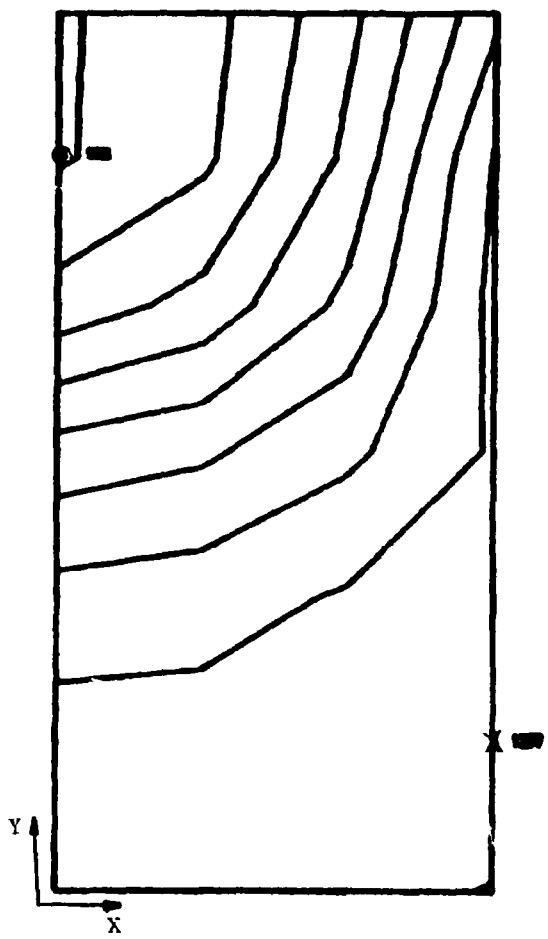

x max: 1387 psi
0 min: 588 psi

FIGURE G.3. MAXIMUM SHEAR STRESS AT CENTROID OF LOWER PLANE OF ELEMENTS - RECTANGULAR WINDOW - EDGE BEAMS ONLY

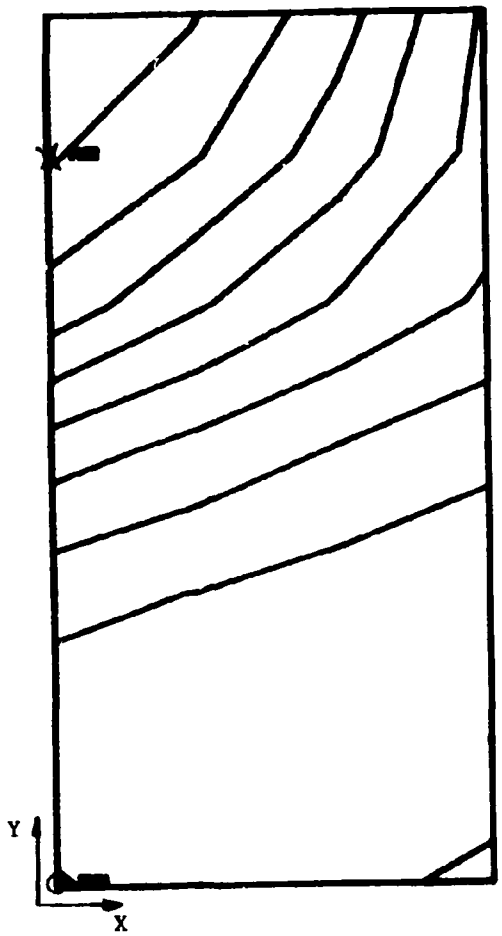

x max: 2805 psi
o min: 1183 psi

FIGURE G.4. MAXIMUM STRESS AT CENTROID OF UPPER PLANE OF ELEMENTS - RECTANGULAR WINDOW - EDGE BEAMS ONLY

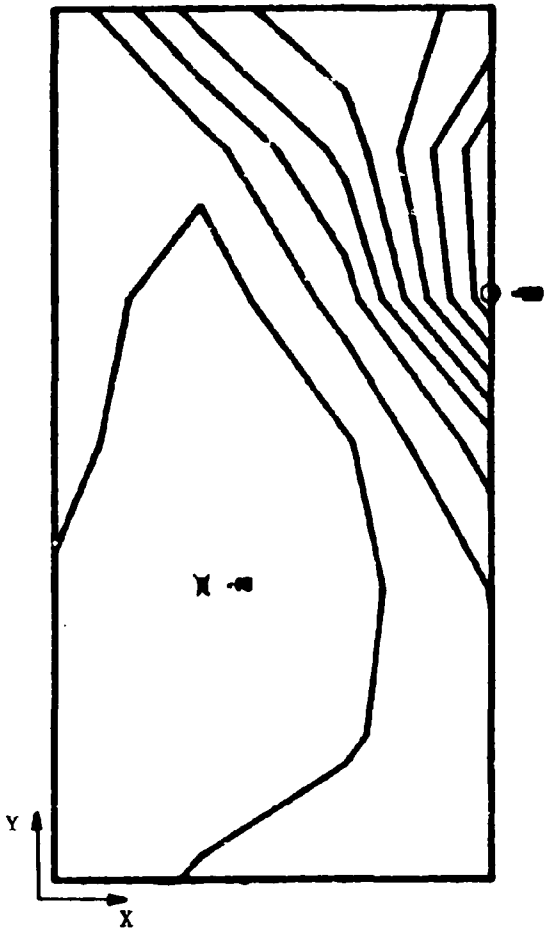

x max: -12 psi
o min: -439 psi

FIGURE G.5. MINIMUM STRESS AT CENTROID OF UPPER PLANE OF ELEMENTS - RECTANGULAR WINDOW - EDGE BEAMS ONLY

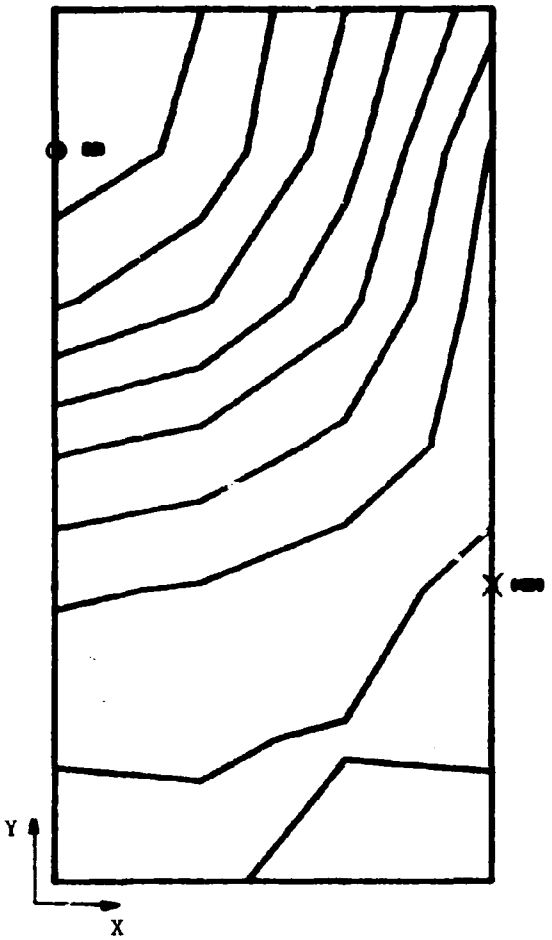

FIGURE G.6. MAXIMUM SHEAR STRESS AT CENTROID OF UPPER PLANE OF ELEMENTS - RECTANGULAR WINDOW - EDGE BEAMS ONLY

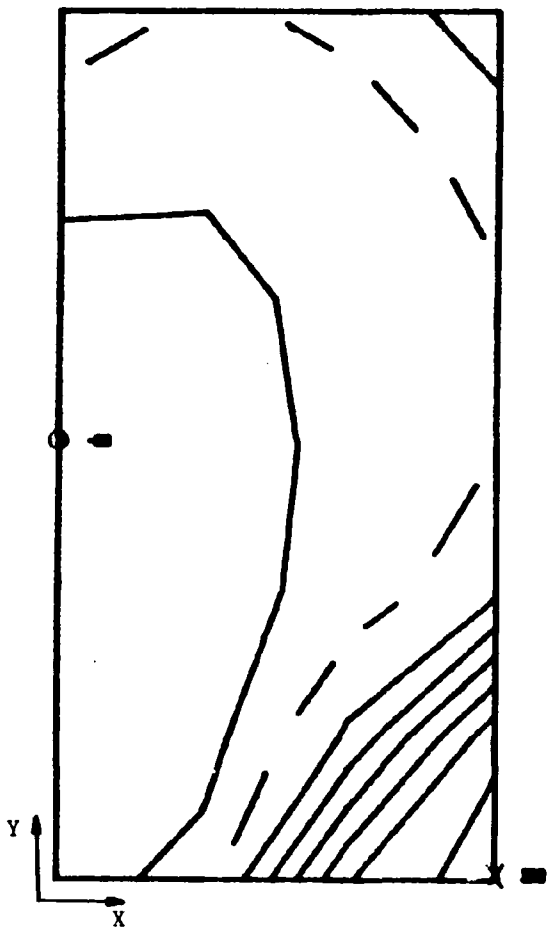

FIGURE G.7. MAXIMUM STRESS AT CENTROID OF LOWER PLANE OF ELEMENTS - RECTANGULAR WINDOW - EDGE BEAMS WITH EPOXY BOND

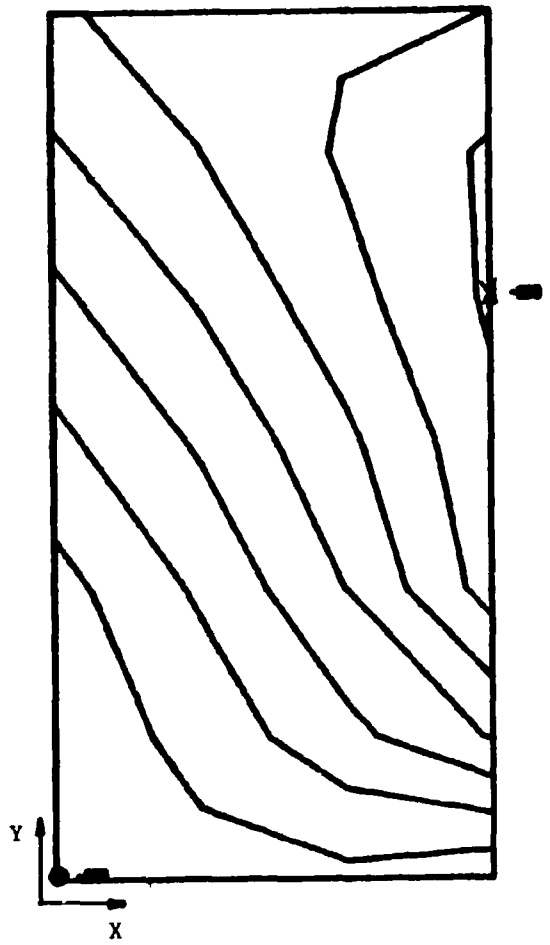

x max: -309 psi
o min: -860 psi

FIGURE G.8. MINIMUM STRESS AT CENTROID OF LOWER PLANE OF ELEMENTS - RECTANGULAR WINDOW - EDGE BEAMS WITH EPOXY BOND

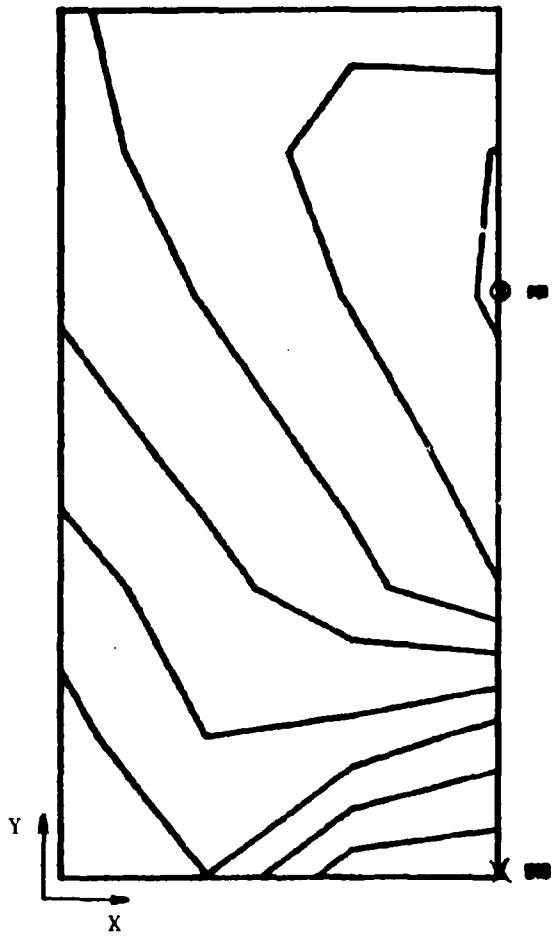

x max: 540 psi
o min: 142 psi

FIGURE G.9. MAXIMUM SHEAR STRESS AT CENTROID OF LOWER PLANE OF ELEMENTS - RECTANGULAR WINDOW - EDGE BEAMS WITH EPOXY BOND

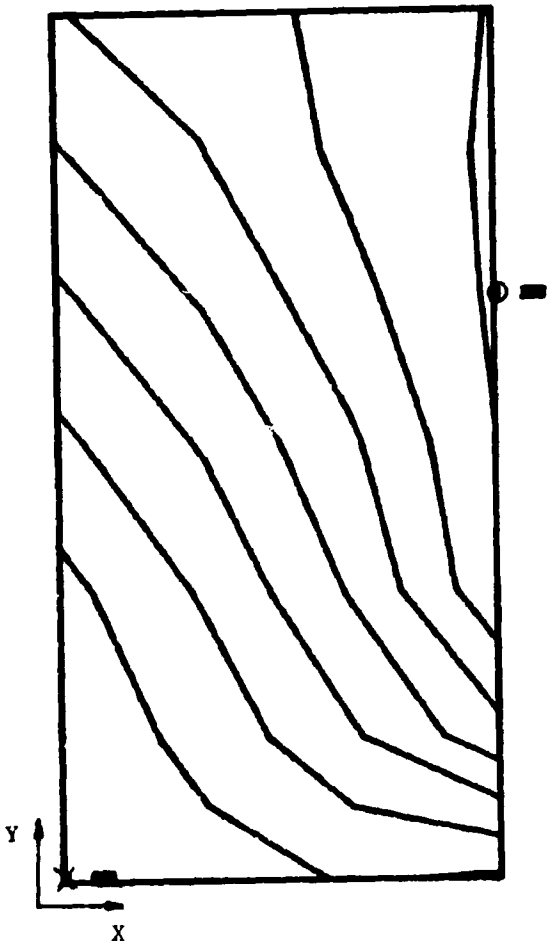

x max: 860 psi
o min: 309 psi

FIGURE G.10. MAXIMUM STRESS AT CENTROID OF UPPER PLANE OF ELEMENTS - RECTANGULAR WINDOW - EDGE BEAMS WITH EPOXY BOND

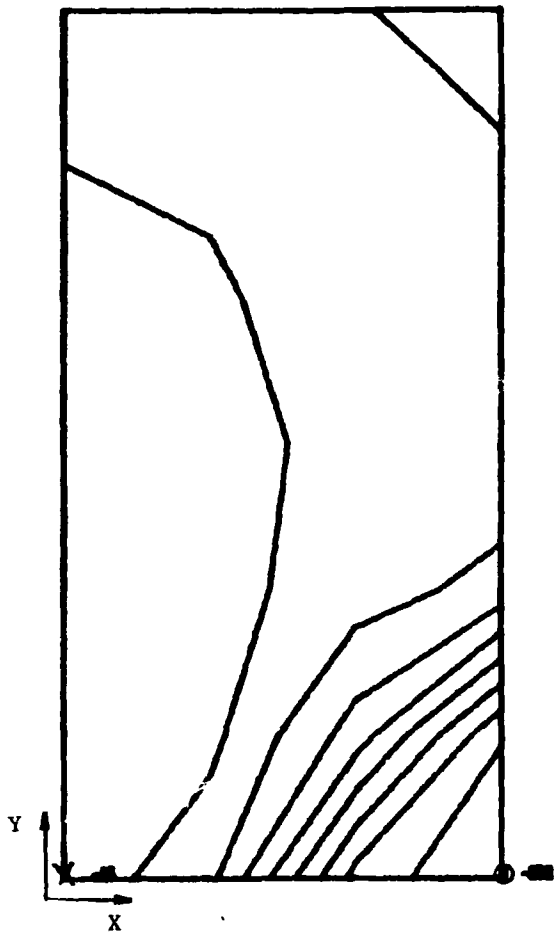

x max: -15 psi
o min: -359 psi

FIGURE G.11. MINIMUM STRESS AT CENTROID OF UPPER PLANE OF ELEMENTS - RECTANGULAR WINDOW - EDGE BEAMS WITH EPOXY BOND

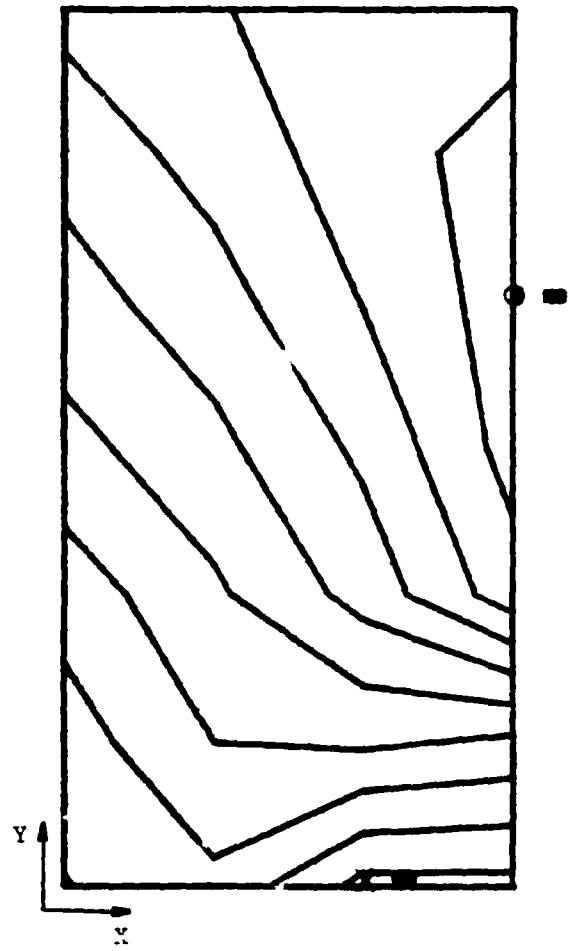

x max: 532 psi
o min: 180 psi

FIGURE G.12. MAXIMUM SHEAR STRESS AT CENTROID OF UPPER PLANE OF ELEMENTS - RECTANGULAR WINDOW - EDGE BEAMS WITH EPOXY BOND

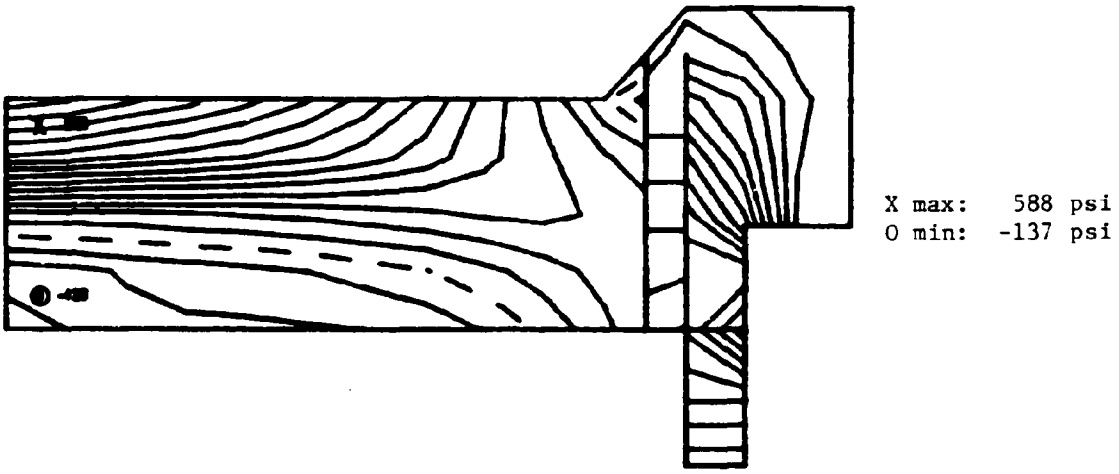

FIGURE G.13. MAXIMUM STRESS - END WINDOW

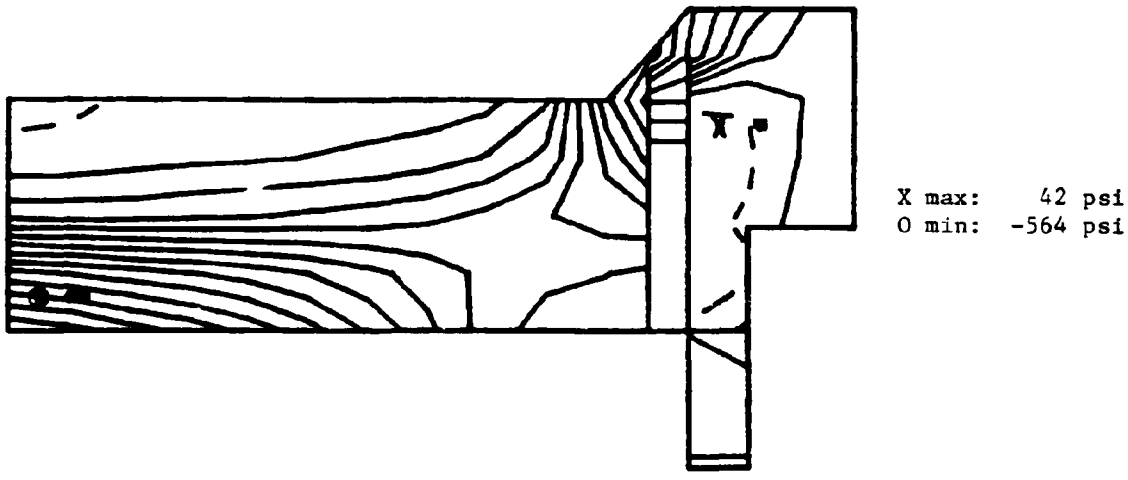

FIGURE G.14. MINIMUM STRESS - END WINDOW

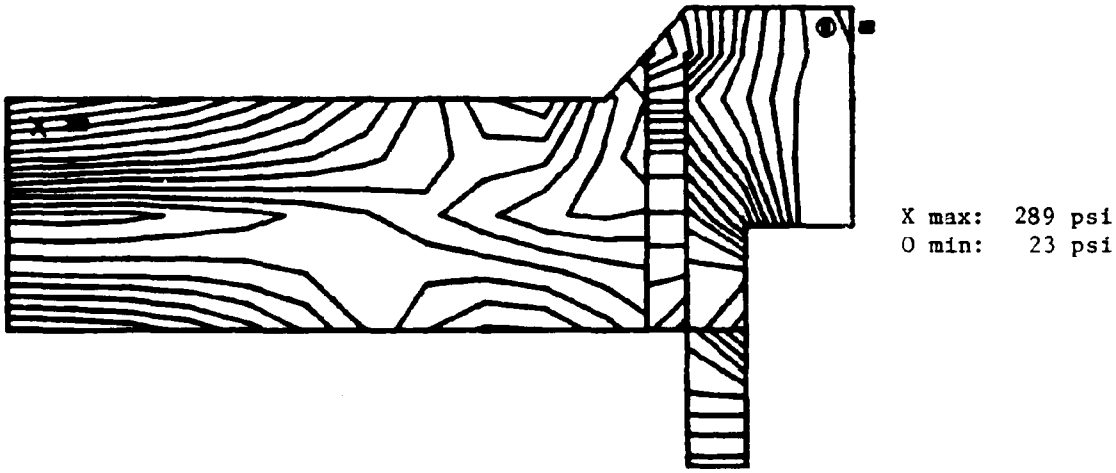

FIGURE G.15. MAXIMUM SHEAR STRESS - END WINDOW

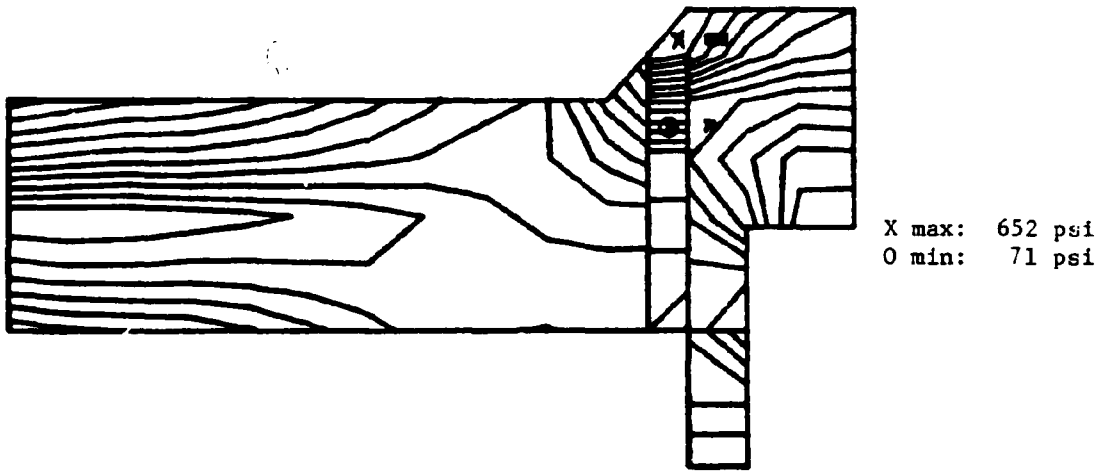

FIGURE G.16. VON MISES EQUIVALENT STRESS - END WINDOW

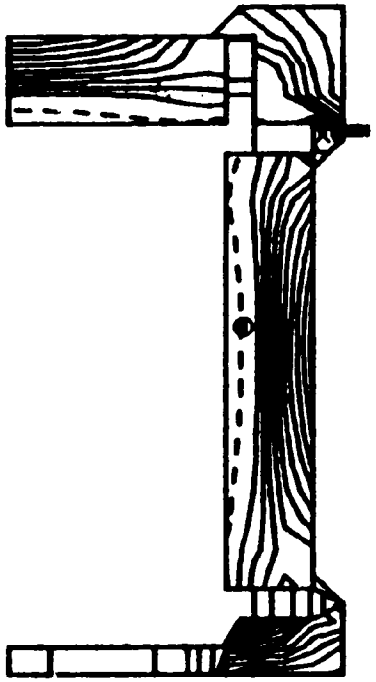

X max: 2081 psi
O min: -88 psi

FIGURE G.17. MAXIMUM STRESS - CROSS-SECTION MODEL

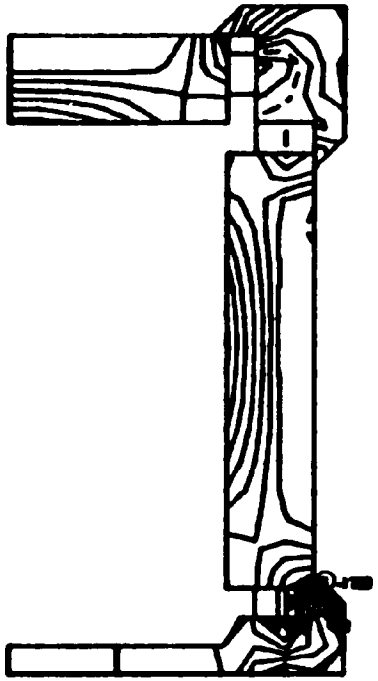

X max: 423 psi
O min: -1738 psi

FIGURE G.18. MINIMUM STRESS - CROSS-SECTION MODEL

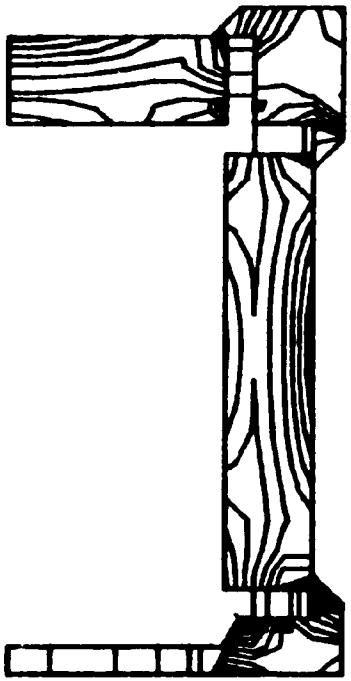

X max: 1376 psi
O min: 37 psi

FIGURE G.19. MAXIMUM SHEAR STRESS - CROSS-SECTION MODEL

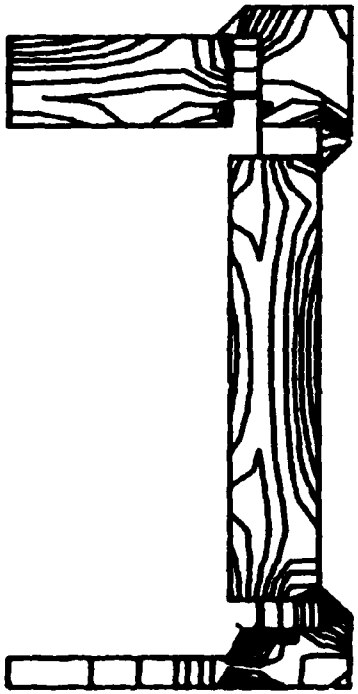

X max: 2753 psi
O min: 97 psi

FIGURE G.20. STRESS INTENSITY - CROSS-SECTION MODEL

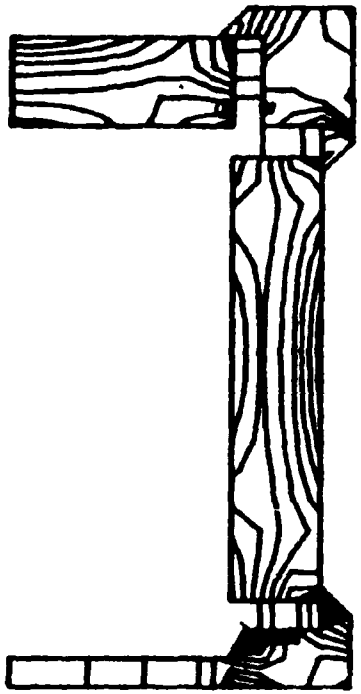

X max: 2400 psi
O min: 88 psi

FIGURE G.21. VON MISES EQUIVALENT STRESS - CROSS-SECTION MODEL

STRESSES IN RECTANGULAR AND CIRCULAR WINDOWS BASED ON HANDBOOK FORMULAS

The stresses computed by the finite element method for rectangular and circular windows can be compared with analytical solutions. Figures H.1 and H.2 were taken from Reference H.1 and give the stress factor, k_1, as a function of the plates' geometries. For a rectangular plate, the minimum bending stress is given by the expression

$$\sigma_m = k_1 \left(\frac{b}{t}\right)^2 p \qquad \text{(H.1)}$$

where

k_1 = curve A when edges are simply supported
k_1 = curve B when edges are clamped
b = smaller plate dimension
t = plate thickness
p = external pressure

For a circular plate, the maximum bending stress is

$$\sigma_m = k_1 \left(\frac{d}{t}\right)^2 p \qquad \text{(H.2)}$$

where

k_1 = 0.3025 when edges are simply supported
k_1 = 0.1875 when edges are clamped
d = plate diameter
t = plate thickness
p = external pressure

As a numerical example, we will take the dimensions of the rectangular and circular plates in Enclosure III. For the rectangular plate

$$\begin{aligned} a &= 7.50 \text{ in.} \\ b &= 3.75 \text{ in.} \\ \frac{a}{b} &= 2.0 \text{ (aspect ratio)} \\ t &= 0.75 \text{ in.} \end{aligned} \qquad \text{(H.3)}$$

and the stress factor from Figure H.1 is

$$k_1 = 0.75 \qquad \text{(H.4)}$$

The maximum bending stress for a 100-psi pressure can be computed to be

$$\begin{aligned} \sigma_m &= 0.61 \left(\frac{3.75}{0.75}\right)^2 100 \text{ psi} \\ &= 1525 \text{ psi} \end{aligned} \qquad \text{(H.5)}$$

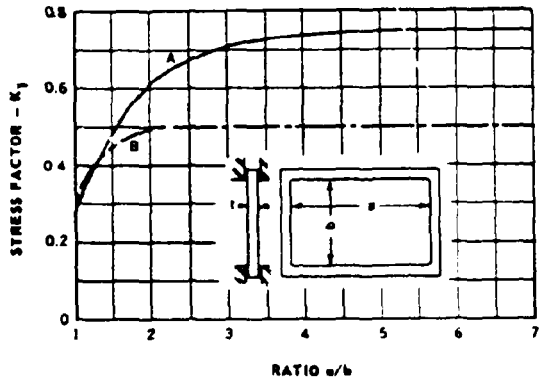

FIGURE H.1. STRESS FACTORS FOR RECTANGULAR PLATES UNDER UNIFORM PRESSURE (ADAPTED FROM TIMOSHENKO). A--Edges free. B--Edges clamped. (From [H.1])

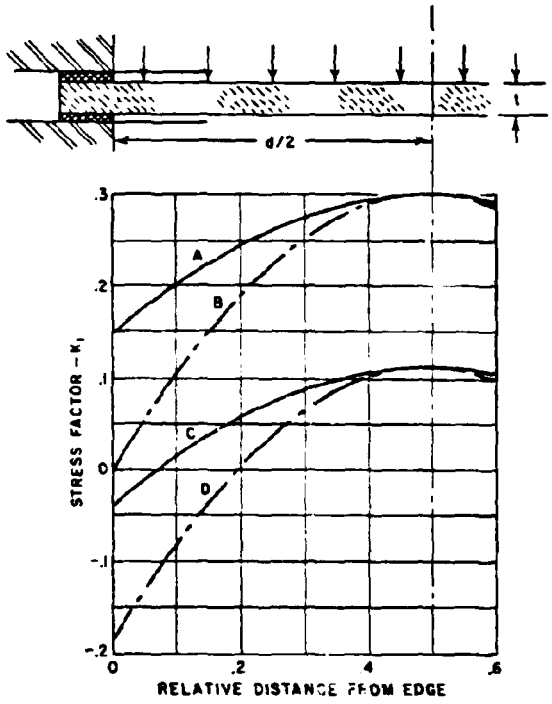

FIGURE H.2. RELATIVE STRESS DISTRIBUTION IN FLAT CIRCULAR PLATES UNDER DISTRIBUTED PRESSURE. A—Edges free—circumferential stress. B—Edges free—radial stress. C—Edges clamped--circumferen ial stress. D--Edges clamped--radial stress. (From [H.1])

This value compares very well with the results for Case IA shown in Figure 4.78.

As the aspect ratio increases, the solution approaches the plane strain case. Figure H.1 shows the stress factor is

$$k_1 = 0.75 \tag{H.6}$$

and the peak bending stress is

$$\sigma_m = 0.75 \left(\frac{3.75}{0.75}\right)^2 100 \text{ psi}$$

$$= 1875 \text{ psi} \tag{H.7}$$

The finite element results for the plane strain model are given in Figure 4.82. The window can be considered as simply supported since the epoxy cement, shown as the shaded portion, will provide little restraint in bending. The surface stresses from Figure 4.82 on the inside and outside of the window should be averaged to give the nominal bending stess, which is

$$\sigma_m = 1877 \text{ psi}$$

and (H.8)

$$\sigma_m = 1937 \text{ psi}$$

at the midsides of the top and side windows, respectively. These values again agree well with Equation H.7.

For the circular plate

$$d = 3.406 \text{ in.}$$

$$t = 0.625 \text{ in.} \tag{H.9}$$

and Equation (H.2) gives

$$\sigma_m = 0.3025 \left(\frac{3.406}{0.625}\right)^2 100 \text{ psi}$$

$$= 898 \text{ psi (simply supported plate)}$$

$$\sigma_m = 0.1875 \left(\frac{3.406}{0.625}\right)^2$$

$$= 557 \text{ psi (clamped plate)} \tag{H.10}$$

The averaged hoop surface stress at the center of the window computed by the finite element method is found in Figure 4.80.

$$\sigma_{hoop} = 771 \text{ psi} \tag{H.11}$$

This value is lower than the results for the simply supported case, but is still higher than the stress for the clamped plate. It is reasonable to expect the stresses computed by the finite element method should fall between the simply supported and clamped cases because the epoxy does provide a small restraint.

The above comparisons indicate that the analytical solutions given in Reference H.1 do provide an accurate method of computing stresses in these simple geometries. They can be used by designers to size the glass windows in the initial design stage or in cases in which deformations in the enclosure are small and do not affect the stress in the windows. Such was not the case for Enclosure III, as discussed in Section 4.3 in the body of the report.

REFERENCES

H.1. Shand, E. B., Glass Engineering Handbook, second edition, McGraw-Hill Book Company, Inc., New York, 1958.

APPENDIX I--EXPLANATORY NOTES FOR USING AWS D14.4 WELDING STANDARD IN FABRICATING EXPLOSION-PROOF ENCLOSURES WITH EXAMPLE COVER LETTER

United States Department of the Interior

BUREAU OF MINES

4800 FORBES AVENUE
PITTSBURGH, PENNSYLVANIA 15213
Pittsburgh Research Center

September 24, 1979

Southwest Research Institute
6220 Culebra Road
Post Office Drawer 28510
San Antonio, Texas 78284

Attn: Mr. P. A. Cox

Dear Sirs:

One aspect of the U.S. Bureau of Mines research programs is the development or improvement of technology that will protect the miner from occupational health and safety hazards. Although, the Mine Safety and Health Administration is the only government agency charged with the task of promulgating federal regulations pertaining to the health and safety of the miner, the Bureau supports their task through research. To this end, the Bureau has been conducting research in the area of explosion-proof enclosures for several years. Our research will culminate with a publication containing recommendations for designing explosion-proof enclosures based on performance standards.

An integral part of this guide will be recommendations for achieving a good quality weld. The Bureau, through its contractor (Southwest Research Institute), has visited several manufacturers of explosion-proof enclosures used in underground mines to review their present welding practices. Also, a thorough review of available welding standards has been conducted. One standard has been selected as best matching the industry's present practices plus offering flexibility for innovations--American Welding Society Standard D14.4-77, Classification and Application of Welded Joints for Machinery and Equipment. The Standard includes information on weld joint design, welder and welding procedure qualifications, inspection criteria, and provisions for qualifying all the present weld joint designs and/or procedures used in the present enclosure manufacturing process.

The Bureau is soliciting comments from representative organizations. Any comments should be addressed to:

Mr. Roger L. King
Technical Project Officer
U.S. Bureau of Mines
Pittsburgh Research Center
4800 Forbes Avenue
Pittsburgh, Pennsylvania 15213
Telephone: (412) 675-6637

Ltr. to Mr. P. A. Cox, Southwest Research Institute, from Roger L. King re Quality of weld for explosion-proof enclosures; 9/24/79

I have attached for your use a copy of AWS D14.4-77 and some supplemental notes to aid you in your understanding of it and how it would apply to the fabrication of explosion-proof enclosures.

Sincerely yours,

Roger L. King
Technical Project Officer

Enclosure

EXPLANATORY NOTES FOR USING AWS D14.4 WELDING STANDARD*

IN FABRICATING EXPLOSION-PROOF ENCLOSURES

Prepared by Southwest Research Institute

Background

It is Southwest Research Institute's recommendation that AWS D14.4 be adopted for fabricating XP enclosures. The use of this standard would not necessarily change weld joint designs or weld quality from existing practice. In fact, of the six companies visited, welding practices conform to, and exceed the design and quality requirements of the Standard; however, none of the companies visited formally recognize the visual examinations performed on final weld surfaces, the class of design used on weldments, and the certification of welders used on XP enclosures. In recommending AWS Standard D14.4 it is intended that the minimum requirement will be used. The specific parts of the standard which would apply to manufacturers of XP enclosures are reviewed in the following paragraphs.

The AWS D14.4 Welding Standard is divided into the following sections:

(1) Scope

(2) Classification of Welded Joints

(3) Welded Joint Design

(4) Workmanship

(5) Quality Control Requirements and Procedures

---

*Unless clearly stated as "in these notes," all references to figures, sections, and pages refer to D14.4.

(6) Qualification

Part A - General Qualification Requirements

Part B - Welding Procedure Qualification

Part C - Welder Qualification

Part D - Welding Operator Qualification

Part E - Qualification of Tackers

(7) Inspection

Part A - Radiographic Inspection

Part B - Ultrasonic Inspection

Part C - Magnetic Particle Inspection

Part D - Liquid Penetrant Inspection

Part E - Visual and Dimensional Inspection

These sections cover three criteria common to all welding codes, which are:

(1) Welding Procedure Specification (Section 2, part of Section 3)

(2) Welding Procedure Qualification (Section 6, Parts A and B)

(3) Welder or Welding Operator Qualification (Section 6, Parts A, C, D, and E).

In addition, D14.4 covers:

(4) Joint Design (Section 3), and

(5) Acceptance Criteria for Weldments (Sections 4 and 7).

A good feature of this code is that it is self contained, i.e., it gives sufficiently detailed information to perform all of the five functions enumerated. We believe that classification of joint efficiencies, and the permissible use of prequalified joints and procedures will be of great benefit to XP enclosure manufacturers. These features are discussed in more detail in the following paragraphs. Those unfamiliar with welding codes may not readily realize that most of the written code addresses requirements for joints which are classified as "other than prequalified." Thus, a majority of the standard does not apply when a prequalified procedure and visual inspection are used. However, all of the provisions for qualification, testing and inspection-methods are given in the event they do become necessary. The following discussions will attempt to show both the simplified, prequalified procedure and also the procedure qualification testing situations.

Applicable Sections

There are some parts of AWS D14.4 that do not apply to manufacture of XP enclosures under present practices. For example, Classes I, II, and III weld joints, which give 100% static joint efficiency, are not presently used for XP enclosures. Therefore, the weld quality requirements for these classes of welds do not apply, and so ultrasonic, radiographic, and magnetic particle

nondestructive testing are not necessary in the design for XP enclosures. Classes I, II or III could be used if at anytime the designer considers it is beneficial to have a higher joint efficiency. It follows that inspection requirements (pages 49-74) usually are not necessary, except for Part E, "Visual and Dimensional Inspection," on pages 70 to 74. The following discussion is intended to cover those welding standard areas of D14.4 that should be applied to present practice.

Joint Efficiency (Section 2)

Joint efficiency is the ratio of the strength of a joint to the strength of the base metal expressed in percent. The selection of joint efficiency depends entirely on the design parameters that are established by each manufacturer to meet the service intended for the part. Past experience and certification testing are also used to determine suitability of joint designs in addition to calculating allowable unit stresses. Allowable unit stresses (σ) most often are calculated by the formula:

$$\sigma = \frac{P}{A} \times \text{safety factor}$$

where P is the joint load

and A is the effective weld cross sectional area per unit length of weld

The allowable maximum stress must then be multiplied by the joint efficiency shown on Figure 2.1 on pages 2 and 3 of the standard to establish the permissible design stress. Fatigue of the weld can also be evaluated as shown in

Figure 3.1.3 on pages 4 and 5. Most XP enclosures are presently built to Class IV and V type of joint designs. The use of joint efficiency in enclosure designs is demonstrated in Example 1 of these notes.

Prequalified Welding Procedures (Section 3)

Prequalification of a welding procedure specification (WPS) refers to the use of certain weld joint details, materials and processes which are permitted in the Welding Standard without performing any procedure qualification or testing. The purpose in qualifying a welding procedure or using a prequalified procedure is to provide assurance that quality welds and strength levels can be produced within a certain range of welding variables using the materials and processes tested. Procedure qualification provides a demonstration that sound welds can be made and offers a measure of quality assurance for product liability.

Details of welded joints (paragraph 3.3 page 1) and the fillet weld details for carbon and low-alloy steels (paragraph 3.3.2, page 6) may be used with the designated welding processes without performing a procedure qualification. Weldments made under these guidelines are designated as prequalified joints. The referenced Figures 3.2.5, 3.3.4.1.2, 3.3.5.1, and 3.3.5.2 pages 8 through 15 show the choices for prequalified procedure, process, and joint parameters.

Welder Qualification Testing (Section 6, Parts A and C)

Three approaches are provided in paragraph 6.3, page 18 for qualifying welders, welding operators, or tackers. Details of welder qualifications provided in Part C of the Standard cover the variables that must be tested in order to match production requirements. A second approach is to accept evidence of previous qualification of the welders, i.e., from previous employment, schooling and certication, state certification, etc. Accepting evidence of previous qualification of a welder is very practical and is based largely on the premise that the welder has continued to make satisfactory welds. This premise is usually valid if the welder has used the welding process within a six month period. Judgement on acceptance of welders is left to the descretion of an Engineer. If previous qualification is accepted the Engineer will normally keep a record on file of the statement of his or the Company's acceptance of the welder's qualification. The third approach provides for welder certification by radiographic examination of a test plate. Welding a grooved test plate of 3/8-inch thickness qualifies a welder or operator for any thickness fillet weld for those welding positions tested. To qualify for groove welds of unlimited thickness, the plates tested must be at least 1 inch thick, using a single-Vee groove as described in paragraph 6.19. The alloy group designation for various weld strength levels for which a welder must qualify, are described in paragraph 6.18.2, page 35. Referring again to Example 1, the welder used to make the fillet welds could be qualified by either Option 1 or 2. Option 1 test is shown in Figure 6.23.1, page 40 which consists of a single fillet-welded T joint, 8 inches long on 1/2-inch plate

which is sectioned for a macro-etch and a break test (paragraph 6.28.2 page 38). Acceptance for the test is provided in paragraph 6.29.2, page 39. Option 2 provides for making fillet welds into root-bend test specimens as shown in Figure 6.23.2, page 41. The two root-bend test specimens (Table 6.27.1, page 43) tested in one of the jigs shown in Figure 6.28.1, page 46 must not exceed a 1/8-inch crack (or defect) on the convex surface of the U bend as required in paragraph 6.29, pages 38 and 39.

The position of welding is an essential variable for welder qualification. The welder must be tested and qualified for the placement and positioning of welding used in production. However, the more difficult positions identified in Figure 6.9.3 page 26 for fillet welds also qualify for the less difficult as summarized in Table 6.24, page 42.

Procedure Qualification Testing and Testing Laboratories (Section 6, Parts B and C)

It is common practice for smaller companies (who do not have their own test facilities) to send both their welder and procedure qualification test coupons to a commercial testing laboratory. Most major cities have testing laboratories capable of testing and reporting results needed for certification. In the event a procedure qualification test is required because the desired joints or welding processes are not considered as prequalified in the Standard, the use of a testing laboratory is very helpful. Mechanical tests are required for procedure qualification which involve both tensile and guided-bend testing as shown in Table 6.11.1.1, page 27. Removal and preparation of test specimens are presented in sufficient detail that any shop or laboratory can make them in accordance with Figures 6.11.1.3, (A) through (K) pages 28 through 35.

For typical explosion-proof enclosure construction, procedure qualification would not be necessary. On the other hand, where the flux cored arc welding (FCAW) process is used for other than fillets, it would be necessary to qualify any groove welding procedure. Example 2 of these notes describes the steps necessary for a procedure qualification.

Inspection (Section 7, Part E)

The final item required by the Standard for a typical XP enclosure would be Part E, "Visual and Dimensional Inspection," page 70. Visual inspection is required in Table 5, "Weld quality assurance requirements," for a Class V weld. Therefore, all of the visual acceptance criteria on pages 70 through 74 apply for final weld surfaces.

In-Process Inspection (Not Specifically Covered in the Standard)

Considerable added quality assurance measures can be provided during fabrication that are not mandatory in the Standard. Nondestructive and visual testing at intervals during welding can avert many of the conditions that produce defects. The quality of the root bead is important as is the interbead cleaning and grinding preparation that are performed. To help ensure the soundness of the welds being made, it is recommend that an inspector be assigned to in-process as well as final weld inspection.

Example 1

A typical prequalified welding procedure that might be used to fabricate explosion-proof enclosures in accordance with AWS D14.4, is described in the following items for a hypothetical case. The items required include:

1. Providing a written procedure.

2. Choosing a prequalified joint design and procedure.

3. Coordinating the weld joint design selection with the efficiency determined by the design engineer.

4. Establishing how fit up will be maintained, i.e., by jigging, tacking, etc.

5. Qualifying the welders and welding operators on the material, thicknesses and positions that are required in production.

Form E-1 (Figure I.4 of these notes) was selected for the written welding procedure specification in this example and is shown in the attachments. The form (E-1) is the sample provided by the AWS D1.1-79, "Structural Steel" Welding Code and is also suitable for use with the D14.4 Welding Standard. Filling out the form is essentially self-explanatory. The welding parameters intended to be used in production need to be provided.

The shielded metal arc welding (SMAW) process and a Class V fillet weld joint is typical for XP enclosures and was selected for this example. Refer to the weld joint details B and C in Figure I.1 of these notes where the plate sides of the box are attached to the frame and the ends are inset to the bottom and side plates then fillet welded. A sketch of the enclosure is given in Figure I.2 of these notes. Calculation of the weld joint stresses for the enclosure is complicated because the box structure is indeterminate; therefore, in this example only the stresses in the weld produced by shear reactions are considered.

Base Material - ASTM A36 Steel Plate - 1/4 Inch - 60 ksi min. tensile, 36 ski min. yield strength

Weld Material - E-7018, AWS A5.1 or A5.5, 70 ksi min. tensile, 57 ksi min. yield strength

Pressure Load Inside Enclossure - 150 psig

Safety Factor - 2X

Sixe of plate receiving maximum load - 1 sq. ft. (144 sq. in.) and 48 in. of weld to receive the load

Size of fillet weld preferred = 3/16 inch

Static joint efficiency to establish permissible design stress - 50% for Class V weld joints.

$$\sigma_{max} = \frac{P}{A} \times \text{Safety Factor};$$

where σ_{max} = allowable maximum stress
P = pressure load
A = area of fillet weld throat

$$\sigma_{max} = \frac{150 \text{ psi} \times 144 \text{ sq. in.} \times 2}{48 \times 3/16 \times 0.707} = 6789.3 \text{ psi}$$

A 50% efficiency gives σ_{max} = 13,579 psi allowable stress

13,579 psi is acceptable since it is much less than either the base or filler material strength (approximately 36 ksi) by a factor of 2.65X.

The coordination of these calculations with the weld joint selected and the resulting efficiency for static loading in shear is fulfilled.

The fitup required for the XP enclosure will be required to have no gaps greater than 1/8 inch spacing before welding between the ends, sides, and bottom on joint C. The tolerance between the sides and the frames will be required to have no gaps greater than 1/16-inch spacing before welding. Clamping is the only means required to hold the parts for welding.

The welders used for this procedure shall be qualified as a minimum to weld on mild carbon steel. Fillet welds are to be made in the 3F (vertical) welding position. Option 1 shown in Figure 6.23.1 on page 40 will be used to test welders using 1/2-inch plate. The 3F welding position for fillet welding is shown in Figure 6.9.3(c) on page 26. Welder qualification in the 3F (vertical)

position qualifies for flat, horizontal and vertical position fillet welding of plate as stated in Paragraph 6.24.3.3 on page 37. The fillet weld break test required by Paragraph 6.27.1 and 6.27.3 on page 38 and Table 6.27.1 on page 43 consists of a visual examination, bending the weld back on itself and also examining a macroetched specimen cut through the weld joint. The test results of each welder's tests will be kept in a permanent record file. Sample Form E-4 (Figure I.6 of these notes) is provided as a suitable welder and welding operator qualification test record.

Example 2

A typical groove welding procedure using the flux cored arc welding (FCAW) process is an example where welding procedure qualification is required by AWS D14.4. Items which must be included in the qualification procedure are the same as for the prequalified welding procedure given in Example 1 of these notes, except that the demonstration and mechanical testing of the procedure must be documented. Items to be included are:

1. Providing a written procedure

2. Choosing a suitable joint design and procedure

3. Coordinating the weld joint design with the efficiency determined by the design engineer.

4. Establishing how fit-up will be maintained, i.e., by jigging, tacking, etc.

5. Perform a procedure qualification on a suitable groove weld test joint.

6. Preparing, testing, and recording of the procedure qualification test information.

7. Qualifying the welders and welding operators on the material, thickness, and positions that are required in production.

The form for the written welding procedure specification chosen for this example is shown in the attachments as Figure I.3 of these notes - Sample Joint Welding Procedure Specification. The welding parameters intended for use in production need to be provided in this form, sometimes referred to as a welding data sheet.

The weld joint design shown in Figure I.3 of these notes is suitable for making a complete or 100% joint connection and will fulfill the requirement for a procedure qualification test joint. But the normal joints provided for XP enclosures, especially on the frame members, are partial penetration joints. Therefore, the joint configuration chosen for this example is Joint A of Figure I.1 of these notes. As shown in the sketches, a single bevel preparation of 50° minimum angle will be machined or ground on the side frame member connections. The frame required is a 2-inch square and the depth for the bevel 3/8 inch for this example. One pass of FCAW weld is required all around this corner joint so that the surfaces can be finish ground or machined flush to make a sealing surface.

Analyses of a typical enclosure have shown that maximum scresses in the frame are quite low, typically less than 20% of the yield strength of the material at a design pressure of 150 psi. The design detail chosen has a static joint efficiency of 80% as shown in Figure 2.1, page 2 of D14.4. Thus, this joint design is more than adequate for the applied loads.

The fit-up of the frames will be butt uptight for welding and will be held in a fixture designed to rotate or turn over in order that all of the flux core welding may be performed in the down-hand, flat, or 1G position.

Procedure qualification for using the FCAW process in a groove weld is required by AWS D14.4. The welding procedure qualification test record if Form E-2 shown in Figure I.5 of these notes. Welding information and the actual parameters used in the welding procedure in production will be expanded from these actual test parameters approximately ±10%. The requirements for essential welding procedure variables listed in Paragraph 6.6.2.4 on page 20 for Flux Cored Arc Welding are considered to be the minimum of information recorded in the Procedure Qualification Record. To match the minimum dimension of weld joint angle, the qualification must also demonstrate the 50° minimum included angle permitted in the procedure, 6.6.2.4(13).

The requirement for testing groove welds, Paragraph 6.7.1 on page 21, includes tensile and bend tests. A flat plate welding position only will be tested as shown in Figure 6.9.1(A) on page 24. In order to qualify for welding on a carbon steel bar of at least 2 inches in thickness, Table 6.11.1.1 on page 27 gives the number and type of test specimens and range of thickness qualified. The test plate thickness must be 25 mm or 1 inch minimum, using one plate sample from which two reduced tensile specimens, and four side-bend test specimens are required. Location of test specimen removal for plates over 3/4-inch is shown in Figure 6.11.1.3(D) on page 29. The specifications for reduced section tensile specimens is shown in Figure 6.11.1.3(F) and the side-bend specimens in Figure 6.11.1.3(J). The tensile strength shall be not less than the minimum of the specified tensile range of the base metal used as per Paragraph 6.13.1 on page 29. For A-36 Steel Plates the required minimum is 60 ksi. In accordance with Paragraph 6.13.2 none of the side-bend test specimens must show any crack or opening in excess of 1/8-inch except on the corners. The results of these tests will be recorded on Form E-2, Welding Procedure Qualification Test Record (Figure I.5 of these notes).

Qualification of operators for the flux cored arc welding process, in accordance with Part C of the Standard, requires a groove weld qualification plate test for plates of unlimited thicknesses. This test plate is described in Paragraph 6.19 page 35 and Figure 6.19A on page 36. Radiographic testing will be used for acceptance of welder plate tests as provided in Paragraph 6.29.4 and Part A of Section 7. Again the same form E-4 will be used to record the radiograph test results for each welding operator. The test plates for this example will be sent to a local testing laboratory and the acceptance criteria of Paragraph 7.3.9 on page 52 will be applied. A permanent record file will be kept for each operator to maintain qualification information.

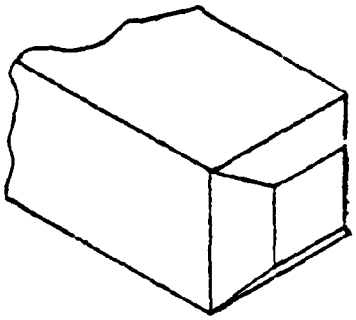

Beveled Bars for
Making Frame Joints

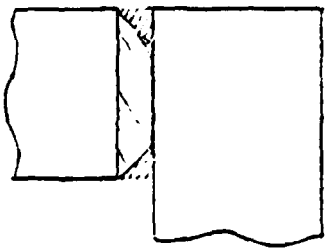

A. Partial Penetration Corner Weld Joint for Frames

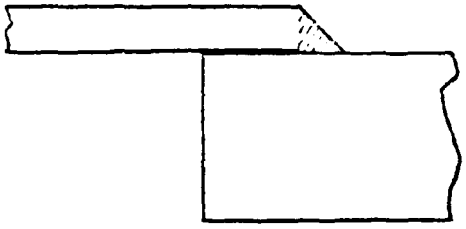

B. Side and Ends Joined by a Lap Joint to the Frame

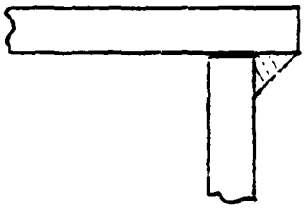

C. Inset Type Fillet Weld Joint for Enclosure Ends using Wrap-Around Sides

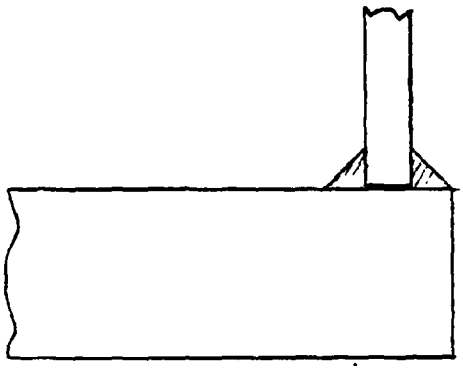

D. Double Fillet Welded Tee Joint for Joining Thin Side to Heavy Bottom Plate, etc.

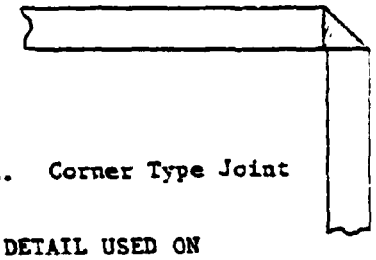

E. Corner Type Joint

FIGURE I.1. EXAMPLES OF WELD JOINT DETAIL USED ON SOME EXPLOSION-PROOF ENCLOSURES

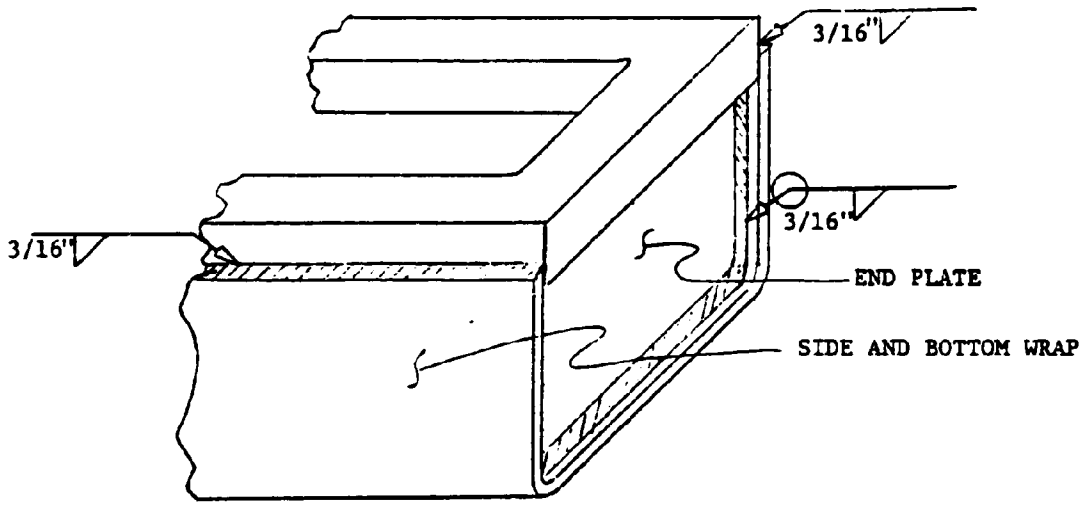

FIGURE I.2. SKETCH OF TYPICAL ENCLOSURE END DETAIL

JOINT WELDING PROCEDURE
SPECIFICATION NO.____
JOINT____

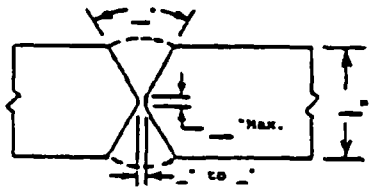

WELDING PROCEDURE - GENERAL

BASE METAL (SPECIFICATION NO.)_____

ELECTRODE (CLASSIFICATION OR TRADE NAME)_____

POWER SOURCE (AC OR DC) AND POLARITY IF DC_____

BACKING OR ROOT TREATMENT_____

PREHEATING_____

POSTHEATING_____

POSITION OF WELDING_____

DETAILS OF WELDING PROCEDURE

PASS NUMBER	ELECTRODE SIZE	CURRENT RANGE	ARC VOLTAGE	LOCATION AND SEQUENCE OF PASSES

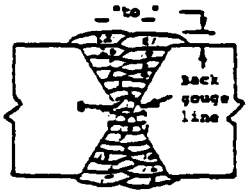

FIGURE I.3. SAMPLE JOINT WELDING PROCEDURE SPECIFICATION

PREQUALIFIED JOINT WELDING PROCEDURE
PROCEDURE SPECIFICATION

Material specification _____
Welding process _____
Manual or machine _____
Position of welding _____
Filler metal specification _____
Filler metal classification _____
Flux _____
Weld metal grade* _____
Shielding gas _____ Flow rate _____
Single or multiple pass _____
Single or multiple arc _____
Welding current _____
Polarity _____
Welding progression _____
Root treatment _____
Preheat and interpass temperature _____
Postheat treatment _____

*Applicable only when filler metal has no AWS classification.

WELDING PROCEDURE

Pass no.	Electrode size	Welding current		Travel speed	Joint detail
		Amperes	Volts		

This procedure may vary due to fabrication sequence, fit-up, pass size, etc., within the limitation of variables given in 4B, C, or D of AWS D1.1, Structural Welding Code.

Procedure no. _____ Manufacturer or contractor _____

Revision no. _____ Authorized by _____

Date _____

Form E-1

FIGURE I.4. FORM E-1

WELDING PROCEDURE QUALIFICATION TEST RECORD

PROCEDURE SPECIFICATION

Material specification _____
Welding process _____
Manual or machine _____
Position of welding _____
Filler metal specification _____
Filler metal classification _____
Weld metal grade* _____
Shielding gas _____ Flow rate _____
Single or multiple pass _____
Single or multiple arc _____
Welding current _____
Welding progression _____
Preheat temperature _____
Postheat treatment _____
Welder's name _____

*Applicable when filler metal has no AWS classification.

GROOVE WELD TEST RESULTS

Reduced-section tension tests
Tensile strength, psi

1. _____
2. _____

Guided-bend tests (2 root-, 2 face-, or 4 side-bend)

Root	Face
1. _____	1. _____
2. _____	2. _____

Radiographic-ultrasonic examination

FILLET WELD TEST RESULTS

Minimum size multiple pass Macroetch	Maximum size single pass Macroetch
1. _____ 3. _____	1. _____ 3. _____
2. _____	2. _____

All-weld-metal tension test

Tensile strength, psi _____
Yield point, psi _____
Elongation in 2 in., % _____

Laboratory test no. _____

WELDING PROCEDURE

Pass No.	Elect. size	Welding current		Speed of travel	Joint detail
		Amperes	Volts		

We, the undersigned, certify that the statements in this record are correct and that the test welds were prepared, welded, and tested in accordance with the requirements of 5B of AWS D1.1, Structural Welding Code.

Procedure no. _____ Manufacturer or contractor _____

Revision no. _____ Authorized by _____

Date _____

Form E-2

FIGURE I.5. FORM E-2

WELDER AND WELDING OPERATOR QUALIFICATION TEST RECORD

Welder or welding operator's name _____ Identification no. _____
Welding process _____ Manual _____ Semiautomatic _____ Machine _____
Position _____
(Flat, horizontal, overhead or vertical – if vertical, state whether upward or downward)
In accordance with procedure specification no. _____
Material specification _____
Diameter and wall thickness (if pipe) – otherwise, joint thickness _____
Thickness range this qualifies _____

FILLER METAL

Specification no. _____ Classification _____ F no. _____
Describe filler metal (if not covered by AWS specification) _____

_____

Is backing strip used? _____
Filler metal diameter and trade name _____ Flux for submerged arc or gas for gas metal arc or flux cored arc welding _____

Guided Bend Test Results

Type	Result	Type	Result

Test conducted by _____ Laboratory test no. _____
per _____

Fillet Test Results

Appearance _____ Fillet size _____
Fracture test root penetration _____ Macroetch _____
(Describe the location, nature, and size of any crack or tearing of the specimen.)
Test conducted by _____ Laboratory test no. _____
per _____

RADIOGRAPHIC TEST RESULTS

Film identification	Results	Remarks	Film identification	Results	Remarks

Test witnessed by _____ Test no. _____
per _____

We, the undersigned, certify that the statements in this record are correct and that the welds were prepared and tested in accordance with the requirements of 5C or D of AWS D1.1, Structural Welding Code.

Manufacturer or contractor _____
Authorized by _____
Date _____

Form E-4

FIGURE I.6. FORM E-4

APPENDIX J--CALCULATIONS OF STRAIN ENERGY AND LOAD FACTORS FOR A CIRCULAR LENS

CALCULATIONS OF STRAIN ENERGY AND DYNAMIC LOAD FACTORS FOR A CIRCULAR LENS

Circular Plate, Simply Supported Edge

To evaluate the strain energy, we start with the static deformed shape of the circular lens [J.1].

$$w = \frac{P}{16\pi D}\left[\frac{3+\nu}{1+\nu}(a^2 - r^2) + 2r^2 \log\frac{r}{a}\right] \tag{J.1}$$

$$w_o = \frac{P}{16\pi D}\left(\frac{3+\nu}{1+\nu}\right) a^2 \tag{J.2}$$

$$P = \frac{w_o}{a^2}\left(\frac{1+\nu}{3+\nu}\right) 2\pi D \tag{J.3}$$

$$w = \frac{w_o}{a^2}\left(\frac{1+\nu}{3+\nu}\right)\left[\frac{3+\nu}{1+\nu}(a^2 - r^2) + 2r^2 \log\frac{r}{a}\right] \tag{J.4}$$

The strain energy can be written as [J.1]:

$$U = \frac{D}{2}\int_0^{2\pi}\int_0^a \left[\left(\frac{\partial^2 w}{\partial r^2} + \frac{1}{r}\frac{\partial w}{\partial r}\right)^2 - 2(1-\nu)\frac{1}{r}\frac{\partial w}{\partial r}\frac{\partial^2 w}{\partial r^2}\right] r\,dr\,d\theta \tag{J.5}$$

Using Equation (J.4), the derivatives are evaluated as:

$$\frac{\partial w}{\partial r} = \frac{w_o}{a^2}\left(\frac{1+\nu}{3+\nu}\right)\left[-2r\frac{3+\nu}{1+\nu} + 4r\log\frac{r}{a} + 2r\right] = \frac{w_o}{a^2}\left(\frac{1+\nu}{3+\nu}\right) \times \left[\frac{-4r}{1+\nu} + 4r\log\frac{r}{a}\right]$$

$$\frac{\partial^2 w}{\partial r^2} = \frac{w_o}{a^2}\left(\frac{1+\nu}{3+\nu}\right)\left[\frac{-4}{1+\nu} + 4\log\frac{r}{a} + 4\right] = \frac{w_o}{a^2}\left(\frac{1+\nu}{3+\nu}\right)\left[\frac{4\nu}{1+\nu} + 4\log\frac{r}{a}\right]$$

$$\left(\frac{\partial^2 w}{\partial r^2} + \frac{1}{r}\frac{\partial w}{\partial r}\right)^2 = \left(\frac{w_o}{a^2}\right)^2\left(\frac{1+\nu}{3+\nu}\right)^2\left[\frac{4\nu}{1+\nu} + 4\log\frac{r}{a} - \frac{4}{1+\nu} + 4\log\frac{r}{a}\right]^2$$

$$= \left(\frac{w_o}{a^2}\right)^2\left(\frac{1+\nu}{3+\nu}\right)^2\left[\frac{-4(1-\nu)}{1+\nu} + 8\log\frac{r}{a}\right]^2$$

$$2(1-\nu)\frac{1}{r}\frac{\partial w}{\partial r}\frac{\partial^2 w}{\partial r^2} = 2(1-\nu)\left(\frac{w_o}{a^2}\right)^2\left(\frac{1+\nu}{3+\nu}\right)^2\left[\frac{-4}{1+\nu}+4\log\frac{r}{a}\right]$$

$$\times\left[\frac{4\nu}{1+\nu}+4\log\frac{r}{a}\right]$$

Substituting these terms into Equation (J.5) and evaluating the integral over a radius $a = 3.1875$ in., we find:

$$U = \left(\frac{D}{2}\right)2\pi\int_o^a\left(\frac{w_o}{a^2}\right)^2\left(\frac{1+\nu}{3+\nu}\right)^2\left[\left(\frac{-4(1-\nu)}{1+\nu}+8\log\frac{r}{a}\right)^2-2(1-\nu)\right.$$

$$\left.\times\left(\frac{-4}{1+\nu}+4\log\frac{r}{a}\right)\left(\frac{4\nu}{1+\nu}+4\log\frac{r}{a}\right)\right]rdr$$

$$= \pi D\left(\frac{w_o}{a^2}\right)^2\left(\frac{1+\nu}{3+\nu}\right)^2\int_o^{3.1875}[41.314-102.842\log r+64\log^2 r$$

$$-1.5(-5.214+4\log r)(-1.214+4\log r)]\,rdr$$

$$= \pi D\left(\frac{w_o}{a^2}\right)^2\left(\frac{1+\nu}{3+\nu}\right)^2\int_o^{3.1875}[41.314-102.842\log r+64\log^2 r$$

$$-9.495+38.568\log r-24\log^2 r]\,rdr$$

$$= \pi D\left(\frac{w_o}{a^2}\right)^2\left(\frac{1+\nu}{3+\nu}\right)^2\int_o^{3.1875}[31.819\,r-64.274\,r\log r+40\,r\log^2 r]\,dr$$

$$= \pi D\left(\frac{w_o}{a^2}\right)^2\left(\frac{1+\nu}{3+\nu}\right)^2\left[15.910\,r^2-32.137\,r^2\log r+16.069\,r^2+20\,r^2\right.$$

$$\left.(\log^2 r-\log r)+10\,r^2\right]_o^{3.1875}$$

$$= \pi D\left(\frac{w_o}{a^2}\right)^2\left(\frac{1+\nu}{3+\nu}\right)^2\times 211.330\ \text{(lb-in.)}$$

$$= w_o^2\times 1.056\times 10^5\ \text{(lb-in.)} \qquad \text{(J.6)}$$

Circular Plate, Fixed Edge

The same procedure is followed for fixed edges as for simply supported edges.

$$w = \frac{Pr^2}{8\pi D} \log \frac{r}{a} + \frac{P}{16\pi D} (a^2 - r^2) \tag{J.7}$$

$$w_o = \frac{P}{16\pi D} a^2 \tag{J.8}$$

$$w = 2 w_o \frac{r^2}{a^2} \log \frac{r}{a} + \frac{w_o}{a^2} (a^2 - r^2) = \frac{w_o}{a^2} \left(2r^2 \log \frac{r}{a} + a^2 - r^2 \right) \tag{J.9}$$

$$\frac{\partial w}{\partial r} = \frac{w_o}{a^2} \left(4r \log \frac{r}{a} + 2r - 2r \right) = \frac{w_o}{a^2} \left(4r \log \frac{r}{a} \right) = \frac{4w_o}{a^2} \left(r \log \frac{r}{a} \right)$$

$$\frac{\partial^2 w}{\partial r^2} = \frac{w_o}{a^2} \left(4 \log \frac{r}{a} + 4 \right) = \frac{4w_o}{a^2} \left(\log \frac{r}{a} + 1 \right)$$

$$\left(\frac{\partial^2 w}{\partial r^2} + \frac{1}{r} \frac{\partial w}{\partial r} \right)^2 = \left(\frac{4w_o}{a^2} \right)^2 \left[\log \frac{r}{a} + 1 + \log \frac{r}{a} \right]^2 = \left(\frac{4w_o}{a^2} \right)^2 \left[2 \log \frac{r}{a} + 1 \right]^2$$

$$2 (1 - \nu) \frac{1}{r} \frac{\partial w}{\partial r} \frac{\partial^2 w}{\partial r^2} = 2 (1 - \nu) \left(\frac{4w_o}{a^2} \right)^2 \left(\log \frac{r}{a} \right) \left(\log \frac{r}{a} + 1 \right) = 2 (1 - \nu)$$

$$\times \left(\frac{4w_o}{a^2} \right)^2 \left(\log^2 \frac{r}{a} + \log \frac{r}{a} \right)$$

$$U = \frac{D}{2} \int_0^{2\pi} \int_0^{a} \left[\left(\frac{\partial^2 w}{\partial r^2} + \frac{1}{r} \frac{\partial w}{\partial r} \right)^2 - 2 (1 - \nu) \frac{1}{r} \frac{\partial w}{\partial r} \frac{\partial^2 w}{\partial r^2} \right] r \, dr \, d\vartheta \tag{J.10}$$

$$= \pi D \left(\frac{4w_o}{a^2} \right)^2 \int_0^{3.1875} \left[\left(2 \log \frac{r}{a} + 1 \right)^2 - 2 (1 - \nu) \left(\log \frac{r}{a} \right) \left(\log \frac{r}{a} + 1 \right) \right] r \, dr$$

$$= \pi D \left(\frac{4w_o}{a^2} \right)^2 \int_0^{3.1875} [-0.0276 \log r + 4 \log^2 r - 1.5 (\log r - 0.503)$$

$$\times (\log r + 0.499)] \, r \, dr$$

$$= \pi D \left(\frac{4w_o}{a^2}\right)^2 \int_o^{3.1875} [\, -0.0276r \log r + 4r \log^2 r - 1.5r \log^2 r + 0.000\, r \log r + 0.375r \,]\, dr$$

$$= \pi D \left(\frac{4w_o}{a^2}\right)^2 \int_o^{3.1875} [\, -0.019r \log r + 2.5r \log^2 r + 0.375\, r \,]\, dr$$

$$= \pi D \left(\frac{4w_o}{a^2}\right)^2 \left[-0.019 \left(\frac{r^2 \log r}{2} - \frac{r^2}{4} \right) + 2.5 \left(\frac{r^2}{2} \log^2 r - \frac{r^2 \log r}{2} + \frac{r^2}{4} \right) + 0.375 \frac{r^2}{2} \right]_o^{3.1875}$$

$$= \pi D \left(\frac{4w_o}{a^2}\right)^2 5.079$$

$$= 2.748 \times 10^5 \, w_o^2 \quad \text{(lb-in.)} \qquad \text{(J.11)}$$

Dynamic Load Factors

Circular Plate with Simply Supported Edge

The frequency equation is

$$f = \frac{1}{2\pi} \frac{\lambda_{ni}}{r_o^2} \sqrt{\frac{D}{\rho h}} \qquad \text{(J.12)}$$

For the fundamental mode,

$$i = 0 \,, \quad n = 0 \,, \quad \text{and} \quad \lambda_{ni} = 4.977 \quad \text{(Reference J.2)}$$

Substituting into Equation (J.12), we find:

$$f = \frac{4.977}{(0.5)^2} \times \frac{1}{2\pi} \sqrt{\frac{1.111 \times 10^5}{2.355 \times 10^{-3}}}$$

$$= 21{,}763 \quad \text{(Hertz)}$$

$$T = 1/f = 0.0460 \quad \text{msec}$$

Now the ratio of the rise time to the fundamental period is

$$\frac{t_o}{T} = \frac{17}{0.0460} = 370$$

Based on Biggs' curve in Reference J.3, the dynamic load factor (DLF) is DLF < 1.05.

Take DLF = 1.05 (J.13)

Circular Plate with Fixed Edge

For the fundamental mode,

$i = 0$, $n = 0$, and $\lambda_{ni} = 10.22$ (Reference J.2)

Using Equation (J.12):

$$f = 44{,}690 \text{ (Hertz)}$$

and

$$T = \frac{1}{f} = 0.0224 \text{ msec}$$

Now

$$\frac{t_o}{T} = 760$$

so that DLF < 1.05.

Take DLF = 1.05 (J.14)

REFERENCES

J.1. Timoshenko, S., and Woinowsky-Krieger, S., Theory of Plates and Shell, 2nd Edition, McGraw-Hill Book Co., New York, 1959.

J.2. Szilard, R., Theory and Analysis of Plates, Classical and Numerical Methods, Prentice-Hall, Inc., Englewood Cliffs, New Jersey, 1974.

J.3. Biggs, J. M., Introduction to Structural Dynamics, McGraw-Hill Book Co., 1964.

APPENDIX K--RECOMMENDED ACCELERATED AGING TEST
FOR POLYCARBONATES AND ADHESIVES

RECOMMENDED ACCELERATED AGING TEST FOR POLYCARBONATES AND ADHESIVES

Objective

Determine the life of sealants, adhesives, and polycarbonate plastics in explosion-proof luminaires under typical operational environments found underground.

Purpose

Generate an adequate data base which would permit extrapolation of one-year fatigue data to at least a three-year period with reasonable confidence.

Scope

The test program shall be limited to two window materials, two sealant materials, two sealant/adhesives, 180 to 300°F ambient temperature range, one lighting condition, and 25 to 150 psi internal pressure range. The window materials selected for the study are borosilicate glass and UV stabilized polycarbonate plastic. Room temperature vulcanizing silicon rubber GE RTV 108 and an epoxy (to be selected) shall serve both as sealants and adhesives for glass and polycarbonate plastic windows. Mercury vapor fluorescent lights shall be utilized for generation of UV radiation. The windows shall operate at distinct temperature levels; polycarbonate plastic at 180°F, 210°F and 240°F and glass at 180°F, 240°F and 300°F. All tests will be run at 100% relative humidity (humid air) with intermittent water spray. The effect of oil on polycarbonates will be evaluated with screening tests. There are too many different oil formulations for oil to be a variable in the long-term tests. The test fixtures containing polycarbonate plastic windows shall be periodically pressurized to 150 psi while those containing glass windows shall be pressurized to 25, 50, 75, 100, 125, or 150 psi.

Test Specimens

Test specimens will be circular windows fabricated from (1) UV stabilized polycarbonate plastic and (2) borosilicate glass.

The thicknesses of polycarbonate discs shall be constant, but their diameters shall be varied to induce different levels of flexure stress into the plastic by internal pressure of 150 psi. The t/D_i ratios chosen for the windows are based on experimental data from ANSI/ASME PVHO Safety Standard for Acrylic Windows, as the tensile strength of polycarbonate plastic is similar to that of acrylic plastic.

The t/D_i ratios selected for experimental evaluation are: 0.135 (i.e., CF2*), 0.152 (i.e., CF4), 0.190 (i.e., CF8), 0.21 (i.e., CF12),

---

*CF - conversion factor, ratio between short term critical pressure and design pressure at room temperature.

and 0.23 (i.e., CF16). These t/D_i ratios correspond approximately to maximum effective stress levels of 5000 psi, 2500 psi, 1250 psi, 830 psi and 625 psi in the center of the window subjected to 150-psi internal pressure. It is predicted that the t/D_i ratios of 0.135 and 0.152 will fail, 0.190 and 0.21 may fail, and 0.23 won't fail during a one-year long pressure cycling program to 150 psi at elevated temperatures.

Polycarbonate test specimens are to be machined from a single sheet of 0.5-in.-thick UV stabilized polycarbonate plastic. Because all windows are of the same thickness, the effect of UV radiation upon the window's material will be the same (i.e., reduction of tensile strength, ductility, impact, strength, etc.) regardless of the stress level induced in the windows with different t/D_i ratios by the 150-psi internal pressure. This would not be the case if the windows differed in the thickness. Also, by cutting all windows from the same sheet of material, the effect of variation in material properties will be minimized.

Glass specimens will be 0.75-in.-thick x 2.5-in.-diameter circular Pyrex annular edge sight glass with 150 psi and 400°F service ratings. This particular window shape was chosen because it is a commercially available off-the-shelf item, and its dimensions preclude it from failing under 150-psi internal pressure during the test program, thus making it an ideal window for evauation of sealants and adhesives in the 150 to 300°F temperature and 25 to 150 psi pressure ranges.

All specimens shall be sealed and/or bonded to the metallic housing after both surfaces have been coated with the appropriate primer.

Test Fixtures

Test fixtures shall be constructed from 6-in.-diameter stainless steel tubes cut and welded to form a tubular pressure vessel. The front of each tube shall be fitted with a retainer for a glass or polycarbonate lens while the back of each tube shall be closed with a flat bulkhead containing feedthroughs for electric power, thermocouples, and compressed air. Typical fixtures are shown in Figures K.1 and K.2 for glass and polycarbonate lenses, respectively.

The test fixtures shall all be attached to the Q.U.V. Accelerated Weathering Tester by special stainless steel adapter plates. A photograph of the weathering chamber with test fixtures attached is shown in Figure K.3. This photograph was borrowed from USBM Contract H0387009 [K.1]. One-half of the test fixtures with polycarbonate windows shall be illuminated with mercury vapor fluorescent lamps, as provided with the Q.U.V. chamber, while the test fixtures containing glass windows require no illumination.

Resistance heaters shall be placed in each fixture and connected to a rheostat for varying the current to the heater. The temperature of interior window surfaces shall be measured with thermocouples and its magnitude controlled by adjustments to the rheostats.

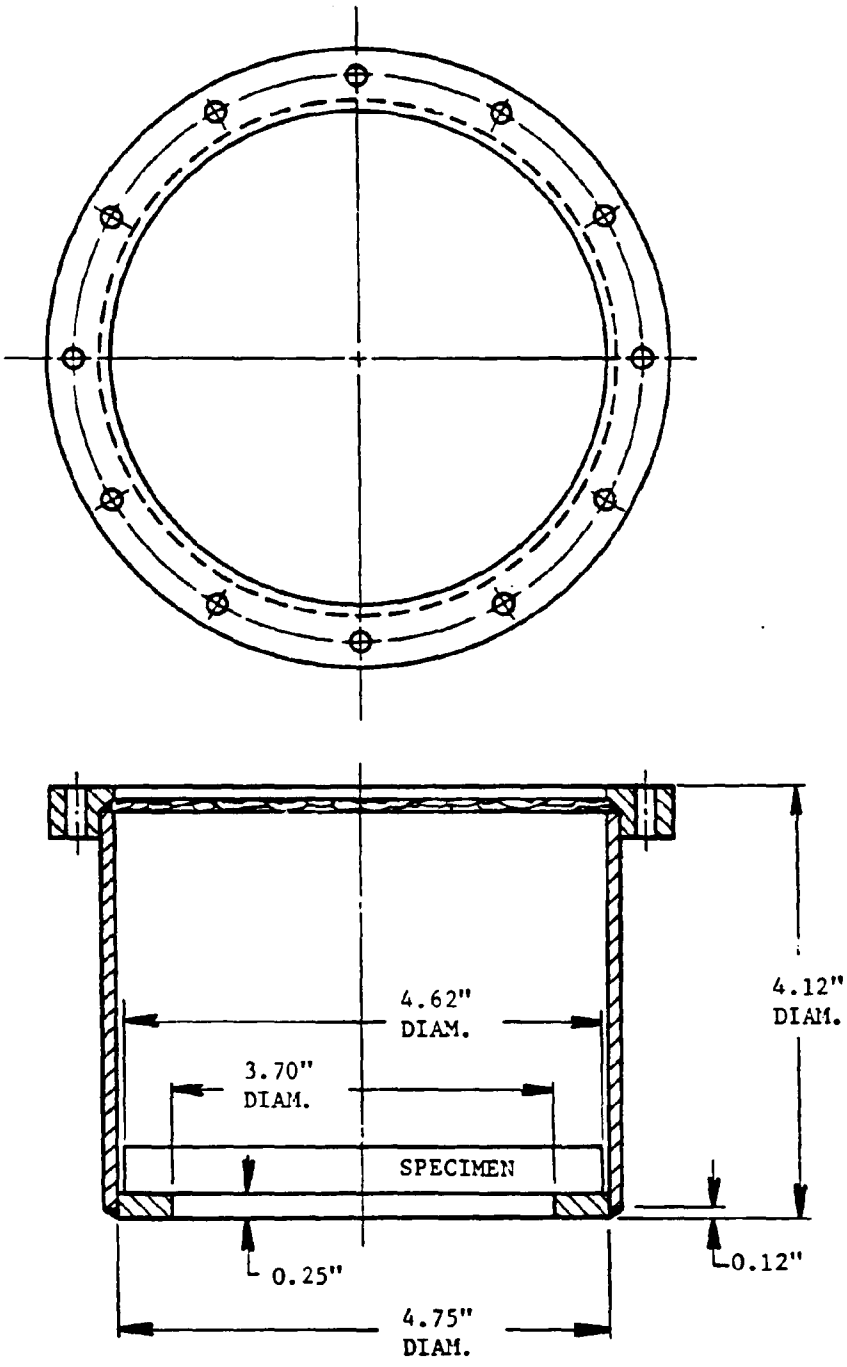

FIGURE K.1. TYPE A FIXTURE FOR POLYCARBONATE LENS SPECIMENS - CLOSURE FLANGE NOT SHOWN

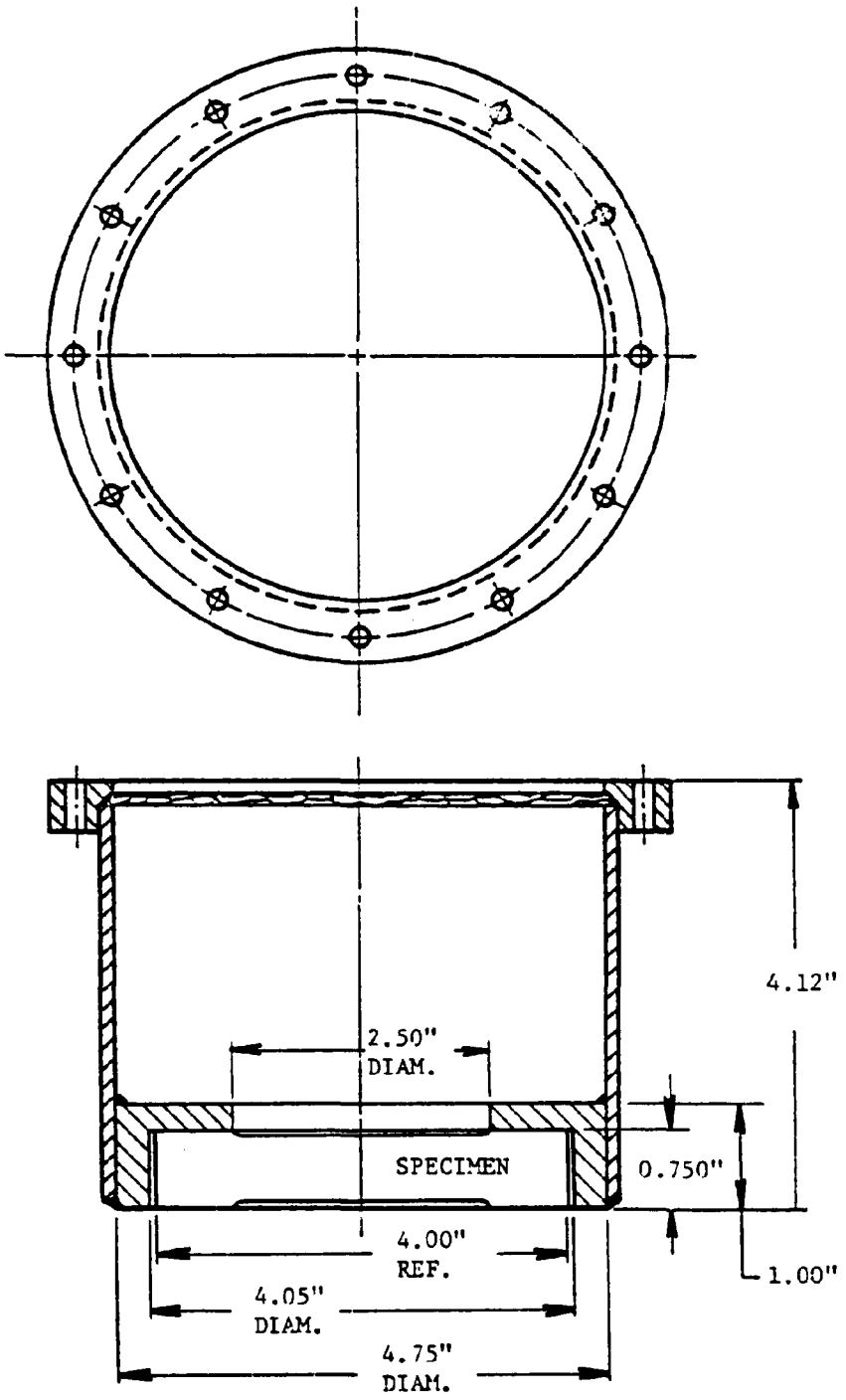

FIGURE K.2. TYPE B FIXTURE FOR GLASS LENS ADHESIVE SPECIMEN - CLOSURE FLANGE NOT SHOWN

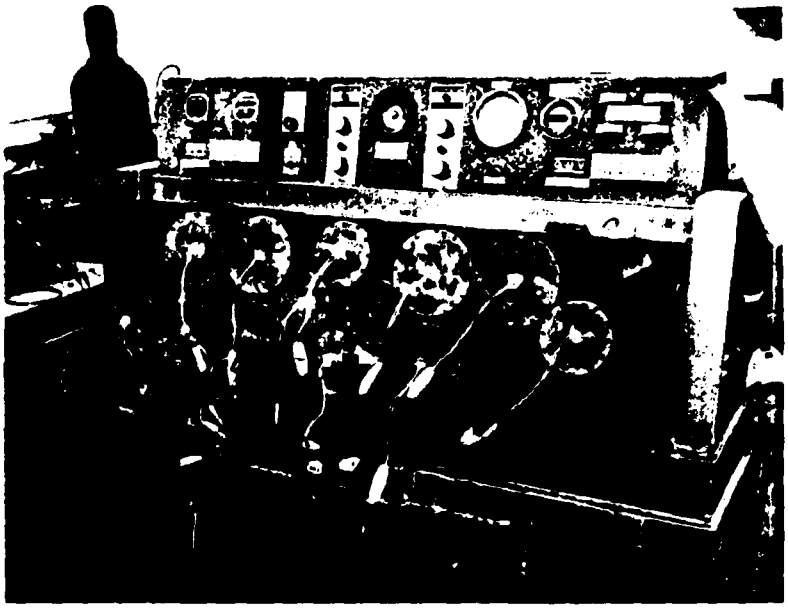

FIGURE K.3. PHOTOGRAPH OF ENVIRONMENTAL CHAMBER WITH FIXTURES INSTALLED

Test Setup

The test setup shall consist of the fixtures, lamps, sealants and test specimens shown in Tables K.1 and K.2. Test fixtures shall be placed in a room, or enclosure, with controlled access so that absence of personnel may be assured during the periods of time when the interiors of fixtures are pressurized with compressed air and failures of windows may take place.

To simulate the exposure of polycarbonate plastic windows to water found underground, fine jets will be located in front of each window that spray water intermittently upon the hot exterior surface of windows. A typical arrangement is shown in Figure K.4. Water from the spray will be collected in the bottom of the chamber. Heaters in the water reservoir will operate to maintain the atmosphere in the chamber at 100% relative humidity.

The internal pressurization and depressurization of each test fixture shall be accomplished from a common manifold by actuation of solenoid operated valves from a control console located outside the enclosure in which the test fixtures are located. The ejection of a window or rapid leakage of air from inside a pressurized fixture should be detected by monitoring the rate of pressure decrease inside the pressurized fixture after the supply of pressurized air to the fixture has been shut off remotely from the control console.

Assembly Procedure

Polycarbonate windows - Prior to mounting of any window into the end closure, a thermocouple is bonded with RTV silicon rubber to the window's interior surface at the center. After 48 hours at room temperature, the window is ready for mounting into the mating end of the Type A test fixture. The mounting of the window into the end closure consists of (1) coating lightly the face of the seat with RTV silicon rubber, (2) centering the window in its seat, and (3) while pressing it with a 1-lb force in place, injecting RTV silicon rubber from a nozzle-equipped tube into the annular space between the edge of the window and the seat in the end closure. Great care will be taken to avoid entrapment of air in the seal, as at high temperatures the entrapped air will expand and rupture the seal. The enclosures with freshly potted windows will be set aside for at least 100 hours in room temperature environment to allow for vulcanization of the silicon seals or heated in a temperature controlled oven to reduce the curing time.

The window-equipped closures are subsequently provided with rubber seals and bolted to the flanges of the fixture. After mounting of a heat source upon the end closure with feedthroughs, it is bolted in place also. The fixture is now considered completed, ready for pressure prooftesting. The pressure prooftest consists of pressurizing the cold assembly to 150 psi and monitoring the rate of pressure drop once the supply of air to the interior of the fixtures has been shut off. If the pressure drop rate exceeds 5 psi in one hour, the seals in the test fixture are considered unacceptable and the test fixture will be taken apart, seals repaired or replaced, and the fixture reassembled. If during the subsequent pressure test the pressure drop rate is found to be less than 5 psi/hour, the test

TABLE K.1. TEST SETUPS FOR POLYCARBONATE WINDOWS OPERATING IN AIR WITH 100% RELATIVE HUMIDITY AND INTERMITTENT WATER SPRAY

	Fixtures 1-5	Fixtures 6-10	Fixtures 11-15
Interior Window Temperature	180°F	210°F	240°F
Sealant	GE RTV 108	Same	Same
Lamp	Hg	Hg	Hg
Closure Type A D_i = 3.70 D_o = 4.75	LEXAN D_w = 4.62 t = 0.50	Same	Same
Closure Type A D_i = 3.29 D_o = 4.24	LEXAN D_w = 4.11 t = 0.5	Same	Same
Closure Type A D_i = 2.63 D_o = 3.42	LEXAN D_w = 3.29 t = 0.5	Same	Same
Closure Type A D_i = 2.38 D_o = 3.11	LEXAN D_w = 2.98 t = 0.5	Same	Same
Closure Type A D_i = 2.17 D_o = 2.84	LEXAN D_w = 2.71 t = 0.5	Same	Same

D_i = internal diameter of opening in closure

D_o = external diameter of window seat
$D_o = D_w + 0.125$

D_w = external diameter of window
$D_w = D_i \times 1.25$

TABLE K.2. TEST SETUPS FOR GLASS WINDOWS OPERATING IN AIR WITH 100% RELATIVE HUMIDITY AND INTERMITTENT WATER SPRAY

	Fixtures 46–50	Fixtures 51–55	Fixtures 56–60
Interior Window Temperature	180°F	240°F	300°F
Lamp	None	Same	Same
Closure Type B D_i = 2.6 D_o = 4.125	Pyrex Glass D_w = 4.0 t = 0.75 GE RTV 108 Sealant	Same	Same
Closure Type B D_i = 2.6 D_o = 4.125	Pyrex Glass D_w = 4.0 t = 0.75 GE RTV 108 Sealant	Same	Same
Closure Type B D_i = 2.6 D_o = 4.125	Pyrex Glass D_w = 4.0 t = 0.75 GE RTV 108 Sealant	Same	Same
Closure Type B D_i = 2.6 D_o = 4.125	Pyrex Glass D_w = 4.0 t = 0.75 Epoxy Sealant	Same	Same
Closure Type B D_i = 2.6 D_o = 4.125	Pyrex Glass D_w = 4.0 t = 0.75 Epoxy Sealant	Same	Same
Cyclic Internal Pressure	150 psi*	150 psi*	150 psi*

D_i = internal diameter of opening in closure

D_o = external diameter of window seat
$D_o = D_w + 0.125$

D_w = external diameter of window

*After adhesive failure, cyclic pressure is reduced by ΔP = 25 psi (Lowest pressure will be P = 25 psi)

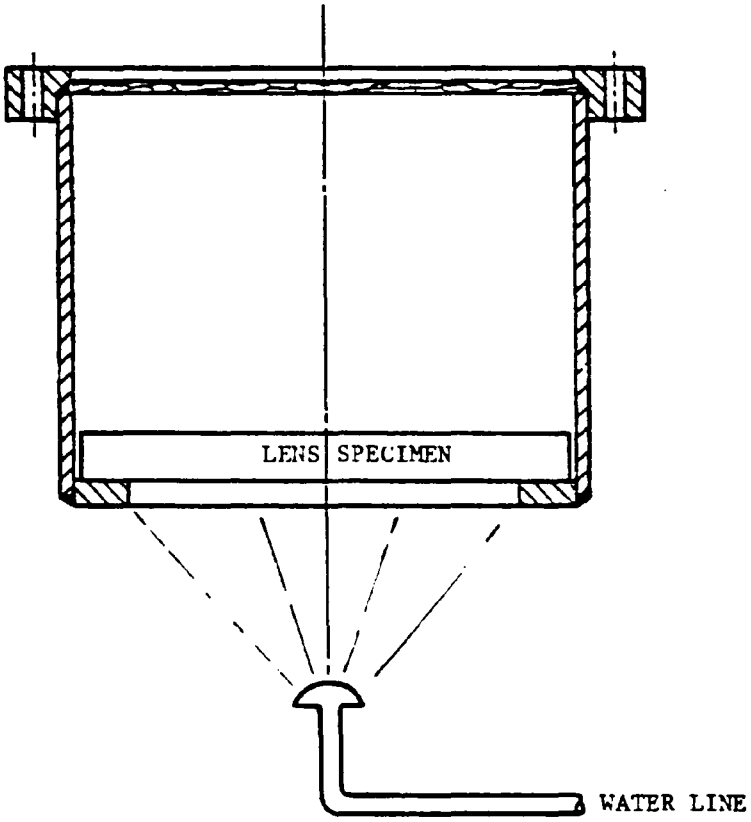

FIGURE K.4. TYPICAL WATER SPRAY NOZZLE

fixture is considered to be properly assembled. During pressurization of the test fixture, the enclosure where the fixture is located must be cleared of all personnel. After release of internal pressure, the heat source is energized and the temperature rise of the windows is monitored with thermocouples connected to a switch and readout unit. The rheostat is adjusted until the temperature of the interior window surfaces reaches the specified temperature level. Once this has been achieved, the test fixture is considered to be operational.

Glass windows - The same procedure is followed with glass windows, except that prior to bonding of thermocouples, each window is first coated all over with the appropriate primer for better adhesion of RTV silicon adhesive. Type B fixtures are utilized for mounting of glass windows. The Type B fixtures are designed to produce tensile stresses in the adhesive, and Type A enclosures are designed to produce shear and compression in the adhesive. The Type A enclosure is primarily for testing the polycarbonate windows, and the Type B enclosure is primarily for testing adhesives. After one cure of the silicon or epoxy seal, the end closure is equipped with a commercial rubber seal and is bolted to the test fixture. During the subsequent leak test, the test fixture is only pressurized to 25 psi to preclude accidental ejection of the window from Type B end closure. The setting of temperature on the internal surfaces of glass windows in the assembled test fixture follows the same procedure as setting of temperature in the fixture with polycarbonate windows. During pressurization of the test fixture, the room or enclosure where the fixture is located must be cleared of all personnel.

Test Procedure

Polycarbonate windows - The objective of the test procedure is to simulate inside the lamp enclosures methane gas explosions which, after the physical properties of the polycarbonate plastic have deteriorated sufficiently due to intermittent exposure to heat, moisture and UV, will cause the windows to fail catastrophically.

The daily test procedure consists of (1) continuous operation of the lamp for 12 hours, followed by 12 hours of darkness, (2) pressurizing the interior of the test fixture to 150 psi at the conclusion of the 12-hour lamp operation period, (3) recording the temperature on the interior window surface at the initiation of internal pressurization and one hour after pressurization initiation, and (4) releasing the remainder of trapped pressurized air from the interior of the test fixture after completion of pressure reading. Test fixtures equipped with spray nozzles shall have the water spray on for one minute every 10 minutes. In case of a window failure the fixture with the failed window will be removed and its fatigue life prior to failure recorded. Another fixture containing an identical window shall be bolted on and the test continued.

Glass windows - The objective of the test procedure is also to simulate inside lamp enclosures methane gas explosions which, after the physical properties of the adhesive have deteriorated sufficiently due to continued exposure to heat, moisture and UV, will cause the windows to leak or be ejected from the fixture. Since the glass windows have been sized not

to fail due to glass fracture, the ejection of any window will reflect only the failure of adhesive.

The test procedure consists of (1) operating the light source continuously, (2) pressurizing the interior of test fixtures once a day to specified pressure (which ranges from 25 to 150 psi, depending on the fixture), (3) recording the temperature prior to pressurization and pressure one hour after pressurization, and (4) releasing the remainder of trapped pressurized air from the interior of the test fixture after completion of pressure reading. The water spray will be turned on for one minute every 10 minutes. In case a window is ejected from its seat, the end closure shall be removed from the fixture and the fatigue life of the failed adhesive prior to failure recorded. Another end closure containing a glass window shall be bolted on and the test continued. If the ejected window is found to be undamaged, it is, after cleaning of the end closure, bonded again in the seat and used for another test.

Data Reduction

The objective of data reduction is to display results in such a manner that the results of a one-year study can be extrapolated into the future for a period of three to five years. Past experience with testing of acrylic plastic windows shows that the static and cyclic fatigue life of plastic structural components can be projected into the future if data are plotted on log-log coordinates. In the case of this study, the coordinates for data resulting from testing of polycarbonate windows should be time vs t/D_i ratio (Figure K.5). For glass windows, the coordinates should be time vs tensile stress in adhesive (Figure K.6). The resulting experimental points will plot linearly, which will allow their extrapolation from 8×10^3 to 4×10^4 hours.

Conclusions

On the basis of the experimental data plots, the designer shall be able to (1) select the appropriate t/D_i ratio for polycarbonate windows rated to withstand periodic 150-psi internal pressure excursions at 180, 210 or 240°F window surface temperature for a period of five years and (2) select the tensile design stress level for RTV 108 adhesive in contact with glass windows at 180, 240, and 300°F that will preclude adhesive failure for a period of five years.

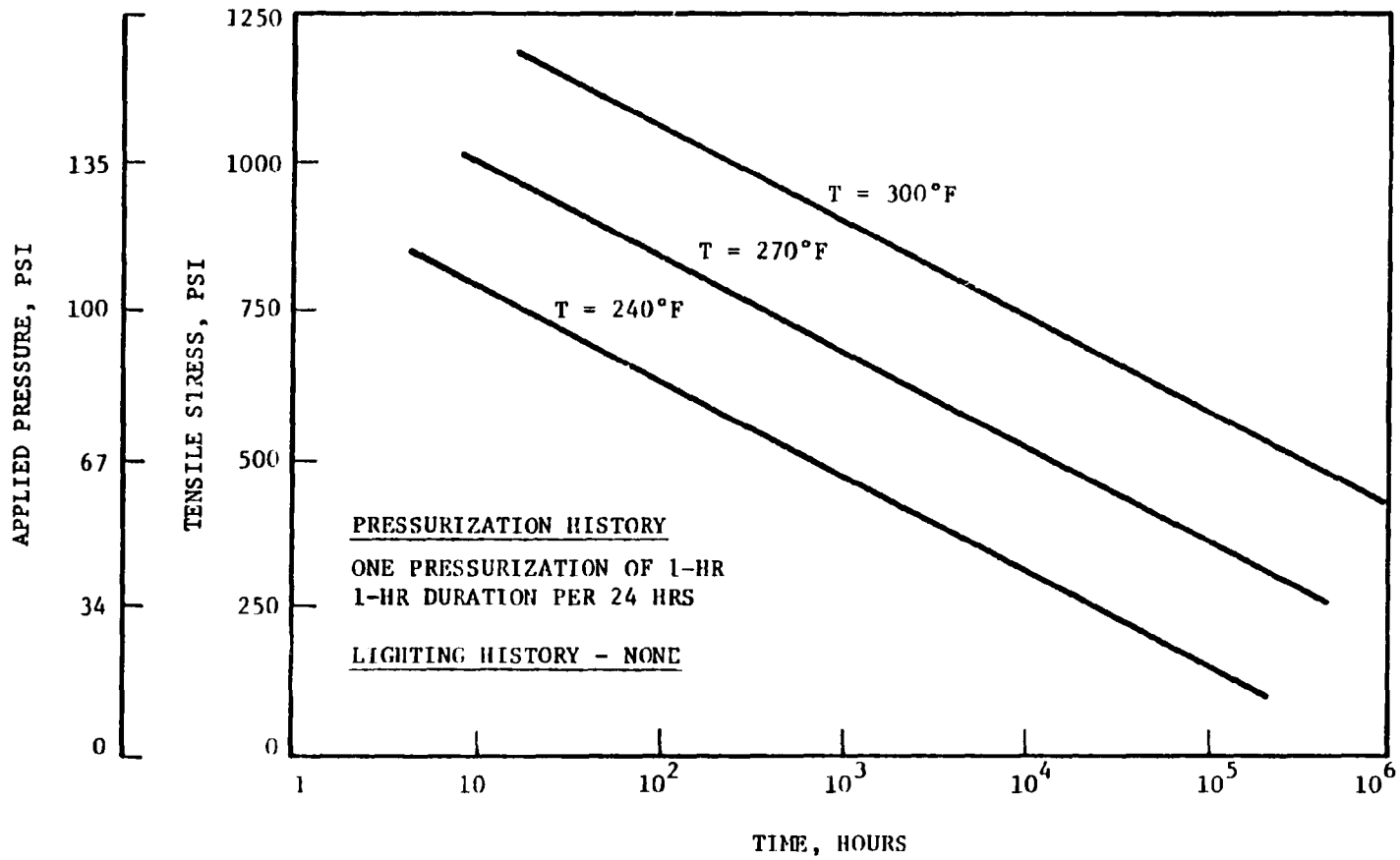

NOTE: THERE WILL BE ONLY ONE PLOT AS SHOWN ABOVE.

FIGURE K.5. TYPICAL DATA PLOT - TENSILE STRENGTH OF RTV 108 SILICON RUBBER UNDER PERIODICALLY APPLIED LOADING

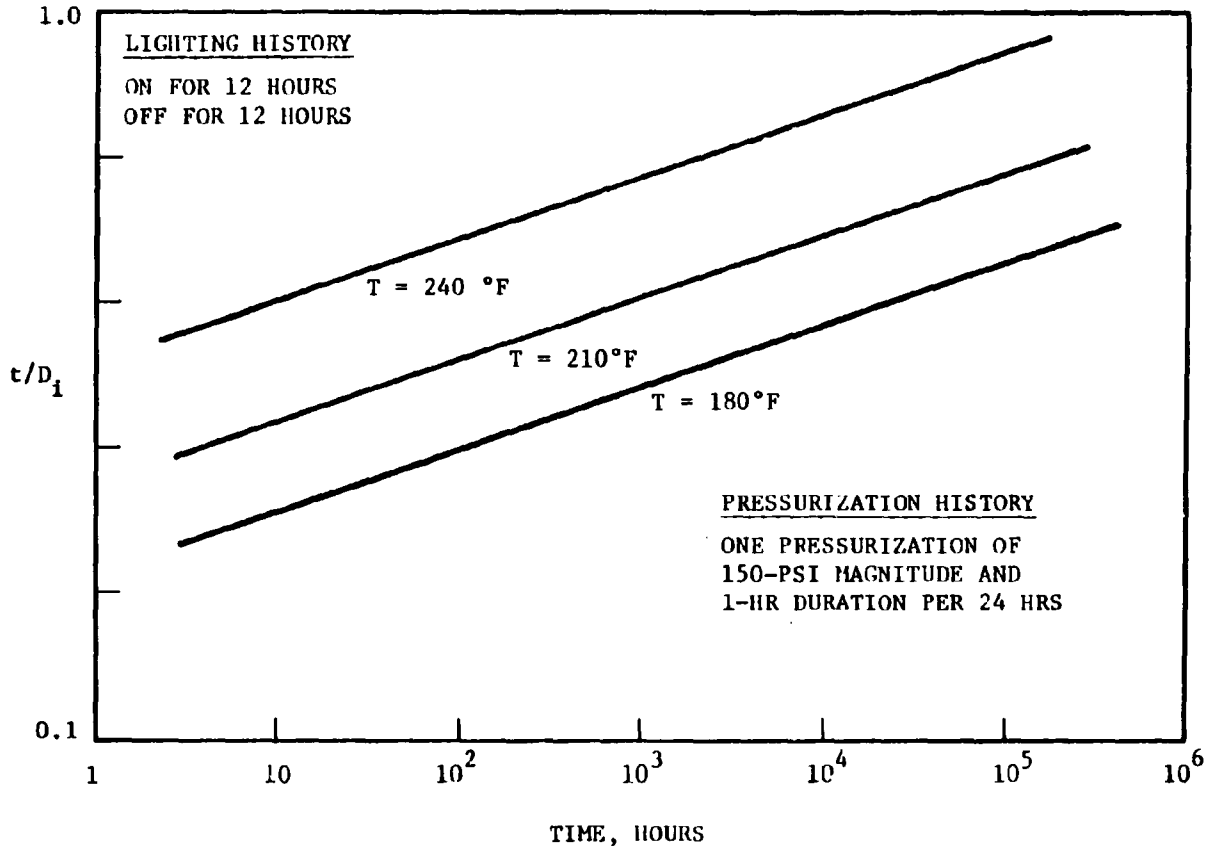

NOTE: THERE WILL BE ONLY ONE PLOT AS SHOWN ABOVE.

FIGURE K.6. TYPICAL DATA PLOT - STRUCTURAL PERFORMANCE OF POLYCARBONATE WINDOWS IN HUMID AIR WITH INTERMITTENT WATER SPRAY

REFERENCES

K.1. U. S. Bureau of Mines Contract No. H0387009, "QA Standards for Bonding Materials Used in Explosion-Proof Enclosures," awarded to Southwest Research Institute, under the technical direction of the Pittsburgh Mining and Safety Research Center, September 1978 (active as of December 1982).

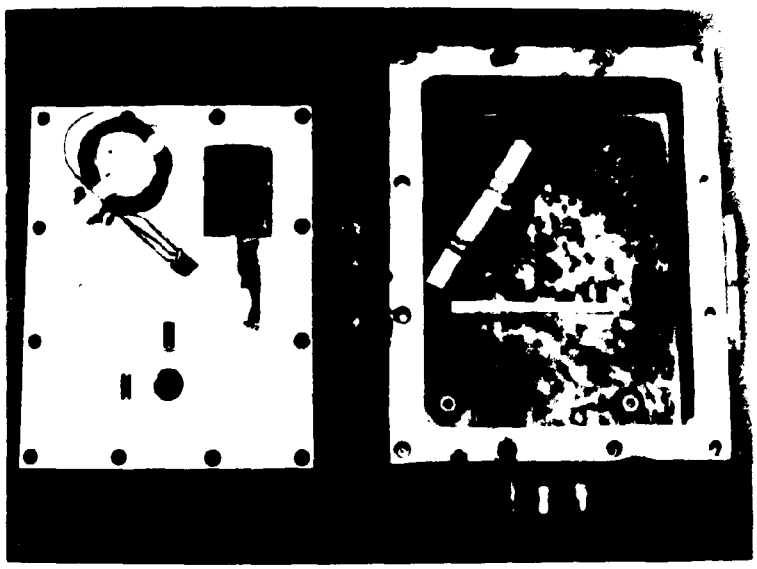

(a)

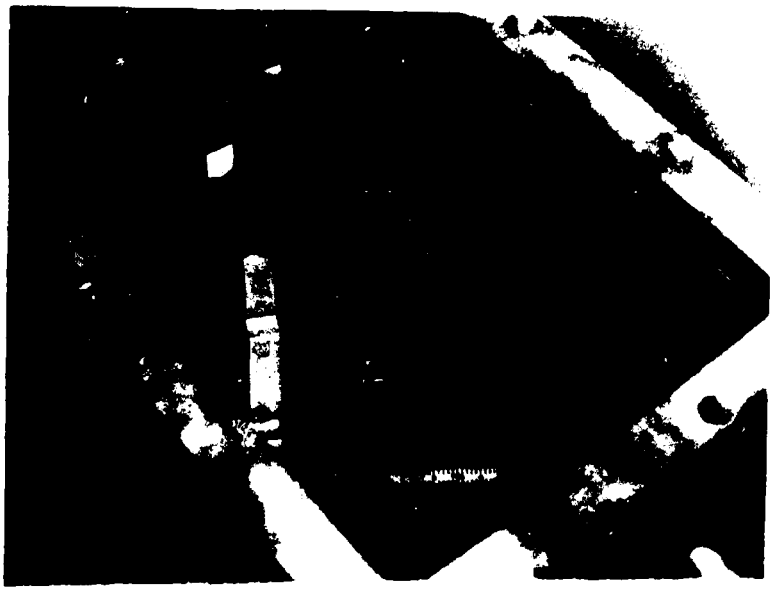

(b)

FIGURE 4.35. INSTRUMENTED 2G ENCLOSURE I

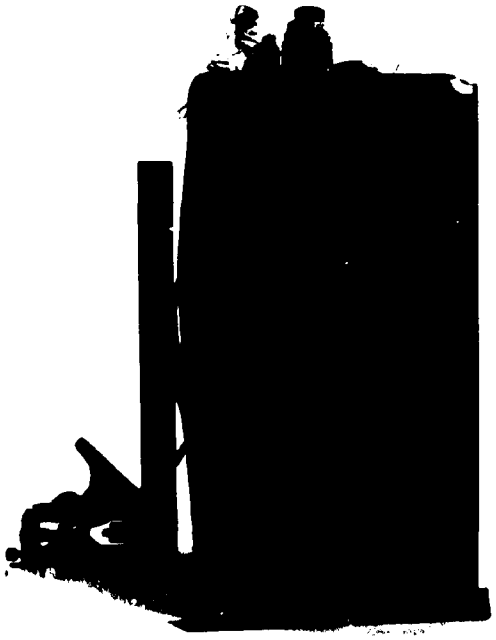

FIGURE 4.36. DEFORMATION OF ENCLOSURE I

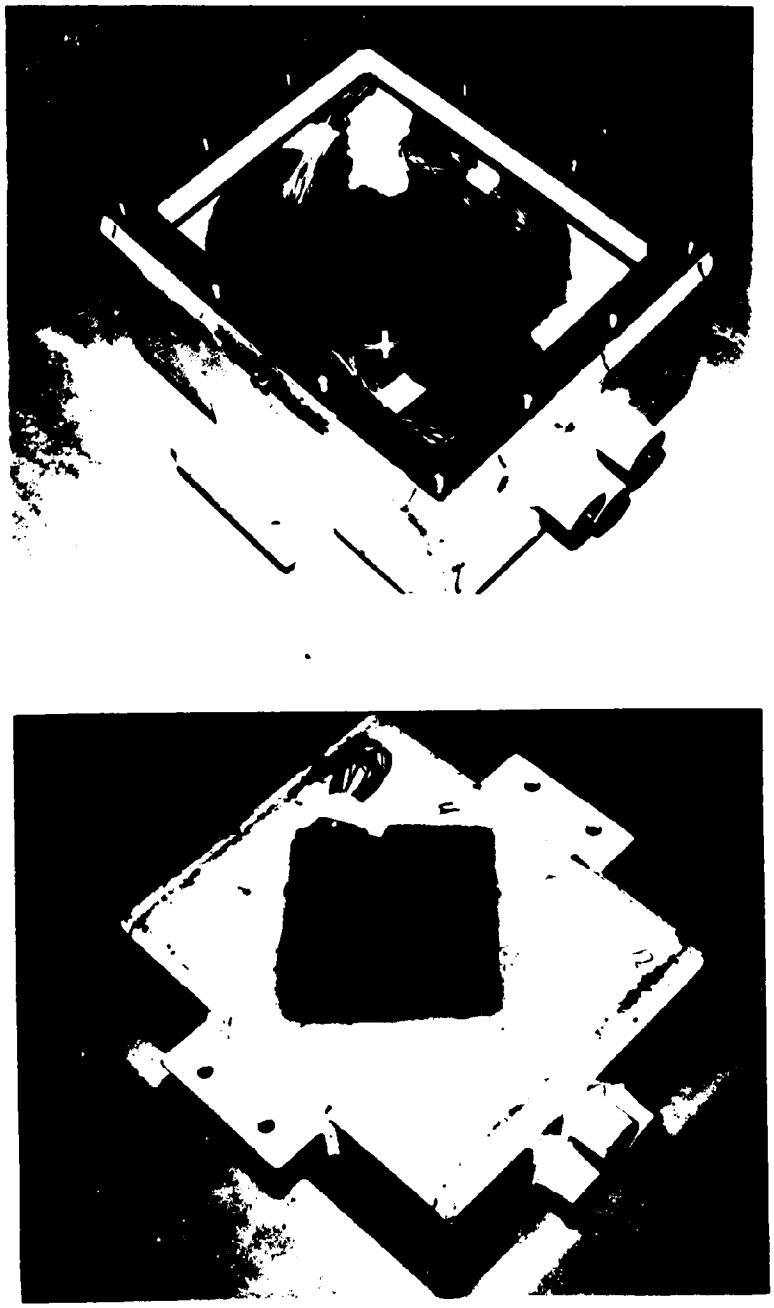

FIGURE 4.44. ENCLOSURE IA INSTRUMENTED WITH FOUR STRAIN GAGE ROSETTES

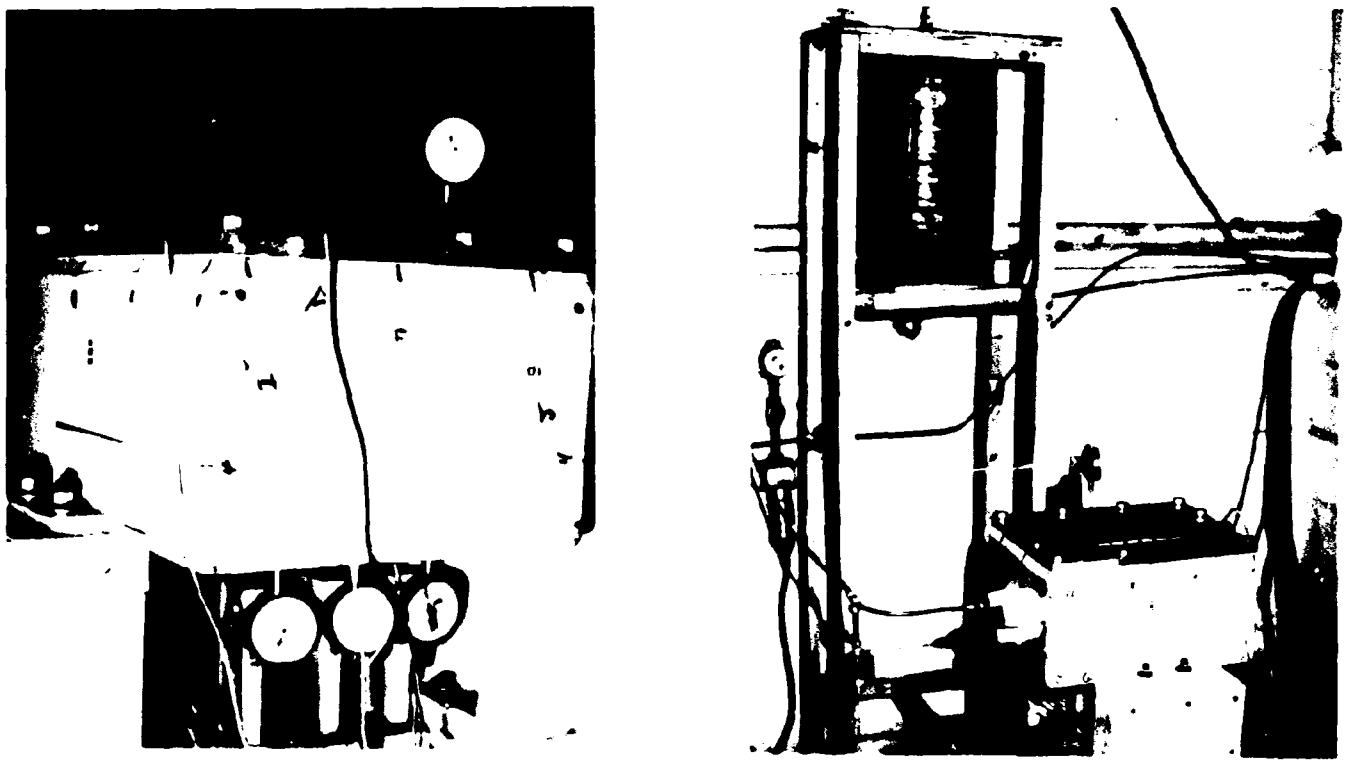

FIGURE 4.45. ENCLOSURE IA READY FOR TESTING

FIGURE 4.46. BOTTOM DEFORMATION
OF ENCLOSURE IA

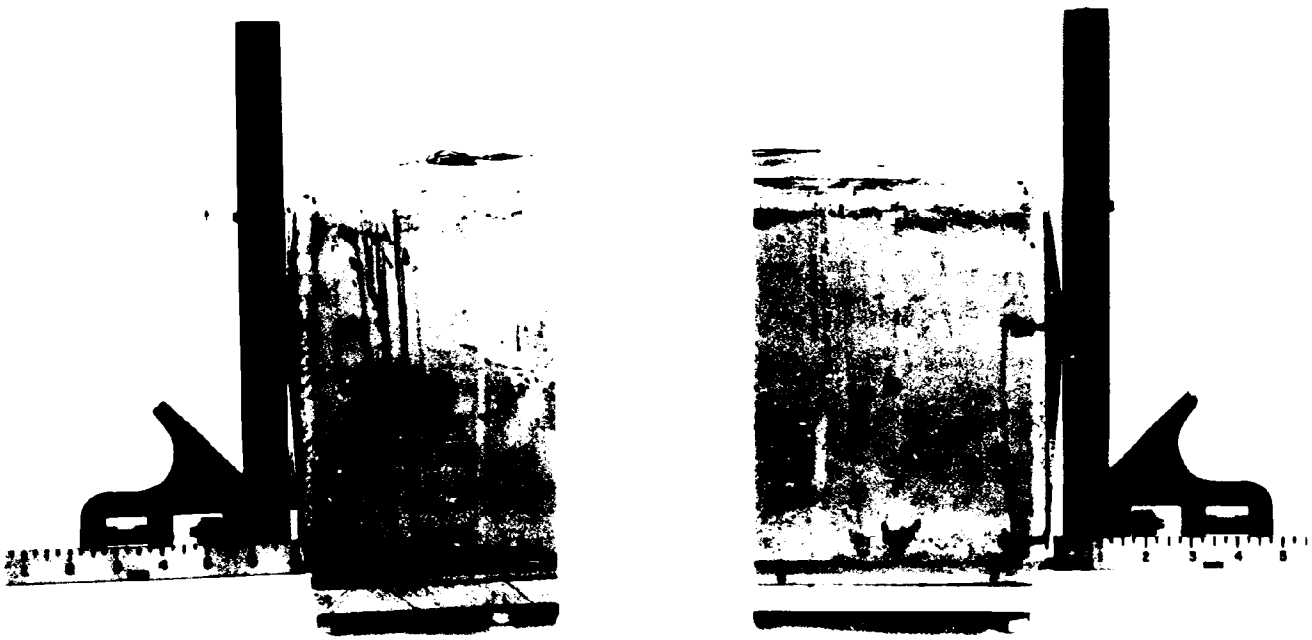

FIGURE 4.47. DEFORMATION OF SIDES ON ENCLOSURE IA

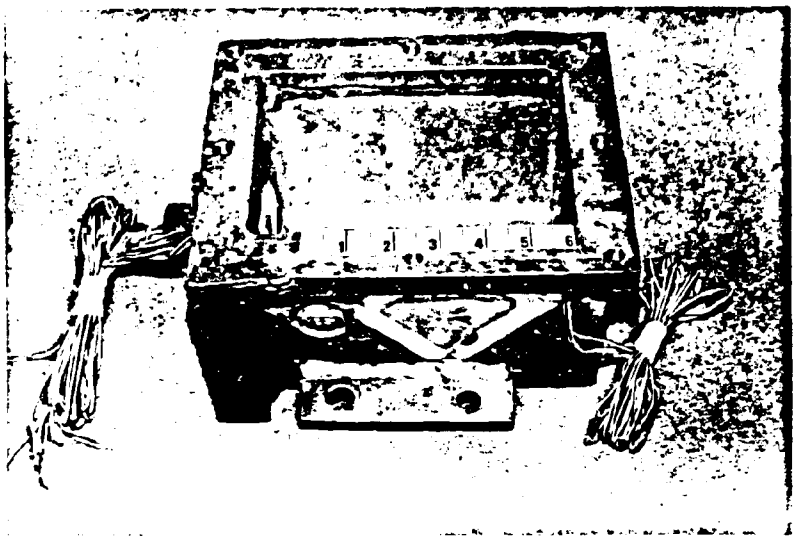

(a) View of Right Side (Front to Left)

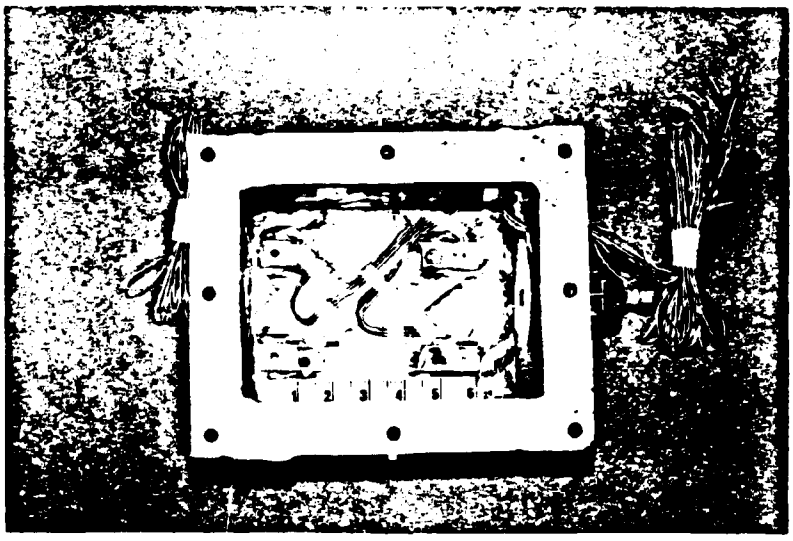

(b) View from Top (Front to Right)

FIGURE 4.64. INSTRUMENTED 2G ENCLOSURE II

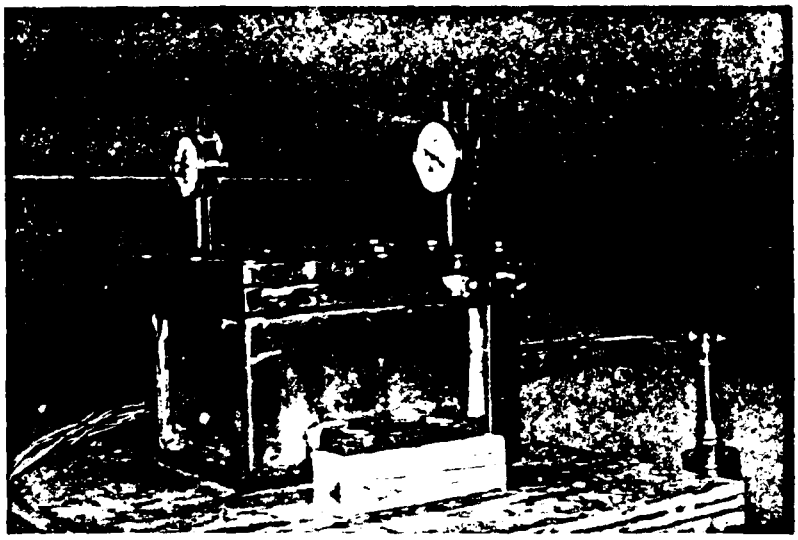

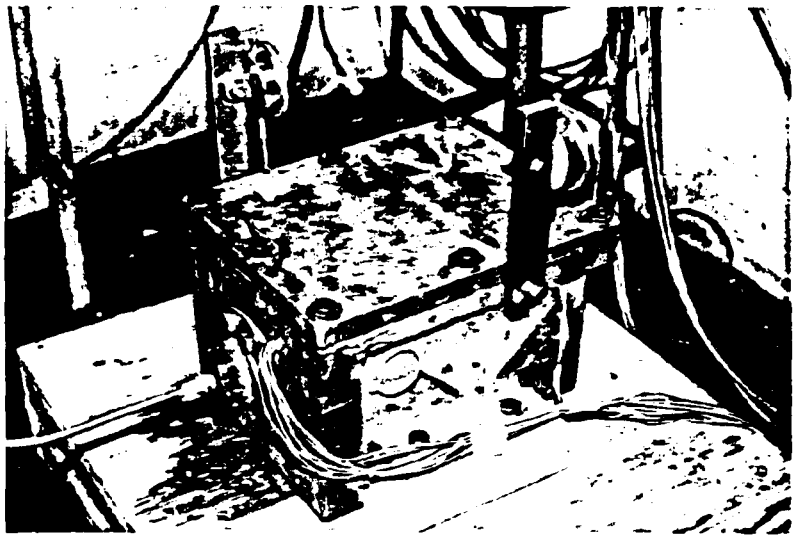

FIGURE 4.65. ENCLOSURE II WITH DIAL GAGES

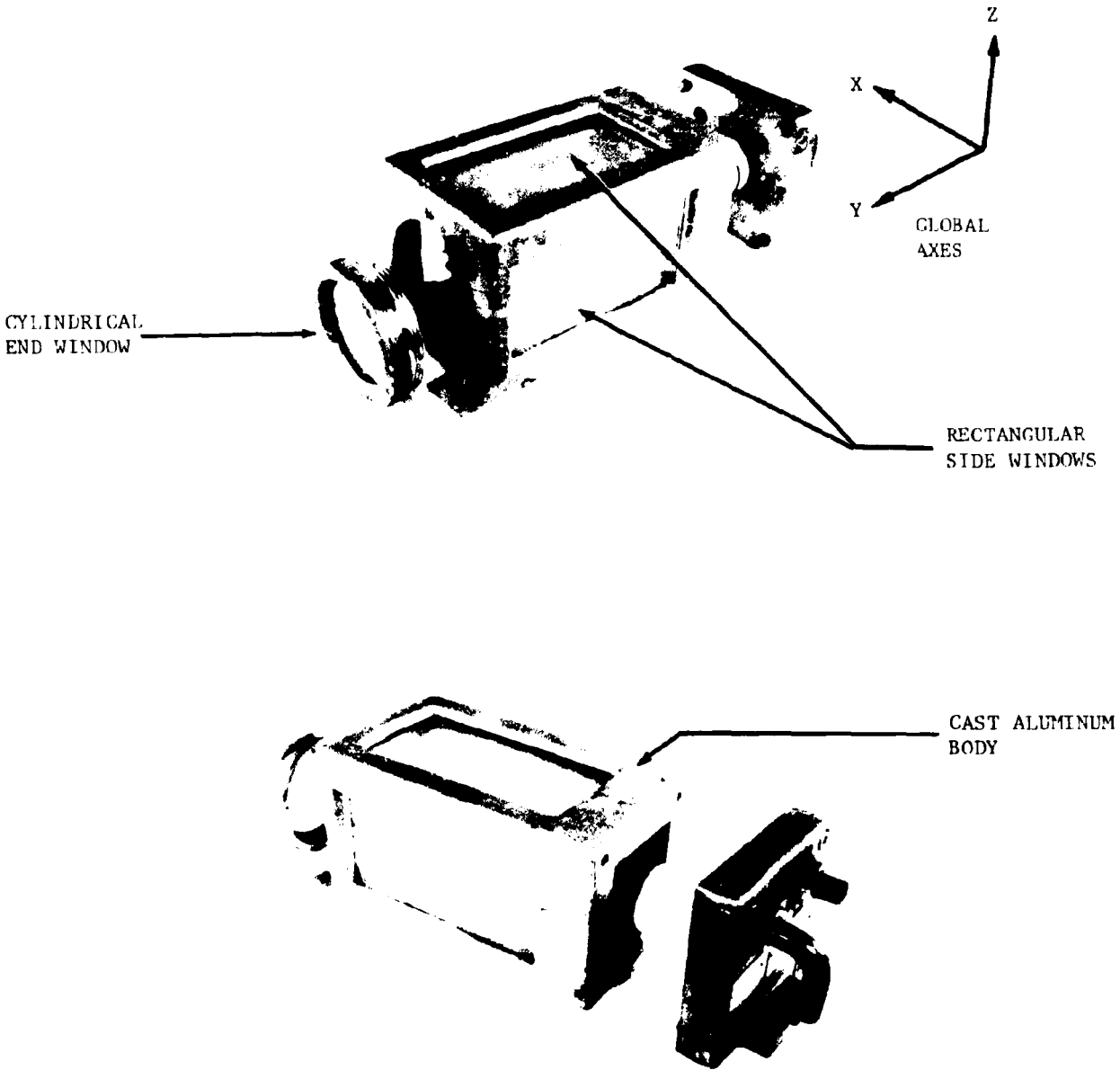

FIGURE 4.70. ENCLOSURE III -
LUMINAIRE WITH WINDOWS

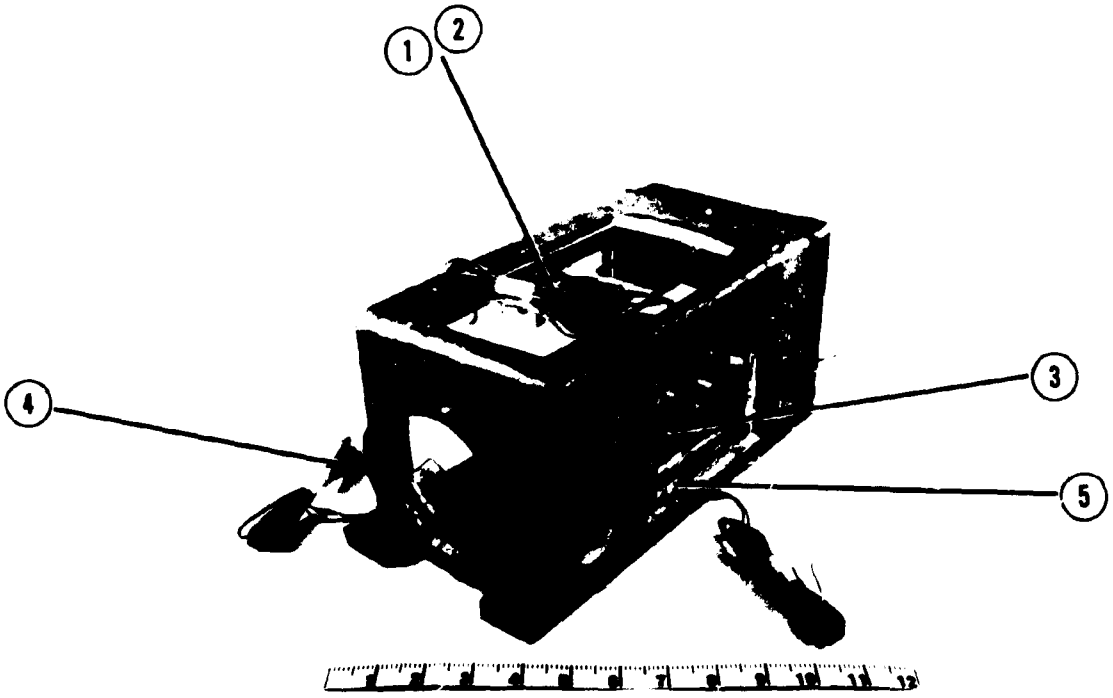

FIGURE 4.83. ENCLOSURE III WITH STRAIN GAGES INSTALLED

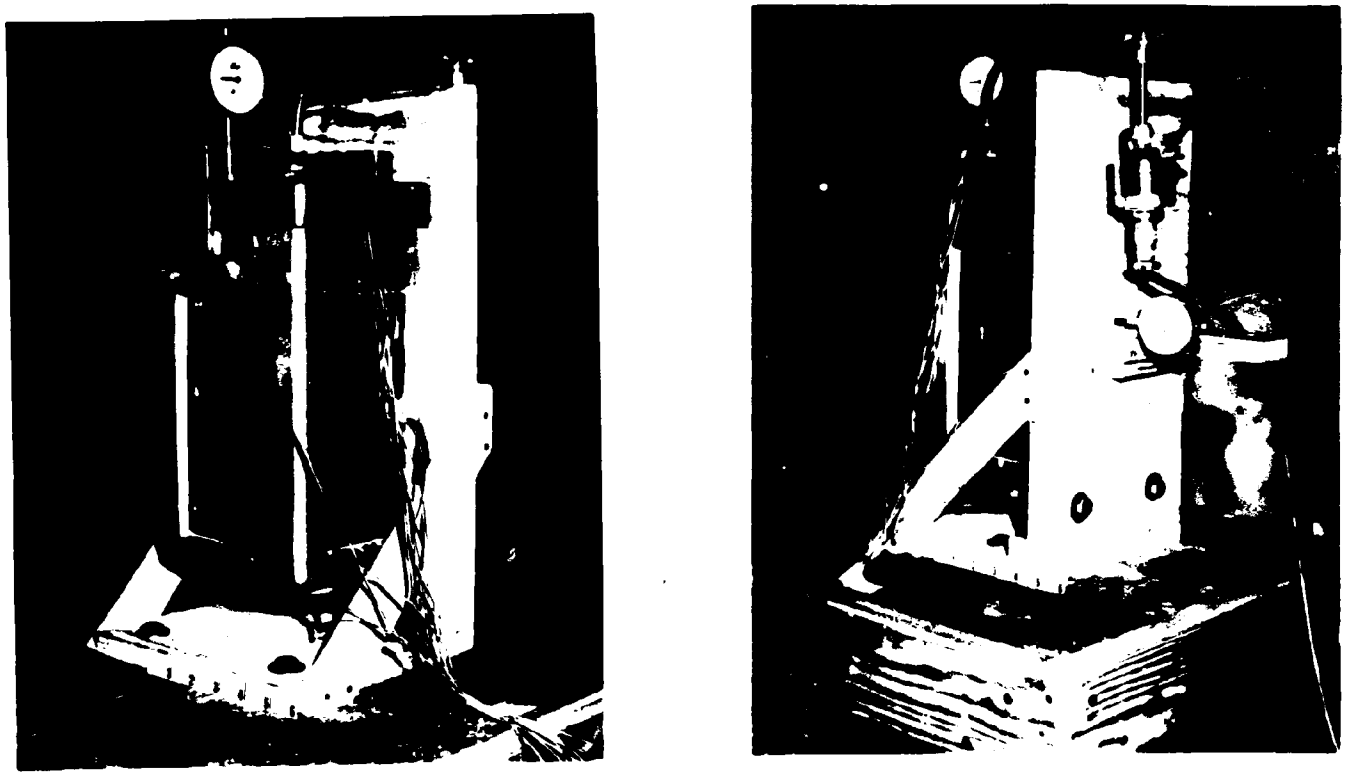

FIGURE 4.84. ENCLOSURE III READY FOR TESTING

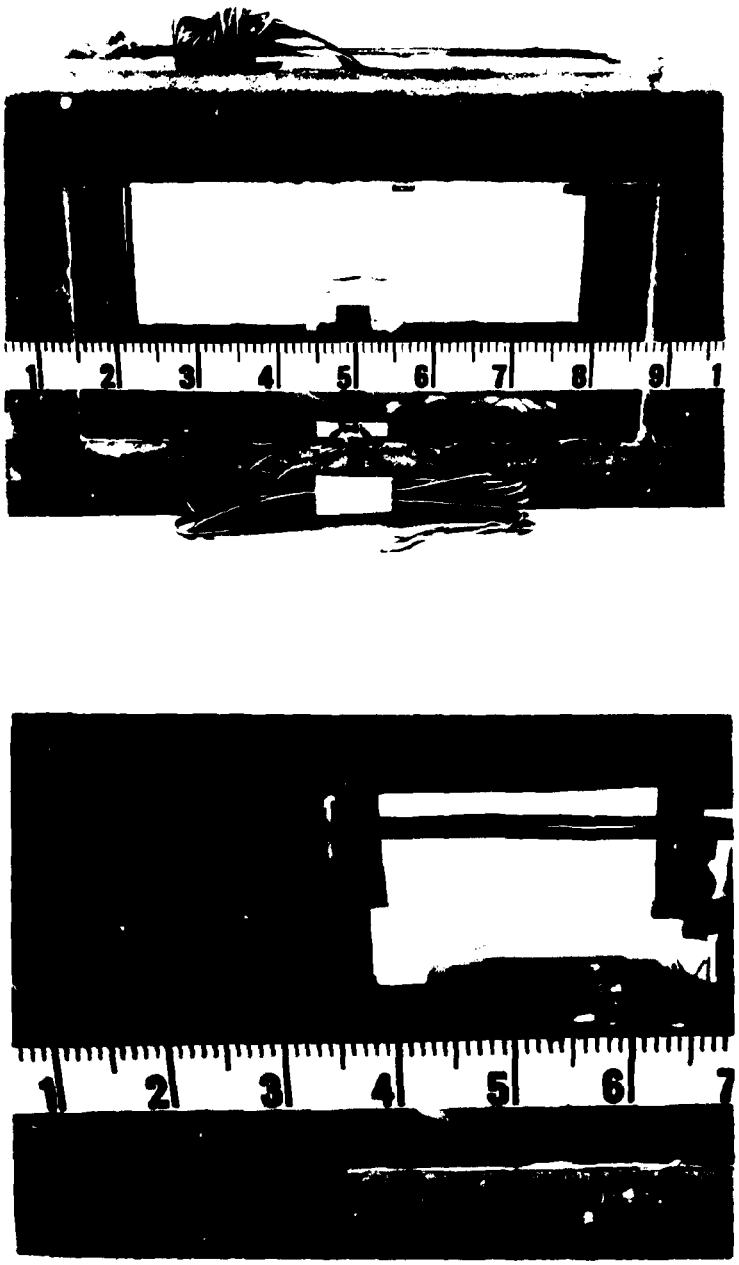

FIGURE 4.85. CRACKS IN THE ALUMINUM CASTING OF ENCLOSURE III WHICH OCCURRED DURING TESTING

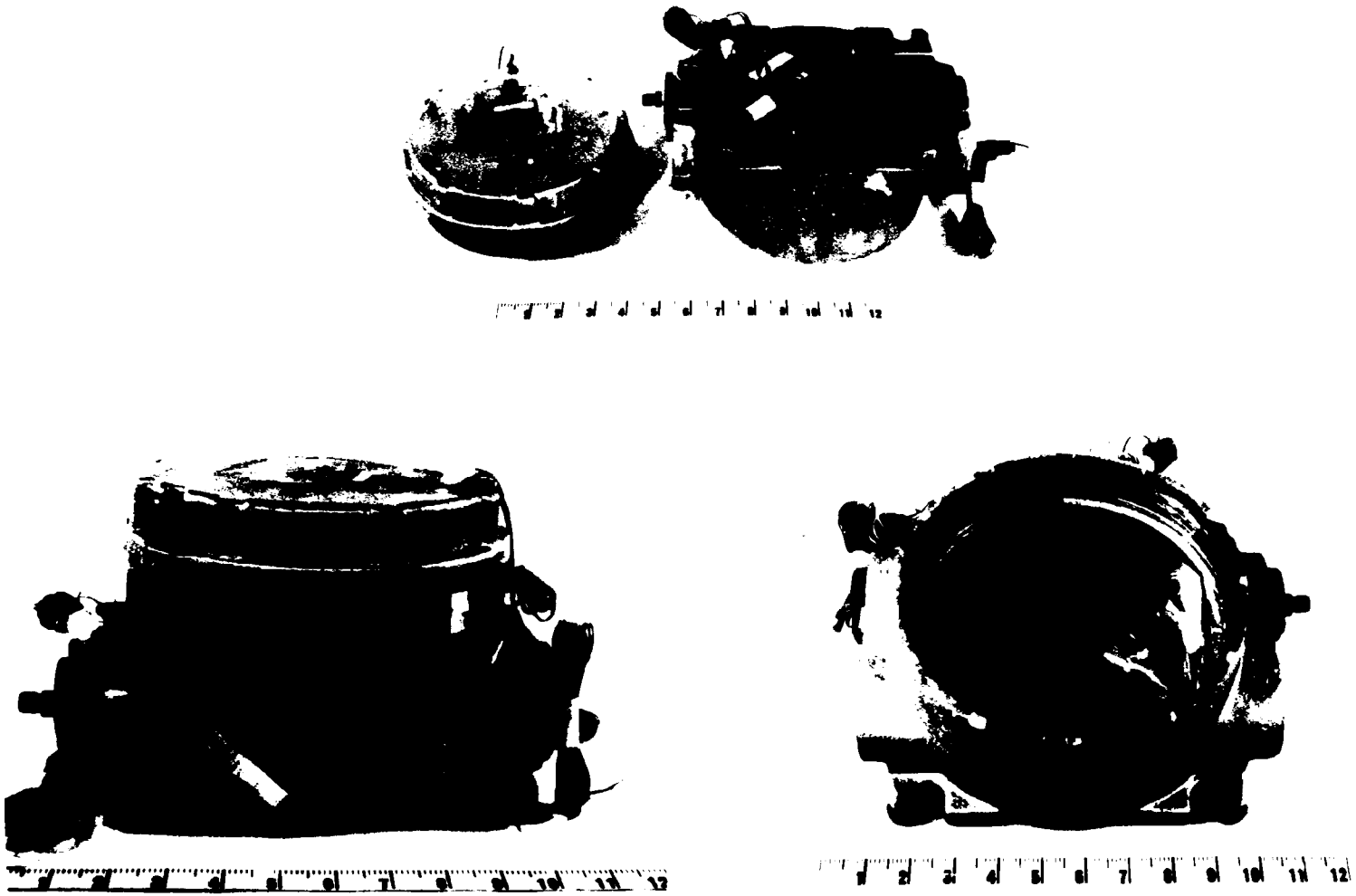

FIGURE 4.90. ENCLOSURE IV WITH STRAIN GAGES INSTALLED

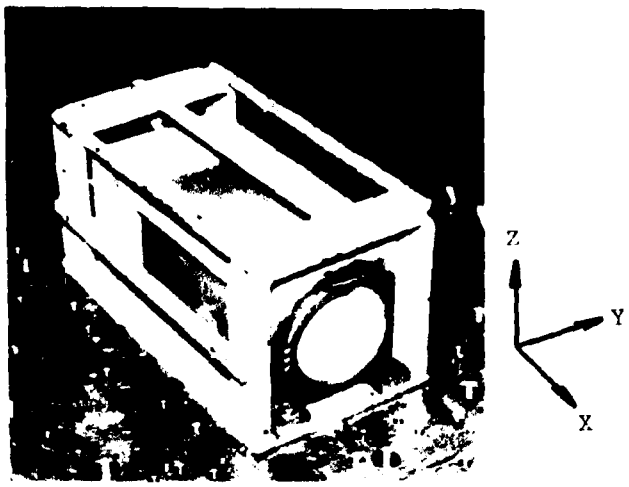

(a) Control Products, Inc., Luminaire

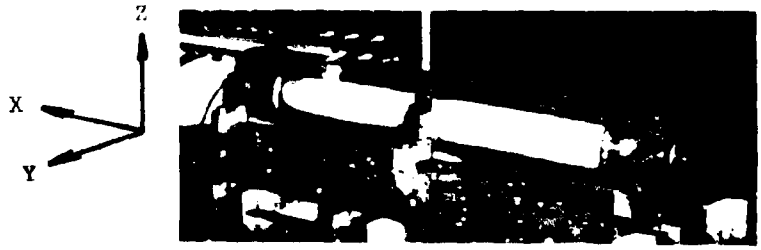

(b) Joy Manufacturing Co. Fluorescent Lamp

(c) Crouse-Hinds Co. MHL Headlight

FIGURE 7.1. REFERENCE AXES FOR VIBRATION TESTING

(a) Velocity = 72 ft/sec

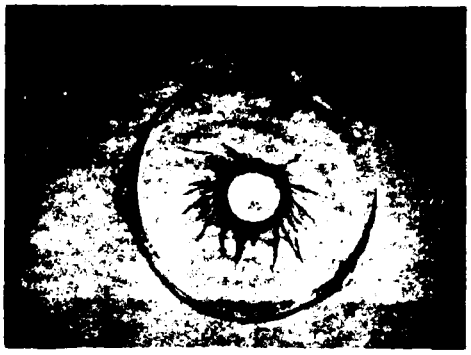

(b) Velocity = 187 ft/sec

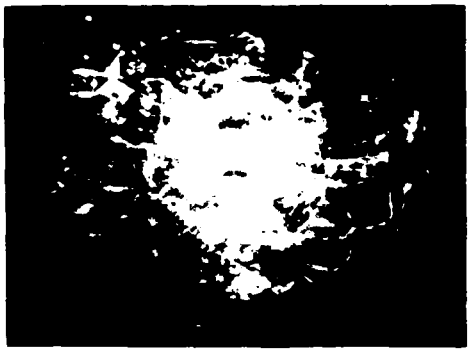

(c) V = 377 ft/sec

FIGURE 7.11. LOCALIZED IMPACT DAMAGE ON SODA-LIME GLASS BY GLASS SPHERES (1.5-mm RADIUS) AT VARIOUS SPEEDS

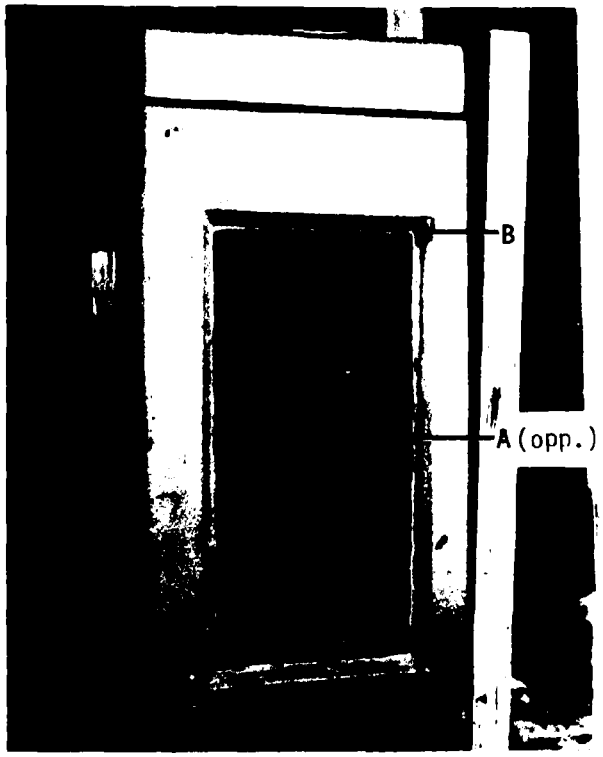

FIGURE 8.2. LUMINAIRE FROM CONTROL PRODUCTS

FIGURE 8.3. GLASS SLIVERS INSIDE
CONTROL PRODUCTS LUMINAIRE

FIGURE 8.4. EDGES OF THE LENS WHERE GLASS BREAKAGE OCCURRED

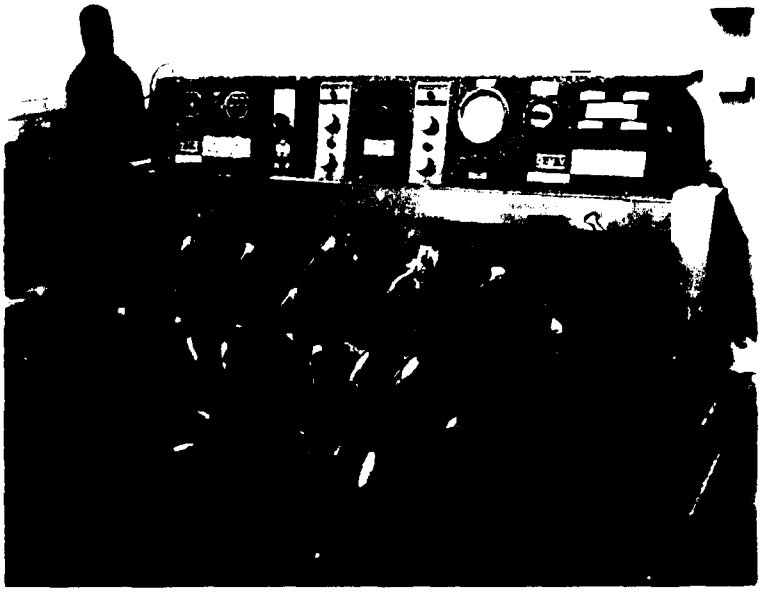

FIGURE K.3. PHOTOGRAPH OF ENVIRONMENTAL CHAMBER WITH FIXTURES INSTALLED